School of Molecular and Life Sciences

A Novel Radiofluorination Method for the Design of Rhenium(I) PET-Optical Hybrid Nuclear Medicines

Mitchell Ashley Klenner

This thesis is presented for the Degree of

Doctor of Philosophy

of

Curtin University

May 2019

Declaration

To the best of my knowledge and belief this thesis contains no material previously published by any other person except where due acknowledgement has been made.

This thesis contains no material which has been accepted for the award of any other degree or diploma in any university.

Signature: .....

Date: 12/05/2019

ACKNOWLEDGEMENTS

I would like to extend my gratitude first and foremost to my three excellent supervisors; Dr. Ben Fraser, Dr. Giancarlo Pascali and Prof. Max Massi for their guidance on matters of organic synthesis, radiochemistry and photophysics, respectively. The wealth of time you have each invested in me has been appreciated beyond measure and has truly helped me to realise my research potential.

I would also like to kindly recognise Dr. Helen Maynard-Casely and Prof. Jack Clegg for obtaining the crystal structures at the Australian Synchrotron, Dr. Gianluca Ciancaleoni for the computational modelling of the reaction mechanisms, as well as Dr. James Howard for being an excellent source of feedback and synthesis advice.

I would particularly like to thank my lab buddies Bo Zhang and Tiffany Mackay for providing support with the radiochemistry work and for the fun times we shared both within the lab and abroad. Not least I have so many friends at ANSTO, particularly within the Human Health group, who have provided me with so much advice, experience and opportunities throughout my studies. I cannot thank you all enough.

I would also like to thank the team at AINSE, especially Michelle Durant, for their overwhelming support and the number of opportunities they have provided me throughout my research.

I would also like to deeply thank my partner Calina Betlazar for her loving support, frequent lab visits and for helping me become a better person in life.

Finally, I owe immeasurable gratitude to my parents, Keith and Christine Klenner. For always encouraging me to pursue my passion, and for all the love and emotional support they have provided along the way.

This thesis work was funded by the Australian Institute for Nuclear Science and Engineering (AINSE) *via* provision of a Postgraduate Research Award (PGRA), Curtin University *via* provision of a Curtin University Postgraduate Scholarship (CUPS) and the Australian Government *via* provision of an Australian Postgraduate Award (APA). In-kind contributions were also made by the Australian Nuclear Science and Technology Organisation (ANSTO).

ABSTRACT

Novel fluorine-18 labelled luminescent rhenium tricarbonyl complexes were synthesised to test their utility as agents for positron emission tomography (PET) and optical hybrid imaging. The complexes were found to afford reasonable quantum yields and lifetimes for use as optical agents and were found to form in high radiochemical yield (RCY) in most cases for use as PET radiotracers. A novel rhenium-activated method was also serendipitously discovered in the process, which enabled the fluorine-18 labelling of 2,2'-bipyridine ligands in high RCYs which were not achievable hitherto. Such an approach was found to work for nucleophilic aromatic substitutions in the *ortho* and *para* positions of the pyridine moiety, though no radiolabelled ligand was observed from substitutions in the *meta* position. Notably, this method also enabled radiofluorination under non-azeotropically dried conditions, which is rarely reported in the literature. The method was also applied to the radiosynthesis of an Alzheimer's disease imaging agent, [^{18}F]CABS13. While the tracer was successfully labelled, the method did not improve upon the RCY reported in literature, though did allow for the radiofluorination of a previously unreported 8-hydroxyquinoline alternative.

ACRONYMS AND ABREVIATIONS

Aβ	Amyloid Beta
AINSE	Australian Institute for Nuclear Science and Engineering
ANSTO	Australian Nuclear Science and Technology Organisation
ATR	Attenuated Total Reflectance
AU	Absorbance Units
BODIPY	Boron-Dipyrromethane
BSA	Bovine Serum Albumin
FDG	Fluorodeoxyglucose
CCD	Charge Coupled Device
CD	Charge Displacement
CPD	Composite Pulse Decoupled
CT	Computed Tomography
CV	Column Volumes / Cone Voltage
CYP	Cytochromes P450
DCM	Dichloromethane
DFB	Difluorobenzene
DFT	Density Functional Theory
DIPEA	*N*,*N*-Diisopropylethylamine
DMF	Dimethylformamide
DMSO	Dimethyl Sulfoxide
DTPA	Diethylenetriaminepentaacetic Acid
EA	Elemental Analysis
EC	Electron Capture
EGFR	Epidermal Growth Factor Receptor
ELS	Evaporative Light Scattering
EpCAM	Epithelial Cell Adhesion Molecule
ER	Endoplasmic Reticulum
ESI	Electrospray Ionisation
ESF	Ethenesulfonyl Fluoride
FEDA	2- Fluoroethyl Iminodiacetic Acid
FET	2-Fluoroethyl-L-Tyrosine
FPyME	1-[3-(2-Fluoropyridin-3-yloxy)Propyl]Pyrrole-2,5-dione
FTIR	Fourier Transform Infrared
GMP	Good Manufacturing Practice
GRPR	Gastrin-Releasing Peptide Receptor
GS	Ground State
Hb	Haemoglobin
HPLC	High Performance Liquid Chromatography
HRMS	High Resolution Mass Spectrometry
IC	Internal Conversion
ICP	Inductively Coupled Plasma
ID	Internal Diameter
ILCT	Intraligand Charge Transfer
IR	Infrared
ISTD	Internal Standard
ISC	Intersystem Crossing
LED	Light Emitting Diode
LMCT	Ligand-Metal Charge Transfer
LRMS	Low Resolution Mass Spectrometry
MC	Metal Centred
MEMS	Microelectromechanical Systems
MMFF	Merck Molecular Force Field
MP	Melting Point
MS	Mass Spectrometry
MSURRF	Mass Spectrometry User Resource and Research Facility
MRI	Magnetic Resonance Imaging
NIR	Near Infrared
NMR	Nuclear Magnetic Resonance
NBO	Natural Bond Order
NOCV	Natural Orbital for Chemical Valance
LC	Ligand Centred
MLCT	Metal-Ligand Charge Transfer
MO	Molecular Orbital
NFT	Neurofibrillary Tangles
NHS	*N*-Hydroxysuccinimide
NP	Normal Phase
PBS	Phosphate Buffered Saline
PDA	Photodiode Array
PEG	Polyethyleneglycol
PET	Positron Emission Tomography
PTFE	Polytetrafluoroethylene
PYFLARE	Pyridine Fluorination Activated by Rhenium
QC	Quality Control
QD	Quantum Dot
RCY	Radiochemical Yield
RF	Radiofrequency
RGD	Arginylglycylaspartic Acid
RHF	Restricted Hartree-Fock
RI	Resolution of Identity
RNA	Ribonucleic Acid
ROS	Reactive Oxygen Species
RP	Reverse Phase
SCF	Self Consistent Field
SFB	*N*-Succinimidyl 4-Fluorobenzoate
SOC	Spin-Orbit Coupling
SRS	Society of Radiopharmaceutical Sciences
SUV	Standardised Uptake Values
SV	Solenoid Valve
SVP	Split Valence Polarisation
SPECT	Single Photon Emission Computed Tomography
TBAF	Tetrabutylammonium Fluoride
TCPE	Trichlorophenylethenesulfonate
TCSPC	Time-Correlated Single Photon Counting
TEA	Tetraethylammonium
TFA	Trifluoroacetic Acid
THF	Tetrahydrofuran
TLC	Thin Layer Chromatography
TMS	Tetramethylsilane
TZVP	Triple-Zeta Valence Polarisation
UV	Ultraviolet
VR	Vibrational Relaxation
WT	Wild Type
XRD	X-Ray Diffraction

TABLE OF CONTENTS

CHAPTER ONE
INTRODUCTION

1.1 Overview of Optical and Positron Emission Imaging Modalities

Discernment between healthy and diseased tissue is of paramount importance in order to excise a disease, such as cancer. Medical practitioners thus benefit from the wealth of data which can be accrued from multiple imaging modalities allowing for more informed decisions to be made. Positron emission tomography (PET) imaging is one such beneficial imaging technique which provides data on the biodistribution of a radioactive tracer administered to a patient. Typically, the radioactive molecule is designed to mimic or interact with known biochemical pathways. Thus, discrepancies concerning the uptake of an administered radiotracer by organs in the patient body often aid in distinguishing a healthy patient from one diagnosed, for instance, with cancer. As with all imaging modalities, however, PET imaging has its own strengths and limitations. While it provides excellent external imaging of a patient *via* detection of deep tissue penetrating gamma radiation photons, the technique is disadvantaged by comparatively low spatial resolution (on the order of millimetres).[1] Thus, efforts have been made to couple PET imaging with other imaging modalities to improve upon the spatial resolution. Both computed tomography (CT), which processes X-ray photons detected from various angles to reconstruct anatomical images of comparative radiodensities, and magnetic resonance imaging (MRI) which maps the distribution of water and lipids in an external magnetic field *via* nuclear magnetic resonance (NMR) of hydrogen nuclei, provide an approximate five-fold improvement in spatial resolution when coupled with PET while still relying on external imaging of the patient.[2] These spatial resolutions are still far from the order of magnitude required to discriminate variations at the cellular level, thus recent efforts have sought to couple the radiotracers used in PET with luminescent molecules which allow for optical imaging of the tracer. Unlike PET imaging, optical imaging provides significantly greater spatial resolution (on the order of nanometres), and while optical imaging does suffer from shallow

tissue penetration, this limitation can likewise be leveraged with the deep tissue penetration afforded by PET imaging.[3] In practice, a PET-optical radiotracer, which provides both the positron emission required for PET imaging and the luminescence required for optical imaging, could enable low resolution external identification of a tumour followed by high resolution internal identification of the same tumour during surgical excision. In pursuit of this goal, this work sought to expand upon a common class of luminescent agents characterised by a rhenium metal centre by chemically bonding them with the most common radioactive isotope used in PET radiotracers, fluorine-18.[4] This laid the framework for the underlying hypothesis, *that a luminescent rhenium complex could be radiolabelled with the fluorine-18 radioisotope and would have desirable properties for use as a PET-optical agent.*

1.2 Fluorine-18 in Positron Emission Tomography

The clinical and research practices of PET imaging rely on the availability of molecular structures labelled with a positron emitting radioisotope. Design of such radiotracers involves chemically bonding the desired radioisotope to a drug or biomolecule, therefore creating a radioactive marker with specific features of interaction with the biological target of interest. Diagnostic PET imaging conventionally necessitates the administration of such radiotracers to monitor the distribution of the associated radioactivity in the patient. The radiotracer consequently accumulates in diseased tissue and radiation emitted from the radioactive decay of the conjugated radioisotope enables imaging by a ring of detectors to locate the site of disease within the patient. The process of PET imaging is summarised in Figure 1, following the administration of the radiotracer to the patient. The radioisotope conjugated to the administered tracer, having a proton rich nucleus, undergoes positron emission decay (β^+ decay) following the spontaneous internal conversion of a proton to a neutron (*via* internal conversion of an up quark to a down quark), as exemplified in Figure 2. This positron emission process can be universally represented by the nuclear decay equation (1), wherein ${}^{A}_{Z}X$ refers to the original radioisotope, ${}_{Z-1}{}^{A}X$ refers to the transmutation product with one lesser proton and v_e refers to an emitted electron neutrino accompanying the positron (β^+).

$$ {}^{A}_{Z}X \rightarrow {}_{Z-1}{}^{A}X' + {}^{0}_{1}\beta^{+} + v_e \qquad (1) $$

The emitted positron, being the antimatter equivalent of an electron, then travels some short distance governed by its excess energy, before complementing the 511 KeV rest mass energy of a nearby electron and ultimately annihilating with it.[5] The annihilation of both particles results in the formation of two 511 KeV gamma radiation photons emitted approximately 180° apart from the annihilation event. The two gamma radiation photons are then detected by two

diametrically opposed scintillator crystals within the PET detector ring. The scintillators each exhibit luminescence upon excitation by the ionising radiation and the emitted photons are absorbed by a photoelectron multiplier tube within the detector block which amplifies the current, such that the signals can be processed for coincidence (*i.e.* that the two gamma radiation photons from the annihilation event indeed interfered with the scintillators within the resolving time of the detectors across an assumed linear line of response). Confirmed coincidence events are then processed by imaging reconstruction software to produce a PET image, which ultimately depicts where in the body (*e.g.* which organs) the radiotracer has accumulated for diagnostic purposes. Figure 3 shows an exemplar diagnostic PET scan of a patient following intravenous administration of the fluorine-18 labelled radiotracer [^{18}F]fluorodeoxyglucose ([^{18}F]FDG). [^{18}F]FDG is commonly used in PET diagnostic scans to map glucose uptake of the organs and consequently to discern diseased tissue as a function of upregulated glucose transporters. Despite the background accumulation of [^{18}F]FDG by the brain, kidneys and heart, as well as radioactive urinary accumulation within the bladder, a significant metastatic tumorous mass can be noticed within the liver, having migrated from a primary colorectal tumour (depicted in dark red from the maximum intensity projection). It is worth noting that PET imaging reconstruction provides only a three-dimensional distribution of the radiotracer within the field of view of the PET camera and imparts no further information regarding the anatomy of the subject. Thus, complementary techniques such as CT or MRI are commonly also applied and fused to the resulting PET image in order to provide correlative anatomical information about radiotracer accumulation within the body.

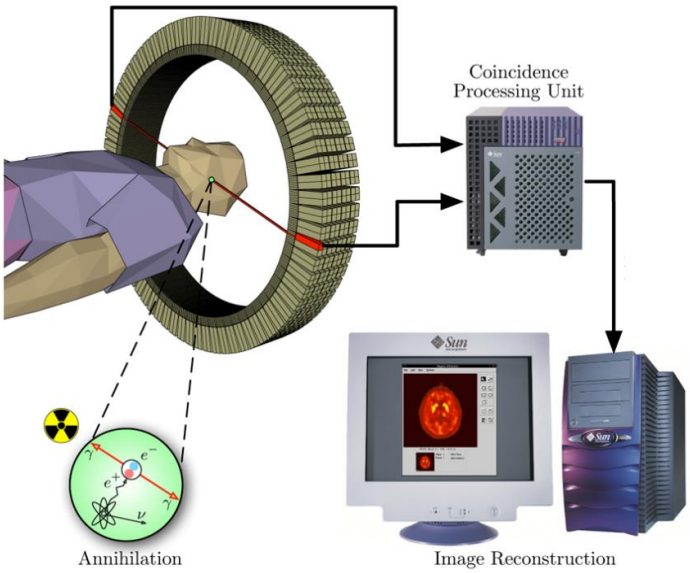

Figure 1. Following administration of a PET radiotracer to a potentially diseased patient, the patient then lies horizontally inside a PET scanner. The radiotracer circulates the blood stream and eventually accumulates at the site of the diseased tissue it was designed to target. Pairs of gamma photons originating from the antimatter annihilation of the emitted positrons from the radiotracer are detected via the detector rings of the PET scanner. Through subsequent coincidence processing and the use of image reconstruction software, a PET image is attained to visually confirm where the radiotracer has accumulated, thus indicating the site of the diseased tissue. Image released into the public domain under the Wikimedia Commons license agreement.

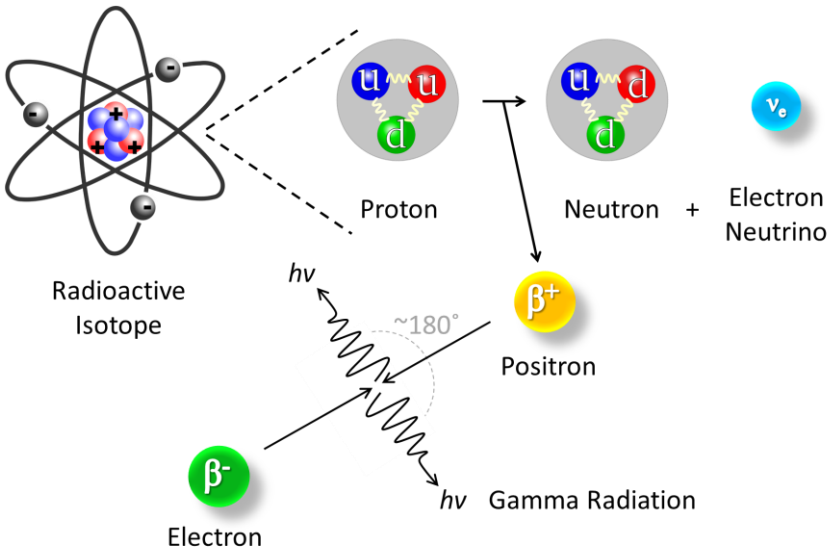

Figure 2. Positron emission from a proton rich nucleus, which occurs following the spontaneous interconversion of an up quark to a down quark within the proton which results in the conversion of a proton to a neutron within the nucleus and the subsequent release of a position (β^+) particle to conserve the charge (alongside an electron neutrino to conserve the energy). The released positron then annihilates with its matter component electron resulting in the formation of two gamma radiation photons (*hν*) spaced approximately 180° apart.

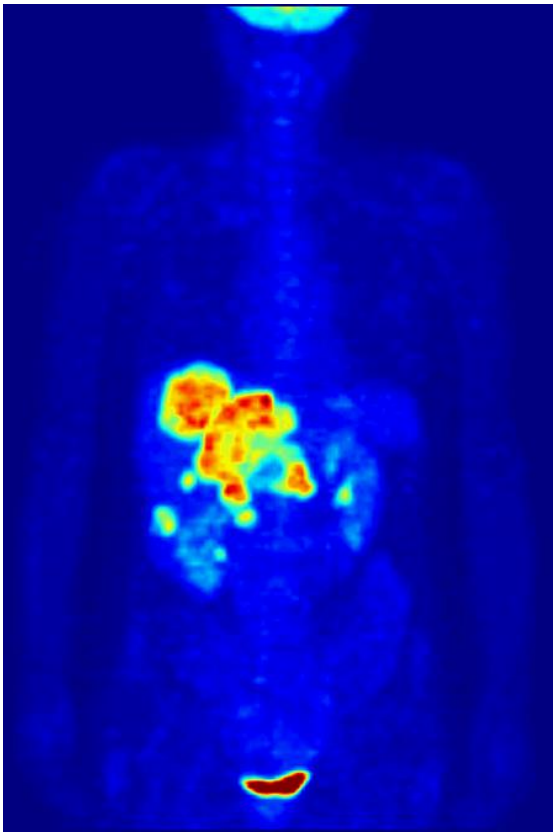

Figure 3. [^{18}F]FDG PET diagnostic scan revealing the metastasis of a primary colorectal tumour (dark red maximum intensity projection) to the site of the liver against the background accumulation of [^{18}F]FDG by the brain, kidneys and heart, as well as radioactive urinary accumulation within the bladder of a 79 kg female patient. Image released into the public domain under the Wikimedia Commons license agreement.

There exist several proton-rich radioisotopes exhibiting β^+ decay which can be implemented within the molecular design of a drug or bioconjugate to serve as a PET radiotracer. Table 1. provides a selective list of the commonly utilised PET radioisotopes, alongside their comparative half-lives, probability of β^+ decay per disintegration (among other decay events such as electron capture (EC)) and the nuclear reactions used to produce the radioisotopes (whereby the absorption and subsequent emission of a deuterium (d), neutron (n), proton (p), helium nucleus (α) or gamma photon (γ) results in the transmutation product).[5,6] Of these radioisotopes fluorine-18, as generated by the ^{18}O(p,n)^{18}F nuclear reaction, is most commonly used in PET imaging due to its ideal half-life of 109.8 mins, which provides sufficient time for synthesis and imaging while reducing the radiation dose to the patient in comparison to longer

lived radioisotopes, and because the majority of its nuclear decay occurs *via* positron emission (97%).[4] Applying the spontaneous conversion of a proton to a neutron within a proton-rich positron emitting nucleus, exemplified in equation (1), to fluorine-18 renders equation (2) which affords the stable oxygen-18 decay product alongside the emission of both a positron and an electron neutrino.

$$^{19}_{9}F \rightarrow \ ^{18}_{8}O + \ ^{0}_{+1}\beta^{+} + \nu_e \qquad (2)$$

Table 1. List of PET radioisotopes in order of atomic number alongside their accompanying physical half-lives, probability of β^+ decay and method of production.[5, 6]

PET radioisotope	**Half-life ($t_{1/2}$)**	**Mode of Decay (%)**	**Methods of Production**
Carbon-11 (^{11}C)	20.4 min	β^+ (100)	^{10}B(d,n)^{11}C ^{14}N(p,α)^{11}C
Nitrogen-13 (^{13}N)	10.0 min	β^+ (100)	^{12}C(d,n)^{13}N ^{16}O(p, α)^{13}N ^{13}C(p,n)^{13}N
Oxygen-15 (^{15}O)	2.0 min	β^+ (100)	^{14}N(d,n)^{15}O
Fluorine-18 (^{18}F)	109.8 min	β^+ (97), EC (3)	^{18}O(p,n)^{18}F ^{20}Ne(d,α)^{18}F
Copper-64 (^{64}Cu)	12.7 hrs	β^+ (18), EC (43), β^- (39)	^{63}Cu(n,γ)^{64}Cu ^{64}Zn(n,p)^{64}Cu ^{64}Ni(p,n)^{64}Cu
Gallium-68 (^{68}Ga)	1.1 hrs	β^+ (89), EC (11)	^{68}Ge–^{68}Ga generator
Iodine-124 (^{124}I)	4.2 days	β^+ (23), EC (77)	^{124}Te(p,n)^{124}I

The most common means of introducing fluorine-18 into a molecule is *via* nucleophilic substitution. However, while [^{18}F]fluoride is prepared from oxygen-18 enriched water *via* cyclotron irradiation, aqueous solutions have typically been found to supress the nucleophilicity of the fluoride rendering most nucleophilic substitutions unreactive.[7] Thus, for most applications the [^{18}F]fluoride requires drying which is most often achieved through the repeated azeotropic distillation of a water-acetonitrile mixture. To enable the solubility of the [^{18}F]fluoride, phase transfer catalysts are typically used to dissolve the [^{18}F]fluoride in

anhydrous organic solvents during radiofluorinations. One such example is Krypotofix 222 (K_{222}), used in the synthesis of [^{18}F]FDG, which complexes the potassium cation thus liberating [^{18}F]fluoride *via* dissolution of the salt as shown in Figure 4. Another commonly employed phase transfer catalyst is 18-crown-6 ether, as a cheaper alternative for complexing the potassium cation. Bulky cationic quaternary ammonium salts such as tetraethylammonium (TEA) bicarbonate are also often used to improve the reactivity of [^{18}F]fluoride in organic solvents.

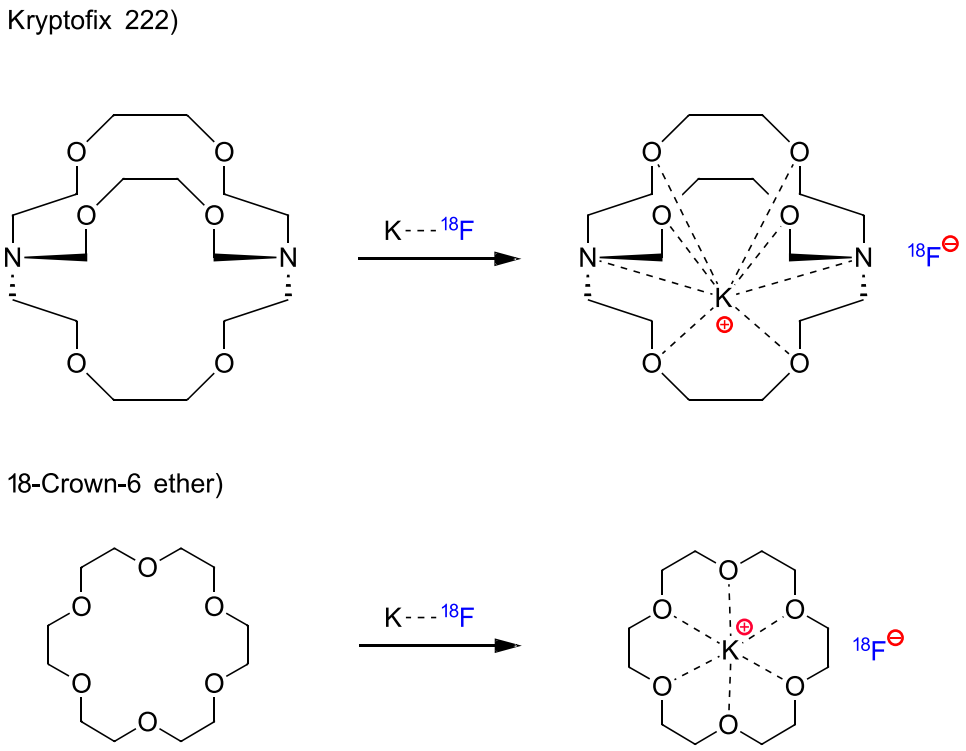

Figure 4. Two common examples of phase transfer catalysts used to dissolve potassium [^{18}F]fluoride into organic media. Kryptofix 222 (top) and 18-crown-6 ether (bottom).[7]

One such example of a nucleophilic substitution used in radiofluorination reactions is the synthesis of [^{18}F]FDG whereby a tetraacetyl mannosyl-2-triflate precursor is reacted with [^{18}F]fluoride dissolved in anhydrous acetonitrile in the presence of Kryptofix 222 and potassium carbonate.[7] The [^{18}F]fluoride substitutes for a triflate leaving group and the acetate

protecting groups are removed *via* acid or base hydrolysis to afford the [^{18}F]FDG product as shown in Figure 5. Electrophilic radiofluorinations can also be achieved, usually *via* labelled fluorine gas ([^{18}F]F_2) or other specialised reagents. The use of [^{18}F]F_2 in radiosyntheses is less common, however, due to the high reactivity which can lead to the formation of side products from unselective reactions, the common use of F_2 gas as a carrier for [^{18}F]F_2 produced from gas or liquid phases which results in lower specific activity of the resulting fluorine-18 labelled tracers, and the 50% probability of incorporating fluorine-19 instead of fluorine-18 isotopes.[8-10] For these reasons and the heightened safety risk involved, neither [^{18}F]F_2 nor any alternative electrophilic radiofluorination reagents were implemented in this study.[5]

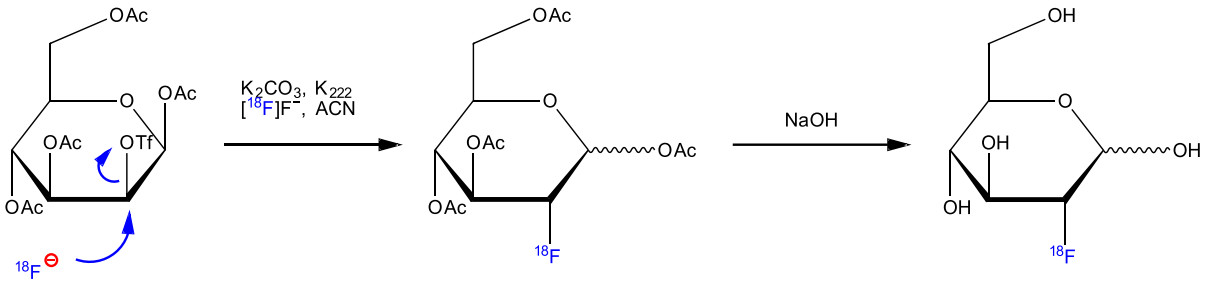

Figure 5. Synthesis of [^{18}F]FDG *via* nucleophilic substitution of [^{18}F]fluoride for a triflate group of [mannosyl etc] aided by a Krypotofix 222 phase transfer catalyst in acetonitrile solution. Subsequent deprotection of acetyl groups by base hydrolysis affords the desired product.

In the synthesis of more complex radiopharmaceuticals, a prosthetic group labelled with a fluorine-18 radioisotope may first be prepared, followed by mild and selective conjugation of the prosthetic group with the biomolecule or drug of interest. A disadvantage of using prosthetic groups is that they require multiple-step radiosyntheses to achieve the final PET tracer (i.e. the fluorine-18 radioisotope is not added in the final step of the synthesis) which can result in a greater loss of radioactivity due to the longer time of synthesis. One advantage, however, is that prosthetic groups can selectively add to positions which may inherently be non-selective for [^{18}F]fluoride. Additionally, while reactions using [^{18}F]fluoride in aqueous

media generally provide no yield, water soluble precursors can alternatively conjugate to a similarly soluble fluorine-18 labelled polar prosthetic group under aqueous conditions, thus widening the scope of radiotracer development. One such example of radiofluorinating *via* the use of a radiolabelled prosthetic group is provided in Figure 6a, whereupon 2-[^{18}F]fluoroethyl tosylate is first prepared through nucleophilic substitution of [^{18}F]fluoride for a tosyl group.[11] Conjugation of the 2-[^{18}F]fluoroethane tosylate prosthetic group with a tyrosine precursor is then used to yield the neurooncological PET tracer [^{18}F]fluoroethyl-L-tyrosine ([^{18}F]FET). Another common example of a fluorine-18 labelled prosthetic group is *N*-succinimidyl 4-[^{18}F]fluorobenzoate ([^{18}F]SFB), which is employed in the labelling of proteins and peptides, such as endothelin-1, neurotensin and human C-peptide.[12-16] The fluorine-18 radiolabelling of a model dipeptide using the [^{18}F]SFB prosthetic group is provided in Figure 6b.

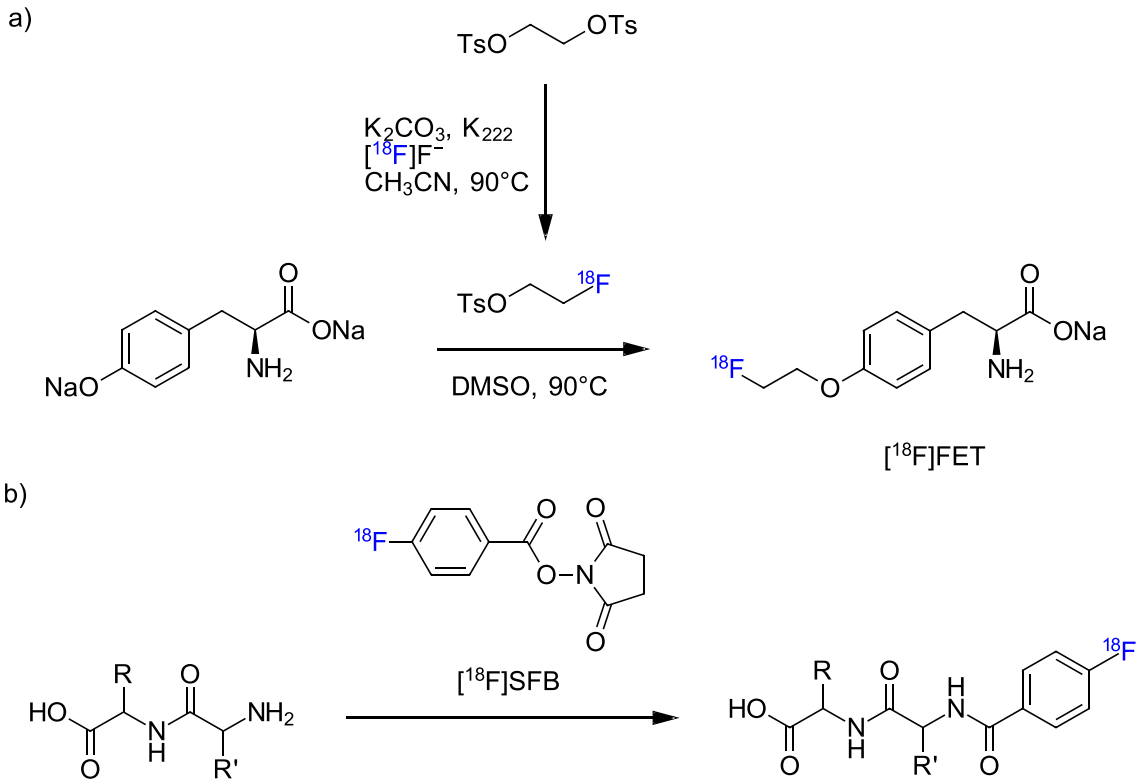

Figure 6. a) Synthesis of [^{18}F]FET *via* a 2-[^{18}F]fluoroethane tosylate prosthetic group.[11] b) Radiolabelling of a model dipeptide using the [^{18}F]SFB prosthetic group.[13]

To measure the incorporation of the fluorine-18 radioisotope into the final tracer product, a few terms need to first be defined. Radioactivity (A) itself is a measure of the decay rate, being the loss of radioisotopes (N) as a function of time (t), which obeys first-order kinetics thus yielding the decay rate constant (λ) as provided in equation (3).[6]

$$A = \frac{-dN}{dt} = \lambda N \tag{3}$$

The half-life ($t_{1/2}$) of a radioisotope, being the time required for an initial quantity of radioactivity to decay to half the amount, is related to the decay rate constant through equation (4). Substituting the 109.8 min half-life of the fluorine-18 radioisotope into this equation, for instance, affords a decay rate constant of approximately 6.3×10^{-3} min^{-1}.

$$\lambda = \ln(2)\left(t_{\frac{1}{2}}\right)^{-1} \tag{4}$$

The calculated decay rate can then be used to decay correct starting amounts of radioactivity back to a single standardised point in time, as per the exponential equation (5), thus allowing for the calculation of the radiochemical yield (RCY).

$$\mathrm{A_t} = \mathrm{A_0} e^{\lambda t} \tag{5}$$

The RCY of a reaction refers to the radioactivity of the product expressed as a percentage of the starting radioactivity. Given the relatively few methods available for selective carbon-fluorine bond formation compared to other halogenation reactions,[17] the limiting time constraints in which such reactions need to be performed given the half-life of the fluorine-18 radioisotope,[18] the general requirement for anhydrous conditions,[19] and that minute amounts of radioactivity can cause otherwise small concentrations of impurities to considerably impact reaction efficiencies,[20] RCYs as low as 2-3% RCY are not uncommon for fluorine-18 labelled tracers (particularly for pyridines) and can still prove sufficient for PET imaging

applications.[21-25] Unless the radioactivity of both the product and starting material are measured at the same time, for example *via* non-isolated radiochromatogram integrated peak ratios, the radioactivity of both chemicals requires decay correction before determining the overall RCY of the reaction. Of considerable importance also in the production of radiotracers is the molar activity (A_m), a measure of the radioactivity per number of moles (n) as described by equation (6).

$$A_m = \left(\frac{-dN}{dt}\right) n^{-1} \quad (6)$$

A greater molar activity is indicative of an efficient radiosynthetic and purification process which encapsulates a greater amount of the radioactivity within a given amount of product and is particularly important for assessing dose administration of a nuclear medicine to a patient. To achieve greater molar activities *no-carrier-added* approaches, whereby the radioisotope is prepared without adding stable carrier isotopes of the same element (e.g. [^{18}F]fluoride formed from oxygen-18 enriched water) are generally used over *carrier-added* approaches where the carrier element has been purposely added, thus diluting the radioactivity per unit mass (e.g. production of electrophilic [^{18}F]F_2 where [^{19}F]F_2 is added to extract the radiofluoride source from the cyclotron target).[7]

In summary, fluorine-18 is the most widely used radioisotope in PET tracers owing to its ideal half-life and positron emission decay profile. The radioisotope is typically produced as *no-carrier-added* [^{18}F]fluoride *via* the ^{18}O(p,n)^{18}F nuclear reaction and azeotropically dried in the presence of a phase transfer catalyst to ensure greater RCYs and molar activities.

1.3 Optical Imaging and Rhenium Photophysics

Optical imaging is a non-invasive medical technique which employs luminescent pharmaceuticals to identify diseased cells. Following administration to a patient, excitation of the tracer is achieved by exposing the tissue to electromagnetic radiation within the visible to near-infrared (NIR) range, which results in the intense emission of red-shifted light from the tracer used to identify where it has accumulated in the tissue. Figure 7 shows an example of optical imaging used to identify metastatic tumour nodules within the liver of a mouse model, performed by Kennedy, *et al.*, following injection of a fluorescein-folate conjugate targeting folate receptors which are over expressed by several cancers (e.g. ovary, breast, kidney, brain and lung cancers).[26] The molecular structure of this fluorescein-folate tracer is shown in Figure 8, whereby the luminescent fluorescein is depicted in red and the folate, bioconjugated *via* an ethylene diamine linker, is depicted in green.

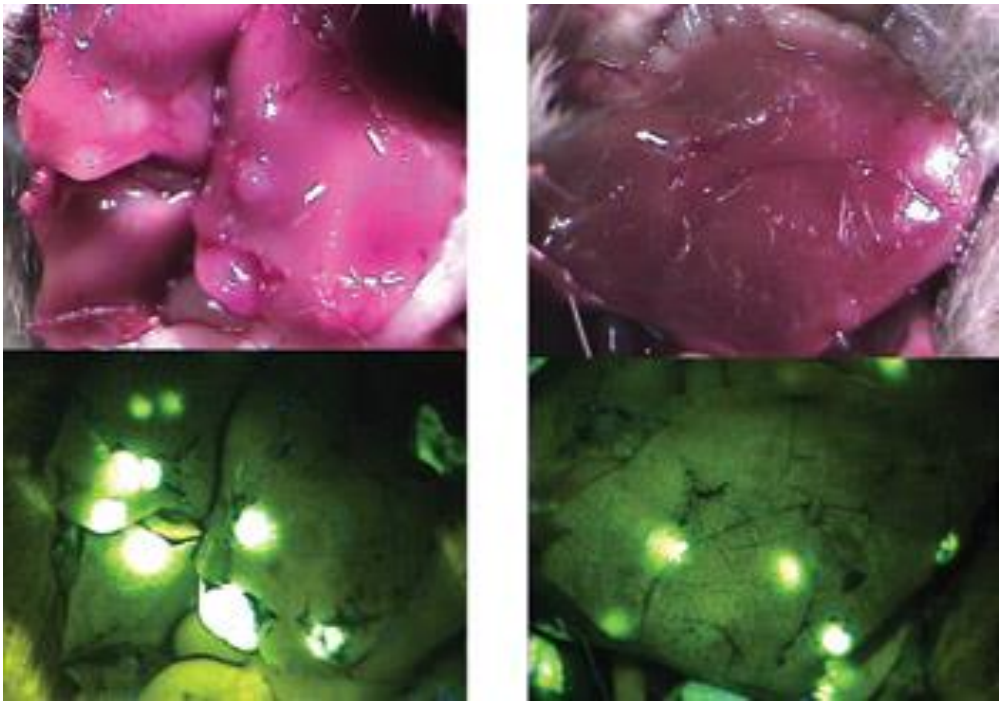

Figure 7. Optical imaging of metastatic tumour nodules (bottom) in the liver of a mouse model (top) following intravenous injection of a folate-fluorescein conjugate by Kennedy, *et al.*[26]

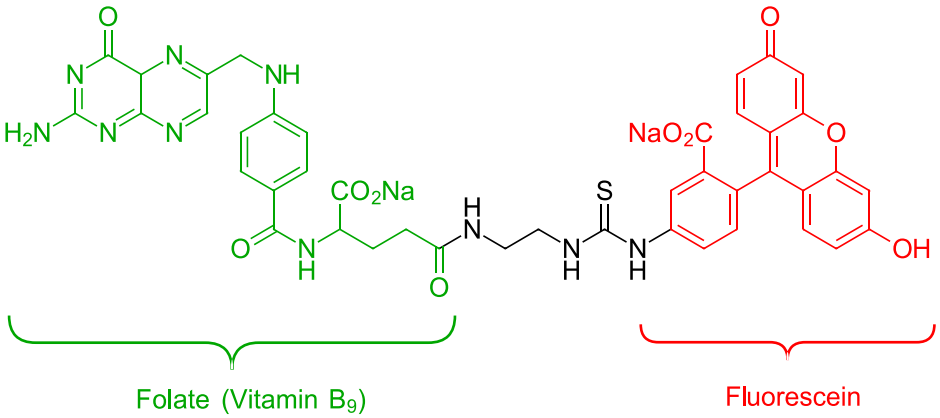

Figure 8. Folate (green) conjugated to Fluorescein (red) thiocyanate linked *via* an ethylene diamine linker, used for the optical imaging of cancers overexpressing folate receptors.

As an entire human patient cannot practically be exposed to a field of the excitation light, recent efforts have endeavoured to create handheld fluorescence scanners for applications in optical imaging during intraoperative surgeries.[27-29] In these devices a continuous-wave laser diode provided the excitation light beam which was converged through a convex lens and delivered to each individual fibre within a fibre optic array. The fibre optics provided the excitation light source through the handheld unit, and the emission light from detection fibre arrays was collected by a charge-coupled device (CCD) camera coupled with a band-pass filter. Imaging within smaller animal subjects can ordinarily be achieved through more simplified set-ups which need not rely on moving the excitation apparatus. An example of an experimental set-up used for the optical imaging of antitumour treatments in a mouse model as implemented by Ntziachritsos, *et al.* is shown in Figure 9.[30] Here the excitation beam was both broadened through a beam expander and passed through an optical filter to illuminate the front of the animal model and concurrently passed through an optical switch, feeding the light through to a fibre optic array, which provided transillumination from the back of the animal imaging chamber. An optical filter was likewise placed in front of the CCD imaging camera to filter the emission wavelength, with the images digitally reconstructed thereafter. Variations of this set-up are commonly applied for *in-vivo* optical imaging experiments within preclinical studies.

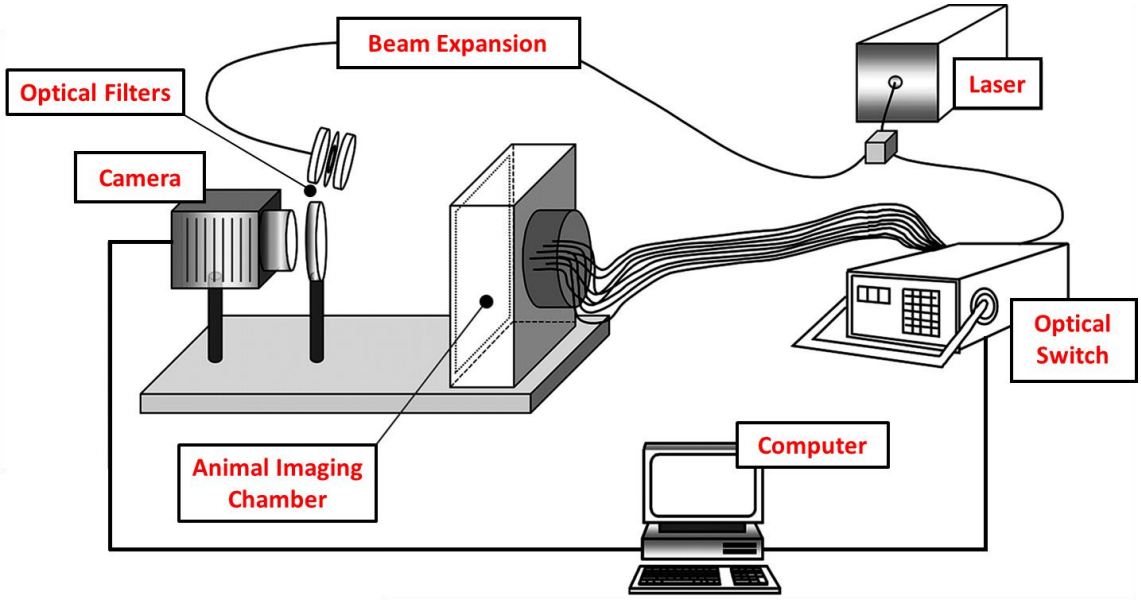

Figure 9. Example of an *in vivo* optical imaging experimental set-up used by Ntziachristos, *et al.*[30] An animal imaging chamber was exposed to a laser, with the beam either expanded for excitation at the front of the chamber or an optical switch enabling excitation from the back. An optical filter was placed in front of the CCD camera to ensure only the emission wavelength was detected.

While excitation and emission within the visible region of the electromagnetic spectrum allows for the optical imaging of exposed surface tissue, the imaging of non-exposed deep tissue typically requires excitation and emission within the NIR region. This is because wavelengths of light within the NIR region are absorbed less by chromophores present within the tissue, thus allowing greater tissue penetration compared to visible light of similar flux.[31] This phenomenon is evident in Figure 10, plotting the molar extinction coefficients of oxyhaemoglobin and deoxyhaemoglobin per wavelength of light, whereupon lesser absorptivity is observed by both chromophores from approximately 600 nm onwards. In many cases excitation within the NIR region can be achieved *via* two photon absorption techniques, which concentrates the flux of NIR photons approximating half the energy of the required excitation frequency, such that the optical tracer can absorb two photons in a given instance of time to transition to an excited electronic state with minimal interference from the biological chromophores present within the tissue.[32]

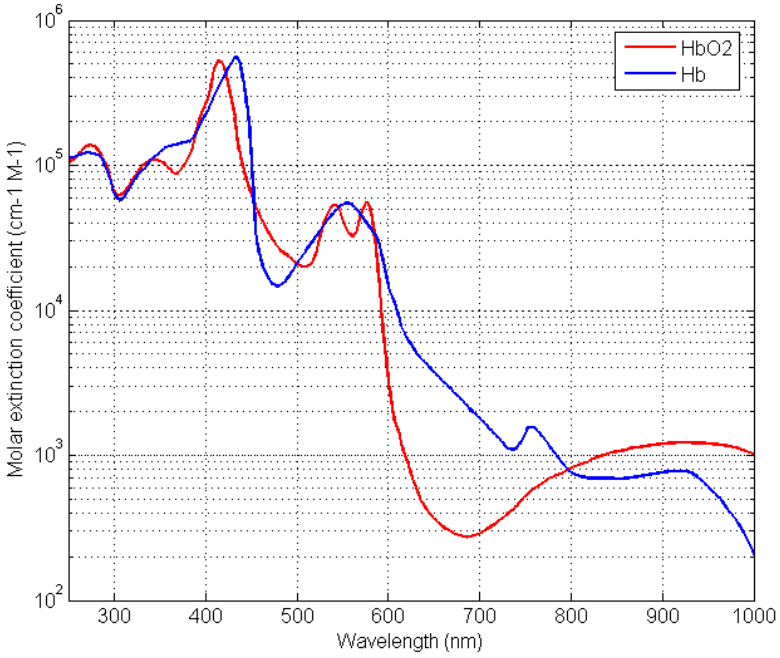

Figure 10. Molar extinction coefficients of oxyhaemoglobin (HbO_2) and deoxyhaemoglobin (Hb) as a function of increasing wavelength. The notable decrease in light absorption by both chromophores at wavelengths longer than 600 nm demonstrations the transparency of biological tissue within the NIR region. Image released into the public domain under the Wikimedia Commons license agreement.

Fortunately, the emission of optical agents is typically red shifted towards more biologically transparent shorter wavelengths compared to the excitation wavelength. This phenomenon can be described by a Jablonski diagram, which vertically plots the quantum states of a molecule as a function of energy and arranges them horizontally as per the spin multiplicity of those states. A detailed Jablonski diagram, depicting the photophysical processes characteristic of a rhenium d^6 complex, is shown in Figure 11, whereupon the electronic quantum states are represented by thick horizontal lines with each vibrational quantum state superimposed by thin horizontal lines. Absorption of a photon of ample energy prompts a transition from the ground electronic singlet state (S_0) to a vibrationally coupled excited electronic singlet state (S_1). Thereafter the molecule will undergo vibrational relaxation (VR), liberating energy to the environment such that it assumes the lowest energy vibrational quantum state of the S_1

electronic state. Three potential deexcitation pathways then arise from a molecule occupying the S_1 electronic state. The excited molecule can either undergo internal conversion (IC) to transition back to the ground state (S_0) vibronically coupled with a vibrational quantum state of equivalent energy, followed by VR to lose the absorbed energy to the environment in the form of heat (i.e. no radiative emission); it can undergo fluorescence, transitioning to any number of vibrationally coupled S_1 electronic states by emitting photons equivalent to the difference in energy (thus accounting for the wide emission bands observed at room temperatures), and then undergoing VR to lose the excess vibrational energy; or, due to the spin-orbit coupling (SOC) exhibited by the larger nucleus of the rhenium atom which perturbs its spin-wavefunction, the molecule may violate the spin-selection rule (which forbids transitions between spin states of differing multiplicities) and undergo intersystem crossing (ISC) to a vibronically coupled excited electronic triplet state (T_1). From the T_1 electronic state the molecule may either undergo ISC back to the S_0 electronic state and lose energy *via* VR or it may undergo phosphorescence, transitioning to vibronically coupled S_0 states and emitting the difference in energy as photons which are even further red shifted with respect to those emitted *via* fluorescence. The orders of magnitude of time required for each of these photophysical processes is listed in Table 2.[33] It is evident from this table that phosphorescent emission occurs over significantly longer periods of time than fluorescent emission, due to the electronic deexcitation from triplet to singlet multiplicities. Thus, agents such as rhenium tricarbonyl complexes which exhibit phosphorescence have found noteworthy applications in time-gated emission, whereupon the emission is imaged some milliseconds after excitation of the tracer to allow for the background decay of autofluorescence from naturally existing biofluorescent molecules present within the biological tissue.[34,35] Added to this advantage is that such phosphorescent metal complexes with d^6 electron configurations also benefit from

significant stokes shifts (typically > 5000 chromo) which allows the emission signal to be easily distinguished from the excitation signal with minimal spectral overlap.[36]

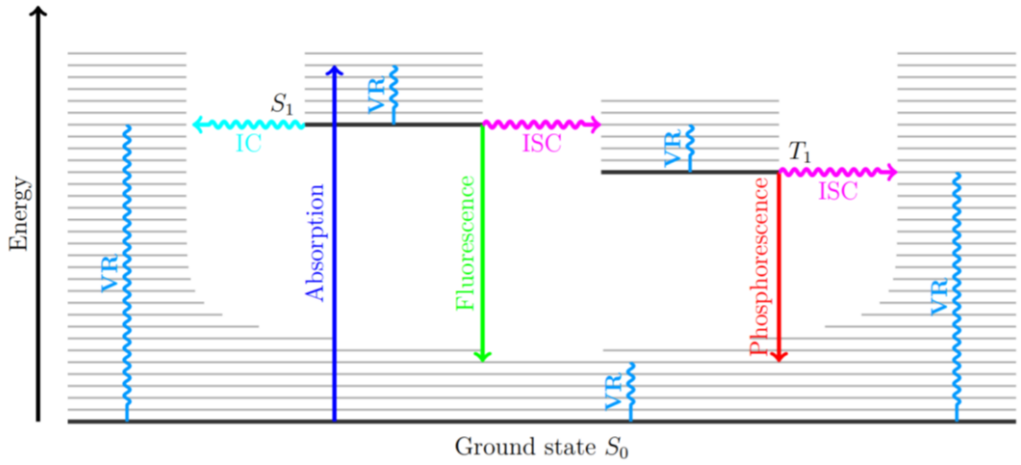

Figure 11. Jablonski diagram showing the photophysical processes of absorption (blue), internal conversion (cyan), intersystem crossing (magenta), vibrational relaxation (azure), fluorescence (green) and phosphoresce (red) between the singlet ground (S_0), singlet excited (S_1) and triplet excited (T_1) electronic quantum states.

Table 2. Duration of time required for the various photophysical processes.[33]

Transition	**Time Scale (s)**
Absorption	10^{-15}
Vibrational Relaxation (VR)	10^{-12} – 10^{-10}
Internal Conversion (IC)	10^{-11} – 10^{-9}
Intersystem Crossing (ISC)	10^{-10} – 10^{-8}
Fluorescence	10^{-10} – 10^{-7}
Phosphorescence	10^{-6} – 10

Due to the advantages afforded from phosphorescent imaging, and aided also by their intrinsic resistance to photobleaching, rhenium tricarbonyl complexes have found widespread applications as optical agents for the imaging of cellular organelles.[37,38] Typically, such rhenium cell imaging agents will consist of a diimine bidentate ligand datively bonded through two nitrogen atoms of the respective *N*-heterocycles, alongside a monodentate ancillary ligand likewise bonded through an *N*-heterocycle. Modulation of either the diimine or ancillary ligand

can induce charge effects or alter the lipophilicity of the complex resulting in the localisation of the rhenium optical agents in differing cellular organelles as a function of these chemical properties. Exemplars of such rhenium tricarbonyl complexes used in the imaging of cellular organelles are provided in Figure 12.[39-42]

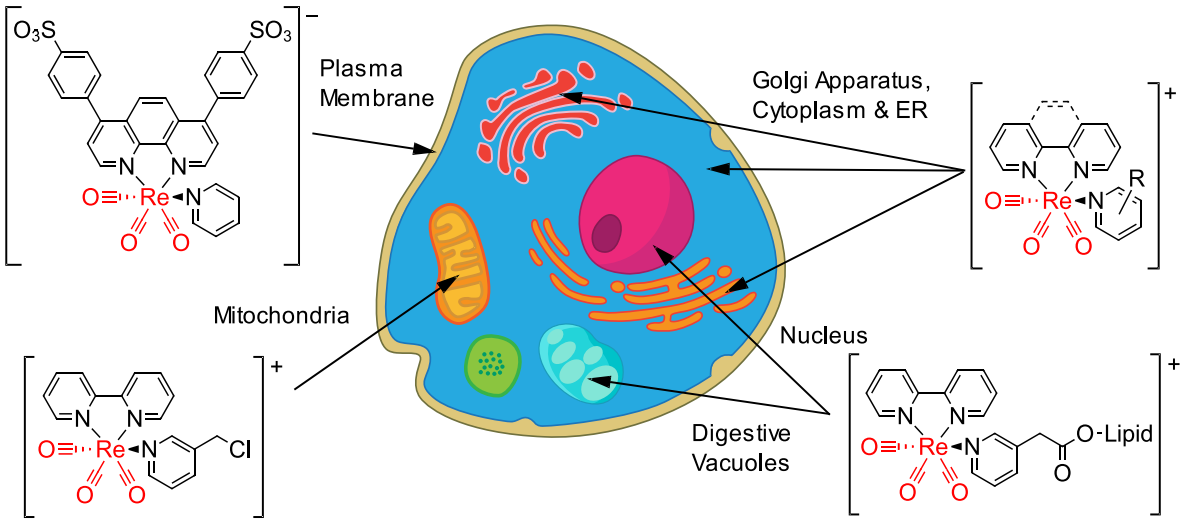

Figure 12. Organelle localisation of some rhenium tricarbonyl imaging complexes as influenced by the modified molecular structure of the diimine and ancillary ligands.[39-42]

The emission observed from rhenium complexes used as imaging agents typically arise from high energy ligand centred (LC) excited states, resulting from electronic transitions occurring within the diimine and/or ancillary ligand, and from a lower energy metal-to-ligand charge transfer (MLCT) excited state, whereupon the electronic transition occurs from a molecular orbital (MO) predominantly centred on the rhenium centre to the π* antibonding orbital of the ligand, thus resulting in a characteristic broad signal highly subject to solvatochromic shifts which can stabilise the positive and negative charge separation arising between the rhenium centre and ligand, respectively. Absorption to the MLCT excited electronic state, denoted as a $d\pi \rightarrow \pi^*$ transition, is characterised by a broad lower energy peak on UV-vis spectra, whereas absorption to the LC states, denoted as $\pi \rightarrow \pi^*$ transitions, are characterised by higher energy,

sharp peaks with greater molar extinction coefficients. These transitions are depicted in Figure 13, which provides a generalised MO diagram for octahedral complexes, such as rhenium tricarbonyl diimine complexes, arising from the superpositioning of the atomic orbitals of the metal with the molecular orbitals of the ligand.[33] Alongside the typical absorption and emission bands observed to and from LC and MLCT excited states, lower energy metal centred (MC) as well as ligand-to-metal charge transfer (LMCT) states are also traced.

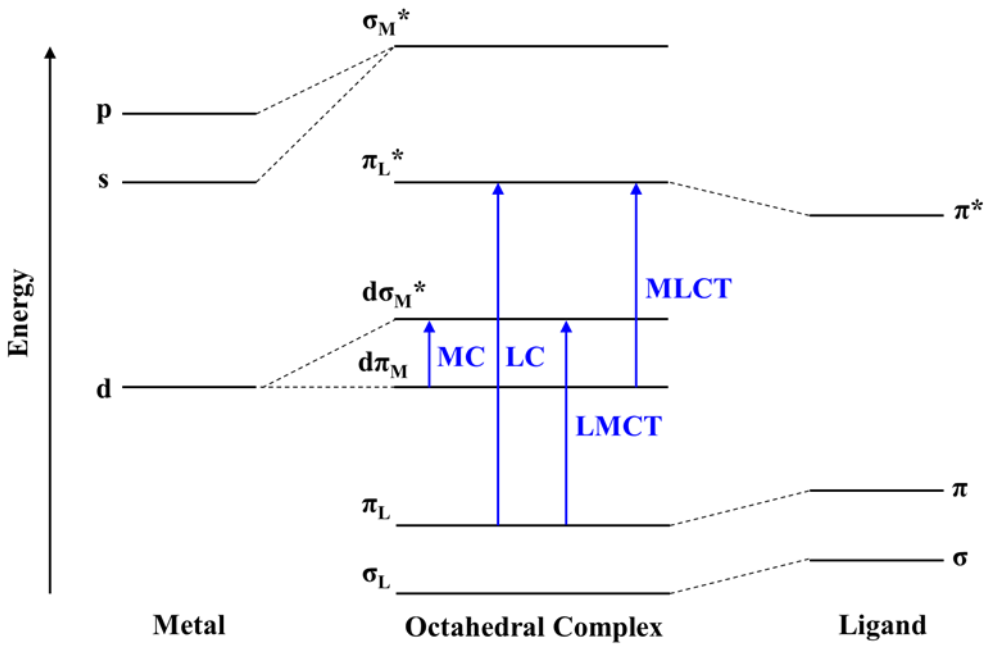

Figure 13. MO diagram for an octahedral metal complex (such as rhenium tricarbonyl diimine complexes) showing the mixing of ligand MOs with the atomic orbitals of the metal centre, alongside some electronic excited states (such as LC and MLCT states) which arise from transitions between the MOs of the complex.

Figure 14 provides a clearer illustration of the orbitals involved in the transition to the MLCT electronic excited state. The dπ orbital occupied in the ground state (GS) of the molecule, consists of electron density centred around the rhenium metal centre and the carbonyl groups, with little electronic density present on the ligand. Upon excitation to the MLCT excited state, a dπ occupied electron transitions to a π* orbital whereby the electronic density is spread over the N-heterocyclic ligand, thus causing a dipole to exist between the ligand and the metal.

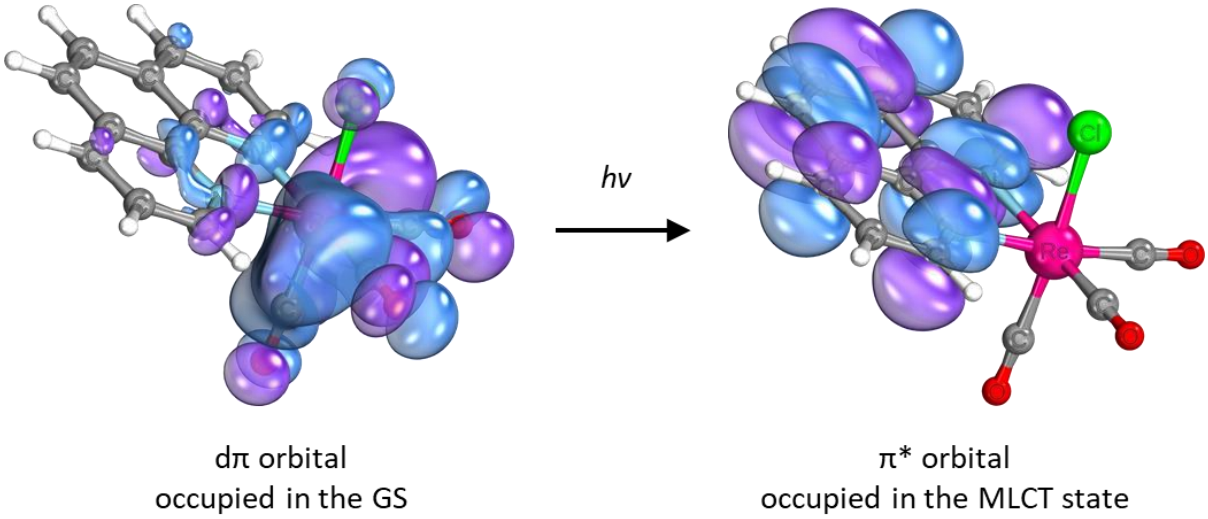

Figure 14. Computational density functional theory (DFT) modelling of a tricarbonyl rhenium(I) complex with a 1,10-phenanthroline diimine ligand, showing the transition of an electron occupying a dπ orbital, centred on the rhenium and carbonyl ligands, to a π* antibonding orbital centred on the diimine ligand upon absorption of a photon. Thus, causing the molecule to transition from the GS to the MLCT excited state and a charged dipole to exist between the negatively and positively charged ligand and metal centre respectively.

Any of these aforementioned transitions can be summarised in part within the simplified photophysical schematic represented by equation (7), whereupon a molecule (M) absorbs a photon (*hv*) as per the absorption rate constant (k_{abs}).[43] The excited state molecule (M*) arising from this transition may then either undergo deexcitation *via* a non-radiative decay channel such as IC determined by the non-radiative decay rate constant (k_{nr}), or alternatively deexcite *via* a radiative decay channel determined by the radiative decay rate constant (k_r), inclusive of fluorescent and phosphorescent emission, to emit a red-shifted photon (*hv*') of lower energy.

$$M + hv \underset{k_{nr}}{\overset{k_{abs}}{\rightleftarrows}} M^* \overset{k_r}{\rightarrow} M + hv' \qquad (7)$$

Aside from the excitation and emission wavelengths required to tune instrumentation to the receiving and output signals appropriate for the tracer, a particularly useful parameter of an optical agent is its luminescent quantum yield (ϕ). The luminescent quantum yield is a measure

of emission efficiency which can be defined by the ratio between the rate of photons emitted (*hv*') and the rate of photons absorbed (*hv*) per given unit of time (t) as per equation (8).

$$\phi = \left(\frac{-d[hv']}{dt}\right)\left(\frac{d[hv]}{dt}\right)^{-1} \quad (8)$$

Similarly of value is the luminescence lifetime (τ) of an optical tracer. The luminescence lifetime is defined as the time required for the luminescence intensity to decay to e^{-1} of its original value and is a key indicator of how long an optical tracer can be efficiently imaged for following excitation. Equation (9) links the lifetime to the scheme provided in equation (7), showing how the concentration of molecules in the excited state ([M*]), indicative of luminescence intensity, exponentially decays as a function of time from its initial value ($[M^*]_0$).

$$[M^*] = [M^*]_0 e^{-\left(\frac{t}{\tau}\right)} \quad (9)$$

The radiative and non-radiative decay rate constants (k_r and k_{nr} respectively), governing the rate of the photophysical processes described by the scheme in equation (7), are intrinsically linked to the quantum yield and lifetime of an optical tracer as per equations (10) & (11).

$$k_r = \phi.\tau^{-1} \quad (10)$$

$$k_{nr} = (1-\phi)\tau^{-1} \quad (11)$$

One final consideration in the design of optical agents is that bioconjugation of a fluorophore or alternative luminescent molecule can potentially inadvertently affect the photophysical properties of the final tracer. Likewise, the attachment of a luminescence appendage can affect the biological properties of the conjugate, such as its receptor binding affinity or rate of metabolism.[44] As such, linker groups are often employed to distance, and hence decouple, the fluorescent group and bioconjugate from influencing the properties of one another. Though these groups can too affect other chemical properties of the system, such as the solubility of the molecule, adding an additional layer of complexity to optical tracer design.[45, 46]

1.4 Fluorine-18 in PET-Optical Hybrid Imaging

Among the first movements towards designing PET-optical hybrid tracers was a radioreceptor binding assay study performed by French, *et al.* in 1993.[47] Several 7α-pentyl substituted estradiols were synthesised in the study to assess estrogen receptor binding affinities, one of which was functionalised with fluorine-18 (**1**) for use as a breast cancer imaging PET tracer and another of which was functionalised with the luminescent boron-dipyrromethene (BODIPY) dye (**2**) for use as an optical agent, as depicted in Figure 15. These contributions laid the framework for fluorine-18 PET-optical imaging, using similar compounds with differing functionalisation tailored to the imaging modality of interest, though no further attempt was undertaken by the group to combine these functions into a single molecule which would behave similarly in both imaging studies.

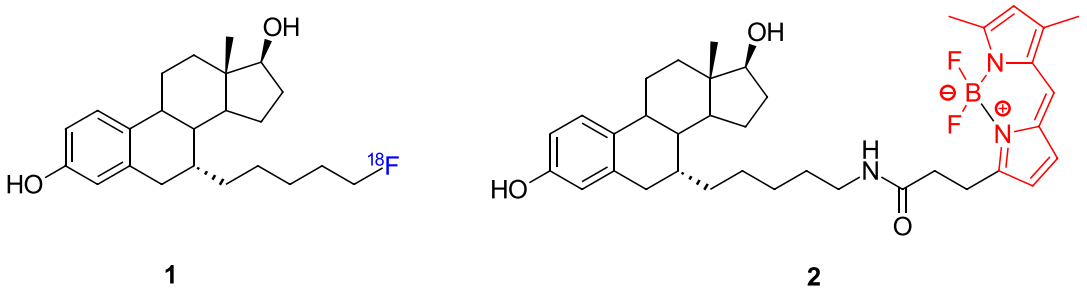

Figure 15. 7α-Pentyl substituted estradiol analogues developed by French, *et al.* bearing a fluorine-18 radioisotope (blue) for PET imaging and a BODIPY dye (red) for optical imaging of breast cancer.[47]

It was not until 2011 that Li, *et al.* published the first communication detailing the fluorine-18 labelling of a BODIPY dye as a structural motif for multimodal PET-optical imaging.[48] The radiolabelling reaction tolerated aqueous conditions, which is rarely reported in the field of radiofluorinations, and afforded the tracer (**4**) in 22 ± 3% RCY as show in

Figure 16 with 925 ± 148 MBq.μmol^{-1} molar activity (though as *carrier-added*). An efficient quantum yield of 14.3% was also measured in chloroform, with 528 nm green light emission.

These photophysical properties were not characterised in water or biological media, however, to discern solvatochromic shifts and changes to the quantum yield in an *in vivo* environment. Despite this, biodistribution studies of the tracer marked one of the first instances of PET-optical hybrid imaging, with the results of both imaging modalities shown in Figure 17. Further studies on analogues of **4** by Liu, *et al.* and Chansaenpak, *et al.* noted significant uptake of the tracer by the heart muscle compared to other organs and thus is currently being investigated as a PET-optical agent for myocardinal perfusion imaging.[49, 50] The confirmed *in vivo* stability of the fluorinated BODIPY agent by Li, *et al.* also inspired subsequent bioconjugations by other research groups.

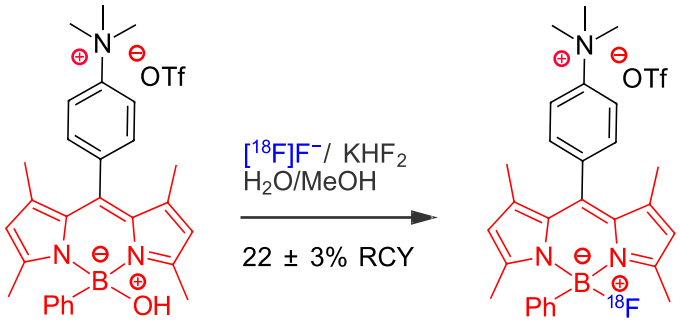

3 **4**

Figure 16. Fluorine-18 radiolabelling of a BODIPY dye with a *c.a.* RCY of 22 ± 3% under aqueous conditions.[48]

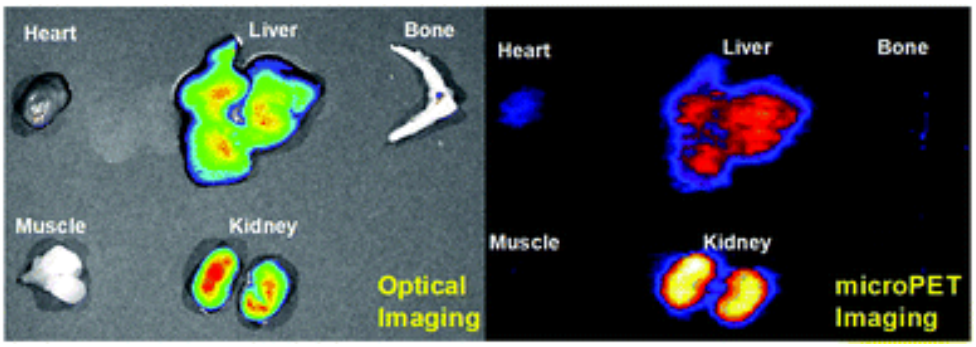

Figure 17. Optical (right) and PET (left) imaging of the organs used for biodistribution analyses performed 4 h post-injection of the fluorine-18 labelled BODIPY agent (**4**) developed by Li, *et al.*[48]

The first experiment to bioconjugate the fluorine-18 labelled BODIPY analogue was published by Liu, *et al.* in 2013, whereby the motif was conjugated to a cyclic arginylglycylaspartic acid (RGD) analogue.[51] As the RGD peptide had been demonstrated to bind to integrin $\alpha_v\beta_3$ receptor proteins in former studies and given that the $\alpha_v\beta_3$ receptor proteins are overexpressed in certain glioblastoma cell lines, the researchers were able to use compound **5** shown in Figure 18 to provide PET and optical imaging of a glioblastoma xenograft mouse model (Figure 19). The radiotracer was afforded in 82% RCY, though with a relatively low molar activity of 703 ± 148 MBq.μmol^{-1} achieved through *carrier-added* $^{18}F/^{19}F$ isotope exchange.

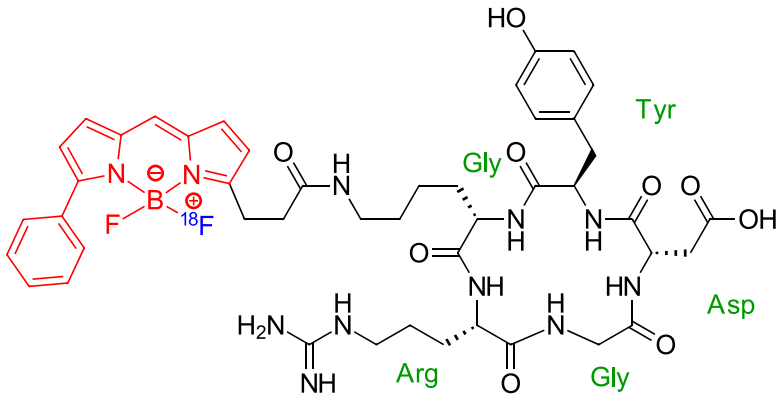

5

Figure 18. Fluorine-18 (blue) labelled BODIPY dye (red) bioconjugated to an RGD peptide analogue for use as a PET-Optical glioblastoma imaging agent.[51]

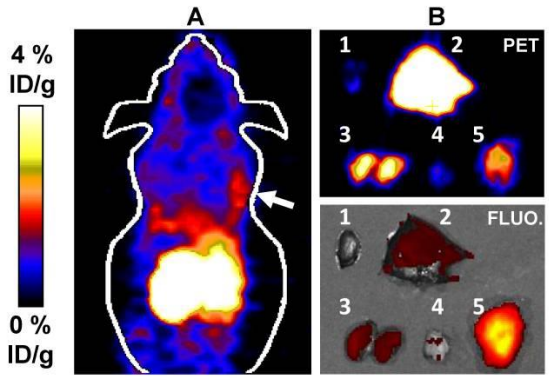

Figure 19. A) PET imaging of a xenograft glioblastoma tumour depicted by the white arrow by Liu, *et al.* B) PET-optical hybrid imaging of the tumour and organs following 0.5 h post-injection of compound **5**. 1: Heart, 2: Liver, 3: Kidneys, 4: Muscle, 5: Tumour.[51]

Later examples of fluorine-18 labelled BODIPY imaging agents encompass bioconjugation to a triglyceride (Figure 20) by Paulus, *et al.* in 2017 for imaging brown adipose tissue, which was formed in 76% RCY and low 220 MBq.μmol^{-1} molar activity with no photophysical characterisation;[52] bioconjugation to a caspase inhibitor (Figure 21), an enzyme family responsible for the regulation of cellular apoptosis, achieved in 11 ± 6% RCY and considerably high molar activity (≥ 166 GBq.μmol^{-1}) with a quantum yield of 12.0 ± 0.5% by Ortmeyer, *et al.* in 2017;[53] and a recent PET-optical prosthetic group developed in 2019 by Kim, *et al.* for the design of neuroimaging agents,[54] whereupon the researchers reported RCYs in the range of 35 – 50% and molar activities in the vicinity of 0.8 – 1.0 GBq.μmol^{-1}.

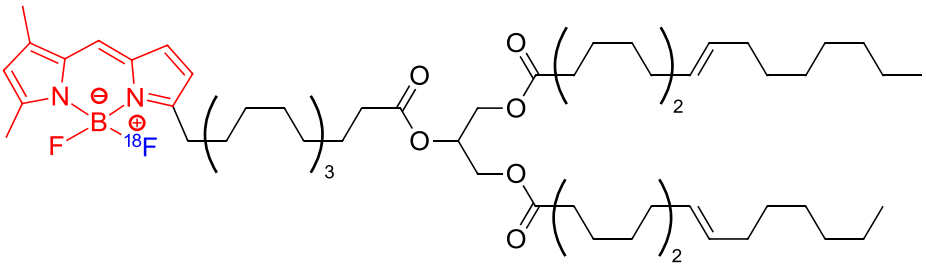

6

Figure 20. Triglyceride molecule functionalised with a radiofluorinated BODIPY dye by Paulus, *et al.* for the PET-optical imaging of brown adipose tissue.[52]

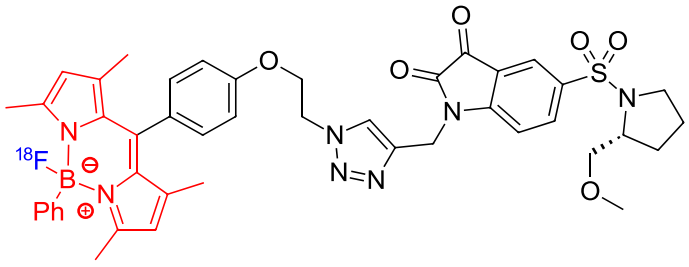

7

Figure 21. Caspase-inhibitor functionalised with a fluorine-18 labelled BODIPY dye by Ortmeyer, *et al.*[53]

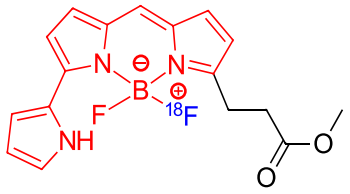

8

Figure 22. PET-optical methyl ester prosthetic group for the development of neuroimaging agents synthesised by Kim, *et al.*[54]

An alternative PET-optical strategy trialled by Ting, *et al.* in 2010 also relied on a boron-fluorine-18 bond *via* a trifluoroborate group, though instead implemented the radioisotope alongside a conjugated heptamethine cyanine (Cy7) dye responsible for the 772 nm NIR emission maximum of the tracer in water.[55] The molecule was bioconjugated to the macromolecular polysaccharide tilmanocept (also marketed as Lymphoseek), consisting of repeating units of diethylenetriaminepentaacetic acid (DTPA) and mannose bonded to a dextran backbone (shown in Figure 23), which was initially designed to complex to technicium-99m for the single photon emission computed tomography (SPECT) imaging of sentinel lymph nodes.[56] The researchers were able to achieve a single step aqueous radiofluorination of the precursor, akin to the protocol used by Li, *et al.* for BODIPY radiolabelling, though no RCYs were reported.[48, 55] The quantum yield of the tracer was calculated as 2.7% in water which, while not as high as those attained by BODIPY analogues in organic solvents, is better representative of the expected fluorescence output in a biological environment and allows for deep-tissue imaging within the NIR window. Discernible PET-optical imaging of the lymph nodes was achieved in animal models, leading to the conclusion that single-injections of tracer **9** may improve sentinel node biopsy over alternative protocols implementing multiple-injection analyses of [^{99m}Tc]Lymphoseek for nuclear imaging and chemically dissimilar isosulfan blue dyes for subsequent optical imaging.[57]

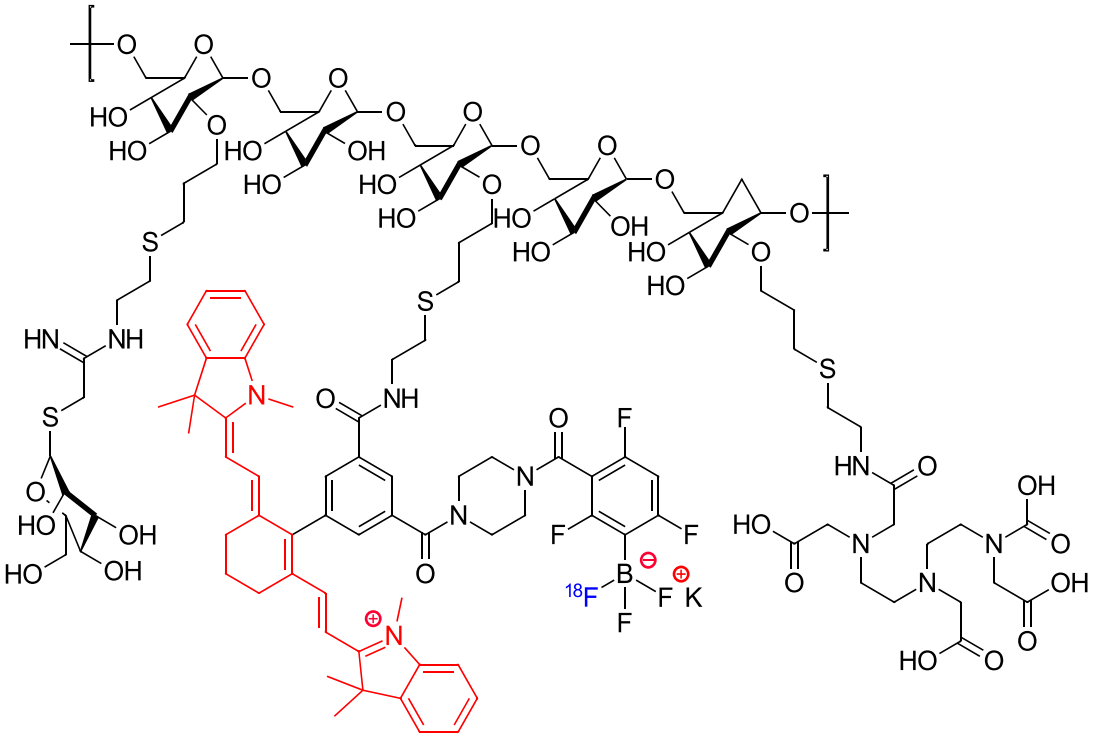

9

Figure 23. DTPA-mannosyl-dextran (Lymphoseek) conjugated to a Cy7 dye (red) for NIR optical imaging and a trifluoroborate group hosting the fluorine-18 radioisotope (blue) for PET imaging, developed by Ting, *et al.* for the PET-optical mapping of sentinel lymph nodes.[55]

Aiming to develop PET-optical tracers of monoclonal antibodies, Rogriguez, *et al.* utilised a similar Cy7 dye as introduced by Ting, *et al.* also incorporating a fluorine-18 boron trap.[58] The 2016 study focussed on coupling two monoclonal antibodies, one being an anti-epithelial cell adhesion molecule (EpCAM) antibody used to label prostate tumours (**10a**) and the other being an anti-epidermal growth factor receptor (EGFR) antibody for labelling lung adenocarcinoma tumours (**10b**). The general structure for both monoclonal antibody-coupled PET-optical tracers is depicted in Figure 24. Significantly greater molar activities were attained for the EpCAM targeting prostate tumour tracer (**10a**) than for the EGFR targeting lung adenocarcinoma tumour tracer (**10b**), affording 592 GBq.μmol^{-1} and 181 MBq.μmol^{-1} respectively.

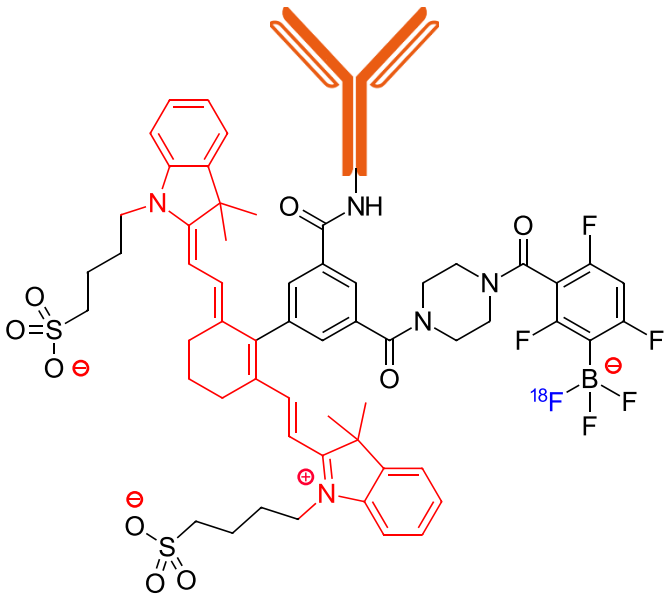

Figure 24. PET-optical tracer designed by Rogriguez, *et al.* incorporating a Cy7 dye (red), boron-bonded fluorine-18 radioisotope (blue) and conjugated to a monoclonal antibody (orange) targeting EpCAM (**10a**) and EGFR (**10b**).[58]

Al-Karmi, *et al.* also sought to radiofluorinate the Cy7 hydrocyanine dye, though for use as a PET coupled on-off optical probe which would fluoresce in the presence of reactive oxygen species (ROS).[59] An initial two-step radiosynthesis of the compound involved nucleophilic aromatic substitution of a nitro-substituted precursor (**11**) using [^{18}F]fluoride with a Kryptofix 222 phase transfer catalyst in dimethylformamide (DMF), followed by reduction of the iminium salt using sodium borohydride, as shown in Figure 25. This approach afforded only 19% RCY, however, and hence direct radiofluorination of the already reduced Cy7 dye (**12**) was instead trialled which afforded the desired tracer (**13**) in 62% RCY and with 5.2 GBq.μmol^{-1} molar activity, thus demonstrating the aforementioned value of simplifying radiosyntheses to a single time-efficient radiofluorination step as to avoid any unnecessary loss of radioactivity.

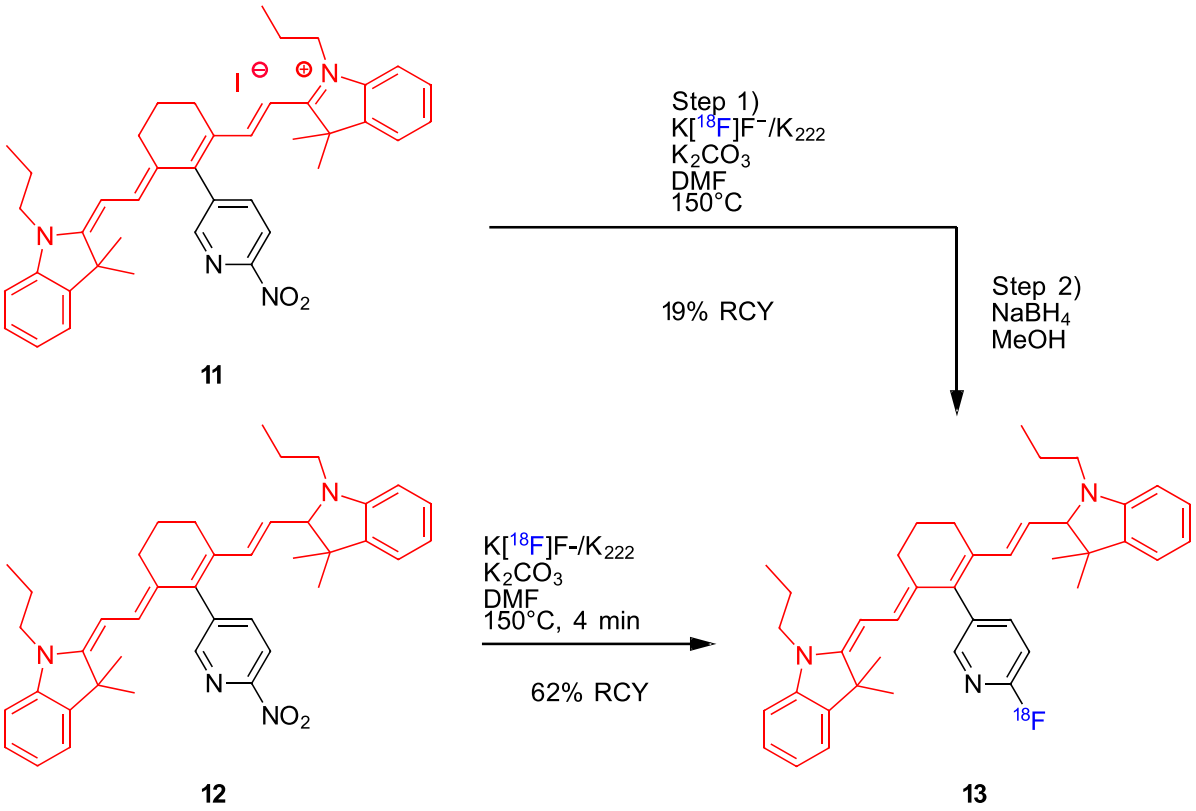

Figure 25. Cy7 dye with a 2-[^{18}F]fluoropyridine prosthetic group for the PET imaging and on-off optical sensing of ROS.[59] Initial syntheses starting from **11** involved a multistep radiofluorination and reduction reaction which afforded **13** in only 19% RCY. An alternative direct single step radiofluorination from the reduced non-radioactive analogue (**12**) afforded **13** in 62% RCY.

An ambitious goal by Wang, *et al.* was to PET-optical label red blood cells, using the alternative trimethine cyanine (Cy3) and pentamethine cyanine (Cy5) dyes coupled with fluorine-18, as a means of imaging intracranial haemorrhages.[60] An initial PET-optical labelling reagent was synthesised by conjugating an *N*-hydroxysuccinimide (NHS) ester to the fluorine-18 labelled Cy3 dye (**14**), which was then demonstrated to react with the free amine groups of lysine units present on the surface of the red blood cells, as shown by the mechanism in Figure 26. The resulting radiolabelled red blood cells were reportedly achieved in greater than 2.96 GBq.μmol^{-1}. Similar red blood cell conjugation experiments were also performed using the Cy5 hydrocyanine dye PET-optical tag (**15**) additionally shown in Figure 26.

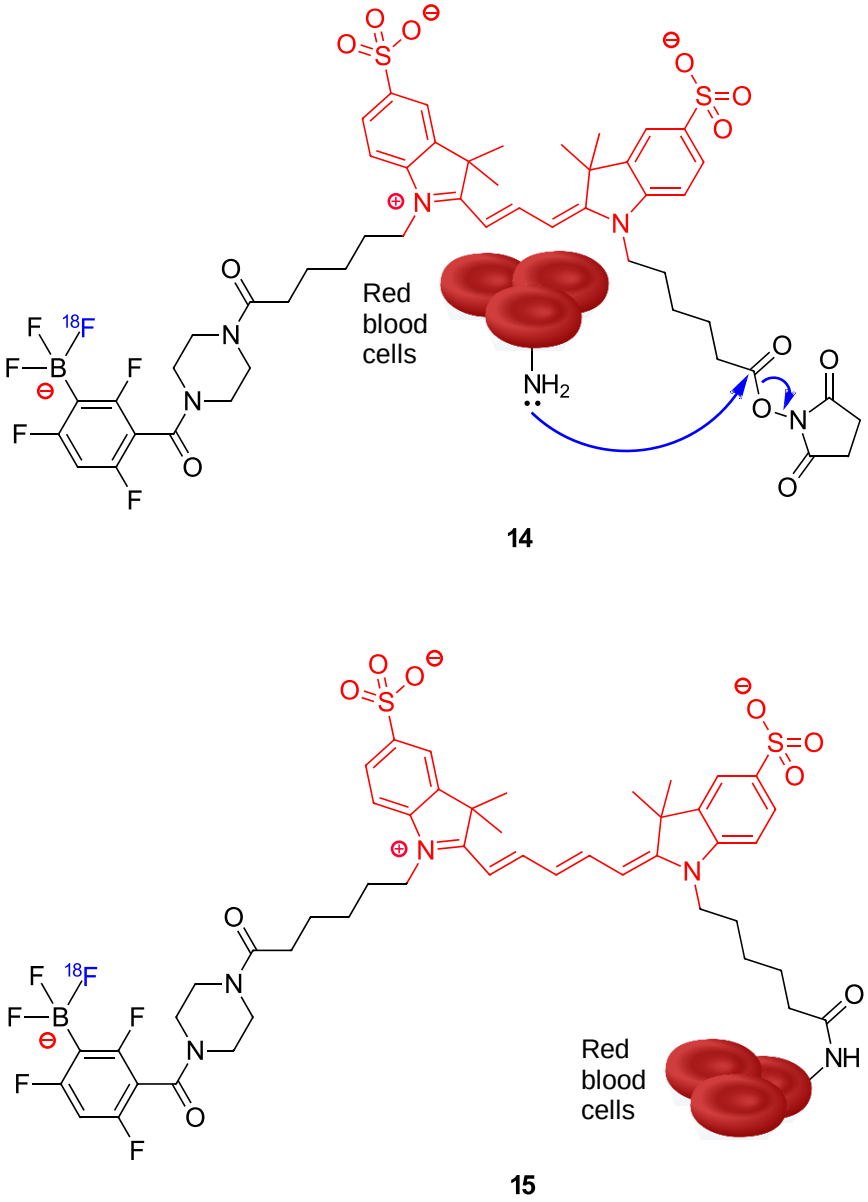

Figure 26. Design of a Cy3 hydrocyanine dye (red) complexed to a fluorine-18 labelled trifluoroborate salt and NHS ester (**14**) by Wang, *et al.*, which allows for bioconjugation to the terminal amino group of lysine residues present on the surface of red blood cells.[60] The resulting PET-optical labelled red blood cells were subsequently used to image intracranial haemorrhages. Substitution for a Cy5 hydrocyanine dye (red) also allowed for an analogous red blood cell conjugate (**15**) with differing excitation and emission properties.

Having developed a novel sulfonated prosthetic group (**16**), shown in Figure 27, as a less lipophilic alternative to the fluorine-18 prosthetic groups which were currently available, Priem, *et al.* also sought to conjugate **16** to an alternative pentamethine cyanine (Cy5.5) dye for development as a PET-optical agent.[61] The Cy5.5 precursor (**17**) reacted with the NHS ester group of the prosthetic group (**16**) in the presence of an *N*,*N*-diisopropylethylamine (DIPEA) base in acetonitrile to afford the PET-optical dye (**17**) in purportedly ≤ 70% RCY, although the molar activity was not specified. Commendably however, the quantum yield of **17** was compared against the original Cy5.5 dye and the precursor derivative **16** to assess its viability as an optical probe. In dimethylsulfoxide (DMSO) solution, probe **17** exhibited a quantum yield of 42%, slightly decreased from the 45% quantum yield of **16**. This trend was inverted, however, when measuring the quantum yields in phosphate-buffered saline (PBS) solution with the 5% addition of bovine serum albumin (BSA) to better represent a biological medium and to prevent the formation of non-emissive aggregates. In such a solution **17** afforded a quantum yield of 38%, slightly greater than **16** which afforded 34% and much greater than the Cy5.5 dye which alone afforded a 23% quantum yield. While the emission maxima of both **17** and **16** were not dissimilar at 712 and 710 nm respectively, both were red shifted with respect to the emission maxima of the Cy5.5 dye at 694 nm in the PBS plus BSA solution. These differences in photophysical parameters demonstrate the importance of measuring the quantum yields and excitation/emission properties not only in organic solvents, though also in aqueous or biological media where solvatochromic effects can influence the efficiency of an optical tracer in its intended environment.

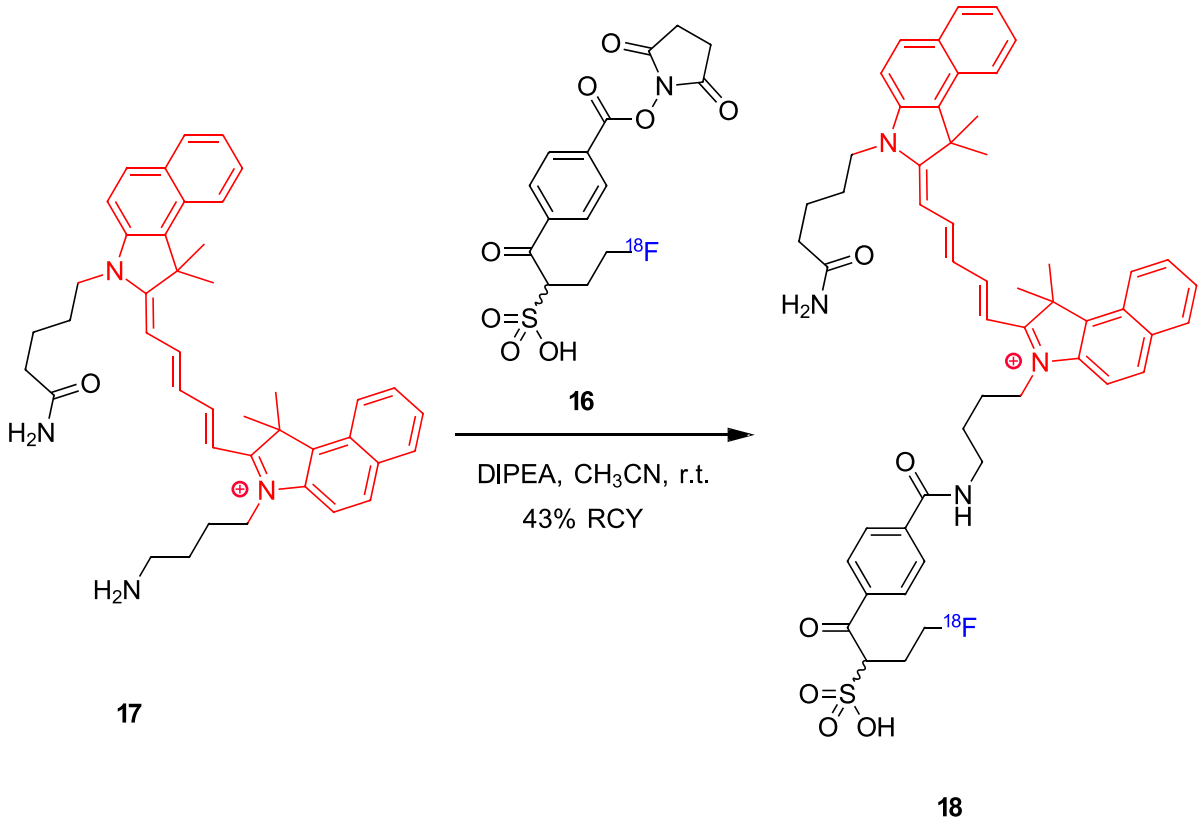

Figure 27. Radiolabelling of a Cy5.5 fluorescent precursor (**17**) with a fluorine-18 labelled NHS ester prosthetic group (**16**) to afford the PET-Optical product (**18**) by Priem, *et al.*[61]

An alternative use of a prosthetic group was also trialled by Heinrich, *et al.* in the radiolabelling of the rhodamine B fluorescing dye for use as a myocardinal perfusion imaging agent, analogous to the mentioned works of Liu, *et al.* and Chansaenpak, *et al.*[62] As shown in Figure 28, the precursor (**19**) was reacted with a 2-[^{18}F]fluoroethyl tosylate prosthetic group heated to reflux in anhydrous acetonitrile in the presence of a DIPEA base, which afforded the fluorine-18 labelled rhodamine B product in 35% decay corrected RCY following purification by solid-phase extraction. While the time of synthesis required approximately 90 mins the PET-optical tracer was still acquired with a satisfactory 1.3 GBq.μmol^{-1} molar activity. Unfortunately, the tracer showed no appreciable uptake in myocardial tissue during subsequent biodistribution studies, invalidating its potential use as a myocardinal perfusion imaging agent, and no

measurements of the quantum yield or other photophysical parameters were undertaken to develop the probe for further PET-optical applications.

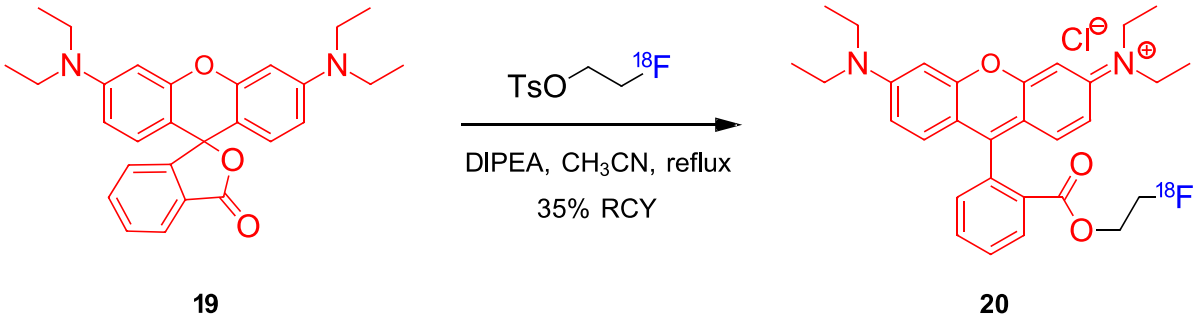

Figure 28. Radiolabelling of Rhodamine B (**20**) using an [^{18}F]fluoroethyl tosylate prosthetic group under basic conditions by Henrich, *et al.* which afforded the tracer in 35% RCY post-purification, though required a synthesis time of approximately 90 mins.[62]

A unique approach to designing PET-optical agents was experimented by Damont, *et al.* whom first sought to conjugate water-soluble biotin (vitamin B_7) to two differing fluorescent dyes, Atto-425 (**21**) and Atto-680 (**22**) as shown in Figure 29.[63] A third biotin precursor (**23**) was also developed which was radiofluorinated *via* a traditional nucleophilic aromatic substitution for a nitro leaving group in anhydrous conditions, affording the 2-[^{18}F]fluoropyridine labelled derivative (**24**) in 44 ± 9% RCY and 153 ± 45 GBq.μmol^{-1} molar activity. Each of the three biotin groups were then bound to avidin, a tetrameric protein capable of binding to four units of biotin with high affinity, in order to create the scaffold for a PET-optical tracer to which a fourth biotin unit could be bound as a targeting vector. Neither the photophysical properties nor the molar activity of the final biotin-bound avidin complex were determined, though the approach demonstrated a novel means by which additional imaging modalities could be appended.

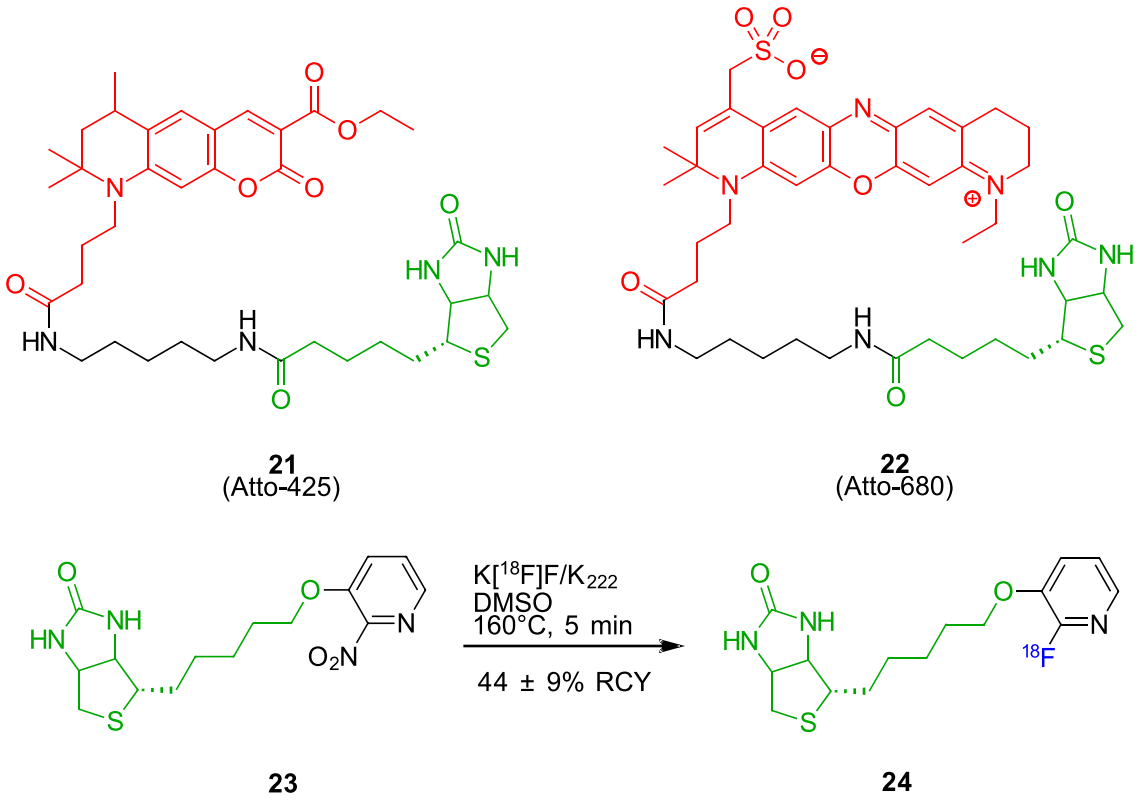

Figure 29. Biotin (green) was conjugated to two fluorescent dyes (red), Atto-425 (**21**) and Atto-680 (**22**). A 2-nitropyridine analogue of biotin (**23**) was radiofluorinated to form a 2-[^{18}F]fluoropyridine biotinylated analogue (**24**). The PET modality (**24**) and optical modality (**21** or **22**) were then combined *via* biotin-avidin binding to develop a novel PET-optical agent.[63]

Aside from the use of organic fluorophores, two researchers have also published work on the fluorine-18 labelling of quantum dots (QDs) as PET-optical agents. The first example, reported in 2008 by Duconge, *et al.*, encapsulated a CdSe/CdZnS core/shell QD within a phospholipid micelle functionalised with thiol groups.[64] A fluorine-18 labelled maleimido reagent, 1-[3-(2-[^{18}F]-fluoropyridin-3-yloxy)propyl]pyrrole-2,5-dione ([^{18}F]FPyME), was then reacted with the thiol groups in order to add PET imaging functionality to the optically emitting QDs (**25**) as shown by the resulting structure in Figure 30. The molar activity of the QDs formed by Duconge, *et al.* ranged from 370 – 740 GBq.μmol^{-1} and while the RCY of the fluorine-18 labelled QDs were not calculated, the radiochemical synthesis hitherto afforded [^{18}F]FPyME in 17 – 20% RCY, though not corrected for decay (as the Society of Radiopharmaceutical

Sciences (SRS) did not publish guidelines requiring decay correction for reported RCYs until 2017).[65] The photophysical properties of the PET-optical functionalised QD (**25)** were unfortunately not measured, however, QDs of this nature have been reported to achieve quantum yields greater than 80% in some instances.[66] An alternative PET-optical fluorine-18 labelled QD tracer developed later by Hu, *et al.* in 2015 sought to bioconjugate not only a cyclic RGD peptide for specific binding to integrin $\alpha_v\beta_3$, similar to the earlier attempts of Liu, *et al.* towards targeting glioblastoma, though also bombesin, an analogue of gastrin-releasing peptide, for targeting the gastrin-releasing peptide receptor (GRPR) which is over-expressed in certain prostate cancers.[67] The researchers utilised ZnS coated CdTe QDs functionalised with polyethyleneglycol (PEG) to which the group bearing the fluorine-18 radioisotope, cyclic RGD peptide and bombesin peptide sequence was attached to give the PET-optical QD (**26**) shown in Figure 30. Despite reasonable tumour uptake of **26** being observed using both modalities in biodistribution experiments of prostate tumour bearing mouse models, neither the photophysical characteristics nor the molar activity and RCY were reported for the final tracer.

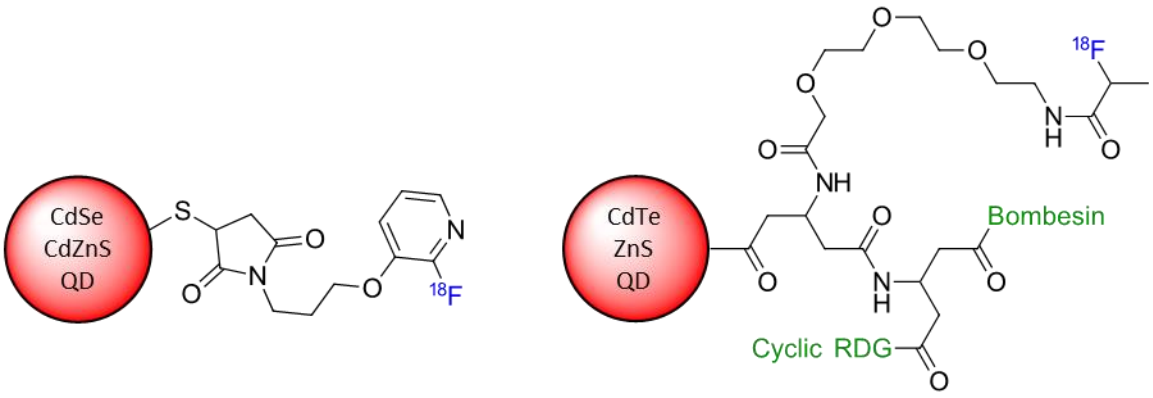

25
Duconge, *et al.*

26
Hu, *et al.*

Figure 30. Two fluorine-18 labelled quantum dots (QDs) for PET-optical imaging designed by Duconge, *et al.* using CdZnS coated CdSe QDs (**25**) and Hu, *et al.* using ZnS coated CdTe QDs bioconjugated to cyclic RGD and a bombesin peptide sequence (**26**).[64, 67]

A final class of PET-optical tracers incorporating [^{18}F]fluoride directly into the core of Yb^{3+} and Er^{3+} upconversion luminescence nanoparticles was developed independently by Liu, *et al.*, Sun, *et al.* and Zhou, *et al.* in 2011.[68-70] The rationale for the use of nanoparticles was the added possibility of co-doping the nanoparticles with paramagnetic Gd^{3+} as a contrast agent for additional MRI trimodal functionality, which was explored in each of these studies *via* the implementation of $NaYF_4$ nanophosphors. Despite the impressive feat of consolidating PET, MRI and optical modalities into a single molecular probe, as well as the wealth of biodistribution data which was acquired from each study, no attempts to bioconjugate these probes for disease diagnosis have since been performed. While Zhou, *et al.* did not report any RCYs for their radiolabelling experiments, leaving the design efficiency in question, Liu, *et al.* and Sun, *et al.* both reported fluorine-18 labelling yields of greater than 90%. No measurements of molar activities, nor quantum yields were commented on, however, and thus remain critical parameters to be explored should the implementation of nanoparticle PET-optical probes be expanded upon.

A comprehensive summary of all the above known fluorine-18 labelled PET-optical tracers in the present literature is provided in Table 3. The table details, where published by the authors, the fluorophore and biological target, RCY, molar activity (A_m), quantum yield (ϕ) and excitation/emission maxima ($\lambda_{ex}/\lambda_{em}$) measured in the listed solvent for each multimodal tracer; save for the fluorine-18 labelled nanoparticles where these experiments were not performed. It is evident from this list that no radiofluorinations of luminescent transition metals, such as rhenium tricarbonyl complexes, have yet been performed and thus signify a critical gap in the research efforts to discover new fluorine-18 PET-optical hybrid agents.

Table 3. Properties of each of the fluorine-18 labelled PET-optical tracers currently reported in literature. *RCY reported was not decay corrected (published before 2017 SRS guidelines required decay corrections for RCYs).[65] **5% BSA also present in the tested PBS solution. ***Radiochemical data is provided for the radiolabelled prosthetic groups rather than the final tracer.

Tracer	Fluorophore	Target	RCY (%)	A_m (GBq.μmol^{-1})	ϕ (%) Solvent	$\lambda_{ex}/\lambda_{em}$ Solvent
4[48]	BODIPY	-	22 ± 3	0.925 ± 0.148	14.3 $CHCl_3$	506/528 $CHCl_3$
5[51]	BODIPY	Integrin $\alpha_v\beta_3$	82	0.703 ± 0.148	-	-
6[52]	BODIPY	Brown adipose tissue	76	0.220	-	-
7[53]	BODIPY	Caspase	11 ± 6	≥166	12.0 ± 0.5 CH_3CN	500/509 CH_3CN
8[54]	BODIPY	-	42.5 ± 7.5	0.900 ± 0.100	-	580/590 MeOH
9[55]	Cy7	Sentinel lymph nodes	-	4.70×10^{-3}	2.7 H_2O	755/772 H_2O
10a[58]	Cy7	EpCAM	-	595	-	-
10b[58]	Cy7	EGFR	-	0.181	-	-
13[59]	Cy7	ROS	62	5.2	-	-
14[60]	Cy3	Red blood cells	-	2.96	-	-
17[61]	Cy5.5	-	≤ 70	-	0.42 DMSO 0.38 PBS**	689/714 DMSO 697/712 PBS**
20[62]	Rhodamine B	Myocardium Tissue	35	1.3	-	-
24[63]***	Atto-425, Atto-680	-	44 ± 9	0.153 ± 0.045	-	-
25[64]***	QD	-	17 – 20*	370 – 740	-	-
26[67]	QD	Integrin $\alpha_v\beta_3$ GRPR	-	-	-	-

1.5 Proposal for Fluorine-18 Labelled Rhenium Complexes as PET-Optical Hybrid Imaging Agents

To date there has only been one example of a fluorine-18 labelled rhenium complex which was performed in 2017 by Lipowska, *et al.* during the time of this thesis investigation.[71] The study involved complexing 2-[^{18}F]fluoroethyl iminodiacetic acid ([^{18}F]FEDA) to a rhenium tricarbonyl source for use as a preclinical PET imaging agent for evaluating renal plasma flow. Figure 31 demonstrates the synthesis of the non-radioactive standard, reacting FEDA with the triaquatricarbonylrhenium(I) cation to obtain **ReFEDA**, alongside the radiosynthesis of **[^{18}F]ReFEDA** which was attained by reacting a tosylated precursor with a source of tetrabutylammonium [^{18}F]fluoride ([^{18}F]TABF). Despite having successfully radiofluorinated the rhenium complex, the potential luminescent properties were lost due to the absence of aromatic diimine and ancillary *N*-heterocyclic ligands (required for the low energy $d\pi \rightarrow \pi^*$ transitions to the MLCT excited state), which were unable to be introduced due to the tridentate nature of the FEDA ligand. Thus, no literature examples have yet existed which posit the fluorine-18 labelling of rhenium (or any other transition metal) complexes as viable PET-optical hybrid imaging agents.

Herein it is proposed that the fluorine-18 radiolabelling of rhenium tricarbonyl diimine complexes could serve as useful PET-optical molecular scaffolds for subsequent bioconjugation. The value of these rhenium complexes in PET-optical imaging is substantiated by their resistance to photobleaching, phosphorescence decay channel and tuneable emission properties as a function of the diimine ligand structure. Towards realising this goal, the research described herein began with the principle aim of synthesising the first radiofluorinated optically emitting rhenium complex, followed by an in-depth evaluation of its radiochemical and photophysical properties (*i.e.* to prove that such a complex can be synthesised in reasonable

RCY and with sufficient molar activity, quantum yield and emission lifetime). While pursuing this objective it was serendipitously also discovered that a novel rhenium-mediated method could fluorine-18 label pyrindyl-bidentate ligands which were unable to be synthesised *via* traditional radiochemical techniques, and thus also redirected research interest towards defining the scope of this novel method and applying it towards the improved radiosynthesis of existing PET nuclear medicines.

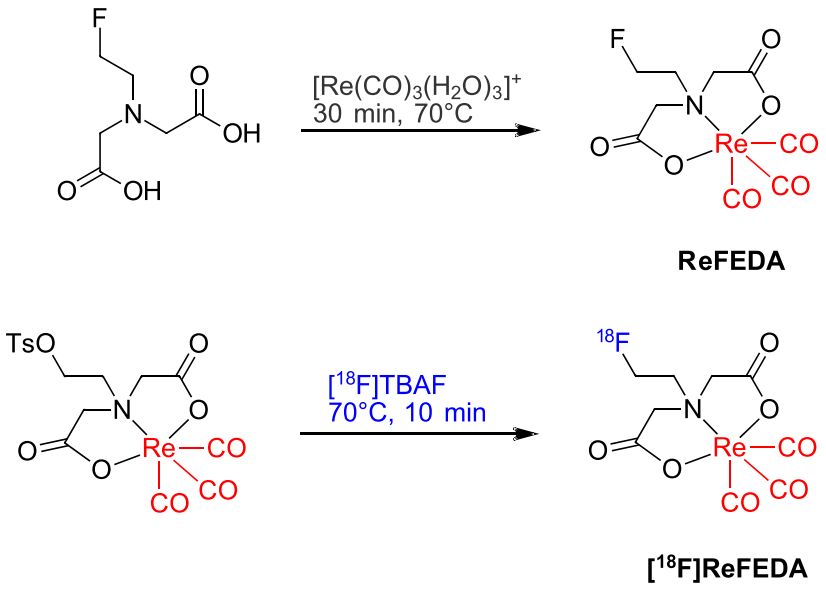

Figure 31. Non-radioactive (top) and radioactive (bottom) syntheses of **ReFEDA** and its radiofluorinated analogue **[^{18}F]ReFEDA**, respectively, by Lipowska, *et al.*[71]

CHAPTER TWO
EXPERIMENTAL METHODS

2.1 Non-Radioactive Syntheses of Standards and Precursors

The synthetic methods required for each of the non-radioactive fluorinated standards and the precursor compounds are described in each separate chapter. The molecular structures and purities of each compound were verified by a suite of analytical techniques prior to radiochemical and photophysical analyses. NMR analyses were performed using a Bruker Spectrospin 400 MHz UltraShield NMR spectrometer. Fourier transform infrared (FTIR) analyses were performed using a Brucker ALPHA-p IR spectrometer. UV-Vis analyses were performed using an Agilent technologies Cary 100 UV-Vis spectrometer. MP analyses were performed using a Stanford Research Systems Optimelt automated MP system with digital imaging processing technology. Low resolution mass spectrometry (LRMS) analyses were performed using a Waters micromass ZQ, equipped with an electrospray ionisation (ESI) source running in positive ionisation mode with the following parameters applied; voltages: 3 kV capillary voltage, 25 V cone voltage for organic molecules or 70 V cone voltage for rhenium complexes (required to dissociate Re–Br & Re–Cl bonds), 5 V extractor voltage and 0.2 V radiofrequency (RF) lens voltage; Temperatures: 45 °C source temperature and 300 °C desolvation temperature; and gas flows: 350 $L.h^{-1}$ desolvation nitrogen gas flow and 90 $L.h^{-1}$ cone nitrogen gas flow. Samples for HRMS were sent to the mass spectrometry user resource and research facility at the University of Wollongong and samples for EA were sent to the Campbell Microanalytical Laboratory at the University of Otago. All synthetic reagents were purchased from Sigma-Aldrich except for trifluoroacetic acid (TFA) and 18-crown-6 ether which were purchased from Alfa Aesar. Any precursor compounds whose syntheses are not described herein were additionally purchased from Bepharm. Finally, all solvents were purchased from Merck and any water used for syntheses and analyses were first purified using a Merck Millipore Milli-Q integral water purification system.

2.2 Assignment of Radiotracer Identities

Radionuclides used in PET diagnostic scans are typically prepared in substantially high molar activities, such that nanomolar to picomolar amounts of the synthesised tracer afford sufficient radioactivity for patient imaging.[72] Most common analytical techniques used in chemistry lack the sensitivity to detect the low picomolar concentrations of the radiotracer produced. Thus, the assignment of radiotracer identities in this study was achieved by equipping a radioactivity detector to a high-performance liquid chromatography (HPLC) instrument, referred to as a radioHPLC. The radioactivity detector was placed in series alongside a photodiode array (PDA) detector to concurrently monitor eluents *via* both channels following injection of the sample. Prior to radiosyntheses, non-radioactive standards of the fluorinated products were injected on the HPLC to determine the retention time *via* the UV-absorbance channel at the PDA detector. Radioproducts whose peaks shared the same retention time *via* radioactivity detection as the non-radioactive standards *via* UV-detection (within a 0.3 min tolerance due to the placement of the detectors) were assigned the same molecular identity. All radiochemical separations were performed on a Chromolith C_{18} reverse phase (RP) monolithic column (Merck 50 × 4.6 mm) demonstrated to have < 8% [^{18}F]fluoride retention in low pH ranges.[73] The standard radioHPLC analyses used in this study consisted of gradient conditions, comprised of water and acetonitrile solvents each containing 0.05% trifluoroacetic acid (TFA) modifier, eluting with a 2 mL.min^{-1} flow rate. The composition of the mobile phase over the 15 min run time is illustrated in Figure 32. The first 3 mins consisted only of 95% water to elute off any residual DMSO or unreacted [^{18}F]fluoride and polar analytes. Thereafter, the composition was ramped from 5% to 95% acetonitrile in water over a period of 7 mins to gradually elute more non-polar analytes as a function of their interaction with the stationary phase. The mobile phase composition was held at 95% acetonitrile for 2 mins to ensure all

remaining lipophilic analytes were eluted from the column and then finally switched back to 5% acetonitrile for 3.5 mins to equilibrate the column in preparation for the subsequent analysis.

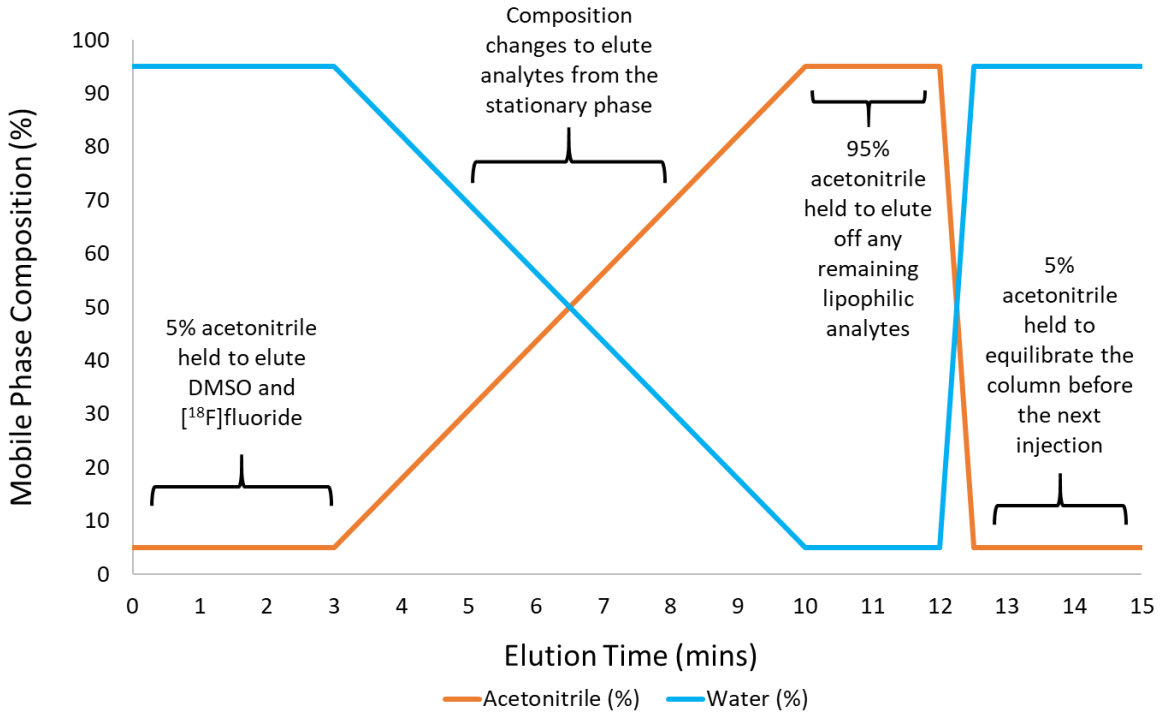

Figure 32. Chromatographic conditions employed for the separation of radioanalytes using a flow rate 2 mL.min^{-1} over a monolithic C_{18} stationary phase. Both water and acetonitrile mobile bases contained 0.05% TFA modifier in solution. 1-3 mins: 95% water held to elute DMSO and unreacted [^{18}F]fluoride. 3-10 mins: gradient switched from 5% to 95% acetonitrile to elute analytes from the stationary phase. 10-12 mins: 95% acetonitrile held to elute off any remaining lipophilic analytes. 12.5-15 mins: 95% water held to equilibrate the column before the next injection.

Each of the radioHPLC analyses were carried out on a Shimadzu system comprised of a CBM-20 controller, LC-20AD pump, SIL-20AHT autoinjector, SPD-M20A PDA detector for the UV analyses and a Lablogic Posi-RAM gamma detector for the radioanalyses. The number of counts detected at the radioactivity detector are proportional to the quantity of the fluorine-18 radioisotope, and thus the radioproduct, as reflected in Equation (3). Thus, non-isolated radioHPLC derived RCYs were calculated *via* the ratio between the integrated peak area (*pA*)

and integrated chromatographic area (cA) expressed as a percentage, as per equation (12). Calculating the amount of radioactivity incorporated within the tracer as a ratio of the total radioactivity, measured in the same instance of time, circumvented the need to correct for decay correction within this equation (assuming negligible loss of radioactivity during the 15 min duration of the HPLC method).

$$RCY = (pA)(cA)^{-1}(10^2) \tag{12}$$

Further confirmation was also achieved, where necessary, by analysing the same samples using thin layer chromatography (TLC) technique. The standard conditions used for these radioTLC analyses involved separation of the radioanalytes on normal phase (NP) silica using an ethyl acetate mobile phase. The radioactive analytes were then imprinted on a phosphor plate and scanned using a PerkinElmer Cyclone Plus phosphor imager to determine the RCYs as per equation (12).

2.3 Automated Radiosyntheses using Microfluidics

Automating reactions is becoming increasingly common in radiopharmaceutical industries which aim to achieve a consistent supply of radiotracers while minimising operating expenses and radiation doses to the chemists involved in production. Assembling such automated synthesisers using microfluidic technologies has a significant number of advantages; namely this reduces costs by using fewer reagents, miniaturises the workstation by occupying less space, improves the molar activity of the final product by reducing the contamination of stable isotopes, affords quicker reaction times due to the smaller volumes requiring heating and is particularly advantageous in the syntheses of products, such as PET radiotracers, where only small quantities are required to be produced.[74] Automated microfluidic systems are also especially valuable in radiochemical research whereupon method development of a radiochemical reaction can be performed multiple times on the same precursor while adjusting one or several parameters in each iteration. Thus, an Advion NanoTek LF Microfluidic Synthesis System was implemented with microfluidic components for the radiosyntheses described herein. A schematic of the automated system constructed for the purposes of this research is shown in Figure 33. Following production on an IBA Cyclone 18 Twin cyclotron particle accelerator hosted at ANSTO using the $^{18}O(p,n)^{18}F$ nuclear reaction, an aqueous solution of [^{18}F]fluoride in oxygen-18 enriched water was drawn into a syringe by pump 1 (P1) and eluted through a QMA ion-exchange cartridge which traps the [^{18}F]fluoride while disposing of the oxygen-18 enriched water solution for recycling. The entrapment of the [^{18}F]fluoride was monitored *via* the placement of a radioactivity detector in proximity of the QMA cartridge. Thereafter tetraethylammonium (TEA) bicarbonate, dissolved in a solution consisting of 10% water in acetonitrile, was passed through the QMA ion-exchange cartridge to elute off TEA [^{18}F]fluoride. A solenoid valve (SV) was switched, thus redirecting the

solution to an azeotropic distillation vial. This process was monitored by the loss of radioactivity measured by the detector located near the QMA cartridge followed by the sharp increase in signal measured by the radioactivity detector placed near the azeotropic distillation vial. To improve the nucleophilicity of the [^{18}F]fluoride we then azeotropically dried the solution by switching two SVs enabling both a nitrogen gas flow and vacuum into and out of the vial while heating. This reduced the volume of the solution such that it could then be reconstituted in an anhydrous acetonitrile solution supplied from a solvent reservoir plumbed to P1. As much as an 84% w/w content of acetonitrile (boiling point of 82 °C) in water (boiling point of 100 °C) under standard pressure conditions can lower the boiling point of the overall solution down to 76 °C *via* formation of an azeotrope, allowing for efficient removal of water from the system.[75] By repeating the process of reducing and reconstituting the [^{18}F]fluoride in anhydrous acetonitrile at least three times in succession, the TEA [^{18}F]fluoride was found to be sufficiently free of water to perform nucleophilic reactions. The TEA [^{18}F]fluoride was thus dissolved in a volume of anhydrous DMSO supplied from P1 thereafter and aspirated into the syringe of pump 2 (P2), whereupon it was dispensed into the P2 storage loop. The solution could be traced from the loss of radioactivity detected at the distillation vial which correlated with the increase in radioactivity sensed by the detector at the storage loop. Simultaneously the precursor solution was loaded by pump 3 (P3) and dispensed into the P3 storage loop. Both the radioactive and precursor solutions in P2 and P3 storage loops respectively were re-aspirated and dispensed three times over to ensure homogeneity of the solutions. Defined volumes of the radioactive and precursor solutions were then concurrently passed through a 15.6 μL microreactor made of fused silica tubing which was coiled tightly into a brass rig containing a thermoresistant polymer to hold the tubing in place. A defined temperature and flow rate were then programmed into the Discovery Mode of the NanoTek software (V1.4.0 GMP Lite) for

each reaction, the latter of which determined the reaction time (t) as defined by equation (13) per volume (V) of solution.

$$t_{reaction} = V\left(\frac{dV}{dt}\right)^{-1} \tag{13}$$

Applying the standard flow rate of 20 µL.min^{-1}, used in most reactions herein, to the 15.6 µL volume of the microreactor, for instance, afforded reaction times of 47 s. The radioactivity was monitored *via* the final detector in the set-up as the solution eluted through and out of the microreactor before finally dispensing in the final product vial for subsequent gamma counting and analyses by radioHPLC and/or radioTLC.

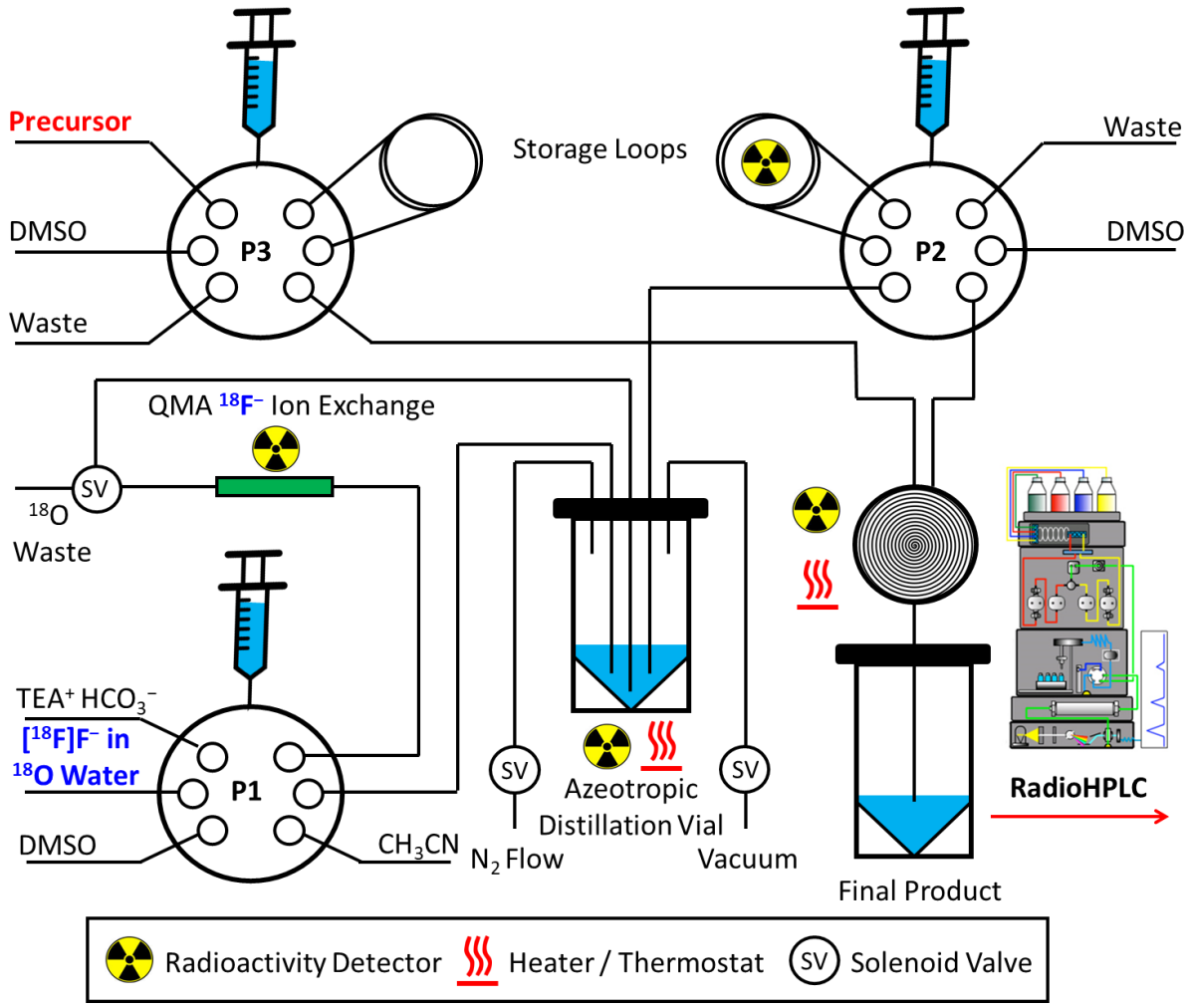

Figure 33. Automated synthesis module assembled for drying and reacting the cyclotron produced [^{18}F]fluoride solution with a precursor for subsequent analysis.

The reaction was likewise monitored *via* the pressure profiles, of which an example is shown in Figure 34. An increase in pressure was observed as P2 and P3 delivered their respective [^{18}F]fluoride and precursor solutions from the storage loop to the microreactor. Thereafter a valve in P2 was switched, thus pumping DMSO to push the [^{18}F]fluoride and precursor solutions through the microreactor where they were heated and reacted under laminar flow regime. It is worth mentioning that no active quenching was applied here to avoid introducing further reagents to the solution and as rapid cooling may have exerted excessive pressure on the pumps. After pumping the precursor solution, the pump valve was turned away from the reactor thus relieving P3 of pressure, whereas P2 maintained its pressure as it supplied inert DMSO solution to push the reaction bolus from the microreactor. After the reaction bolus exited the heated microreactor the flow rate was increased (typically to 150 $\mu L.min^{-1}$) to quickly transfer the resulting radiotracer solution to the final product vial. The increase in flow rate created greater back pressure, particularly at lower temperatures due to the high viscosity of DMSO, though exhibited a characteristic sharp dip in pressure as P2 momentarily paused to adjust to the newly set transfer rate. Ensuring the same pressure profile was observed between each radiolabelling experiment was imperative as it confirmed that the same reaction environments were being consistently maintained.

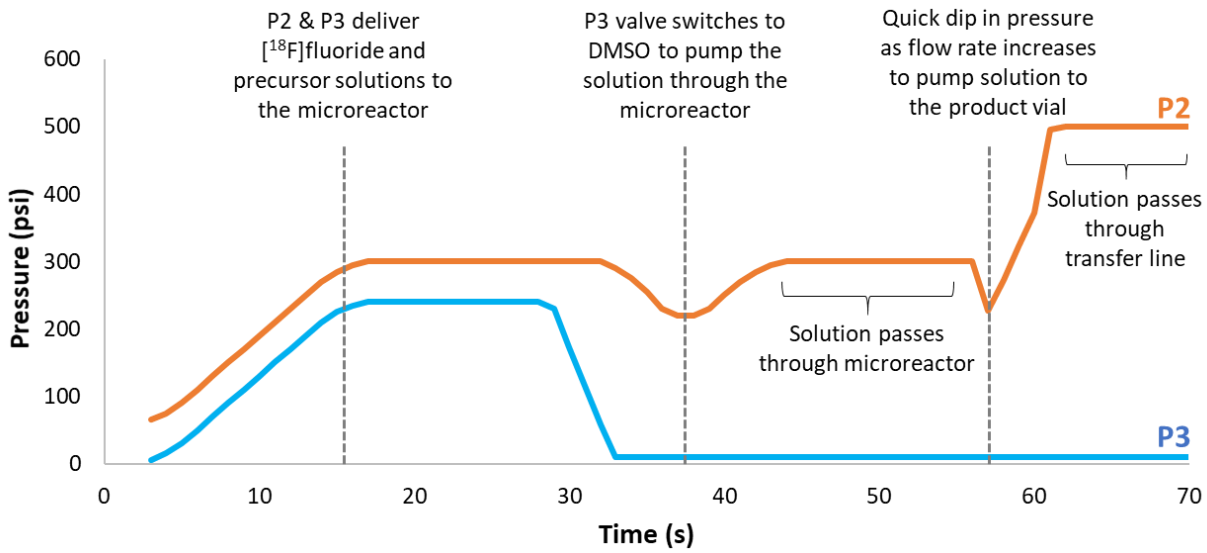

Figure 34. Pressure profiles observed in between radiolabelling reactions for P2 supplying the [^{18}F]fluoride solution and P3 supplying the precursor solution. This consistent pressure profile was maintained during each experiment to ensure the repeatability of each reaction.

2.4 Photophysical Analyses of Quantum Yields and Lifetimes

The photophysical analyses were performed using an Edinburg FLS980 photospectrometer. Following confirmation of the excitation wavelength for the $d\pi \rightarrow \pi^*$ transition to the MLCT excited state using UV-vis spectroscopy, emission scans of the rhenium complexes were subsequently performed on the same solution with the excitation wavelength set to the MLCT absorption maxima. The excitation light was emitted from a 450 W xenon arc lamp source and passed through a monochromator to selectively filter the excitation wavelength. Integration of the emission spectrum then provided an area representative of the number of emitted photons. The process was repeated with a reference standard, tris(bipyridine)ruthenium(II) chloride ($[Ru(BiPy)_3]Cl_2$), in an aqueous solution of known quantum yield (0.028). By substituting the quantum yield (ϕ) of the reference solution as well as correction factors for the integrated area of the emission spectra (I), absorbances of the solutions at the MLCT excitation wavelengths (A) and the refractive indices of the solvents (n) for both the reference and the analyte solution into equation (14) the quantum yield of the rhenium complexes were able to be determined.

$$\phi = \phi_r \left[\frac{(I)(A_r)(n^2)}{(I_r)(A)(n_r^2)}\right] \tag{14}$$

The luminescent lifetimes were determined using time-correlated single photon counting (TCSPC) to detect emissive photons with picosecond resolution. Excitation was achieved using a 377 nm pulsed picosecond light emitting diode (LED) and photon counting was performed after each iteration of the pulsed excitation. The goodness of fit of the attained data was assessed by minimising the reduced chi-squared (χ^2) function and by visual inspection of the weighted residuals.

CHAPTER THREE

RHENIUM-PHENANTHROLINE RADIOFLUORINATION TO CIRCUMVENT AZEOTROPIC DISTILLATION

3.1 Initial Rhenium Radiofluorination Strategies and Non-Radioactive Syntheses

Towards testing the hypothesis that a rhenium complex could be labelled with the fluorine-18 radioisotope for PET-optical imaging, initial radiolabelling experiments were trialled to directly radiofluorinate the rhenium centre. Verifying the identity of the radioproduct first required the synthesis of a non-radioactive standard as shown by the Re–F bond in Figure 35. While analogues of this product had been reported by Horn, *et al.* in the Australian Journal of Chemistry, the authors also noted that such complexes were particularly unstable and would consistently polymerize to form the non-luminescent $[Re(CO)_3F]_4.4H_2O$ tetranuclear cluster instead.[76,77] No Re–F bonds of tricarbonyl complexes had been published since. Indeed, all attempted syntheses of fluorinated rhenium tricarbonyl centres bearing phenanthroline ligands performed within the scope of this thesis work were found to be unsuccessful, despite employing a range of fluorinating media and reaction conditions. Thus, an alternative synthetic target was conceived which involved appending the fluorine atom to the phenanthroline ligand as shown in Figure 35.

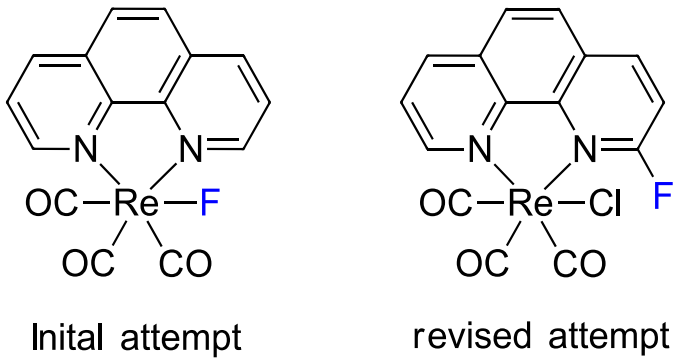

Figure 35. Initial attempt of fluorinating the rhenium centre (left) proved to be unsuccessful, thus leading to the revised attempt to fluorinate the phenanthroline ligand (right).

The revised fluorinated standard, tricarbonylchloro(2-fluoro-1,10-phenanthroline)rhenium(I) (**Re2FPhen**), was synthesised *via* the scheme depicted in Figure 36. In brief, N-oxidation of 1,10-phenanthroline (**Phen**) afforded 1,10-phenanthroline-N-oxide (**Phen-NO**) based on literature examples.[78-80] Thereafter, generation of a Vilsmeier reagent from DMF and phosphorous(V) oxychloride allowed for selective chlorination *ortho* to the oxidised nitrogen atom of **Phen-NO**, thus forming 2-chloro-1,10-phenanthroline (**2ClPhen**). Nucleophilic aromatic substitution of **2ClPhen** using fluoride in the presence of a phase transfer catalyst then yielded 2-fluoro-1,10-phenantholine (**2FPhen**), which was then complexed to a source of rhenium to afford the desired **Re2FPhen** non-radioactive standard. Tricarbonylchloro(2-chloro,1,10-phenanthroline)rhenium(I) (**Re2ClPhen**) was envisioned to also be a precursor which, if successfully radiolabelled, would eliminate the need for a multiple step radiosynthesis. The synthesis of **Re2ClPhen** was likewise achieved by complexing **2ClPhen** to a source of rhenium.

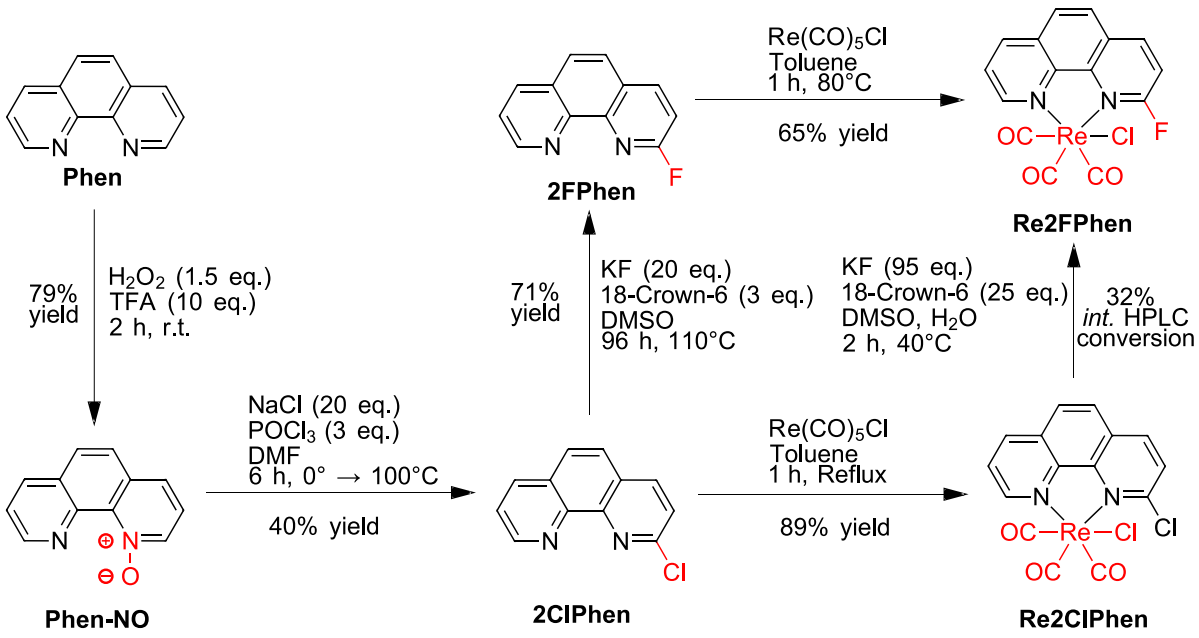

Figure 36. Synthetic route used to synthesise the desired radiolabelling precursor **Re2ClPhen** and the fluorinated standard **Re2FPhen**, annotated with the optimal reaction conditions discovered and the corresponding yields for each reaction.

3.1.1 Imine Oxidation of 1,10-Phenanthroline

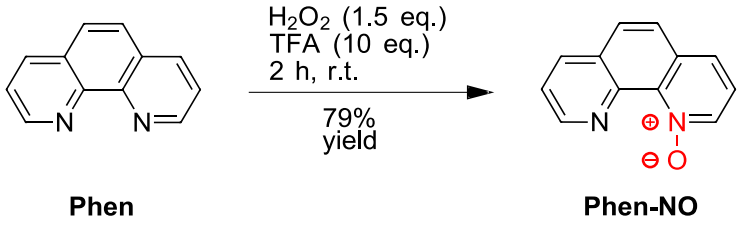

Figure 37. Ideal reaction conditions discovered to afford **Phen-NO** from **Phen** in 79% yield.

A volume of TFA (42.8 mL, 554.9 mmol, 10.0 eq.) was slowly added to a mass of **Phen** (10.0 g, 55.5 mmol, 1.0 eq.). The dissolution of **Phen** in TFA was exothermic and temperature monitoring was employed to ensure that the reaction mixture did not exceed 30 °C to avoid the formation of a 1,10-phenanthroline-*N*,*N*-dioxide by-product. Upon cooling the reaction mixture to 5 °C on an ice bath, hydrogen peroxide (30% w/v, 9.4 mL, 83.2 mmol, 1.5 eq.) was added drop wise and the solution was stirred at room temperature for 3 hours. A volume of sodium hydroxide solution (150 mL, 6 mol.L^{-1}) was then added to adjust the solution to pH 9 while the temperature was kept below 20 °C, which resulted in the formation of a white solid. The solution was filtered and then extracted with DCM (6 x 100 mL). The organic extracts were combined, dried over magnesium sulphate, vacuum filtrated and evaporated under reduced pressure to yield a white solid. The crude product was purified *via* hot filtration recrystallisation from ethanol, yielding off-white crystals (8.630 g).

Initial synthesises of this compound did not account for the exothermic dissolution of **Phen** in TFA solvent, nor the exothermic addition of hydrogen peroxide. For these reasons an additional eluting compound, suspected to be the 1,10-phenanthroline-*N*,*N*-dioxide by-product based upon literature reports,[81, 82] was shown to elute in quality control (QC) HPLC analyses, as shown in Figure 38. The formation of this by-product prevented sufficient recovery of the

desired **Phen-NO** compound, affording no greater than 45% yield until repeated under cold conditions. Nonetheless, purification of **Phen-NO** from this by-product was still able to be achieved by recrystallisation from hot ethanolic solvent.

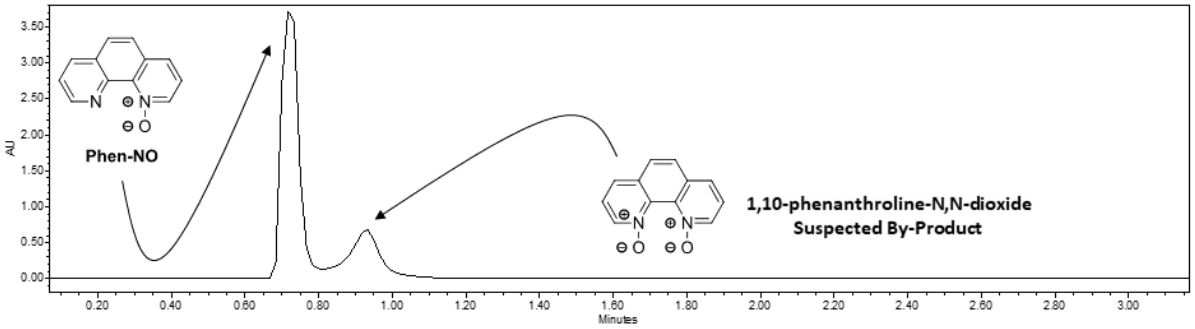

Figure 38. HPLC chromatogram depicting the formation of a suspected 1,10-phenanthroline-N,N-dioxide by-product (*approx.* 0.9 mins) forming from the N-oxidation of **Phen** to obtain **Phen-NO** (*approx.* 0.75 mins). PDA detection wavelength was 254 nm. Separation performed using a water/acetonitrile gradient mobile phase on a C_{18} stationary phase column.

Confirmation of the **Phen-NO** product was easily assessed by ^{1}H-NMR due to the loss of symmetry which now formed eight unique proton environments, unlike the four unique proton environments exhibited in the C_{2V} point group of **Phen**. Figure 39 illustrates the aromatic region of the ^{1}H-NMR spectrum for **Phen-NO**, with peak area integrations which approximate the eight expected protons. The same loss of symmetry is reflected also in the ^{13}C-NMR spectrum, shown in Figure 40, which similarly exhibits twelve carbon signals rather than six, due to the loss of molecular symmetry. Figure 41 depicts the LRMS spectrum which further attests to the formation of **Phen-NO**, given an observed *m/z* ratio of 197.27 against the calculated 197.07. This was additionally backed up by HRMS results in Figure 42 which provided several signals for *m/z* ratios, arising from protonation of the molecule (*m/z* 197.07094 calculated *vs. m/z* 197.07108 observed (Δ 0.71 ppm) for $[M+H]^+ = C_{12}H_9N_2O^+$); protonation with subsequent loss of oxygen (*m/z* 181.07657 calculated *vs. m/z* 181.07615 observed (Δ 2.30 ppm) for $[M+H-O]^+ = C_{12}H_9N_2^+$); and loss of oxygen and hydrogen atoms (*m/z* 179.06092

calculated *vs.* 179.06052 observed (Δ -2.23 ppm) for $[M\text{-}OH]^+$ = $C_{12}H_7N_2^+$). Further confirmation was attained in the FTIR spectrum, which exhibited weak absorption bands at 3060 and 3008 cm^{-1} for the expected C–H bond stretches exhibiting sp^2 hybridised orbitals, alongside absorption peaks at 1519, 1411 and 1335 cm^{-1} corresponding to the C=C π-aromatic bond stretches of the phenanthroline ring. Hartree-Fock calculations were performed to assign the IR band associated with N–O bond stretching, with an input generated by first constraining an initial **Phen-NO** structure (with formal changes of +1 and -1 applying to the N and O atoms of the N-oxide respectively) *via* the Merck Molecular Force Field 94 (MMFF94) using the steepest descent algorithm (2000 steps, 10E-10 convergence) to attain the required Z-matrix. Geometry optimisation, followed by frequency optimised restricted Hartree-Fock (RHF) calculations, were then applied using the split-valance polarization def2-SVP basis set, a restricted self-consistent field (SCF) of normal accuracy, and the RijCosX approximation to reduce computational demand. The computation revealed a strong N–O stretching frequency at 1474 cm^{-1} (coupled with other C=C and C–H vibrational modes), which roughly matches the observed IR absorption band at 1432 cm^{-1} given similar amplitudes and the accuracy of the quantum modelling performed. The experimental and theoretically obtained spectra can be viewed in Figure 43 and Figure 44, respectively.

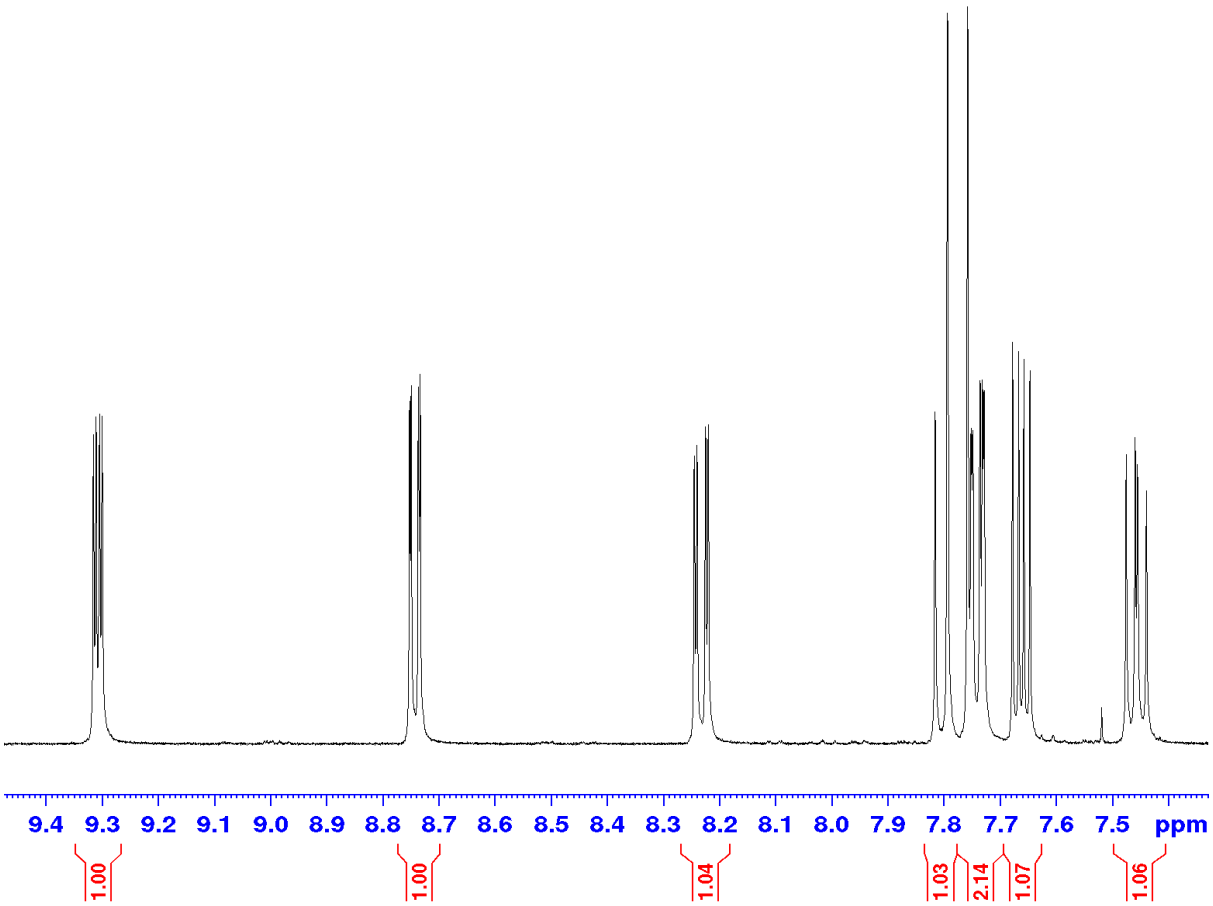

Figure 39. ^{1}H-NMR spectrum of **Phen-NO**, showing the expected peak area integration for eight protons in the aromatic region.

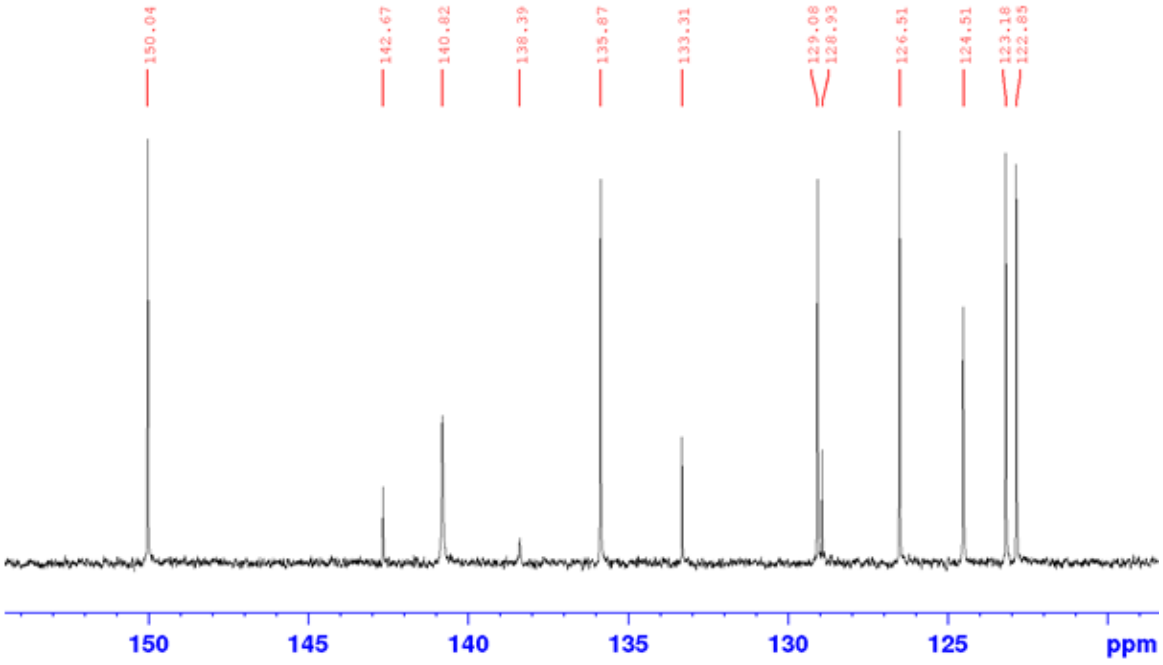

Figure 40. ^{13}C-NMR spectrum of **Phen-NO**, showing the expected twelve carbon signals in the aromatic region.

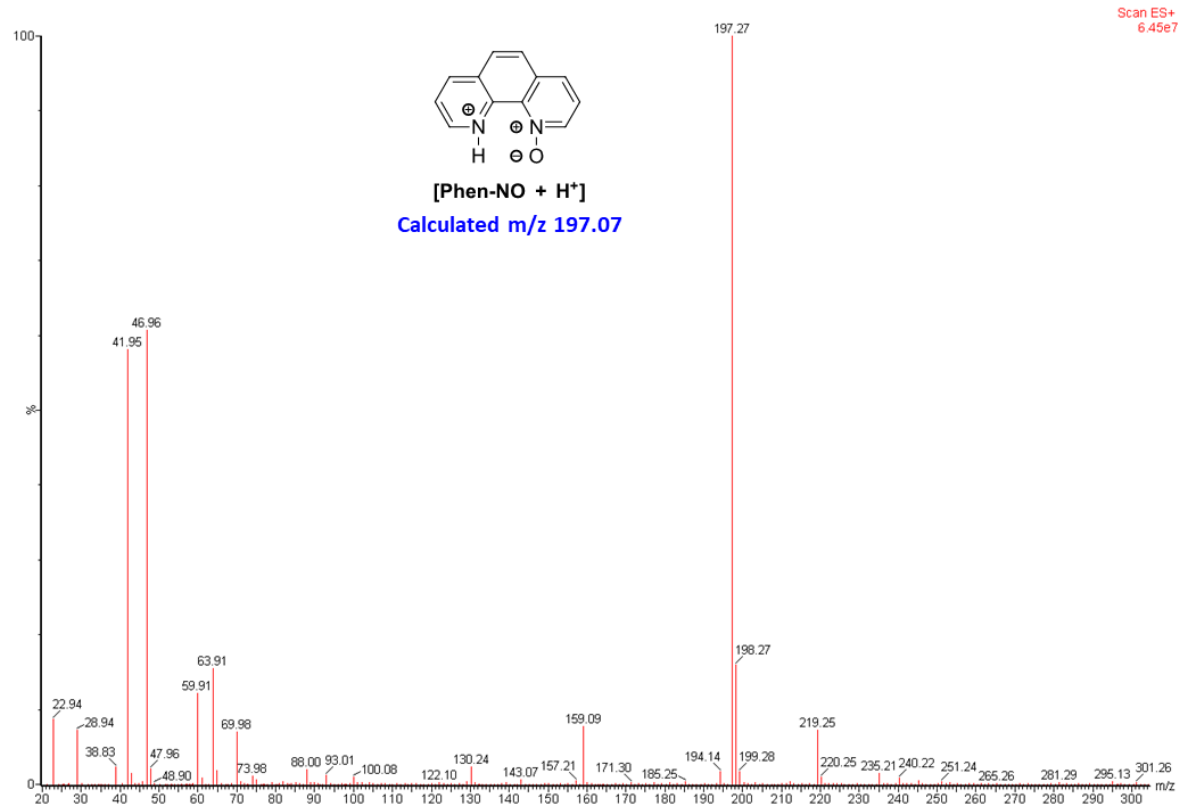

Figure 41. LRMS spectrum showing the major observed *m/z* ratio of 197.27, which corresponds with the protonated analogue of **Phen-NO** having a calculated m/z ratio of 197.07.

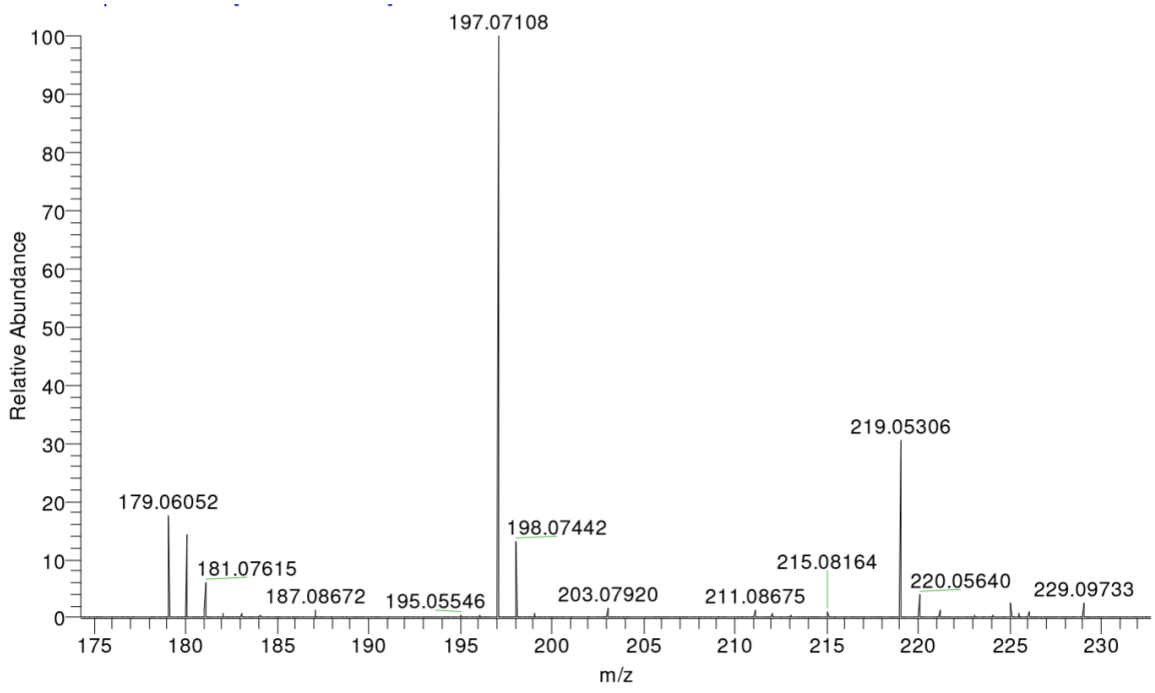

Figure 42. HRMS spectrum complimenting the LRMS data of **Phen-NO** by showing more detailed *m/z* ratios for alternative ions; such as the expected $[M+H]^+$ *m/z* ratio of 197.07108 (Δ 0.71 ppm), the $[M+H-O]^+$ *m/z* ratio of 181.07615 (Δ 2.30 ppm) and $[M-OH]^+$ *m/z* ratio of 179.06052 (Δ -2.23ppm).

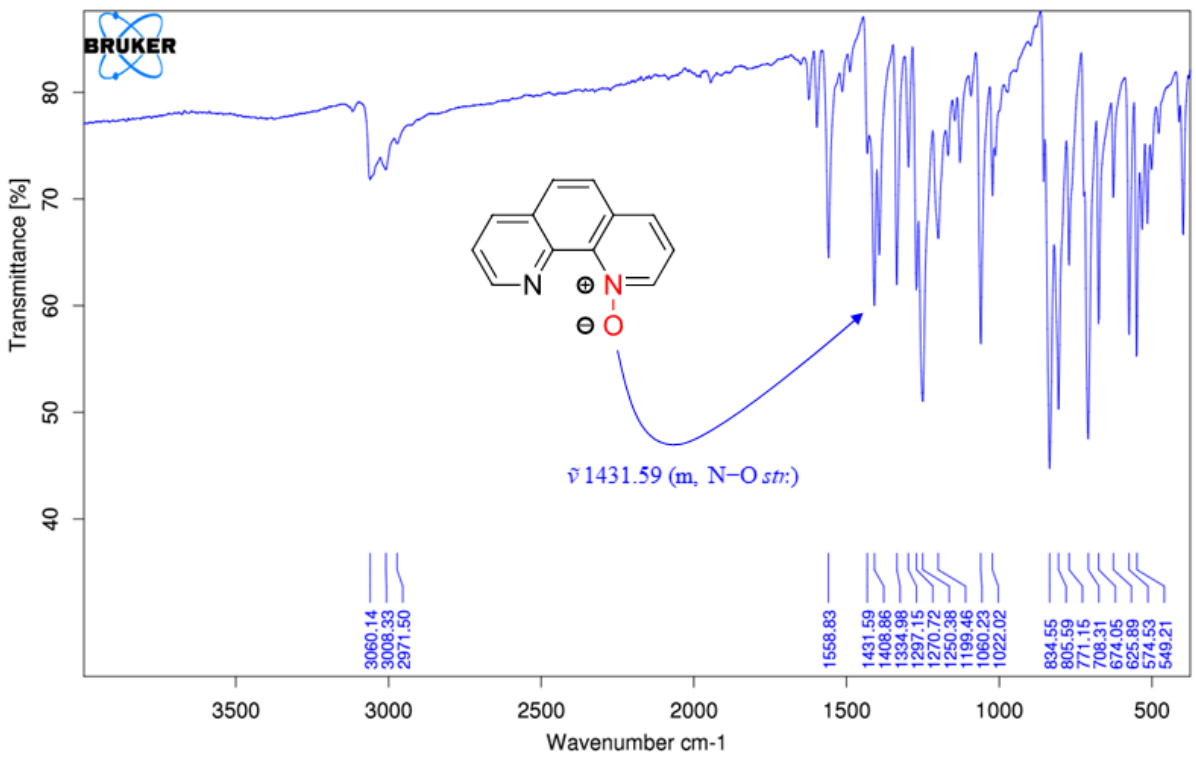

Figure 43. FTIR spectrum of PhenNO, showing the IR absorption band for the N−O stretching frequency at 1432 cm^{-1}, as determined from theoretical RHF geometry and frequency optimisation calculations, alongside distinctive C−H vibrational excitations at higher wavenumbers (3060 cm^{-1} & 3008 cm^{-1}).

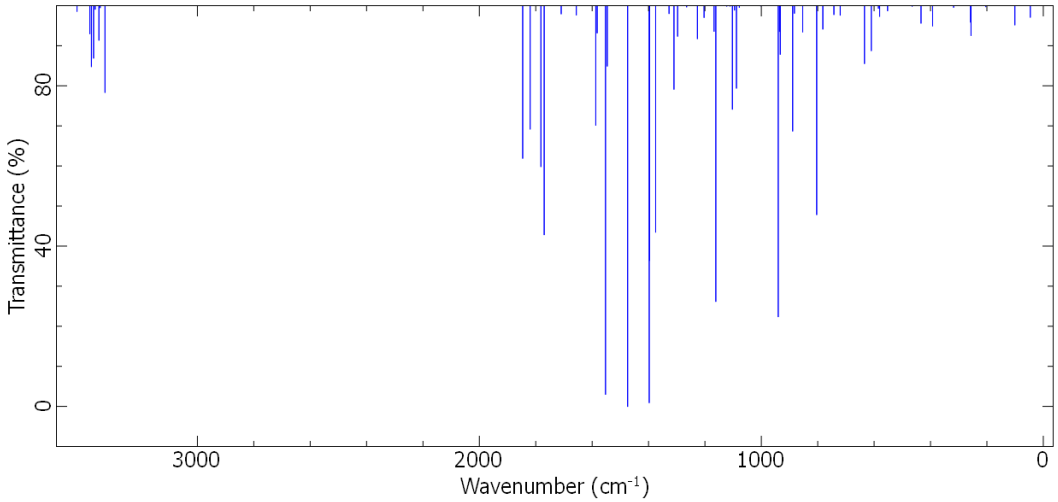

Figure 44. Theoretical IR spectrum for **Phen-NO** calculated from RHF quantum modelling using geometry and frequency optimisation methods with the def2-SVP basis set to determine the stretching frequency of the N-O bond (calculated as 1474 cm^{-1}).

3.1.2 Attempted Coordination of 1,10-Phenanthroline-N-Oxide to a Rhenium Pentacarbonyl Complex

To by-pass the chlorination step, we hypothesised that complexing the **Phen-NO** ligand to the rhenium would enable a single step fluorination of the complex. Acetonitrile was used as the solvent, as it was hypothesised that displacement of the carbonyl ligands by the solvent at high temperatures may aid in the complexation of the oxygen atom in the *N*-oxide functional group, based off literature examples. Intriguingly however, NMR spectroscopic data revealed that **RePhen** formed instead of **RePhen-NO**. A summary of this discovery is shown in Figure 45.

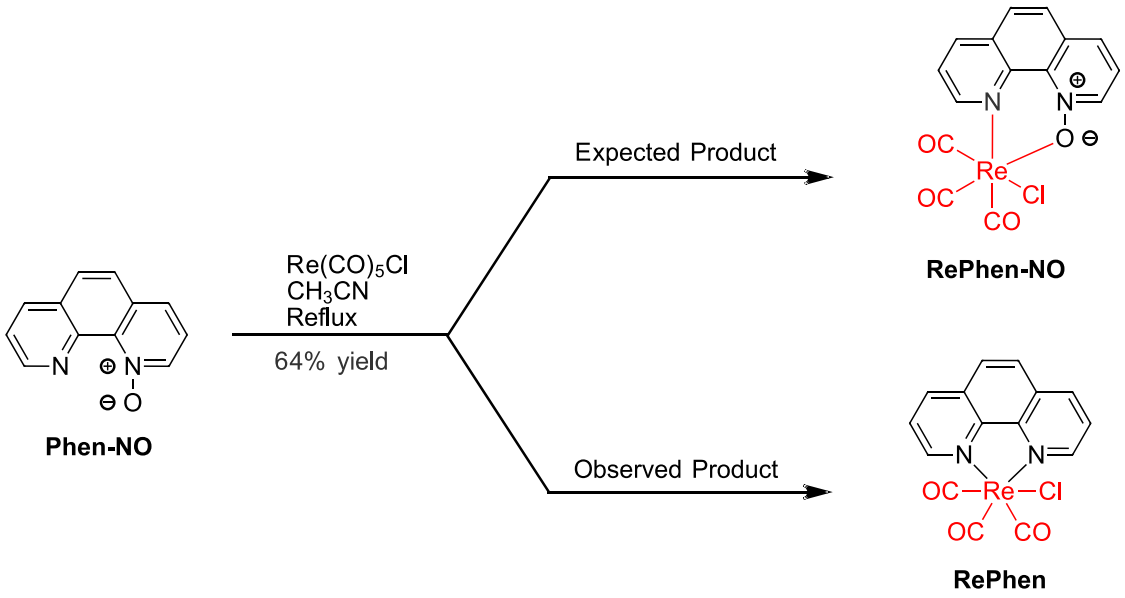

Figure 45. Complexation of **Phen-NO** to pentacarbonylchlororhenium(I) was hypothesised to form the **RePhen-NO** complex *via* co-ordination through the nitrogen atom of the imine, and the oxygen atom of the oxide. However, it was instead discovered that **RePhen** formed.

3.1.3 Chlorination of 1,10-Phenanthroline-*N*-Oxide *via* a Vilsmeier Reagent

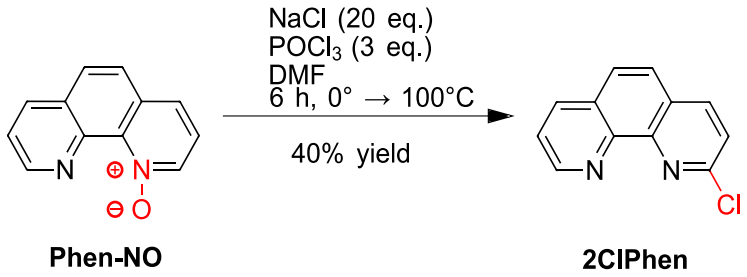

Figure 46. Ideal reaction conditions which afforded **2ClPhen** from **Phen-NO** in 40% yield.

A mass of **Phen-NO** (2.000 g, 10.194 mmol, 1.0 eq.) and sodium chloride (11.910 g, 203.799 mmol, 20.0 eq.) were suspended in a volume of anhydrous DMF (35 mL). A volume of phosphorus(V) oxychloride (2.8 mL, 30.6 mmol, 3.0 eq.) was added drop wise while the reaction temperature was kept below 10°C. The reaction was then heated to 100°C while stirring under a constant stream of nitrogen gas for 8 hours, during which time the solution turned from white to yellow to brown in colour. The reaction was then added to a volume of water (200 mL) and adjusted to pH 9 via the addition of ammonia solution (25% w/v). The solution was then extracted with chloroform (10 x 100 mL), whereupon the organic extracts were combined and then washed with water (8 x 100 mL). The organic layer was then filtered to remove brown particulates, dried over sodium sulphate and the chloroform removed under reduced pressure to yield a light yellow solid. The crude **2ClPhen** was then dissolved in DCM (20 mL) and purified *via* NP chromatography using a silica column (330 g, 40 µm). Using an AB solvent system where A = Ethyl Acetate and B = Hexane, and a 55 mL.min^{-1} flow rate; a gradient was then applied where B% was ramped from 10% to 30% over 2.3 CV, from 30% to 70% over 3.3 CV, from 70% to 76% over 1.1 CV and finally from 76% to 100% over 8.7 CV. The eluents absorbing at a wavelength of 254 nm were combined and evaporated down under reduced pressure to yield a purified product. Further purification was achieved by dissolving

the product in a volume of methanol/acetonitrile (3:1, 10 mL) and performing a series of 100 µL injections via RP preparative HPLC, whereby an Alltima C_{18} column (10 µm, 250 x 22 mm) was employed alongside an isocratic mobile phase consisting of 30% acetonitrile and 70% water. A flow rate of 20 $mL.min^{-1}$ was applied. Eluents absorbing at a wavelength of 254 nm were then combined, evaporated down under vacuum to remove excess acetonitrile and finally dried by lyophilisation to yield a white powder (880 mg).

Figure 47 illustrates the proposed mechanism of reaction for the formation of **2ClPhen** from **Phen-NO**. The DMF solvent catalyses the formation of the Vilsmeier reagent, which is believed to enable selective chlorination in the 2-position due to its spatial proximity of the chlorine upon forming an ether group with the oxygen atom from the *N*-oxide. The phosphorus(V) oxychloride is consumed from the reaction, however, and is subject to hydrolysis to hydrochloric and phosphoric acids if not performed under strictly anhydrous conditions. Thus, a three-equivalence molar excess of phosphorus(V) oxychloride was added in order to maintain production of the Vilsmeier reagent during the reaction. Twenty molar equivalence of sodium chloride was also added, as it provided a continuous source of chloride from the biphasic mixture which is a driving force to produce the Vilsmeier reagent, as demonstrated in an early step of the mechanism.

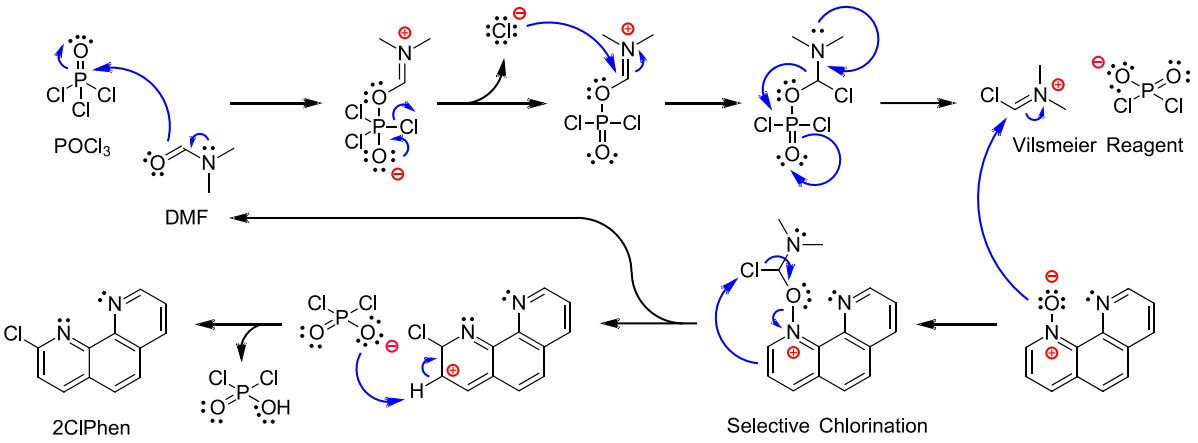

Figure 47. Proposed mechanism for the chlorination of **Phen-NO** to form **2ClPhen**, showing how the Vilsmeier reagent is understood to be formed from DMF and phosphorus(V) oxychloride ($POCl_3$), as well as how the Vilsmeier reagent enables selective chlorination in the 2-position of the molecule.

Confirmation of **2ClPhen** was evident by the integration of seven unique proton environments in the ^{1}H-NMR spectrum of the molecule, as opposed to eight for **Phen-NO**, as one of the hydrogen atoms had been displaced for a chlorine. Figure 48 illustrates this integration of the ^{1}H-NMR spectrum. The ^{13}C-NMR spectrum still exhibited the expected twelve signals as shown in Figure 49, albeit these signals experienced an overall downfield shift with chemical shift ranges between 123 and 152 ppm in the aromatic region. The LRMS spectrum for **2ClPhen** in Figure 50 shows the expected approximate 3:1 ratio of *m/z* signals corresponding to the ^{35}Cl isotope with 75.78% abundance, affording an *m/z* ratio of 215.24 against a calculated *m/z* ratio of 215.04; and the ^{37}Cl isotope with 24.22% abundance, which afforded an *m/z* ratio of 217.24 with a similar mass difference to the calculated *m/z* ratio of 217.04. Identification of the major *m/z* signal was further verified in the HRMS spectrum, shown in Figure 51, for protonation of **2ClPhen** (*m/z* 215.03705 calculated *vs.* *m/z* 215.03726 observed (Δ 0.96 ppm) for $[M+H]^+$ = $C_{12}H_8N_2Cl^+$), alongside the charge-induced loss of a chlorine atom (*m/z* calculated 179.06050 *vs.* *m/z* 179.06092 observed (Δ 2.36 ppm) for $[M-Cl]^+$ = $C_{12}H_7N_2^+$). The FTIR spectrum of **2ClPhen**, shown in Figure 52 shows the distinctive sp^2 hybridised C–H

vibrational stretching frequencies consistent with the hydrogens on the phenanthroline ring, and UV/Vis spectroscopy revealed $\pi \rightarrow \pi^*$ excitations with maxima at wavelengths 266, 229 and 201 nm in acetonitrile, with respective molar absorptivities of 31022, 50456 and 17929 $L.mol^{-1}.cm^{-1}$. Elemental analysis attested to the purity of the ligand by returning experimental compositions of 66.66% carbon, 3.42% hydrogen and 12.95% nitrogen against theoretical values of 67.15% carbon, 3.29% hydrogen and 13.05% nitrogen.

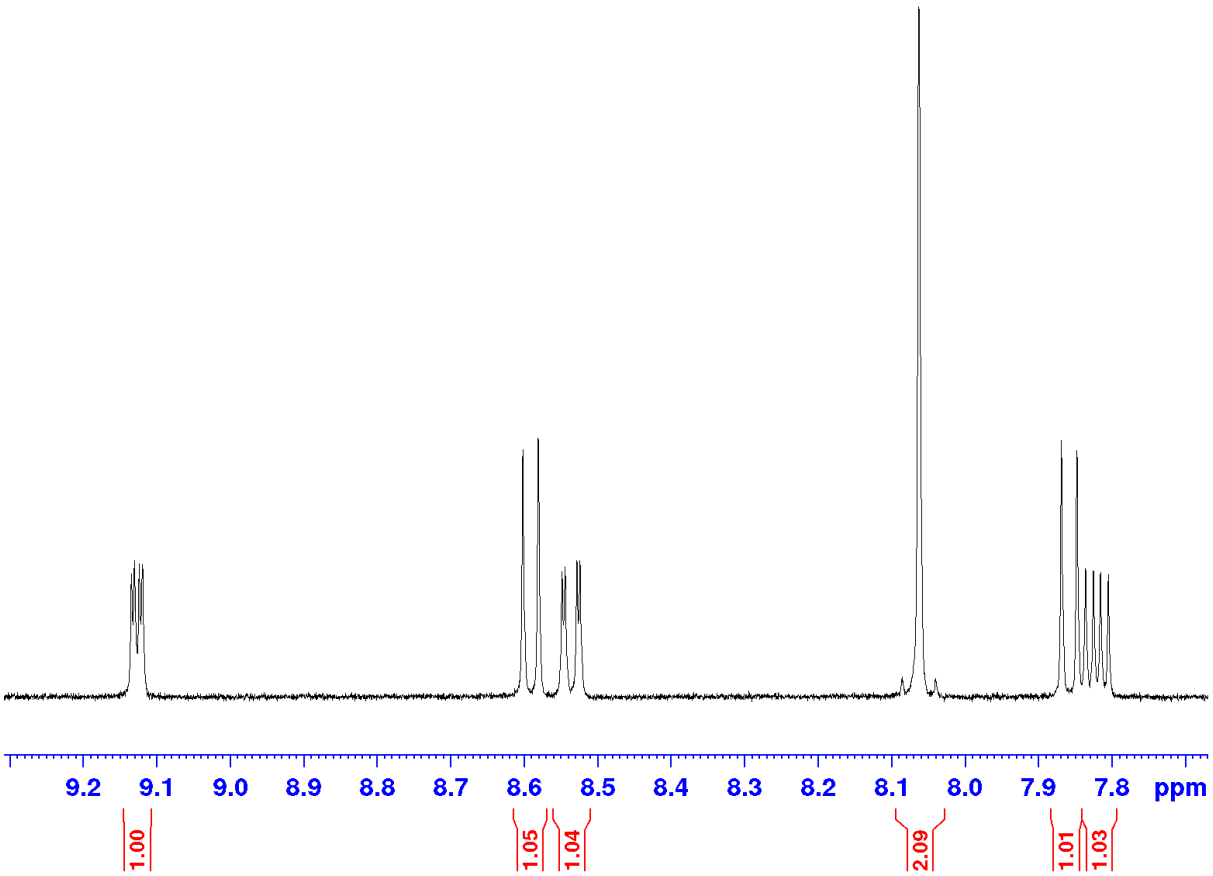

Figure 48. ^{1}H-NMR spectrum of **2ClPhen** in DMSO-d_6, showing the expected peak area integration for seven protons in the aromatic region.

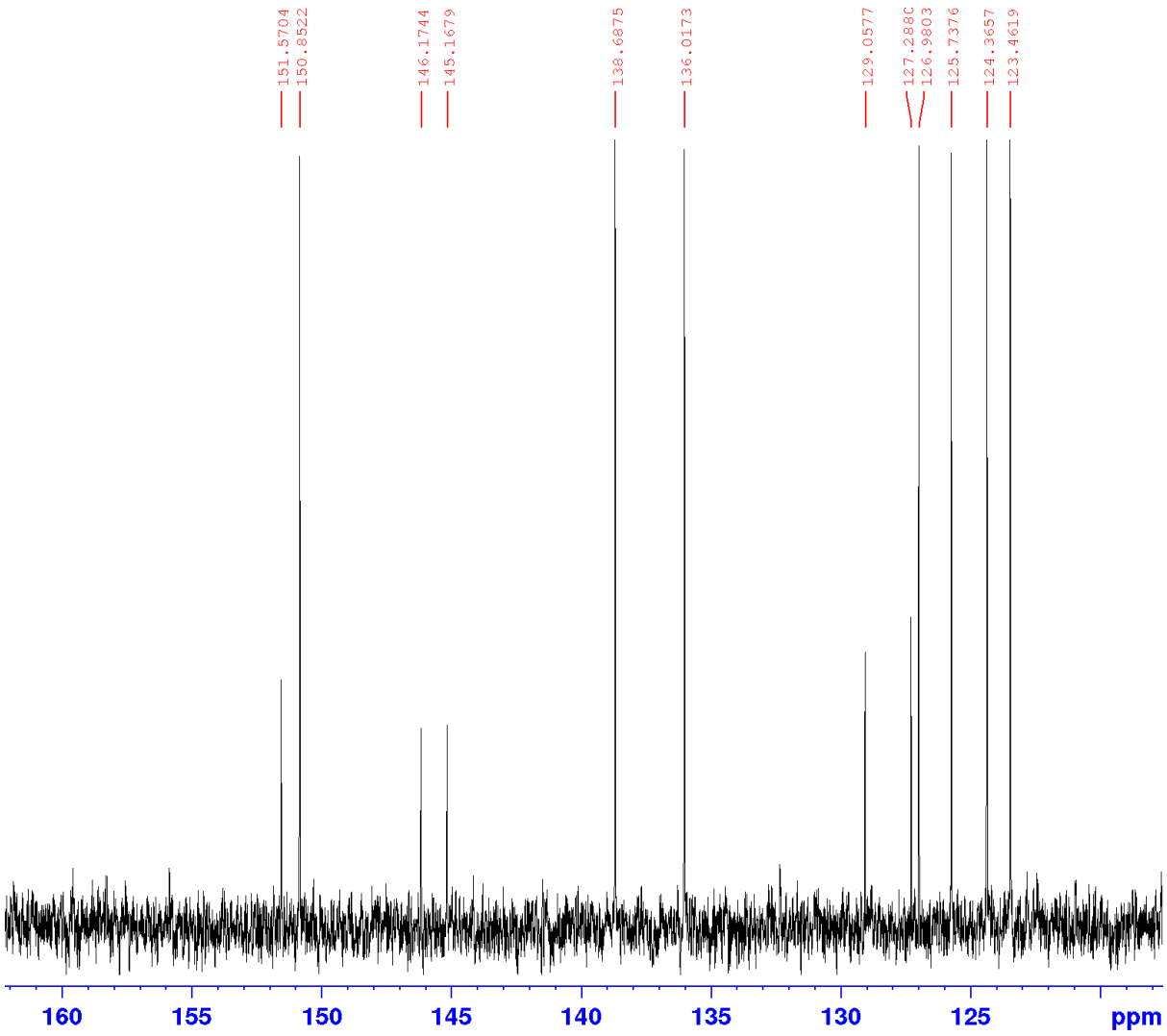

Figure 49. ^{13}C-NMR spectrum of **2ClPhen** in chloroform-d, showing the expected twelve signals for carbon-13 nuclei in the aromatic region.

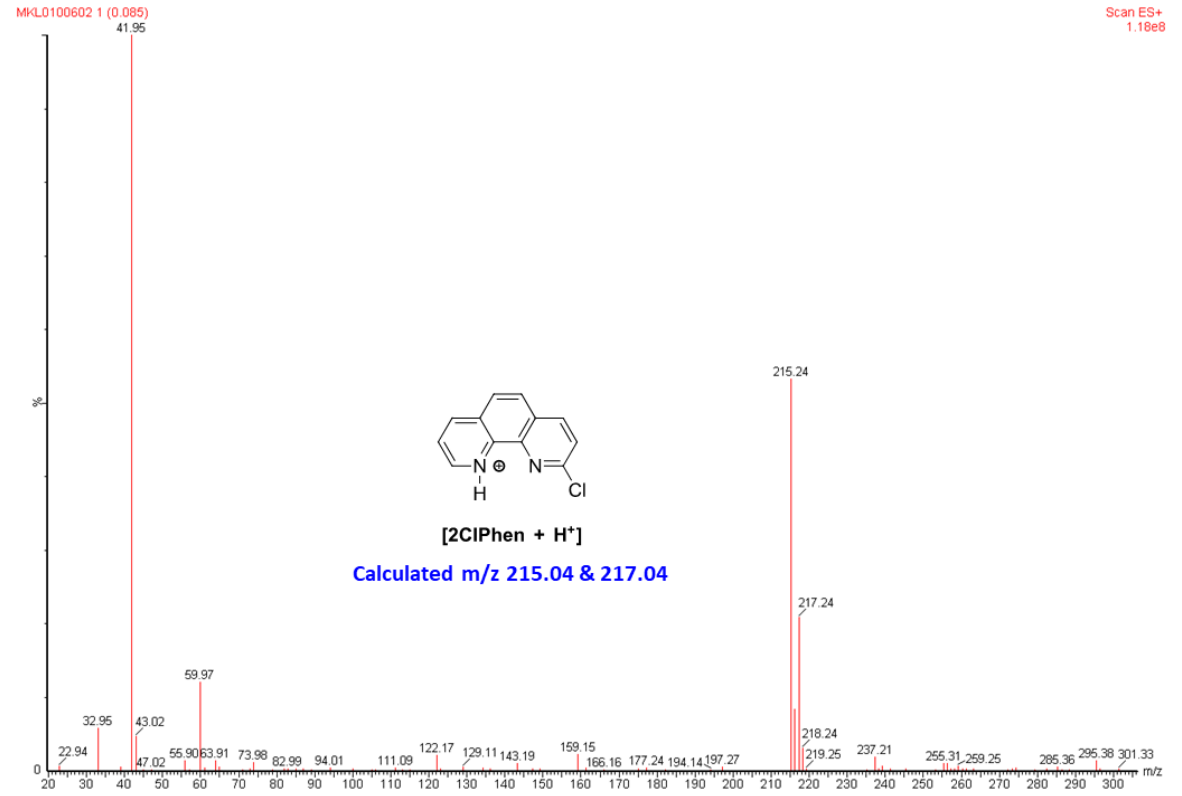

Figure 50. LRMS spectrum showing the major observed m/z ratios of 215.24 and 217.24, consistent with the expected isotopic abundances for ^{35}Cl (75.78%) and ^{37}Cl (24.22%), which correspond with the protonated analogue of **2ClPhen** having calculated m/z ratios of 215.04 and 217.04.

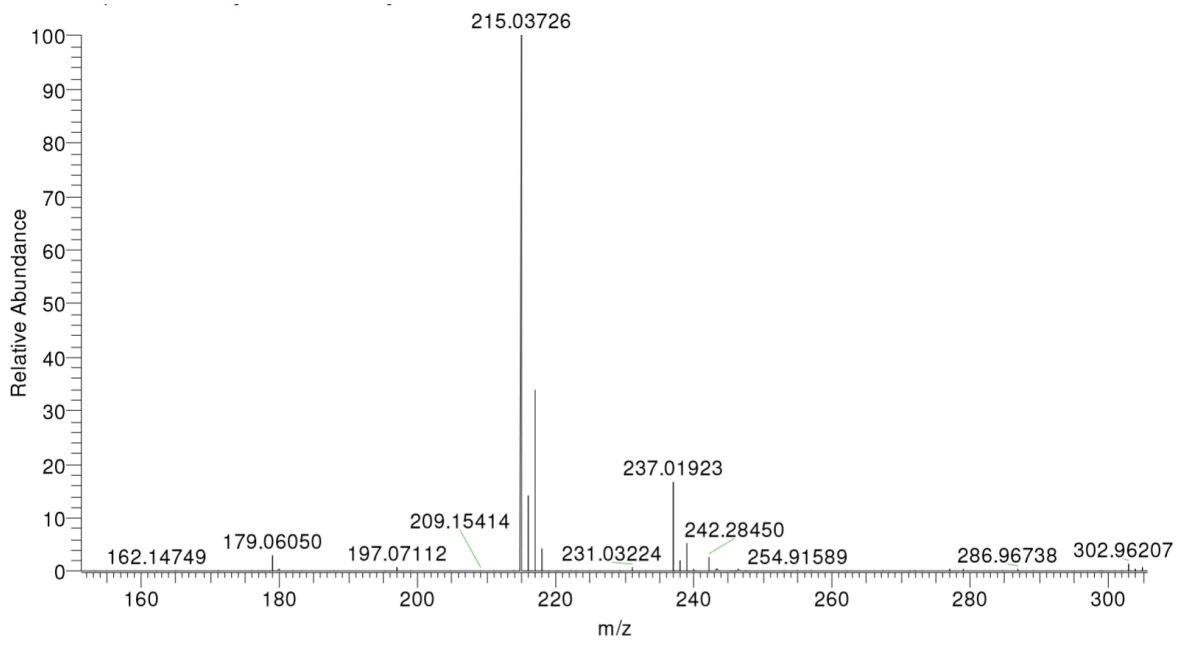

Figure 51. HRMS spectrum further verifying the presence of the major $[M+H]^+$ signal with an observed m/z ratio of 215.03726 against a calculated m/z ratio of 215.03705 (Δ 0.96 ppm). Also present is the $[M-Cl]^+$ signal generated from loss of a chlorine atom, with an observed m/z ratio of 179.06092 against a calculated m/z ratio of 179.06050 (Δ 2.36 ppm).

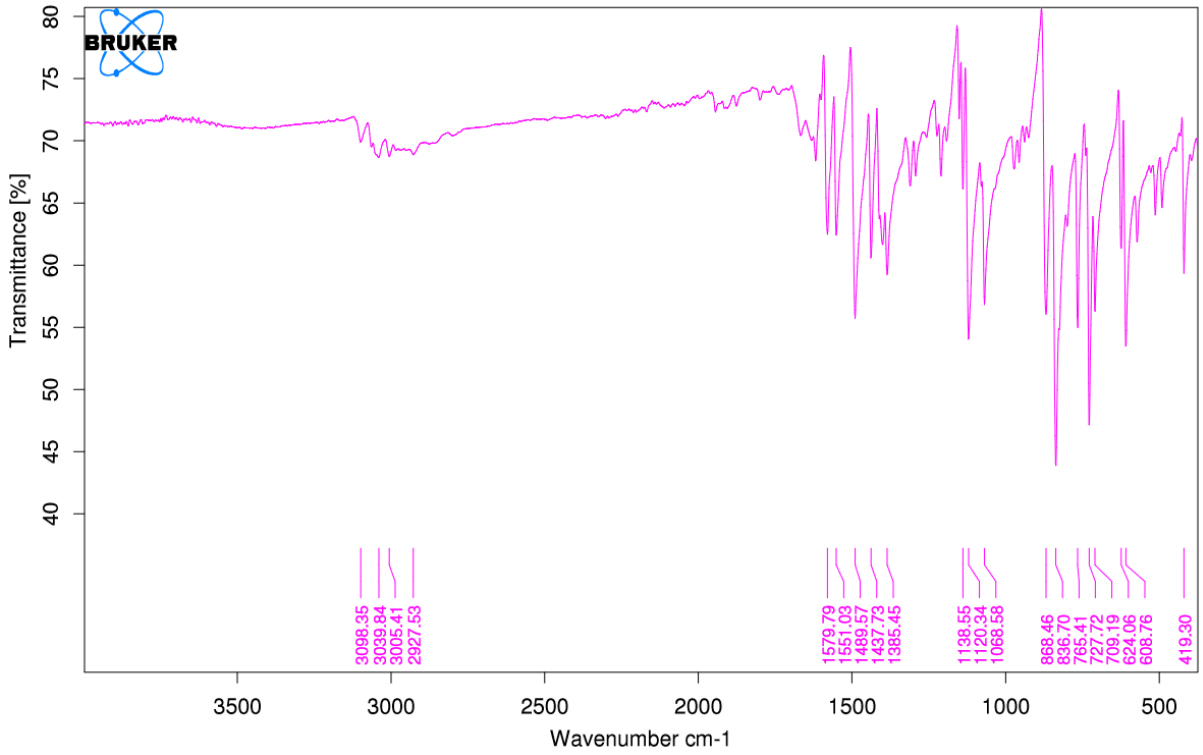

Figure 52. FTIR spectrum of **2ClPhen** showing the distinctive sp^2 hybridised C−H stretching frequencies at higher wavenumbers, representative examples include 3098 cm^{-1} and 3040 cm^{-1}.

3.1.4 Fluorination of 2-Chloro-1,10-Phenanthroline *via* Nucleophilic Aromatic Substitution

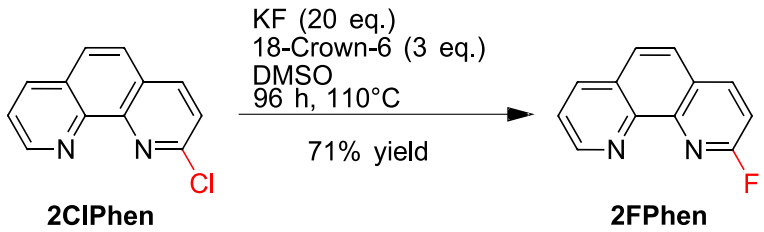

2ClPhen **2FPhen**

Figure 53. Ideal reaction conditions which afforded **2FPhen** from **2ClPhen** in 71% yield.

Masses of 18-crown-6 ether (1.110 g, 4.199 mmol, 3.0 eq.) and potassium fluoride (1.626 g, 28.986 mmol, 20.0 eq.) were azeotropically dried *via* the addition of 20 x 1 mL aliquots of anhydrous acetonitrile while heating at 90°C under a constant stream of nitrogen gas. A mass of **2ClPhen** (300 mg, 1.398 mmol, 1.0 eq.) was then added to the resulting hot crust, followed by a volume of anhydrous DMSO (10 mL). The reaction mixture was then stirred at 110°C for 92 h. Afterwards the reaction was removed from heat and allowed to cool to room temperature. The crude **2FPhen** in DMSO solution was then purified *via* RP chromatography using a C_{18} column (40 g, 40 µm). Using an AB solvent system where A = water and B = acetonitrile, and a 40 mL.min^{-1} flow rate; a gradient was then applied where B% was ramped from 5% to 35% over 6.7 CV, held at 35% for 4.0 CV and then finally ramped from 35% to 100% over 13.9 CV. The fractions with significant absorbance at a wavelength of 254 nm were then combined, evaporated under vacuum to remove excess acetonitrile and finally dried by lyophilisation to yield a white powder (249 mg). Further purification was then achieved by dissolving the product in a volume of methanol (450 µL) and performing a series of 20 µL injections via RP preparative HPLC, whereby an Alltima C18 column (10 µm, 250 x 22 mm) was employed alongside an isocratic mobile phase consisting of 30% acetonitrile and 80% water containing 0.1% TFA modifier, and a flow rate of 25 mL.min^{-1} applied. Eluents absorbing at 254 nm were

then combined, evaporated under reduced pressure to remove excess acetonitrile and then dried *via* lyophilisation to afford a pink salt (the TFA salt of the compound). The pink solid was then reconstituted in water (10 mL) and extracted with DCM (15 x 100 mL). The organic phases were then combined, dried over sodium sulphate for 15 mins, vacuum filtrated and then evaporated under reduced pressure to yield a white solid (196 mg).

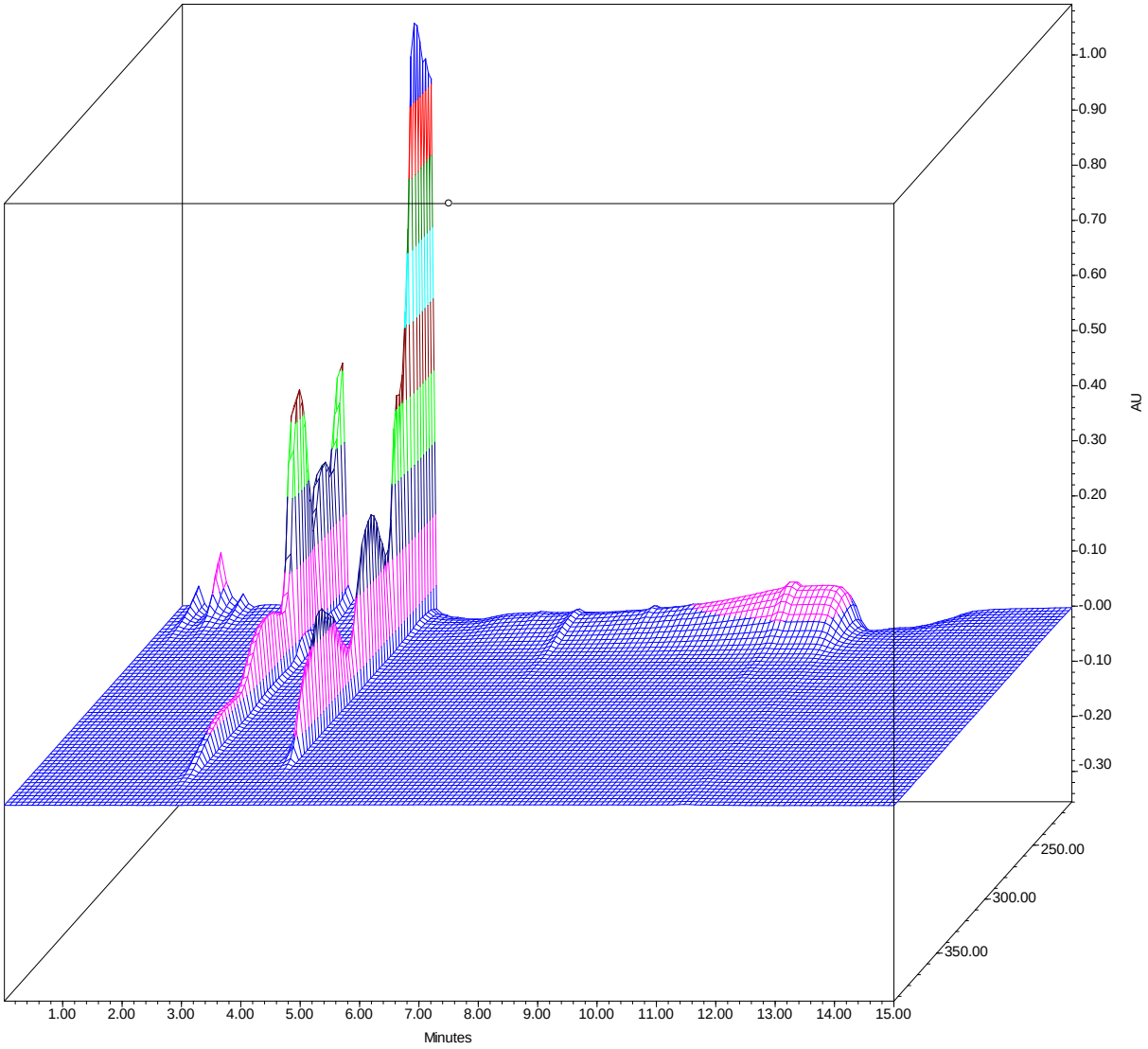

Figure 54. Formation of **2FPhen** (rt = 2.6 mins) from **2ClPhen** (rt = 4.2 mins) *via* HPLC monitoring using PDA detection across multiple wavelengths (200 – 400 nm). Water/acetonitrile gradient mobile phase employed on a C_{18} RP stationary phase.

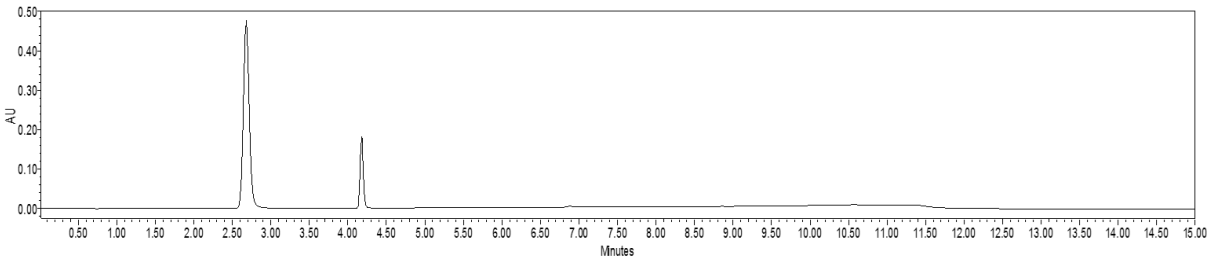

Figure 55. Selective chromatogram at detection wavelength λ = 245nm for fluorination of **2ClPhen** (r_t = 4.2 mins) to form **2FPhen** (r_t = 2.6 mins).

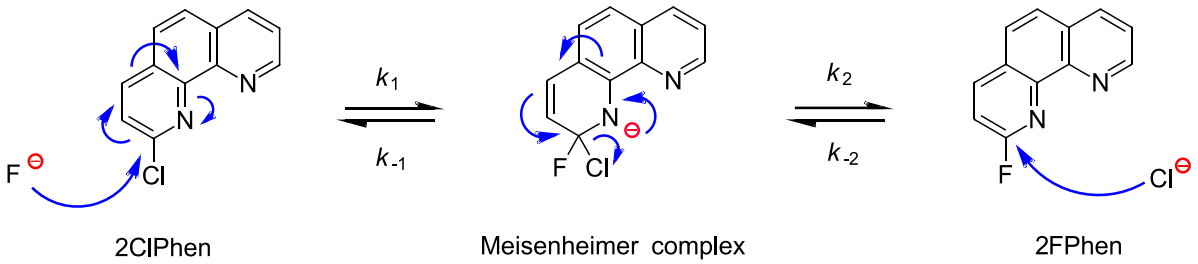

Figure 56. Mechanism for the fluorination of **2ClPhen** to afford **2FPhen** via nucleophilic aromatic substitution. The mechanism involves the formation of a Meisenheimer complex intermediate, which is generated faster from the consumption of **2FPhen** (k_{-2}) than from **2ClPhen** (k_1).

The mechanism in Figure 56 illustrates the competing nucleophilic aromatic substitutions of both chloride and fluoride anions to form the intermediate Meisenheimer complex, alongside the associated qualitative rate constants (k_x). Reactions with rate constants k_1 and k_{-2} are slower processes as they result in the loss of aromaticity, thus requiring higher activation energy barriers. Conversely, the reactions with rate constants k_{-1} and k_2 are faster processes as they restore aromaticity, thus requiring only low activation energy barriers. From a qualitative point of view, k_{-2} is also a slightly larger rate constant than k_1, because the already present fluorine has a greater electron inductive withdrawal effect to stabilise the Meisenheimer complex. Also apparent is that k_{-1} should be slightly smaller than k_2 in theory, because fluoride is typically a poor leaving group given the intramolecular strength of the C−F bond (evident by the lower internal energy of 326.7 KJ.mol^{-1} for **2FPhen** *vs.* 331.7 KJ.mol^{-1} for **2ClPhen** calculated using the steepest descent algorithm with the MMFF94 force field constraint in Avogadro). Thus, in

order of magnitude it can be qualitatively assigned that $k_2 > k_{-1} >> k_{-2} > k_1$. The synthetic challenge this presents is that while the production of **2FPhen** is slightly more favoured than **2ClPhen** when restoring aromaticity, it is still thermodynamically more favourable for **2FPhen** to be consumed than **2ClPhen** to form the Meisenheimer complex, which is the rate-determining step of the reaction. Thus to counter this unfavourable fluorination process, the reaction equilibrium was shifted in favour of consuming the **2ClPhen** reactant by increasing the molar equivalence of fluoride in the system, increasing the reaction temperature to overcome the high activation energy barrier associated with the formation of the Meisenheimer complex, and the reaction left for a considerably long time with daily HPLC monitoring to determine when the reaction had achieved equilibrium. A phase transfer reagent was also used to aid in solubilising the potassium fluoride in the organic DMSO solution. Early attempts at this synthesis applied TBAF as the source of fluorine, however, yields no greater than 7% were able to be attained due to the highly hygroscopic nature of TBAF which reduced the nucleophilicity of the fluoride rendering it less susceptible to nucleophilic aromatic substitution. Improved yields were obtained upon switching to an 18-crown-6 ether phase transfer catalyst instead. Also, of great importance was the need to azeotropically distil the potassium fluoride while immersed in a heated solution of the 18-crown-6 ether to efficiently remove water from the reaction mixture. In the early instances of relying on vacuum techniques to dry the fluoride source, an unintended 1,10-diaza-1H-phenanthren-2-one by-product formed from what was hypothesised to be the reaction between hydroxides generated from the residual water and the 2-chloro or 2-fluoro substituted phenanthrolines, followed by subsequent tautomerisation as proposed by the mechanism shown in Figure 57.

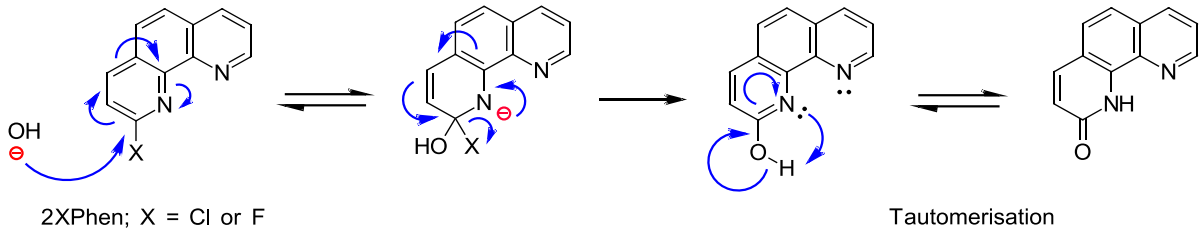

Figure 57. Mechanism for the formation of the hydroxy-substituted by-product in the presence of non-azeotropically distilled conditions, which tautomerises to form 1,10-diaza-1H-phenanthren-2-one.

The water catalysed by-product was isolated and spectroscopically characterised to determine whether the 2-hydroxy-1,10-phenanthroline or 1,10-diaza-1H-phenanthren-2-one tautomerized product had formed. The first confirmation was attained by FTIR spectroscopy, with the spectrum shown in Figure 58. The spectrum provides evidence in favour of the 1,10-diaza-1H-phenanthren-2-one product given the absence of the broad O–H stretching frequency at higher wavenumbers which is characteristic of alcohols, and the presence of both a strong secondary amide N–H amide vibrational band at 3345 cm^{-1} and amide C=O vibrational band at 1654 cm^{-1}, having been shifted to slightly lower wavenumbers due to the resonance stabilisation afforded within the aromatic ring. The ^{1}H-NMR spectrum of the compound also supported the assignment of the 1,10-diaza-1H-phenanthren-2-one by-product by not only integrating for the eight expected ^{1}H nuclei within the molecule, though by also including a broad downfield shifted signal for the ^{1}H nuclear resonance within an N–H bond.

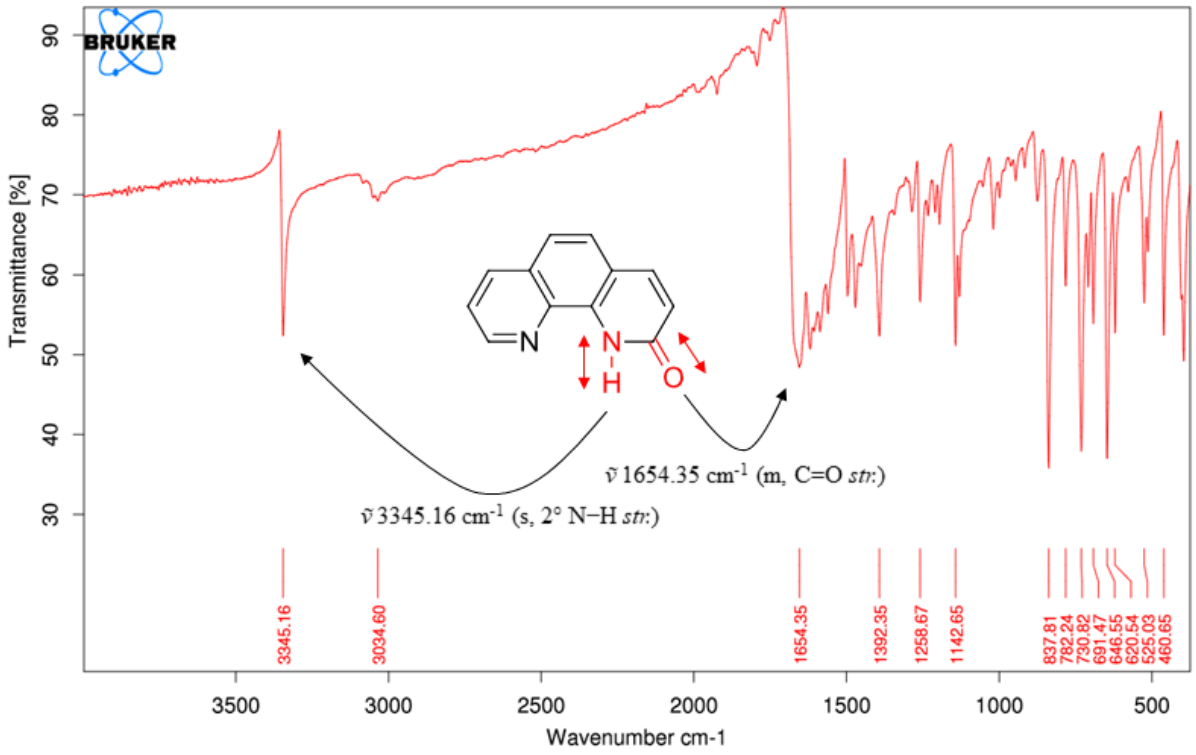

Figure 58. FTIR spectrum of the non-azeotropically dried by-product. The presence of a strong secondary N–H amide vibrational band at 3345 cm^{-1}, alongside the resonance stabilised C=O stretching frequency at 1654 cm^{-1} and the absence of a broad O–H stretching signal at higher wavenumbers provides evidence for the assignment of the 1,10-diaza-1H-phenanthren-2-one product.

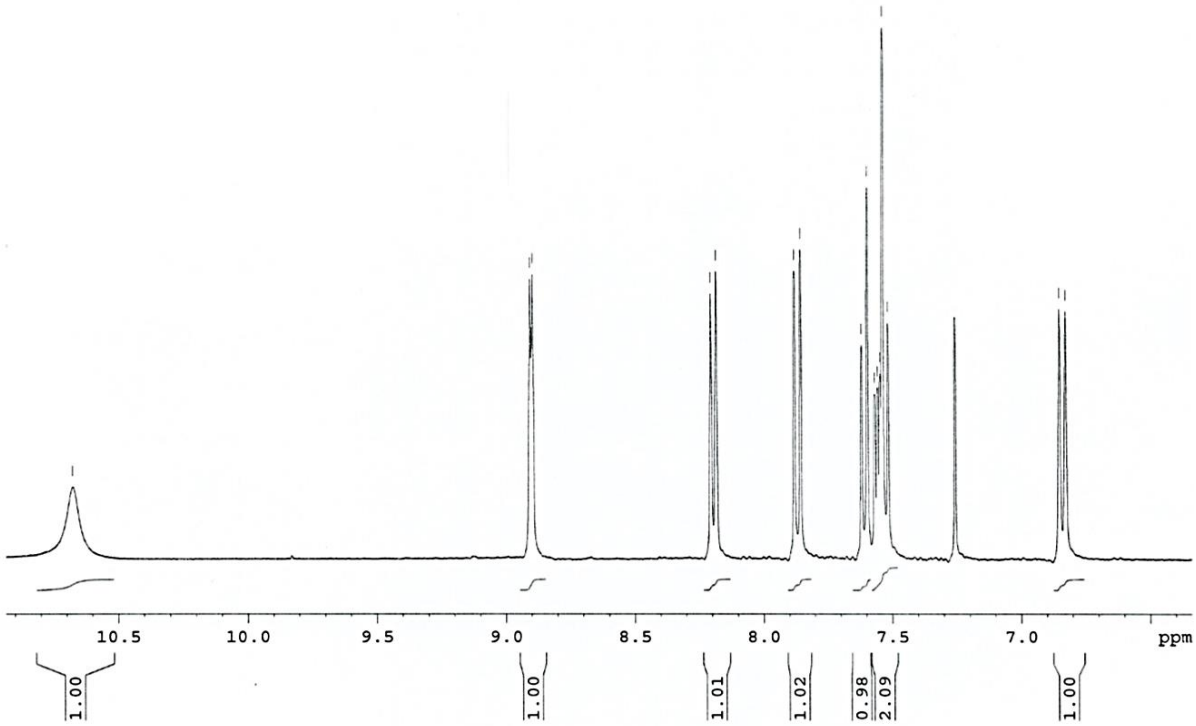

Figure 59. ^{1}H-NMR spectrum of the 1,10-diaza-1H-phenanthren-2-one by-product, depicting the eight expected signals for ^{1}H nuclei within the molecule, inclusive of a broad downfield shifted signal characteristic of the ^{1}H nuclear resonance within an N–H bond.

Figure 60 illustrates the expected peak area integration for the seven protons in the attained **2FPhen** 1H-NMR spectrum. The spectrum exhibited noticeable shifts from the **2ClPhen** ^{1}H-NMR spectrum due to the difference in electron withdrawal effects from the more electronegative fluorine atom, and differences in peak splitting due to the additional spin-spin coupling with the fluorine-19 isotope which consists of a spin ½ nucleus and high gyromagnetic ratio. The differences in these chemical shifts and peak splitting patterns are evident in Figure 61, which superimposes the two ^{1}H-NMR spectra for **2ClPhen** and **2FPhen**. The ^{13}C-NMR spectrum for **2FPhen**, shown in Figure 62, also depicts the presence of three additional carbon-13 signals resulting from the spin-spin coupling between the carbon-13 and fluorine-19 spin ½ nuclei. The coupling within the ^{19}F-NMR spectrum is likewise evident in Figure 63. The LRMS spectrum further confirms the identity of the **2FPhen** compound with an *m/z* ratio of 199.27 for the protonated $[M+H]^{+}$ ion being apparent against the calculated *m/z* ratio of 199.07, as

shown in figure 4.1.26. The presence of this *m/z* signal was further verified in the HRMS spectrum which not only illustrated the observed protonated cation (*m/z* 199.06660 calculated *vs. m/z* 199.06673 observed (Δ 0.64 ppm) for $[M+H]^+ = C_{12}H_8N_2F^+$), though also the positive charge induced loss of a fluorine atom (*m/z* calculated 179.06092 *vs. m/z* 179.06050 observed (Δ 2.36 ppm) for $[M-F]^+ = C_{12}H_7N_2^+$), which was similarly observed in the HRMS spectrum for **2ClPhen** as well. The FTIR spectrum of **2FPhen** exhibited the expected C–H stretching vibrational frequencies at higher wavenumbers consist with the 1,10-phenanthroline analogue, as shown in Figure 66, and UV/Vis spectroscopy revealed similar $\pi \rightarrow \pi^*$ excitations to **2ClPhen**, with absorption maxima at 262, 227 and 283 nm though with slightly lower molar absorptivities of 28596, 47402 and 16445 $L.mol^{-1}.cm^{-1}$ respectively in acetonitrile solution.

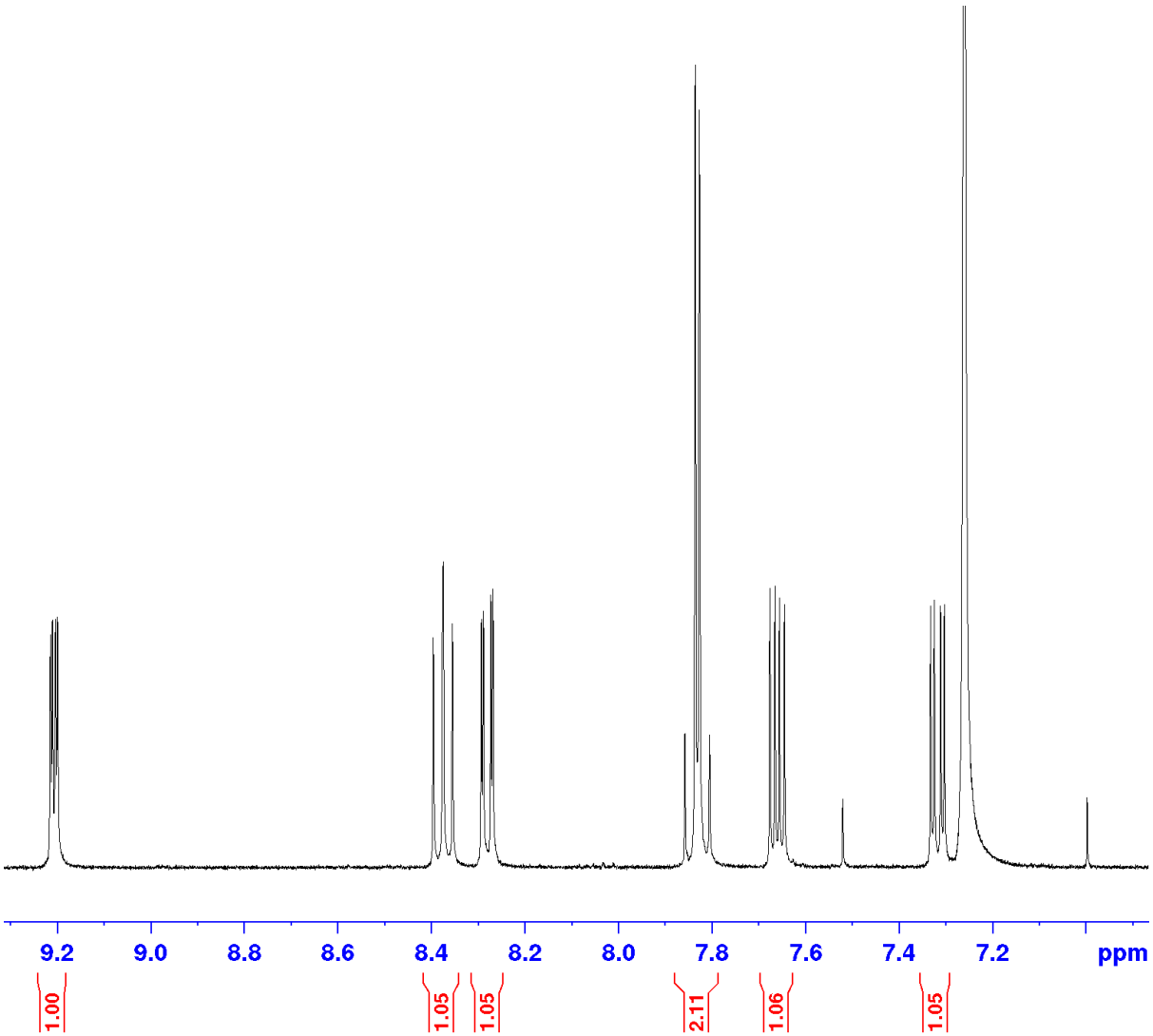

Figure 60. ^{1}H-NMR spectrum of **2FPhen** in chloroform-d, showing the expected peak area integration for seven protons in the aromatic region.

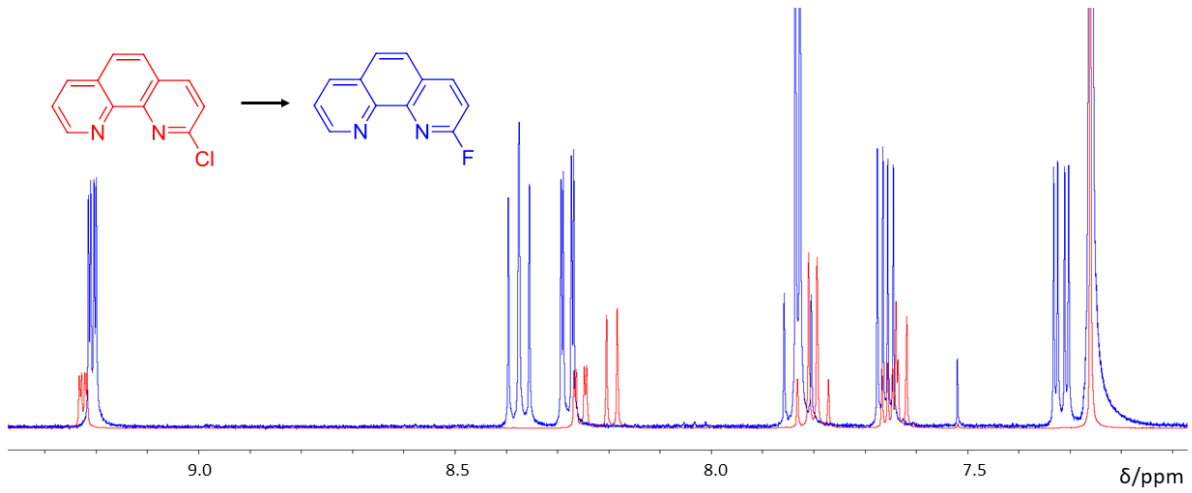

Figure 61. Differences arising in the chemical shifts and peak splitting from spin-spin couplings between **2ClPhen** (red) and **2FPhen** (blue) in chloroform-d within the superimposed ^{1}H-NMR spectra.

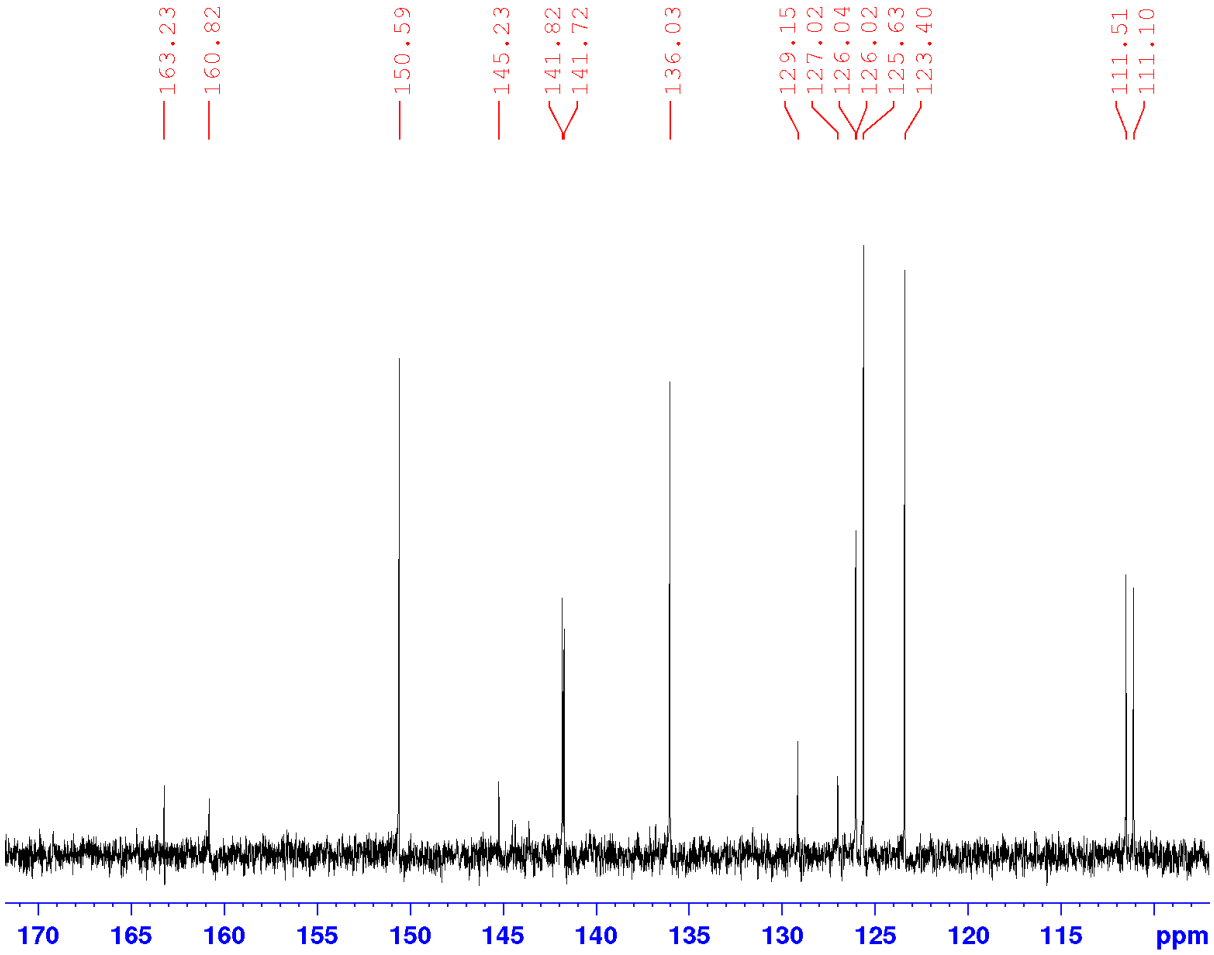

Figure 62. ^{13}C-NMR spectrum of **2FPhen** in chloroform-d. Three additional ^{13}C signals are present due to the coupling between the ^{19}F nucleus present in the molecule.

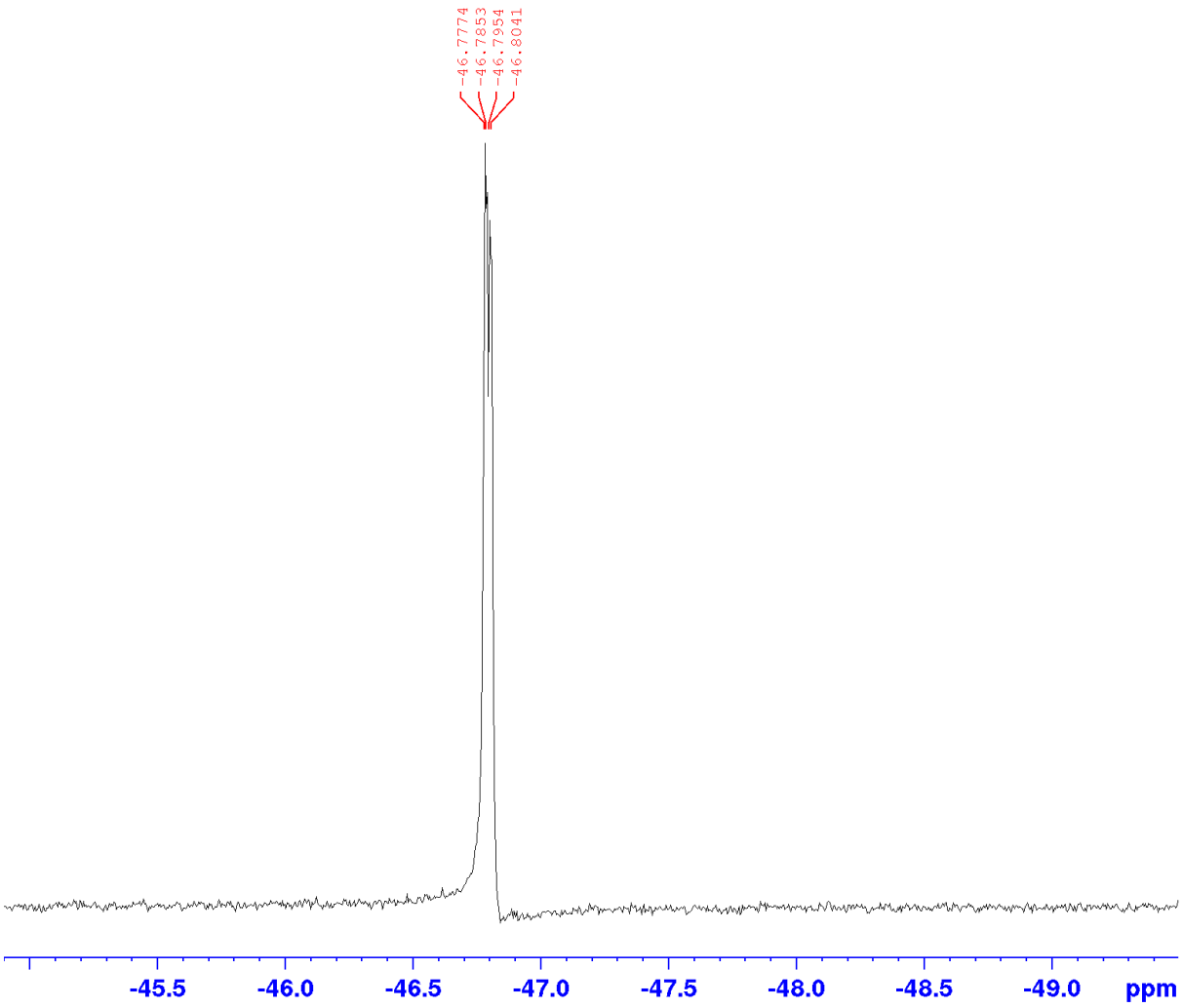

Figure 63. ^{19}F-NMR spectrum of **2FPhen** in chloroform-d, showing the single peak arising for the fluorine atom in the molecule.

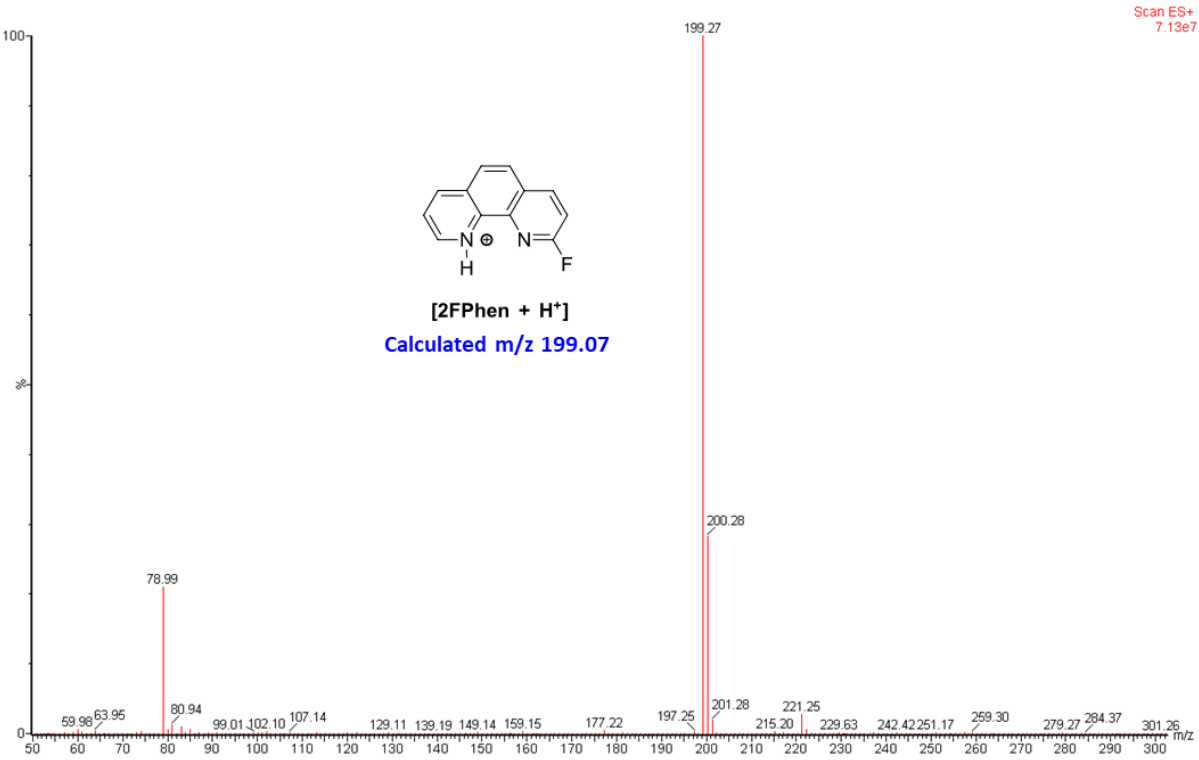

Figure 64. LRMS spectrum showing the major observed *m/z* ratio of 199.27, which corresponds with the protonated analogue of **2FPhen** having a calculated *m/z* ratio of 199.07.

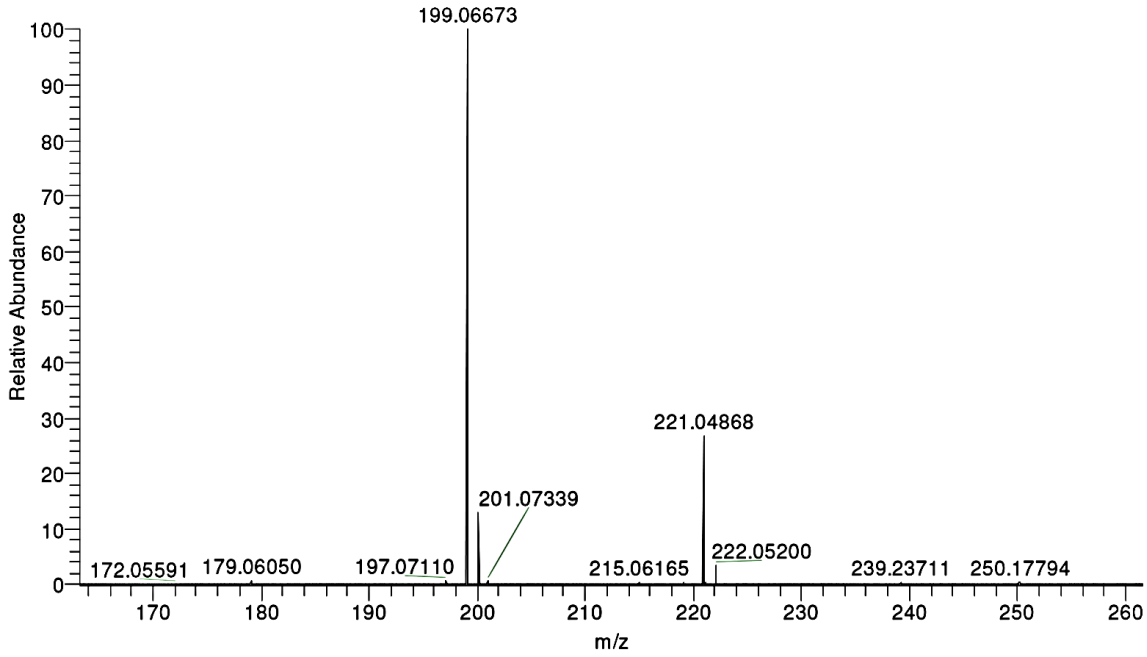

Figure 65. HRMS spectrum further verifying the presence of the major $[M+H]^+$ signal with an observed *m/z* ratio of 199.06673 against a calculated *m/z* ratio of 199.06660 (Δ 0.64 ppm). Also present is the $[M-F]^+$ signal generated from loss of a fluorine atom, with an observed *m/z* ratio of 179.06050 against a calculated *m/z* ratio of 179.06092 (Δ 2.36 ppm).

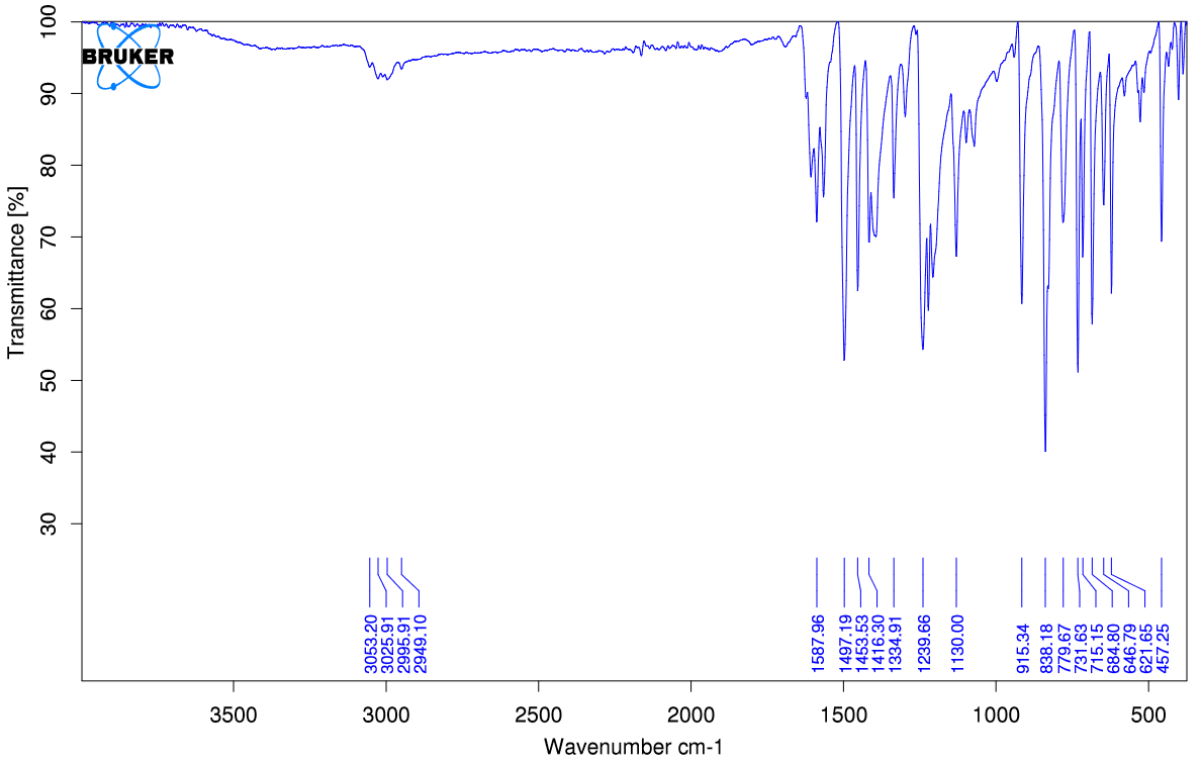

Figure 66. FTIR spectrum of **2FPhen** exhibiting the typical C−H stretching vibrational frequencies (2949 – 3053 cm^{-1}) consist with the 1,10-phenanthroline analogue.

3.1.5 Rhenium Complexation of 2-Chloro-1,10-Phenanthroline

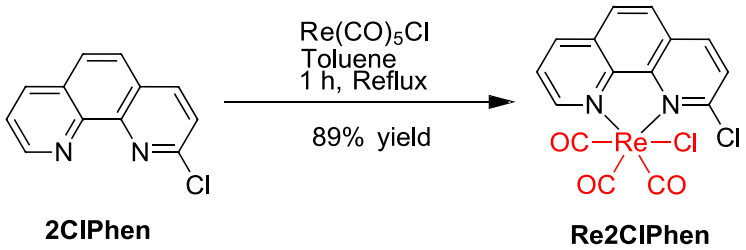

Figure 67. Ideal reaction conditions discovered to afford **Re2ClPhen** from **2ClPhen** in 89% yield.

A mass of 2-chloro-1,10-phenanthroline (100 mg, 466 µmol, 1.1 eq.) was dissolved in a volume of toluene (15 mL), to which a mass of pentacarbonylchlororhenium(I) (150 mg, 415 µmol, 1.0 eq.) was added. The solution was heated at reflux for 2 h, after which a yellow solid precipitate formed from solution. The solution was then cooled to around 4°C to encourage further precipitation. The yellow solid was isolated *via* vacuum filtration and washed with *n*-hexane to afford a pure product (216 mg).

Initial purity of the product was assessed by QC HPLC, whereupon the rhenium complex demonstrated an increased retention time on the C_{18} reverse phase column in comparison with the free ligand. This result is consistent with the expected polarity of the compounds given the presence of a TFA modifier in the mobile phase, as the free amine of the ligand is easily protonated to increase polarity and elute earlier. The formation of a rhenium complex was first confirmed by FTIR spectroscopy, whereupon the two distinctive IR active carbonyl stretching frequencies belonging to the A'(1) and co-exciting A'(2) and A'' vibrational modes exhibited strong absorbances around 2021 cm^{-1} and 1889 cm^{-1} wavenumbers respectively. Weak sp^2 hybridised C–H bond stretches were also observed, with a distinctive stretching frequency occurring at approximately 3042 cm^{-1}. These stretching frequencies can be viewed in the ATR

corrected FTIR spectrum of **RePhenCl** in Figure 68. The A(1), A'' and A'(2) vibrational modes of the carbonyl groups are also illustrated in the highlighted FTIR spectrum in Figure 69.

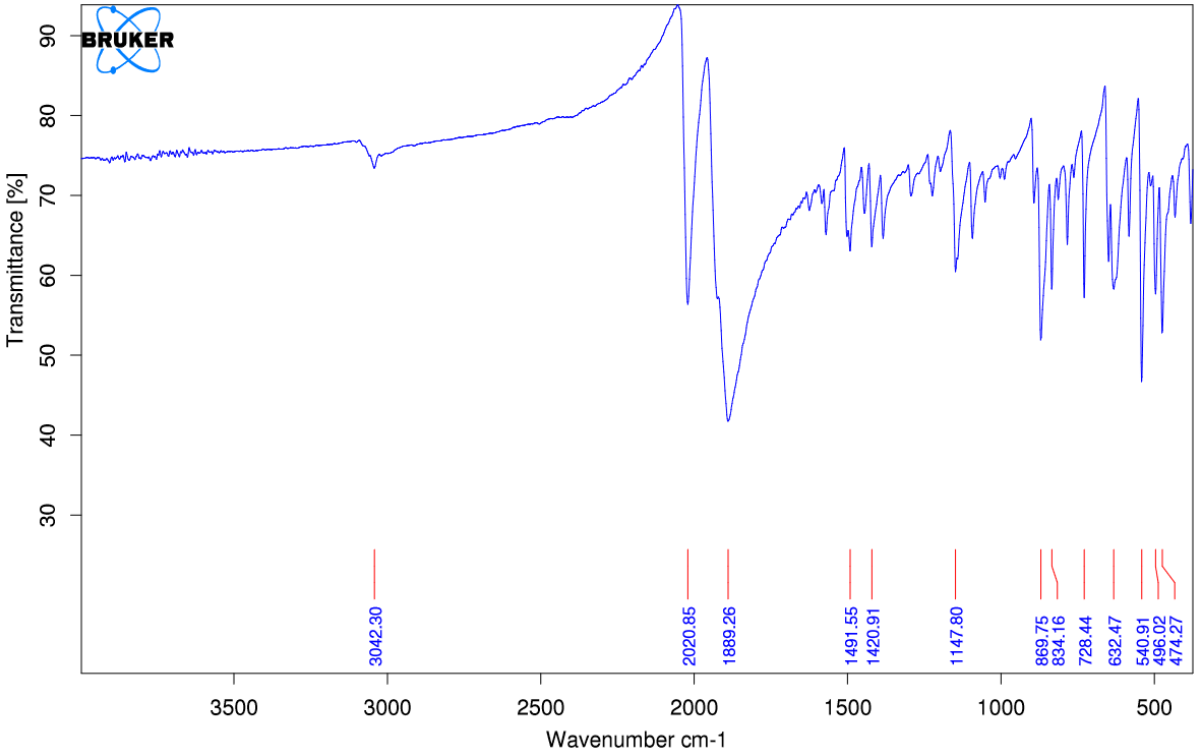

Figure 68. FTIR spectrum of **Re2ClPhen** exhibiting the two distinctive C≡O stretching IR absorption bands at 2020 cm^{-1} and 1889 cm^{-1} belonging to A'(1) and A'(2) & A'' coupled irreducible representations respectively. A weak sp^2 hybridised C−H bond stretch is also observed at 3042 cm^{-1} from the phenanthroline ligand.

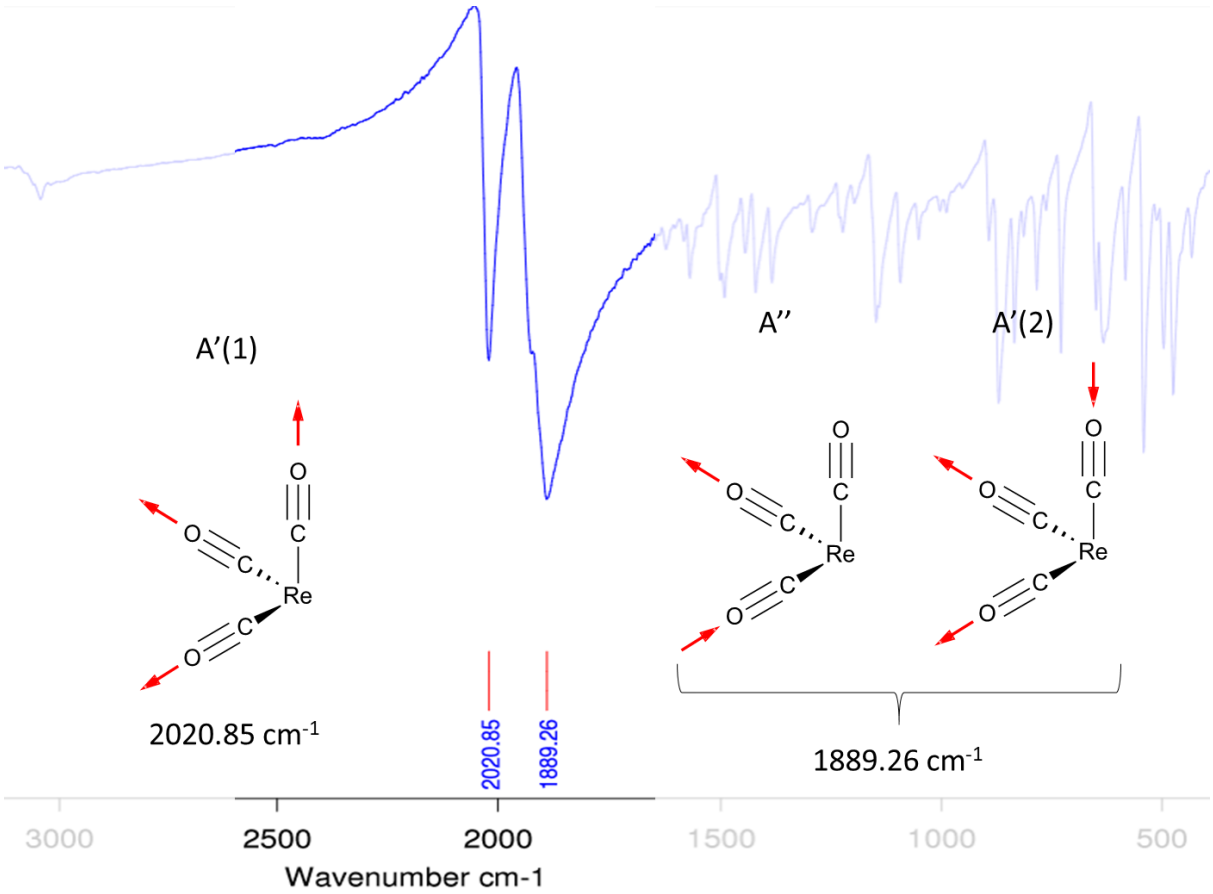

Figure 69. Carbonyl vibrational modes corresponding to the A'(1) irreducible representation at 2021 cm^{-1} and the overlapping A'' and A'(2) irreducible representations in the FTIR spectrum of **Re2ClPhen**.

The acquired NMR spectrum also support the formation of the **Re2ClPhen** complex with the ^{1}H-NMR spectrum exhibiting the expected integration for seven protons in the aromatic region (Figure 70), alongside simple splitting patterns which occur upfield from those chemical shifts observed in the **2ClPhen** ligand, as shown in Figure 71, suggesting an electron withdrawal effect consistent with complexation to the rhenium tricarbonyl centre. In Figure 72, the ^{13}C-NMR spectrum of **Re2ClPhen** exhibits the expected fifteen carbon-13 environments. Twelve of the carbon-13 signals occur between 120 – 160 ppm, corresponding to the twelve carbon atoms of the substituted phenanthroline ring. The remaining three carbon-13 signals occur between 185 – 200 ppm and correspond to the carbon nuclei in the C≡O carbonyl ligands bonded to the rhenium through the carbon atom. These carbon atoms are significantly electron

withdrawn due to the π-back bonding effect thus resulting in their downfield chemical shift to higher resonant frequencies. Additionally, these ^{13}C-NMR signals are significantly less intense due to the long spin-lattice (T1) relaxation times resulting from the metal-carbonyl bond.[83]

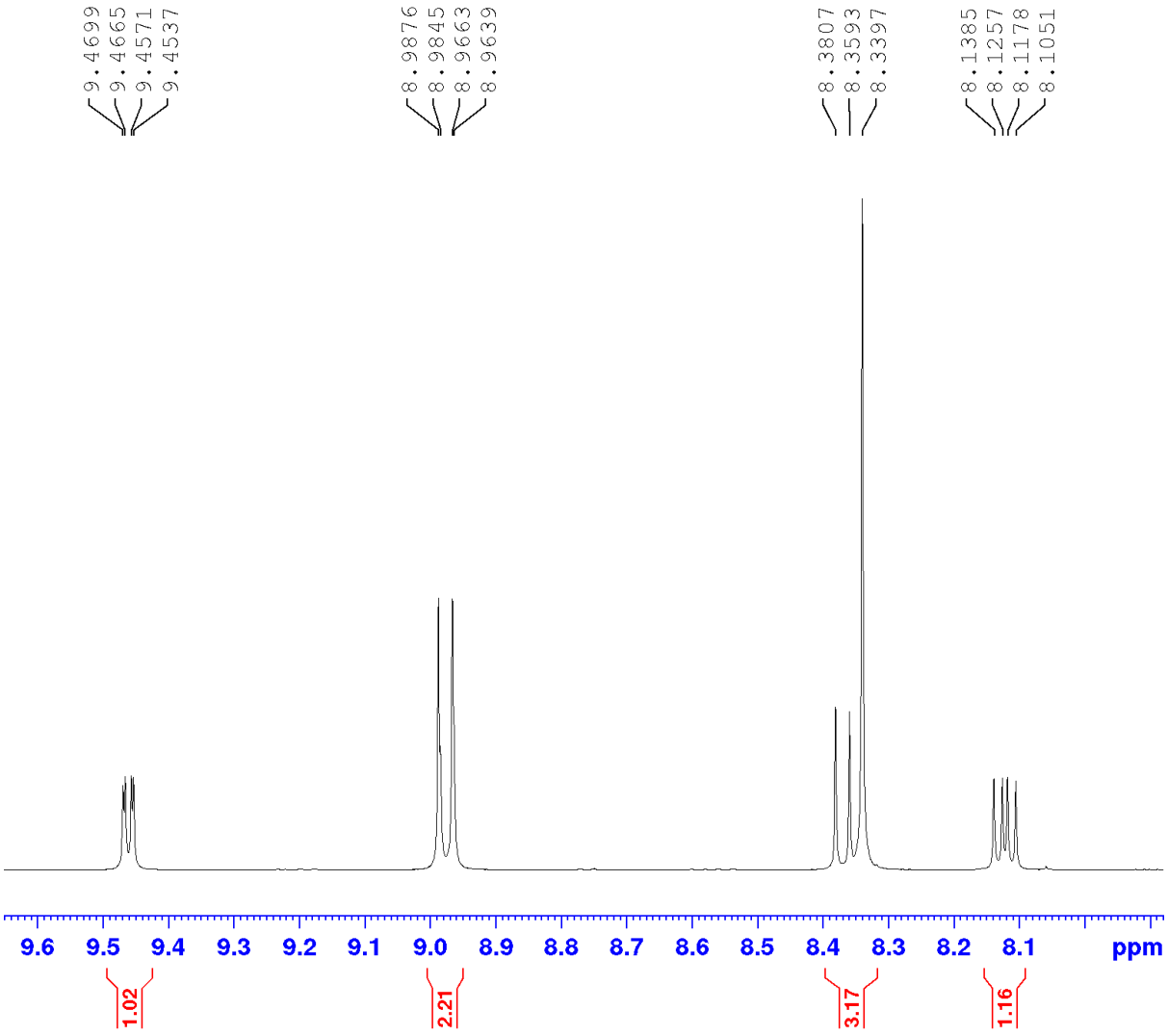

Figure 70. ^{1}H-NMR spectrum of **Re2ClPhen** showing the expected integration for seven protons in the aromatic region, alongside simplified splitting patterns and the corresponding chemicals shifts for each signal in DMSO-d_6 solution.

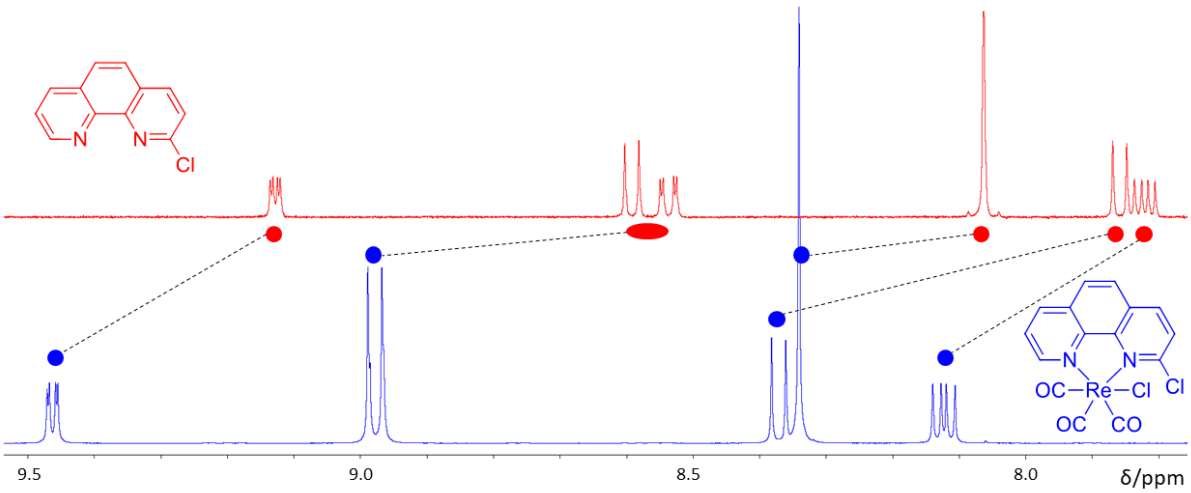

Figure 71. Downfield shift of aromatic ^{1}H-NMR signals caused by electron withdrawal in the π-aromatic phenanthroline ring by having complexed the **2ClPhen** ligand (red, above) to form the **Re2ClPhen** complex (blue, below).

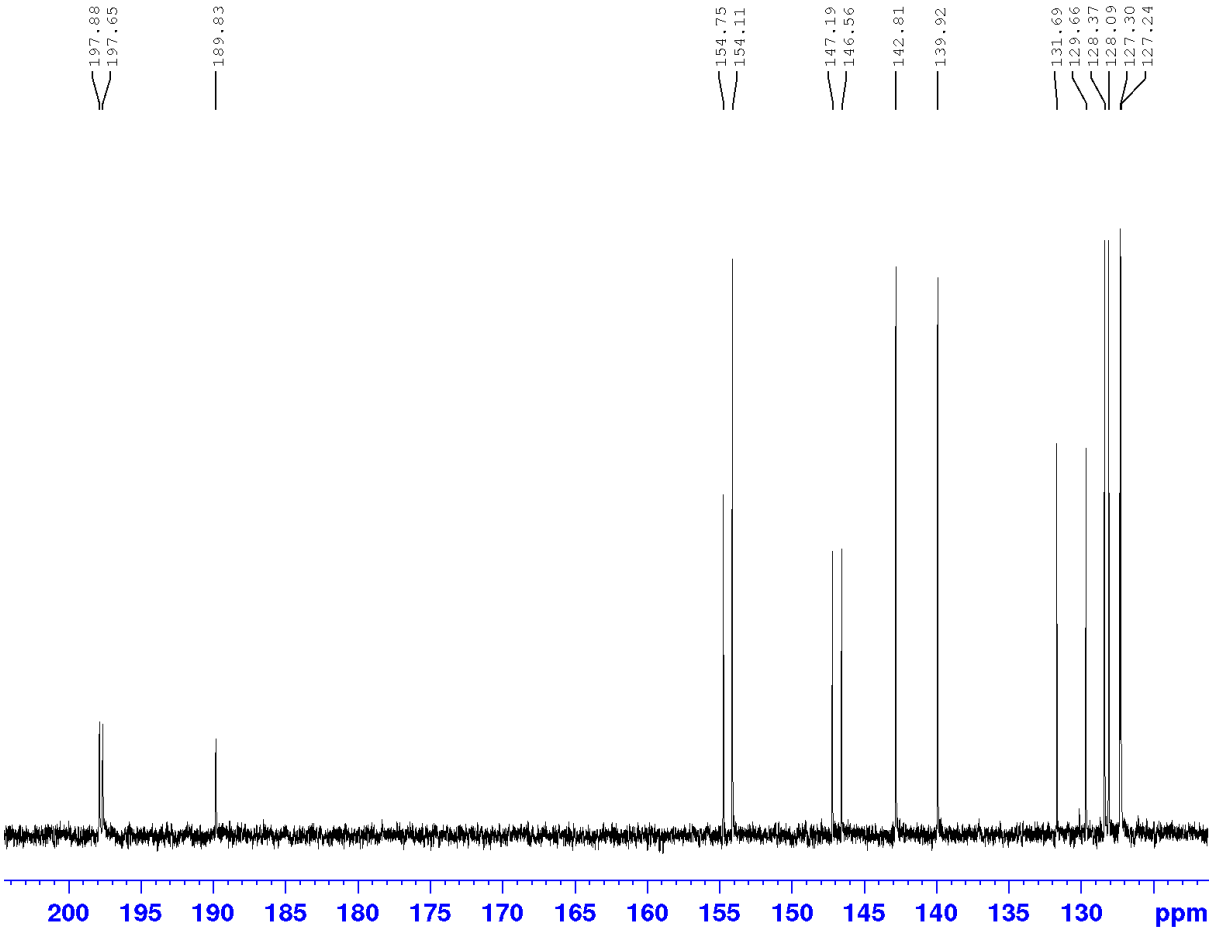

Figure 72. ^{13}C-NMR spectrum of **Re2ClPhen** showing the expected fifteen carbon signals for each carbon nuclei within the molecule. The twelve carbon-13 signals between 120 – 160 ppm correspond with the carbon atoms on the phenanthroline ring, whereas the three less intense signals between 185 – 200 ppm correspond with the heavily electron withdrawn carbonyl groups bonded to the rhenium centre.

The transition to the MLCT excited state for **Re2ClPhen** is depicted by the characteristic broad low-energy dπ → π* absorption band at 368 nm shown in the UV-Vis spectrum in Figure 73, alongside the higher energy π → π* absorption bands to LC excited states. The HRMS spectrum provides further confirmation of the **Re2ClPhen** complex through the presence of the bromine-dissociated sodium adduct ion signal (*m/z* 540.9261 calculated *vs.* 540.9266 observed (Δ 0.5 ppm) for $[M\text{-}Br+Na]^+ = {}^{185}ReC_{15}H_7N_2O_3Na^+$) for both the ^{185}Re and ^{187}Re isotopes as shown in Figure 74. As none of these prior mentioned analyses were able to verify the identity of the chloro ancillary ligand the compound was sent off for elemental analysis specifically to quantity the chlorine composition of the complex. An experimental composition of 13.55% was returned which aligned closely with the theoretical composition of 13.65% chlorine. Molecular compositions of 34.45% carbon, 0.95% hydrogen and 5.36% nitrogen were also measured against calculated compositions of 34.62% carbon, 1.36% hydrogen and 5.38% nitrogen. A crystal structure was also attainted from XRD analysis at the Australian Synchrotron, as shown in Figure 75, which provided unequivocal evidence for the assigned molecular structure of **Re2ClPhen**.

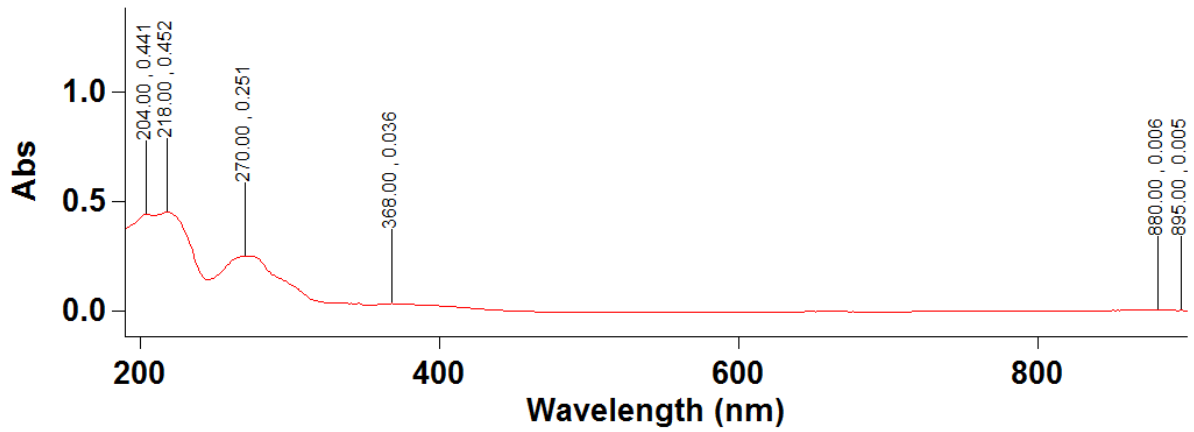

Figure 73. UV-Vis spectrum of **Re2ClPhen** exhibiting the typical dπ → π* transition to the MLCT excited state at 368 nm. Higher energy transitions at the lower wavelengths correspond to the intraligand π → π* electronic transitions with greater molar absorptivities.

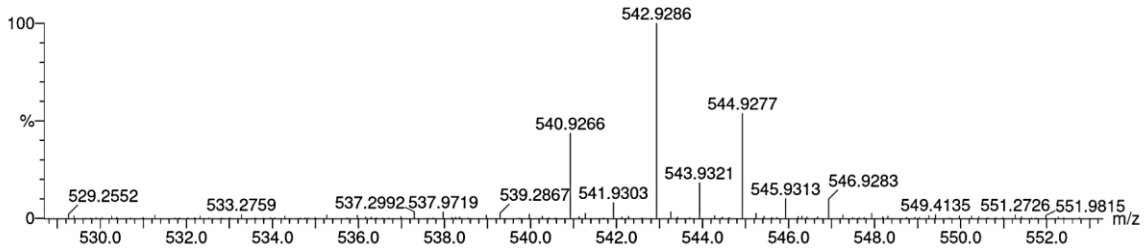

Figure 74. HRMS spectrum of **Re2ClPhen** verifying the presence of the bromine dissociated $[Na+M-Br]^+$ sodium-adduct ion signal with an observed m/z ratio of 540.9266 against a calculated m/z ratio of 540.9261 (Δ 0.5 ppm) for the ^{185}Re isotope (37.4% abundance). The accompanying MS signal for the more abundant ^{187}Re isotope (62.6 %) is also observed at m/z 542.9286.

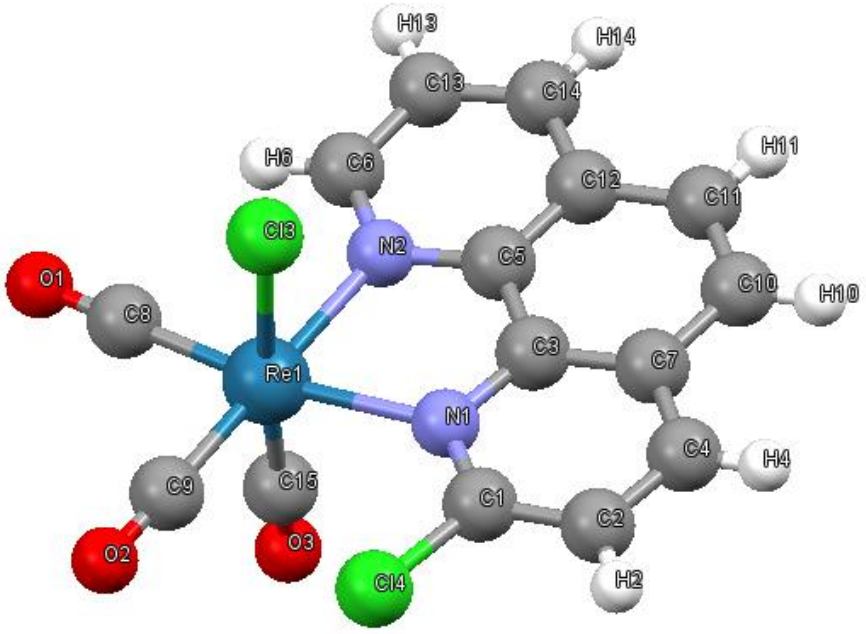

Figure 75. Crystal structure obtained for **Re6ClPhen** *via* XRD analysis at the Australian Synchrotron. Crystals were grown from the slow evaporation of DMSO solution.

3.1.6 Rhenium Complexation of 2-Fluoro-1,10-Phenanthroline

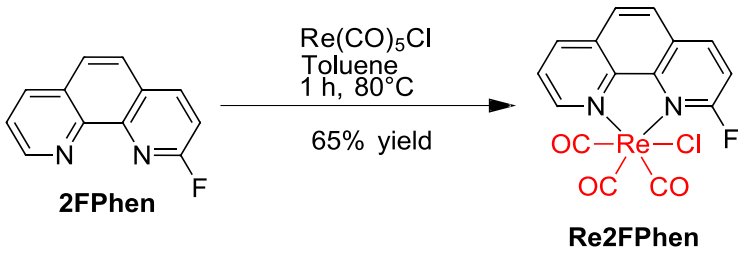

Figure 76. Ideal reaction conditions discovered to afford Re2FPhen from 2FPhen in 65% yield.

A mass of 2-fluoro-1,10-phenanthroline (39 mg, 198 µmol, 1.1 eq.) was dissolved in a solution of toluene (6 mL), to which a mass of pentacarbonylchlororhenium(I) (65 mg, 180 µmol, 1.0 eq.) was added. The solution was then heated 80°C for 1 h, whereupon a yellow solid formed. The solution was then cooled to room temperature to promote further precipitation of the solid. The yellow solid was isolated *via* vacuum filtration and washed with cold *n*-hexane to yield a pure product (65 mg).

The FTIR spectrum in Figure 77 shows the two distinctive absorption bands for the C≡O IR stretching frequencies at 2021 cm^{-1} (A'(1) irreducible representation) and 1890 cm^{-1} (A'(2) & A'' irreducible representations). Weak sp^2 hybridised C–H bond stretching frequencies from the phenanthroline ligand are also observed at higher wavenumbers. The ^{1}H-NMR spectrum of **Re2FPhen** in Figure 78 depicts the expected integration for seven protons, downfield shifted with respect to the proton resonance signals of **2FPhen** due to the electron withdrawing nature of the rhenium centre, alongside complex splitting patterns due to coupling between the protons and the fluorine-19 nucleus. The complex splitting patterns are likewise observed in the ^{13}C-NMR spectrum shown in Figure 79 and the 19F-NMR spectrum shown in Figure 80. The UV-Vis spectrum in Figure 81 shows the expected $d\pi \rightarrow \pi^*$ absorption to the MLCT excited state

at 368 nm, alongside higher energy $\pi \rightarrow \pi^*$ absorptions to LC excited states characteristic of rhenium tricarbonyl diimine complexes. The HRMS spectrum is also indicative of the **Re2FPhen** complex with the presence of the chlorine-dissociated sodium adduct ion signal (*m/z* 524.9557 calculated *vs.* 524.9579 observed (Δ 2.2 ppm) for $[M\text{-}Cl+Na]^+$ = $^{185}ReC15H7N2O3Na^+$) for the ^{185}Re isotopic signal in 37.4% abundance, accompanied also by the analogous ^{187}Re isotopic signal in 62.6% abundance at *m/z* 526.9622, shown in Figure 82. To verify the identity of the chloro ancillary ligand, which could not be assigned due to dissociation of the Re−Cl bond, the sample was sent off for elemental analysis specifically to measure the composition of chlorine in the complex. The analysis returned an experimental composition of 6.83% chlorine against a closely aligned theoretical composition of 7.04% chlorine, suggesting that the chloro group was indeed the ancillary ligand. Measurements of 35.73% carbon, 0.98% hydrogen and 5.59% nitrogen against calculated compositions of 35.75% carbon, 1.40% hydrogen and 5.56% nitrogen also attested to the purity of the ligand.

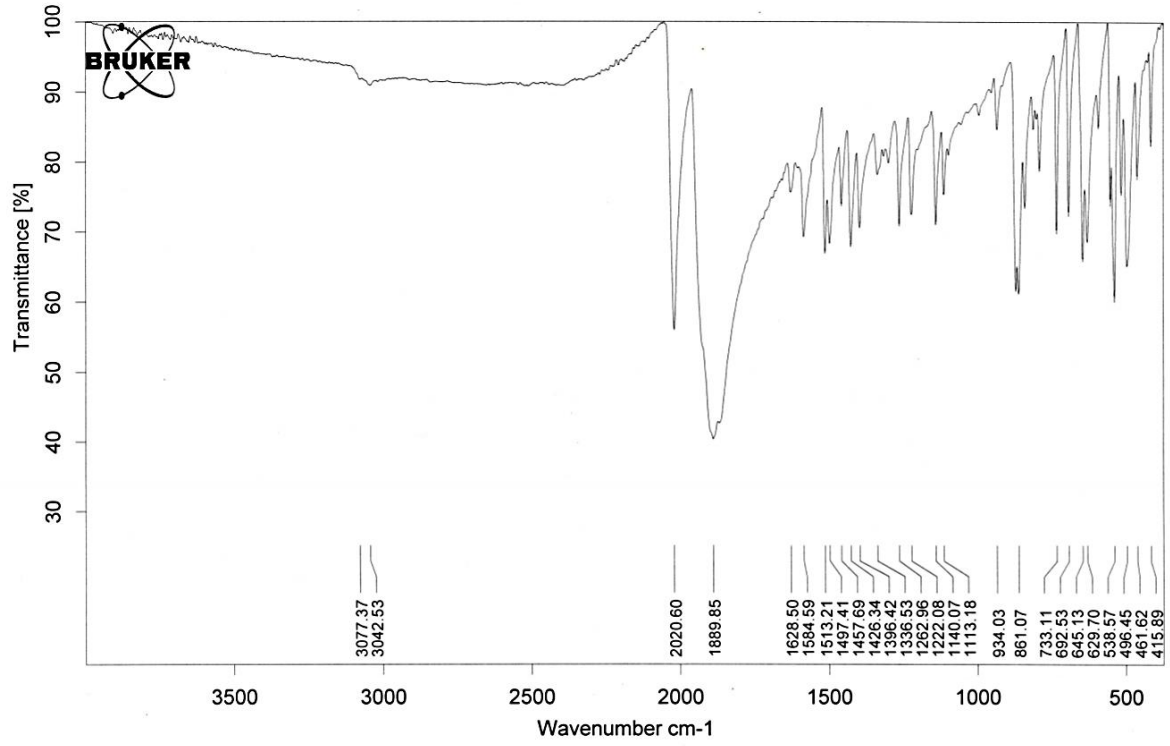

Figure 77. FTIR spectrum of **Re2FPhen** exhibiting the two distinctive C≡O stretching IR absorption bands at 2021 cm^{-1} and 1890 cm^{-1} with A'(1) and A'(2) & A'' coupled irreducible representations respectively. Weak sp^2 hybridised C−H bond stretches are also observed at 3077 cm^{-1} and 3043 cm^{-1} from the complexed phenanthroline ligand.

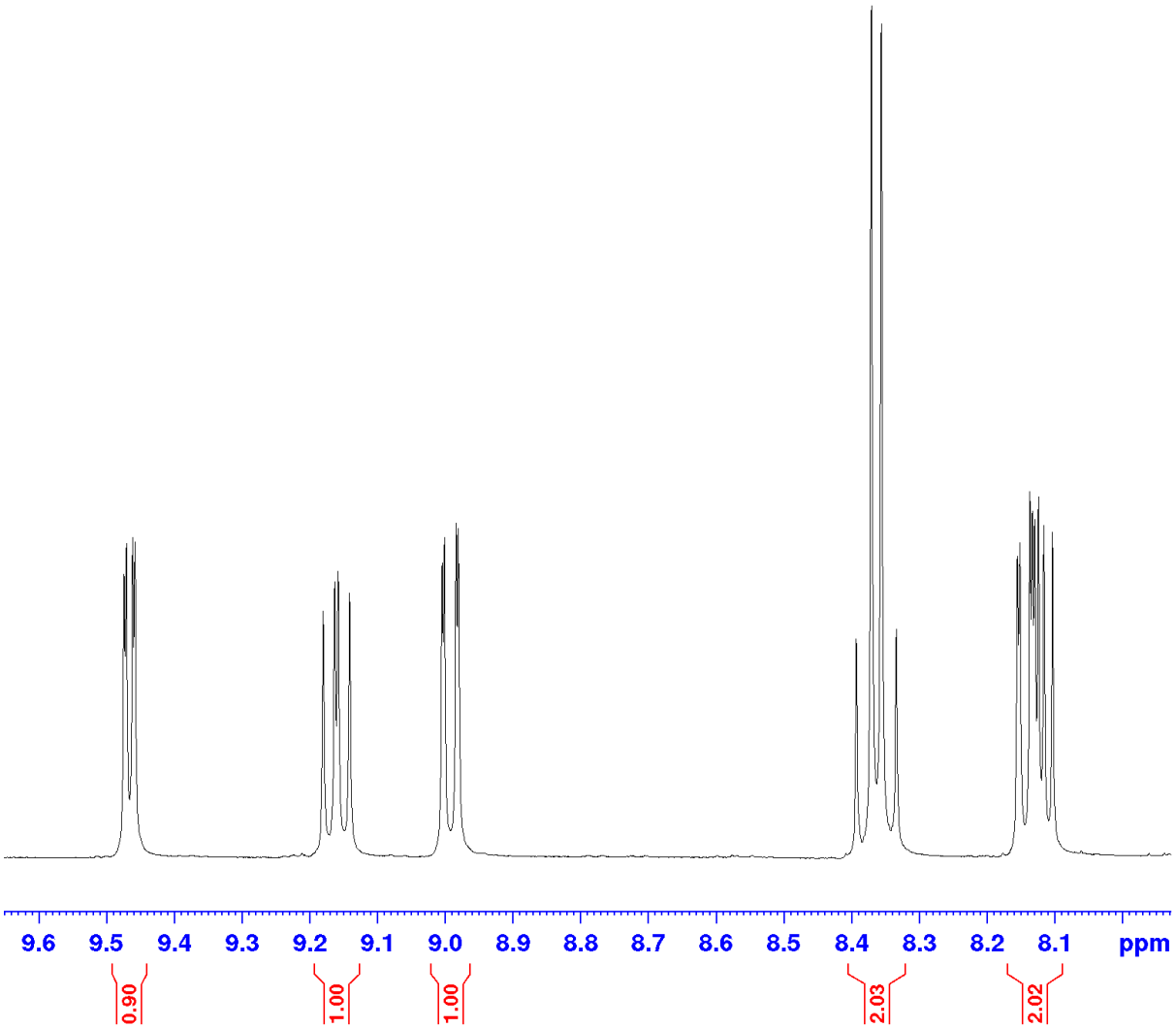

Figure 78. ^{1}H-NMR spectrum of **Re2FPhen** showing the expected integration for seven protons in the aromatic region in DMSO-d_6 solution. The splitting patterns are slightly more complicated due to the additional spin-spin coupling between the hydrogen protons and NMR active fluorine-19 nucleus.

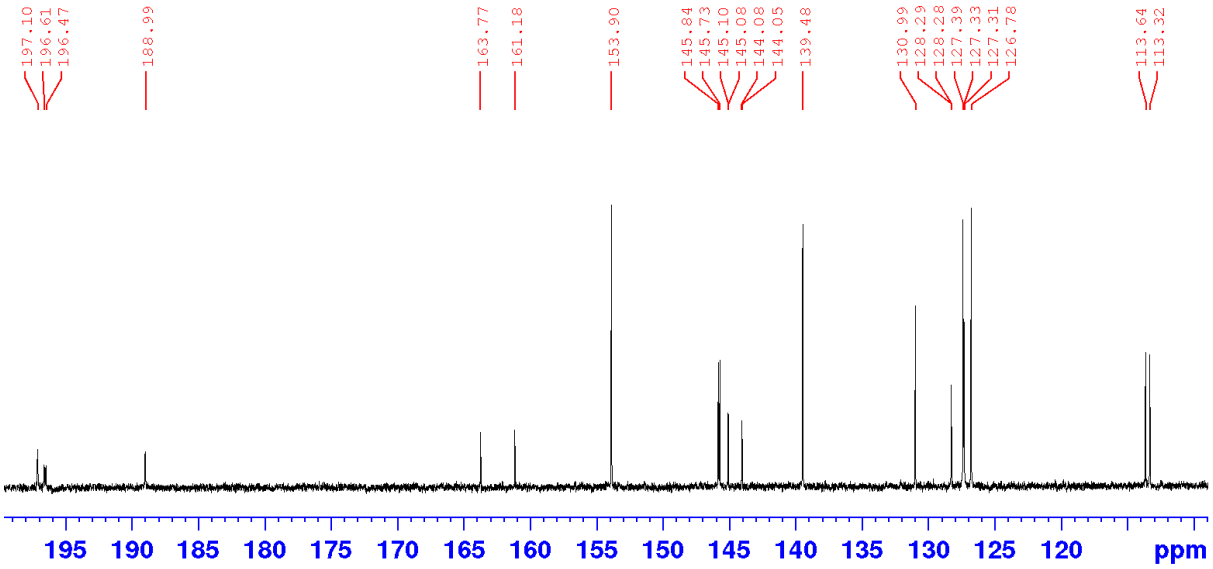

Figure 79. Complex splitting patterns observed in the ^{13}C-NMR spectrum of **Re2FPhen** in DMSO-d_6 due to coupling with the fluorine-19 nucleus.

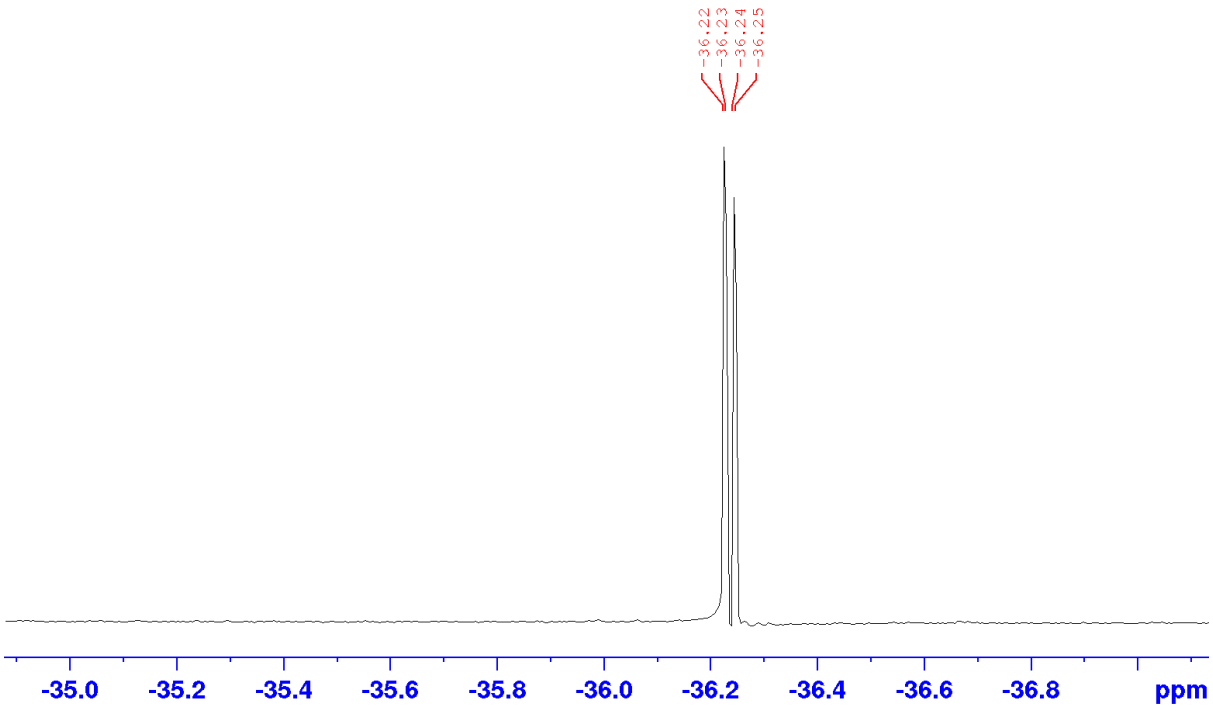

Figure 80. Coupling observed in the ^{19}F-NMR spectrum of **Re2FPhen** in DMSO-d_6 leads to a doublet of doublets splitting pattern arising from unequal F−H coupling constants.

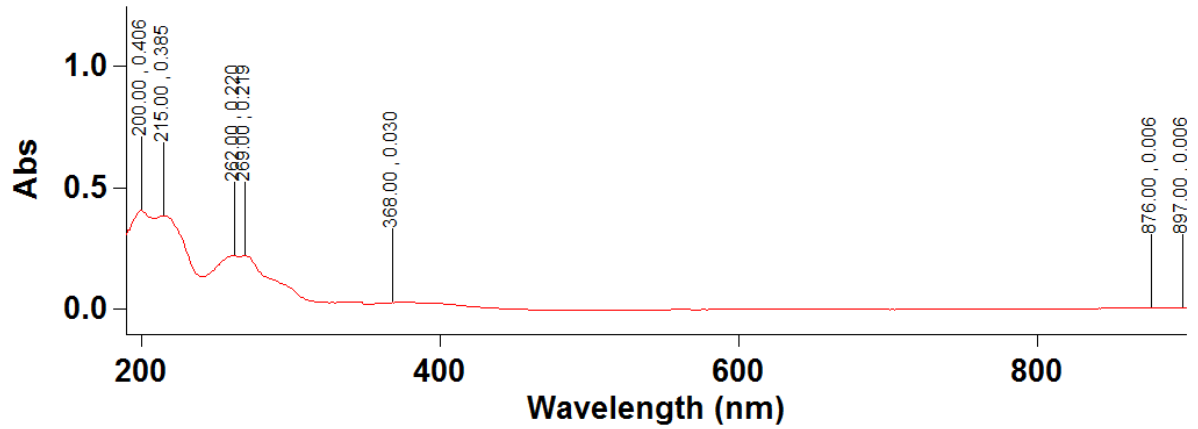

Figure 81. UV-Vis spectrum of **Re2FPhen** exhibiting the typical dπ → π* transition to the MLCT excited state at 368 nm. Higher energy transitions at the lower wavelengths correspond to the intraligand π → π* electronic transitions with greater molar absorptivities.

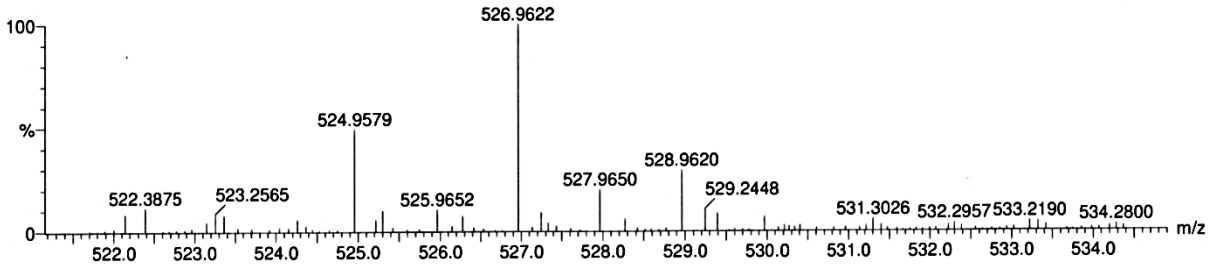

Figure 82. HRMS spectrum of **Re2FPhen** verifying the presence of the chlorine dissociated $[Na+M-Cl]^+$ sodium-adduct ion signal with an observed *m/z* ratio of 524.9579 against a calculated *m/z* ratio of 524.9557 (Δ 2.2 ppm) for the ^{185}Re isotope (37.4% abundance). The accompanying MS signal for the more abundant ^{187}Re isotope (62.6%) is also observed at *m/z* 526.9622.

3.1.7 Characterisation Data for Products and Intermediates in the Synthesis of 2-Chloro and 2-Fluoro Substituted Phenanthroline Complexes

1,10-phenanthroline-N-oxide (**Phen-NO**). White Solid; MP: 185°C (*dec.*); 79% yield. ^{1}H NMR (400 *MHz*, DMSO-d_6, *δ/ppm*): δ 9.31 (dd, J^d=4.36, 1.88 *Hz*, 1H), δ 8.74 (dd, J^d = 6.32, 1.16 Hz, 1H), δ 8.23 (dd, J^d = 8.08, 1.88 Hz, 1H), δ 7.74 (dd, J^d = 8.12, 1.16 Hz, 1H), δ 7.66 (dd, J^d = 8.08, 4.36 Hz, 1H), δ 7.46 (dd, J^d = 8.08, 6.32 Hz, 1H). ^{13}C{^{1}H} NMR (100 MHz, $CDCl_3$, δ/ppm): δ 150.04, δ 142.67, δ 140.82, δ 138.39, δ 135.87, δ 133.31, δ 129.08, δ 128.93, δ 126.51, δ 124.51, δ 123.18, δ 122.85. FTIR (ATR *corr. ṽ/cm^{-1}*): *ṽ* 3060 (w, C−H sp^2 *str.*), *ṽ* 3008 (w, C−H sp^2 *str.*), *ṽ* 1519 (s, C=C π_{Ar} *str.*), *ṽ* 1432 (s, N −O *str.*), *ṽ* 1411 (s, C=C π_{Ar} *str.*), *ṽ* 1335 (s, C=C π_{Ar} *str.*). UV/Vis (CH_3CN, λ/*nm*, ε/*L.mol^{-1}.cm^{-1}*): λ 335 (*π→π**, ε 4197.08), λ 271 (*π→π**, ε 14324.82), λ 243 (*π→π**, ε 21304.74), λ 211 (*π→π**, ε 20118.61), λ 194 (*π→π**, ε 19160.58). LRMS (ESI^+): $[M+H]^+$ *m/z* calc. 197.07, *m/z obsv.* 197.27. HRMS (ESI^+): $[M+H]^+$ *m/z calc.* 197.07094 ($C_{12}H_9N_2O^+$), *m/z obsv.* 197.07108 (Δ 0.71 *ppm*); $[M+H-O]^+$ *m/z calc.* 181.07657 ($C_{12}H_9N_2^+$); *m/*z *obsv.* 181.07615 (Δ 2.30 ppm). $[M-O-H]^+$ *m/z calc.* 176.06092 ($C_{12}H_7N_2^+$); *m/*z *obsv.* 197.06052 (Δ 2.25 ppm).

2-chloro-1,10-phenanthroline (**2ClPhen**). White solid; MP: 127°C; 40% yield. ^{1}H NMR (400 *MHz*, DMSO-d_6, *δ/ppm*): δ 9.22 (dd, J^d=4.32, 1.72 *Hz*, 1H), δ 8.25 (dd, J^d = 8.08, 1.72 Hz, 1H), δ 8.19 (d, J^d = 8.36 Hz, 1H), δ 7.80 (d, J^d = 24.2 Hz, 1H), δ 7.80 (d, J^d = 6.6 Hz, 1H), δ 7.65 (dd, J^d = 8.08, 4.36 Hz, 1H), δ 7.63 (d, J^d = 8.36 Hz, 1H). ^{13}C{^{1}H} NMR (100 MHz, $CDCl_3$, δ/ppm): δ 151.55, δ 150.84, δ 146.14, δ 145.13, δ 138.71, δ 136.04, δ 129.05, δ 127.28, δ 126.99, δ 125.75, δ 124.37, δ 123.48. FTIR (ATR *corr. ṽ/cm^{-1}*): *ṽ* 3098 (w, C−H sp^2 *str.*), *ṽ* 3040 (w, C−H sp^2 *str.*), *ṽ* 1580 (s, C=C π_{Ar} *str.*), *ṽ* 1490 (s, C=C π_{Ar} *str.*), *ṽ* 1385 (s, C=C π_{Ar} *str.*). UV/Vis (CH_3CN, λ/*nm*, ε/*L.mol^{-1}.cm^{-1}*): λ 266 (*π→π**, ε 31021.90), λ 229 (*π→π**, ε 50456.20), λ 201

($\pi\rightarrow\pi^*$, ε 17928.83). LRMS (ESI^+): $[M+H]^+$ *m/z calc.* 215.04 & 217.04, *m/z obsv.* 215.24 & 217.24. HRMS (ESI^+): $[M+H]^+$ *m/z calc.* 215.03705 ($C_{12}H_8N_2Cl^+$); *m/z obvs.* 215.03726 (Δ 0.96 ppm); $[M-Cl]^+$ *m/z calc.* 179.06092 ($C_{12}H_7N_2^+$); *obsv.* 179.06050 (Δ 2.36 ppm).

2-fluoro-1,10-phenanthroline (**2FPhen**). White solid; MP: 123°C; 71% yield. ^1H NMR (400 *MHz*, DMSO-d_6, *δ/ppm*): δ 9.21 (dd, J^d = 4.32, 0.43 Hz, 1H), δ 8.37 (*app.* t, J^t = 8.44, 1H), δ 8.28 (dd, J^d = 8.12, 0.43 Hz, 1H), δ 7.83 (d, J^d = 21.16, 1H), δ 7.83 (d, J^d = 3.52 Hz, 1H), δ 7.66 (dd, J^d = 8.12, 1.08 Hz, 1H), δ 7.32 (dd, J^d = 8.56, 0.79 Hz, 1H). $^{13}C\{^1H\}$ NMR (100 MHz, $CDCl_3$, δ/ppm): δ 163.23, δ 160.82, δ 150.59, δ 145.23, δ 141.77 (d, J^d = 10.06 Hz), δ 136.03, δ 129.15, δ 127.02, δ 126.03 (d, J^d = 2.01 Hz), δ 125.63, δ 123.40, δ 111.31 (d, J^d = 41.25 Hz). ^{19}F NMR (376 MHz, DMSO-d_6, δ/ppm): δ -46.79 (dd, J^d = 3.27, 10.05 Hz), δ -106.00 (ISTD: *para*-DFB). FTIR (ATR *corr.* $\tilde{\nu}/cm^{-1}$): $\tilde{\nu}$ 3053 (w, C−H sp^2 *str.*), $\tilde{\nu}$ 3026 (w, C−H sp^2 *str.*), $\tilde{\nu}$ 1588 (s, C=C π_{Ar} *str.*), $\tilde{\nu}$ 1497 (s, C=C π_{Ar} *str.*), $\tilde{\nu}$ 1416 (s, C=C π_{Ar} *str.*). UV/Vis (CH_3CN, λ/nm, $\varepsilon/L.mol^{-1}.cm^{-1}$): λ 262 ($\pi\rightarrow\pi^*$, ε 28595.96), λ 227 ($\pi\rightarrow\pi^*$, ε 47402.32), λ 200 ($\pi\rightarrow\pi^*$, ε 16444.83). LRMS ($ESI^+$): $[M+H]^+$ *m/z calc.* 199.07, *m/z obsv.* 199.27. HRMS (ESI^+): $[M+H]^+$ *m/z calc.* 199.06660 ($C_{12}H_8N_2F^+$); *m/z obsv.* 199.06673 (Δ 0.64 ppm); $[M-F]^+$ *m/z calc.* 179.06092 ($C_{12}H_7N_2^+$); *m/*z *obsv.* 179.06050 (Δ 2.36 ppm).

1,10-diaza-1H-pehanthren-2-one. White solid. ^1H NMR (400 *MHz*, DMSO-d_6, *δ/ppm*): δ 10.68 (br. s, 1H), δ 8.90 (d, J^d = 4.20 Hz, 1H), δ 8.20 (d, J^d = 7.87 Hz, 1H), δ 6.84 (d, J^d = 9.52 Hz, 1H), δ 7.55 (dd, J^d = 8.64, 4.52 Hz, 1H), δ 7.57 (dd, J^d = 32.08, 8.40 Hz, 1H). FTIR (ATR *corr.* $\tilde{\nu}/cm^{-1}$): $\tilde{\nu}$ 3345 (s, 2° N−H *str.*), $\tilde{\nu}$ 3035 (w, C−H sp^2 *str.*), $\tilde{\nu}$ 1654 (s, C=O *str.*).

Tricarbonylchloro(2-chloro-1,10-phenanthroline)rhenium(I) (**Re2ClPhen**). Yellow solid; MP: 316°C (*dec.*); 89% yield. ^1H NMR (400 *MHz*, DMSO-d_6, *δ/ppm*): δ 9.46 (dd, J^d = 5.12, 1.36 Hz, 1H), δ 8.98 (d, J^d = 8.52 Hz, 1H), δ 8.97 (d, J^d = 8.24 Hz, 1H), δ 8.37 (d, J^d = 8.56, 1H), δ 8.34 (s, 2H), δ 8.12 (dd, J^d = 8.24, 5.12 Hz, 1H). $^{13}C\{^1H\}$ NMR (100 MHz, $CDCl_3$, δ/ppm): δ

197.88 (**C**≡O), δ 197.65 (**C**≡O), δ 189.83 (**C**≡O), δ 154.75, δ 154.11, δ 147.19, δ 146.56, δ 142.81, δ 139.92, δ 131.69, δ 129.66, δ 128.37, δ 128.09, δ 127.30, δ 127.24. FTIR (ATR *corr.* $\tilde{\nu}/cm^{-1}$): $\tilde{\nu}$ 3042 (w, C–H sp^2 *str.*), $\tilde{\nu}$ 2021 (s, A'(1) C≡O *str.*), $\tilde{\nu}$ 1889 (s, A'(2) & A'' C≡O *str.*). UV/Vis (CH_3CN, λ/*nm*, ε/$L.mol^{-1}.cm^{-1}$): λ 368 (Re*(dπ)*→π*, ε 374.65), λ 270 (π→π*, ε 2612.13), λ 218 (π→π*, ε 4703.92), λ 204 (π→π*, ε 4589.45). LRMS (ESI^+): $[M\text{-}Cl]^+$ *m/z* calc. 484.97, *m/z obsv.* 485.07. HRMS (ESI^+): $[M+Na]^+$ *m/z calc.* 540.9261 ($C_{15}H_7N_2O_3FCl_2ReNa^+$); *m/z obsv.* 540.9266 (Δ 0.90 ppm). EA (%): *calc.* C 34.62, H 1.36, N 5.38, Cl 13.63; *obsv.* C 34.45, H 0.95, N 5.36, Cl 13.55.

Tricarbonylchloro(2-fluoro-1,10-phenanthroline)rhenium(I) (**Re2FPhen**). Yellow solid; MP: 314°C (*dec.*); 65% yield. ^1H NMR (400 *MHz*, DMSO-d_6, *δ/ppm*): δ 9.47 (dd, J^d = 5.04, 1.32 Hz, 1H), δ 9.16 (dd, J^d = 8.84, 6.80 Hz, 1H), δ 8.99 (dd, J^d = 8.32, 1.32 Hz, 1H), δ 8.36 (*app.* q, J^q = 14.72, 8.84 Hz, 2H), δ 8.14 (dd, J^d = 8.84, 1.48 Hz, 1H), δ 8.12 (dd, J^d = 8.32, 5.04 Hz, 1H). $^{13}C\{^1H\}$ NMR (100 MHz, $CDCl_3$, δ/ppm): δ 197.10 (**C**≡O), δ 196.54 (d, J^d = 14 Hz, **C**≡O), δ 189.99 (**C**≡O), δ 163.77, δ 161.18, δ 153.90, δ 145.79 (d, J^d = 11 Hz), δ 145.09 (d, J^d = 2 Hz), δ 144.07 (d, J^d = 3 Hz), δ 139.48, δ 130.99, δ 128.29 (d, J^d = 1 Hz), δ 127.32 (d, J^d = 2 Hz), δ 127.09 (d, J^d = 61 Hz), δ 113.48 (d, J^d = 32 Hz). ^{19}F NMR (376 MHz, DMSO-d_6, δ/ppm): δ -36.75 (dd, J^d = 6.92, 1.92 Hz), δ -106.00 (ISTD: *para*-DFB). FTIR (ATR *corr.* $\tilde{\nu}/cm^{-1}$): $\tilde{\nu}$ 3077 (w, C–H sp^2 *str.*), $\tilde{\nu}$ 2021 (s, A'(1) C≡O *str.*), $\tilde{\nu}$ 1890 (s, A'(2) & A'' C≡O *str.*). UV/Vis (CH_3CN, λ/*nm*, ε/$L.mol^{-1}.cm^{-1}$): λ 375 (Re*(dπ)*→π*, ε 2720.95), λ 343 (π→π*, ε 2821.73), λ 269 (π→π*, ε 22069.94), λ 262 (π→π*, ε 22170.71), λ 215 (π→π*, ε 38798.75), λ 200 (π→π*, ε 40915.05).). LRMS (ESI^+): $[M\text{-}Cl]^+$ *m/z* calc. 469.00, *m/z obsv.* 469.12. HRMS (ESI^+): $[M+Na]^+$ *m/z calc.* 524.9557 ($C_{15}H_7N_2O_3FClReNa^+$); *m/z obsv.* 524.9579 (Δ 4.20 ppm). EA (%): *calc.* C 3575, H 1.40, N 5.56, Cl 7.04; *obsv.* C 35.73, H 0.98, N 5.59, Cl 6.83.

3.2 Rhenium-Phenanthroline Fluorine-18 Labelling and Testing of Non-Azeotropically Distilled Conditions

Drying by azeotropic distillation is typically required for nucleophilic reactions involving [^{18}F]fluoride, in order to increase the nucleophilicity of the fluoride which is otherwise hindered in the presence of water.[7] It remains a time-consuming process (> 15 mins), however, during which radioactivity (≥ 10%) is lost due to the radioactive decay of the fluorine-18 radioisotope and non-specific adsorption of [^{18}F]fluoride to the surface of the azeotropic distillation vial.[84, 85] Following the synthesis of the **2ClPhen** phenanthroline precursor and its rhenium tricarbonyl complex, radiofluorination attempts were attempted *via* nucleophilic aromatic substitution for [^{18}F]fluoride. However, during the radiolabelling experiments it was discovered that the solenoid valves enabling nitrogen gas flow and vacuum flow to and from the azeotropic distillation vial were not operating, as marked by the red crosses in in Figure 83. Thus, indicating that the [^{18}F]fluoride was not being properly dried prior to the radiolabelling experiments. Despite the lack of azeotropically dried conditions, the radiolabelling of the rhenium complexes progressed unexpectedly and afforded considerable RCYs. This led to an ongoing investigation in each of the subsequent chapters whereupon azeotropically dried (*dry*) conditions and non-azeotropically dried (*wet*) conditions, which still containing a 10% v/v content of water, were compared in the radiolabelling of some rhenium complexes. In each case it was found that the radiolabelling of rhenium complexes can circumvent the requirement for azeotropic distillation of the [^{18}F]fluoride media.

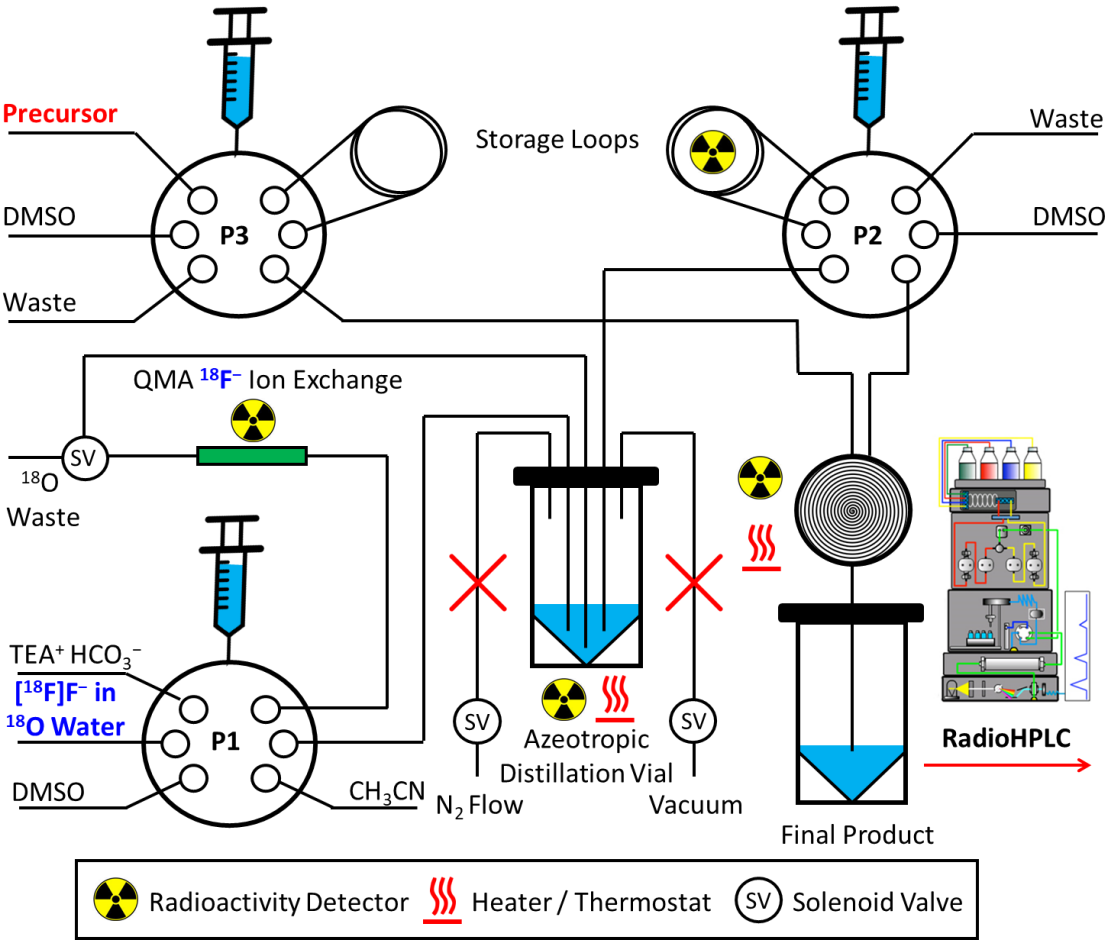

Figure 83. Solenoid valves supplying nitrogen gas and vacuum flow to and from the azeotropic distillation vial were not operating (marked by red crosses) within the microfluidic set-up, thus resulting in non-azeotropically dried reaction conditions during some radiolabelling experiments.

3.2.1 Fluorine-18 Labelling of 2-Chloro-1,10-Phenanthroline

The first strategy developed for attaining the radiofluorinated rhenium complex was to first radiolabel the 2-chloro-1,10-phenanthroline ligand *via* nucleophilic aromatic substitution for [^{18}F]fluoride and then subsequently complex the ligand to source of rhenium *via* a multistep synthesis outlined in Figure 84. To first verify the retention time of **[^{18}F]2FPhen**, a non-radioactive standard of **2FPhen** was injected on the HPLC using an isocratic mobile phase consisting of 8% acetonitrile and 82% water, each containing 0.05% TFA modifier, with a 1 mL.min^{-1} flow rate. The retention time was determined to be approximately 3.0 mins, as shown by the chromatogram in Figure 85. An example radiochromatogram of the reaction affording **[^{18}F]2FPhen** is shown in Figure 86, alongside the UV absorption chromatogram attained for the same reaction at 190 °C which shows the remaining unreacted **2ClPhen** and a very minor UV peak forming, of value for determining molar absorptivities. A series of reactions were performed using the same precursor concentrations, amount of radioactivity and reaction time (0.08 µmol, 29±10 MBq and 47 s, respectively) under *dry* conditions, though with varying temperature conditions ranging from 50 to 190 °C in 20 °C increments. The non-isolated RCYs determined for each of these reaction temperatures by radioHPLC analysis is shown in Figure 87. Under *wet* conditions no RCY was obtained for the radiolabelling of **2ClPhen**, which was not surprising given that most radiofluorination reactions do not afford radioproducts in the presence of water due to the suppressed nucleophilicity of the [^{18}F]fluoride.[7] Under *dry* conditions, however, **[^{18}F]2FPhen** did indeed form, though only at temperatures greater than 130 °C. Moderate RCYs of 24% and 38% were observed when using reaction temperatures of 150 °C and 170 °C, respectively. Maximum RCYs of 49, 54 and 60% were attained from triplicate analyses at 190 °C. Higher temperatures were not trialled as the microfluidic module

could not heat at temperatures greater than 210 °C and it was not desirable to operate at this limit for multiple analyses. These results were also mirrored by radioTLC analyses, shown in Figure 88, attained from separating the radioactive species using an ethyl acetate mobile phase on a silica plate stationary phase. No **[^{18}F]2FPhen** was found to form at temperatures below 130 °C by radioTLC, and RCYs of 23, 38 and 58% were attained at the higher temperatures of 130, 150 and 190 °C, respectively.

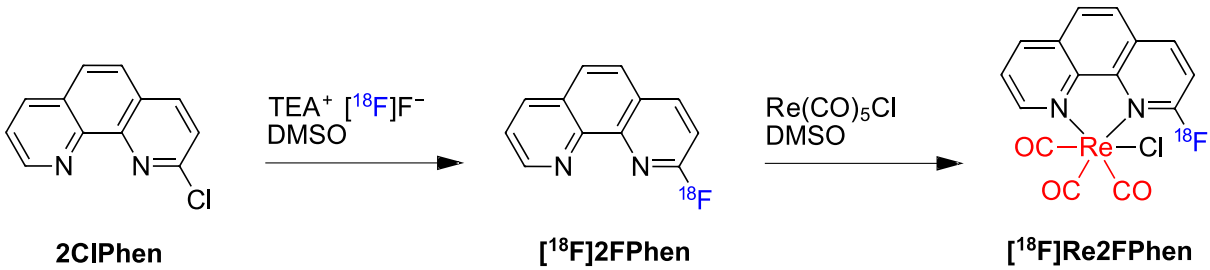

Figure 84. Multiple-step radiosynthesis involving the radiofluorination of **2ClPhen** to attain **[^{18}F]2FPhen**, followed by rhenium complexation to attain **[^{18}F]Re2FPhen**.

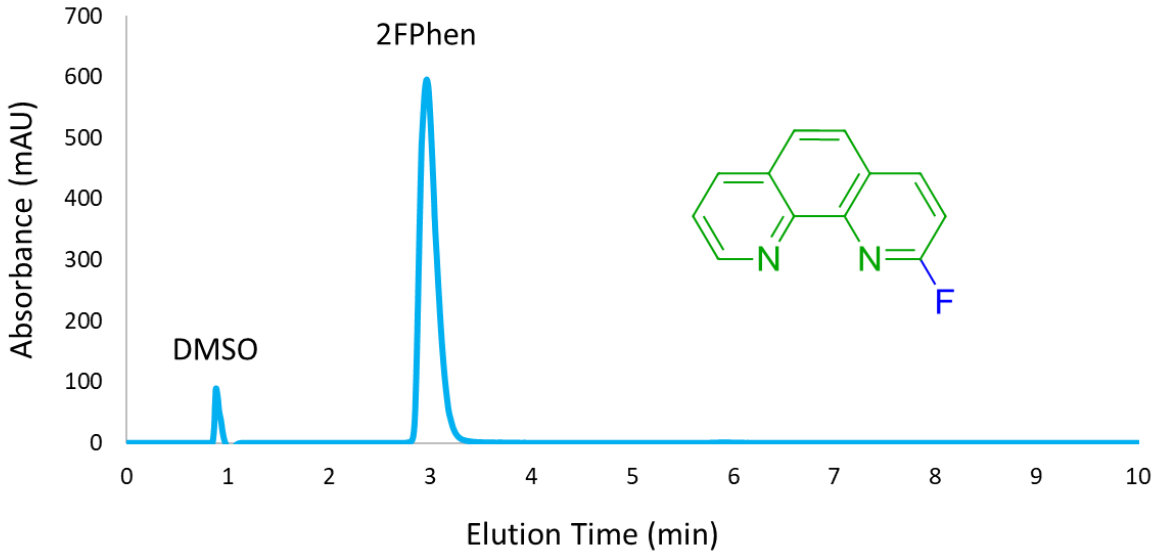

Figure 85. UV-absorbance chromatogram of the **2FPhen** standard, providing a retention time of approximately 3.0 mins using an isocratic mobile phase consisting of 8% acetonitrile and 82% water (each containing 0.05% TFA) with a flow rate of 1 mL.min^{-1}.

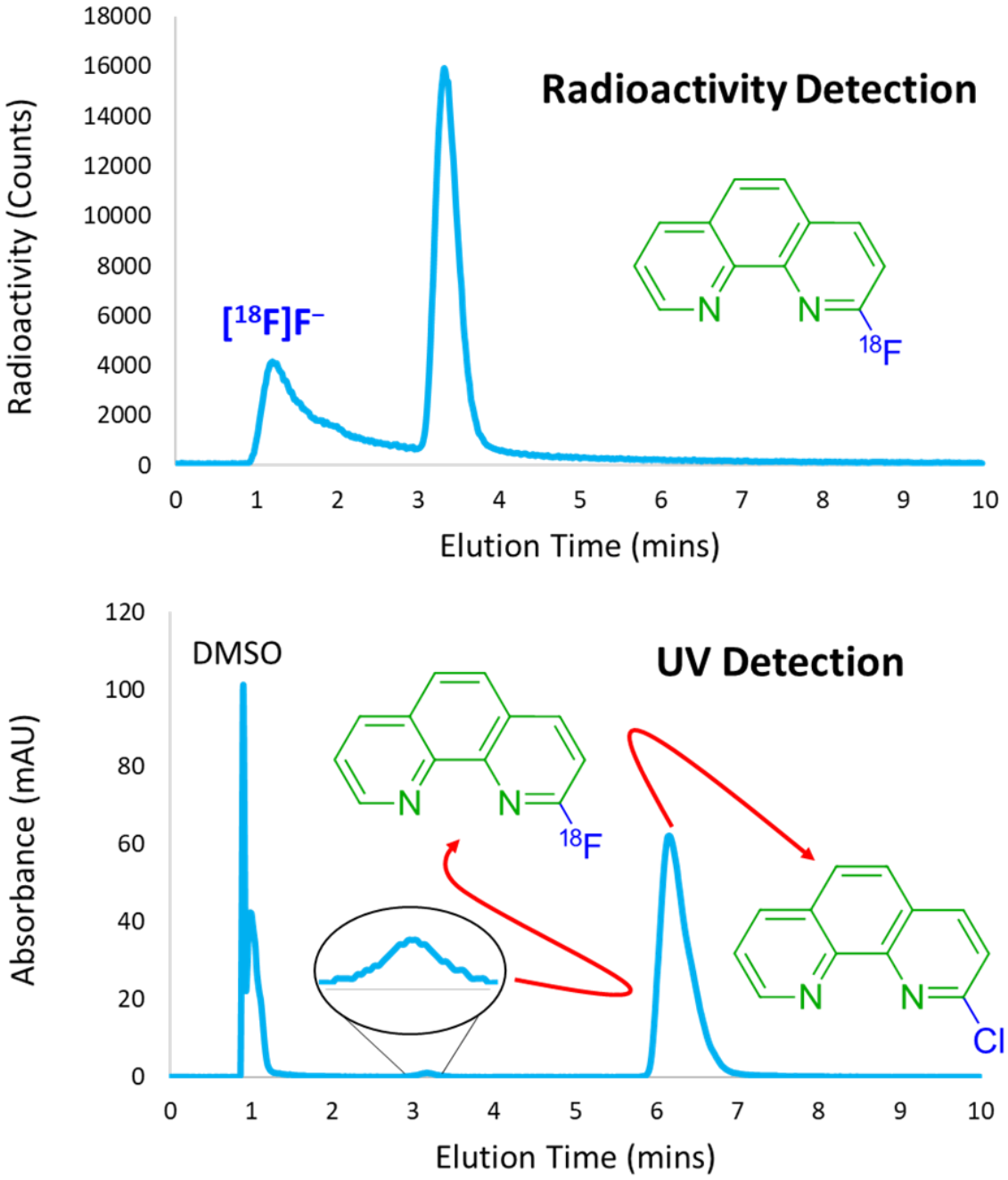

Figure 86. Radiochromatogram for the formation of **[^{18}F]2FPhen** (top) at 190°C, with an RCY of 60% calculated from the peak area integration ratio between the **[^{18}F]2FPhen** peak (3.3 min) and the entire radiochromatogram inclusive of the unreacted [^{18}F]fluoride (1.3 min). The UV absorbance chromatogram (bottom) for the same reaction shows the early eluted DMSO (0.9 min) and the later eluting unreacted **2ClPhen** (6.2 min) alongside a small UV absorbance peak with a retention time aligned with the **[^{18}F]2FPhen** radioproduct.

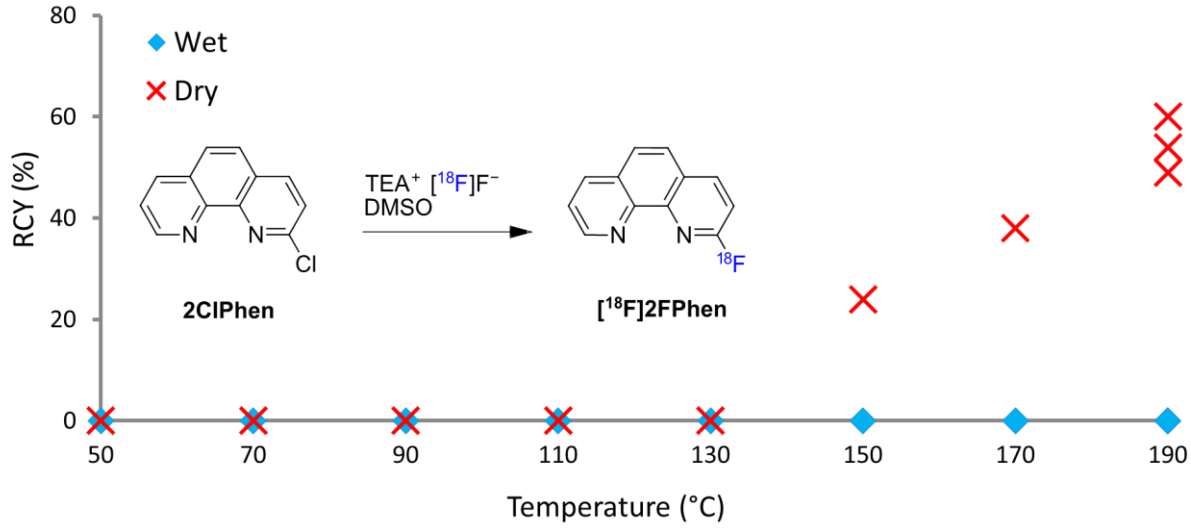

Figure 87. Non-isolated RCYs for **[^{18}F]2FPhen** determined by radioHPLC as a function of reaction temperature for both *wet* (blue diamonds) and *dry* (red crosses) reaction conditions.

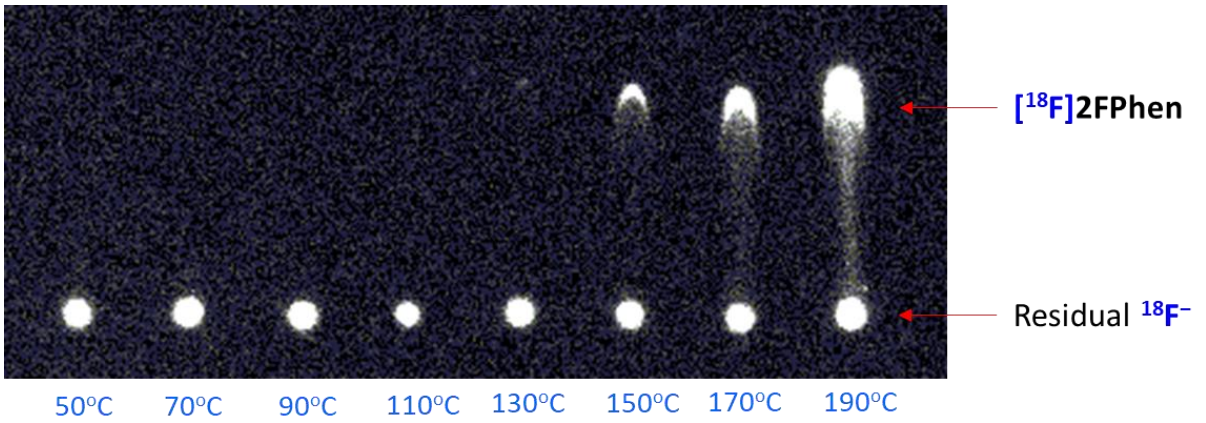

Figure 88. RadioTLC results for the radiofluorination reactions forming **[^{18}F]2FPhen** at varying temperatures under *dry* conditions (0.08 µmol of precursor, 29±10 MBq of radioactivity, 47 s reaction time). The results suggest that radiolabelling could only be achieved at temperatures greater than 130°C. Separations were achieved using an ethyl acetate mobile phase on a silica plate stationary phase.

3.2.2 Multiple Step Fluorination and Complexation of [^{18}F]2-Fluoro-1,10-Phenanthroline with Rhenium

Using the optimal 190 °C *dry* temperature conditions for the radiosynthesis of **[^{18}F]2FPhen**, a fourth pump (P4) was then connected in series to the microfluidic set-up in order to provide a second precursor solution and second microreactor in flow, as shown in Figure 89. The second precursor consisted of pentacarbonylchlororhenium(I) of differing equivalents in DMSO solution, and the temperature of the second microreactor was trialled between 70 and 190 °C in 30 °C increments in order to determine the ideal temperature for rhenium complexation and thus the formation of **[^{18}F]Re2FPhen**. The UV-absorbance chromatogram for the non-radioactive **Re2FPhen** standard is shown in Figure 90 using chromatographic conditions consisting of 35% acetonitrile and 65% water, each containing 0.05% of TFA modifier. The RCY for the formation of **[^{18}F]Re2FPhen** for each given temperature of the second microreactor is shown in Figure 91 for one, five and eight equivalences (*i.e.* 0.08, 0.40 and 0.64 µmol) of pentacarbonylchlororhenium(I). No RCY was obtained at 70 and 100 °C, however at 130 °C RCYs of 5% and 21% were obtained for one and five equivalences, respectively. At 160 °C one equivalence of the rhenium source afforded 14% RCY of **[^{18}F]Re2FPhen** with the same yield afforded at 190 °C. Whereas using both five and eight equivalences of the pentacarbonylchlororhenium(I) precursor provided the greatest yield at 190 °C with both affording 35% RCY. In order to determine the molar activity of the **[^{18}F]Re2FPhen** product, differing concentrations of the non-radioactive **Re2FPhen** standard were injected onto the HPLC, as shown in Table 4. The integrated UV peak areas determined for each sample in DMSO were then plotted against the calculated molar amounts in order to construct the calibration curve shown in Figure 92. The correlation co-efficient (R^2) value for the curve was

0.9992 signifying a good linear fit of the curve and provided equation (15) linking the integrated peak area (*pA*) at 254 nm with the molar amount (*n*) of **Re2FPhen**.

$$pA = 0.9298(n) - 2.7325 \quad (15)$$

Rearrangement of equation (15) allows the molar amount (*n*) to be substituted into the previously discussed equation (6) which, provided the radioactivity (*A*) of the sample was measured at the time of injection, can be used to determine the molar activity (A_M) of **[^{18}F]Re2FPhen** by yielding equation (16).

$$A_M = 0.9298(A)(2.7325 + pA)^{-1} \quad (16)$$

The molar activities of **[^{18}F]Re2FPhen** determined for three of the reaction temperatures (130, 160 and 190 °C) at the second microreactor are provided in Table 5. The injected radioactivity, UV integrated peak area and molar amounts used to calculate the molar activity *via* equations (15) and (16) are also provided in the table. Taking the mean of the three determined molar activities provides an average of 1.2 ± 0.2 MBq.nmol^{-1} for **[^{18}F]Re2FPhen** using this multiple step radiosynthetic approach.

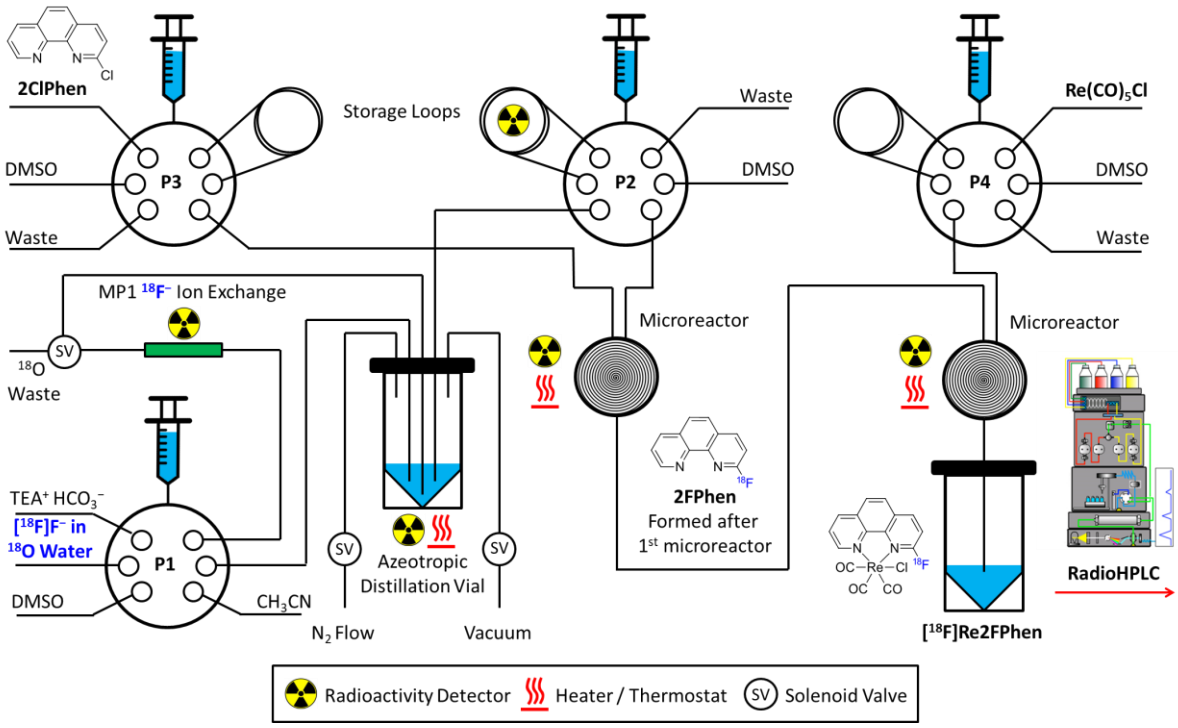

Figure 89. Automated microfluidic module set-up for the two-step radiosynthesis forming **[^{18}F]Re2FPhen**. **[^{18}F]2FPhen** was formed at the first reactor from **2ClPhen** at a consistent 190 °C reaction temperature. Thereafter a fourth pump (P4) was plumbed to deliver the $Re(CO)_5Cl$ precursor, alongside a second microreactor whereby the **[^{18}F]2FPhen** was complexed at varying reaction temperatures to synthesise the **[^{18}F]Re2FPhen** radioproduct for HPLC analysis.

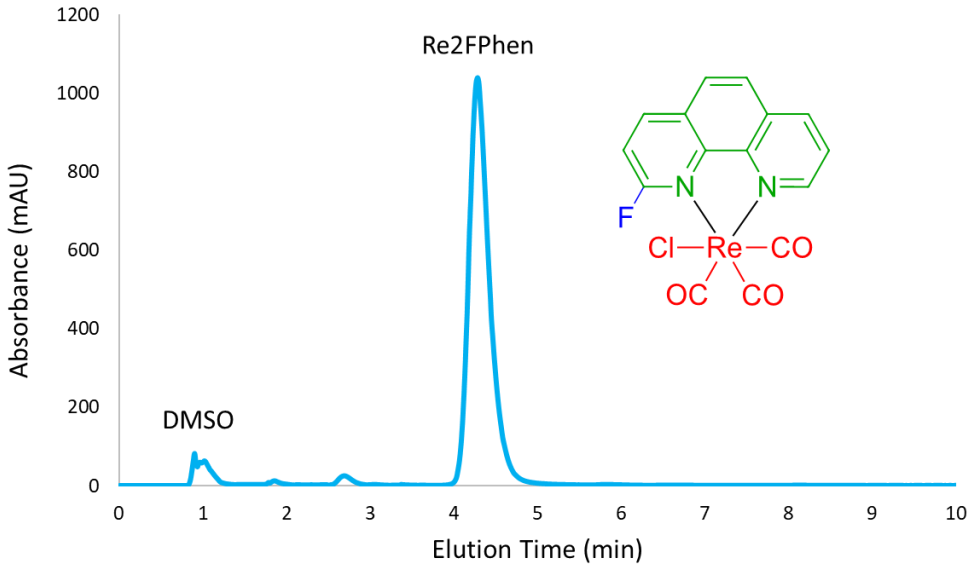

Figure 90. UV-absorbance chromatogram of **Re2FPhen** providing a retention time of approximately 4.2 mins while using a mobile phase consisting of 35% acetonitrile and 65% water, each containing 0.05% TFA modifier, and a flow rate of 1 mL.min^{-1}.

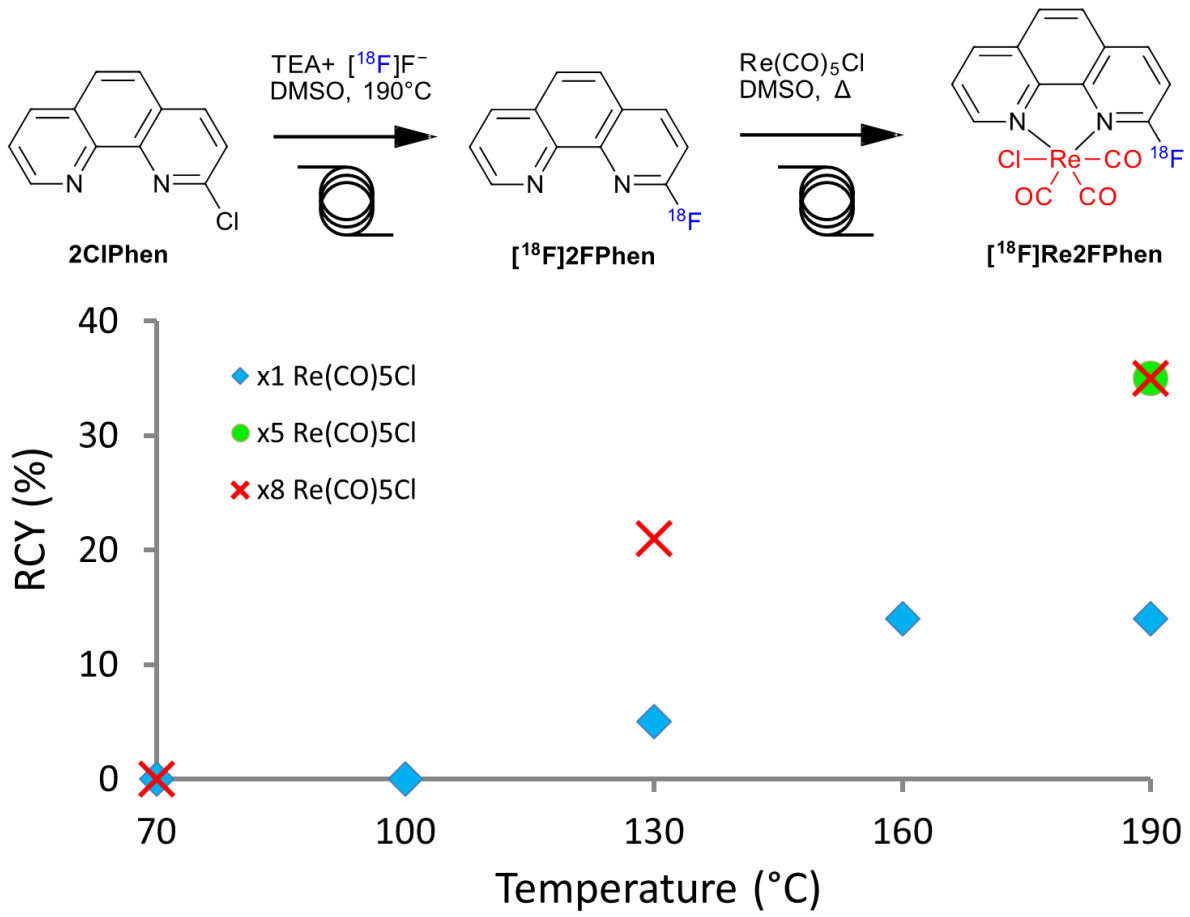

Figure 91. RCY of **[^{18}F]Re2FPhen** plotted as a function of the complexation reaction temperature at the second microreactor. RCYs are plotted for one equivalence (0.08 µmol, blue diamonds), five equivalence (0.40 µmol, red crosses) and eight equivalence (0.64 µmol, green circle) of the $Re(CO)_5Cl$ precursor.

Table 4. Concentration of **Re2FPhen** standards used to construct a calibration curve for the determination of the molar activity of the radioproduct. 10 µL of each standard was injected into the HPLC in order to plot the calculated molar amount against the integrated UV peak area determined for the sample.

Concentration (ug/mL)	Mass in 10uL (ng)	Molar Amount (pmol)	UV Integrated Peak Area (mAu.s)
8.00	80.0	158.8	143.9
4.00	40.0	79.4	73.1
2.00	20.0	39.7	34.7
1.00	10.0	19.8	14.1
0.50	5.0	9.9	7.9
0.25	2.5	5.0	0.5

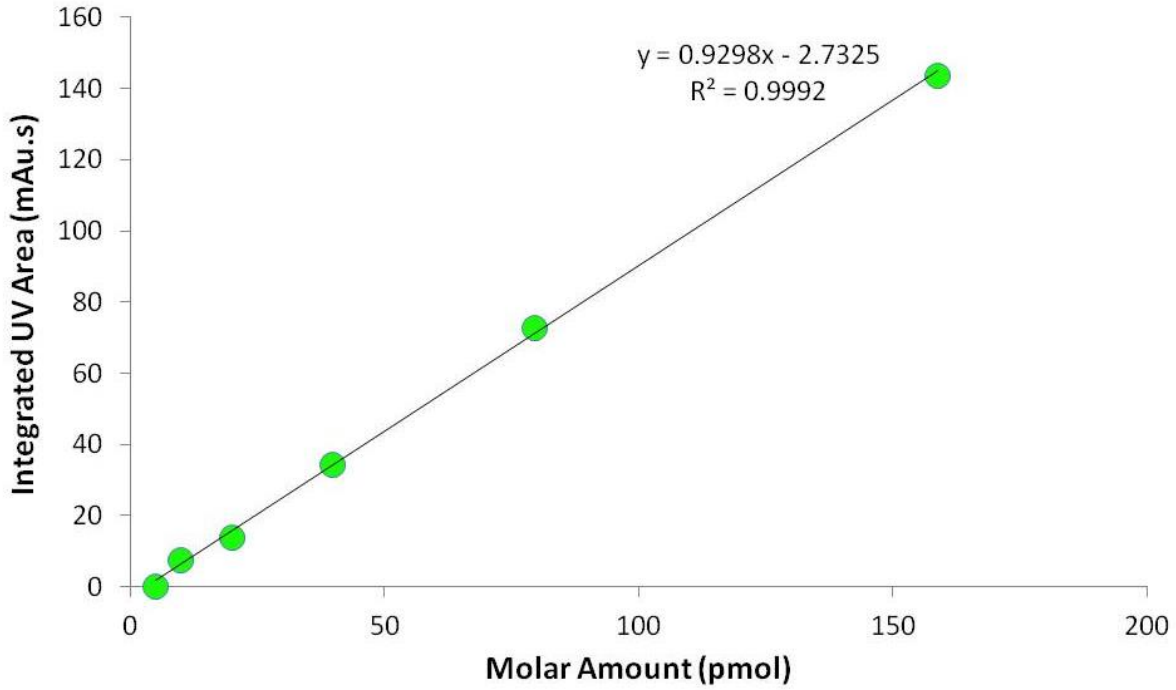

Figure 92. Calibration curve plotting the molar amount of **Re2FPhen** against the integrated UV peak area afforded from each sample in order to determine the molar activity of the **[^{18}F]Re2FPhen** radioproduct.

Table 5. Molar activities determined from the injected activity, molar amount and integrated UV peak area for the multiple step radiosynthesis of **[^{18}F]Re2FPhen** at three differing temperatures of the second microreactor.

Temperature (°C)	**Activity Injected (MBq)**	**UV Integrated Area (mAu.s)**	**Molar Amount (pmol)**	**Molar Activity (MBq/nmol)**
130	0.033	120.6	132.6	0.245
160	0.049	470.6	509.1	0.096
190	0.098	285.0	309.5	0.317

3.2.3 Radiofluorination of 2-Chloro-1,10-Phenanthroline Complexed to Rhenium

To improve upon the low molar activity of **[^{18}F]Re2FPhen** attained from the multiple-step radiosynthesis, a single-step radiosynthesis was trialled using the **Re2ClPhen** precursor. The same reactions conditions were employed (0.08 µmol of precursor, 29±10 MBq of activity and 47 s reaction time) in DMSO solvent, as per the radiosynthesis of **[^{18}F]2FPhen** and *wet* and *dry* conditions were likewise tested also. The only change in variable was the reaction temperature, whereupon different reactions were tested from 30 to 170 °C in 20 °C increments. Intriguingly, a noticeable difference in the radiochromatograms was observed for the same reaction temperatures under *wet* and *dry* conditions. These differences are shown in Figure 93, whereupon under dry conditions less of the **[^{18}F]Re2FPhen** radioproduct (3.9 mins) formed at all, despite more of the **Re2ClPhen** precursor (6.2 mins) being consumed. The increased presence of an early eluting UV absorbing by-product (3.0 mins) appears to account for the loss of precursor. Surprising, under *dry* conditions for the same given temperature the UV absorbing by-product formed in much lesser abundance. This was corelated with an increased RCY of **[^{18}F]Re2FPhen** forming from the available **Re2ClPhen** precursor. The determined RCYs for each reaction temperature under *wet* and *dry* conditions are plotted in Figure 94. Under *dry* conditions the **[^{18}F]Re2FPhen** product was found to form at most in 19% RCY at 30 °C, with reliable RCYs of 14, 15 and 17% being measured in triplicate at 50 °C. Thereafter RCYs of 14, 15, 10 and 6% formed at temperatures of 70, 90, 110 and 130 °C, respectively, and formed no yield at higher temperatures. The *wet* conditions, however, afforded much greater RCYs of 69, 70 and 78% forming at 50 °C, which likewise decreased to 38, 53, 29 and 16% RCY at temperatures of 70, 90, 110 and 130 °C, respectively, before affording no **[^{18}F]Re2FPhen** product at higher temperatures. This result was in contrast with the RCYs

obtained for **[^{18}F]2FPhen** forming from **2ClPhen** which not only required temperatures greater than 130 °C to obtain a radioproduct, though which also did not afford any radioproduct under *wet* conditions. In the case of **[^{18}F]Re2FPhen** formation, *wet* conditions and lower temperatures (< 150 °C) appeared to be favourable in forming the radioproduct. The UV-absorbing by-product was confirmed to be base-mediated *via* the spiked addition of sodium hydroxide (5 µL, 5 mol.L^{-1}) to an HPLC injected solution of **Re2ClPhen** which indeed formed the UV by-product which was unobservable hitherto. Thus, the increased RCY of **[^{18}F]Re2FPhen** under *wet* conditions may be a consequence of increased basicity of the media.

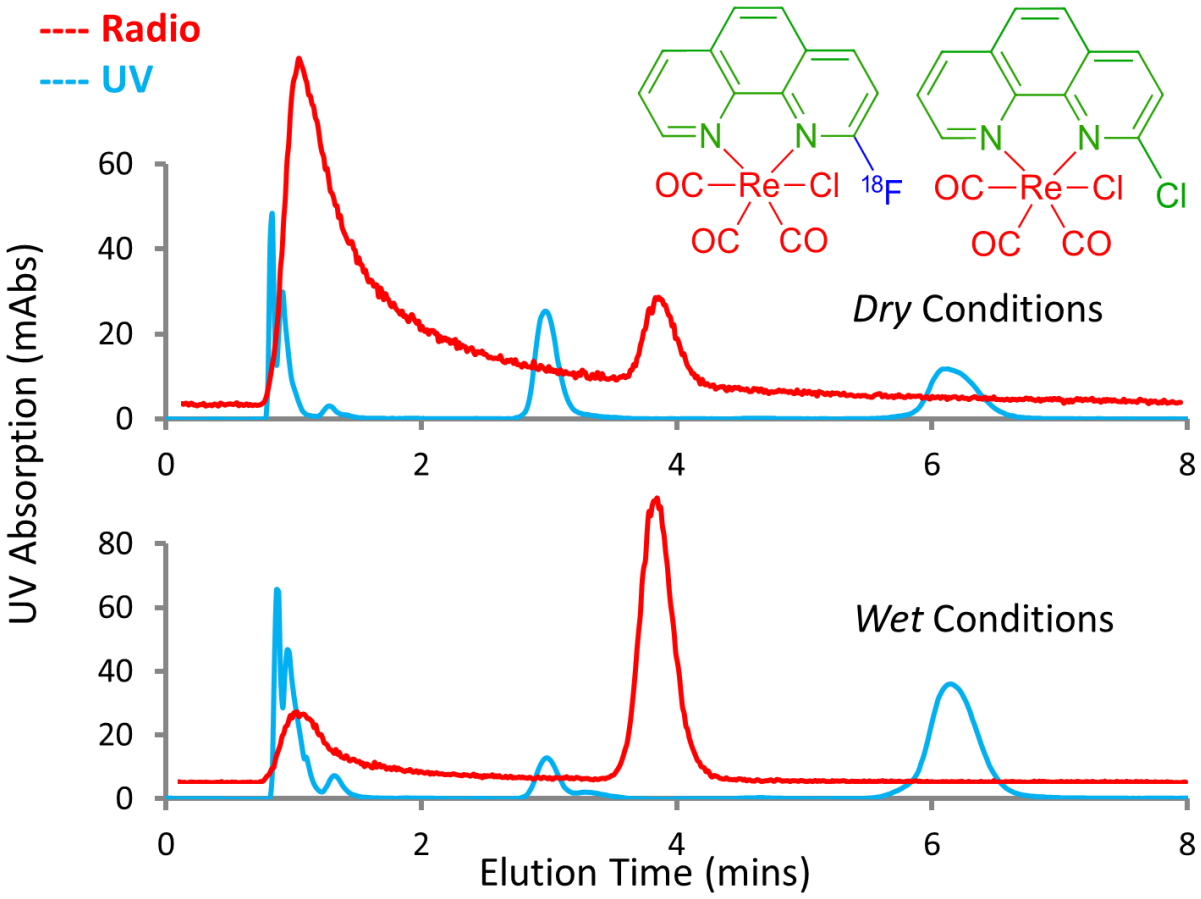

Figure 93. UV absorbance chromatogram (254 nm, blue) and superimposed radioactive (red) profiles for the *wet* and *dry* analogous conditions (top and bottom) used to radiosynthesise **[^{18}F]Re2FPhen**. A UV degradation by-product is observed at 3.0 mins alongside the unreacted **Re2ClPhen** precursor at 6.2 mins (absorbance from the DMSO solvent is also observed at around 1 min). The radiochromatogram shows the elution of the unreacted [^{18}F]fluoride at 1.0 min and the **[^{18}F]Re2FPhen** radioproduct at 3.9 min elution time.

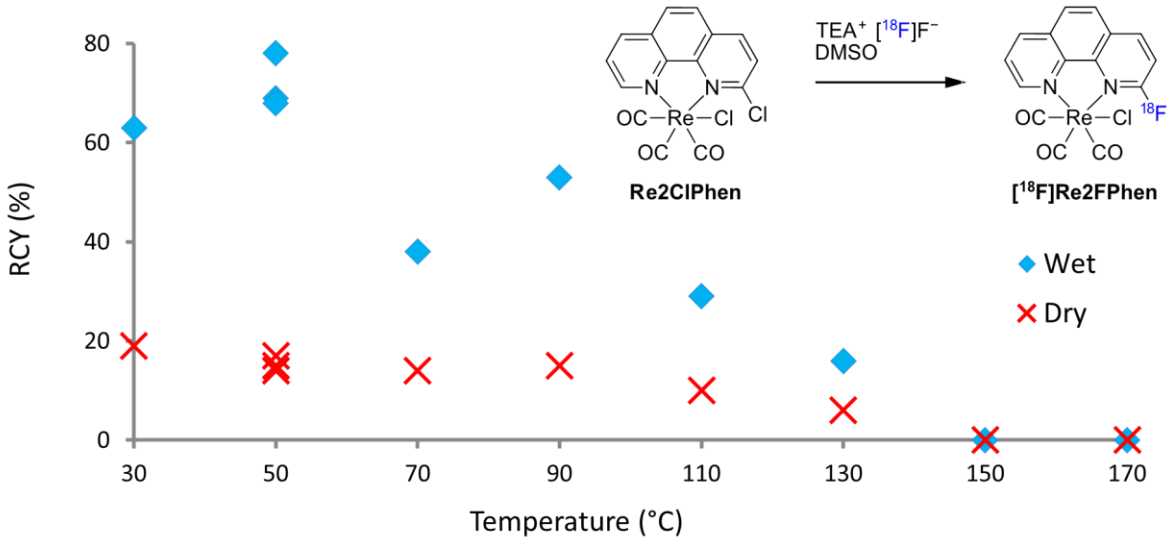

Figure 94. RCY of **[^{18}F]Re2FPhen** forming from **Re2ClPhen** as a function of reaction temperature under *wet* (blue diamonds) and *dry* (red crosses) conditions. The reaction was found to afford greater yield under low temperature, *wet* conditions which is the opposite trend of typical nucleophilic radiofluorinations.

To determine the molar activity of **[^{18}F]Re2FPhen** formed in these single step radiosynthetic reactions the injected activity, UV integrated peak areas and molar amounts were all recorded for each of these tested reaction temperatures which yielded a radioproduct (Table 6). Substituting these values into equations (15) and (16) then allowed for the determination of the molar activity which, taken as an average, was calculated as 71±29 MBq.nmol^{-1}. The comparative molar activities for the single-step and multiple-step radiosyntheses of **[^{18}F]Re2FPhen** are shown in Figure 95.

Table 6. Molar activities determined from the injected activity, molar amount and integrated UV peak area for the single step radiosynthesis of **[^{18}F]Re2FPhen** from **ReClPhen** at each of the reaction temperatures affording a radioproduct.

Temperature (°C)	Activity Injected (MBq)	UV Integrated Area (mAu.s)	Molar Amount (pmol)	Molar Activity (MBq/nmol)
30	1.244	13.9	17.9	69.6
50	0.949	7.9	11.4	83.0
70	0.523	4.0	7.2	72.2
90	0.596	5.4	8.7	68.2
110	0.363	2.6	5.7	63.2
130	0.160	1.4	4.4	36.0

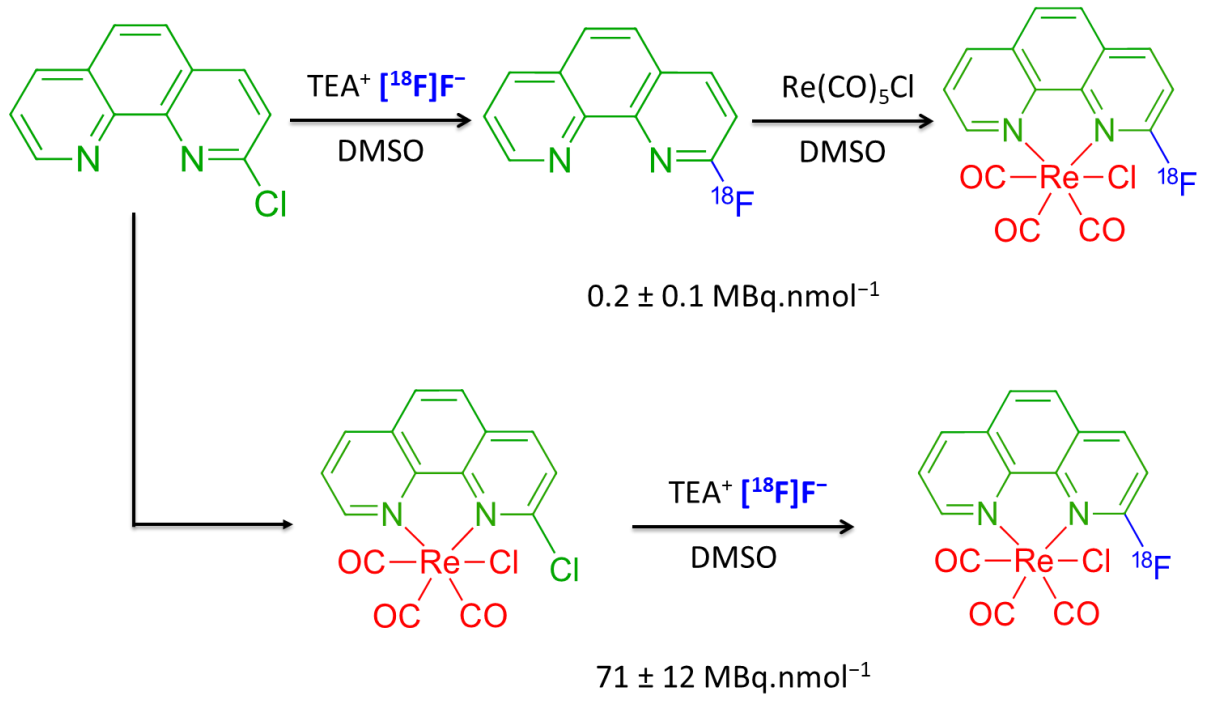

Figure 95. Difference in molar activities acquired for the multiple-step radiosynthesis (top, 0.2±0.1 MBq.nmol^{-1}) and single-step radiosynthesis (bottom, 71±12 MBq.nmol^{-1}) of **[^{18}F]Re2FPhen**.

Alternative experiments were also trialled, by adjusting the reaction time and the **Re2ClPhen** precursor amount, to increase the RCY of **[^{18}F]Re2FPhen**. In Figure 96, increasing the reaction time was found to steadily increase the yield of the radioproduct with shorter reaction times of 8, 12 and 24 seconds found to afford lesser RCYs of 27, 34 and 42%, respectively, when employing the optimal reaction temperature of 50 °C alongside the usual 0.08 µmol concentration of the **Re2ClPhen** precursor and 29±10 MBq of [^{18}F]fluoride under *dry* conditions. Triplicate analyses with a reaction time of 47 s afforded between 49 and 60% RCY, as expected based upon the previous temperature dependent reactions. Intriguingly though, a longer reaction time of 94 seconds only afforded only 56% RCY, no greater than the RCYs attained at from the 47 second reaction time experiments. Adjusting the precursor amount, however, did not appear to have such a varied influence on the amount of **[^{18}F]Re2FPhen** synthesised. Figure 97 plots the RCY as a function of differing precursor amounts used while keeping the reaction temperature (50 °C), reaction time (47 s) and radioactivity (29±10 MBq) constant. From these experiments, RCYs of 53, 49, 61 and 44% were observed when employing half (0.04 µmol), standard (0.08 µmol), approximately double (0.15 µmol) and approximately five times (0.38 µmol) the amount of **Re2ClPhen** in each of the reactions.

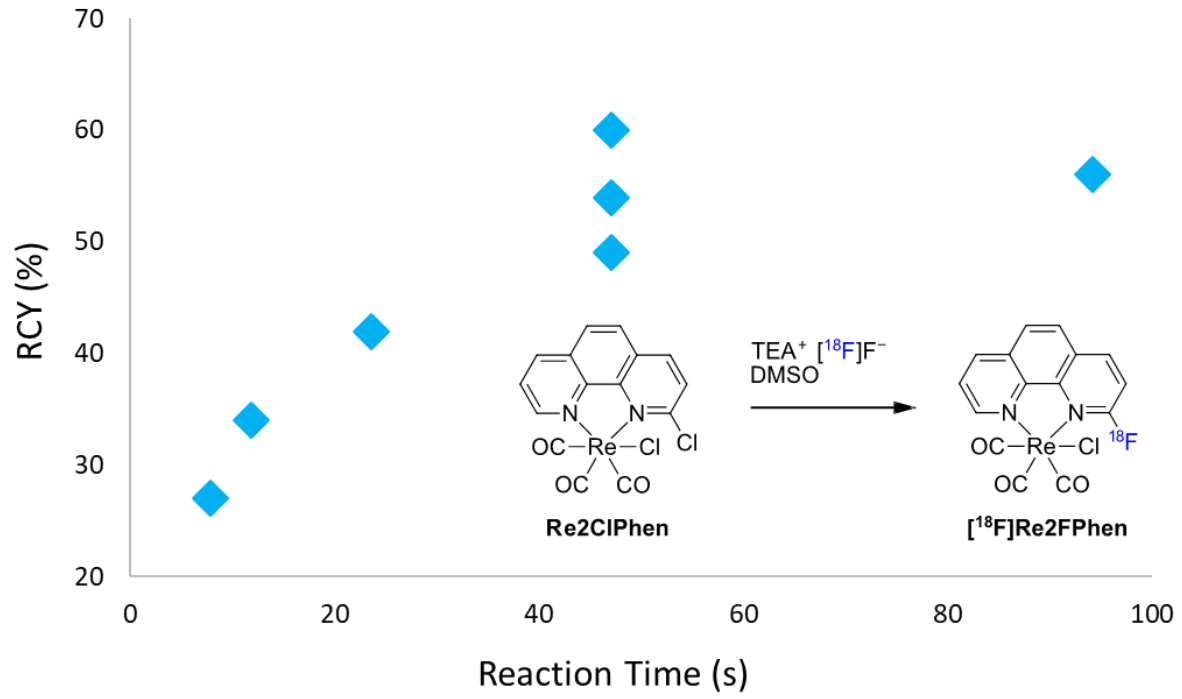

Figure 96. Effect on the RCY of **[^{18}F]Re2FPhen** obtained when changing the reaction time while keeping all other parameters constant (*i.e.* 50 °C reaction temperature, 0.08 µmol of **Re2ClPhen** precursor and 29±10 MBq of [^{18}F]fluoride).

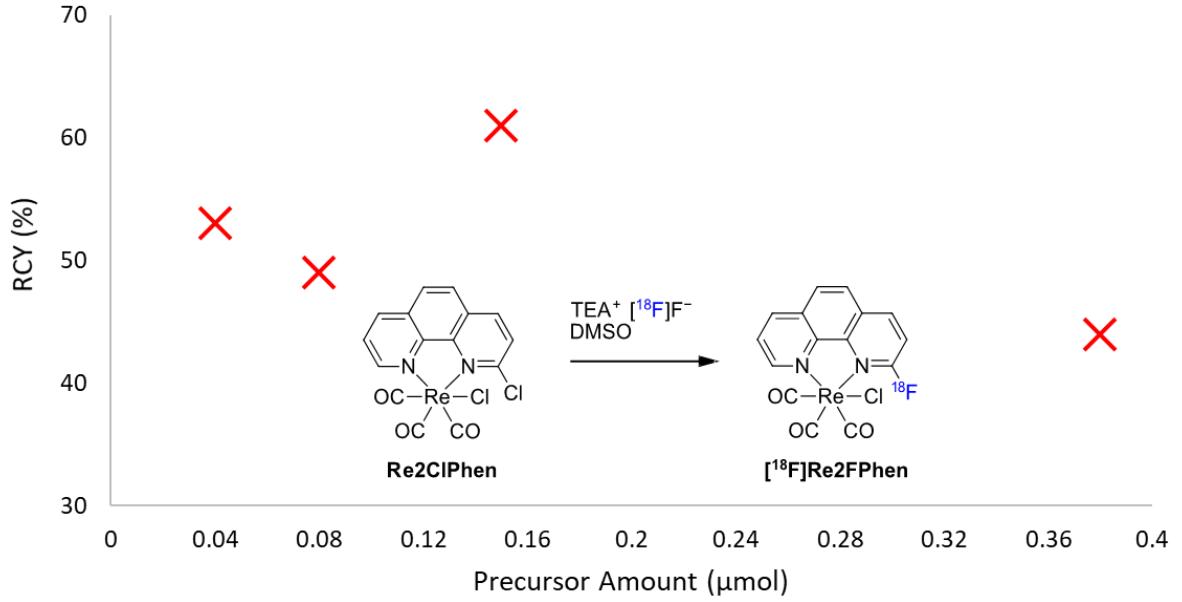

Figure 97. Adjusting the precursor amount of **Re2ClPhen** used in the reaction while keeping the other reaction parameters constant (50 °C temperature, 47 s reaction time and 29±10 MBq of radioactivity) did not afford any substantial difference in the RCY of **[18F]2FPhen**.

3.3 Photophysical Analyses of Rhenium-Phenanthroline Complexes

In accordance with the goal to evaluate the use of radiofluorinated rhenium tricarbonyl complexes as PET-optical probes, the photophysical properties of both the **Re2ClPhen** precursor and **Re2FPhen** standard were measured. An emission spectrum was initially obtained for **Re2ClPhen** in DMSO solution (10^{-4} mol.L^{-1}) by applying a monochromatic excitation wavelength of 370 nm, which aligned closely with the MLCT absorption maxima of the complex determined by UV-Vis spectroscopy. The emission maximum was determined to be 654 nm. Thus, a wavelength of 650 nm was set to be detected to acquire the excitation spectrum of the complex. The excitation spectrum notably deviated from the expected gaussian shaped peak profile due to inner filter effects arising from the solution. These inner filter effects may have been caused by the reabsorption of emitted photons, or a too greater concentration of the absorbing analyte, such that the intensity of excitation photons was not homogeneous within the solution. Nonetheless an excitation maximum of 382 nm was measured. Figure 98 shows the overlaid emission and excitation spectra of **Re2ClPhen**. The same experiment was performed on a solution of **Re2FPhen** in DMSO (10^{-4} mol.L^{-1}), whereupon an emission spectrum was first obtained using a set excitation wavelength of 370 nm. From this spectrum the **Re2FPhen** complex was verified to have an emission maximum of 654 nm. The excitation spectrum which was subsequently obtained by applying a fixed monochromatic emission wavelength of 650 nm, though also appeared to be subject to inner filter effects. An excitation maximum of 382 nm was nonetheless determined for **Re2FPhen**, akin to the excitation maximum observed for **Re2ClPhen**. An overlay of the normalised emission and excitation spectra attained for **Re2FPhen** is provided in Figure 99. Experimental uncertainties are estimated to be ±5 nm for the absorption and emission peaks.

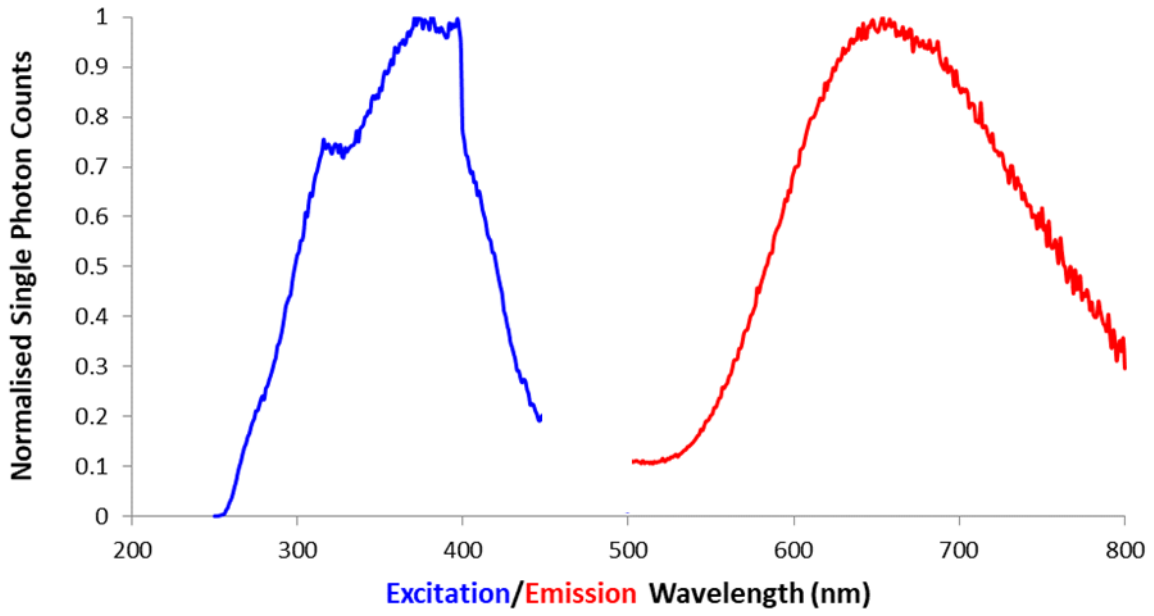

Figure 98. Normalised spectra exhibiting overlaid emission maxima of 654 nm and excitation maxima of 382 nm (subject to inner filter effects) for a solution of **Re2ClPhen** in DMSO, given fixed excitation and emission wavelengths of 370 nm and 650 nm, respectively.

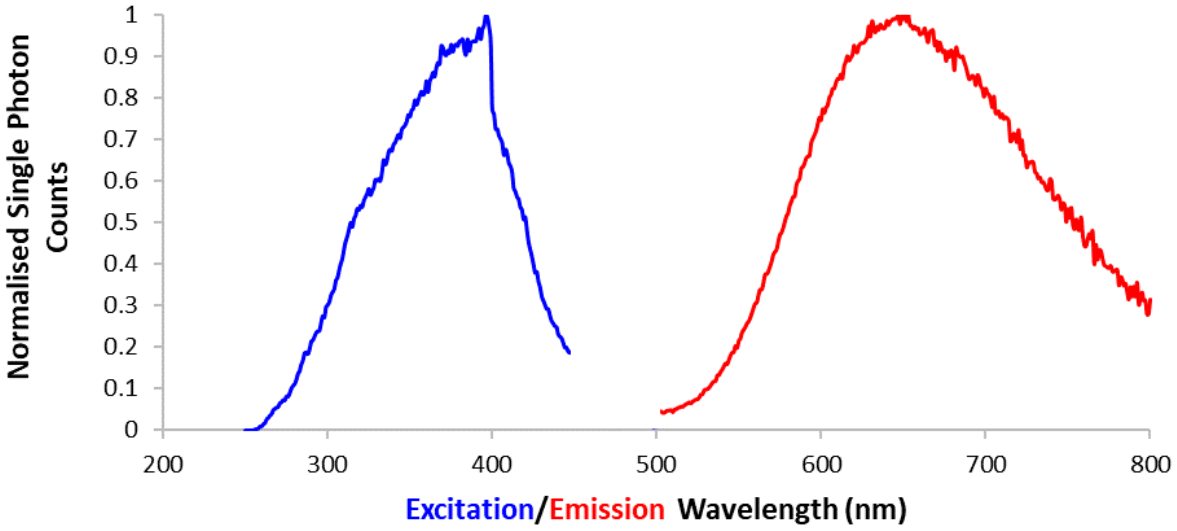

Figure 99. Normalised spectra exhibiting overlaid emission maxima of 653 nm and excitation maxima of 396 nm (subject to inner filter effects) for a solution of **Re2FPhen** in DMSO, given fixed excitation and emission wavelengths of 370 nm and 650 nm, respectively.

3.3.1 Quantum Yield Determination of 2-Chloro and 2-Fluoro Phenanthroline Complexes

The quantum yields of the **Re2ClPhen** and **Re2FPhen** complexes were determined for comparison with other optical emission agents. The quantum yield was determined from correction factors applied using a $[Ru(BiPy)_3]Cl_2$ reference standard in water solution, which consisted of a quantum yield of 0.028, an absorbance intensity of 0.045 at 410 nm and refractive index of 1.333. Integration of the emission spectrum of $[Ru(BiPy)_3]Cl$, acquired through a fixed monochromatic excitation wavelength of 410 nm, afforded 4.71×10^6 counts·nm. The quantum yield of both **Re2ClPhen** and **Re2FPhen** were measured in both air equilibrated DMSO solution and an aqueous solution consisting of 5% DMSO to aid solubility, consisting of refractive indices of 1.479 and 1.339, respectively. The absorbances of the **Re2ClPhen** solutions at 410 nm were 0.169 and 0.333 for the complex dissolved in DMSO and 5% DMSO solution, respectively. Integration of the emission spectrum obtained from a fixed monochromatic excitation wavelength of 410 nm afforded 1.46×10^6 counts·nm and 3.00×10^6 counts·nm for **Re2ClPhen** dissolved in DMSO and 5% DMSO solutions, respectively. Likewise, absorbances of **Re2FPhen** at 410 nm were 0.284 and 0.193 in DMSO and 5% DMSO solutions, respectively. Integrations of the emission spectra obtained *via* a 410 nm excitation wavelength afforded values of 2.51×10^6 counts·nm and 1.52×10^6 counts·nm in DMSO and 5% DMSO respectively. These parameters, tabulated in Table 7, were substituted into equation (14) to afford the quantum yields of **Re2ClPhen** and **Re2FPhen**. The quantum yields were calculated to be 0.3% for both **Re2ClPhen** and **Re2FPhen** in DMSO solution, and 0.2% for both **Re2ClPhen** and **Re2FPhen** in 5% DMSO solution. Experimental uncertainties are estimated to be ±0.1% for the quantum yields.

Table 7. Air equilibrated quantum yields calculated for the **Re2ClPhen** and **Re2FPhen** complexes *via* comparison to a $[Ru(BiPy)_3Cl]$ reference standard with correction factors applying for the refractive index of the media, absorbance at the 410 nm excitation wavelength and the integration of the emission spectrum.

Analyte	Solvent	Refractive Index	Absorbance	Emission Integration (counts·nm)	Quantum Yield (%)
$[Ru(BiPy)_3]Cl$	Water	1.333	0.045	4.71×10^6	2.8%
Re2ClPhen	DMSO	1.479	0.169	1.46×10^6	0.3%
	5% DMSO	1.339	0.333	3.00×10^6	0.2%
Re2FPhen	DMSO	1.479	0.284	2.51×10^6	0.3%
	5% DMSO	1.339	0.193	1.52×10^6	0.2%

The quantum yields obtained for these rhenium tracers thus fell within the ranges reported for the cyanine dyes used in PET-optical tracer development. For instance, the Cy5.5 fluorescent precursor used in the radiosynthesis of a PET-optical marker by Priem, *et al.* afforded a quantum yield of 0.4% when measured in DMSO solution.[61] Not dissimilar to the 0.3% and 0.2% quantum yields measured in DMSO and 5% DMSO solution for both rhenium complexes. These results are still at least an order of magnitude less than the quantum yields acquired for the BODPY conjugated PET-optical probes however which, as reported for both Li, *et al.* and Paulus, *et al.*, measured within the range of 11 to 15%.[48, 52] Much greater quantum yields of rhenium complexes have been reported, however, when displacing the chloro ancillary ligands for π-conjugated N-heterocycles.[86-88] Such future work may thus provide competitive quantum yields for PET-optical tracers based on rhenium probes, however this work was not pursued in favour of developing alternative rhenium mediated radiofluorination methods based on the interesting radiochemical results obtained.

3.3.2 Luminescent Lifetimes and Decay Rates of 2-Chloro and 2-Fluoro Phenanthroline Complexes

The lifetimes of the rhenium complexes were determined by TCSPC technique following excitation with a 377 nm picosecond LED. The monoexponential decay profiles are shown in Figure 100 and Figure 101 for **Re2ClPhen** and **Re2FPhen** in DMSO solution, respectively. The profiles do not differ significantly for both complexes, however, from these decay profiles **Re2ClPhen** was determined to have a luminescent lifetime of 27 ns (χ^2 = 0.876) and **Re2FPhen** was determined to have a luminescent lifetime of 41 ns (χ^2 = 0.974). When testing these complexes in 5% DMSO solution the luminescent lifetimes proved to be shorter, with a lifetime of 10 ns determined for **Re2ClPhen** (χ^2 = 1.148) and a lifetime of 14 ns determined for **Re2FPhen** (χ^2 = 1.156). By substituting the lifetime and quantum yields into equation (10) the radiative decay rate constants were determined to be 1.05×10^{-4} and 7.04×10^{-5} for **Re2ClPhen** and **Re2FPhen** in DMSO solution, respectively. In 5% DMSO solution, these radiative decay rate constants were determined to be 1.64×10^{-4} and 1.60×10^{-4} for **Re2ClPhen** and **Re2FPhen**, respectively. Conversely, the non-radiative decay rate constants calculated from the lifetimes and quantum yields using equation (11) were determined to be 3.76×10^{-2} and 2.41×10^{-2} for **Re2ClPhen** and **Re2FPhen** in DMSO solution, respectively. In 5% DMSO solution, these non-radiative decay rate constants were determined to be 1.01×10^{-1} and 6.96×10^{-2} for **Re2ClPhen** and **Re2FPhen**, respectively. These photophysical properties are listed in Table 8 for **Re2ClPhen** and **Re2FPhen** in both DMSO and 5% DMSO solutions. Experimental uncertainties are estimated to be ±8% for the luminescent lifetime determinations.

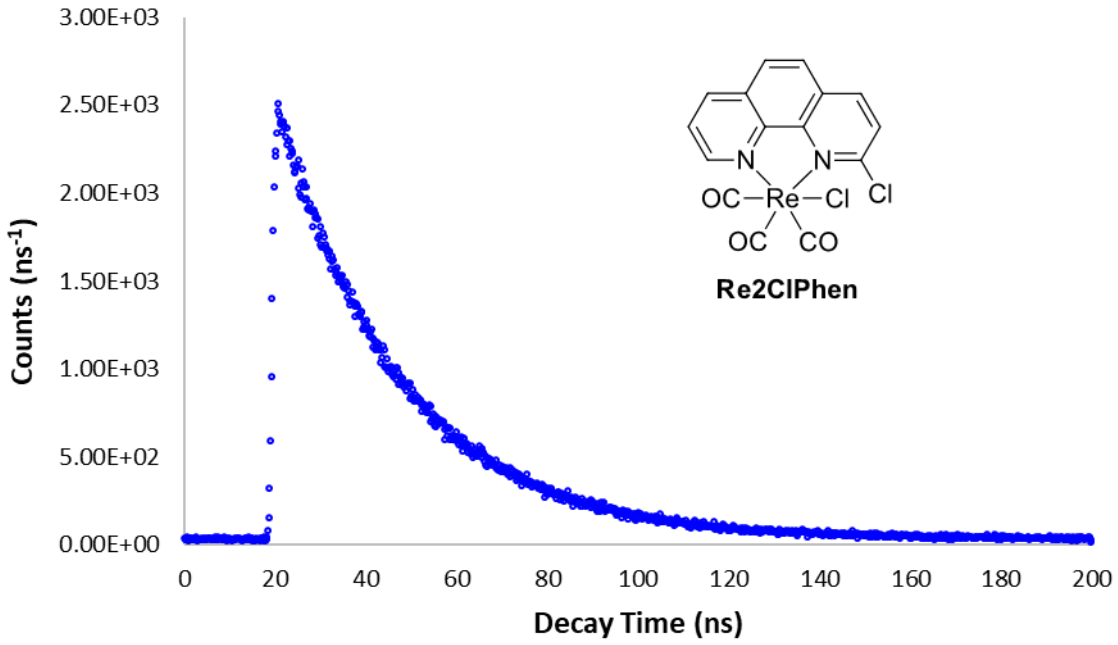

Figure 100. Monoexponential decay profile of **Re2ClPhen** in DMSO *via* TCSPC following excitation with a 377 nm pulsed picosecond LED. The phosphorescent lifetime in DMSO was determined to be 27 ns with $\chi^2 = 0.876$.

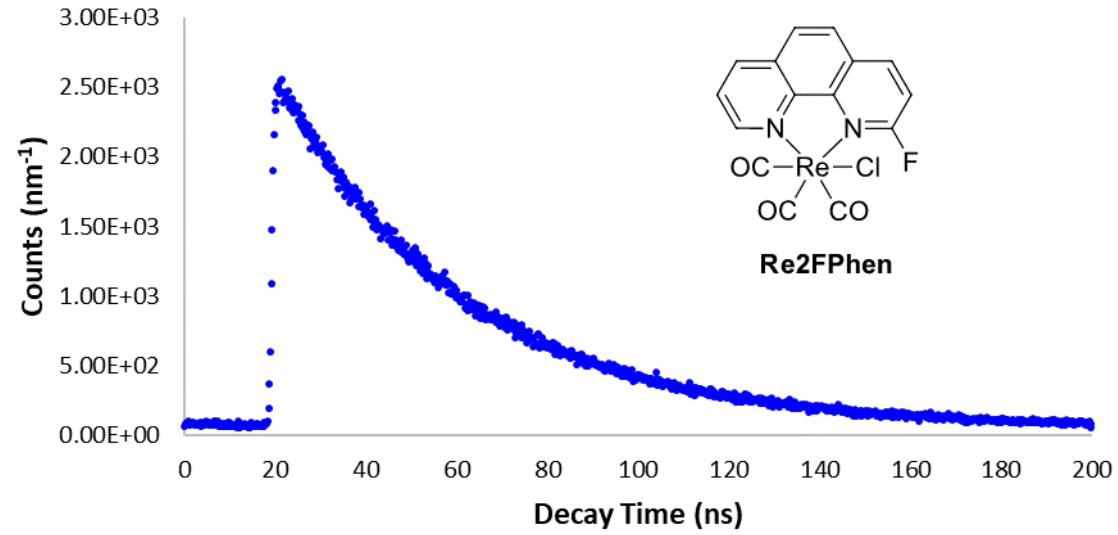

Figure 101. Monoexponential decay profile of **Re2FPhen** in DMSO *via* TCSPC following excitation with a 377 nm pulsed picosecond LED. The phosphorescent lifetime in DMSO was determined to be 41 ns with $\chi^2 = 0.974$.

Table 8. Comparison of air equilibrated quantum yields, lifetimes with associated goodness of fit, and radiative and non-radiative decay rate constants for **Re2ClPhen** and **Re2FPhen** in DMSO and 5% DMSO in water solvents.

Re Complex (solvent)	Luminescent Quantum Yield (ϕ)	Luminescent Lifetime (τ)	Goodness of Fit (χ^2)	Radiative Decay Rate Constant (k_r)	Non-Radiative Decay Rate Constant (k_{nr})
Re2ClPhen (DMSO)	2.85×10^{-3}	27 ns	0.876	1.05×10^{-4}	3.76×10^{-2}
Re2FPhen (DMSO)	2.91×10^{-3}	41 ns	0.974	7.04×10^{-5}	2.41×10^{-2}
Re2ClPhen (5% DMSO)	2.43×10^{-3}	10 ns	1.148	1.64×10^{-4}	1.01×10^{-1}
Re2FPhen (5% DMSO)	2.12×10^{-3}	14 ns	1.156	1.60×10^{-4}	6.96×10^{-2}

CHAPTER FOUR

RHENIUM-BIPYRIDINE DECOMPLEXATION AS A NOVEL METHOD FOR PRODUCING RADIOTRACERS

4.1 Synthesis of 6-Substituted 2,2'-Bipyridine Rhenium Tricarbonyl Complexes

Following the successful radiofluorination of **Re2ClPhen**, it was hypothesised that rhenium complexed 2-2'bipyridine could afford similar RCYs under analogous conditions. Additionally, due to the commercial availability of the chlorinated precursor ligands, such complexes were an opportunity to assess how rhenium activation could assist fluorine-18 radiolabellings on different positions of the molecule. Three chlorinated ligands were selected to trial substitution reactions for [^{18}F]fluoride in the *ortho*, *meta* and *para* positions; these ligands being 6-chloro-2,2'-bipyridine (**6ClBiPy**), 5-chloro-2,2'-bipyridine (**5ClBiPy**) and 4-chloro-2,2'-bipyridine (**4ClBiPy**). Additionally, the fluorinated analogues of each ligand were required as non-radioactive standards. Initial syntheses of these fluorinated ligands *via* palladium-catalysed Suzuki-Miyaura cross-coupling reactions with the corresponding pyridinyl halides and trifluoroborate salts provided unsuccessful, despite the reported syntheses of similar compounds *via* this method.[89-92] Thus, 6-fluoro-2,2'-bipyridine (**6FBiPy**) and 4-fluoro-2,2'-bipyridine (**4FBiPy**) were synthesised *via* nucleophilic aromatic substitution of the chlorinated ligands with a source of potassium fluoride and in the presence of an 18-crown-6 ether phase transfer catalyst. The 5-fluoro-2,2'-bipyridine (**5FBiPy**) was unfortunately unable to be synthesised *via* this method and no alternative synthetic routes were explored in the interest of time. Each of the chlorinated ligands were synthesised to form their respective rhenium complexed precursors, tricarbonylchloro(6-chloro-2,2'-bipyrine)rhenium(I) (**6ClBiPy**), tricarbonylchloro(5-chloro-2,2'-bipyrine)rhenium(I) (**5ClBiPy**) and tricarbonylchloro(4-chloro-2,2'-bipyrine)rhenium(I) (**4ClBiPy**). Both synthesised fluorine substituted ligands were also complex with a source of pentacarbonylchlororhenium(I) to form the non-radioactive standards of tricarbonylchloro(6-fluoro-2,2'-bipyrine)rhenium(I) (**6FBiPy**) and

tricarbonylchloro(4-fluoro-2,2'-bipyrine)rhenium(I) (**4FBiPy**). Each of these precursors and non-radioactive standards are illustrated in Figure 102.

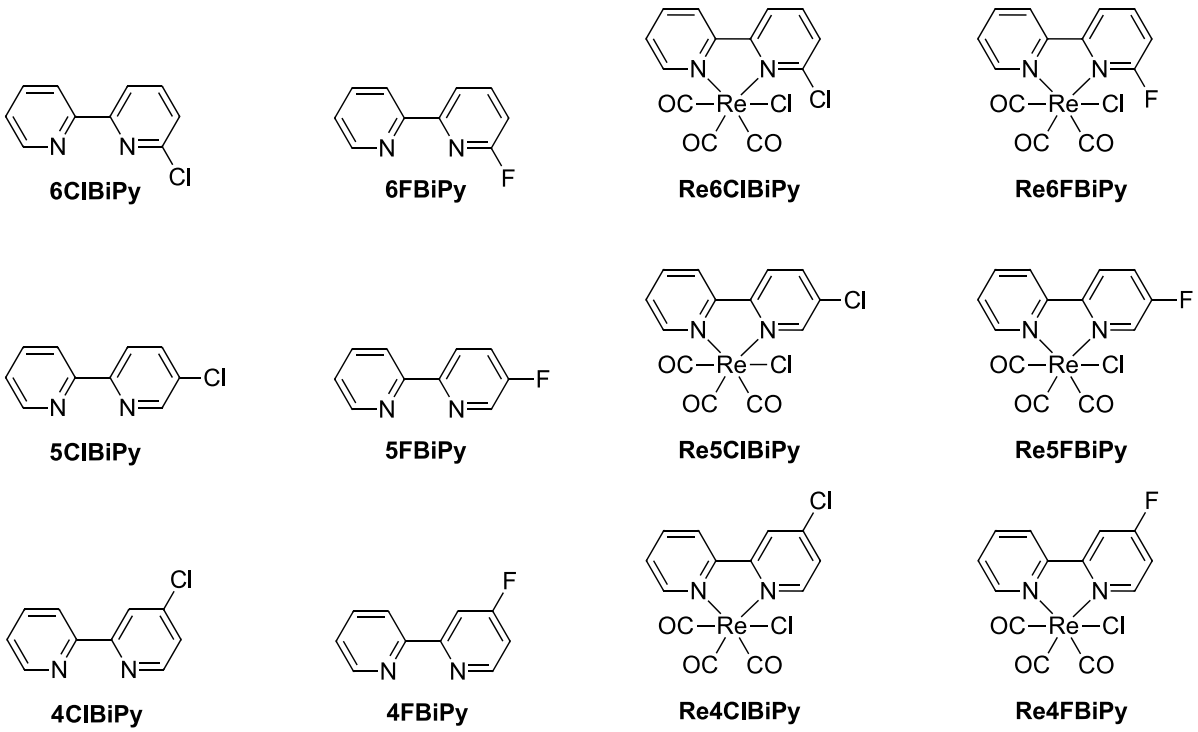

Figure 102. Each of the precursors and non-radioactive standards prepared for the radiolabelling experiments of 2,2'-bipyridine ligands and their corresponding rhenium complexes. Note that the syntheses of **5FBiPy** and by extension **Re5FBiPy** were unsuccessful, though are listed due to their importance in later discussion.

4.1.1 Fluoride substitution of 6-Chloro-2,2'-Bipyridine

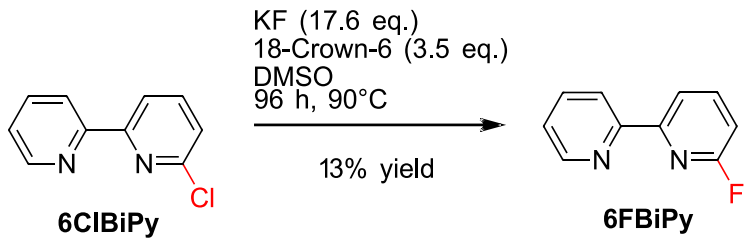

Figure 103. Synthesis of **6FBiPy** *via* nucleophilic aromatic substitution for fluoride provided by a potassium salt azeotropically dried in DMSO solvent in the presence of an 18-crown-6 ether phase transfer catalyst. The reaction afforded 13% yield following stirring at 90°C for 96 h under an inert nitrogen gas environment.

A mass of **6ClBiPy** (318.7 mg, 1.672 mmol, 1.0 eq.) was dried under high vacuum and back-filled with nitrogen gas over three cycles. A volume of DMSO was distilled over calcium hydride and further dried over 4 Å molecular sieves. Masses of potassium fluoride (1.712 g, 29.466 mmol, 17.6 eq.) and 18-crown-6 ether (1.567 g, 5.928 mmol, 3.5 eq.) were azeotropically dried *via* small additions of acetonitrile (20 × 1 mL), with evaporation of the azeotrope occurring between additions, at 90°C under a constant flow of nitrogen gas. A homogeneous white crust resulted which was subsequently vacuumed and back-filled with nitrogen gas over three cycles. A volume of the recently distilled anhydrous DMSO (10 mL) was then added to dissolve the 6-chloro-2,2'-bipyridine which turned yellow in solution and was then transferred to the potassium fluoride- crown ether complex under inert conditions. No product was afforded at room temperature, nor any temperature approaching 90°C while stirring in an inert nitrogen gas environment. Thus, the solution was left to stir at 90°C until the reaction achieved equilibration and no increase in the peak area of the product was identified, as confirmed by HPLC and MS monitoring (96 h). The reaction was thus cooled to room temperature and afforded a brown solution. The solution was loaded onto a silica column wet-packed with hexane and eluted over gradient conditions with a mobile phase ramped from

0% to 20% ethyl acetate in hexane. Fractions containing the co-eluting 6-chloro-2,2'-bipyrine and 6-fluoro-2,2'-bipyridine were then evaporated down under reduced pressure which afforded a white crystalline powder. The crude white powder was then dissolved in a minimum of methanol (2.2 mL) for preparative chromatography and a series of optimised 32 μL injections were loaded onto an Atlantis T3 C_{18} reverse phase column (5 μm, 4.6 × 150 mm) and eluted with an isocratic mobile phase consisting of 9% acetonitrile and 91% of Milli-Q water with 0.1% TFA modifier at a flow rate of 1.5 $mL.min^{-1}$ and PDA detection wavelength set at 254 nm. The collected fractions were combined and evaporated under reduced pressure to remove the acetonitrile before sublimating off the water *via* overnight lyophilisation, which afforded a pink salt. The pink salt was dissolved in a minimum of water (20 mL), neutralised with saturated sodium bicarbonate solution and extracted into DCM (15 × 10 mL) *via* liquid-liquid extraction. The resulting organic fractions were then combined, dried over sodium sulphate, vacuum filtered and evaporated under reduced pressure before dried under high vacuum which afforded a white powder (39.2 mg).

Confirmation of **6FBiPy** was verified by ^{1}H-NMR which affirmed the expected peak area integration for seven protons in the aromatic region, as shown in Figure 104. The ^{13}C-NMR spectrum of **6FBiPy**, shown in Figure 105, afforded twelve signals in the aromatic region due to two of the ten carbon-13 nuclei exhibiting coupling with the fluorine-19 nucleus. The CPD ^{19}F{^{1}H}-NMR spectrum of the compound shows the signal for the lone fluorine-19 nucleus in Figure 106, alongside the *para*-DFB internal standard.

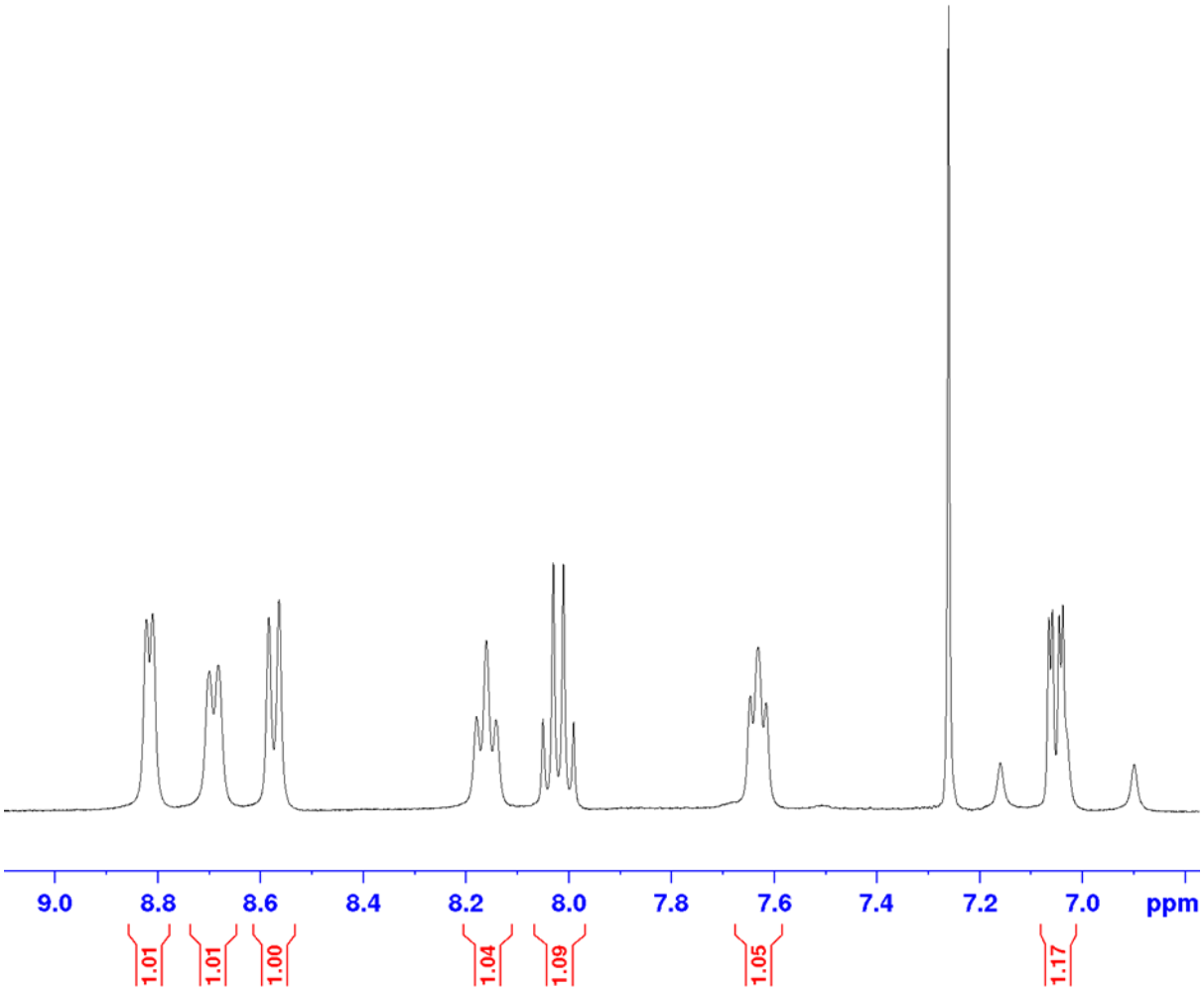

Figure 104. ^{1}H-NMR spectrum of **6FBiPy** in $CDCl_3$, showing the expected peak area integration for seven protons in the aromatic region. Note the non-integrated peaks belong to the solvent signal and two satellite peaks of the upfield doublet of doublets.

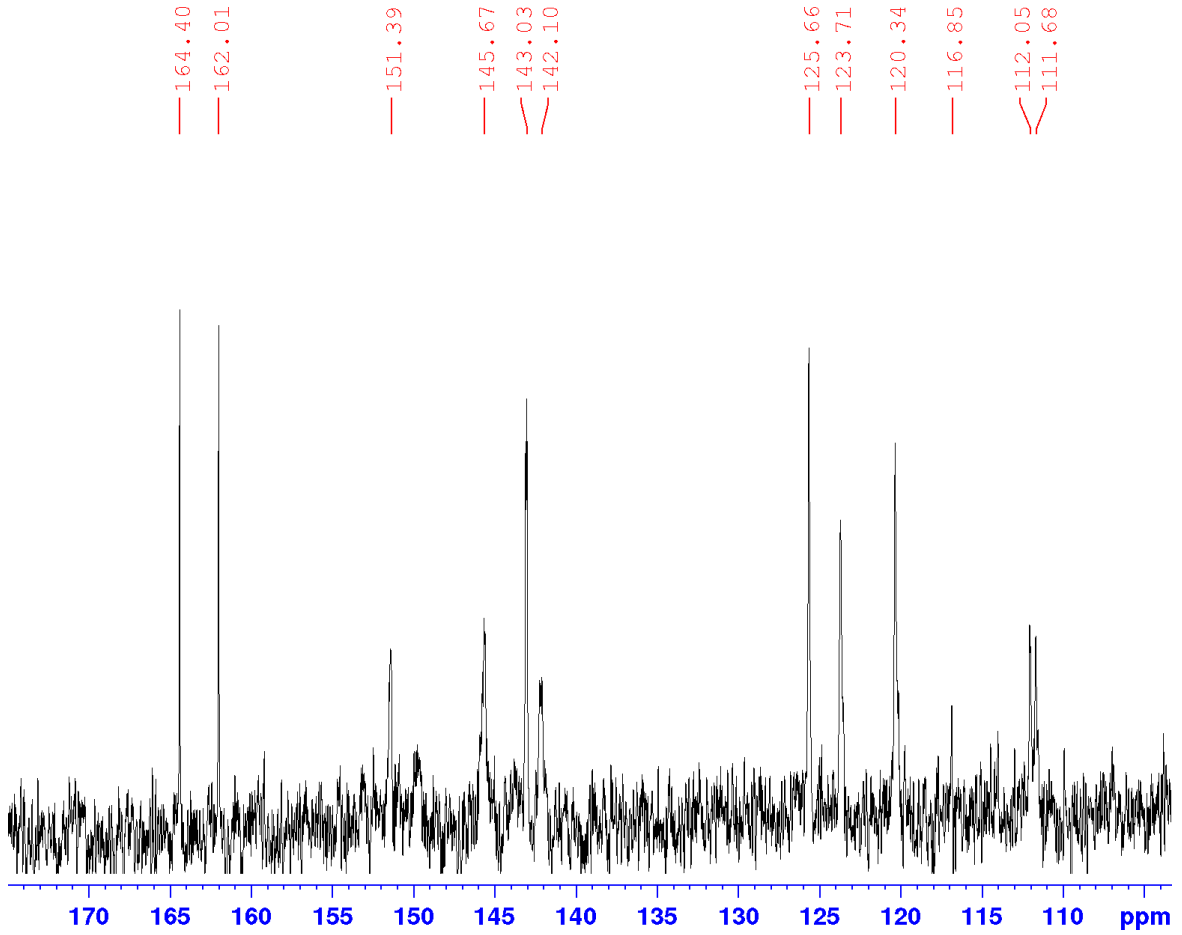

Figure 105. ^{13}C-NMR spectrum of **6FBiPy** in $CDCl_3$, affording twelve signals in the aromatic region due to two additional signals appearing from two of the ten carbon atoms exhibiting observable coupling with the ^{19}F nucleus present in the molecule.

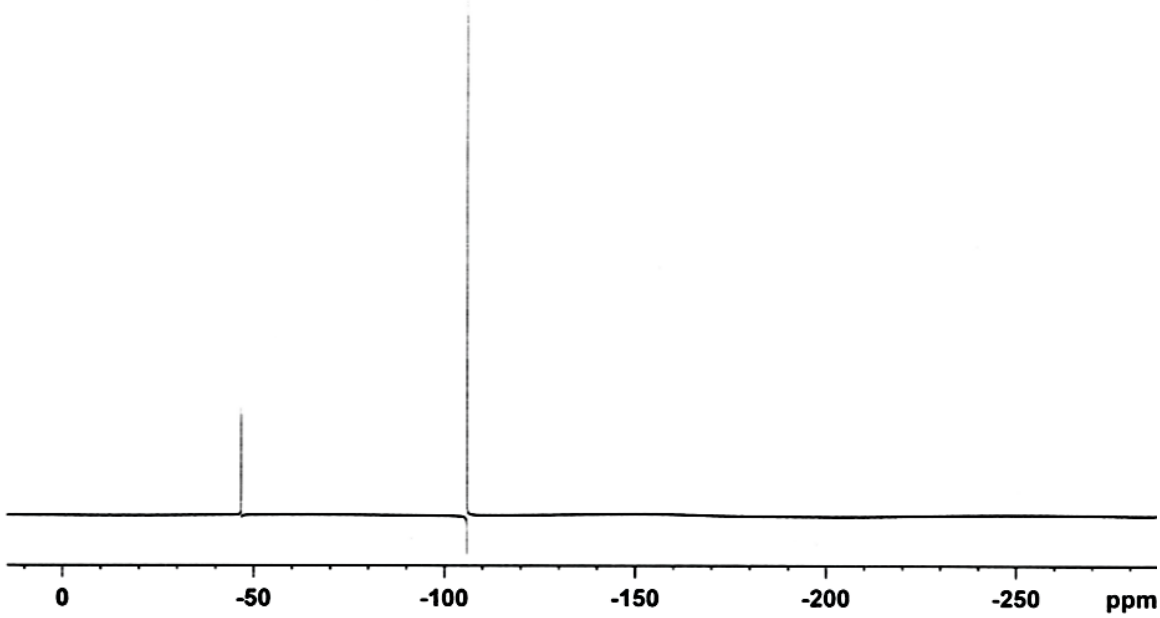

Figure 106. CPD ^{19}F{^{1}H}-NMR spectrum of **6FBiPy** in $CDCl_3$. The signal at -106.00 ppm is the *para*-DFB internal standard.

4.1.2 Rhenium Complexation of 6-Chloro-2,2'-Bipyridine

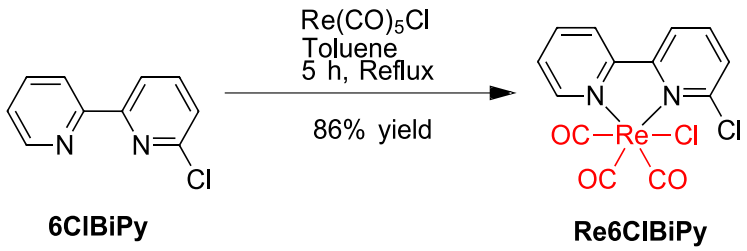

Figure 107. Synthesis of **Re6ClBiPy** *via* reflux of pentacarbonylchlororhenium(I) with **6ClBiPy** in toluene which afforded the desired product in 86% yield.

A mass of **6ClBiP** (277.5 mg, 1.456 mmol, 1.1 eq.) was dissolved in a volume of anhydrous toluene (5 mL) prompting the solution to turn beige in colour. A mass of pentacarbonylchlororhenium(I) (478.7 mg, 1.3234 mmol, 1.0 eq.) was then added and the solution was stirred at reflux under an inert nitrogen environment (5 h) causing the biphasic mixture to turn orange in colour. The solution was then cooled to room temperature and further cooled to -20°C to induce greater precipitation. The solution was then filtered *via* vacuum filtration and washed first with cold toluene, followed by diethyl ether. The resulting yellow solid was then dissolved in a minimum of DCM (7 mL) and loaded onto neutral alumina normal phase column (Brockman grade II, 120 g) wet packed with DCM and was eluted using an isocratic mobile phase consisting of only DCM. Fractions confirmed to contain the desired product by HPLC, MS and TLC analyses were combined and evaporated under reduced pressure to afford a yellow powder (564.2 mg).

Confirmation of rhenium complexation was affirmed by ^{1}H-NMR, with signals integrating for the expected seven protons as shown in Figure 108 with each signal shifted downfield with respect to the ligand; ^{13}C-NMR as shown in Figure 109 which exhibited ten carbon-13 signals from the bipyridine ring and an additional three downfield shifted carbon-13 signals for the carbonyl ligands; FTIR which showed the expected A'(1) C≡O stretching IR absorption band

at 2018 cm^{-1} and the overlapping A'(2) & A'' C≡O stretching band at 1882 cm^{-1} indicative of the carbonyl ligands alongside a weak sp^2 hybridised C–H bond stretch at 3075 cm^{-1} from the bipyridine ligand as shown in Figure 110; as well as HRMS which demonstrated the chlorine-dissociated $[M\text{-}Cl]^+$ ion signal observable at *m/z* 460.9694 against the calculated *m/z* 460.9703 (Δ -0.9 ppm) as shown in Figure 111. Additionally the UV-Vis spectrum of **Re6ClBiPy** shows the expected absorption band for the dπ → π* transition to the MLCT excited state, as shown in Figure 112, as well as higher energy absorption bands with greater molar absorptivities for π → π* transitions to LC excited states. Elemental analysis further confirmed the purity of the complex with compositions of 13.59% carbon, 1.17% hydrogen and 5.70% nitrogen measured against the theoretical compositions of 31.46% carbon, 1.42% hydrogen and 5.64% nitrogen. Finally, the XRD structure shown in Figure 113 provided unequivocal evidence for the structure of **Re6ClBiPy**.

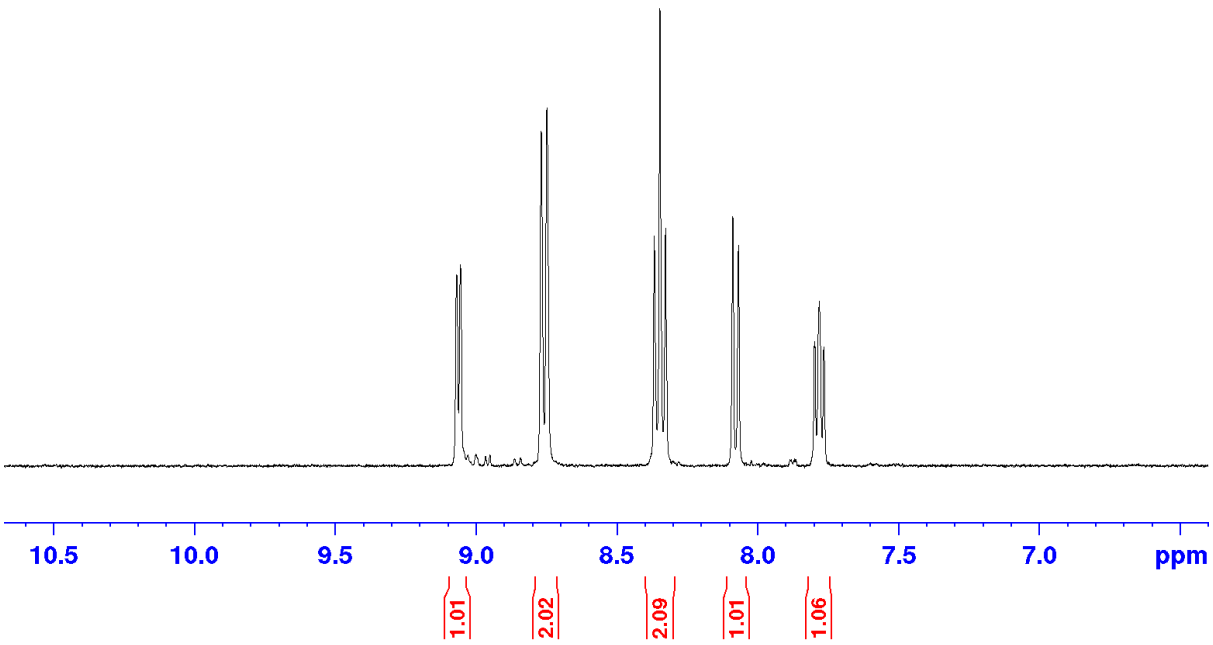

Figure 108. ^{1}H-NMR spectrum of **Re6ClBiPy** in DMSO-d_6, showing the expected peak area integration for the seven protons in the aromatic region which were shifted downfield with respect to the ligand.

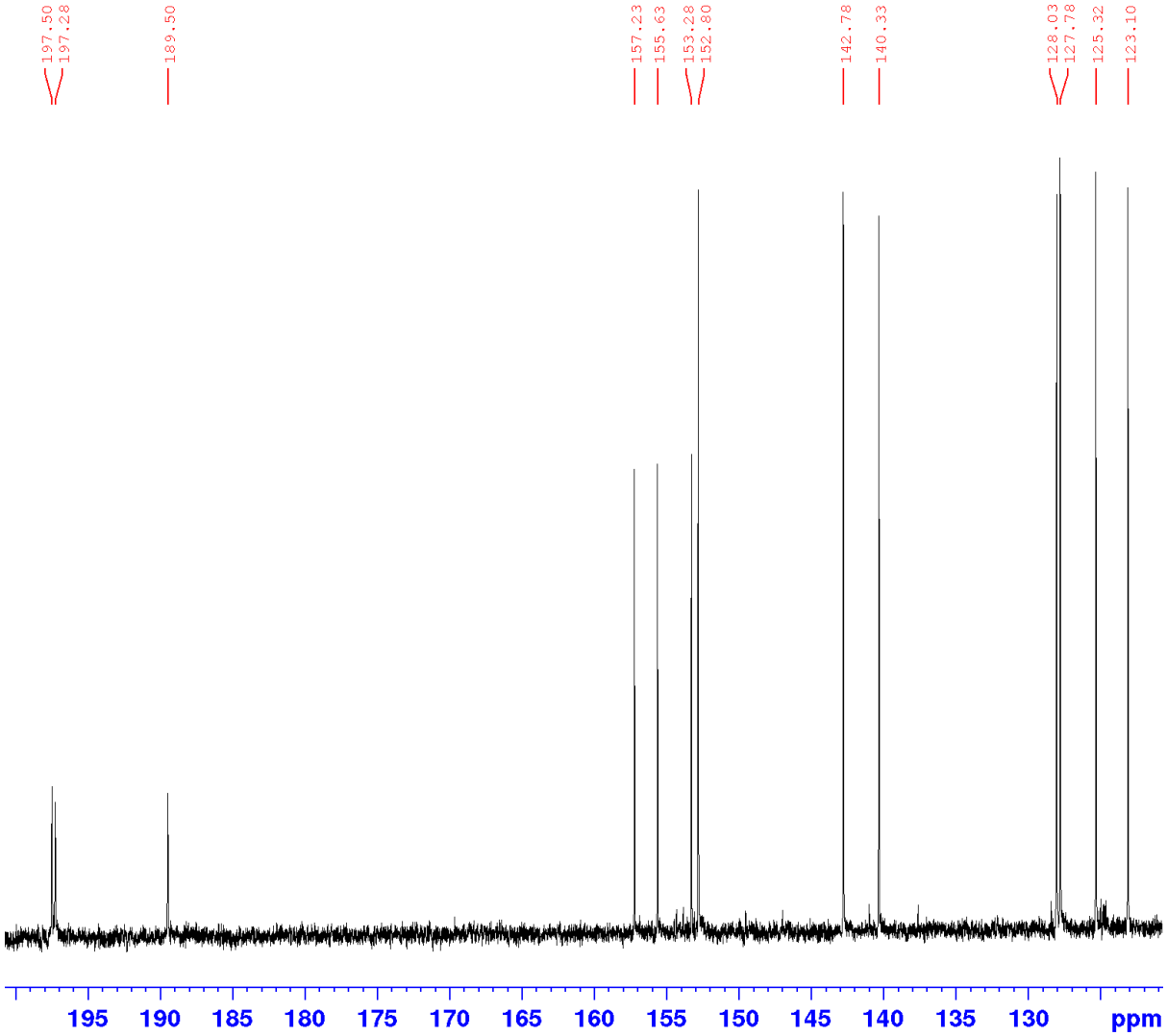

Figure 109. ^{13}C-NMR spectrum of **Re6ClBiPy** in DMSO-d_6, exhibiting not only the ten aromatic carbon-13 signals from the bipyridine system though also showing the three downfield shifted carbonyl signals of the rhenium complex (189.5, 197.3 & 197.5 ppm).

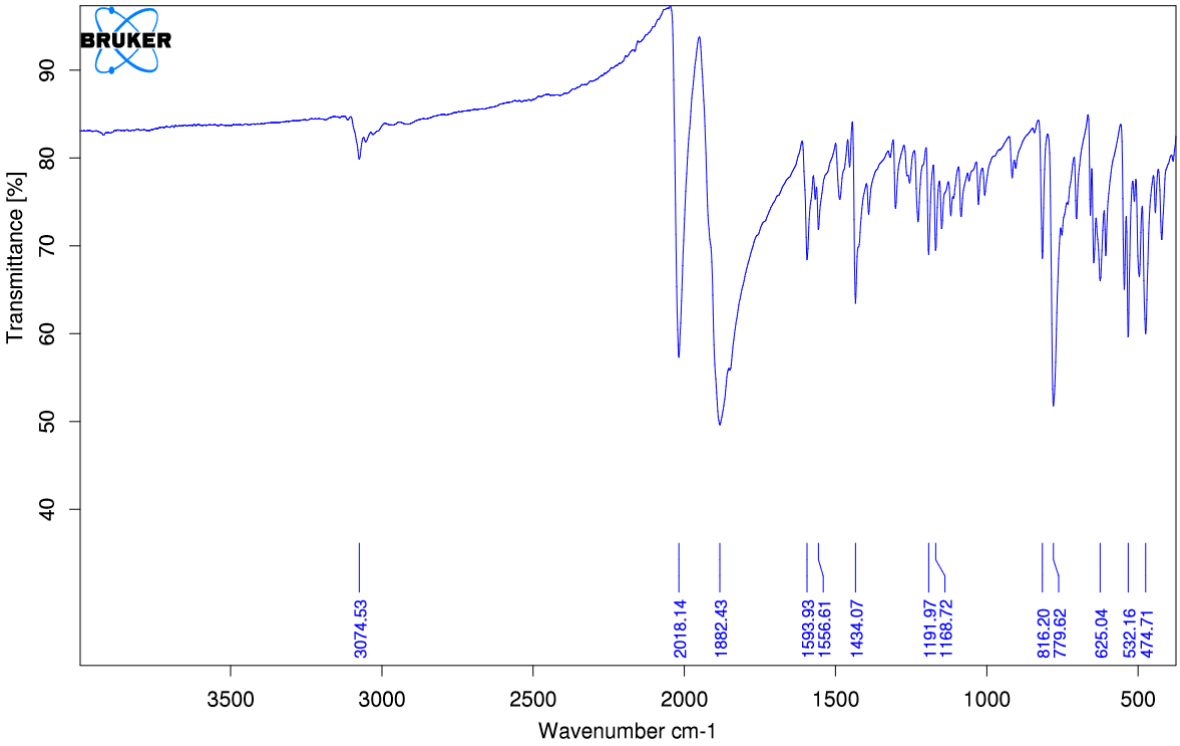

Figure 110. FTIR spectrum of **Re6ClBiPy** exhibiting the distinctive A'(1) C≡O stretching IR absorption band at 2018 cm^{-1} and the overlapping A'(2) & A'' C≡O stretching band at 1882 cm^{-1}. A weak sp^2 hybridised C–H bond stretch is also observed at 3075 cm^{-1} from the bipyridine ligand.

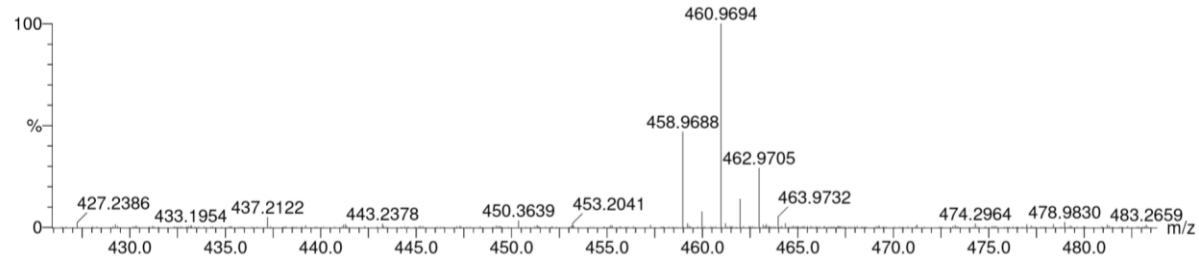

Figure 111. HRMS spectrum of **Re6ClBiPy** depicting the chlorine-dissociated $[M\text{-}Cl]^+$ ion signal observable at *m/z* 460.9694 with a calculated ratio of m/z 460.9703 (Δ -0.9 ppm) for the complex incorporating the ^{187}Re isotope in 62.6% natural abundance. An additional signal with *m/z* 458.9688 is also observed for the same ion incorporating the ^{185}Re isotope in 37.4% natural abundance.

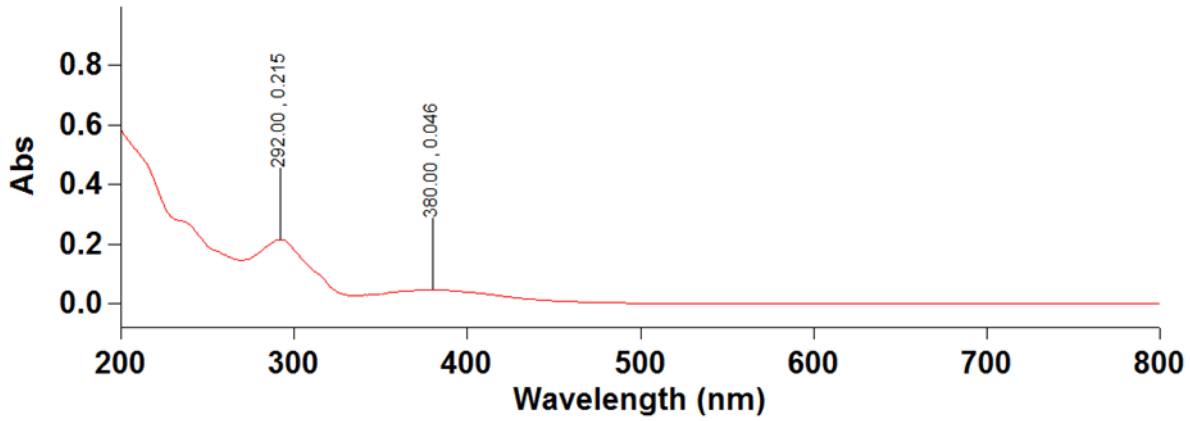

Figure 112. UV-Vis spectrum of **Re6ClBiPy** (2 μg.mL^{-1} in acetonitrile) showing the absorption band for the dπ → π* electronic transition to the MLCT excited state at 380 nm, alongside higher energy π → π* transitions to LC excited states with greater molar absorptivities.

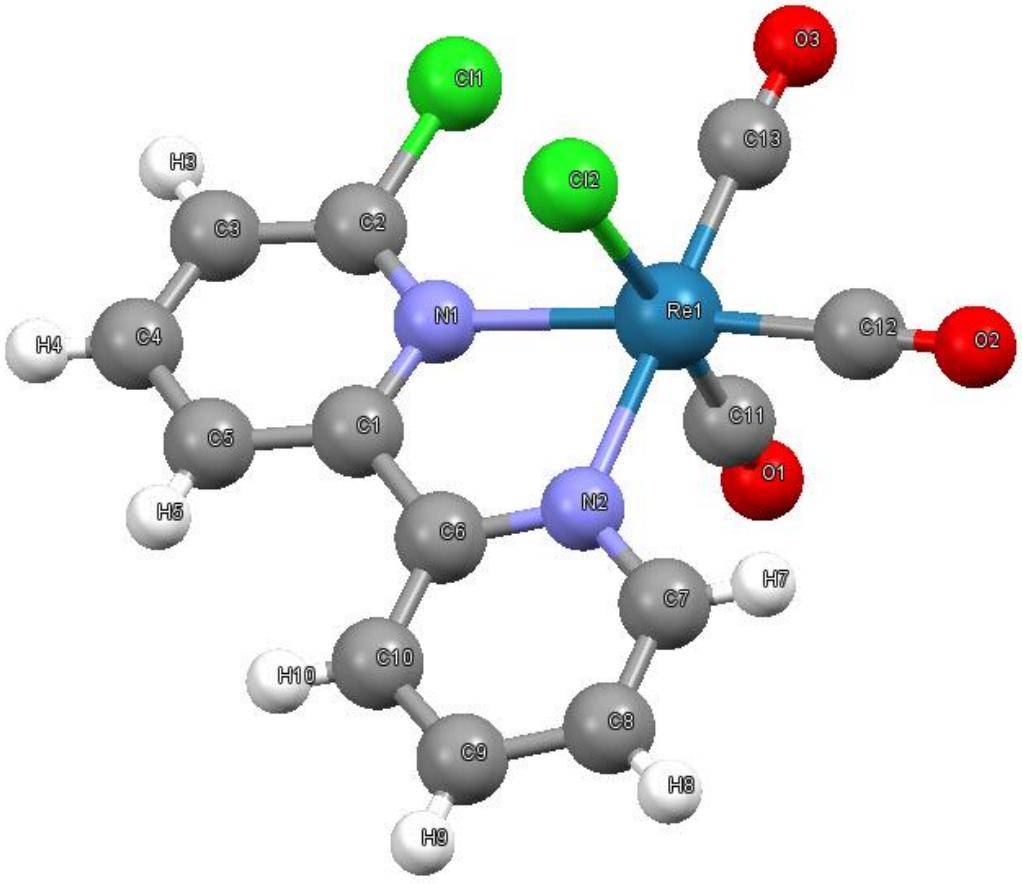

Figure 113. Crystal structure obtained for **Re6ClBiPy** *via* XRD analysis at the Australian Synchrotron. Crystals were grown from the slow evaporation of DMSO solution.

4.1.3 Rhenium Complexation of 6-Fluoro-2,2'-Bipyridine

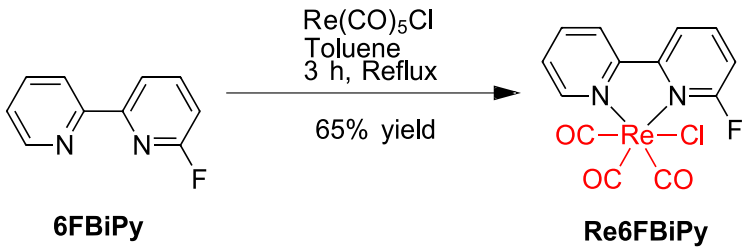

Figure 114. Synthesis of **Re6FBiPy** *via* reflux of pentacarbonylchlororhenium(I) with **6FBiPy** in toluene which afforded the desired product in 65% yield.

A mass of **6FBiPy** (65.3 mg, 363 µmol, 1.1 eq.) was dissolved in a volume of anhydrous toluene (8 mL), to which was added a mass of pentacarbonylchlororhenium(I) (120.0 mg, 332 µmol, 1.0 eq.). The solution was stirred at reflux under an inert nitrogen environment (3 h) during which time the solution turned yellow in colour. The solution was cooled thereafter first to room temperature, then to -20°C to induce further precipitation. The resulting yellow solid was isolated *via* vacuum filtration and was washed with cold toluene followed by diethyl ether. The solid was then dissolved in a minimum of DCM (4 mL) and was loaded onto a Sepaflash neutral alumina column (80 g) whereupon the product was eluted over gradient conditions with the mobile phase ramped from 0 to 10% acetonitrile in ethyl acetate. The fractions containing the desired product, as confirmed by HPLC, TLC and MS, were combined and evaporated under reduced pressure to afford a yellow powder (104.1 mg).

Confirmation of rhenium complexation to the 2-fluoro-2,2'-bipyridine ligand was affirmed by 1H-NMR as shown in Figure 115, which integrated for the expect seven aromatic protons with more complex splitting patterns when compared to the chloro substituted analogue due to the additional coupling between the protons and fluorine-19 isotope. Complex splitting patterns are also observed between the carbon-13 and fluorine-19 nuclei as shown by the ^{13}C-NMR spectrum in Figure 116, which also distinctly shows the Re−C≡O carbon-13 signals shifted

downfield with respect to the aromatic bipyridine carbon-13 signals. The CPD ^{19}F-NMR spectrum shows just the one signal pertaining to the sole fluorine-19 nucleus in the molecule, as shown in Figure 117. Additional confirmation was also affirmed by the FTIR spectrum which showed the expected A'(1) C≡O stretching IR absorption band at 2016 cm^{-1} and the overlapping A'(2) & A'' C≡O stretching band at 1880 cm^{-1} indicative of the carbonyl ligands alongside weak sp^2 hybridised C–H bond stretches around 3039 cm^{-1} from the bipyridine ligand as shown in Figure 118. The UV-Vis spectrum of **Re6FBiPy**, as shown in Figure 119, depicts the absorption band for the $d\pi \rightarrow \pi^*$ electronic transition to the MLCT excited state at 369 nm. Absorption bands to LC excited states are also observed due to $\pi \rightarrow \pi^*$ transitions at higher energies. Purity of the complex was also further assessed *via* elemental analysis which yielded compositions of 32.59% carbon, 1.16% hydrogen and 5.88% nitrogen against closely aligned theoretical compositions of 32.54% carbon, 1.47% hydrogen and 5.64% nitrogen.

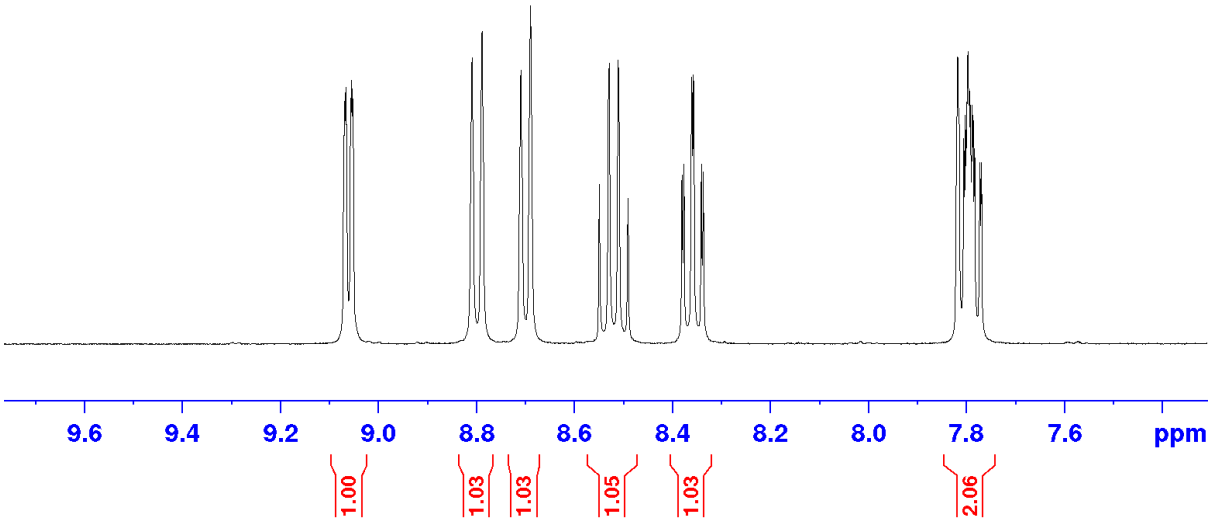

Figure 115. ^{1}H-NMR spectrum of **Re6FBiPy** in DMSO-d_6, showing the expected peak area integration for the seven protons in the aromatic region which were shifted downfield with respect to the ligand. The peaks exhibit more complex splitting patterns on account of the coupling between the fluorine-19 isotope present in the molecule.

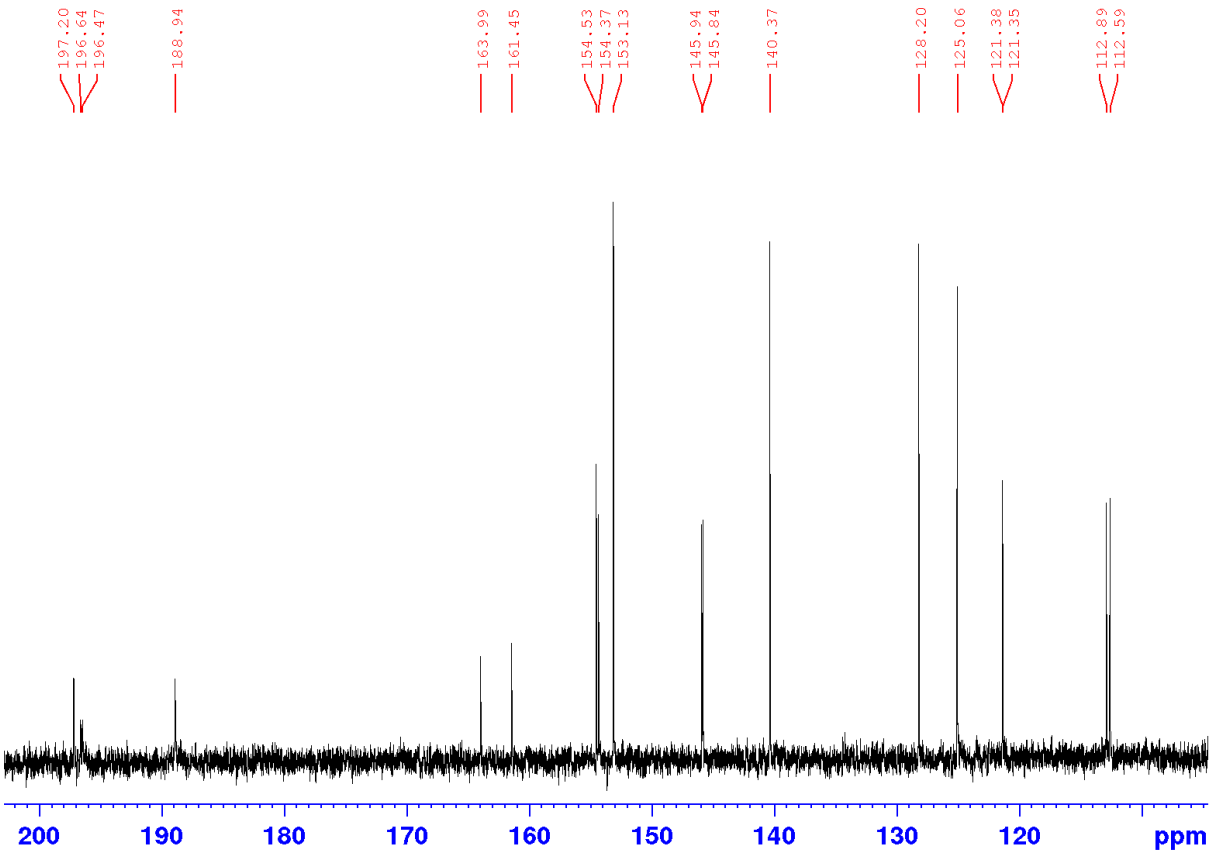

Figure 116. ^{13}C-NMR spectrum of **Re6FBiPy** in DMSO-d_6, showing the downfield shifted carbonyl signals with respect to the carbon-13 aromatic signals from the bipyridine ring. Complex splitting is observed due to the coupling between the carbon-13 and fluorine-19 nuclei.

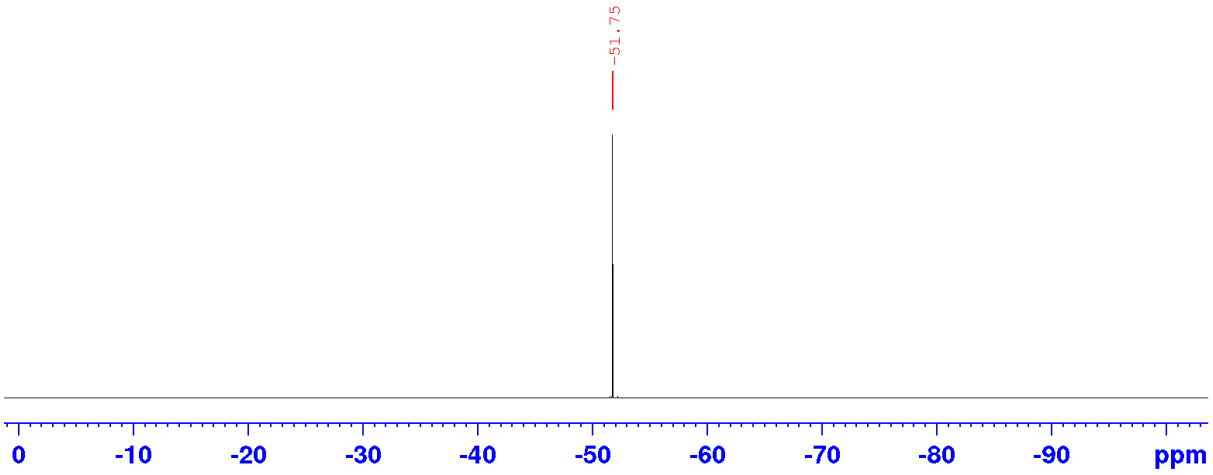

Figure 117. Decoupled ^{19}F-NMR spectrum of **R62FBiPy** in DMSO-d_6 displaying the signal for the sole fluorine-19 nucleus in the molecule at -50.75 ppm.

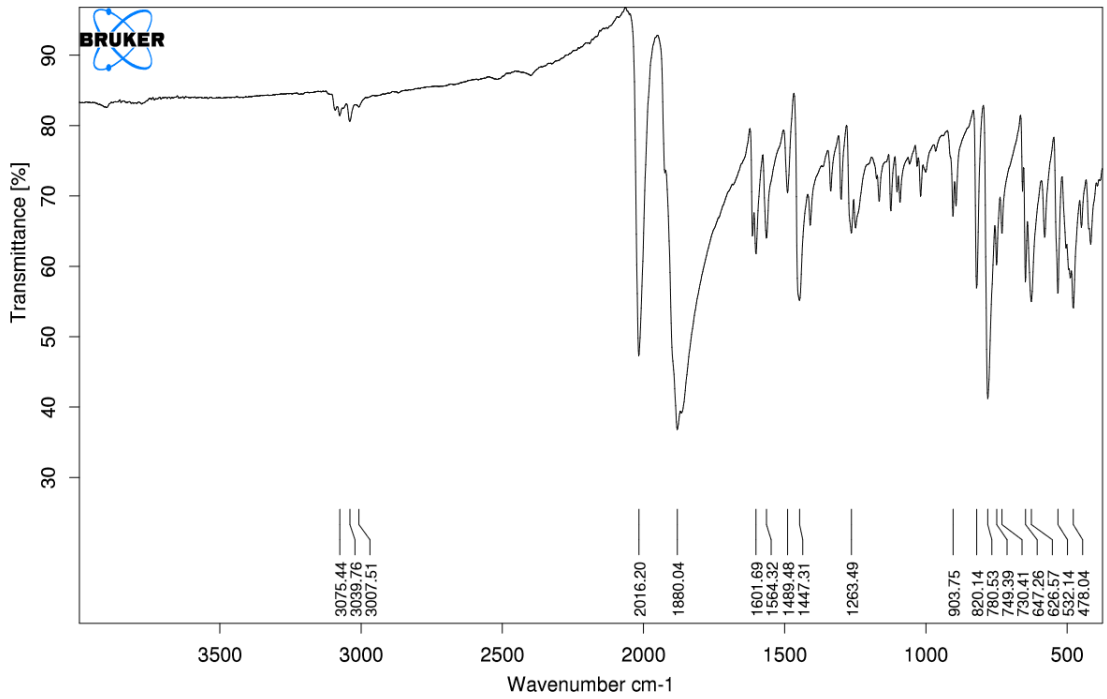

Figure 118. FTIR spectrum of **Re6FBiPy** exhibiting the distinctive A'(1) C≡O stretching IR absorption band at 2016 cm^{-1} and the overlapping A'(2) & A'' C≡O stretching band at 1880 cm^{-1}. Weak sp^2 hybridised C−H bond stretches are also observed at higher wavenumbers (*circa* 3039 cm^{-1}) from the bipyridine ligand.

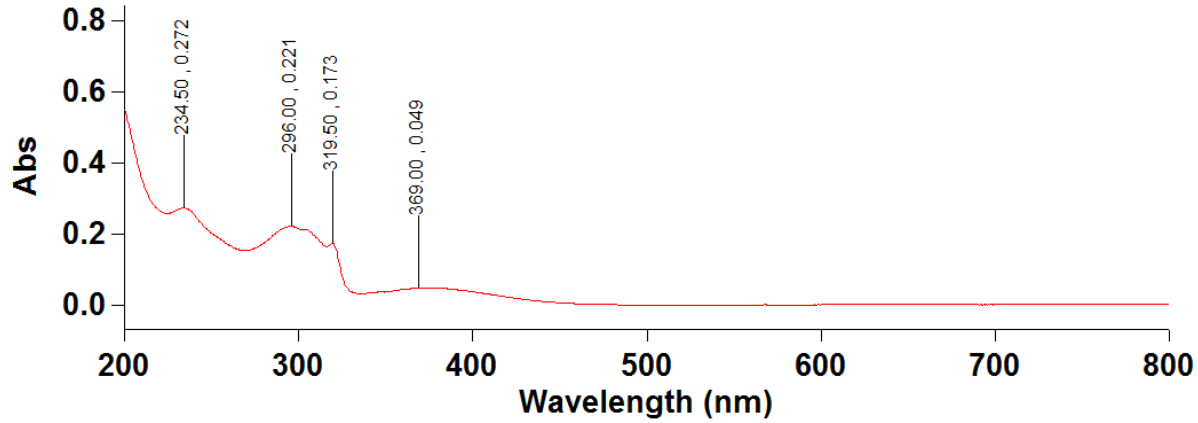

Figure 119. UV-Vis spectrum of **Re6FBiPy** (2 µg.mL^{-1} in acetonitrile) showing the absorption band for the dπ → π* electronic transition to the MLCT excited state at 369 nm, alongside higher energy π → π* transitions to LC excited states with greater molar absorptivities.

4.1.4 Fluorine substitution of 4-Chloro-2,2'-Bipyridine

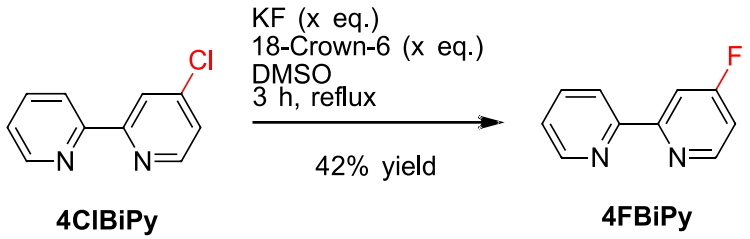

4ClBiPy **4FBiPy**

Figure 120. Synthesis of **4FBiPy** *via* nucleophilic aromatic substitution for fluoride provided by a potassium salt azeotropically dried in DMSO solvent in the presence of an 18-crown-6 ether phase transfer catalyst. The reaction afforded 42% yield following stirring at reflux for 3 h under an inert nitrogen gas environment.

A mass of 18-crown-6 ether (4.060 g, 0.0154 mol, 9.8 eq.) was added alongside a mass of potassium fluoride (1.890 g, 0.0325 mol, 20.8 eq.) and dried under high vacuum before heating under an inert nitrogen environment to form a yellow crust which was then azeotropically dried *via* the dropwise addition of acetonitrile to the heated solid. A mass of **4ClBiPy** (298.2 mg, 1.564 mmol, 1.0 eq.) was then dried under high vacuum and backfilled with nitrogen gas in a separate flask before being dissolved in a volume of anhydrous DMSO (4 mL) resulting in a pale-yellow solution. The solution was then transferred to the potassium fluoride-crown ether complex and was heated at reflux whilst stirring in an inert nitrogen environment (3 h). The solution was then cooled to room temperature following HPLC-UV and MS confirmation of the desired product. The cooled solution was filtered through PTFE membrane filters (0.2 µm) to remove the excess potassium fluoride and the filtered solution was then loaded onto a C_{18} RP column (80 g) primed with 0.1% TFA in water and eluted over 20 column volumes with a flow rate of 40 $mL.min^{-1}$ with increasing acetonitrile composition (0 to 100%). Each of the eluted fractions were analysed for purity by HPLC, TLC and MS. Those fractions confirmed to contain the purified product were combined and evaporated under reduced pressure to remove the acetonitrile before freeze-drying the resulting aqueous suspension overnight. A

yellow oil resulted which was washed first with chloroform and evaporated under reduced pressure to afford a yellow solid. The yellow solid was then dissolved in a minimum of water and extracted with DCM (10 × 20 mL). The organic extracts were then combined, dried over sodium sulphate, filtered *via* vacuum filtration and evaporated under reduced pressure to afford a white solid which was then further dried under high vacuum and weighed (115.1 mg).

^{1}H-NMR analysis of the final product (Figure 121) showed the expected integration for seven protons in the aromatic region, ^{13}C-NMR analysis (Figure 122) showed splitting of three of the ten carbon-13 nuclei due to coupling to the fluorine-19 nucleus, the resonance signal of which is shown in the CPD ^{19}F-NMR spectrum of **4FBiPy** in Figure 123. The LRMS spectrum of **4FBiPy**, shown in Figure 124, shows a detected signal for the $[M+H]^{+}$ ion at *m/z* 175.12 closely matching the calculated *m/z* ratio of 175.07.

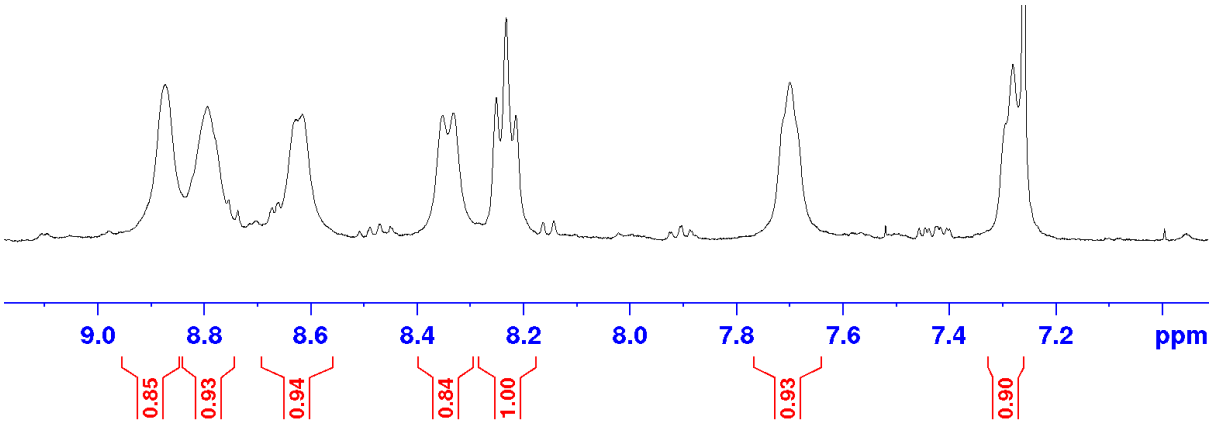

Figure 121. ^{1}H-NMR spectrum of **4FBiPy** in chloroform-d, showing the expected peak area integration for seven protons in the aromatic region. Note that the most upfield shifted peak integral overlaps with the solvent signal.

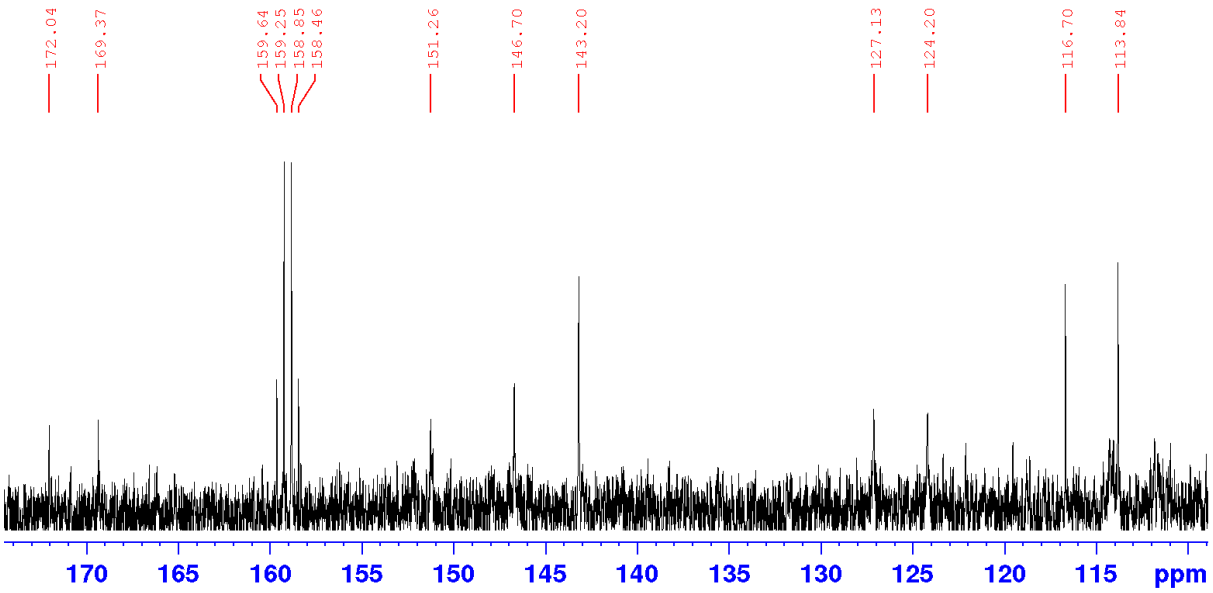

Figure 122. ^{13}C-NMR spectrum of **4FBiPy** in chloroform-d, affording thirteen signals in the aromatic region due to three additional signals appearing from three of the ten carbon nuclei exhibiting observable coupling with the fluorine-19 nucleus present in the molecule.

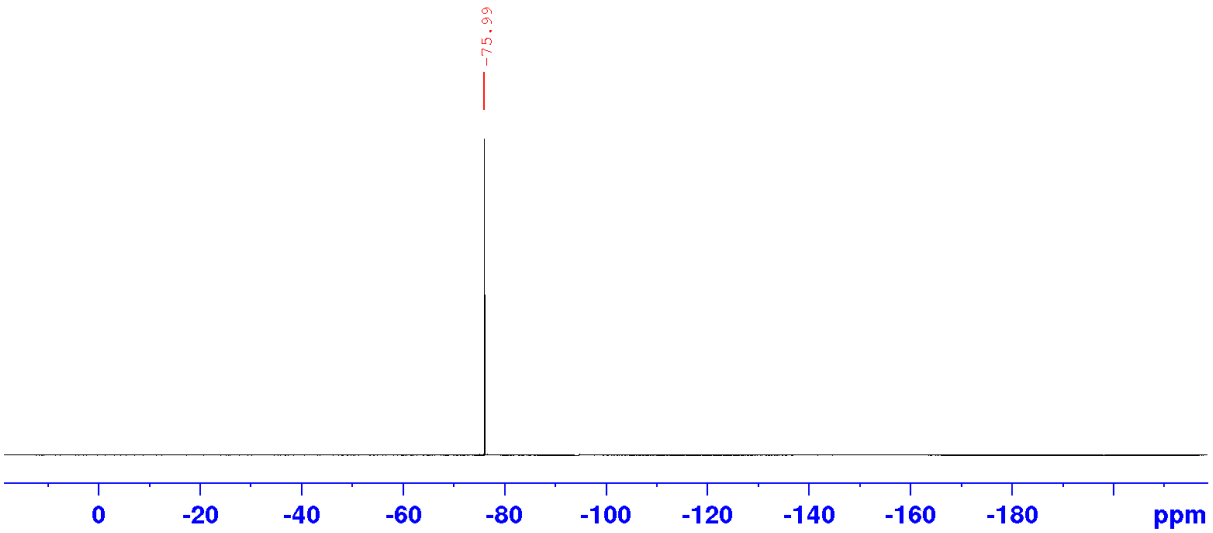

Figure 123. CPD ^{19}F-NMR spectrum for **4FBiPy** exhibiting one lone single for the sole fluorine-19 nucleus in the molecule at -75.99 ppm.

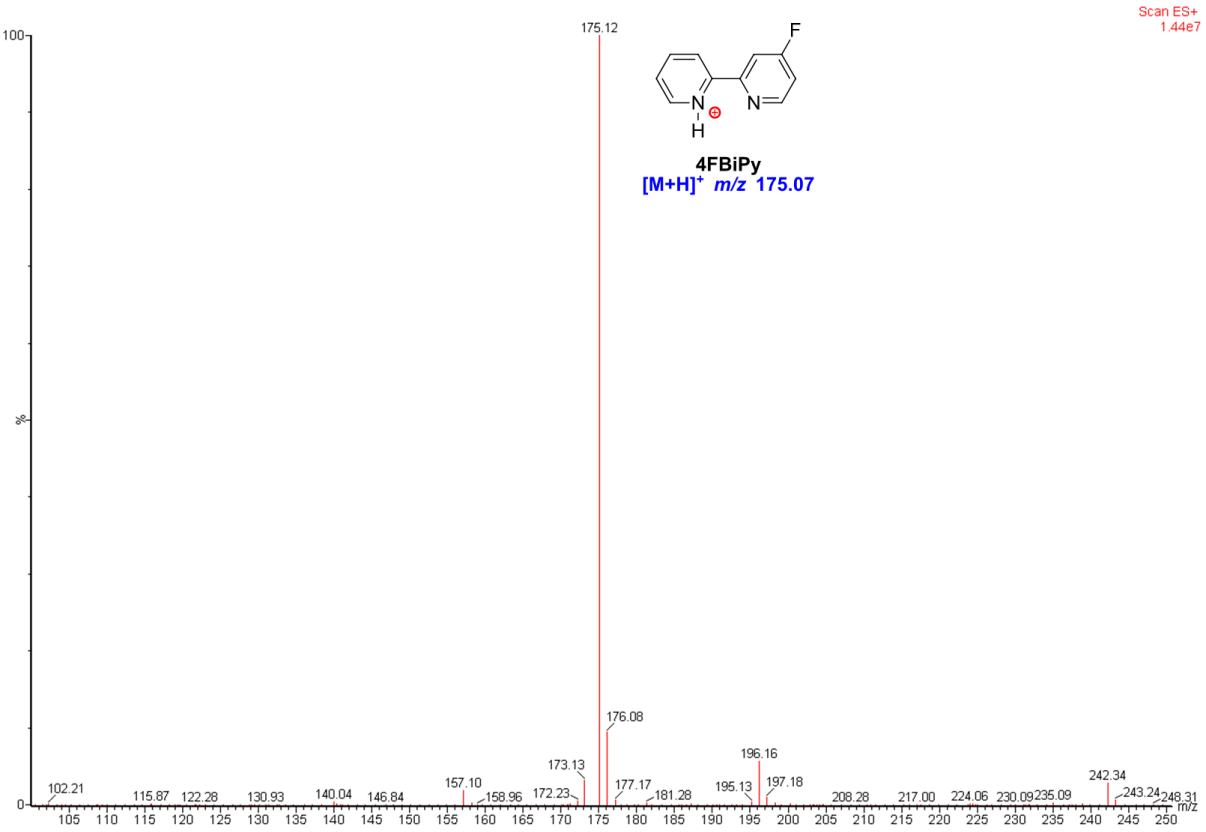

Figure 124. LRMS spectrum of **4FBiPy** showing detection of the $[M+H]^+$ ion at *m/z* 175.12 against a calculated ratio of *m/z* 175.07.

4.1.5 Rhenium Complexation of 4-Chloro-2,2'-Bipyridine

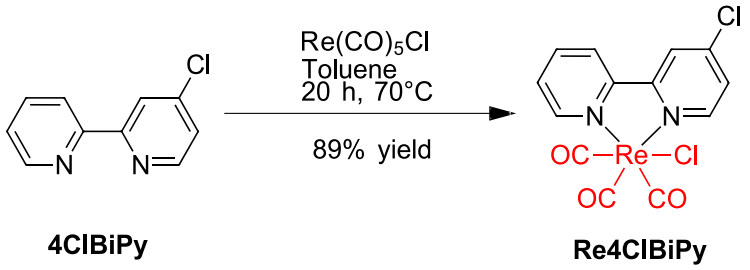

Figure 125. Synthesis of **Re4ClBiPy** via complexation of **4ClBiPy** with pentacarbonylchlororhenium(I) for 20 h at 70°C in toluene which afforded the desired product in 89% yield.

A mass of **4ClBiPy** (181.5 mg, 952.1 mmol, 1.1 eq.) was dissolved in a volume of anhydrous toluene (5 mL) and to this solution was added a mass of pentacarbonylchlororhenium(I) (315.0 mg, 870.9 mmol, 1.0 eq.). The solution was then stirred at 70°C under an inert nitrogen environment (20 h) promoting the formation of a yellow reaction product. The reaction mixture was then cooled to room temperature, further cooled to -20°C to aid the precipitation of the solid, filtered *via* vacuum filtration and washed with cold toluene followed by diethyl ether. The resulting yellow solid was then dried under high vacuum, dissolved in DCM and purified on a neutral alumina NP column Brockman grade II, 90 g) wet packed with DCM and eluted with 100% DCM. Fractions containing the desired product were then combined, evaporated under reduced pressure and dried under high vacuum to afford a yellow powder (386.1 mg).

Formation of the 4-chloro-2,2'bipyridine rhenium complex was verified by ^{1}H-NMR as shown in Figure 126, which exhibited the expected seven signals of similar integration in the aromatic region, each shifted downfield with respect to the ligand. The ^{13}C-NMR spectrum, shown in in Figure 127, also exhibited the expected thirteen carbon-13 signals, three of which pertaining to the carbonyl ligands were significantly downfield shifted compared to the other aromatic signals. The FTIR spectrum of the compound (Figure 128) also provided additional

confirmation that the ligand was complexed to the rhenium, due to the observable A'(1) C≡O stretching and overlapping A'(2) & A'' C≡O stretching IR absorption bands at 2019 cm^{-1} and 1884 cm^{-1}, respectively. IR absorptions of C−H sp^2 hybridised bond stretches were also observed at higher wavenumbers (*circa* 3073 cm^{-1}), evidencing the presence of the bipyridine ring. The HRMS spectrum of **Re4ClBiPy**, shown in Figure 129, shows detection of the chlorine-dissociated $[M\text{-}Cl]^+$ ion signal ($ReC_{13}H_7N_2O_3Cl$) observable at *m/z* 460.9712 against a calculated ratio of *m/z* 460.9703 (Δ 0.9 ppm) for the complex incorporating the ^{187}Re isotope in 62.6% natural abundance. An additional signal with *m/z* 458.9691 is also observed for the same ion incorporating the ^{185}Re isotope in 37.4% natural abundance. The UV-Vis spectrum of **Re6FBiPy** in Figure 130 also shows the absorption band for the dπ → π* electronic transition to the MLCT excited state at 369 nm, alongside the expected higher energy π → π* transitions to LC excited states. Purity of the complex was also further evaluated by elemental analysis which measured compositions of 32.52% carbon, 1.33% hydrogen and 5.81% nitrogen against calculated compositions of 32.54% carbon, 1.47% hydrogen and 5.84% nitrogen.

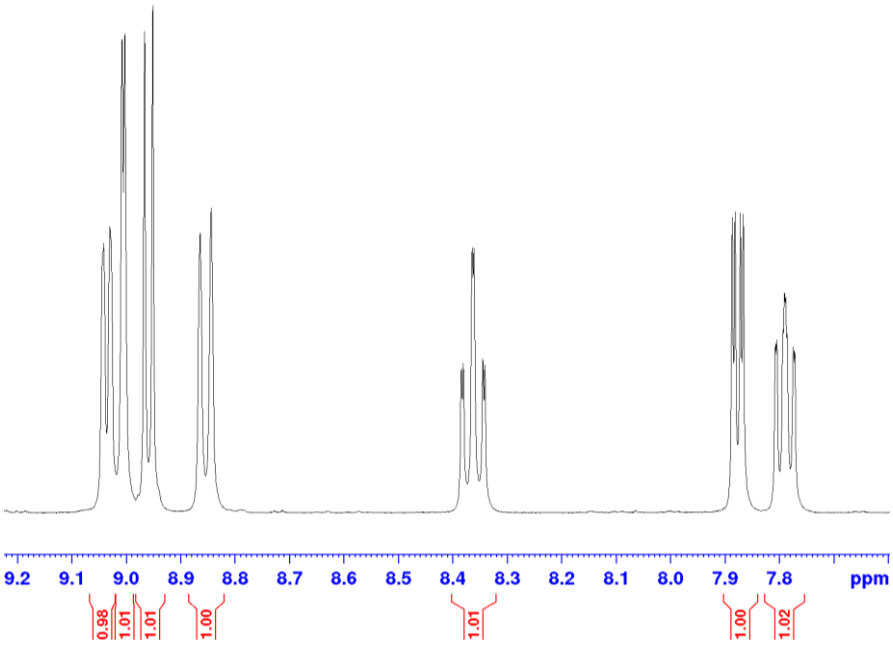

Figure 126. ^1H-NMR spectrum of **Re4ClBiPy** in DMSO-d_6, showing the expected peak area integration for the seven protons in the aromatic region which were shifted downfield with respect to the ligand.

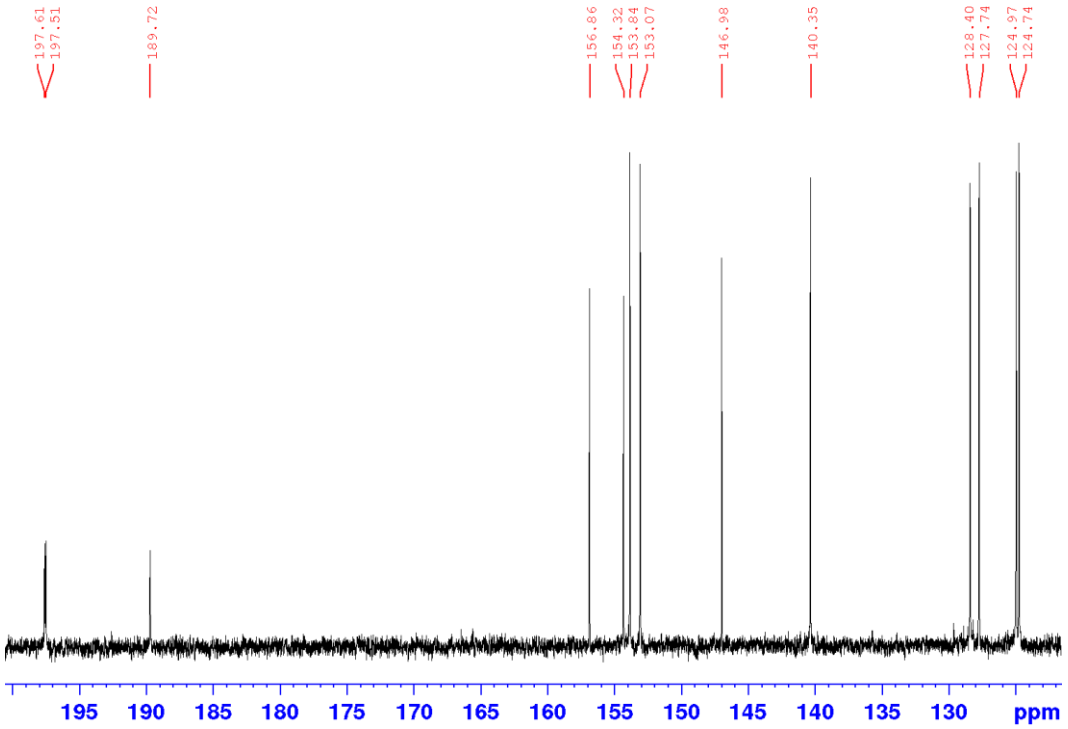

Figure 127. ^{13}C-NMR spectrum of **Re4ClBiPy** in DMSO-d_6, showing the three downfield shifted carbonyl signals with respect to the carbon-13 aromatic signals from the bipyridine ring.

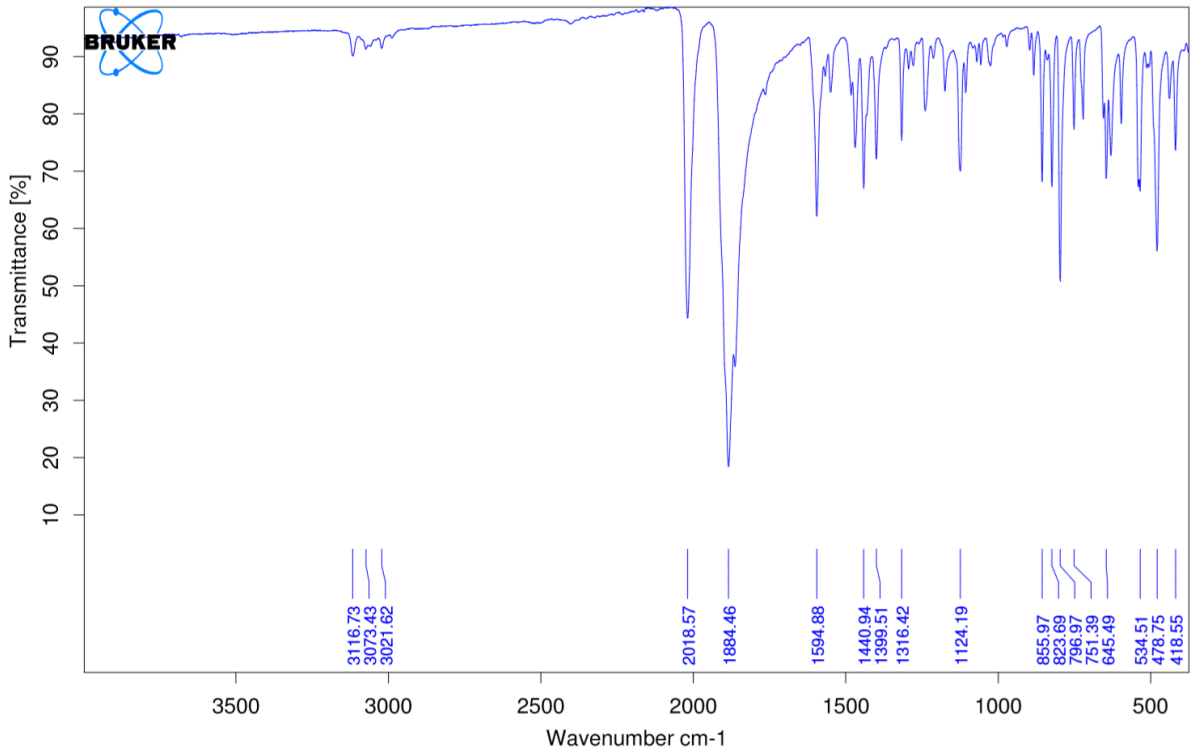

Figure 128. FTIR spectrum of **Re4ClBiPy** exhibiting the distinctive A'(1) C≡O stretching IR absorption band at 2019 cm^{-1} and the overlapping A'(2) & A'' C≡O stretching band at 1884 cm^{-1}. Weak sp^2 hybridised C–H bond stretches are also observed at higher wavenumbers (*circa* 3073 cm^{-1}) from the bipyridine ligand.

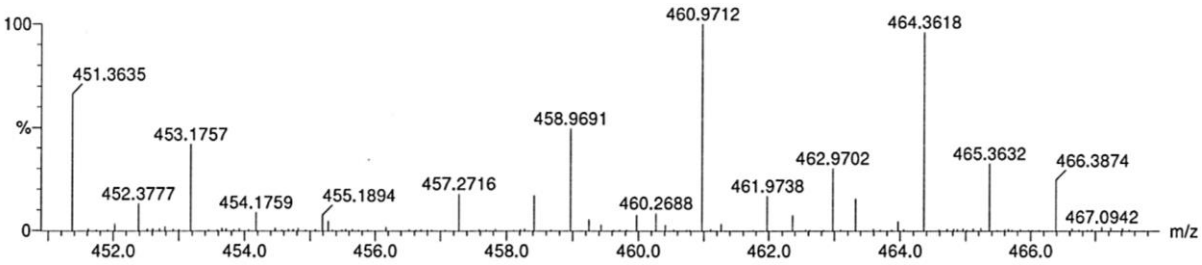

Figure 129. HRMS spectrum of **Re4ClBiPy** depicting the chlorine-dissociated $[M\text{-}Cl]^+$ ion signal observable at *m/z* 460.9712 with a calculated ratio of *m/z* 460.9703 (Δ 0.9 ppm) for the complex incorporating the ^{187}Re isotope in 62.6% natural abundance. An additional signal with *m/z* 458.9691 is also observed for the same ion incorporating the ^{185}Re isotope in 37.4% natural abundance.

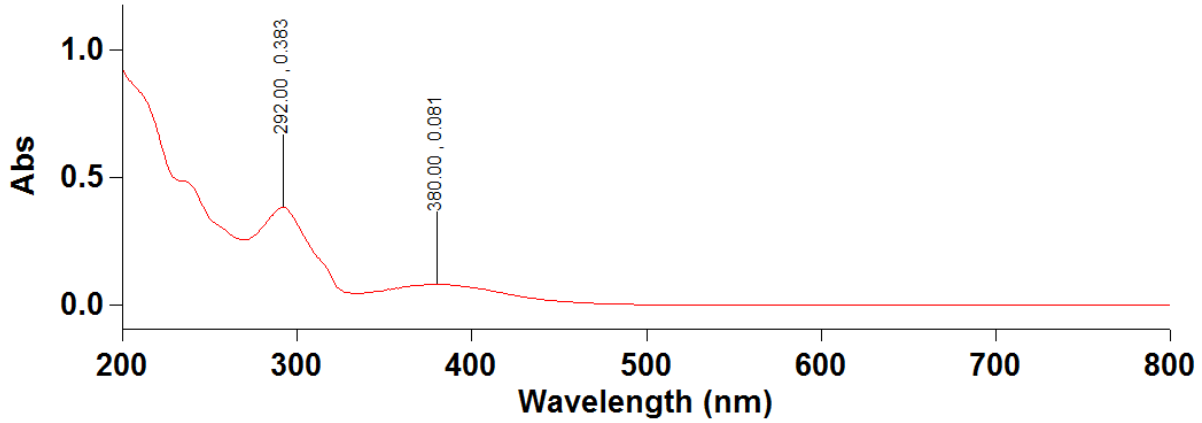

Figure 130. UV-Vis spectrum of **Re4ClBiPy** (5 μg.mL^{-1} in acetonitrile) showing the absorption band for the dπ → π* electronic transition to the MLCT excited state at 369 nm, alongside higher energy π → π* transitions to LC excited states with greater molar absorptivities.

4.1.6 Rhenium Complexation of 4-Fluoro-2,2'-Bipyridine

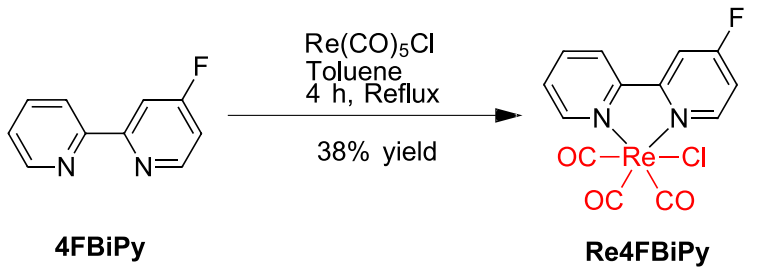

4FBiPy **Re4FBiPy**

Figure 131. Synthesis of **Re4FBiPy** via reflux of **4FBiPy** with pentacarbonylchlororhenium(I) in toluene which afforded the desired product in 38% yield.

A mass of **4FBiPy** (6.0 mg, 34.5 mmol, 1.0 eq.) was dissolved in a volume of anhydrous toluene (1 mL) to which was added a mass of pentacarbonylchlororhenium(I) (12.5 mg, 34.6 mmol, 1.0 eq.). The solution was then stirred and heated at reflux (4 h). The resulting yellow solid was then cooled to 4°C to promote precipitation and was isolated *via* vacuum filtration and washed with toluene and diethyl ether. The yellow product was then loaded onto a neutral alumina stationary phase (Brockmann grade II) in a glass pipette and eluted with DCM. The eluents confirmed to contain the product were combined, evaporated under reduced pressure and dried under high vacuum to attain a yellow powder (6.2 mg).

Integration of the ^{1}H-NMR spectrum in Figure 132 provides a value of approximately seven as expected for the seven protons present in the bipyridine ring of **Re4FBiPy**. The ^{13}C-NMR exhibits seventeen carbon-13 resonance signals, three of which correspond to the downfield shifted carbon-13 nuclei of the carbonyl ligands at 197.61, 197.58 and 189.94 ppm. The remaining fourteen carbon-13 resonance signals correspond to the ten carbon atoms of the bipyridine ring, though with the fluorine-19 nucleus coupling with four of those carbon-13 nuclei, thus giving rise to the additional four signals. The CPD ^{19}F-NMR spectrum of **Re4FBiPy**, as shown in Figure 134, shows the lone magnetic resonance signal for this fluorine-

19 nucleus. The FTIR spectrum in Figure 135 provides evidence for the rhenium tricarbonyl center with the distinctive A'(1) C≡O stretching frequency being notably excited at 2018 cm^{-1} and the overlapping A'(2) & A'' C≡O stretching vibrations being co-excited at 1884 cm^{-1}.

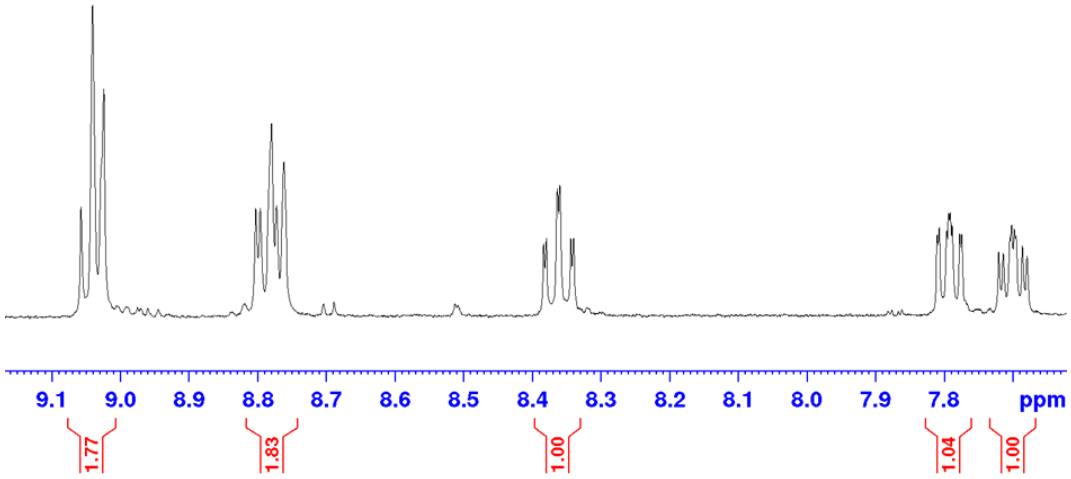

Figure 132. ^{1}H-NMR spectrum of **Re4FBiPy** in DMSO-d_6, showing the expected peak area integration for the seven protons in the aromatic region which were shifted downfield with respect to the ligand. The peaks exhibit more complex splitting patterns on account of the coupling between the fluorine-19 isotope present in the molecule.

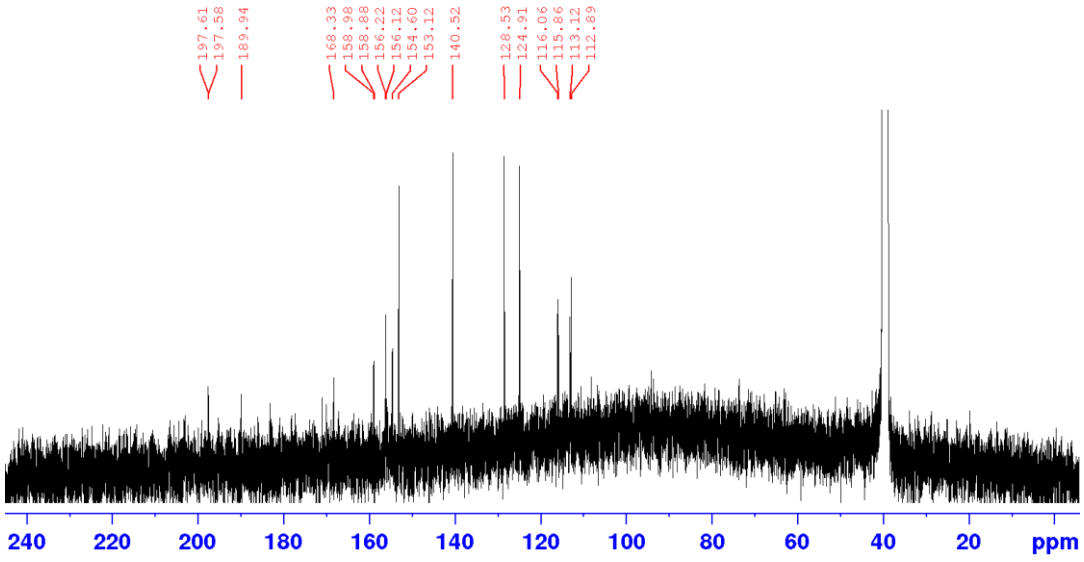

Figure 133. ^{13}C-NMR spectrum of **Re4FBiPy** in DMSO-d_6, showing the downfield shifted carbonyl signals with respect to the carbon-13 aromatic signals from the bipyridine ring. Complex splitting is observed due to the coupling between the carbon-13 and fluorine-19 nuclei.

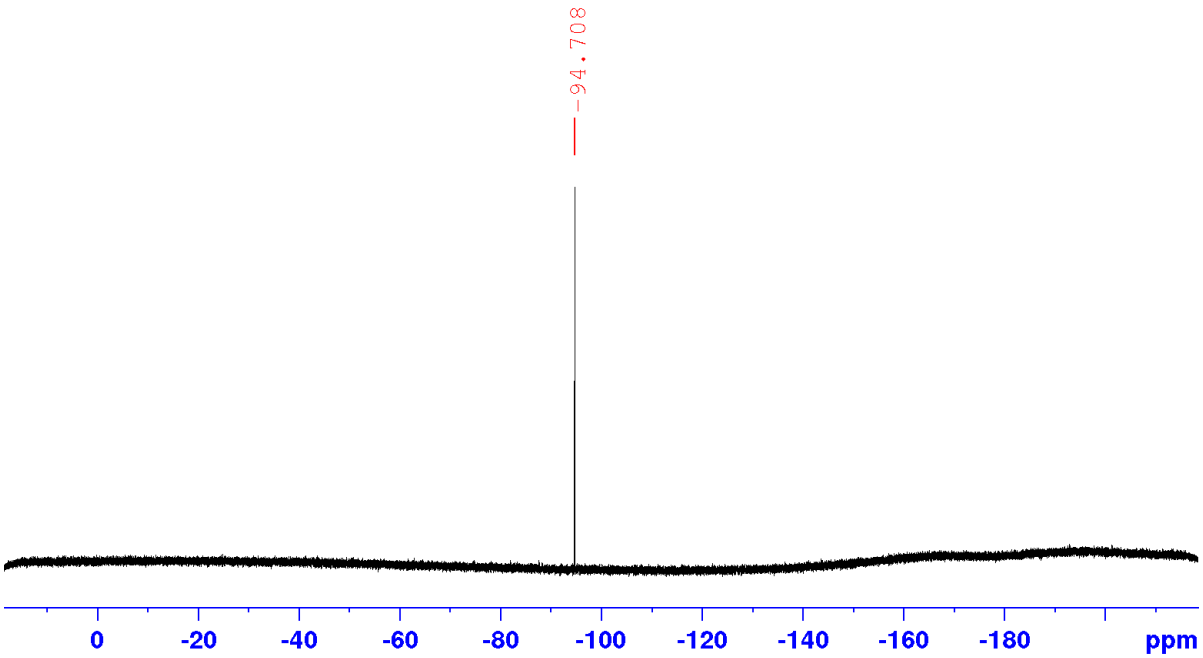

Figure 134. CPD ^{19}F-NMR spectrum of **Re4FBiPy** in DMSO-d_6 displaying the signal for the sole fluorine-19 nucleus in the molecule at -94.71 ppm.

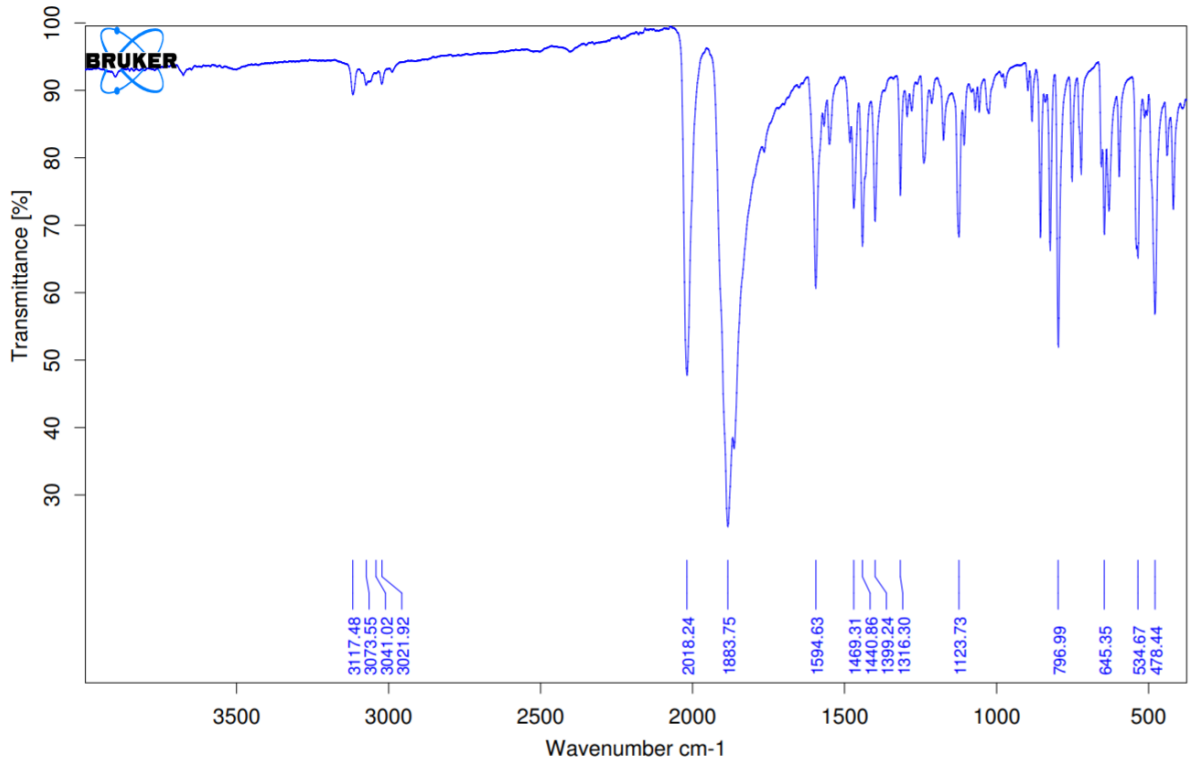

Figure 135. FTIR spectrum of **Re4FBiPy** exhibiting the distinctive A'(1) C≡O stretching IR absorption band at 2018 cm^{-1} and the overlapping A'(2) & A'' C≡O stretching band at 1884 cm^{-1}. Weak sp^2 hybridised C−H bond stretches are also observed at higher wavenumbers (*circa* 3041 cm^{-1}) from the bipyridine ligand.

4.1.7 Rhenium Complexation of 5-Chloro-2,2'-Bipyridine

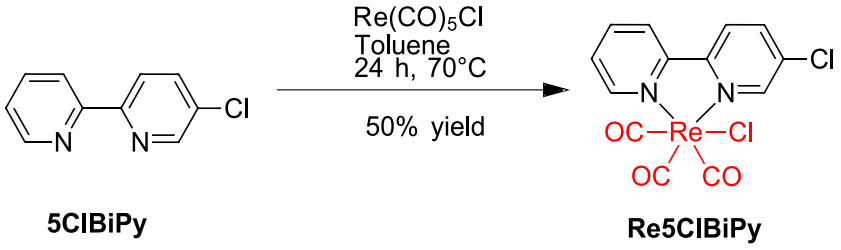

5ClBiPy **Re5ClBiPy**

Figure 136. Synthesis of **Re5ClBiPy** via reflux of **5ClBiPy** with pentacarbonylchlororhenium(I) in toluene which afforded the desired product in 50% yield.

A mass of **5ClBiPy (**195.3 mg, 1.024 mmol, 1.0 eq.) was dissolved in a volume of anhydrous toluene (10 mL) resulting in a pale blue coloured solution. A mass of pentacarbonylrhenium(I) (337.9 mg, 0.934 mmol, 1.1 eq.) was then added to the solution and heated to 70°C in an inert nitrogen atmosphere while stirring (24 h). The solution was then cooled first to room temperature, then to 4°C to induce further precipitation before isolating *via* vacuum filtration and washing with both cold toluene and diethyl ether. The yellow product was then dissolved in a minimum of DCM and purified on a mobile phase consisting of Brockmann grade II neutral alumina (*approx.* 30 g) eluting with an isocratic gradient of DCM. Those fractions containing the desired product were combined, evaporated under reduced pressure and dried under high vacuum to afford a yellow powder (232.6 mg).

Complexation of the 5-chloro-2,2'-bipyridine ligand to the source of tricarbonyl rhenium(I) was confirmed by ^{1}H-NMR and ^{13}C-NMR spectroscopy, shown in Figure 137 & Figure 138 respectively, which affirmed the expected peak area integration for seven protons and ten carbon-13 signals in the aromatic region alongside an additional three downfield shifted signals for the carbon-13 nuclei present in the carbonyl ligands. The IR absorption bands for these carbonyl ligands were also observed in the FTIR spectrum shown in Figure 139, which depicts

the A'(1) C≡O and overlapping A'(2) & A'' C≡O stretching frequencies at 2021 cm^{-1} and 1883 cm^{-1} respectively. Bipyridyl C−H sp^2 hybridised bond stretches also gave rise to IR absorption bands around 3064 cm^{-1}. The HRMS spectrum of **Re5ClBiPy** shown in Figure 140 depicts the chlorine-dissociated $[M\text{-}Cl]^+$ ion signal ($ReC_{13}H_7N_2O_3Cl^+$) observable at *m/z* 460.9730 against a calculated ratio of *m/z* 460.9703 (Δ 5.9 ppm) for the complex incorporating the ^{187}Re isotope in 62.6% natural abundance. An additional signal with *m/z* 458.9718 is also observed for the same ion incorporating the ^{185}Re isotope in 37.4% natural abundance. The UV-Vis spectrum of **Re5ClBiPy** in Figure 141 shows the absorption band for the dπ → π* electronic transition to the MLCT excited state at 379 nm and higher energy π → π* transitions to LC excited states at 299 and 241 nm. Elemental analysis further attested to the purity of the complex with measured composition of 31.61% carbon, 1.14% hydrogen and 5.44% nitrogen against calculated compositions of 31.46% carbon, 1.42% hydrogen and 5.64% nitrogen.

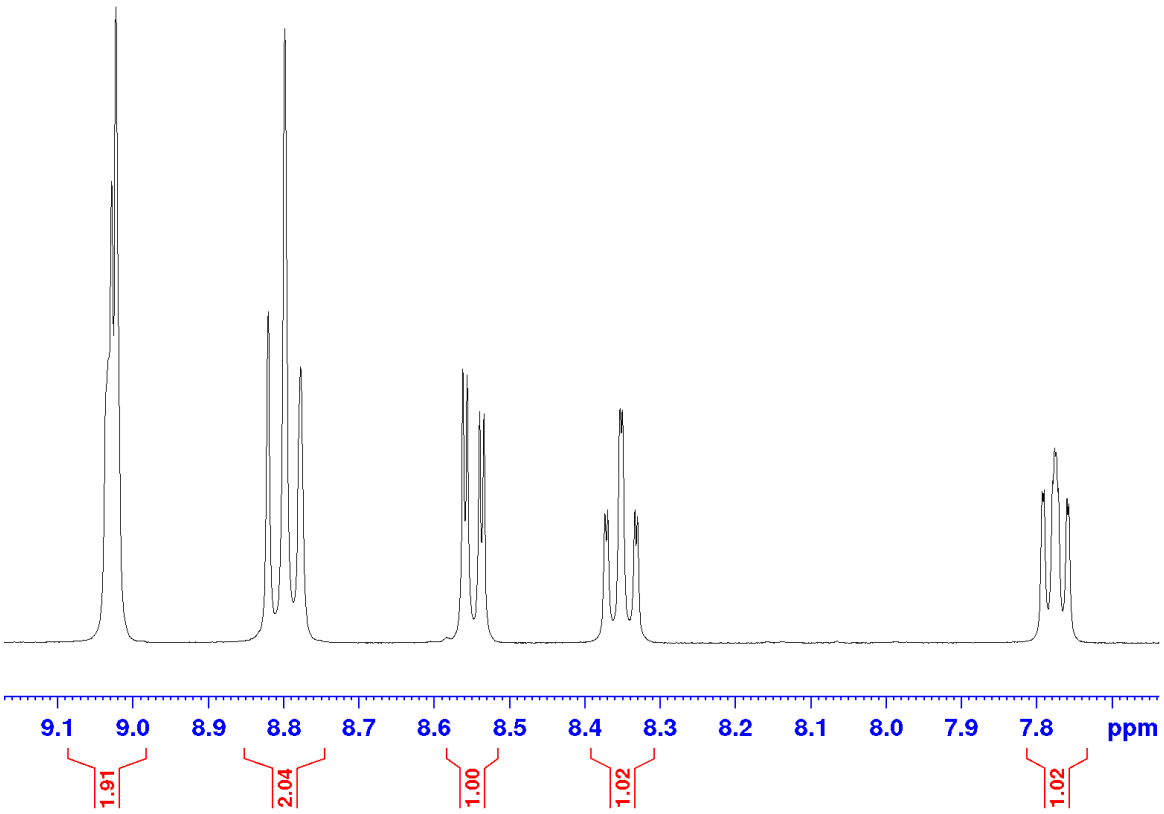

Figure 137. ^1H-NMR spectrum of **Re5ClBiPy** in DMSO-d_6, showing the expected peak area integration for the seven protons in the aromatic region which were shifted downfield with respect to the ligand.

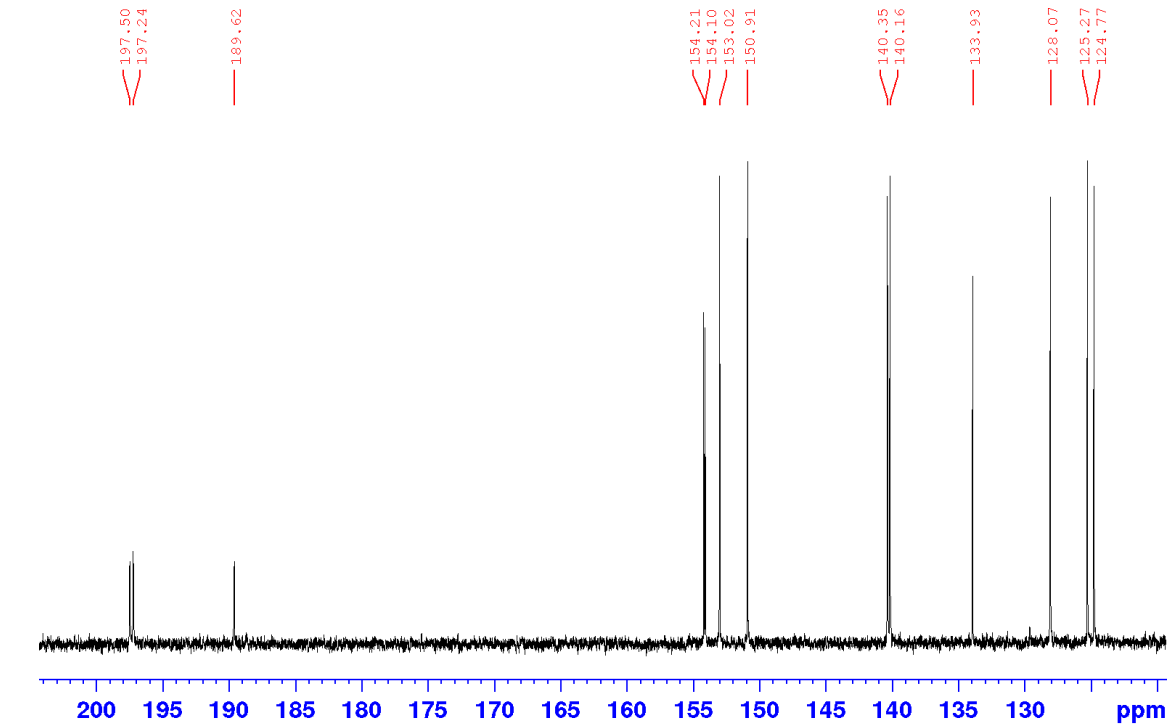

Figure 138. ^{13}C-NMR spectrum of **Re5ClBiPy** in DMSO-d_6, showing the three downfield shifted carbonyl signals with respect to the carbon-13 aromatic signals from the bipyridine ring.

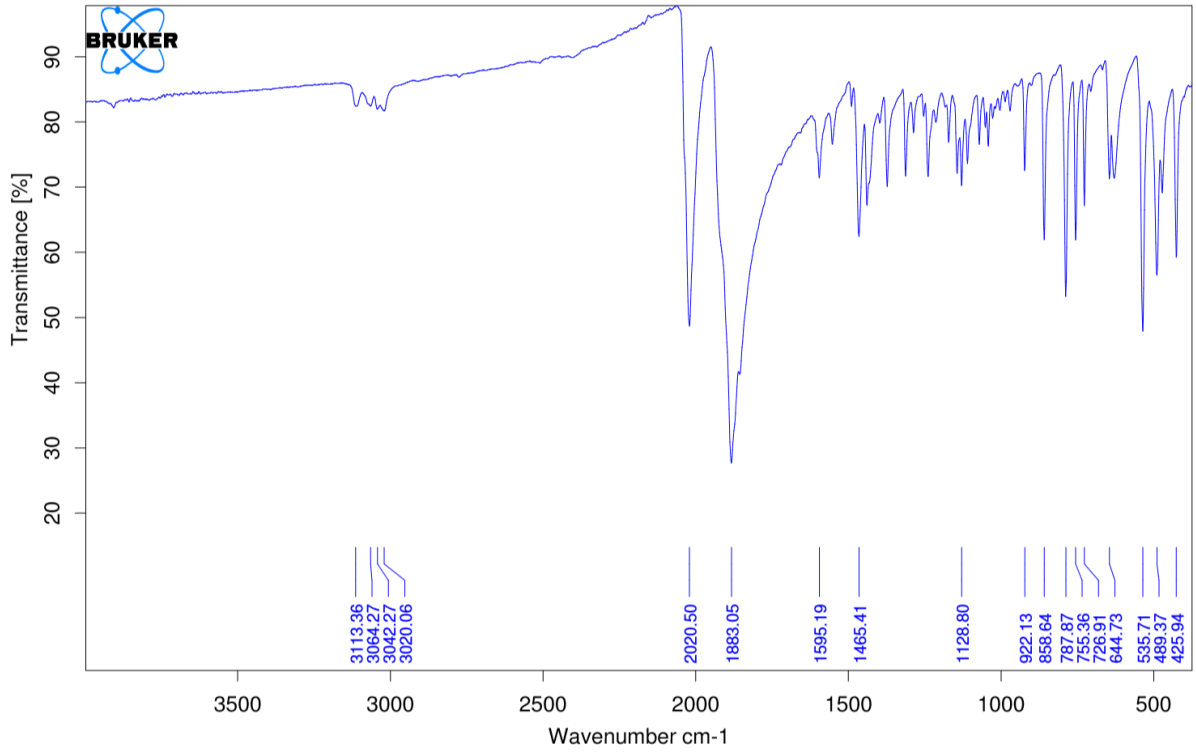

Figure 139. FTIR spectrum of **Re5ClBiPy** exhibiting the distinctive A'(1) C≡O stretching IR absorption band at 2021 cm^{-1} and the overlapping A'(2) & A'' C≡O stretching band at 1883 cm^{-1}. Weak sp^2 hybridised C−H bond stretches are also observed at higher wavenumbers (*circa* 3064 cm^{-1}) from the bipyridine ligand.

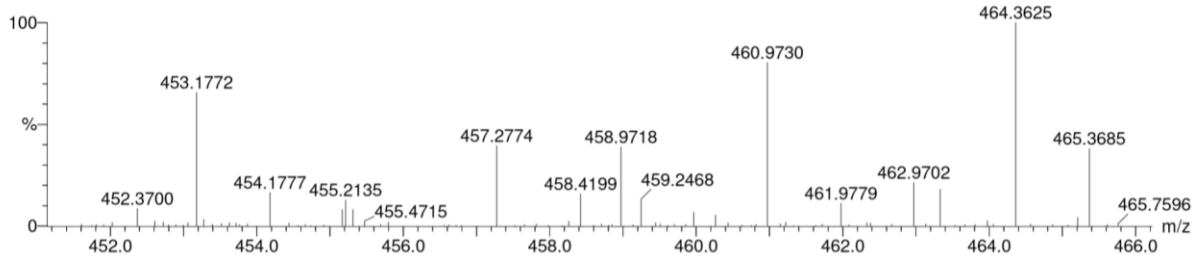

Figure 140. HRMS spectrum of **Re5ClBiPy** depicting the chlorine-dissociated $[M\text{-}Cl]^+$ ion signal observable at *m/z* 460.9730 with a calculated ratio of *m/z* 460.9703 (Δ 5.9 ppm) for the complex incorporating the ^{187}Re isotope in 62.6% natural abundance. An additional signal with *m/z* 458.9718 is also observed for the same ion incorporating the ^{185}Re isotope in 37.4% natural abundance.

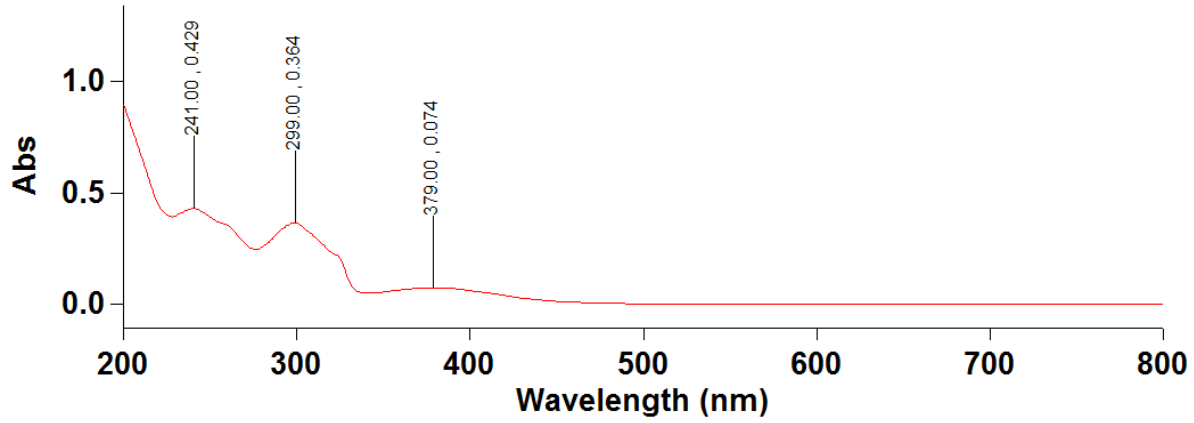

Figure 141. UV-Vis spectrum of **Re5ClBiPy** (5 μg.mL^{-1} in acetonitrile) showing the absorption band for the dπ → π* electronic transition to the MLCT excited state at 379 nm, alongside higher energy π → π* transitions to LC excited states with greater molar absorptivities.

4.1.8 Rhenium Complexation of 6-Bromo-2,2'-Bipyridine

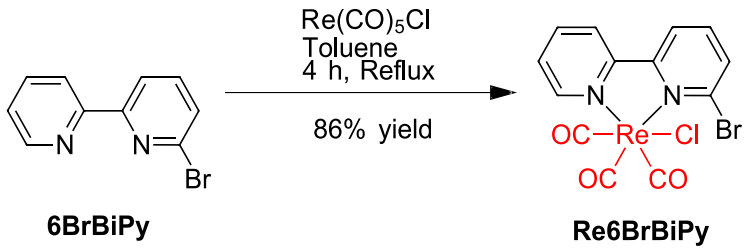

6BrBiPy **Re6BrBiPy**

Figure 142. Synthesis of **Re6BrBiPy** *via* reflux of **6BrBiPy** with pentacarbonylchlororhenium(I) in toluene which afforded the desired product in 86% yield.

A mass of **6BrBiPy** (157.0 mg, 0.6679 mmol, 1.1 eq.) was dissolved in a volume of anhydrous toluene (5 mL). A mass of pentacarbonylchlororhenium(I) (219.7 mg, 0.6074 mmol, 1.0 eq.) was added to the solution, which was then then purged with inert nitrogen gas and stirred at reflux (4 h). The solution was then cooled to room temperature thereafter and further cooled to -20°C to induce further precipitation of the solid. The yellow solid was then isolated *via* vacuum filtration, washed with sold toluene and diethyl ether, then dried under high vacuum. The resulting solid was then dissolved in a minimum of DCM and loaded onto a neutral alumina column (Brockmann grade II, *approx.* 80 g) and eluted using an isocratic mobile phase consisting solely of DCM. The fractions containing the purified product of interest were combined, evaporated under reduced pressure and dried under high vacuum to afford the yellow powder (311.9 mg).

The ^{1}H-NMR spectrum for **Re6BrBiPy**, shown in Figure 143, shows the expected integration for the seven protons in the aromatic region all downfield shifted with respect to the resonance signals of the ligand. In Figure 144 the ^{13}C-NMR spectrum gives rise to the expected thirteen carbon-13 nuclei resonance signals, ten of which exist within the aromatic region and pertain to the to the atoms within the bipyridine ring, and the other three being significantly downfield shifted at 190.0, 197.2 and 198.1 ppm pertaining to the carbonyl ligands. The FTIR spectrum

of **Re6BrBiPy**, shown in Figure 145, exhibits the distinctive A'(1) C≡O stretching IR absorption band at 2017 cm^{-1} and the overlapping A'(2) & A'' C≡O stretching bands at 1884.31 cm^{-1}. A weak sp^2 hybridised C−H bond stretch is also observed at 3074 cm^{-1} from the bipyridine ligand. The purity of the **Re6BrBiPy** complex was also verified by elemental analysis which measured compositions of 28.90%, 1.05% and 5.21% for carbon, hydrogen and nitrogen, respectively. These values closely align with the theoretical compositions of 28.87%, 1.30% and 5.18% for carbon, hydrogen and nitrogen, respectively.

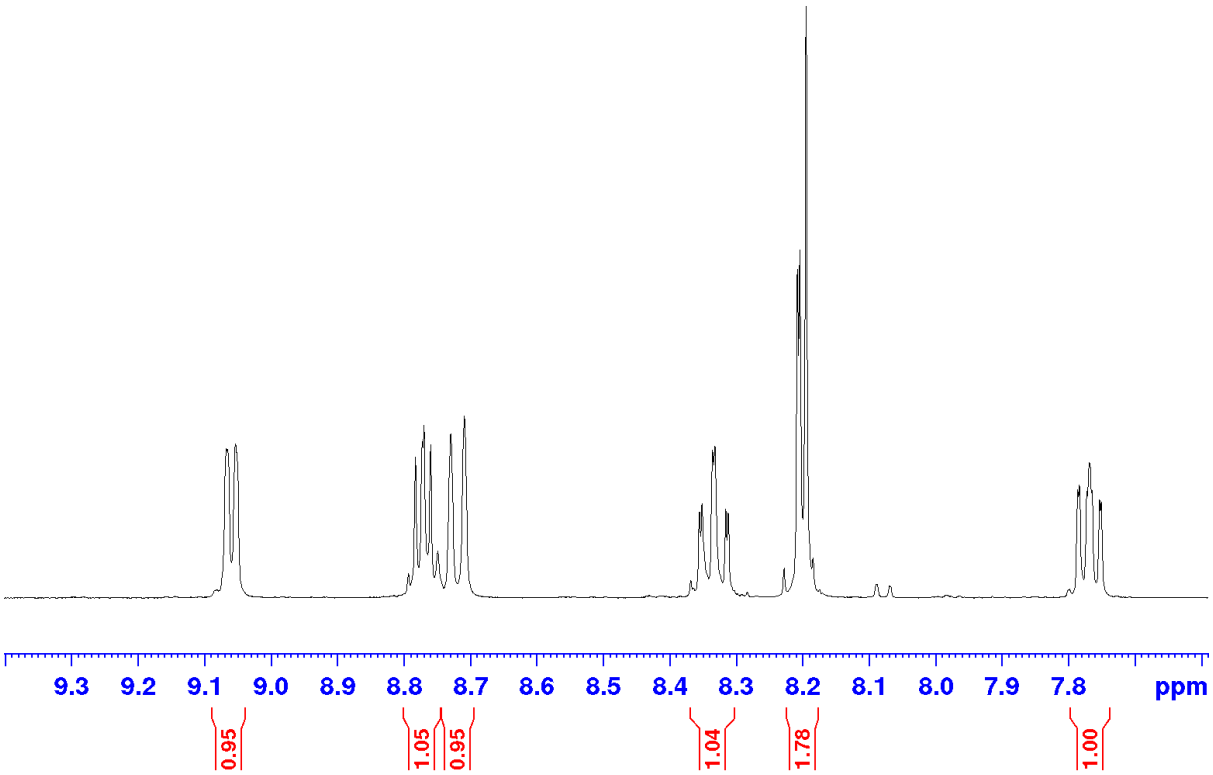

Figure 143. ^{1}H-NMR spectrum of **Re6BrBiPy** in DMSO-d_6, showing the expected peak area integration for the seven protons in the aromatic region which were shifted downfield with respect to the ligand.

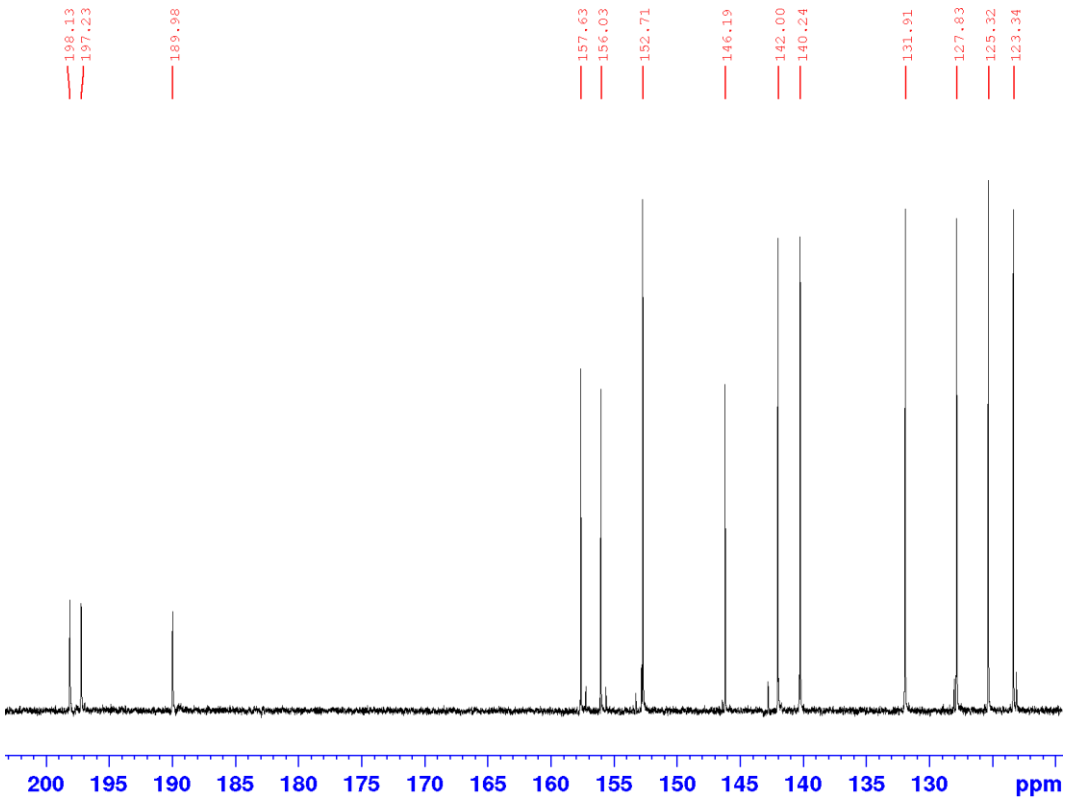

Figure 144. ^{13}C-NMR spectrum of **Re6BrBiPy** in DMSO-D_6, exhibiting not only the ten aromatic carbon-13 signals from the bipyridine system though also showing the three downfield shifted carbonyl signals of the rhenium complex (190.0, 197.2 & 198.1 ppm).

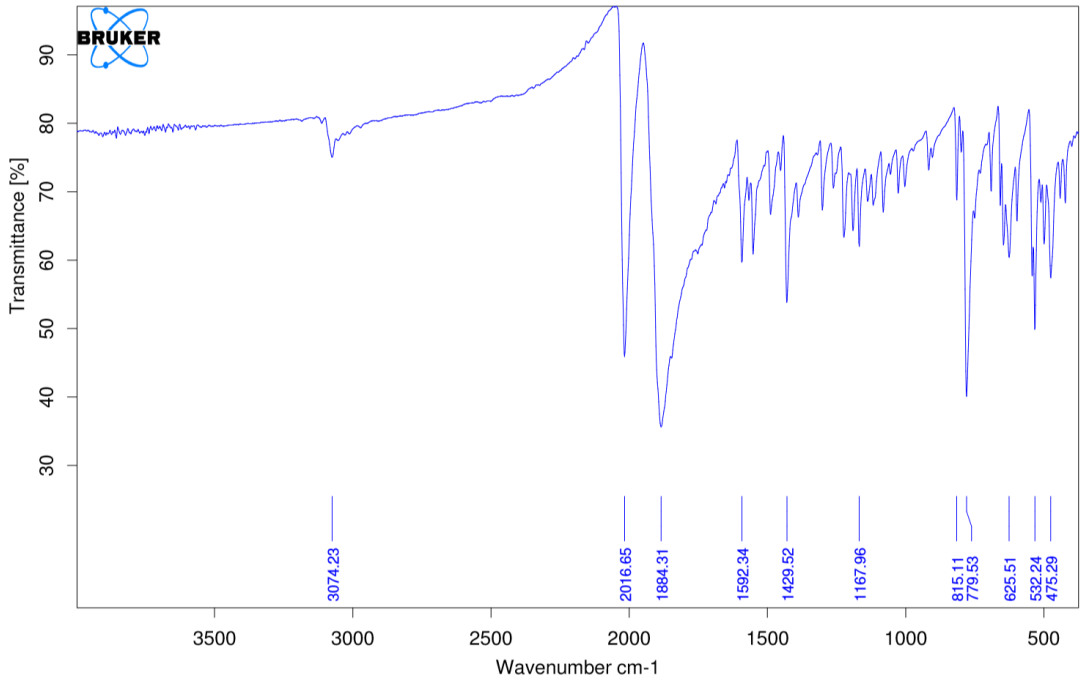

Figure 145. FTIR spectrum of **Re6BrBiPy** exhibiting the distinctive A'(1) C≡O stretching IR absorption band at 2017 cm^{-1} and the overlapping A'(2) & A'' C≡O stretching band at 1884 cm^{-1}. A weak sp^2 hybridised C–H bond stretch is also observed at 3074 cm^{-1} from the bipyridine ligand.

4.1.9 Characterisation Data for the Rhenium Complexed 2,2-Bipyridine Standards and Precursors

Tricarbonylchloro(6-chloro-2,2'-bipyridine)rhenium(I) (**Re6ClBiPy**) Yellow solid; MP: 255 °C; 86% yield. ^{1}H NMR (400 *MHz*, DMSO-d$_6$, *δ*/*ppm*): δ 9.06 (d, J^{d}=4.76 *Hz*, 1H), δ8.76 (d, J^{d}=8.12 *Hz*, 2H), δ 8.35 (*app.* td, J^{d}=1.96, J^{t}=8.04 *Hz*, 2H), δ 8.08 (dd, J^{d}=0.68, 8.04 *Hz*, 1H), δ 7.78 (*app.* td, J^{d}=1.80, J^{t}=4.56 *Hz*, 1H). ^{13}C{^{1}H} NMR (100 *MHz*, DMSO-d$_6$, δ/*ppm*): δ 197.5$_{C\equiv O}$, δ 197.3$_{C\equiv O}$, δ 189.5$_{C\equiv O}$, δ 157.2, δ 155.6, δ 153.2, δ 152.8, δ 142.7, δ 140.3, δ 128.0, δ 127.7, δ 125.3, δ 123.1. FTIR (ATR *corr.* $\tilde{\nu}$/*cm*$^{-1}$): $\tilde{\nu}$ 3075 (w, C−H sp^2 *str.*), $\tilde{\nu}$ 2018 (s, A'(1) C≡O *str.*), $\tilde{\nu}$ 1882 (s, A'(2) & A'' C≡O *str.*). UV/Vis (λ/*nm*, ε/*L.mol*$^{-1}$.*cm*$^{-1}$): λ 380 (*dπ*→*π**, ε 3375.36), λ 301 (*π*→*π**, ε 14990.57), λ 326 (*π*→*π**, ε 10920.28), λ 233 (*π*→*π**, ε 19259.41). LRMS (ESI^{+}): [M-Cl]$^{+}$ *m/z* cald: 460.97, *m/z* obvs 460.95. HRMS (ESI^{+}): [M-Cl]$^{+}$ *m/z* cald: 460.9703, *m/z* obvs 460.9694 (Δ -2.0 *ppm*). EA (%): *calc.* C 31.46, H 1.42, N 5.64. *found* C 31.59, H 1.17, N 5.70.

Tricarbonylchloro(6-fluoro-2,2'-bipyridine)rhenium(I) (**Re6FBiPy**) Yellow solid; MP: 294 °C, 65% yield. ^{1}H NMR (400 *MHz*, DMSO-d$_6$, *δ*/*ppm*): δ 9.06 (*app.* tq, J^{t} =5.48 *Hz*, J^{q}=0.80 *Hz*, 1H), δ 8.80 (d, J^{d}=8.16 *Hz*, 1H), δ 8.70 (d, J^{d}=7.92 *Hz*, 1H), δ 8.52 (q, J^{q}=8.04 *Hz*, 1H), δ 8.36 (td, J^{t}=8.08 *Hz*, J^{d}=1.52 *Hz*, 1H), δ 7.80 (m, 2H). ^{13}C{^{1}H} NMR (100 *MHz*, DMSO-d$_6$, δ/*ppm*): δ 197.2$_{C\equiv O}$, δ 196.6$_{C\equiv O}$ (d, J^{d}=16.59 *Hz*), δ 188.9$_{C\equiv O}$, δ 164.0, δ 161.5, δ 154.4 (d, J^{d}=15.92 *Hz*), δ 153.1, δ 145.9 (d, J^{d}=10.15 *Hz*), δ 140.4, δ 128.2, δ 125.1, δ 121.4 (d, J^{d}=2.94 *Hz*), δ 112.7 (d, J^{d}=30.19 *Hz*). ^{19}F{^{1}H} NMR (376 *MHz*, DMSO-d$_6$, *δ*/*ppm*): δ -51.75. FTIR (ATR *corr.* $\tilde{\nu}$/*cm*$^{-1}$): $\tilde{\nu}$ 3040 (w, C−H sp^2 *str.*), $\tilde{\nu}$ 2016 (s, A'(1) C≡O *str.*), $\tilde{\nu}$ 1880 (s, A'(2) & A'' C≡O *str.*). UV/Vis (λ/*nm*, ε/*L.mol*$^{-1}$.*cm*$^{-1}$): λ 369 (*dπ*→*π**, ε 2768.36), λ 296 (*π*→*π**, ε 12485.88), λ 235 (*π*→*π**, ε 15367.33). LRMS (ESI^{+}): [M-Cl]$^{+}$ *m/z* cald: 445.00, *m/z* obvs 445.10. EA (%): *calc.* C 32.54, H 1.47, N 5.84. *found* C 32.59, H 1.16, N 5.88.

4-fluoro-2,2'-bipyridine (**4FBiPy**). White solid; 42% yield. ^{1}H NMR (400 *MHz*, DMSO-d_6, *δ/ppm*): δ 8.87 (s, 1H), δ 8.79 (s, 1H), δ 8.62 (d, J^d=5.58 *Hz*, 1H), δ 8.34 (t, J^t=7.28 *Hz*, 1H), δ 7.70 (s 1H), 7.28 (s 1H). ^{13}C{^{1}H} NMR (100 *MHz*, DMSO-d_6, δ/*ppm*): δ 127.04, δ 169.37, δ 159.4 (d, J^d=39 *Hz*), δ 158.7 (d, J^d=39 *Hz*), δ 151.26, δ 146.70, δ 143.20, δ 125.7 (d, J^d=239 *Hz*), δ 116.70, δ 113.84. ^{19}F{^{1}H} NMR (376 *MHz*, DMSO-d_6, *δ/ppm*): δ -75.99. LRMS (ESI^+): $[M+H]^+$ *m/z* cald: 175.07, *m/z* obvs175.12.

Tricarbonylchloro(4-chloro-2,2'-bipyridine)rhenium(I) (**Re4ClBiPy**). Yellow solid; MP: 283 °C; 89% yield. ^{1}H NMR (400 *MHz*, DMSO-d_6, *δ/ppm*): δ 9.04 (d, J^d=4.68 *Hz*, 1H), δ 9.01 (d, J^d=2.04 *Hz*, 1H), δ 8.96 (d, J^d=6.00 *Hz*, 1H), δ 8.85 (d, J^d=8.16 *Hz*, 1H), δ 8.36 (*app.* td, J^t=8.04 *Hz*, J^d=1.32, 1H), δ 7.88 (dd, J^d=2.12, 6.00 *Hz*, 1H), δ 8.36 (*app.* td, J^d=1.12, J^t=5.56 *Hz*, 1H). ^{13}C{^{1}H} NMR (100 *MHz*, DMSO-d_6, δ/*ppm*): δ 197.6$_{C\equiv O}$, δ 197.5$_{C\equiv O}$, δ 189.7$_{C\equiv O}$, δ 156.9, δ 154.3, δ 153.8, δ 153.1, δ 147.0, δ 140.3, δ 128.4, δ 127.7, δ 125.0, δ 124.7. FTIR (ATR *corr.* $\tilde{\nu}/cm^{-1}$): $\tilde{\nu}$ 3117 (w, C–H sp^2 *str.*), $\tilde{\nu}$ 2019 (s, A'(1) C≡O *str.*), $\tilde{\nu}$ 1884 (s, A'(2) & A'' C≡O *str.*). UV/Vis (λ/*nm*, ε/$L.mol^{-1}.cm^{-1}$): λ 380 ($d\pi\rightarrow\pi^*$, ε 7548.93), λ 292 ($\pi\rightarrow\pi^*$, ε 38022.44), λ 235 ($\pi\rightarrow\pi^*$, ε 48347.07). LRMS (ESI^+): $[M-Cl]^+$ *m/z* cald: 460.97, *m/z* obvs 460.95. HRMS (ESI^+): $[M-Cl]^+$ *m/z* cald: 460.9703, *m/z* obvs 460.9712 (Δ 2.0 *ppm*). EA (%): *calc.* C 31.46, H 1.42, N 5.64. *found* C 31.81, H 1.20, N 5.32.

Tricarbonylchloro(4-fluoro-2,2'-bipyridine)rhenium(I) (**Re4FBiPy**). Yellow solid; MP: 302 °C; 38% yield. ^{1}H NMR (400 *MHz*, DMSO-d_6, *δ/ppm*): δ 9.04 (*app.* t, J^t=6.72 *Hz*, 2H), δ 8.78 (m, 2H), δ 8.36 (td, J^d=1.44, J^t=7.92 *Hz*, 1H), δ 7.79 (qd, J^d=1.12, J^q=7.56 *Hz*, 1H), δ 7.69 (qd, J^d=1.00, J^q=7.36 *Hz*, 1H). ^{13}C{^{1}H} NMR (100 *MHz*, DMSO-d_6, δ/*ppm*): δ 197.6$_{C\equiv O}$, δ 197.6$_{C\equiv O}$, δ 189.9$_{C\equiv O}$, δ 168.3, δ 168.3, δ 158.9 (d, J^d=10.26 *Hz*), δ 156.2 (d, J^d=9.99 *Hz*), δ 154.6, δ 153.1, δ 140.5, δ 128.5, δ 124.9, δ 116.0 (d, J^d=19.7 *Hz*), δ 113.0 (d, J^d=22.79 *Hz*). ^{19}F{^{1}H} NMR (376 *MHz*, DMSO-d_6, *δ/ppm*): δ -94.71. FTIR (ATR *corr.* $\tilde{\nu}/cm^{-1}$): $\tilde{\nu}$ 3117 (w, C–H sp^2 *str.*), $\tilde{\nu}$ 2018 (s, A'(1) C≡O *str.*), $\tilde{\nu}$ 1884 (s, A'(2) & A'' C≡O *str.*). LRMS (ESI^+): [M-

Cl]$^{+}$ *m/z* cald: 445.00, *m/z* obvs 444.92. EA (%): *calc.* C 32.54, H 1.47, N 5.84. *found* C 32.52, H 1.33, N 5.81.

Tricarbonylchloro(5-chloro-2,2'-bipyridine)rhenium(I) (**Re5ClBiPy**). Yellow solid; MP: 292 °C, 50% yield. ^{1}H NMR (400 *MHz,* DMSO-d$_6$, *δ/ppm*): δ 9.03 (d, J^{d}=2.28 *Hz*, 2H), δ 8.80 (t, J^{t}=8.92 *Hz*, 2H), δ 8.55 (dd, J^{d}=8.84, 2.28 *Hz*, 1H), δ 8.35 (td, J^{t}=8.04 *Hz,* J^{d} = 1.32 *Hz*, 1H), δ 7.77 (*app.* qd, J^{q}=5.68 *Hz,* J^{d}=1.16 *Hz*, 1H). ^{13}C{^{1}H} NMR (100 *MHz,* DMSO-d$_6$, δ/*ppm*): δ 197.5$_{C\equiv O}$, δ 197.2$_{C\equiv O}$, δ 189.6$_{C\equiv O}$, δ 154.2, δ 154.1, δ 153.0, δ 150.9, δ 140.4, δ 140.2, δ 133.9, δ 128.1, δ 125.3, δ 124.8. FTIR (ATR *corr.* $\tilde{\nu}$/*cm*$^{-1}$): $\tilde{\nu}$ 3113 (w, C−H sp^2 *str.*), $\tilde{\nu}$ 2021 (s, A'(1) C≡O *str.*), $\tilde{\nu}$ 1883 (s, A'(2) & A'' C≡O *str.*). UV/Vis (λ/*nm*, ε/*L.mol*$^{-1}$*.cm*$^{-1}$): λ 379 (*dπ→π**, ε 7346.37), λ 299 (*π→π**, ε 36136.21), λ 241 (*π→π**, ε 42589.10). LRMS (ESI^{+}): [M-Cl]$^{+}$ *m/z* cald: 460.97, *m/z* obvs 460.95. HRMS (ESI^{+}): [M-Cl]$^{+}$ *m/z* cald: 460.9703, *m/z* obvs 460.9730 (Δ 5.9 *ppm*). EA (%): *calc.* C 31.46, H 1.42, N 5.64. *found* C 31.61, H 1.14, N 5.44.

Tricarbonylchloro(6-bromo-2,2'-bipyridine)rhenium(I) (**Re6BrBiPy**). Yellow solid; MP: 260 °C, 86% yield. ^{1}H NMR (400 *MHz,* DMSO-d$_6$, *δ/ppm*): δ 9.06 (dd, J^{d}=5.48 *Hz,* 0.80 *Hz*, 1H), δ 8.77 (q, J^{q}=5.16 *Hz,* 4.08 *Hz*, 1H), δ 8.71 (d, J^{d}=8.24 *Hz*, 1H), δ 8.33 (td, J^{t}=8.08 *Hz*, J^{d}=1.52 *Hz*, 1H), δ 8.20 (d, J^{d}=1.40 Hz, 1H), δ 8.19 (s, 1H), δ 7.76 (qd, J^{q}=5.52 *Hz,* 1.24 *Hz,* J^{d}=1.04 *Hz,* 1H). ^{13}C{^{1}H} NMR (100 *MHz,* CD$_3$CN, δ/*ppm*): δ 198.1$_{C\equiv O}$, δ 197.2$_{C\equiv O}$, δ 190.0$_{C\equiv O}$, δ 157.6, δ 156.0, δ 152.7, δ 146.2, δ 142.0, δ 140.2, δ 131.9, δ 127.8, δ 125.3, δ 123.3. FTIR (ATR *corr.* $\tilde{\nu}$/*cm*$^{-1}$): $\tilde{\nu}$ 3074 (w, C−H sp^2 *str.*), $\tilde{\nu}$ 2017 (s, A'(1) C≡O *str.*), $\tilde{\nu}$ 1884 (s, A'(2) & A'' C≡O *str.*). LRMS (ESI^{+}): [M-Cl]$^{+}$ *m/z* cald: 504.92, *m/z* obvs 505.04. EA (%): *calc.* C 28.87, H 1.30, N 5.18. *found* C 28.90, H 1.05, N 5.21.

4.2 Radiosyntheses of Rhenium-Bipyridine Complexes

4.2.1 Fluorine-18 Radiolabelling of Rhenium Complexed 6-Chloro-2,2'-Bipyridine

The synthesised non-radioactive standards of **6FBiPy** and **Re6FBiPy** were first injected onto the radio-HPLC using the standard chromatographic conditions described in the experimental. The UV-absorption profiles of both compounds are superimposed on the chromatogram in Figure 146 and affirm an approximate 2.1 min elution time for **6FBiPy** and 7.7 min for **Re6FBiPy** which were then used to identify the radioproducts. A series of radiolabelling reactions were then performed on the **Re6ClBiPy** precursor under *dry* microfluidic conditions using standard reaction conditions (0.08 μmol of precursor, 29±10 MBq of [^{18}F]fluoride and 47 s reaction time) with the temperature raised by 20 °C between each experiment, ranging from 50 to 190 °C. Surprisingly, not only was fluorine-18 labelling of the complex observed to form **[^{18}F]Re6FBiPy** though the radiolabelled complex was also found to dissociate at higher temperatures to afford the **[^{18}F]6FBiPy** ligand. This phenomenon is illustrated by the superimposed radiochromatographic profiles for the reaction at 130 °C (blue trace) and 190 °C (orange trace) in Figure 147. At temperatures of 130 °C and lower the reaction was found to reliably form **[^{18}F]Re6FBiPy**, with little or no dissociation observed at all. At temperatures greater than 170 °C, dissociation of the complex appeared to form the **[^{18}F]6FBiPy** radiolabelled ligand in greater concentration than the initial **[^{18}F]Re6FBiPy** product. An unknown by-product was also found to form concurrently with the dissociation process, however, with a retention time of 6.6 mins between both the ligand and precursor. This uncharacterised compound could potentially be due to [^{18}F]fluoride substitution for the chloro ancillary ligand bonded to the rhenium, however a non-radioactive standard of such a compound would first need to be synthesised to assign such an identity.

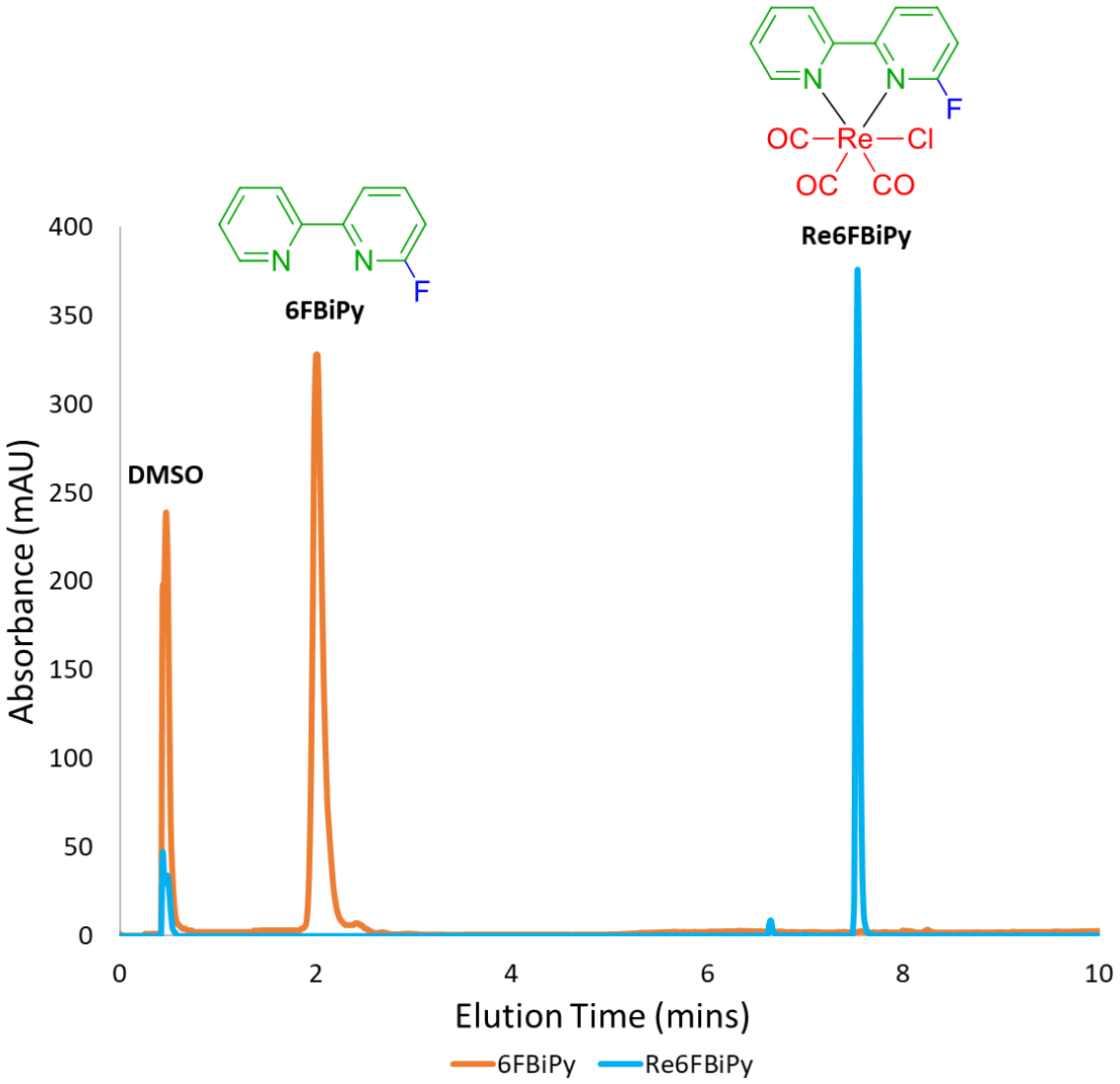

Figure 146. UV-absorbance chromatograms for **6FBiPy** (orange trace) and **Re6FBiPy** (blue trace) providing approximate elution times of 2.1 min and 7.7 min, respectively, which were used to assign the identities of the radioproducts. DMSO is also observed to elute early at 0.5 min with the initially aqueous mobile phase.

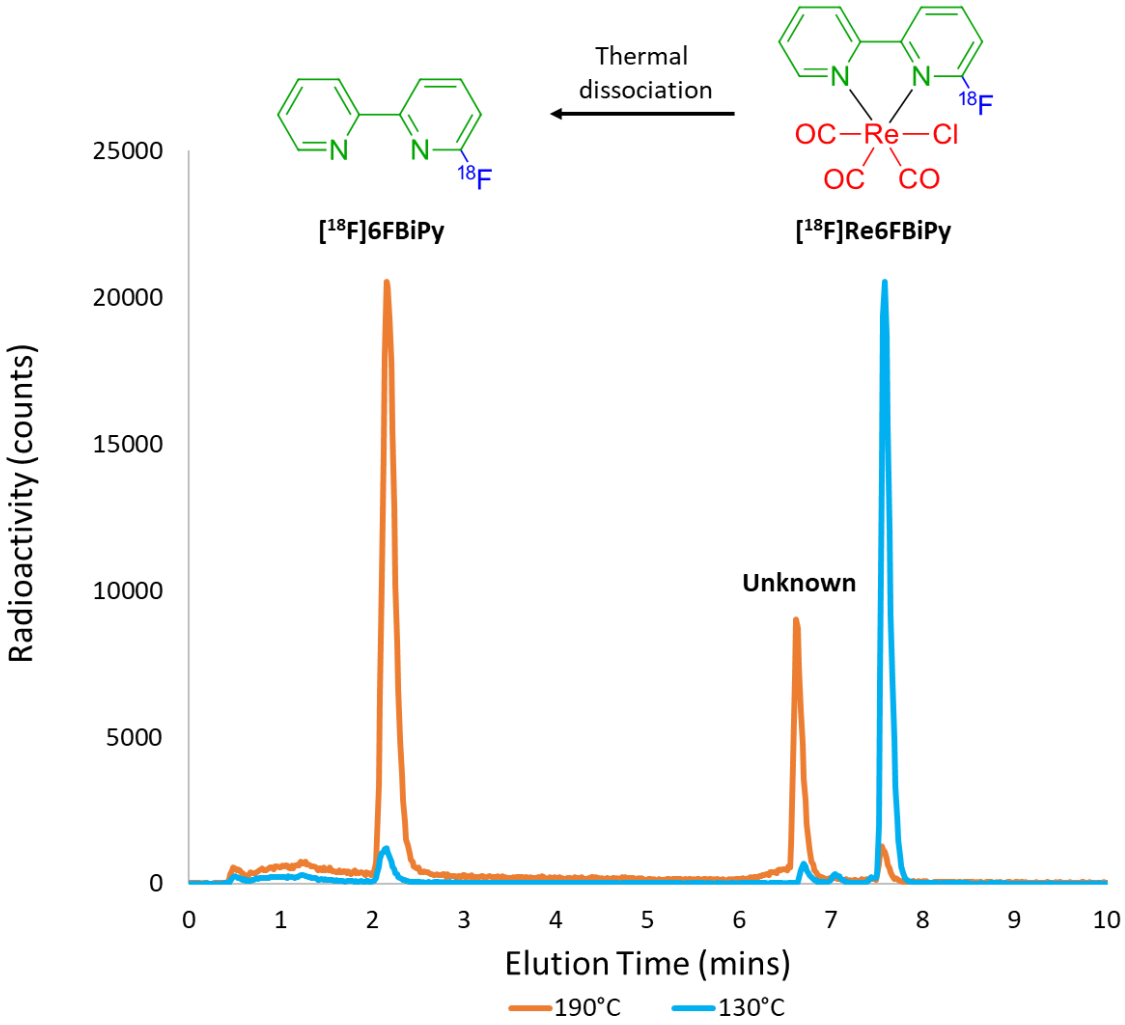

Figure 147. Radiochromatogram profiles for the fluorine-18 radiolabelling of **Re6ClBiPy** at 130 °C (blue trace) and 190 °C (orange trace). At 130 °C **[^{18}F]Re6FBiPy** (7.6 min) reliably forms, whereas at 190 °C the complex dissociates to form the otherwise unobtainable **[^{18}F]6FBiPy** (2.2 min) as well as an unknown by-product (6.6 min).

To confirm that the **Re6ClBiPy** precursor was not in fact dissociating to form the **6ClBiPy** ligand, which in turn may have been radiolabelled to afford the observed **[^{18}F]6FBiPy** radioproduct, we performed the same reactions under analogous conditions using the only the **6ClBiPy** precursor. To our surprise, despite several attempts the **6ClBiPy** would not radiolabel to afford the **[^{18}F]6FBiPy** radioproduct. Thus, it was found that the **[^{18}F]6FBiPy** radiolabelled ligand could only be attained by radiolabelling the **Re6ClBiPy** precursor with [^{18}F]fluoride under temperatures which also enabled decomplexation to liberate **[^{18}F]6FBiPy**. This process is illustrated in Figure 148, which also plots the RCYs of the **[^{18}F]Re6FBiPy**, **[^{18}F]6FBiPy** and unknown radioproducts as a function of the reaction temperature. Within this plot we observe the RCY of **[^{18}F]Re6FBiPy** increase from 8% at 50 °C to a maximum of 82% at 130 °C, where after the complex dissociates forming only 3% at a higher temperature of 190 °C. Meanwhile, **[^{18}F]6FBiPy** was not found to form at 70 °C or lower, though did start to form in 5% RCY at 90 °C and steadily increased at higher temperatures affording 65% RCY at 190 °C. The unidentified by-product appeared to form in a similar trend to the ligand, forming in only 2% RCY at 90 °C and then steadily increasing at higher temperatures to yield 20% at 190 °C. In an effort to increase the RCY of the **[^{18}F]6FBiPy**, experiments were further trialled under the same conditions at 190 °C though with the flow rate adjusted to 5 µL.min^{-1} and 2 µL.min^{-1} (reaction times of 3.12 min and 7.8 min, respectively). In the reaction applying a flow rate of 5 µL.min^{-1}, **[^{18}F]6FBiPy** was found to form in 56% RCY and the uncharacterised product was found to form in 27%. Whereas in the reaction applying a flow rate of 2 µL.min^{-1}, **[^{18}F]6FBiPy** was found to form in 38% RCY and the unknown product was found to form in 25%, suggesting that longer reaction times were inhibiting the formation of the **[^{18}F]6FBiPy** radioproduct. In both experiments the **[^{18}F]Re6FBiPy** radioproduct did not form in any measurable yield. Given that none of these reactions formed greater than 65% RCY observed using a flow rate of 20 µL.min^{-1} a 190 °C, the reaction was again repeated though using a ten-

fold equivalence of the **Re6ClBiPy** precursor (0.80 µmol) while applying a 4 µL.min^{-1} flow rate (3.9 min reaction time). In this experiment **[^{18}F]Re6FBiPy** was found to form in 66% RCY, though **[^{18}F]6FBiPy** only dissociated to form in 20% RCY. These conditions did suppress the formation of the unknown product, however, which only formed in 3% RCY.

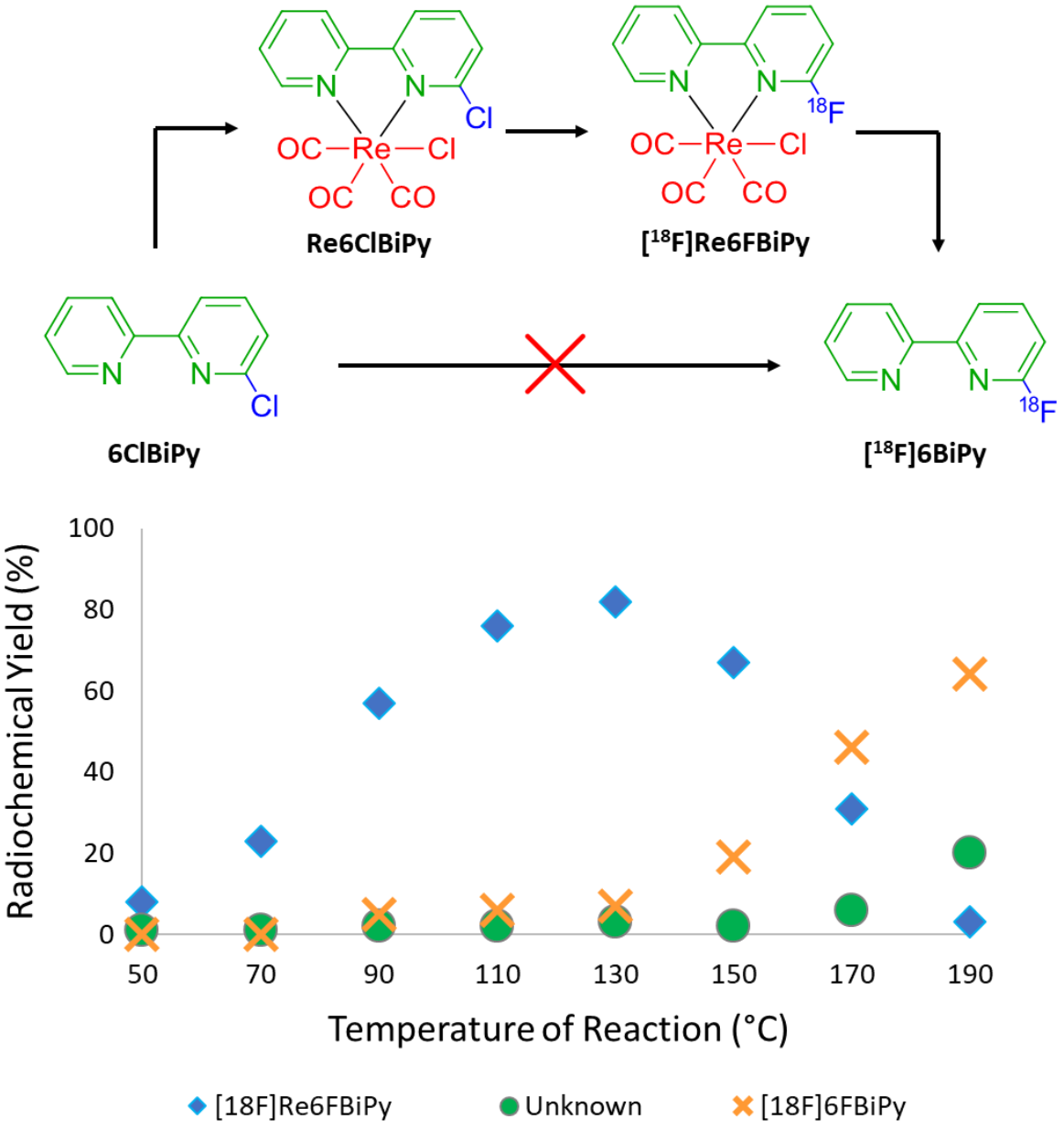

Figure 148. RCYs of **[^{18}F]Re6FBiPy** (blue diamonds), **[^{18}F]6FBiPy** (orange crosses) and the unknown by-product (green circles) as a function of the reaction temperature. The above scheme also shows how the fluorine-18 radiolabelling of **6ClBiPy** was unable to afford the **[^{18}F]6FBiPy** radioproduct, whereas the complex **Re6ClBiPy** was able to form the **[^{18}F]Re6FBiPy** radioproduct which could then be thermally dissociated to form the **[^{18}F]6FBiPy** ligand in considerable RCY.

The reactions were also performed under *wet* conditions, given how the 10% v/v content of water improved the yield of the fluorine-18 labelled rhenium complexes of the phenanthroline ligands. The RCY of **[^{18}F]Re6FBiPy**, **[^{18}F]6FBiPy** and the unknown product are each plotted in Figure 149 as a function of the reaction temperature for these experiments employing the same reaction conditions (0.08 µL of **Re6ClBiPy**, 29±10 MBq of radioactivity and a 47 s reaction time) though with *wet* DMSO solvent. These experiments greatly favoured the formation of the unidentified by-product which formed in 15% RCY for the experiment at 90 °C and then stabilised with maximal RCYs of 37%, 41%, 42% and 36% for reactions at temperatures of 110 °C, 130 °C, 150 °C and 170 °C, respectively. The yield of uncharacterised by-product then decreased considerably to 4% RCY when performing the reaction at 190 °C. By contrast, **[^{18}F]Re6FBiPy** revealed the same reaction profile, whereupon the RCY of the reaction steadily increased as a function of reaction temperature before steadily decomplexing at higher temperatures; as evident by 1% RCY forming at 50 °C, 3% RCY forming at 70 °C, 6% RCY forming at 90 °C, 17% RCY forming at 110 °C and a maximum 29% RCY forming at 130 °C, before decreasing to 25% RCY at 150 °C, 6% RCY forming at 170 °C and finally forming again only 1% RCY at 190 °C. The fluorine-18 labelled **[^{18}F]6FBiPy** ligand also followed the expected trend, though with no radioproduct forming up to 110 °C, followed by an incremental increase to 7% RCY at 130 °C, 15% RCY at 150 °C, 22% RCY at 170 °C and 24% RCY at 190 °C as the **[^{18}F]Re6FBiPy** radioproduct steadily decomplexed. These experiments were also repeated at 190 °C while applying different flow rates of 5 µL.min^{-1} and 2 µL.min^{-1} as per the *dry* conditions. With the *wet* reaction conditions repeated at 5 µL.min^{-1}, **[^{18}F]6FBiPy** formed in 15% RCY and the unknown by-product formed in 27% RCY, whereas **[^{18}F]Re6FBiPy** did not form at all. When repeating the reaction at 2 µL.min^{-1} **[^{18}F]6FBiPy** formed in 10% RCY and the unidentified by-product formed in 26% RCY, with the **[^{18}F]Re6FBiPy** again forming 0% RCY. A final experiment performed under *wet* conditions

applied a flow rate of 4 µL.min^{-1} with a ten-fold increase of the precursor amount to 0.80 µmol of **Re6ClBiPy** (analogous to the *dry* reaction experiment), which afforded 54% of **[^{18}F]Re6FBiPy**, 5% of **[^{18}F]6FBiPy** and 19% of the uncharacterised product, respectively. Thus, unlike the *dry* reaction conditions, applying a greater molar amount of the precursor under the *wet* reaction conditions afforded a considerably greater yield of the fluorine-18 labelled rhenium complex.

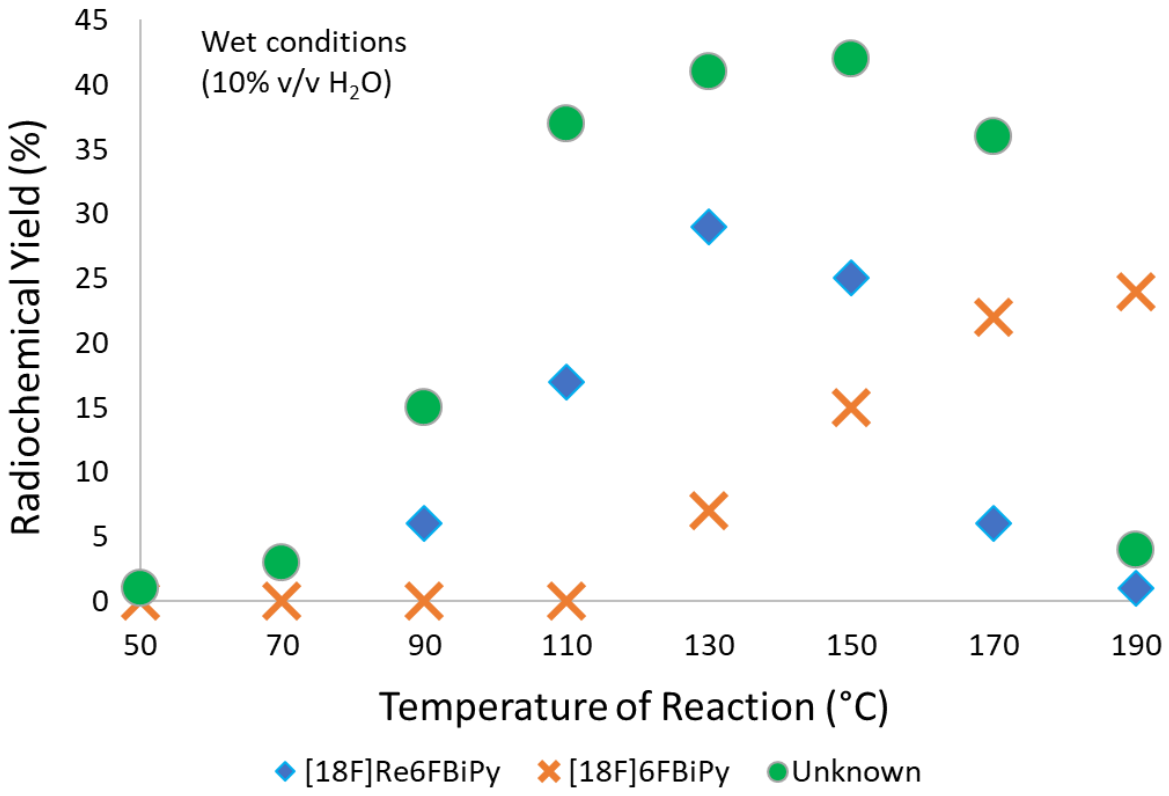

Figure 149. RCYs of **[^{18}F]Re6FBiPy** (blue diamonds), **[^{18}F]6FBiPy** (orange crosses) and the unknown by-product (green circles) plotted as function of reaction temperature for the same reaction parameters employing *wet* DMSO solvent (10% v/v content of water).

4.2.2 Fluorine-18 Radiolabelling of Rhenium Complexed 6-Bromo-2,2'-Bipyridine

Given the successful fluorine-18 radiolabelling of **Re6ClBiPy** and its thermal decomplexation to yield the **[^{18}F]6FBiPy** ligand, which could not be attain *via* traditional fluorine-18 labelling of the ligand, the reactions were again repeated using the **Re6BrBiPy** precursor to determine whether grater RCYs for both the **[^{18}F]Re6FBiPy** complex and **[^{18}F]6FBiPy** ligand could be achieved. Figure 150 shows the superimposed radiochromatographic profiles for the fluorine-18 radiolabelling of **Re6BrBiPy** at 110 °C (blue trace) and 190 °C (orange trace). A similar trend was observed whereupon the **[^{18}F]Re6FBiPy** labelled complex reliably formed at temperatures up to 110 °C. At 190 °C the **[^{18}F]Re6FBiPy** radioproduct had almost entirely dissociated to liberate the earlier eluting radiolabelled **[^{18}F]6FBiPy** ligand, as well as an unknown by-product. Curiously, this radioactive by-product formed from the high-temperature radiolabelling of **Re6BrBiPy** shared the same 6.6 min retention time as the uncharacterised by-product formed from the fluone-18 labelling of **Re6ClBiPy**. This may suggest either suggest that the familiar by-product is not due to [^{18}F]fluoride substitution for the chloro ancillary ligand bonded to the rhenium, or that the rhenium-[^{18}F]fluoride bonded complexes were not dissimilar enough in their chemical properties to be separated given the standard chromatographic conditions employed. The radiolabelling of the **6BrBiPy** precursor gave no radioproduct, akin to the results attained for the **6ClBiPy** precursor. Thus the **[^{18}F]6FBiPy** ligand could only be radiosynthesised *via* fluorine-18 radiolabelling and subsequent decomplexation of the **Re6BrBiPy** and **Re6ClBiPy** precursors. Figure 151 plots the RCY of **[^{18}F]Re6FBiPy**, **[^{18}F]6FBiPy** and the unidentified product formed from the radiolabelling of **Re6BrBiPy** as a function of reaction temperature. Evidently the plot exhibited a similar trend to the radiolabelling of **Re6ClBiPy**, with **[^{18}F]Re6FBiPy** having formed in 5% RCY at 50 °C before plateauing with maximum RCYs of 69%, 72% and 70% at temperatures of 90 °C,

110 °C and 130 °C, respectively. The RCY of **[^{18}F]Re6FBiPy** then decreased at higher temperature conditions, eventually forming only 4% RCY at 190 °C. Conversely, the **[^{18}F]6FBiPy** radiolabeled ligand did not form at 50 °C, though afforded 5% RCY at 70 °C and continued to synthesise in greater amounts peaking at 51% RCY at 190 °C as **[^{18}F]Re6FBiPy** decomplexed. The unknown product, also not forming at 50 °C, appeared in only trace amounts between 1 to 3% RCY for reaction temperatures between 70 and 150 °C, before also increasing to form in 8% and 25% RCY at temperatures of 170 °C and 190 °C, respectively.

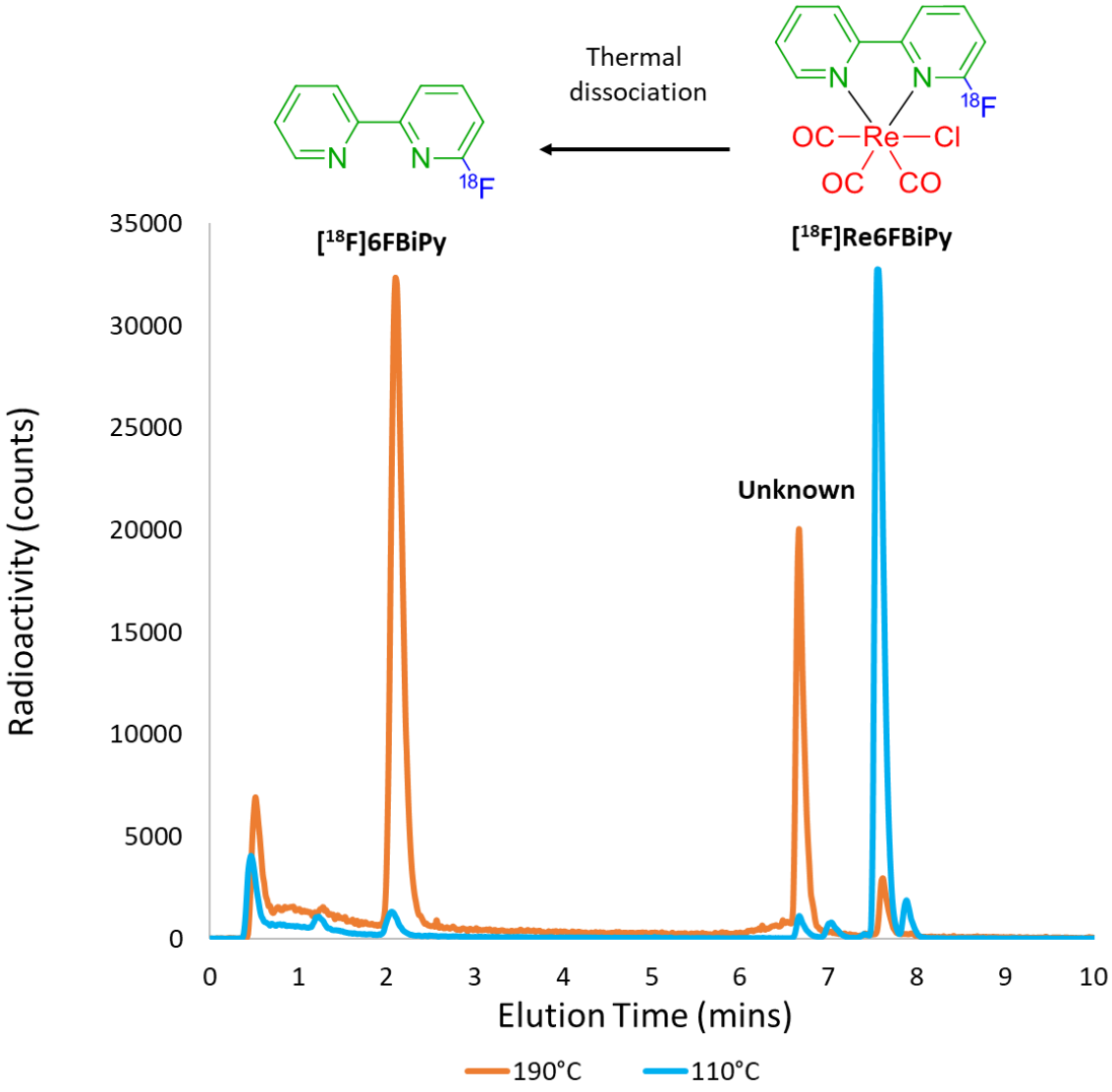

Figure 150. Radiochromatogram profiles for the fluorine-18 radiolabelling of **Re6BrBiPy** at 110 °C (blue trace) and 190 °C (orange trace). At 110 °C **[^{18}F]Re6FBiPy** (7.6 min) reliably forms, whereas at 190 °C the complex dissociates to form the otherwise unobtainable **[^{18}F]6FBiPy** (2.2 min) as well as an unknown by-product (6.6 min).

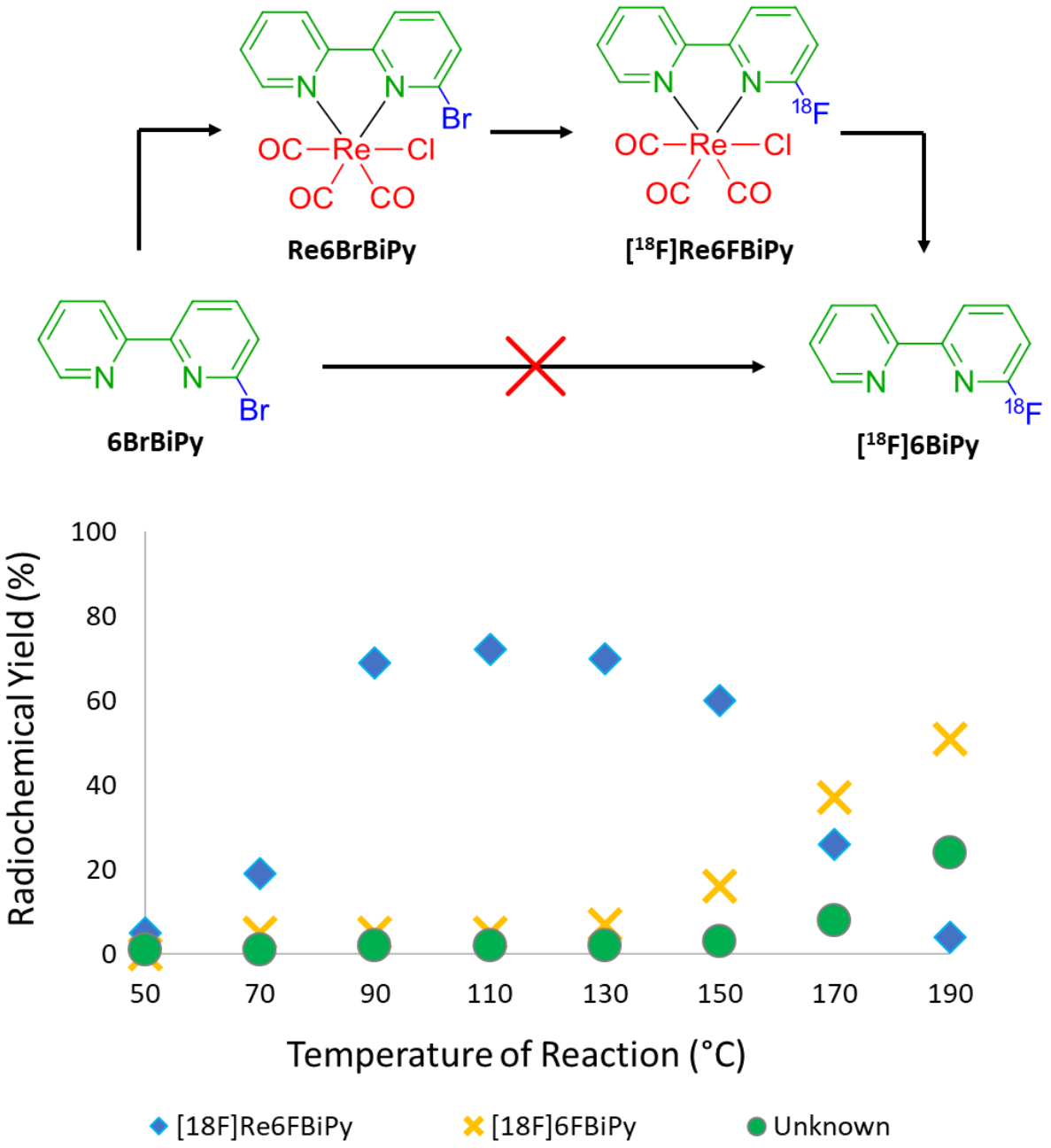

Figure 151. RCYs of **[^{18}F]Re6FBiPy** (blue diamonds), **[^{18}F]6FBiPy** (orange crosses) and the unknown by-product (green circles) as a function of the reaction temperature. The above scheme also shows how the fluorine-18 radiolabelling of **6BrBiPy** was unable to afford the **[^{18}F]6FBiPy** radioproduct, whereas the rhenium complexed **Re6BrBiPy** was able to form the **[^{18}F]Re6FBiPy** radioproduct which could then be thermally dissociated to form the **[^{18}F]6FBiPy** ligand in considerable RCY.

4.2.3 Fluorine-18 Radiolabelling of Rhenium Complexed 4-Chloro-2,2'-Bipyridine

To determine whether rhenium complexation could also mediate [^{18}F]fluoride radiolabelling in the *para* position of 2,2'-bipyridine rings, radiofluorinations were additionally performed on the **Re4ClBiPy** precursor. The non-radioactive standards were again injected on the radio-HPLC to determine their retention times *via* UV-absorption detection. The UV-absorption chromatograms of both the **4FBiPy** and **Re4FBiPy** standards are superimposed in Figure 152 and affirm approximate retention times of 2.1 mins and 7.6 mins, respectively. Figure 153 shows the profile of the radiochromatogram obtained for the fluorine-18 radiolabelling of **Re4ClBiPy** at 130 °C (blue trace) and 190 °C (orange trace). At 130 °C the **[^{18}F]Re6FBiPy** is found to form almost exclusively, as expected based upon the radiolabeling of **Re6ClBiPy** and **Re6BrBiPy**. However, while decomplexation did occur to form the **[^{18}F]4FBiPy** radioligand in considerable RCY, the unknown product was instead found to form in slightly higher abundance from integration of the radiochromatographic peak areas. The unidentified peak forming from **Re4ClBiPy** was found to elute at 6.7 mins, slightly offset from the shared identity of the unknown peak forming from both **Re6ClBiPy** and **Re6BrBiPy**, further supporting the theory that the product could be due to [^{18}F]fluorine substitution at site of the Re−Cl bond.

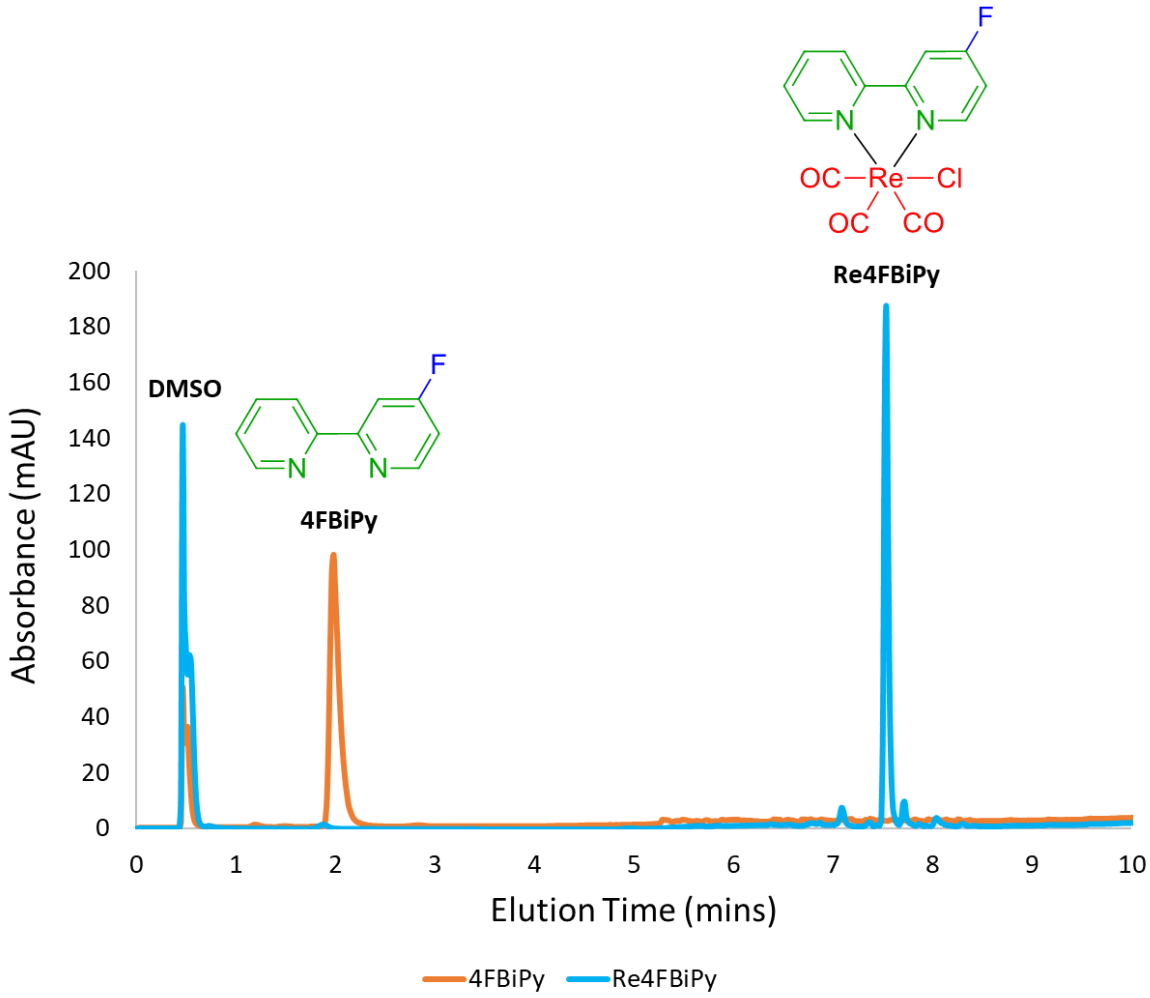

Figure 152. UV-absorbance chromatograms for **4FBiPy** (orange trace) and **Re4FBiPy** (blue trace) providing approximate elution times of 2.1 min and 7.6 min, respectively, which were used to assign the identities of the radioproducts. DMSO is also observed to elute early at 0.5 min with the initially aqueous mobile phase.

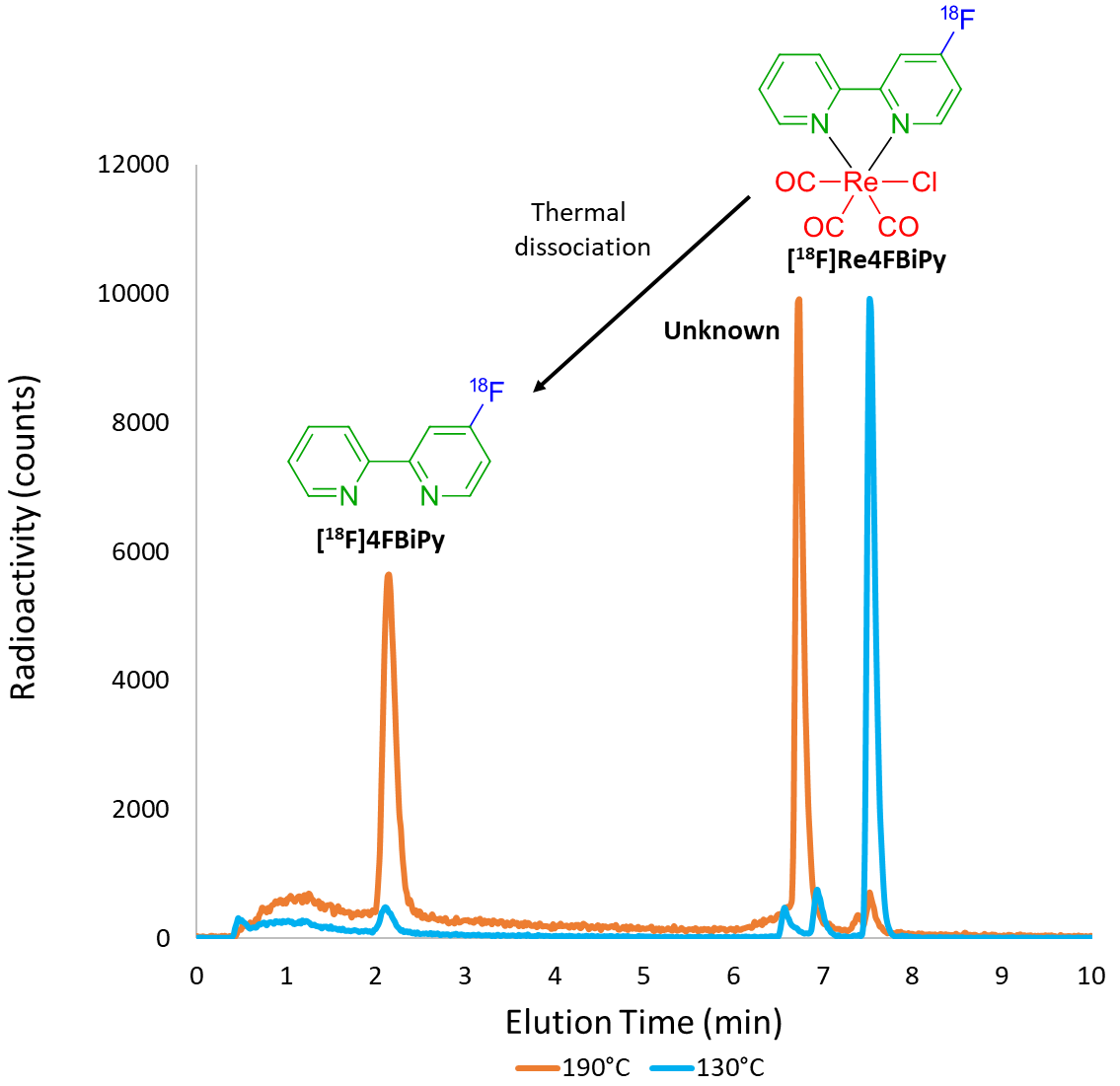

Figure 153. Radiochromatogram profiles for the fluorine-18 radiolabelling of **Re4ClBiPy** at 130 °C (blue trace) and 190 °C (orange trace). At 130 °C **[^{18}F]Re4FBiPy** (7.5 min) reliably forms, whereas at 190 °C the complex dissociates to form the otherwise unobtainable **[^{18}F]4FBiPy** (2.1 min) as well as an unknown by-product (6.7 min).

To likewise confirm that the radioligand was not being radiosynthesised from [^{18}F]fluoride substitution with the **4ClBiPy** ligand thermally decomplexed from the **Re6ClBiPy** precursor, analogous radiolabelling experiments were performed solely on the ligand in the absence of rhenium. In each of these experiments, under analogous conditions, no **[^{18}F]4FBiPy** product was observed, which was unsurprising given no radioproduct had formed from fluorine-18 labelling experiments with the **6ClBiPy** and **6BrBiPy** precursors either. Thus, it was discovered that **[^{18}F]4FBiPy** could also only form from subsequent decomplexation of the **[^{18}F]Re4FBiPy** radioproduct. Figure 154 portrays a representation of this scheme, alongside a plot detailing the RCYs obtained for **[^{18}F]Re4FBiPy**, **[^{18}F]4FBiPy** and the unknown by-product as a function of reaction temperature for the fluorine-18 labelling of the **Re4ClBiPy** precursor. The RCY of **[^{18}F]Re4FBiPy** was found to increase with temperature up until 130 °C, with RCYs of 5%, 11%, 35%, 54% and 68% forming at temperatures of 50 °C, 70 °C, 90 °C, 110 °C and 130 °C respectively. Thereafter, decomplexation resulted in lower RCYs for reaction temperatures greater than 130 °C, decreasing to as low as 2% RCY at 190 °C. With the rise in reaction temperature, **[^{18}F]4FBiPy** was found to first form in 6% RCY at 130 °C, followed by 16% RCY at 150 °C, 24% RCY at 170 °C and finally plateauing in 27% RCY at 190 °C. The reason for **[^{18}F]4FBiPy** not forming until 130 °C, whereas **[^{18}F]6FBiPy** had decomplexed at temperatures as low as 50 °C or 70 °C, is likely due to the slightly lesser RCY yielded for **[^{18}F]Re4FBiPy** compared to **[^{18}F]Re6FBiPy**, which in turn would suggest there was less of the radiolabeled complex available for thermal dissociation to liberate the radiolabeled ligand. The surprising quantity of the radioactive by-product, having formed from the radiofluorination of **Re4ClBiPy**, is also observed in 2% to 6% RCY between 90 °C and 150 °C, before rising to 17% RCY at 170 °C and ultimately surpassing the concentration of **[^{18}F]4FBiPy** with 31% RCY forming at 190 °C. *Wet* reaction temperatures were not tested

given the considerable yield of the by-product that was observed when radiolabellings **Re6ClBiPy** under such conditions.

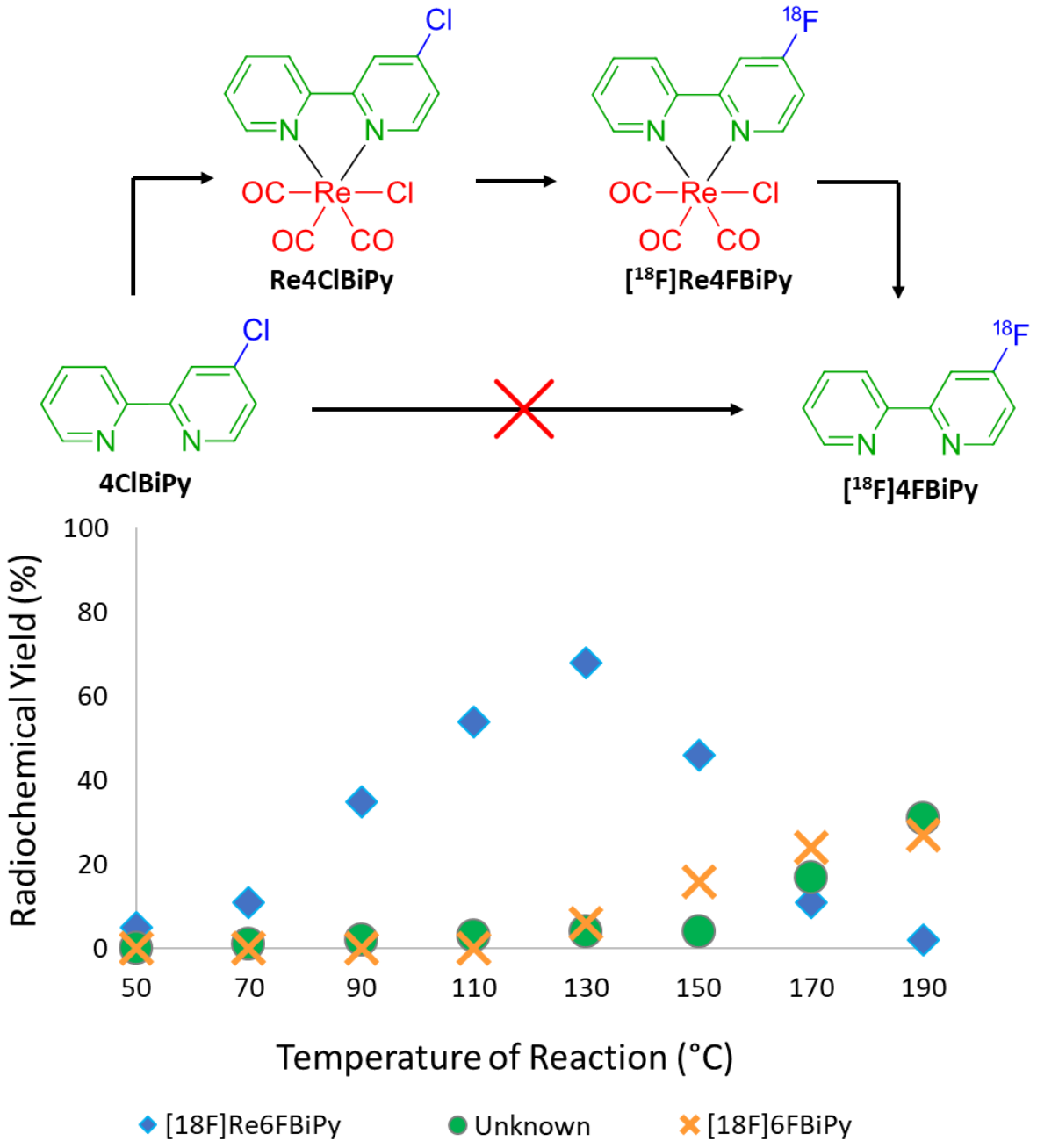

Figure 154. RCYs of **[^{18}F]Re4FBiPy** (blue diamonds), **[^{18}F]4FBiPy** (orange crosses) and the unknown by-product (green circles) as a function of the reaction temperature. The above scheme also shows how the fluorine-18 radiolabelling of **4ClBiPy** was unable to afford the **[^{18}F]4FBiPy** radioproduct, whereas the rhenium complexed **Re4ClBiPy** was able to form the **[^{18}F]Re4FBiPy** radioproduct which could then be thermally dissociated to form the **[^{18}F]4FBiPy** ligand in considerable RCY.

4.2.4 Fluorine-18 Radiolabelling of Rhenium Complexed 5-Chloro-2,2'-Bipyridine

The fluorine-18 radiolabelling of **Re5ClBiPy** was also trialled in order to determine whether nucleophilic aromatic substitution for [^{18}F]fluoride could be achieved in the *meta* position of 2,2'-bipyridine ligands. This test was important towards determining whether rhenium-mediated nucleophilic aromatic substitution for [^{18}F]fluoride could occur in an electronically unfavoured position on the molecule. The reason for the *meta* position of **Re5ClBiPy** being resistant to radiofluorination compared to the *ortho* and *para* positions of the **Re6ClBiPy** and **Re4ClBiPy** complexes could likely be due to the inability of the complex to form a resonance stabilised intermediate following nucleophilic substitution, as shown by the proposed reaction mechanisms in Figure 155. Such radiofluorinations in these *meta* positions of pyridinyl compounds are reportedly difficult to achieve and it was questioned whether metal activation from the rhenium centre could aid in such radiolabellings. However, under analogous conditions to the previous reaction no radioproduct was observed. A peak of comparatively low signal-to-noise ratio was however observed at 190°C when decreasing the flow rate from 20 µL.min^{-1} down to 5 µL.min^{-1} (*i.e.* from a 47 s reaction time to a 188 s reaction time as per equation (14)). This peak eluted at 5.1 min, as shown in Figure 156, using non-standard chromatographic conditions which omitted the 3 min held aqueous phase and thus consisted of only a 12 min run time. The peak occurs alongside a significant amount of unreacted [^{18}F]fluoride, and peak area integration revealed the radioproduct to have only formed in less than 1% RCY. This peak is hypothesised to correspond to the radiolabelled **[^{18}F]Re5FBiPy** complex, however, because the non-radioactive standard was unable to be synthesised there is currently no means of assigning an identity to the radioproduct.

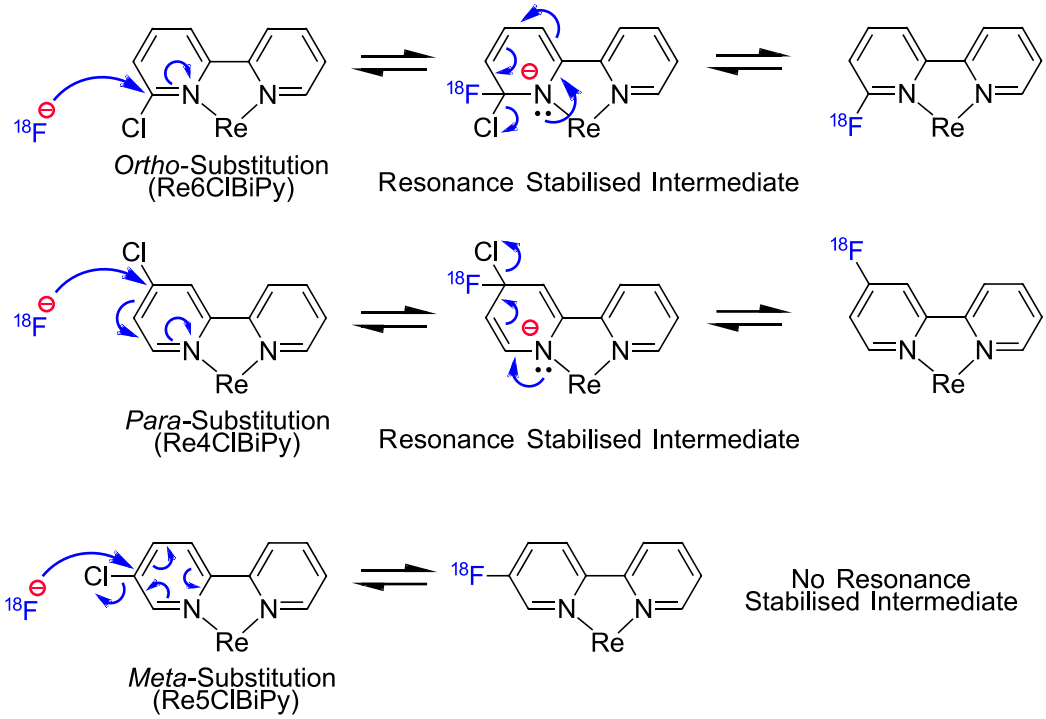

Figure 155. Unlike the *ortho* and *para* substituted **Re6ClBiPy** and **Re4ClBiPy** complexes, the *meta* substituted **Re5ClBiPy** formed no resonance stabilised intermediate during nucleophilic aromatic substitution for [^{18}F]fluoride.

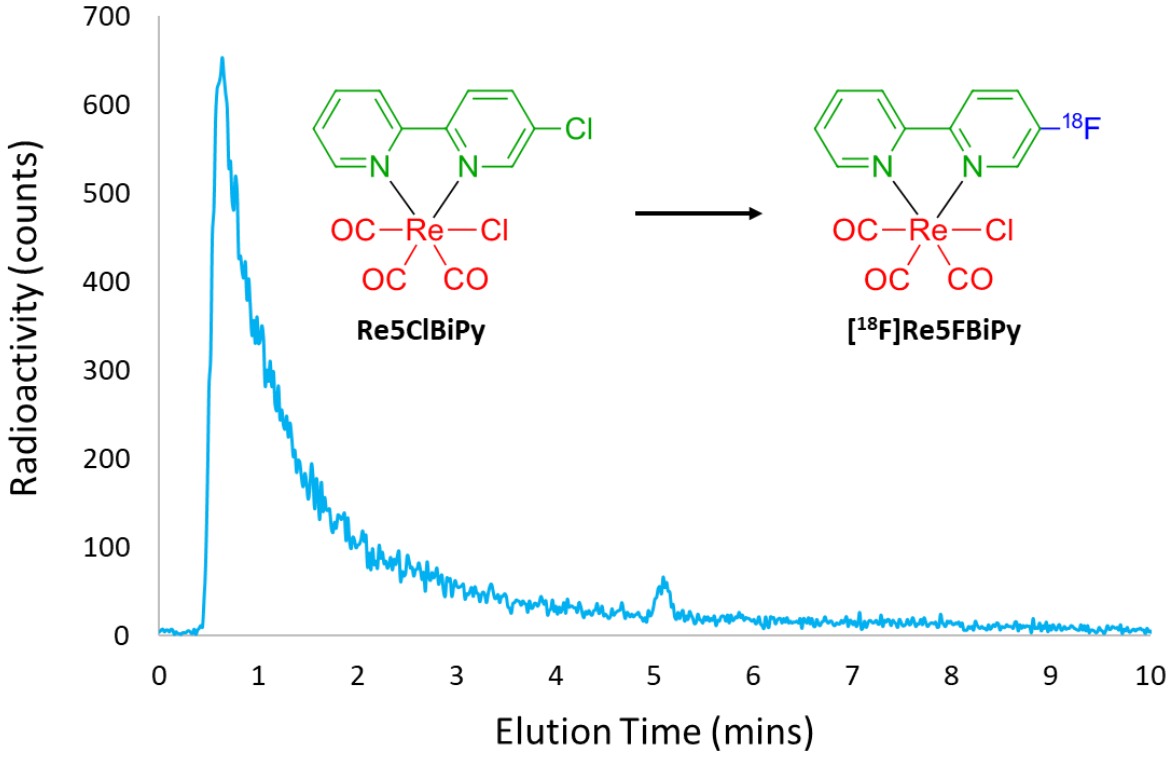

Figure 156. Radiochromatogram for the radiolabelling of **Re5ClBiPy** with [^{18}F]fluoride (0.65 min). A small peak is observed at 5.1 min which may pertain to the **[^{18}F]Re5FBiPy** radioproduct, however a non-radioactive standard was unable to be synthesised to confirm the identity.

With a mechanistic understanding of the differing reaction pathways, two microreactors used in series could potentially improve the RCYs of the desired fluorine-18 labelled ligands using such a rhenium complexation-dissociation approach. Figure 157 illustrates the reaction pathways which are known to lead to the radiolabelled complex and ligands, therein simply labelled as **[^{18}F]ReFBiPy** and **[^{18}F]FBiPy** to express that the scheme could represent fluorine-18 labelling in any position of the bipyridine ligand. Because **[^{18}F]FBiPy** has been shown not to form from the radiofluorination of the ligand precursor *via* nucleophilic aromatic substation, any rate of **ReXBiPy** precursor dissociation (k_{pd}) would inhibit the ligand from being radiofluorinated due to the absence of the rhenium activation effect. Thus, the rate constant for radiofluorination (k_{rf}) of the rhenium precursor would need to compete with this process, such that subsequent **[^{18}F]ReFBiPy** radioproduct dissociation (k_{rd}) could afford the maximum amount of the radiolabelled **[^{18}F]FBiPy** ligand. As the ideal reaction conditions influencing the processes defined by the k_{pd} and k_{rd} rate constants are likely to be similar, future work could be used to determine the optimal temperature conditions which would allow for the optimisation of the radiofluorination process governed by the k_{rf} rate constant. The first microreactor in the series would then ideally afford a lower temperature to optimise the rate of radiofluorination (k_{rf}) while reducing the rate of precursor dissociation (k_{pd}), thus producing the maximum amount of **[^{18}F]ReFBiPy**. The second microreactor, thereafter, would ideally afford a higher temperature which would optimise radioproduct dissociation (k_{rd}) to produce more of the **[^{18}F]FBiPy** ligand. Multiple analyses would need to be undertaken, however, to ensure that the radioproduct is not lost due to the formation of the uncharacterised by-product whose identity, and thus reaction pathways, are currently unknown. The minor non-radioactive impurities indicated by the chromatographic peaks at *circa* 7 mins in both Figure 146 and Figure 152 for the **[^{18}F]Re6FBiPy** and **[^{18}F]Re4FBiPy** standards, if removed or isolated, could potentially aid identification of these uncharacterised by-products in future experiments.

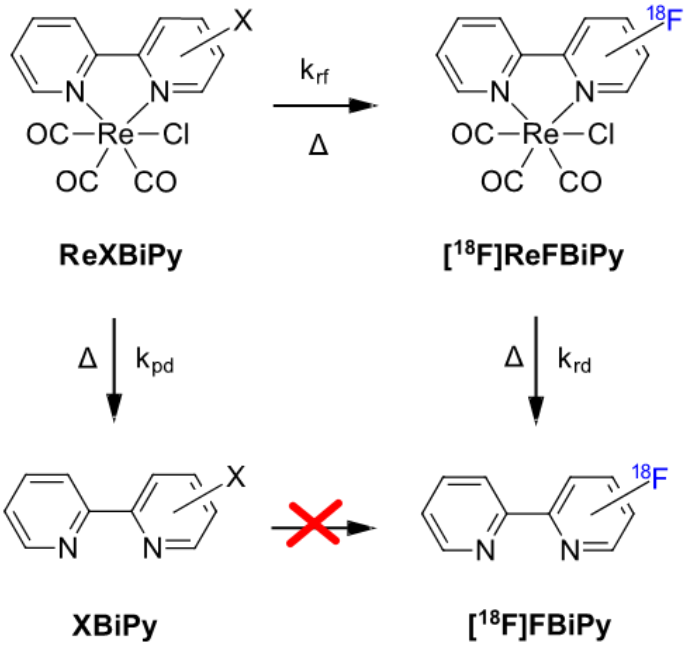

Figure 157. Differing optimal temperature conditions (among other factors) may influence the dissociation of the rhenium precursor (k_{pd}) and the radiofluorination of the rhenium complex (k_{rf}) prior to its dissociation to form the radiolabelled ligand (k_{rd}) which could not be attained from the radiofluorination of any of the ligand precursors.

4.3 Determination of Rhenium-Bipyridine Quantum Yields

Quantum yields were determined for **Re6ClBiPy**, **Re5ClBiPy**, **Re4ClBiPy** and **Re6FBiPy** complexes in DMSO solution. Figure 158 to Figure 161 illustrate the emission spectra for each complex following fixed monochromatic excitation at 410 nm, the integration of which were substituted into equation (14) alongside the 1.479 refractive index of the DMSO solvent the compounds were dissolved in and the absorbance of the compounds at 410 nm, each listed in Table 9. The refractive index, absorbance at 410 nm and integration of the emission spectrum attained from a 410 nm excitation wavelength for the $[Ru(BiPy)_3]Cl$ reference standard were likewise substituted into equation (14) to attain the quantum yield for each complex in DMSO solution. The quantum yield of **Re6ClBiPy** proved to be 0.5% given an absorbance of 0.337 at 410 nm and an emission integration of 5.14×10^6 counts·nm. Comparatively the quantum yield of **Re5ClBiPy** proved to be twice as large at 1.0% given an absorbance of 0.321 at 410 nm and an emission integration of 9.57×10^6 counts·nm. The quantum yields of both **Re4ClBiPy** and **Re6FBiPy** were determined to be 0.6% given absorbances of 0.369 and 0.2380 at 410 nm and emission integrations of 6.19×10^6 counts·nm and 4.95×10^6 counts·nm, respectively. Experimental uncertainties are estimated to be ±0.1% for each of these determined quantum yields. While each of these quantum yields are greater than the 0.3% quantum yield determined for both **Re2ClPhen** and **Re2FPhen** phenanthroline coordinated complexes, they were still an order of magnitude below the quantum yields reported for BODIPY based PET-Optical tracers. Thus, reinforcing the need for coordination of an N-heterocyclic ligand to the ancillary ligand, to improve quantum yields as reported in the literature, though which feel outside of the scope for the work reported herein.[86-88]

Table 9. Quantum yields calculated for the **Re6ClBiPy**, **Re5ClBiPy**, **Re4ClBiPy** and **Re6FBiPy** complexes *via* comparison to a $[Ru(BiPy)_3]Cl_2$ reference standard with correction factors applied for the refractive index of the media, absorbances at the 410 nm excitation wavelength and the integrations of the emission spectra.

Analyte	Solvent	Refractive Index	Absorbance	Emission Integration (counts·nm)	Quantum Yield (%)
$[Ru(BiPy)_3]Cl$	Water	1.333	0.045	4.50×10^6	2.8%
Re6ClBiPy	DMSO	1.479	0.337	5.14×10^6	0.5%
Re5ClBiPy	DMSO	1.479	0.321	9.57×10^6	1.0%
Re4ClBiPy	DMSO	1.479	0.369	6.19×10^6	0.6%
Re6FBiPy	DMSO	1.479	0.280	4.95×10^6	0.6%

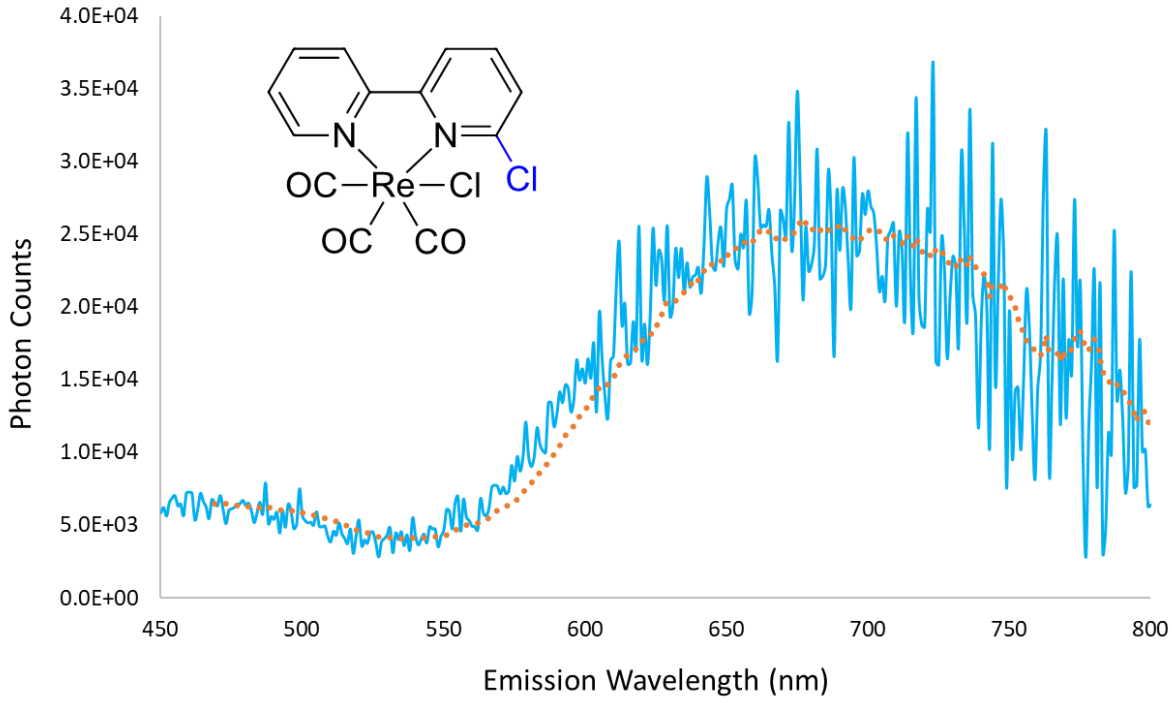

Figure 158. Emission spectrum of **Re6ClBiPy** in DMSO solution obtained using a 410 nm excitation wavelength. Dashed orange line is a moving average over 20 periods to help visualise the spectrum. The 5.14×10^6 counts·nm integration of this spectrum was used to calculate the quantum yield.

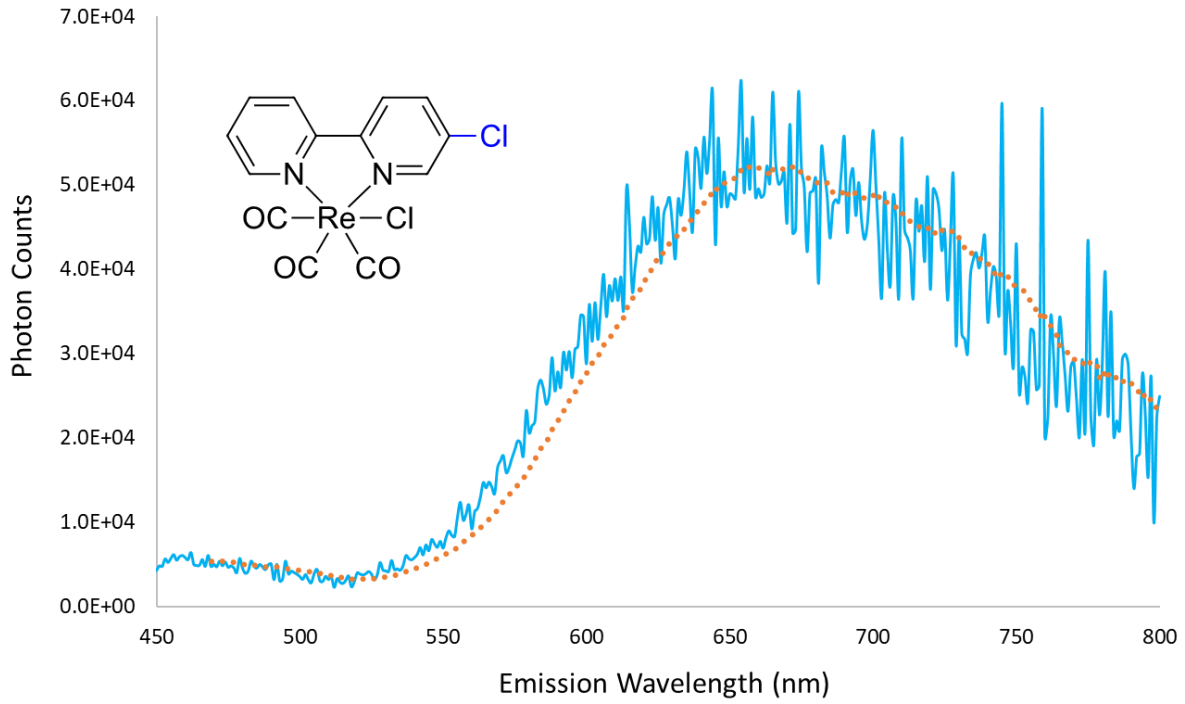

Figure 159. Emission spectrum of **Re5ClBiPy** in DMSO solution obtained using a 410 nm excitation wavelength. Dashed orange line is a moving average over 20 periods to help visualise the spectrum. The 9.57×10^6 counts·nm integration of this spectrum was used to calculate the quantum yield.

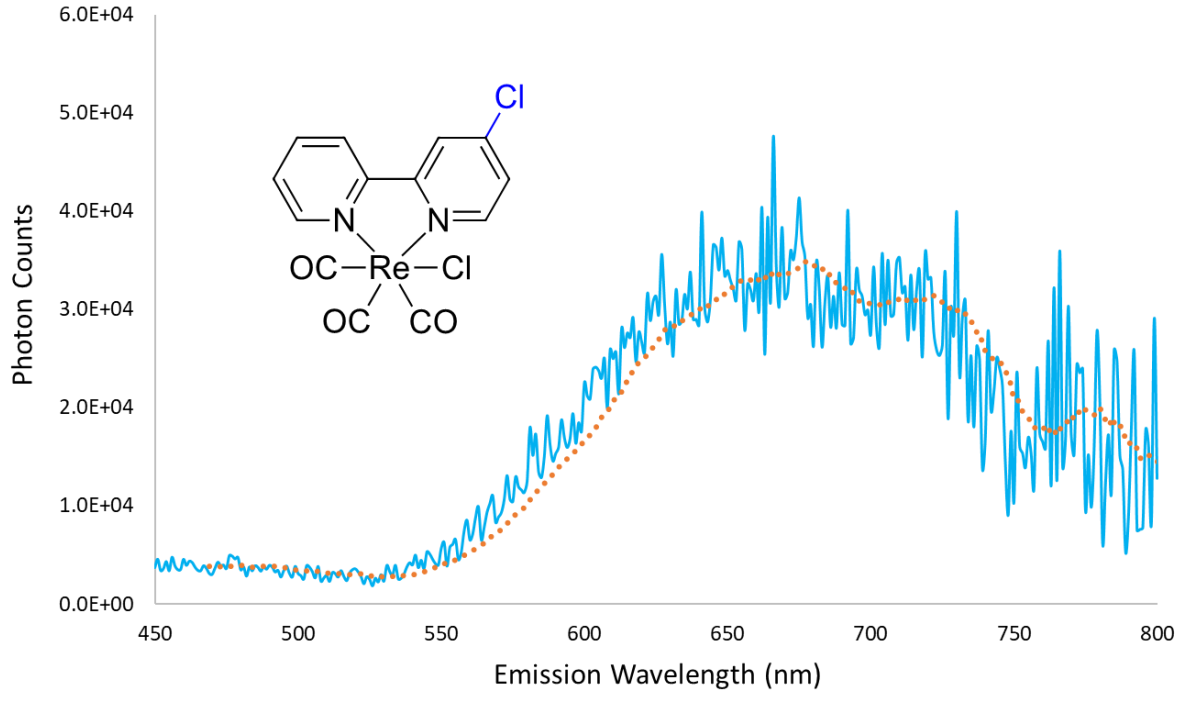

Figure 160. Emission spectrum of **Re4ClBiPy** in DMSO solution obtained using a 410 nm excitation wavelength. Dashed orange line is a moving average over 20 periods to help visualise the spectrum. The 6.19×10^6 counts·nm integration of this spectrum was used to calculate the quantum yield.

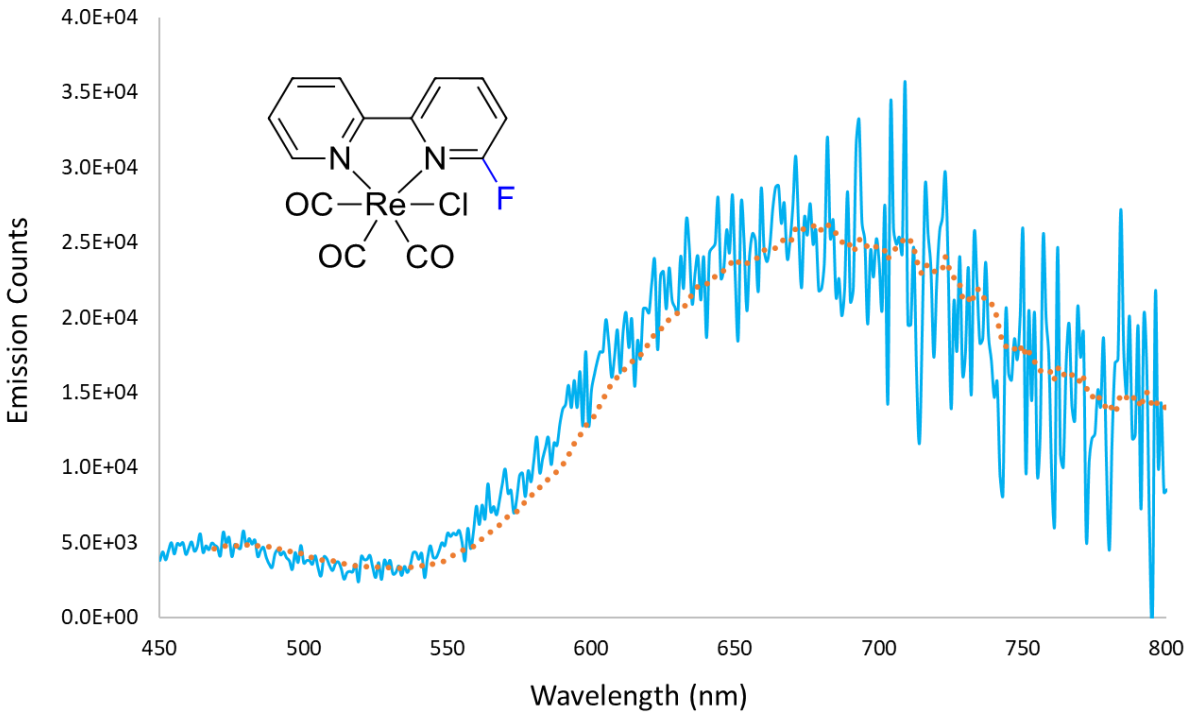

Figure 161. Emission spectrum of **Re6FBiPy** in DMSO solution obtained using a 380 nm excitation wavelength. Dashed orange line is a moving average over 20 periods to help visualise the spectrum. The 4.95×10^{6} counts·nm integration of this spectrum was used to calculate the quantum yield.

CHAPTER FIVE

RHENIUM-HYDROXYQUINOLINE PRECURSORS FOR ALZHEIMER'S DISEASE IMAGING

5.1 Role of Fluorine-18 Labelled 8-Hydroxyquinolines in the PET imaging of Alzheimer's Disease

Alzheimer's disease is a neurodegenerative disease which can be characterised by two pathological markers in the cerebral cortex. One of these markers is neurofibrillary tangles, which are characterised by the disaggregation of tau proteins within the neuron.[93, 94] The second diagnostic marker is amyloid beta (Aβ) plaques which form from the aggregation of Aβ proteins between the neurons, thus disrupting synaptic connections as shown in Figure 162a.[95, 96] Many diagnostics designed for the treatment of Alzheimer's disease are based on the metal hypothesis, which postulates that elevated concentrations of iron, zinc and copper ions in the brain provide a nucleation site for the Aβ proteins, thus accelerating the rate of Aβ plaque aggregation.[97-99] One PET diagnostic agent designed for the imaging of Alzheimer's disease was [^{18}F]CABS13 which, as a fluorine-18 labelled hydroxyquinoline, has been shown to chelate to metal ionophores to not only image Aβ plaques *in vivo*, though to also promote the disaggregation of these plaques by displacing the entangled proteins *in vitro* as a potential Alzheimer's disease treatment.[100-102] Administration of [^{18}F]CABS13 to transgenic mouse models of Alzheimer's disease performed by Liang, *et al.* exhibited far greater brain uptake and retention of the radiotracer when compared to a wild type (WT) mouse model, with example PET-CT scans shown in Figure 162b.[103] The radiotracer did fail, however, when translated to a non-human primate due to rapid metabolism and low brain uptake.[104] Other fluorinated hydroxyquinolines have shown greater promise as Aβ plaque diagnostic agents, based on ionophore and disaggregation assays.[100] These alternative agents were unable to be fluorine-18 labelled *via* traditional means, however. Thus, it was hypothesised that the rhenium complexation-dissociation strategy, formerly discovered to radiolabel challenging bipyridine structures, could be used to improve the radiosynthesis of [^{18}F]CABS13 and enable the fluorine-18 labelling of alternative hydroxyquinoline systems.

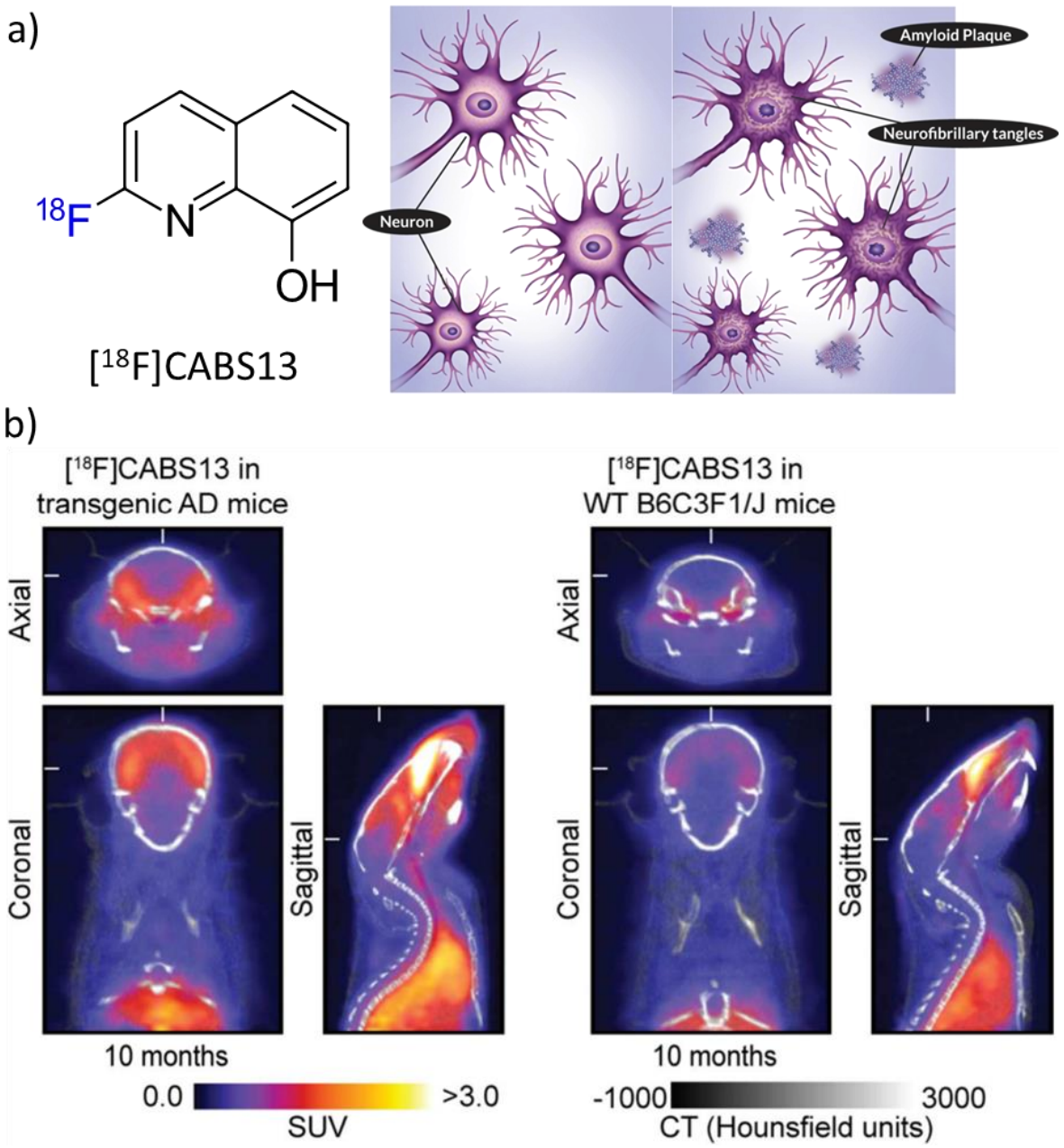

Figure 162. a) Molecular structure of the [^{18}F]CABS13 PET Alzheimer's disease imaging agent (left), alongside a representation of Aβ plaques between neurons and tau neurofibrillary tangles within neurons which are known pathological markers for the characterisation of Alzheimer's disease (right), and b) PET-CT scans acquired 5-10 mins post-injection following tail vein administration of [^{18}F]CABS13 to a transgenic mouse model of Alzheimer's disease (left) and to a WT mouse model (right). Standardised uptake values (SUV) revealed greater brain uptake and retention of the radiotracer in the diseased model than compared to the WT model. Scans performed by Liang, *et al.*[103]

To test this hypothesis a non-radioactive analogue of [^{18}F]CABS13 (referred to herein as **2F8HQ**) first required synthesis and chelation to rhenium to form the acetonitriletricarbonyl(2-fluoro-8-hydroxyquinolinato)rhenium(I) (**Re2F8HQ**) standard. While the chlorinated precursor 2-chloro-8-hydroxyquinoline (**2Cl8HQ**) was readily available, subsequent rhenium complexation was also required to attain the acetonitriletricarbonyl(2-chloro-8-hydroxyquinolinato)rhenium(I) (**Re2Cl8HQ**) precursor for fluorine-18 labelling. Benzyl protection of **2Cl8HQ**, thus forming 2-chloro-8-benzoxyquinoline (**2Cl8HQ-OBn**), enabled fluorination *via* nucleophilic aromatic substitution without side reactions occurring with the hydroxyl group on the molecule. The 2-fluoro-8-benzoxyquinoline (**2F8HQ-OBn**) product was then subsequently deprotected using hydrogen gas in the presence of palladium on carbon catalysts, which afforded the desired **2F8HQ** product. Complexation of **2F8HQ** with pentacarbonylchlororhenium(I) in acetonitrile then afforded the required **Re2F8HQ** standard. This synthetic route is shown in Figure 163. Precursors to [^{18}F]5-fluoro-8-hydroxyquinoline (**[^{18}F]5F8HQ**), an alternative analogue of [^{18}F]CABS13, were also synthesised by complexing 5-chloro-8-hydroxyquinoline (**5Cl8HQ**) and 5-nitro-8-hydroxyquinoline (**5NO$_2$8HQ**) ligands with pentacarbonylchlororhenium(I) thus forming acetonitriletricarbonylchloro(5-chloro-8-hydroxyquinolinato)rhenium(I) (**Re5Cl8HQ**) as well as acetonitriletricarbonylchloro(5-nitro-8-hydroxyquinolinato)rhenium(I) (**Re5NO$_2$8HQ**), respectively. While the **5F8HQ** non-radioactive standard was commercially available, rhenium complexation of the compound was required to obtain the acetonitriletricarbonylchloro(5-fluoro-8-hydroxyquinolinato)rhenium(I) (**Re5F8HQ**) standard.

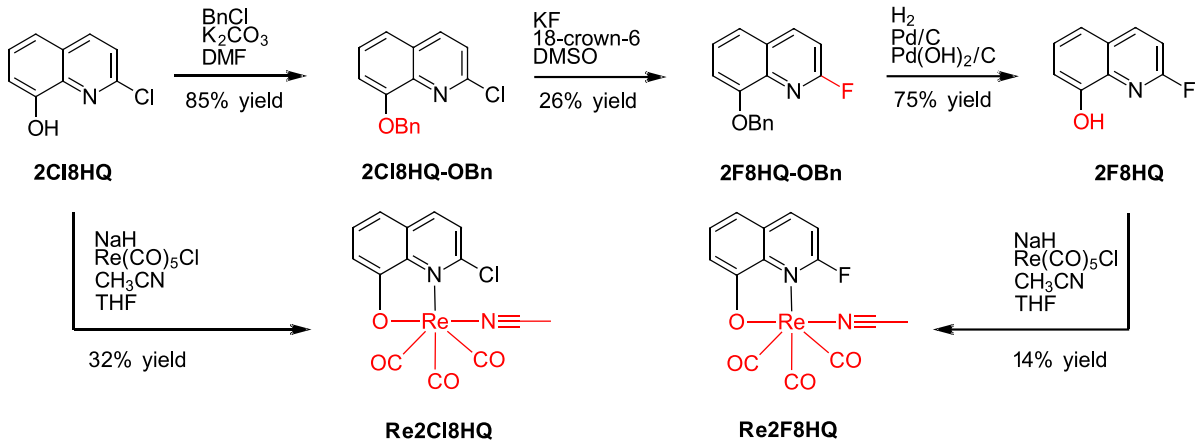

Figure 163. Synthetic route used to obtain the **Re2Cl8HQ** precursor as well as the **2F8HQ** (CABS13) and **Re2F8HQ** non-radioactive standards for the radiosynthesis of the [^{18}F]CABS13 Alzheimer's disease imaging agent.

5.1.1 Benzyl Protection of 2-Chloro-8-Hydroxyquinoline

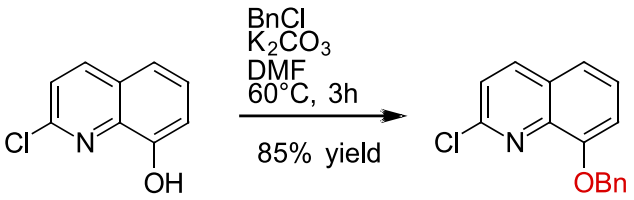

Figure 164. Protection of the **2Cl8HQ** alcohol in the 8-position using benzyl chloride to afford **2Cl8HQ-OBn** in 85% yield.

A mass of **2Cl8HQ** (2.40 g, 13.362 mmol, 1.0 eq.) was dissolved in a volume of anhydrous DMF (2.5 mL) to which a mass of potassium carbonate (3.69 g, 26.693 mmol, 2.0 eq.) was added. A volume of benzyl chloride (3.1 mL, 27.360 mmol, 2.0 eq.) was then added dropwise to the solution. The reaction mixture was stirred at 60 °C for 3 hours, where after HPLC reaction monitoring confirmed near complete conversion to the product. The product was extracted into DCM (20 × 10 mL) and the combined organic fractions were back extracted with brine (2 × 20 mL). The organic layer was then dried over sodium sulphate, filtered *via* vacuum filtration and evaporated under reduced pressure to afford a light pink solid. The solid was then recrystallised from hot ethanolic solution and filtered *via* vacuum filtration to afford a purified pink product (3.02 g).

Confirmation of the product was simply assessed by NMR analysis, with the ^{1}H-NMR spectrum of **2Cl8HQ-OBn** shown in Figure 165 exhibiting the expected integration for twelve protons. Ten of which existed in the aromatic region, pertaining to the hydrogen atoms bonded within the quinoline and benzene rings, and the other two being relatively upfield shifted as expected for the methylene group protons. The ^{13}C-NMR spectrum, shown in in Figure 166, further evidenced the assigned structure with fourteen carbon-13 nuclear resonance signals found present, as expected given the similar magnetic environment for two pairs of the sixteen carbon atoms.

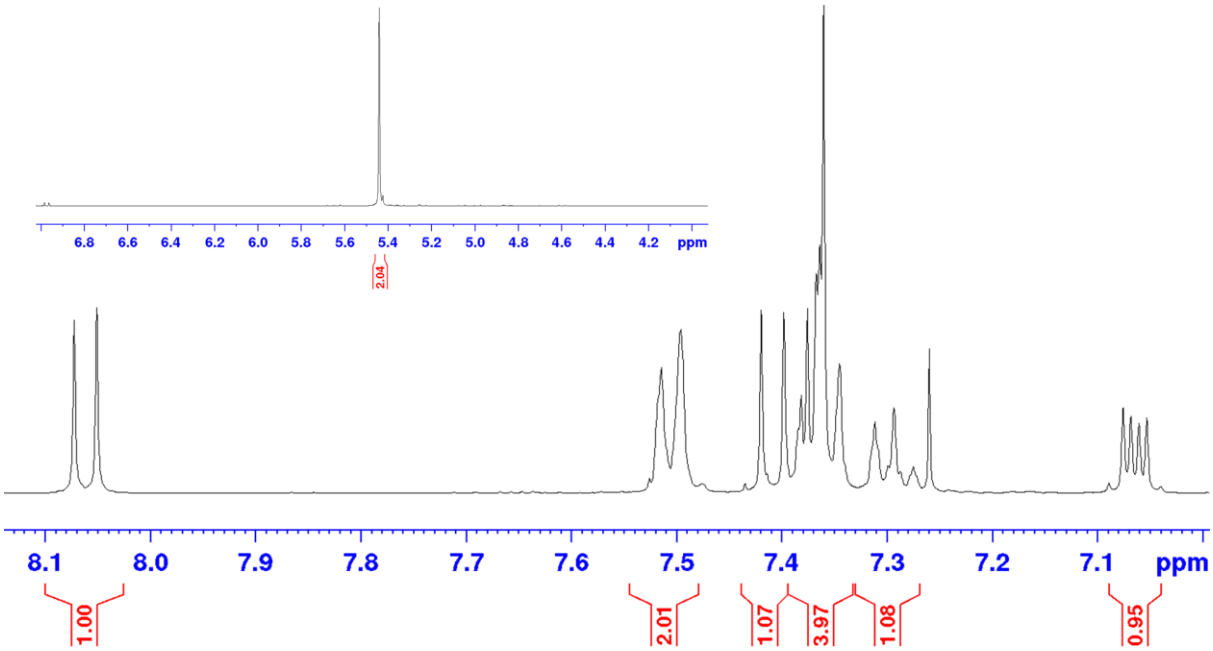

Figure 165. ^{1}H-NMR spectrum depicting the integrations of the resonance signals for the twelve expected protons in **2Cl8HQ-OBn**. Ten of these protons exhibit resonance in the aromatic region, whereas the two protons of the methyl group are upfield shifted by comparison (top left corner).

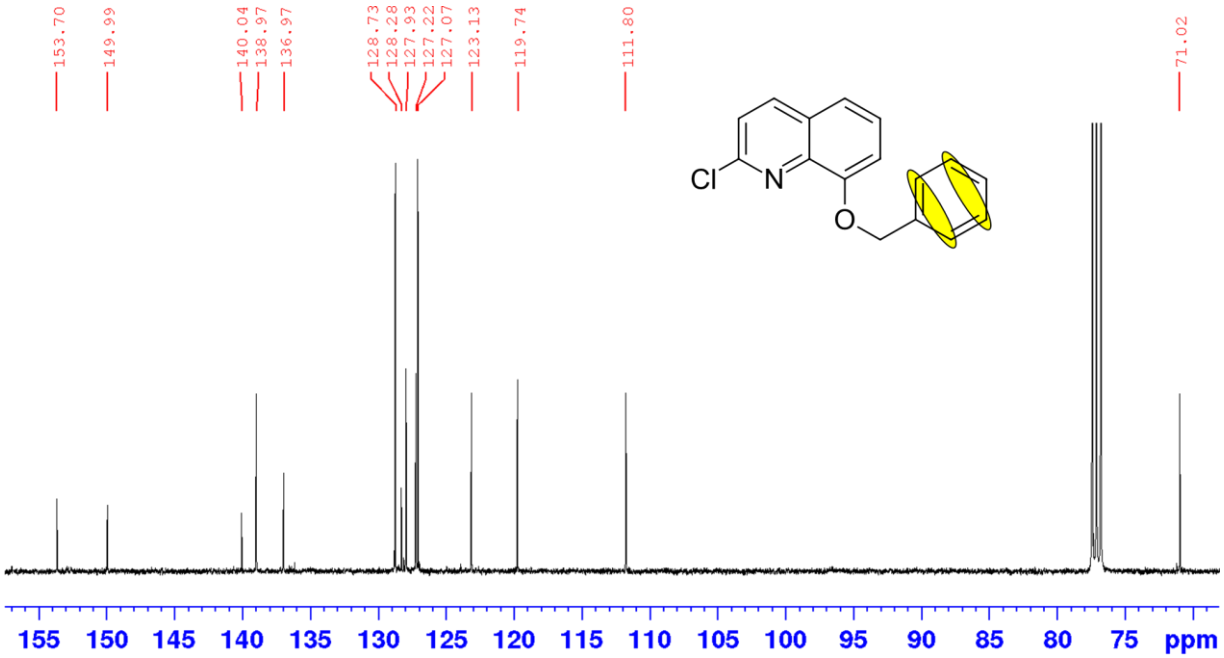

Figure 166. ^{13}C-NMR spectrum of **2Cl8HQ-OBn** in chloroform-d, depicting the fourteen expected fourteen signals for the sixteen carbon-13 nuclei as two pairs of carbon atoms share the same magnetic environment as shown by the yellow highlighted regions of the molecule. The carbon-13 nucleus of the methyl group is notably upfield shifted by comparison.

5.1.2 Fluorination of 2-Chloro-8-Benzoxyquinoline

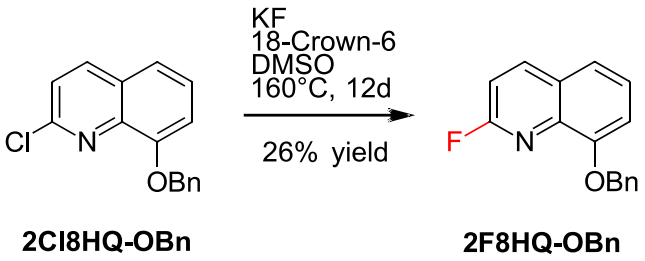

2Cl8HQ-OBn **2F8HQ-OBn**

Figure 167. Fluorination of **2Cl8HQ-OBn** using potassium fluoride and an 18-crown-6 ether phase transfer catalyst to afford **2F8HQ-OBn** in 26% yield.

A mass of **2Cl8HQ-OBn** (1.48 g, 5.487 mmol, 1.0 eq.) was purged under nitrogen and vacuum before being dissolved in a volume of freshly distilled, anhydrous DMSO (10 mL). Masses of potassium fluoride (3.84 g, 66.093 mmol, 12.0 eq.) and 18-crown-6 ether (5.84 g, 22.094 mmol, 4.0 eq.) were azeotropically dried at 90 °C *via* the dropwise addition of anhydrous acetonitrile under an inert nitrogen environment. The ligand in DMSO solution was then transferred to the potassium-crown ether complex and the solution was slowly heated to 160 °C and stirred in an inert nitrogen environment for 12 days. As reaction monitoring suggesting no greater product formation was eventuating, the solution was then cooled to room temperature. The solution was then filtered through a PTFE membrane (0.2 µm) before loading onto a C_{18} reverse phase column (220 g, 40 µm) and eluted over a gradient mobile phase consisting of 1 to 100% acetonitrile in water, each containing 0.1% TFA modifier. Fractions found to contain the desired **2F8HQ-OBn** product were combined and evaporated under reduced pressure to remove the acetonitrile before freeze-drying overnight to pink salt. The presumed TFA salt was then dissolved in a minimum volume of water and extracted into DCM (10 × 5 mL). The combined organic extracts were then dried over sodium sulphate, filtered *via* vacuum filtration and evaporated under reduced pressure to afford the pure product (357.4 mg).

^{1}H-NMR spectrometry revealed differing splitting patterns, owing to coupling with the fluorine-19 nucleus, though still retained the expected integration for twelve protons with ten of those signals existing within the aromatic region of the spectrum, shown in Figure 168, as expected. The ^{13}C-NMR spectrum, shown in Figure 169, exhibited twenty-one signals due to five instances of carbon-13 nuclei coupling to the sole fluorine-19 nucleus whose resonance signal is shown at -31.07 ppm in the ^{19}F-NMR spectrum of **2F8HQ-OBn**, as shown in Figure 170.

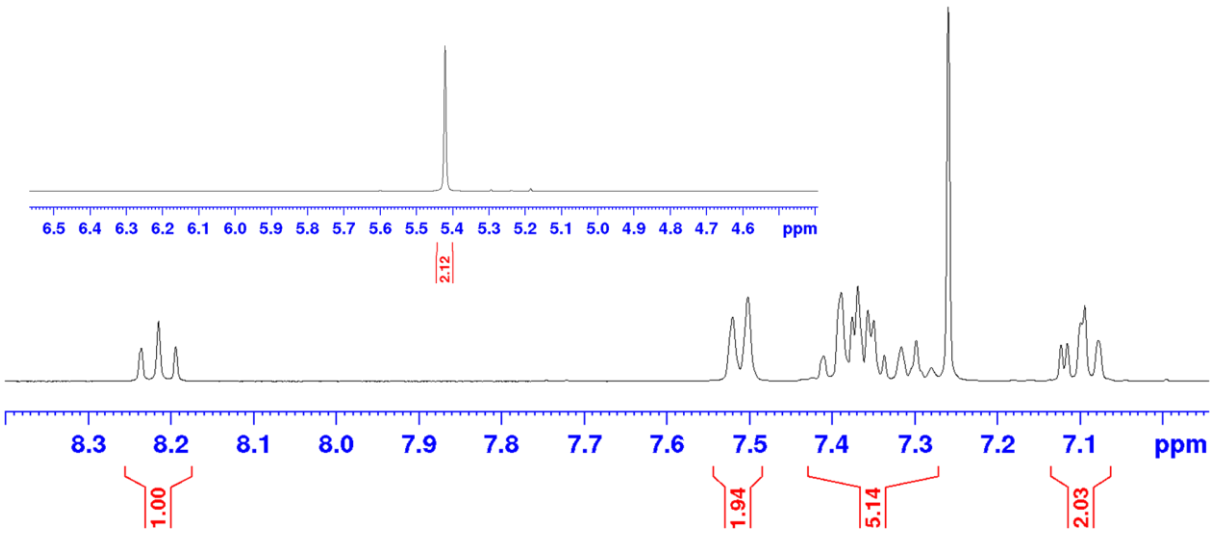

Figure 168. ^{1}H-NMR spectrum depicting the integrations of the resonance signals for the twelve expected protons in **2F8HQ-OBn**. Ten of these protons exhibit resonance in the aromatic region, whereas the two protons of the methyl group are upfield shifted by comparison (top left corner).

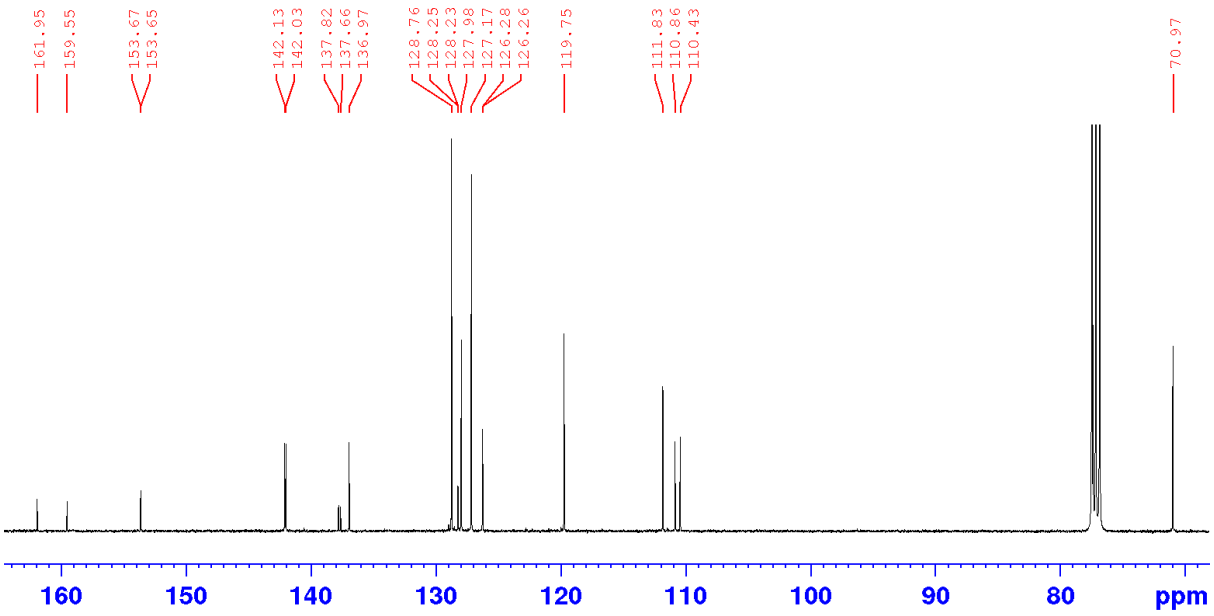

Figure 169. ^{13}C-NMR spectrum of **2F8HQ-OBn** in chloroform-d exhibiting twenty-one resonance signals due to five of the carbon-13 nuclei coupling to the fluorine-19 nucleus.

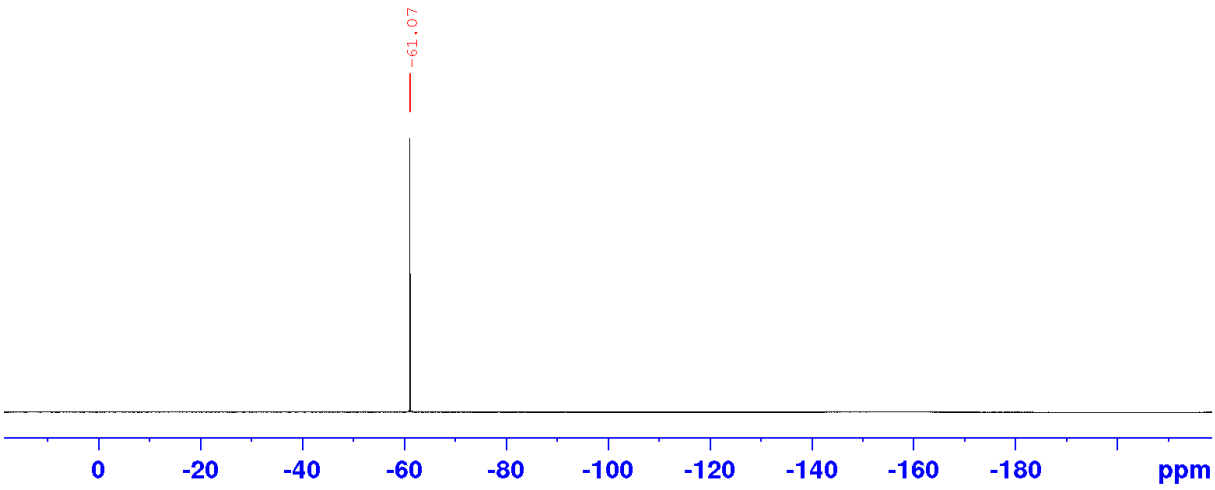

Figure 170. CPD ^{19}F-NMR spectrum of **2F8HQ-OBn** in chloroform-d showing the fluorine-19 magnetic resonance signal at -61.07 ppm pertaining to the lone fluorine-19 nucleus in the molecule.

5.1.3 Deprotection of 2-Fluoro-8-Benzozyquinoline

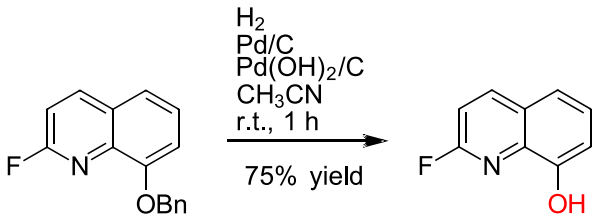

2F8HQ-OBn **2F8HQ**

Figure 171. Deprotection of **2F8HQ-OBn** using hydrogen gas in the presence of palladium on activated carbon catalysts to afford **2F8HQ** in 75% yield.

A mass of **2F8HQ** (217.6 mg, 0.859 mmol, 1.0 eq.) was dissolved in a volume of acetonitrile (6 mL). Masses of 10% wt. palladium on activated carbon (123.4 mg) and 20% wt. palladium hydroxide on activated carbon (124.7 mg) were added to the reaction mixture under an inert nitrogen gas environment. The nitrogen gas was then displaced with hydrogen gas and the mixture left to stir for 1 hour. The solution was then filtered over diatomaceous earth *via* vacuum filtration to afford a pale-yellow solution which was evaporated under reduced pressure to afford a golden crystalline solid (105.7 mg).

The ^{1}H-NMR spectrum of the product (Figure 172) shows the expected integration for six protons in the aromatic region alongside a broad and significantly downfield shifted signal suggestive of the O−H bond. The ^{13}C-NMR spectrum in Figure 173 exhibits fourteen carbon-13 nuclear resonance signals due to coupling of five carbon-13 nuclei with the fluorine-19 nucleus. This fluorine-19 nucleus is evident from the single resonance signal in the CPD ^{19}F-NMR spectrum of **2F8HQ** in Figure 174.

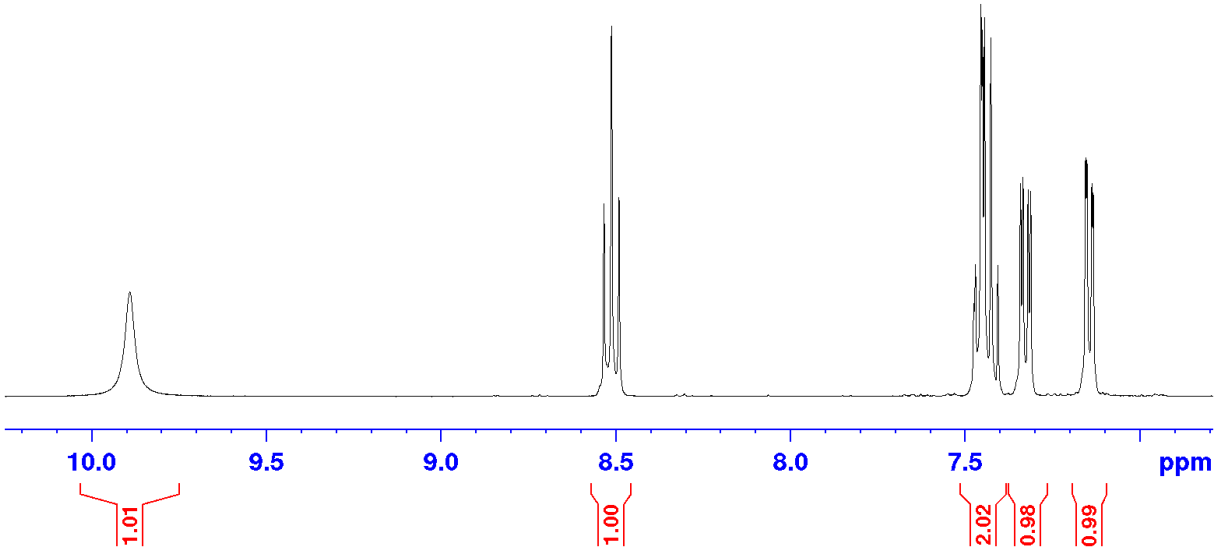

Figure 172. ^{1}H-NMR spectrum of **2F8HQ** in DMSO-d_6 showing the expected integration for six protons in the aromatic region including a broad signal pertaining to the O−H bonded hydrogen atom.

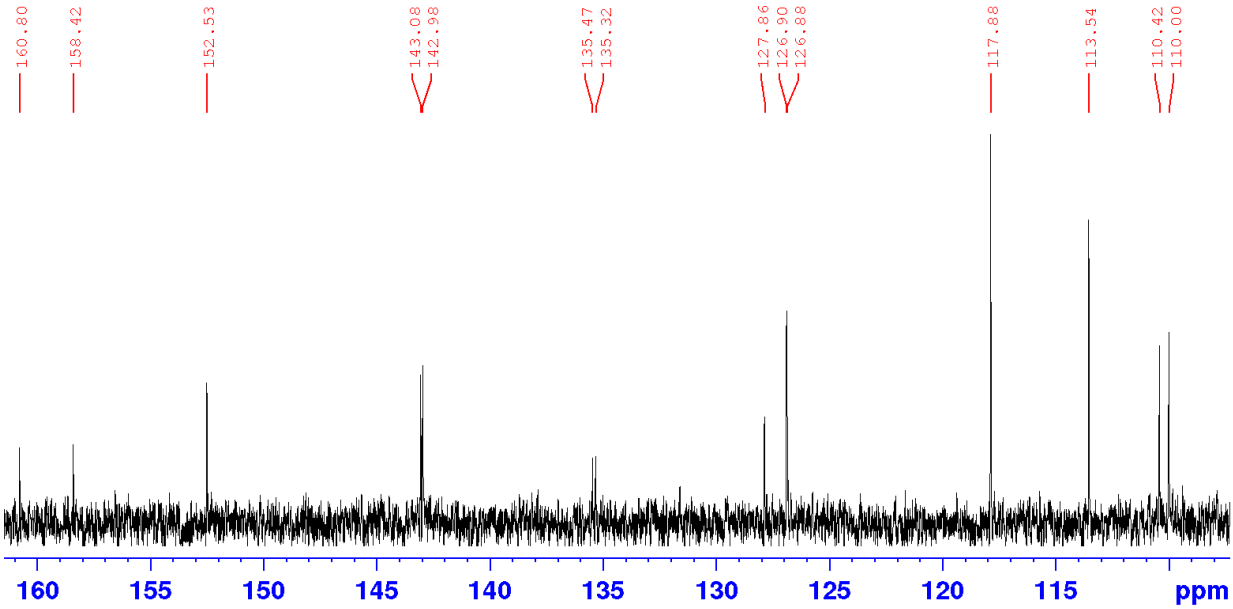

Figure 173. ^{13}C-NMR spectrum of **2F8HQ** in DMSO-d_6 showing fourteen carbon-13 nuclear resonance signals due to the carbon-13 nuclei in the pyridinyl ring coupling with the fluorine-19 nucleus.

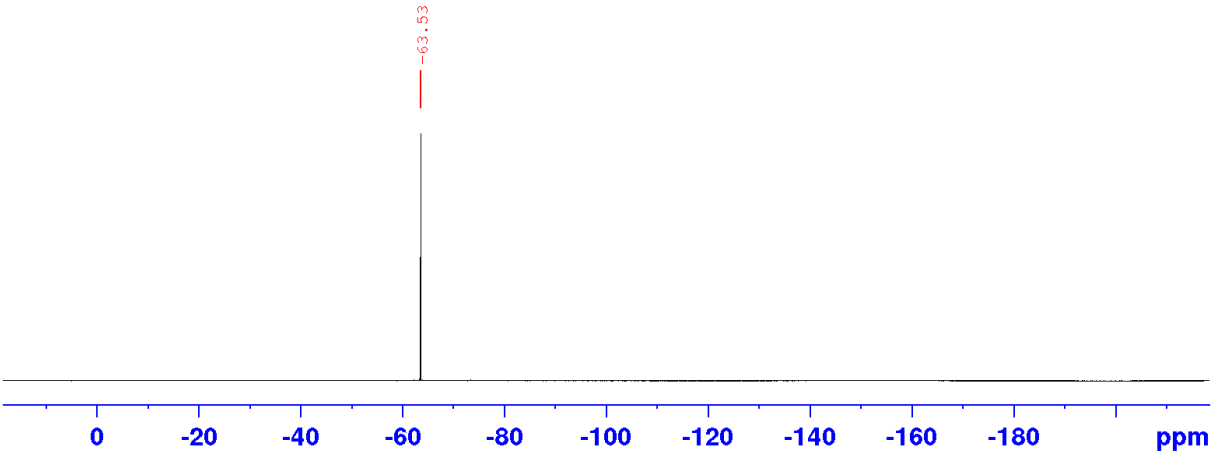

Figure 174. CPD ^{19}F-NMR spectrum of **2F8HQ** showing the resonance single for the sole fluorine-19 nucleus in the molecule at -63.53 ppm.

5.1.4 Rhenium Complexation of 2-Chloro-8-Hydroxyquinoline

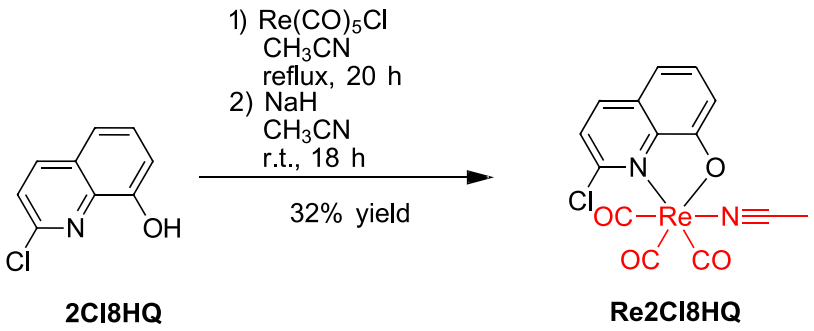

2Cl8HQ **Re2Cl8HQ**

Figure 175. Rhenium complexation with **2Cl8HQ** *via* the formation of a diacetonitrilo intermediate to form the **Re2Cl8HQ** precursor.

A mass of pentacarbonylchlororhenium(I) (116.1 mg, 0.321 mmol, 1.0 eq.) was purged under nitrogen gas followed by vacuum (3 cycles) before being suspended in a volume of anhydrous acetonitrile (10 mL). The solution was refluxed for 20 hours in an inert nitrogen gas environment to form the diacetonitrilotricarbonylchlororhenium(I) intermediate which was monitored by both HPLC and FTIR spectroscopy. To a separate flask a mass of sodium hydride (60% wt/wt in mineral oil, 48.0 mg, 2.000 mmol, 6.2 eq.) was washed three times in hexane and then dried under vacuum. A mass of **2Cl8HQ** (63.4 mg, 0.3530 mmol, 1.1 eq.) dissolved in a volume of anhydrous acetonitrile (2 mL) was then added to the white sodium hydride powder and stirred for 1 hour to ensure deprotonation of the alcohol. The ligand solution was then filtered through a PTFE membrane (0.2 µm) and added dropwise to the rhenium solution, causing a vibrant colour change from green to orange. The reaction mixture was then left to stir for 18 hours at room temperature, whereupon reaction monitoring confirmed the formation of **Re2Cl8HQ**. The orange solution was then added to a volume of aqueous triflic acid (0.1 $mol.L^{-1}$, 10 mL) and evaporated under reduced pressure to remove the acetonitrile, thus precipitating out a yellow solid in the remaining aqueous suspension. The crude yellow solid was isolated *via* vacuum filtration, dissolved in acetonitrile and eluted over neutral alumina

(Brockmann grade II) using an isocratic acetonitrile mobile phase. The eluents containing the product were subsequently combined and evaporated down under reduced pressure to afford the pure yellow powder (49.8 mg).

The ^{1}H-NMR spectrum of the product, as shown in Figure 176, afforded five distinctly split signals each providing an integration of one, thus totalling the five expected protons in the aromatic region for **Re2Cl8HQ**. This was further verified by ^{13}C-NMR spectroscopy, in Figure 177, which not only revealed the expected nine carbon-13 resonance signals for the nuclei pertaining to the quinoline moiety, though also exhibited the three typically downfield shifted signals of low intensity characteristic of the carbonyl ligands coordinated to the rhenium centre. The FTIR spectrum of the compound (Figure 178) exhibited the distinctive A'(1) C≡O and overlapping A'(2) & A'' C≡O stretching frequencies at 2017 cm^{-1} and 1880 cm^{-1}, respectively, clearly demonstrating the existence of the rhenium tricarbonyl centre. Evidently, the absence of a broad O−H vibrational band at higher wavenumbers in the FTIR spectrum, alongside the absence of a broad downfield shifted NMR signal, suggested the loss of a hydroxyl group through which the quinoline had coordinated to the rhenium centre. Due to the presence of a neutral acetonitrile ancillary ligand, whose resonance signals were masked by the residual protonated solvent signal in the NMR analyses but may be the cause of the sharp IR absorption bands *circa* 2303 cm^{-1}, the complex was unable to yield reliable *m/z* ratios *via* LRMS or HRMS analysis as no charges could be induced by dissociating the rhenium to ancillary ligand bond. The compound was examined by elemental analysis, however, which attested to both the purity and assigned molecular identity of **Re2Cl8HQ** (including the acetonitrilo ancillary ligand) by affording experimental compositions of 34.89% carbon, 1.54% hydrogen and 5.60% nitrogen against theoretically calculated compositions of 34.32% carbon, 1.65% hydrogen and 5.72% nitrogen. The $d\pi \rightarrow \pi^*$ electronic transition to the MLCT excited state of **Re2Cl8HQ** is also present at 437 nm in the UV-Vis spectrum in Figure 179.

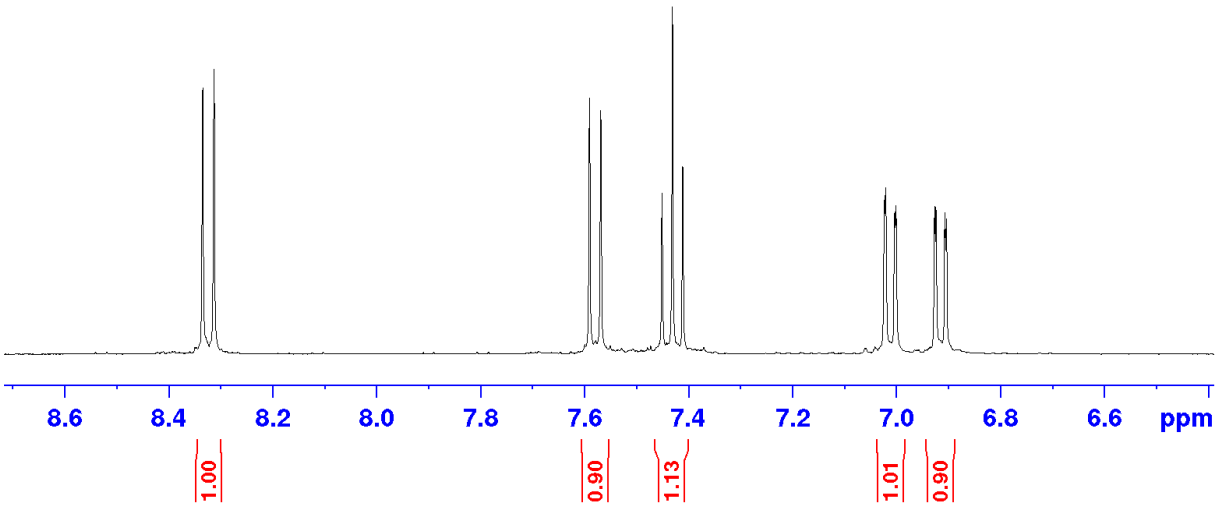

Figure 176. ^{1}H-NMR spectrum of **Re2Cl8HQ** in acetonitrile-d_3 showing the expected integration for five protons in the aromatic region. The resonance signal for the methyl group of the acetonitrilo ancillary ligand is masked behind the residual solvent peak.

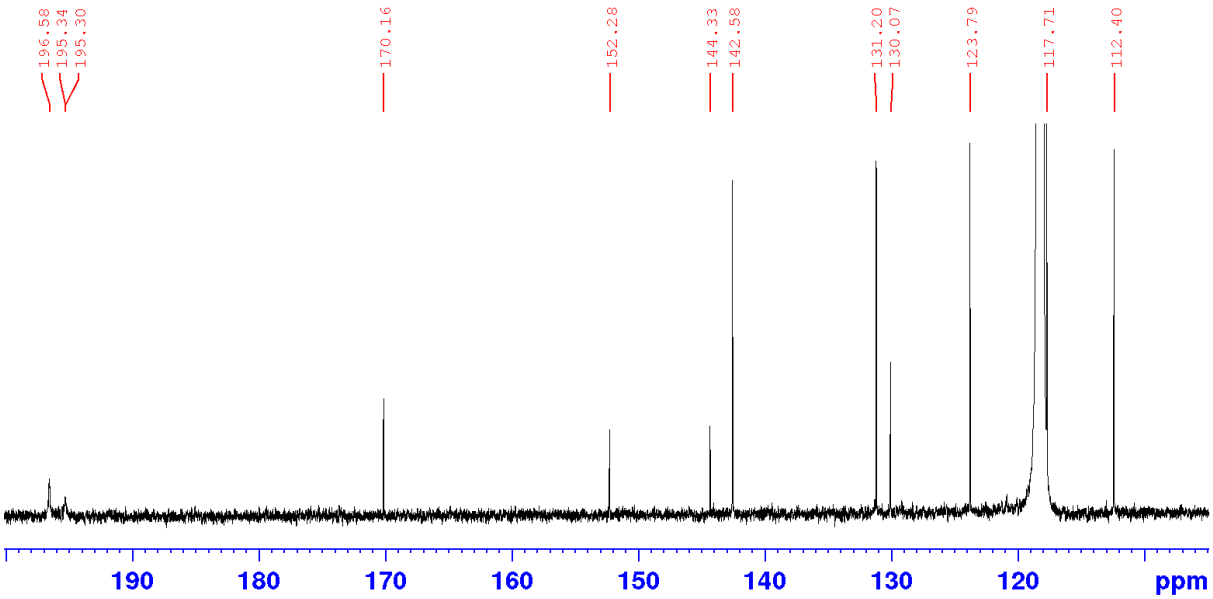

Figure 177. ^{13}C-NMR spectrum of **Re2Cl8HQ** in acetonitrile-d_3 showing the three downfield shifted carbon-13 resonance signals of the carbonyl ligands and the nine carbon-13 resonance signals of the quinoline ring.

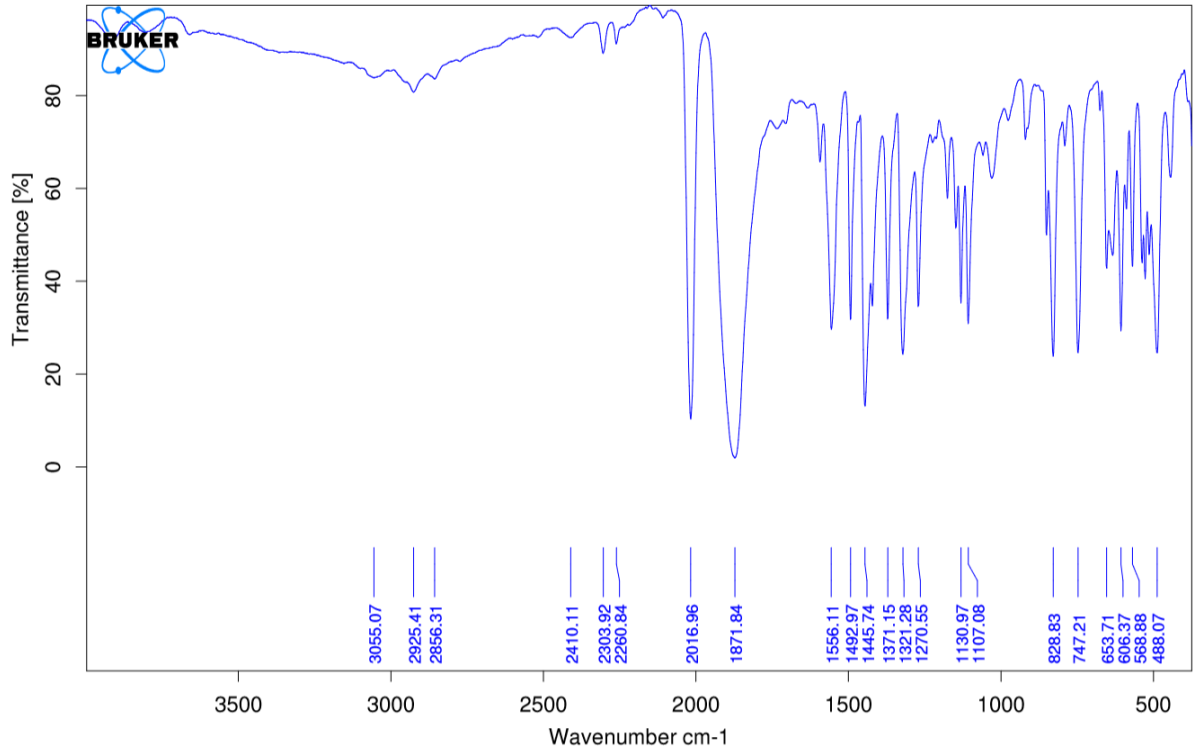

Figure 178. FTIR spectrum of **Re2Cl8HQ** exhibiting the distinctive A'(1) C≡O stretching frequency at 2017 cm^{-1} and the overlapping A'(2) & A'' C≡O stretching frequencies at 1880 cm^{-1}. Weaker sp^2 hybridised C−H bond stretches are also observed at higher wavenumbers (*circa* 2925 cm^{-1}) from the quinoline ring, and the absence of a broad O−H vibrational band at higher wavenumbers suggests the absence, and thus the coordination, of the hydroxyl group.

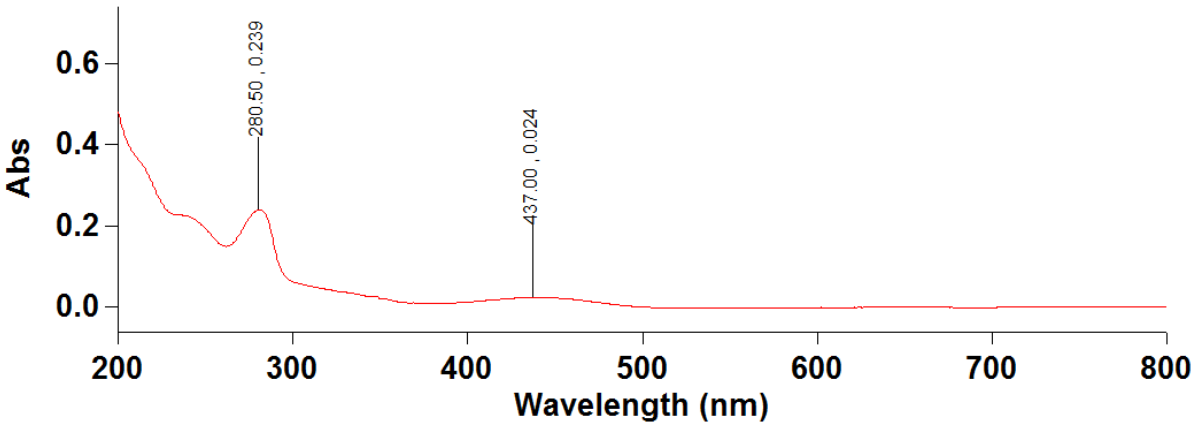

Figure 179. UV-Vis spectrum of **Re2Cl8HQ** (5 µg.mL^{-1}) in acetonitrile exhibiting the absorption band for the dπ → π* electronic transition to the MLCT excited state at 437 nm, alongside a very distinctive π → π* transition to a LC excited state at 281 nm.

5.1.5 Rhenium Complexation of 2-Fluoro-8-Hydroxyquinoline

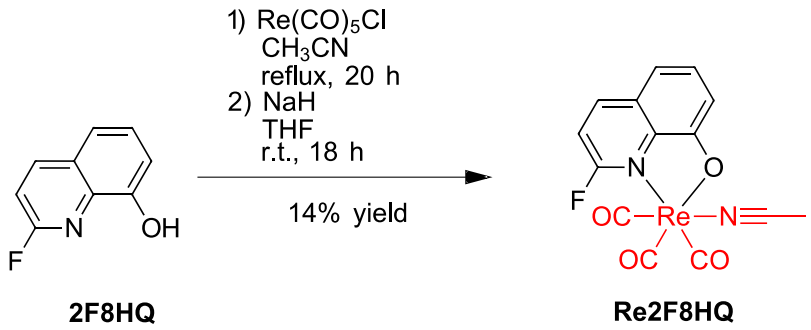

Figure 180. Rhenium complexation with **2F8HQ** *via* the formation of a diacetonitrilo intermediate to form the **Re2F8HQ** precursor.

A mass of pentacarbonylchlororhenium(I) (79.6 mg, 0.220 mmol, 1.0 eq.) was purged under nitrogen gas and vacuum (3 cycles) before being suspended in a volume of anhydrous acetonitrile (4 mL). The solution was refluxed for 20 hours in an inert nitrogen gas environment, which dissolved the powder to form the diacetonitriletricarbonylchlororhenium(I) intermediate which was verified by HPLC and FTIR spectroscopy. To a separate flask a mass of sodium hydride (60% wt/wt in mineral oil, 7.2 mg, 0.300 mmol, 1.4 eq.) was washed three times in hexane and then dried under high vacuum. A mass of **2F8HQ** (31.9 mg, 0.955 mmol, 0.4 eq.) dissolved in a volume of anhydrous tetrahydrofuran (THF, 2 mL) was then added to the white sodium hydride powder and stirred for 1 hour over a 0 °C ice bath to ensure deprotonation of the alcohol. The ligand solution was filtered through a PTFE membrane (0.2 µm) and added dropwise to the rhenium solution, causing a vibrant colour change from green to yellow. The reaction mixture was then left to stir for 18 hours at room temperature to ensure complete consumption of the ligand starting material. The yellow solution was then added to a volume of aqueous triflic acid (0.1 $mol.L^{-1}$, 10 mL) and evaporated under reduced pressure to remove the acetonitrile, thus precipitating out a yellow solid in the remaining aqueous suspension. The crude yellow solid was isolated *via* vacuum filtration, dissolved in acetonitrile and eluted over

neutral alumina (Brockmann grade II) using an isocratic acetonitrile mobile phase. The eluents containing the product were subsequently combined and evaporated down under reduced pressure to afford the pure yellow powder (12.6 mg).

The ^{1}H-NMR spectrum of the compound, depicted in Figure 181, provided the expected integration for five protons in the aromatic region. The ^{13}C-NMR spectrum depicted the three highly downfield shifted and low intensity signals corresponding to the carbon-13 nuclei within the three carbonyl ligands, alongside fourteen carbon-13 resonance signals in the aromatic region due to the coupling of five carbon nuclei with the fluorine-19 nucleus. The resonance signal corresponding to the fluorine-19 nucleus is shown at -56.94 ppm in the CDP ^{19}F-NMR spectrum in Figure 183. Furthermore, the FTIR spectrum of **Re2F8HQ**, as shown in Figure 184, showed the distinctive A'(1) C≡O and overlapping A'(2) & A'' C≡O stretching frequencies at 2020 cm^{-1} and 1875 cm^{-1}, respectively. Higher sp^2 hybridised C−H bond stretches were observed around 2926 cm^{-1} from the quinoline ring and, more significantly, the absence of an O−H vibrational band suggested coordination through the nitrogen and oxygen atoms of the quinoline ligand.

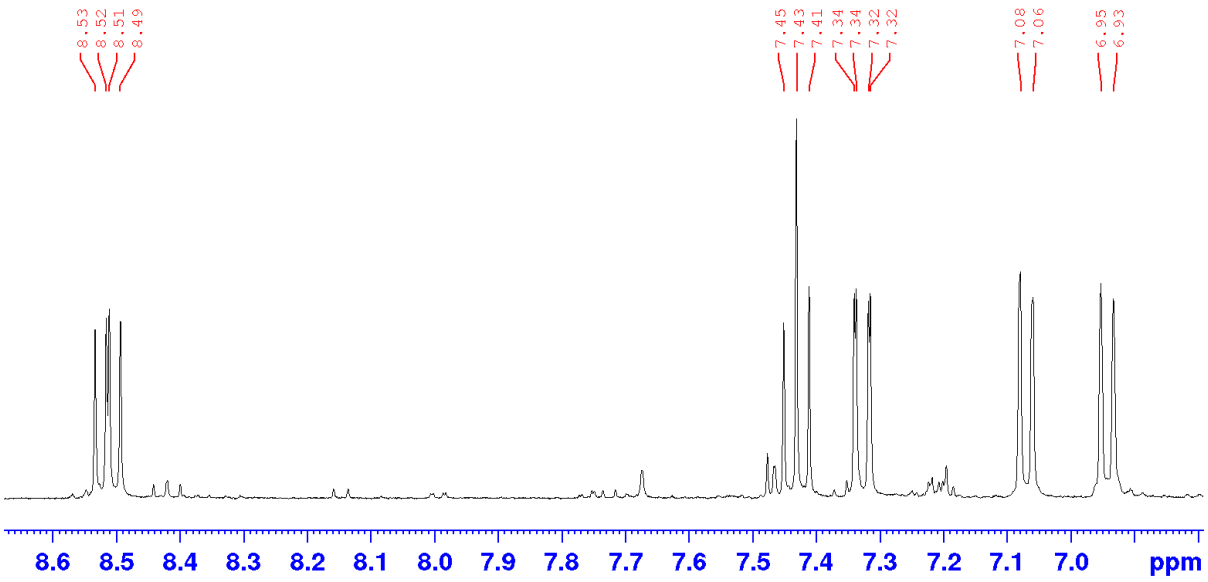

Figure 181. ^{1}H-NMR spectrum of **Re2F8HQ** in acetonitrile-d_3 showing the expected integration for five protons in the aromatic region. The resonance signal for the methyl group of the acetonitrilo ancillary ligand is masked behind the residual solvent peak.

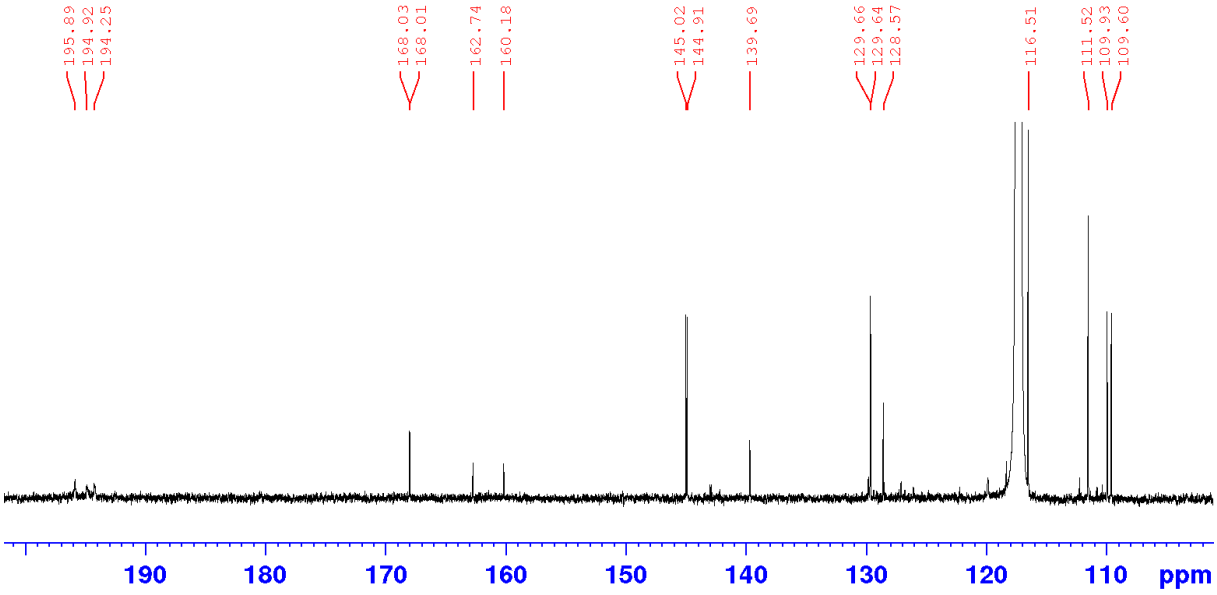

Figure 182. ^{13}C-NMR spectrum of **Re2F8HQ** in acetonitrile-d_3 showing the three downfield shifted carbon-13 resonance signals of the carbonyl ligands and the nine carbon-13 resonance signals (five split into doublets due to fluorine-19 coupling) of the quinoline ring.

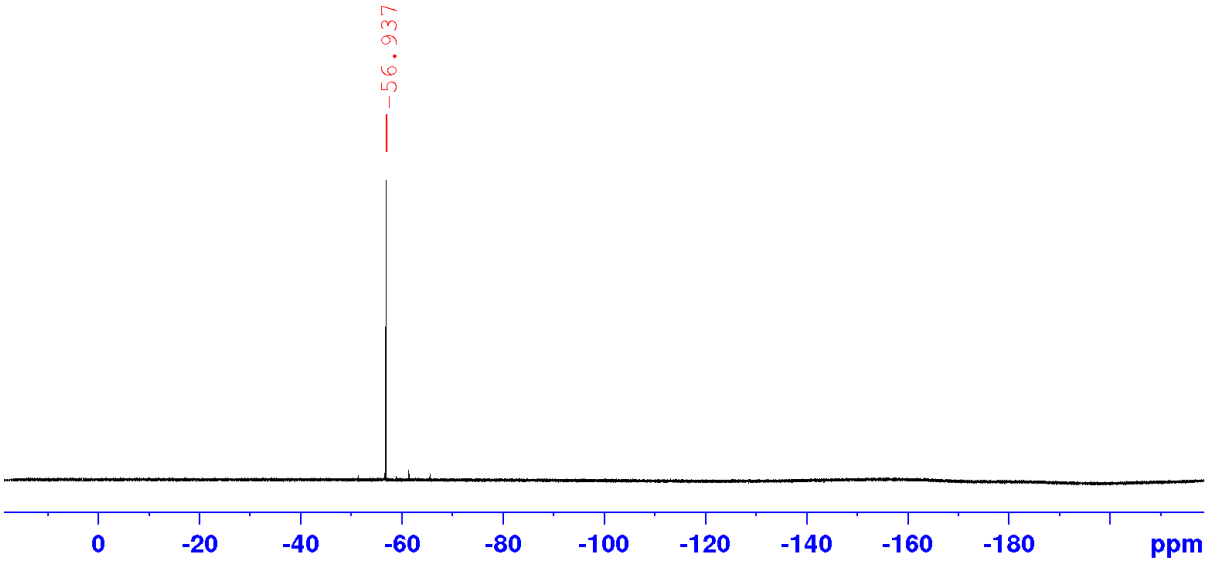

Figure 183. CPD ^{19}F-NMR spectrum of **Re2F8HQ** in acetonitrile-d_3, showing the magnetic resonance signal for the sole fluorine-19 nucleus in the molecule at -56.94 ppm.

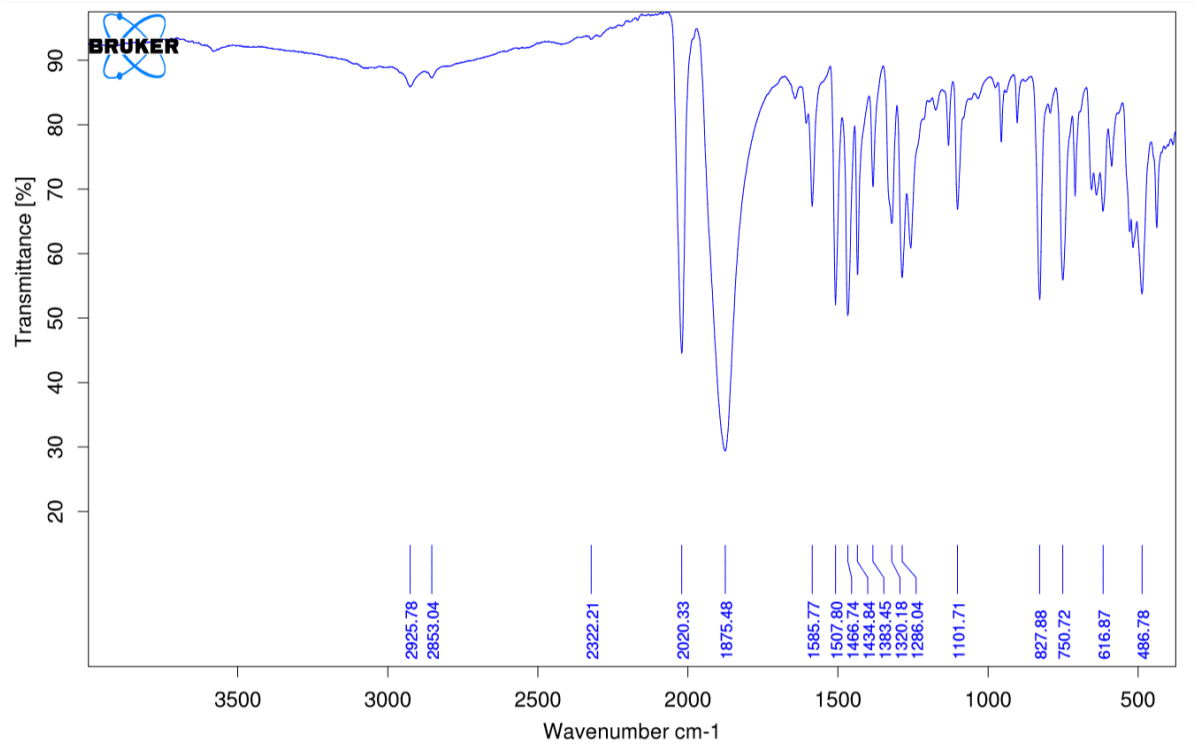

Figure 184. FTIR spectrum of **Re2F8HQ** exhibiting the distinctive A'(1) C≡O stretching frequency at 2020 cm^{-1} and the overlapping A'(2) & A'' C≡O stretching frequencies at 1875 cm^{-1}. Weaker sp^2 hybridised C−H bond stretches are also observed at higher wavenumbers (*circa* 2926 cm^{-1}) from the quinoline ring, and the absence of a broad O−H vibrational band at higher wavenumbers suggests the absence, and thus the coordination, of the hydroxyl group.

5.1.6 Rhenium Complexation of 5-Nitro-8-Hydroxyquinoline

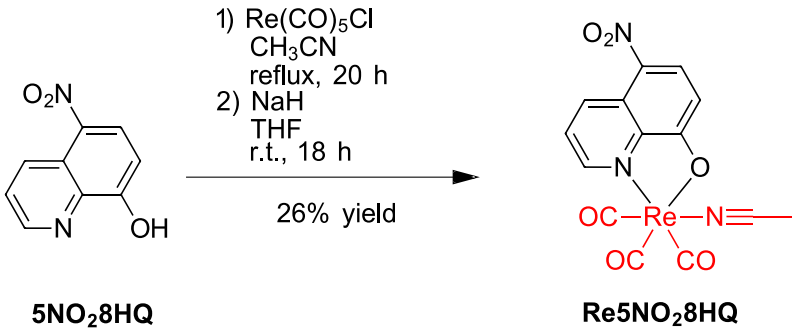

5NO$_2$8HQ **Re5NO$_2$8HQ**

Figure 185. Rhenium complexation with **5NO$_2$8HQ** *via* the formation of a diacetonitrilo intermediate to form the **Re5NO$_2$8HQ** precursor.

A mass of pentacarbonylchlororhenium(I) (112.4 mg, 0.311 mmol, 1.0 eq.) was suspended in a volume of anhydrous acetonitrile (4 mL) following 3 cycles of nitrogen gas and vacuum purging of the environment. The solution was refluxed for 20 hours overnight in an inert nitrogen environment to form a diacetonitrilo intermediate, which was monitored *via* FTIR spectroscopy and HPLC analysis. Separate to this system, a mass of **5NO$_2$8HQ** (65.0 mg, 0.342 mmol, 1.1 eq.) was dissolved in a volume of THF (5 mL) within an inert nitrogen environment. A mass of 60% wt/wt sodium hydride in mineral oil (8.2 mg, 0.342 mmol, 1.1 eq.) was then washed three times in hexanes and dried under vacuum to afford a white powder. The ligand solution was then injected dropwise over the sodium hydride in a 0 °C ice bath. The solution turned a vibrant green and was left to stir at 0 °C for an hour to ensure complete deprotonation. The deprotonated ligand solution was then injected over the rhenium solution, immediately transitioning to a vibrant orange solution. The reaction mixture was left to stir overnight at room temperature for 18 hours, where after the solution was filtered through a 0.2 µm PTFE membrane filter. The solution was then loaded onto a neutral alumina phase column (Brockmann grade II) and eluted with an acetonitrile isocratic mobile phase. The eluted

fractions containing **Re5NO$_2$8HQ** were then combined and evaporated under reduced pressure to afford a pure yellow powder (41.0 mg).

The ^{1}H-NMR and ^{13}C-NMR spectra of **Re5NO$_2$8HQ** show the expected integration for five protons in the aromatic region and the expected nine signals for carbon-13 nuclei in the aromatic region in Figure 186 and Figure 187, respectively. Additionally, three additional signals are present at much higher chemical shifts due to the three carbon-13 resonance signals from the carbonyl ligands. The FTIR spectrum also shows the two distinctive high intensity carbonyl stretching frequencies at 2019 cm^{-1} and 1900 cm^{-1}, pertaining to the A'(1) and overlapping A'(2) and A'' irreducible representations. Weaker sp^2 hybridised C–H stretching frequencies are also present around 2918 cm^{-1} as shown in Figure 188. A crystal structure of **Re5NO$_2$8HQ** attained *via* XRD analysis at the Australian Synchrotron, grown from the slow evaporation of DMSO solvent, is shown in Figure 189 which assigned unequivocal evidence for the assigned molecular identity.

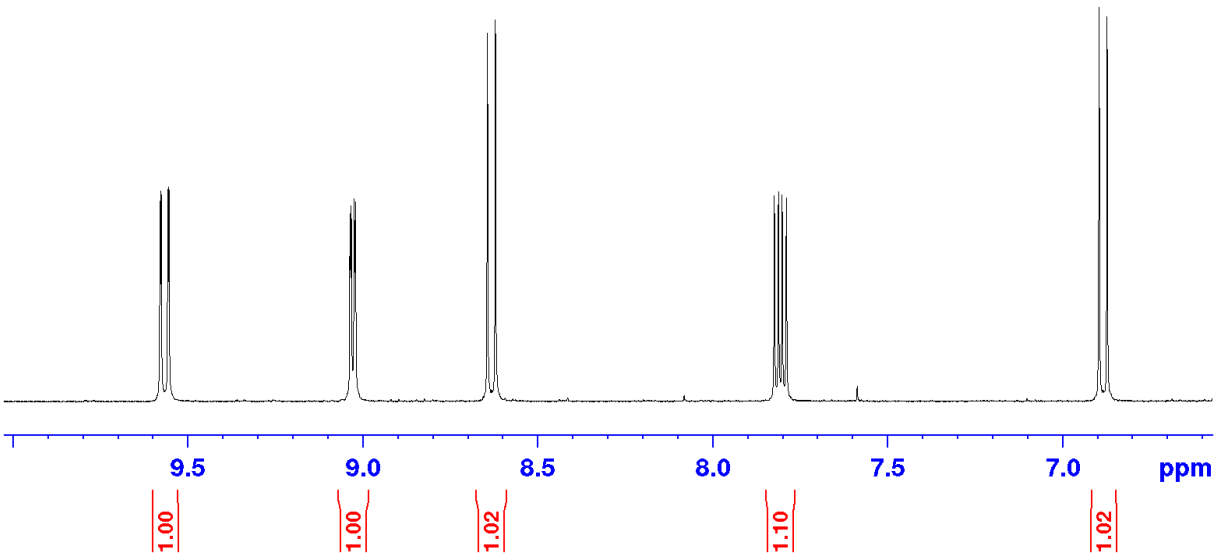

Figure 186. ^{1}H-NMR spectrum of **Re5NO$_2$8HQ** in acetonitrile-d$_3$ showing the expected integration for five protons in the aromatic region. The resonance signal for the methyl group of the acetonitrilo ancillary ligand is masked behind the residual solvent peak.

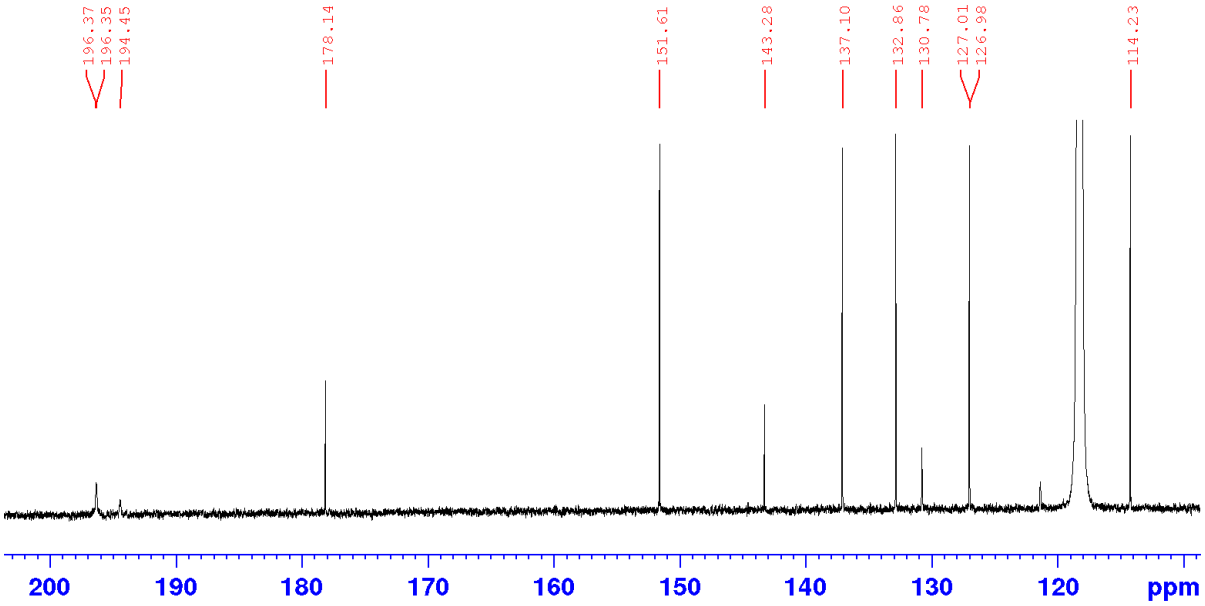

Figure 187. ^{13}C-NMR spectrum of **Re5NO$_2$8HQ** in acetonitrile-d$_3$ showing the three downfield shifted carbon-13 resonance signals of the carbonyl ligands and the nine carbon-13 resonance signals of the quinoline ring.

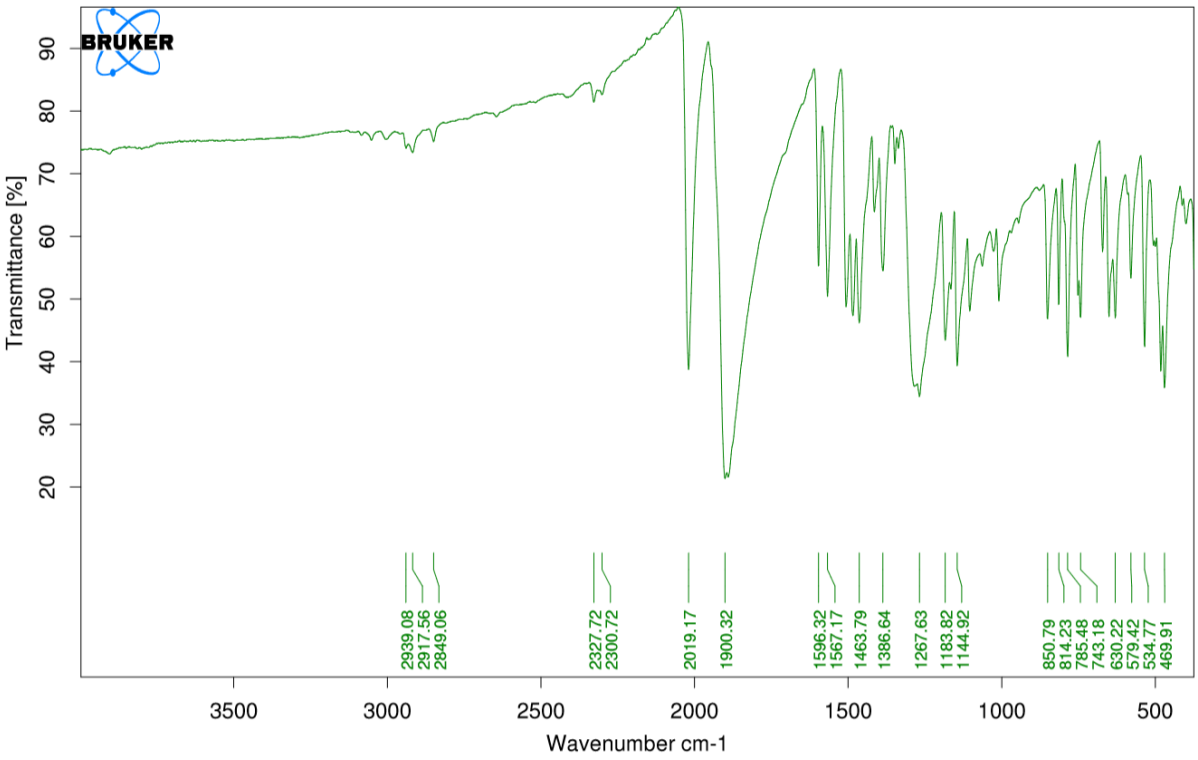

Figure 188. FTIR spectrum of **Re5NO$_2$8HQ** exhibiting the distinctive A'(1) C≡O stretching frequency at 2019 cm^{-1} and the overlapping A'(2) & A'' C≡O stretching frequencies at 1900 cm^{-1}. Weaker sp^2 hybridised C−H bond stretches are also observed at higher wavenumbers (*circa* 2918 cm^{-1}) from the quinoline ring, and the absence of a broad O−H vibrational band at higher wavenumbers suggests the absence, and thus the coordination, of the hydroxyl group.

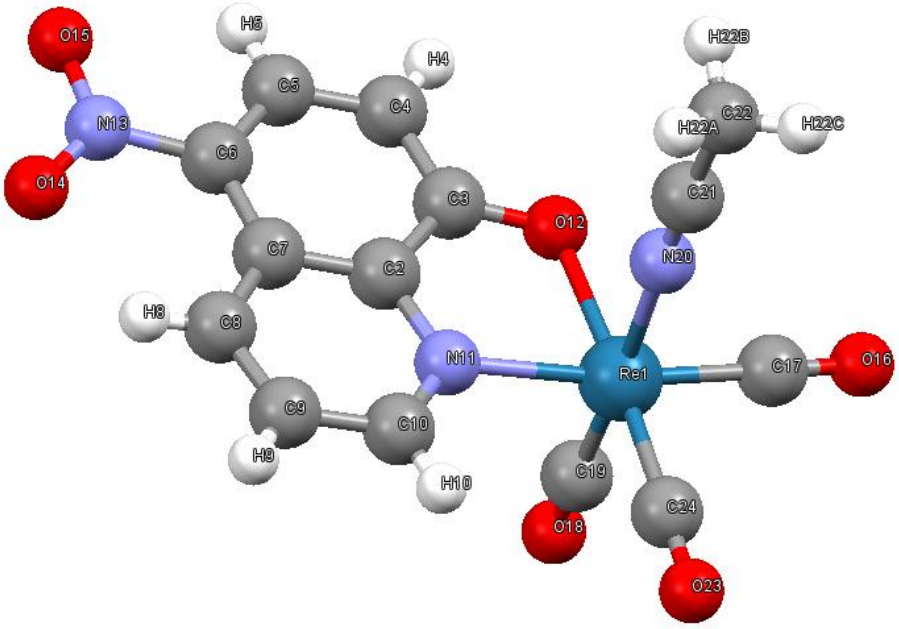

Figure 189. Crystal structure of **Re5NO$_2$8HQ** attained *via* XRD analysis at the Australian Synchrotron.

5.1.7 Rhenium Complexation of 5-Fluoro-8-Hydroxyquinoline

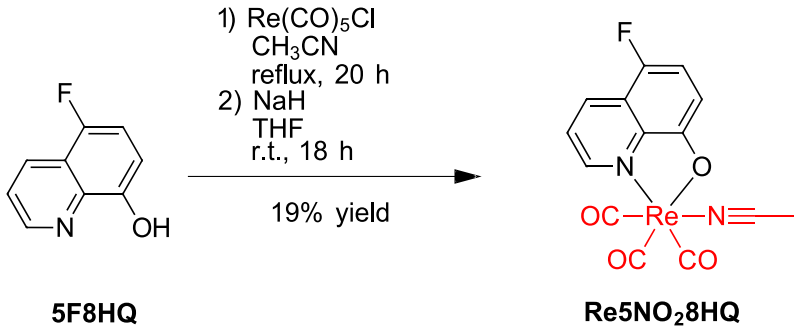

5F8HQ **Re5NO$_2$8HQ**

Figure 190. Rhenium complexation with **5F8HQ** *via* the formation of a diacetonitrilo intermediate to form the **Re5F8HQ** precursor.

A mass of pentacarbonylrhenium(I) (104.0 mg, 0.288 mmol, 1.0 eq.) was refluxed in a volume of anhydrous acetonitrile (3 mL) under an inert nitrogen environment for 20 hours, thus forming a diacetonitrile intermediate which was verified by peak shifts in HPLC and FTIR spectroscopic reaction monitoring. A mass of **5F8HQ** (51.6 mg, 0.316 mmol, 1.1 eq.) was dissolved in a volume of anhydrous THF (2 mL) in an inert nitrogen environment. A mass of 60% wt/wt sodium hydride in mineral oil (8.2 mg, 0.342 mmol, 1.2 eq.) was washed three times in hexanes and dried under high vacuum. The volume of **5FHQ** in THF was then added to the hydride powder over a 0 °C ice bath and stirred for 1 hour resulting in a green solution. This solution was then added to the solution containing rhenium, prompting a colour change to orange. The solution was then allowed to stir at room temperature for 18 hours. Thereafter the solution was filtered through a PTFE membrane (0.2 µm), loaded onto a Brockmann II neutral alumina column and eluted using a 100% acetonitrile gradient. The eluents containing the **Re5NO$_2$8HQ** complex were combined and evaporated under reduced pressure to afford a pure yellow powder (25.5 mg).

NMR analysis of **Re5F8HQ** show the expected integration for five protons in the aromatic region from the ^{1}H-NMR spectrum show in in Figure 191, twenty carbon-13 signals due to

three downfield shifted carbonyl ligand signals and nine carbon-13 nuclei of the quinoline ring coupling to the fluorine-19 nucleus from the ^{13}C-NMR spectrum in Figure 192, and the sole fluorine-19 resonance signal expected from the only fluorine atom in the molecule in the CPD ^{19}F-NMR in Figure 193. The FTIR spectrum also exhibits the expected carbonyl stretching frequencies belonging to the A'(1) C≡O and the overlapping A'(2) & A'' irreducible representations at 2019 cm^{-1} and 1892 cm^{-1}, as shown in Figure 194 respectively. Curiously the UV-vis spectrum of **Re5F8HQ** (Figure 195) exhibited an absorption band at 437 nm, formerly assigned to the typical dπ → π* electronic transition to the MLCT excited state, though with a much higher molar absorptivity (17570 L.mol^{-1}.cm^{-1}) than the other synthesised rhenium complexes of similar 5 µg.mL^{-1} concentration in acetonitrile, suggesting that this transition may instead account for an electronic transition to an intraligand charge transfer (ILCT) excited state. Other π → π* transitions to LC excited states at are also observed at shorter wavelengths as expected.

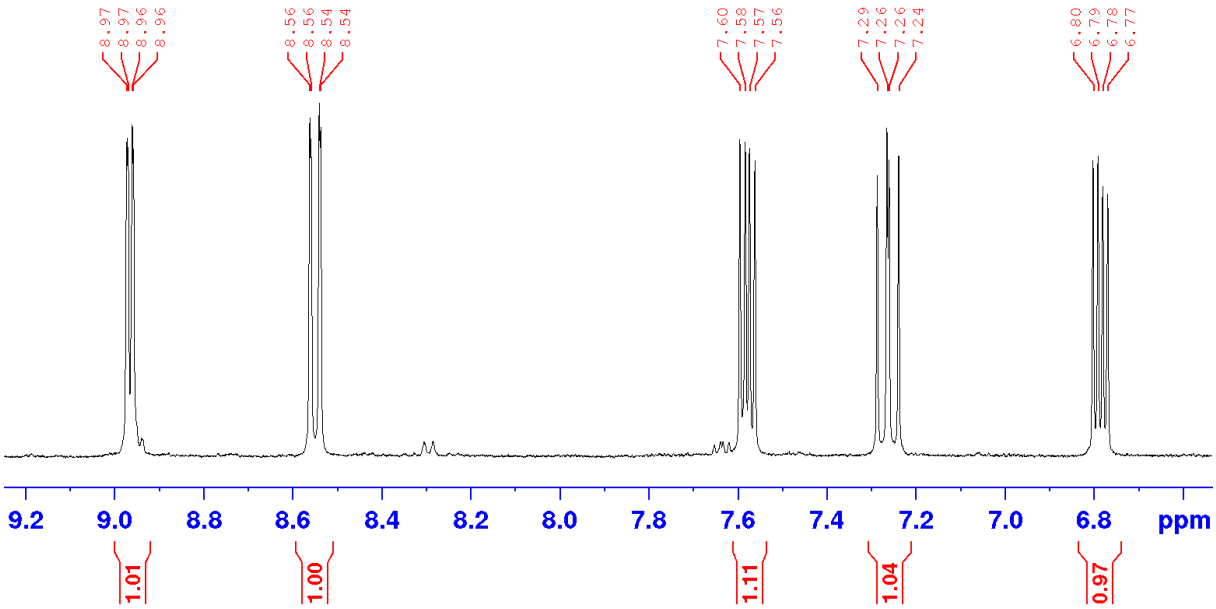

Figure 191. ^{1}H-NMR spectrum of **Re5F8HQ** in acetonitrile-d$_3$ showing the expected integration for five protons in the aromatic region. The resonance signal for the methyl group of the acetonitrilo ancillary ligand is masked behind the residual solvent peak.

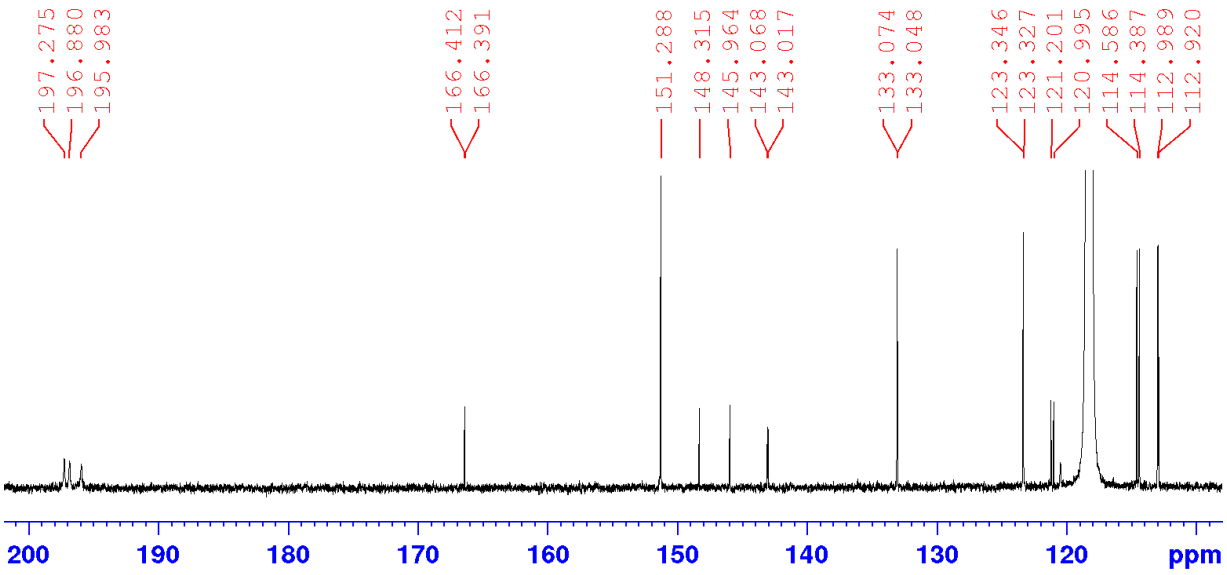

Figure 192. ^{13}C-NMR spectrum of **Re5NO$_2$8HQ** in acetonitrile-d$_3$ showing the three downfield shifted carbon-13 resonance signals of the carbonyl ligands and seventeen carbon-13 resonance signals in the aromatic region due to nine of the quinoline carbon-13 nuclei coupling with the fluorine-19 nucleus.

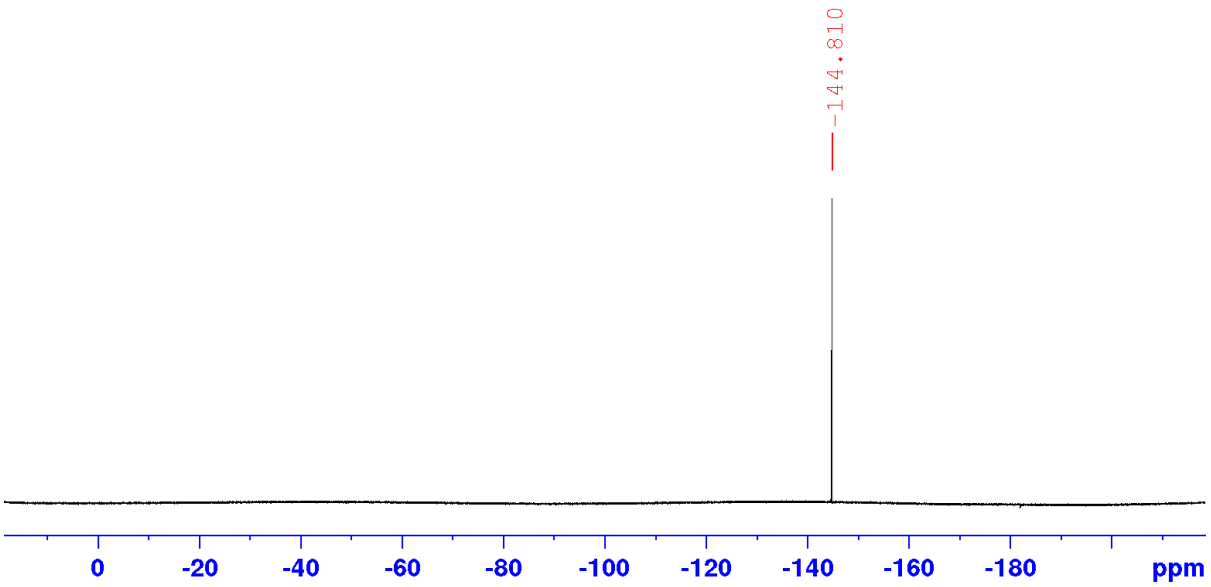

Figure 193. Lone magnetic resonance signal of the fluorine-19 nucleus in the CPD ^{19}F-NMR spectrum of **Re5F8HQ**.

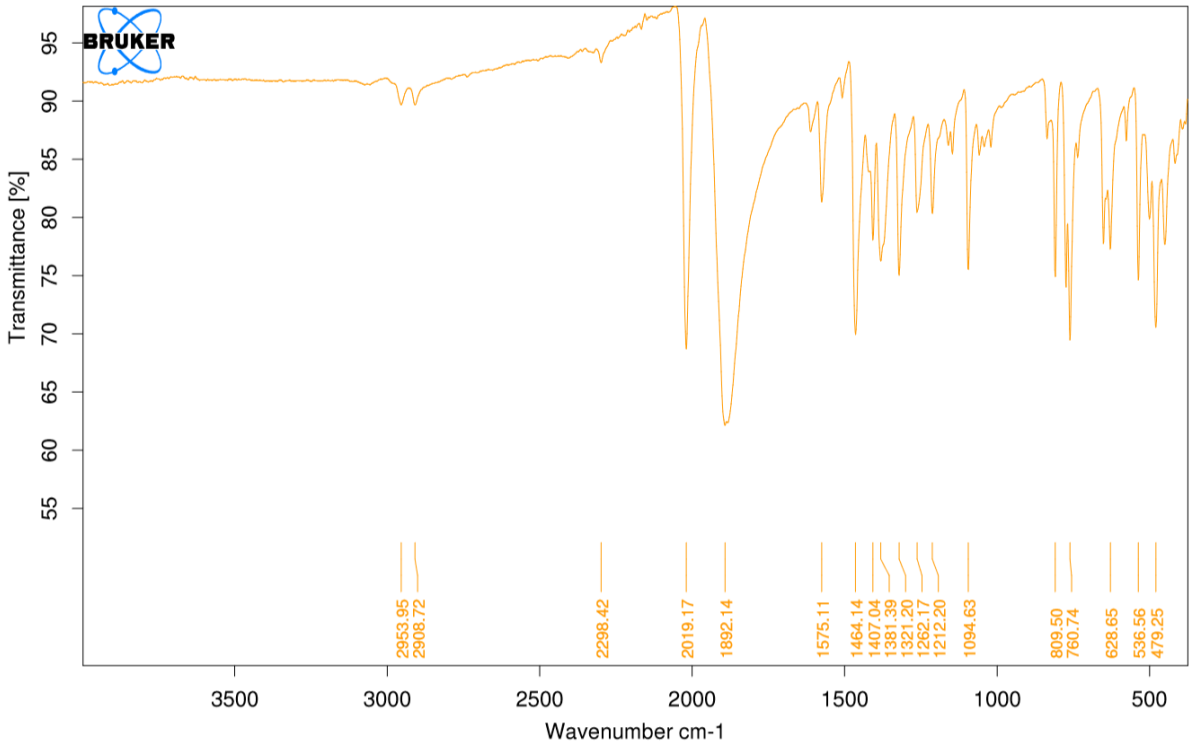

Figure 194. FTIR spectrum of **Re5F8HQ** exhibiting the distinctive A'(1) C≡O stretching frequency at 2019 cm^{-1} and the overlapping A'(2) & A'' C≡O stretching frequencies at 1892 cm^{-1}. Weaker sp^2 hybridised C−H bond stretches are also observed at higher wavenumbers (*circa* 2953 cm^{-1}) from the quinoline ring, and the absence of a broad O−H vibrational band at higher wavenumbers suggests the absence, and thus the coordination, of the hydroxyl group.

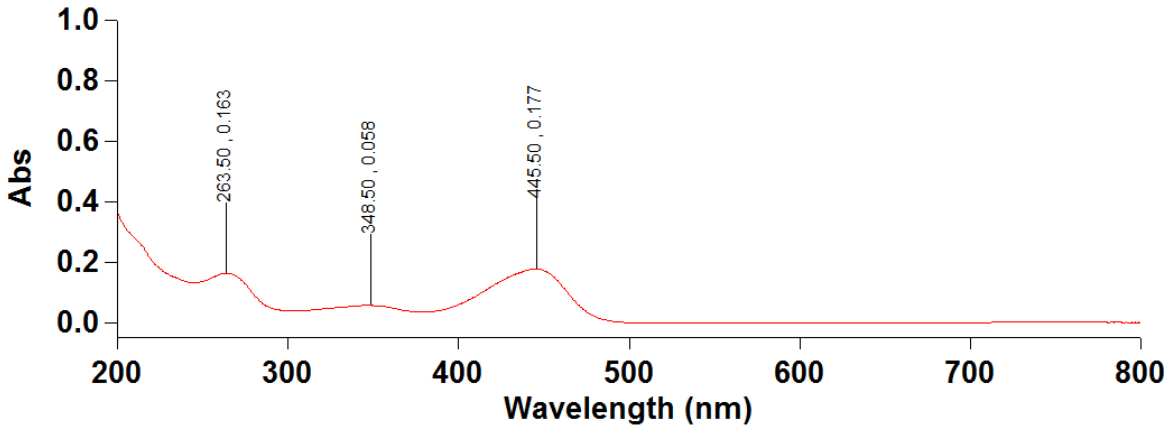

Figure 195. UV-Vis spectrum of **Re5F8HQ** (5 µg.mL^{-1}) in acetonitrile exhibiting an absorption band for an electronic transition to either the MLCT excited state of uncharacteristically high molar absorptivity (17570 L.mol^{-1}.cm^{-1}) or an ILCT excited state at 437 nm. $\pi \rightarrow \pi^*$ transitions to LC excited states at are also observed at shorter wavelengths.

5.1.8 Characterisation Data for the 8-Hydroxyquinoline Ligands and their Rhenium Complexes

2-chloro-8-benzoxyquinoline (**2Cl8HQ-OBn**) Pink solid; MP: 101 °C, 85% yield. ^{1}H NMR (400 *MHz*, $CDCl_3$, *δ*/*ppm*): δ 8.06 (d, J^d=8.60 Hz, 1H), δ 7.50 (d, J^d=7.36 Hz, 1H), δ 7.40 (d, J^d=8.56 Hz, 1H), δ 7.36 (m, 1H), δ 7.30 (d, J^d=7.06 Hz, 1H), δ 7.06 (dd, J^d=6.08, 3.00 Hz, 1H). ^{13}C{^{1}H} NMR (100 *MHz*, $CDCl_3$, δ/*ppm*): δ 153.7, δ 150.0, δ 140.0, δ 138.7, δ 137.0, δ 128.7, δ 128.3, δ 127.9, δ 127.2, δ 127.1, δ 127.1, δ 123.1, δ 119.7, δ 111.8, δ 71.0.

2-fluoro-8-benzoxyquinoline (**2F8HQ-OBn**) Pink solid; MP: 107 °C, 26% yield. ^{1}H NMR (400 *MHz*, $CDCl_3$, *δ*/*ppm*): δ 8.22 (d, J^d=8.40 Hz, 1H), δ 7.51 (d, J^d=7.40 Hz, 1H), δ 8.35 (m, 5H), δ 7.10 (m, 2H), δ 5.42 (s, 1H). ^{13}C{^{1}H} NMR (100 *MHz*, $CDCl_3$, δ/*ppm*): δ 162.0, δ 159.5, δ 153.6 (J^d=2 *Hz*), δ 142.1 (J^d=9 *Hz*), δ 137.7 (J^d=15 *Hz*), δ 137.0, δ 128.8, δ 128.2 (J^d=2 *Hz*), δ 128.0, δ 127.2, δ 126.3 (J^d=9 *Hz*), δ 119.7, δ 111.8, δ 110.9, δ 110.4. ^{19}F{^{1}H} NMR (376 *MHz*, DMSO-d_6, *δ*/*ppm*): δ -61.07.

2-fluoro-8-hydroxyquinoline (**2F8HQ** or **CABS13**) Yellow solid; MP: 62 °C, 75% yield. ^{1}H NMR (400 *MHz*, DMSO-d_6, *δ*/*ppm*): δ 9.89 (br. s, 1H), δ 8.51 (t, J^t=8.60 *Hz*), δ 7.45 (m, 2H), δ 7.32 (dd, J^d=8.80, 2.76 *Hz*, 1H), δ 7.14 (dd, J^d=7.20, 1.64 *Hz*, 1H). ^{13}C{^{1}H} NMR (100 *MHz*, CD_3CN, δ/*ppm*): δ 159.6 (d, J^d=238 *Hz*), δ 152.5, δ 143.0 (d, J^d=10 *Hz*), δ 135.4 (d, J^d=15 *Hz*), δ 127.9, δ 126.9 (d, J^d=2 *Hz*), δ 117.9, δ 113.5, δ 110.2 (d, J^d=42 *Hz*). ^{19}F{^{1}H} NMR (376 *MHz*, DMSO-d_6, *δ*/*ppm*): δ -63.53. FTIR (ATR *corr.* $\tilde{\nu}/cm^{-1}$): $\tilde{\nu}$ 2473 (br. m, O-H *str.*).

Acetonitriletricarbonyl(2-chloro-8-quinolinolate)rhenium(I) (**Re2Cl8HQ**) Amber solid; MP: 130 °C (dec.), 32% yield. ^{1}H NMR (400 *MHz*, CD_3CN, *δ*/*ppm*): δ 8.32 (d, J^d=8.68 *Hz*, 1H), δ 7.58 (d, J^d=8.68 *Hz*, 1H), δ 7.43 (t, J^t=7.96 *Hz*, 1H), δ 7.01 (dd, J^d=7.96, 0.96 *Hz*, 1H), δ 6.92 (dd, J^d=7.96, 1.04 *Hz*, 1H), δ 1.96 (s, 3H). ^{13}C{^{1}H} NMR (100 *MHz*, CD_3CN, δ/*ppm*): δ 196.6$_{C\equiv O}$, δ 195.3$_{C\equiv O}$, δ 195.3$_{C\equiv O}$, δ 170.2, δ 152.3, δ 144.3, δ 142.6, δ 131.2, δ 130.1, δ 123.8,

δ 120.8, δ 117.7, δ 112.4, δ 30.3. FTIR (ATR *corr. ṽ/cm^{-1}*): *ṽ* 2925 (w, C−H sp^2 *str.*), *ṽ* 2304 (w, N≡C *str.*), *ṽ* 2017 (s, A'(1) C≡O *str.*), *ṽ* 1872 (s, A'(2) & A'' C≡O *str.*). UV/Vis (λ/*nm*, ε/*L.mol^{-1}.cm^{-1}*): λ 437 (*dπ→π**, ε 235.06), λ 281 (*π→π**, ε 2340.84), λ 237 (*π→π**, ε 3104.80). EA (%): *calc.* C 34.32, H 1.65, N 5.72. *found* C 34.89, H 1.54, N 5.60.

Acetonitriletricarbonyl(2-fluoro-8-quinolinolate)rhenium(I) (**Re2F8HQ**) Amber solid; MP: 134 °C (dec.), 14% yield. ^{1}H NMR (400 *MHz*, CD_3CN, *δ/ppm*): δ 8.51 (dd, J^d=8.92, 7.04 *Hz*, 1H), δ 7.43 (t, J^t=7.96 *Hz*, 1H), δ 7.33 (dd, J^d=8.92, 1.24 *Hz*, 1H), δ 7.06 (d, J^d=8.00 *Hz*, 1H), δ 6.94 (d, J^d=7.92 *Hz*, 1H). ^{13}C{^{1}H} NMR (100 *MHz*, CD_3CN, δ/*ppm*): δ 195.9$_{C≡O}$, δ 194.9$_{C≡O}$, δ 194.2$_{C≡O}$, δ 168.0 (d, J^d=2 *Hz*), δ 161.5 (d, J^d=256 *Hz*), δ 145.0 (d, J^d=2 *Hz*), δ 139.7, δ 129.6 (d, J^d=2 *Hz*), δ128.6, δ 116.5, δ 111.5, δ 109.8 (d, J^d=33 *Hz*). ^{19}F{^{1}H} NMR (376 *MHz*, CD_3CN, *δ/ppm*): δ -56.94. FTIR (ATR *corr. ṽ/cm^{-1}*): *ṽ* 2925 (w, C−H sp^2 *str.*), *ṽ* 2853 (w, C−H sp^2 *str.*), *ṽ* 2322 (w, N≡C *str.*), *ṽ* 2020 (s, A'(1) C≡O *str.*), *ṽ* 1875 (s, A'(2) & A'' C≡O *str.*).

Acetonitriletricarbonyl(5-chloro-8-quinolinolate)rhenium(I) (**Re5Cl8HQ**) Yellow solid, MP: 159-170 °C (dec.), 26% yield. ^{1}H NMR (400 *MHz*, CD_3CN, *δ/ppm*): δ 9.98 (dd, J^d=4.84, 1.24 *Hz*, 1H), δ 8.64 (dd, J^d=8.64, 1.28 *Hz*, 1H), δ 7.64 (dd, J^d=8.64, 4.84 *Hz*, 1H), δ 7.55 (d, J^d=8.52 *Hz*, 1H), δ 6.85 (d, J^d=8.52 *Hz*, 1H), δ 1.96 (s, 3H). ^{13}C{^{1}H} NMR (100 *MHz*, CD_3CN, δ/*ppm*): δ 197.1$_{C≡O}$, δ 196.8$_{C≡O}$, δ 195.7$_{C≡O}$, δ 169.6, δ 151.0, δ 144.9, δ 136.5, δ 130.9, δ 128.9, δ 124.1, δ 115.4, δ 113.2. FTIR (ATR *corr. ṽ/cm^{-1}*): *ṽ* 2959 (w, C−H sp^2 *str.*), *ṽ* 2911 (w, C−H sp^2 *str.*), *ṽ* 2322 (w, N≡C *str.*), *ṽ* 2016 (s, A'(1) C≡O *str.*), *ṽ* 1874 (s, A'(2) & A'' C≡O *str.*).

Acetonitrilecarbonyl(5-fluoro-8-quinolinolate)rhenium(I) (**Re5F8HQ**) Yellow solid, MP: 171-184 °C (dec.), 26% yield. ^{1}H NMR (400 *MHz*, CD_3CN, *δ/ppm*): δ 8.97 (dd, J^d=4.84, 1.08 *Hz*, 1H), δ 8.55 (dd, J^d=8.56, 1.12 *Hz*, 1H), δ 7.58 (dd, J^d=8.56, 4.84 *Hz*, 1H), δ 7.26 (q, J^q=10.52, 8.72 *Hz*, 1H), δ 6.78 (dd, J^d=4.40, 8.72 *Hz*, 1H).). ^{13}C{^{1}H} NMR (100 *MHz*, CD_3CN, δ/*ppm*): δ 197.3$_{C≡O}$, δ 196.9$_{C≡O}$, δ 196.0$_{C≡O}$, δ 166.4 (d, J^d=2 *Hz*), δ 151.3, δ 147.1 (d, J^d=235 *Hz*), δ

143.0 (d, J^d=5 *Hz*), δ 133.1 (d, J^d=3 *Hz*), δ 123.3 (d, J^d=2 *Hz*), δ 121.1 (d, J^d=21 *Hz*), δ 144.5 (d, J^d=20 *Hz*), δ 113.0 (d, J^d=7 *Hz*). $^{19}F\{^1H\}$ NMR (376 *MHz,* CD_3CN, *δ/ppm*): δ -144.8. FTIR (ATR *corr. ṽ/cm*$^{-1}$): *ṽ* 2954 (w, C−H sp^2 *str.*), *ṽ* 2909 (w, C−H sp^2 *str.*), *ṽ* 2298 (w, N≡C *str.*), *ṽ* 2019 (s, A'(1) C≡O *str.*), *ṽ* 1892 (s, A'(2) & A'' C≡O *str.*).

Acetonitriletricarbonyl(5-nitro-8-quinolinolate)rhenium(I) (**Re5NO$_2$8HQ**) Yellow solid, MP: 190 - 194 °C (dec.), 26% yield. ^1H NMR (400 *MHz,* CD_3CN, *δ/ppm*): δ 9.57 (dd, J^d=9.00, 1.28 *Hz*, 1H), δ 9.03 (dd, J^d=4.84, 1.28 *Hz*, 1H), δ 8.63 (d, J^d=9.24 *Hz*, 1H), δ 7.81 (dd, J^d=9.00, 4.84 *Hz*, 1H), δ 6.88 (d, J^d=9.24 *Hz,* 1H). $^{13}C\{^1H\}$ NMR (100 *MHz,* CD_3CN, δ/*ppm*): δ 196.3$_{C\equiv O}$, δ 194.4$_{C\equiv O}$, δ 178.1$_{C\equiv O}$, δ 151.6, δ 143.3, δ 137.1, δ 132.9, δ 130.8, δ 127.0, δ 126.9, δ 121.4, δ 114.2. FTIR (ATR *corr. ṽ/cm*$^{-1}$): *ṽ* 2939 (w, C−H sp^2 *str.*), *ṽ* 2918 (w, C−H sp^2 *str.*), *ṽ* 2328 (w, N≡C *str.*), *ṽ* 2019 (s, A'(1) C≡O *str.*), *ṽ* 1900 (s, A'(2) & A'' C≡O *str.*).

5.2 Fluorine-18 Radiolabellings of 8-Hydroxyquinoline Rhenium Complexes

5.2.1 Radiosynthesis of the [^{18}F]CABS13 Alzheimer's Disease Imaging Agent *via* Rhenium Complexation

Non-radioactive standards of CABS13 (**2F8HQ**) and its corresponding rhenium complex (**Re2F8HQ**) were injected onto the radioHPLC using the standard chromatographic conditions described in the experimental section. The UV-absorption profiles of both compounds are superimposed upon one another in Figure 196 and provide retention times of 6.38 mins for **2F8HQ** and 7.60 mins for **Re2F8HQ**, which were used to match the retention times of the radioproducts to affirm their molecular identities. Radiolabelling studies of the **2Cl8HQ** precursor afforded no radiochemical yield, as affirmed by prior studies whom sought to protect the alcohol. Thus fluorine-18 radiolabelling experiments were instead performed on the **Re2Cl8HQ** using the standard *dry* conditions of 0.08 μmol of precursor, 29±10 MBq of [^{18}F]fluoride and a reaction time of 47 s within a laminar flow afforded by the microfluidic set-up. The temperature was progressive raised by 20 °C between each experiment, beginning at 50 °C for the first experiment and ending at 190 °C for the final experiment. The hypothesis for using **Re2Cl8HQ** was that it would not only improve the nucleophilic aromatic substitution for [^{18}F]fluoride in the *ortho*-position due to the rhenium activated electron withdrawal effect exhibited in the previous radiosyntheses of **[^{18}F]Re2FPhen** and **[^{18}F]Re6ClBiPy**, though would also protect the alcohol due to coordination through the oxygen atom of the alcohol group, thus circumventing the need for the multiple step radiosyntheses employed by other research groups. The **[^{18}F]2F8HQ** was then hypothesised to thermally dissociate from the radiolabelled **[^{18}F]Re2F8HQ** complex thereafter to afford the desired radiotracer in heightened RCY. Figure 197 shows a plot of the RCY of **[^{18}F]Re2F8HQ** and **[^{18}F]2F8HQ** formed as a

function of the reaction temperature from the **Re2Cl8HQ** precursor in DMSO. At both 50 °C and 70 °C neither radioproduct as formed, however from 90 °C to 150 °C a noticeable 2% RCY of the **[^{18}F]Re2F8HQ** has formed, though in absence of the **[^{18}F]2F8HQ** radiolabelled ligand. Evidently not enough heat had been supplied to the system at these temperatures to facilitate the thermal decomplexation of the ligand from the complex. Indeed, at a higher temperature of 190 °C not only was 2% of the **[^{18}F]Re2F8HQ** found to have formed, though this was also accompanied by the liberation of 2% of the **[^{18}F]2F8HQ** ligand. Alternative experiments were trialled to improve upon the RCY of **[^{18}F]2F8HQ**. These included adjusting the flow rate from 20 µL.min^{-1} to 5 µL.min^{-1} and 2 µL.min^{-1} (reaction times of 3.12 mins and 7.80 mins as per equation (13), respectively), while maintaining same amount of precursor and radioactive at a temperature of 190 °C. For the reaction at 5 µL.min^{-1}, RCYs of 2% were attained for both **[^{18}F]Re2F8HQ** and **[^{18}F]2F8HQ** indicating no improvement over the reaction conditions employed using a 20 µL.min^{-1} flow rate. For the reaction at 2 µL.min^{-1} **[^{18}F]2F8HQ** formed in only 1% RCY and **[^{18}F]Re2F8HQ** did not even form at all. This may have implied that the **Re2Cl8HQ** was thermally degrading a rate faster than it was being radiofluorinated, thus providing very little of the **[^{18}F]Re2F8HQ** radioproduct to dissociate to the desired **[^{18}F]2F8HQ** ligand. Thus, the reaction was repeated using a 2 µL.min^{-1} flow rate, 29±10 MBq of [^{18}F]fluoride and reaction temperature of 190 °C though with ten-fold increase of the precursor amount to 0.80 µmol. In this experiment a 10% RCY of **[^{18}F]Re2F8HQ** was obtained alongside a 2% RCY of **[^{18}F]2F8HQ**. Intriguingly however, a repeat experiment performed using the same parameters (though analysed with a slightly modified chromatographic condition which only held the 95% water mobile phase of the standard conditions described in the experimental section for 1 min) afford **[^{18}F]Re2F8HQ** in 18% RCY and the radiolabelled **[^{18}F]2F8HQ** ligand in a slightly greater 5% RCY, as shown by the radiochromatograms in Figure 198.

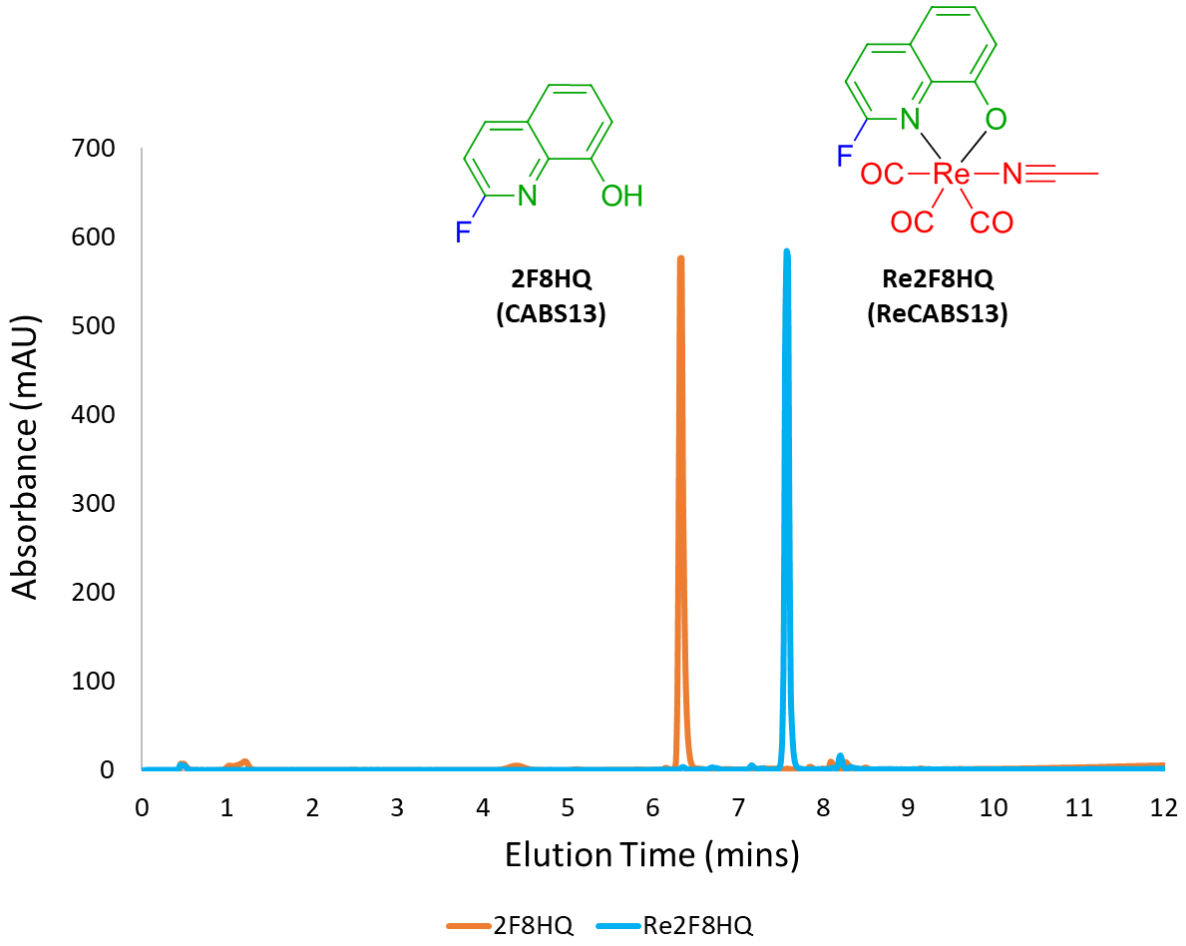

Figure 196. Superimposed UV-absorbance profiles for the non-radioactive standards of **2F8HQ** (CABS13, orange line) and **Re2F8HQ** (ReCABS13, blue line) providing retention times of 6.38 mins and 7.60 mins for both compounds, respectively, which were used to assign the identity of the radioproducts analysed by radioHPLC.

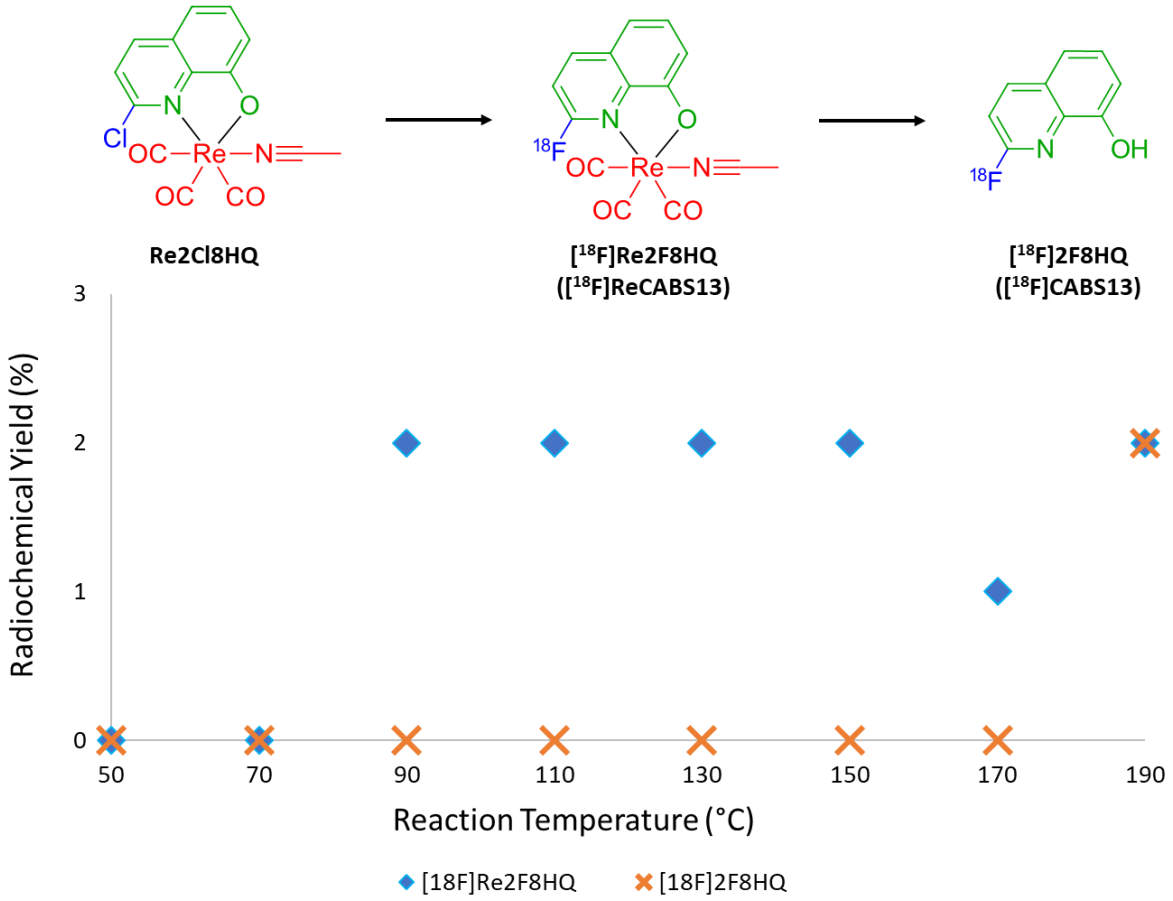

Figure 197. RCYs of **[^{18}F]Re2F8HQ** ([^{18}F]ReCABS13, blue diamonds) and **[^{18}F]2F8HQ** ([^{18}F]CABS13, orange crosses) synthesised from the **Re2Cl8HQ** precursor as a function of reaction temperature while employing the same reaction conditions of 0.08 µmol of the **Re2Cl8HQ** precursor, 29±10 MBq of [^{18}F]fluoride and a 47 s reaction temperature in *dry* DMSO solvent.

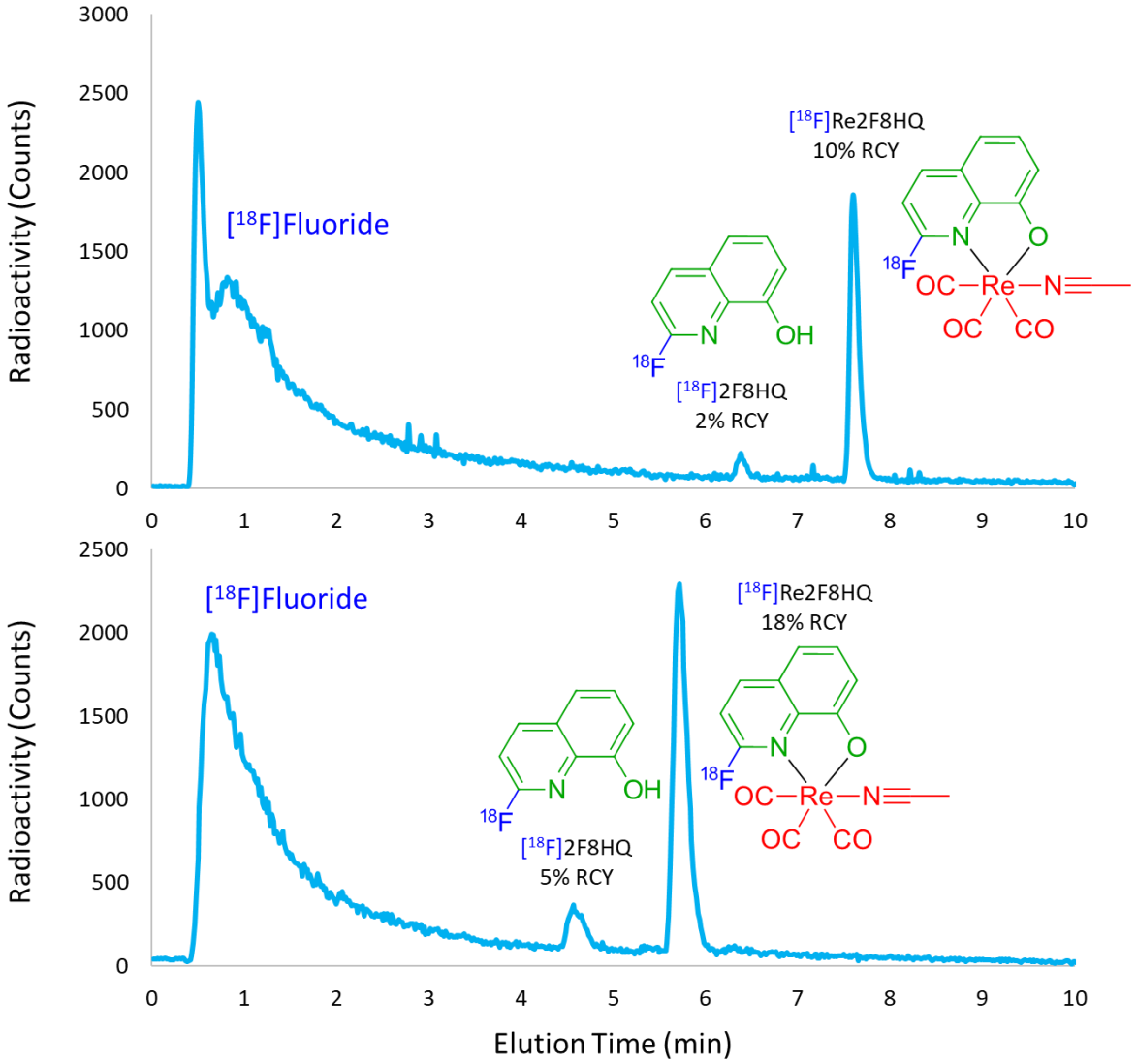

Figure 198. Radiochromatograms obtained using two different chromatographic conditions for two separate experiments affording the maximum RCYs for **[^{18}F]2F8HQ** and **[^{18}F]Re2F8HQ** using 0.80 µmol of **Re2Cl8HQ**, 29±10 MBq of [^{18}F]fluoride, a reaction time of 468 s (7.80 mins) and a reaction temperature of 190 °C. The experiment analysed by the standard chromatographic conditions described in the experimental section (top) afforded 10% RCY of **[^{18}F]Re2F8HQ** (7.58 min) and 2% RCY of **[18F]2F8HQ** (6.32 min). Whereas the experiment analysed with the initial 95% water phase held for only 1 min (bottom) afforded 18% RCY of **[^{18}F]Re2F8HQ** (5.72 mins) and 5% RCY of **[^{18}F]2F8HQ**.

The approach undertaken by Liang, *et al.* to synthesis the [^{18}F]CABS13 Alzheimer's disease diagnostic agent is shown in Figure 199.[104] Beginning with **2Cl8HQ**, the group first protected the alcohol using benzyloxymethyl chloride. This then afforded the benzyloxymethyl protected precursor which was subsequently reacted with TEA [^{18}F]fluoride in DMF solution at 140 °C for 15 mins, allowing nucleophilic aromatic substitution for [^{18}F]fluoride to occur in exchange for the chloro leaving group. Thereafter, a second reaction was required to deprotect the resulting radioproduct. The fluorine-18 labelled benzyloxymethyl protected quinoline was treated with TFA in DMF solution at 130 °C for 10 mins to afford the desired **[^{18}F]CABS13** nuclear medicine. Repeat analyses revealed an RCY of 19±5% for the radiotracer. In contrast, the work described herein as also shown in Figure 199, complexed the **2Cl8HQ** ligand to a source of pentacarbonylchlororhenium(I) to acquire the **Re2Cl8HQ** precursor. Fluorine-18 radiolabelling of this precursor required only a single reaction step to afford the **[^{18}F]CABS13** tracer while consuming lesser reagents and requiring a comparatively quicker reaction time of only 7.8 mins. Despite these advantages, however, only 5% RCY of **[^{18}F]CABS13** was able to be afforded, and thus did not improve substantially on the method developed by Liang, *et al.*

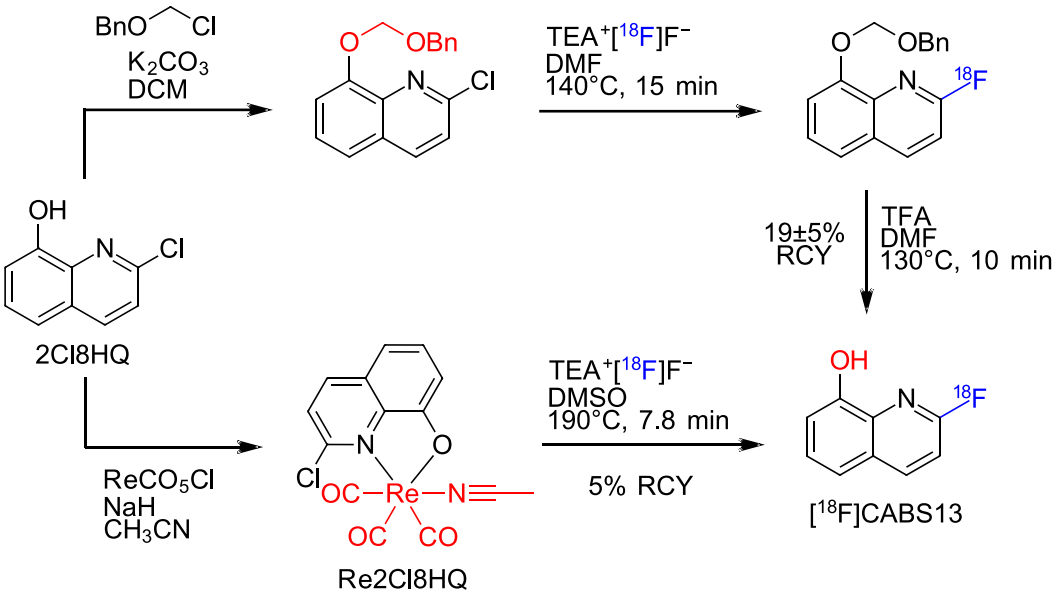

Figure 199. Comparison of the radiosynthetic routes used to obtain the **[^{18}F]CABS13** Alzheimer's disease imaging agent performed by Liang, *et al.* and in this work. While the multiple step method used by Liang, *et al.* required at least 25 mins of synthesis and more reagents (top) it nonetheless produced **[^{18}F]CABS13** in 19±5% RCY.[104] Whereas using the single step rhenium complexation-dissociation approach described herein required less than 8 mins with fewer reagents, though only produced **[^{18}F]CABS13** in 5% RCY at most.

Additional experiments were also performed, whereupon the radiofluorinations of the **Re2Cl8HQ** precursor were undertaken in *wet* conditions (i.e. a 10% v/v content was present in the DMSO solvent). These conditions applied the same precursor amount (0.08 µmol), radioactivity (29±10 MBq) and reaction time (47 s) as the standard *dry* reaction experiments. Figure 200 plots the RCY attained for each experiment against the reaction temperature which varied in 20 °C increments from 50 to 190 °C. A noticeable difference is that **[^{18}F]2F8HQ** did not form at all from these reactions, with **[^{18}F]Re2F8HQ** being the only observable radioproduct. The RCY of **[^{18}F]Re2F8HQ** was 0% for the first three experiments tested at 50 , 70 and 90 °C. Thereafter the RCY increased to 1% at 110 °C, 2% at 130 °C and 3% at 150 °C. Overall, the reaction conditions afforded no more than 4% RCY of **[^{18}F]Re2F8HQ** at 190 °C. Modifications to the flow rate of the reaction afforded 3% RCY and 4% RCY of [^{18}F]**Re2F8HQ** at flow rates of 5 µL.min^{-1} and 2 µL.min^{-1} (187 s and 468 s), respectively,

when holding the temperature at 190 °C with the other reaction parameters kept the same. Thus, alternatively the **Re2Cl8HQ** precursor amount was increased to 0.80 µmol while applying a flow rate of 4 µL.min^{-1} (234 s) at 190 °C with the same amount of [^{18}F]fluoride (29±10 MBq) applied. While the reaction produced significantly more of **[^{18}F]Re2F8HQ** with an RCY of 10%, it also produced a small 2% RCY of **[^{18}F]2F8HQ**. Hence, demonstrating that the [^{18}F]CABS13 Alzheimer's disease imaging agent can be produced under non-azeotropically dried conditions, but that such conditions notably inhibit the yield produced *via* the rhenium complexation-dissociation approach.

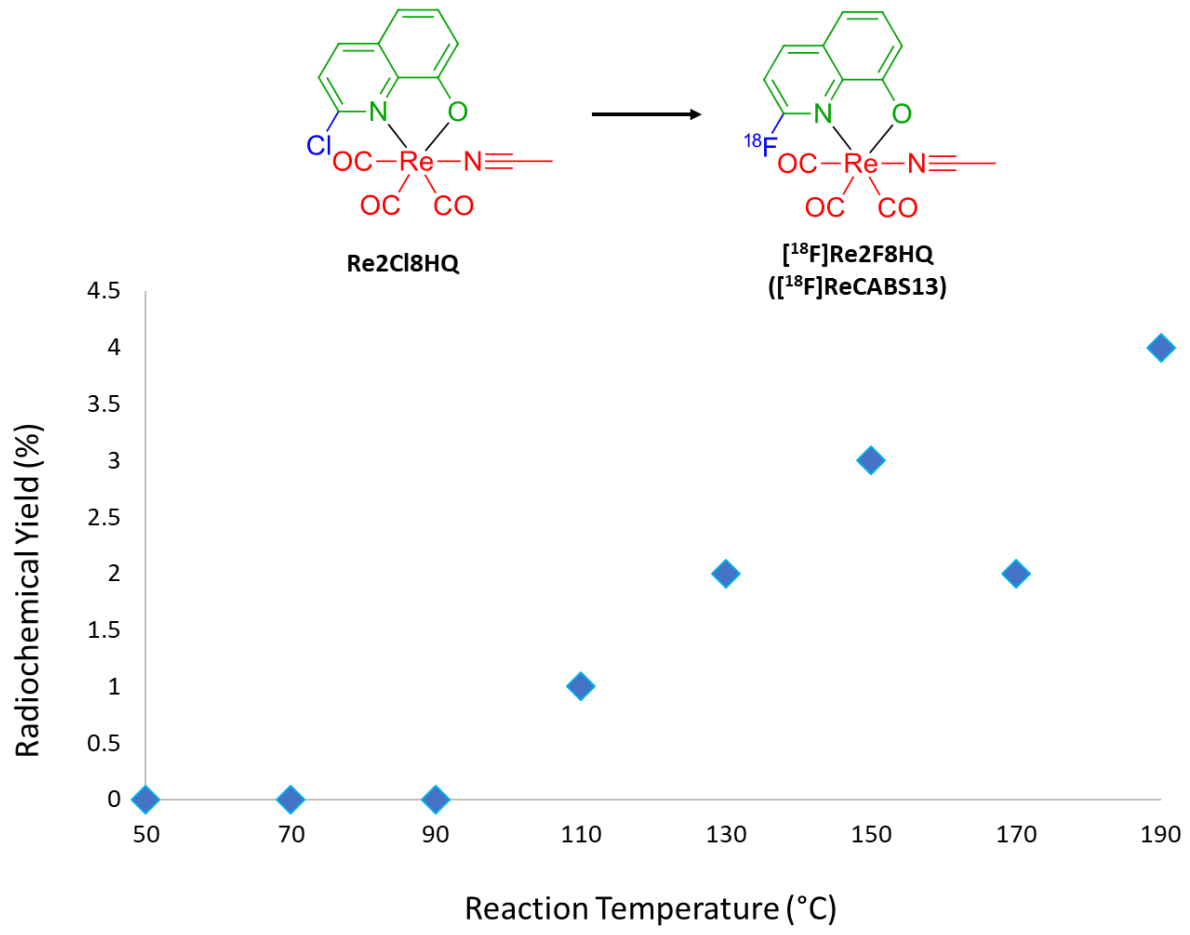

Figure 200. RCY of **[^{18}F]Re2F8HQ** ([^{18}F]ReCABS13) synthesised from the **Re2Cl8HQ** precursor under *wet* conditions as a function of reaction temperature while employing the same reaction conditions of 0.08 µmol of the **Re2Cl8HQ** precursor, 29±10 MBq of [^{18}F]fluoride and a 47 s reaction temperature in *wet* DMSO solvent. **[^{18}F]2F8HQ** ([^{18}F]CABS13) did not form from these reactions.

5.2.2 An Alternative [^{18}F]5-Fluoro-8-Hydroxyquinoline Radiotracer for Alzheimer's Disease PET Imaging

A 2015 study performed by Liang, *et al.* sought to test several fluorinated 8-hydroxyquinoline analogues of CABS13 towards validating the metal hypothesis for Alzheimer's disease.[100] In this study it was shown that positioning the fluorine atom elsewhere on the quinoline aromatic ring was able to improve properties for an Alzheimer's diagnostic agent in some cases. Among the molecules tested **5F8HQ** had a half maximal effective concentration (EC_{50}) of 21.5±15.9 µmol.L^{-1} in a study assessing the concentration of 8-hydroxyquinoline compounds required to disaggregate zinc-induced Aβ oligomers, whereas **CABS13** required concentrations greater than 120 µmol.L^{-1}. Greater copper uptake within an *in vitro* neuronal cell model (SH-SY5Y cells) was also observed when treated with 20 µMol.L^{-1} of **5F8HQ** for 6 hours than compared to the same concentration of **CABS13**, with approximately 6 times the concentration of cellular metal measured relative to **CABS13** and the basal control as determined by inductively coupled plasma (ICP) mass spectrometry analysis. Despite these *in vitro* studies which suggested that **5F8HQ** could have been a superior medicine for the treatment of Aβ plaques over **CABS13**, the drug was not radiolabelled due to the difficulties associated with incorporating the fluorine-18 radioisotope in the 5-position of the molecule. Thus, it was hypothesised that the rhenium complexation-dissociation approach explored previously with **[^{18}F]CABS13** and the radiofluorinated 2-2'-bipyridine analogues could provide an electron withdrawal effect and simultaneous protection of the alcohol in the 8-position which would allow for the previously unachievable **[^{18}F]5F8HQ** for the potential PET imaging and dissociation of Aβ plaques in Alzheimer's disease. Towards testing this hypothesis, the non-radioactive standards of **Re5F8HQ** and **5F8HQ** were injected onto the radioHPLC to determine the retention times whereby the radioproducts would be expected to elute. Figure 201 shows the retention time

determined for these two compounds when running the standard chromatographic conditions though omitting the initial 2 mins of constantly held 95% water in acetonitrile in the method (thus resulting in substantially shifted retention times compared to the **Re2F8HQ** and **Re5F8HQ** chromatographic results). Applying this method resulted in retention times of 3.42 mins and 5.87 mins for **5F8HQ** and **Re5F8HQ**, respectively. A series of experiments were then performed which used 0.08 µmol of a **Re5Cl8HQ** precursor, 29±10 MBq of [^{18}F]fluoride and a 47 s reaction time while tuning the reaction temperature from 50 to 190 °C in 20 °C increments. Figure 203 plots the RCYs for each of these reactions performed in *dry* DMSO against the reaction temperature. 2% RCY of **[^{18}F]Re5F8HQ** was found to form from all experiments with reaction temperatures between 50 and 100 °C. 3% RCY of **[^{18}F]Re5F8HQ** was then achieved at reaction temperatures of 130 and 150 °C, which then decreased to 2% RCY at 170 °C and 1% RCY at 190 °C. Meanwhile, no **[^{18}F]5F8HQ** was found to form at reaction temperatures of 50 and 70 °C, though thermal dissociation of **[^{18}F]Re5F8HQ** enabled the radiosynthesis of **[^{18}F]5F8HQ** in 1% RCY at all temperatures of 90 °C and higher. Figure 202 shows an example radiochromatogram obtained at 150 °C which afforded 1% RCY and 5% RCY of **[^{18}F]Re5F8HQ,** respectively. The effect of the change of flow rate on the RCY of the radioproducts was also tested, as was also performed for the CABS13 and bipyridine analogues. Unfortunately, adjusting the flow rate to 5 µL.min^{-1} and 2 µL.min^{-1} at 190 °C afforded only 1% RCY of **[^{18}F]5F8HQ** and none of the **[^{18}F]Re5F8HQ** radioproduct in both cases. Adjusting the flow rate to 4 µL.min^{-1} at 190 °C while increasing the precursor amount to 0.80 µmol produced no RCY of **[^{18}F]5F8HQ** nor **[^{18}F]Re5F8HQ**. The same reactions were also performed using *wet* DMSO to assess the differences in RCY of the radioproducts produced. Only **[^{18}F]Re5F8HQ** was obtained from the reactions applying a 20 µL.min^{-1} flow rate with 29±10 MBq of [^{18}F]fluoride and 0.08 µmol of the **Re5Cl8HQ** precursor. Figure 204 plots the formation of **[^{18}F]Re5F8HQ** as a function of the reaction temperature ranging from

50 to 190 °C. The RCY of **[^{18}F]Re5F8HQ** fluctuated between 0% and 1% RCY for reaction temperatures between 50 °C and 130 °C. Thereafter the RCY of **[^{18}F]Re5F8HQ** increased to 2% RCY at 150 and 170 °C and finally increased to 3% RCY at 190 °C. Adjusting the flow rate to 5 and 2 µL.min^{-1} at 190 °C still only afforded 3% RCY of **[^{18}F]Re5F8HQ** and using a ten-fold equivalence of the **Re5Cl8HQ** precursor with an applied flow rate of 4 µL.min^{-1} yielded only 2% RCY, each in the absence of any radiolabeled **[^{18}F]5F8HQ** ligand.

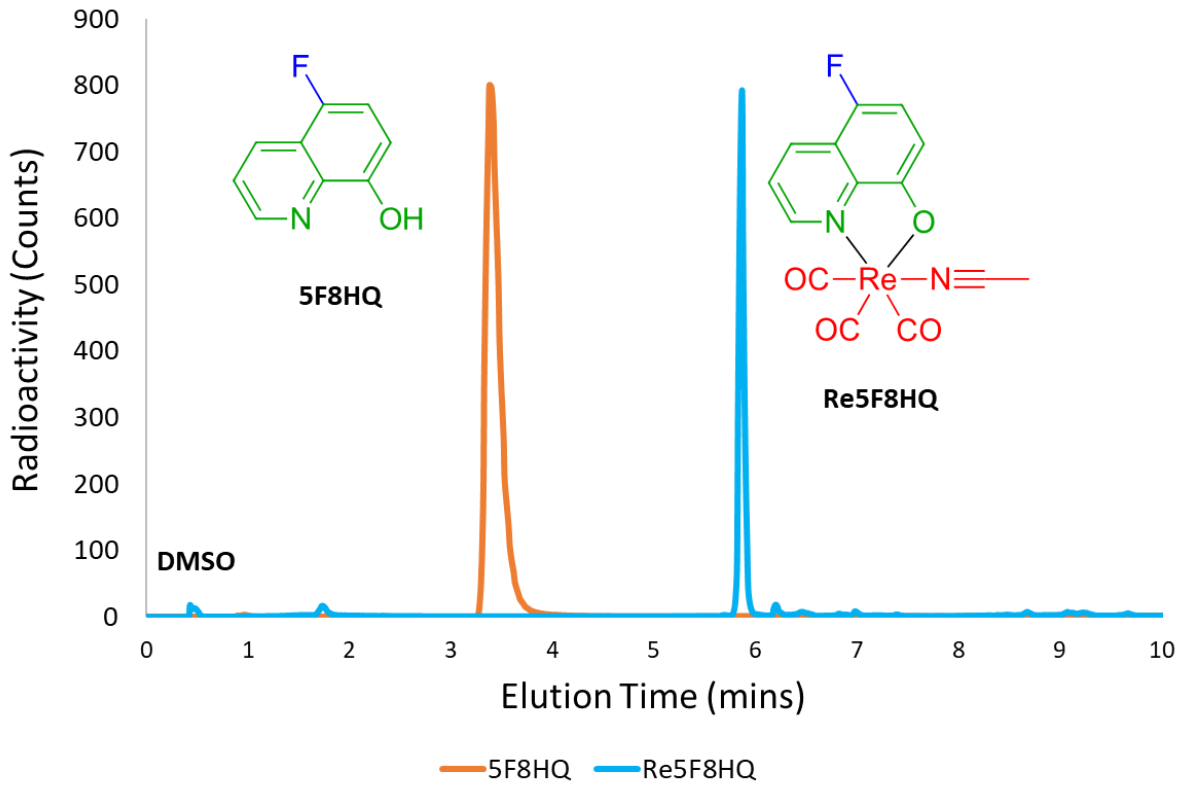

Figure 201. Superimposed UV-absorbance profiles for the non-radioactive standards of **5F8HQ** (orange trace) and **Re5F8HQ** (blue trace) providing retention times of 3.42 mins and 5.87 mins for both compounds, respectively, which were used to assign the identity of the radioproducts analysed by radioHPLC. These retention times were acquired from the standard chromatographic conditions omitting 2 mins of the initial hold of the 95% water mobile phase.

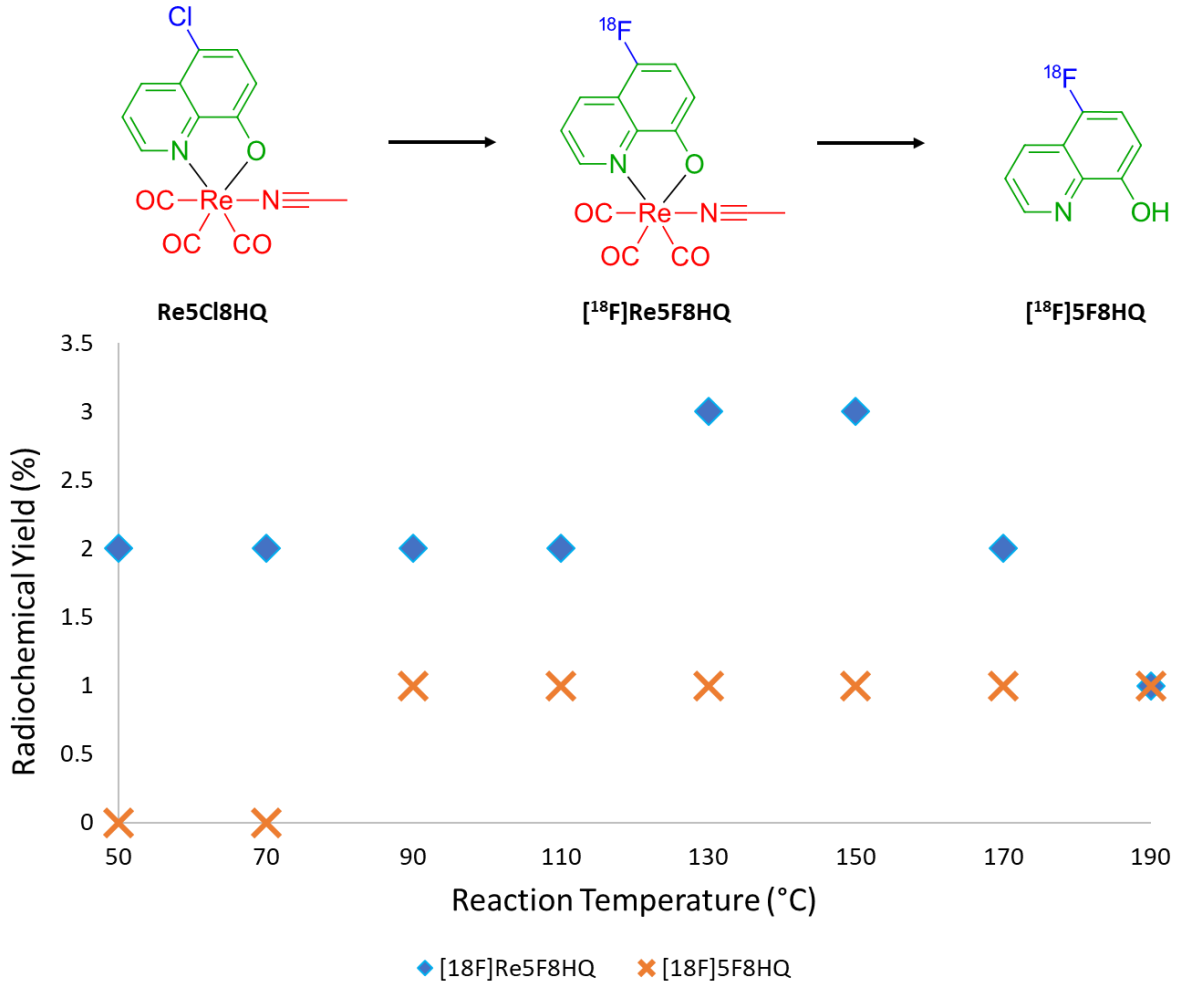

Figure 202. RCY of **[^{18}F]Re5F8HQ** (blue diamonds) and **[^{18}F]5F8HQ** (orange crosses) synthesised from the **Re5Cl8HQ** precursor as a function of reaction temperature while employing the same reaction conditions of 0.08 µmol of the **Re5Cl8HQ** precursor, 29±10 MBq of [^{18}F]fluoride and a 47 s reaction temperature in *dry* DMSO solvent.

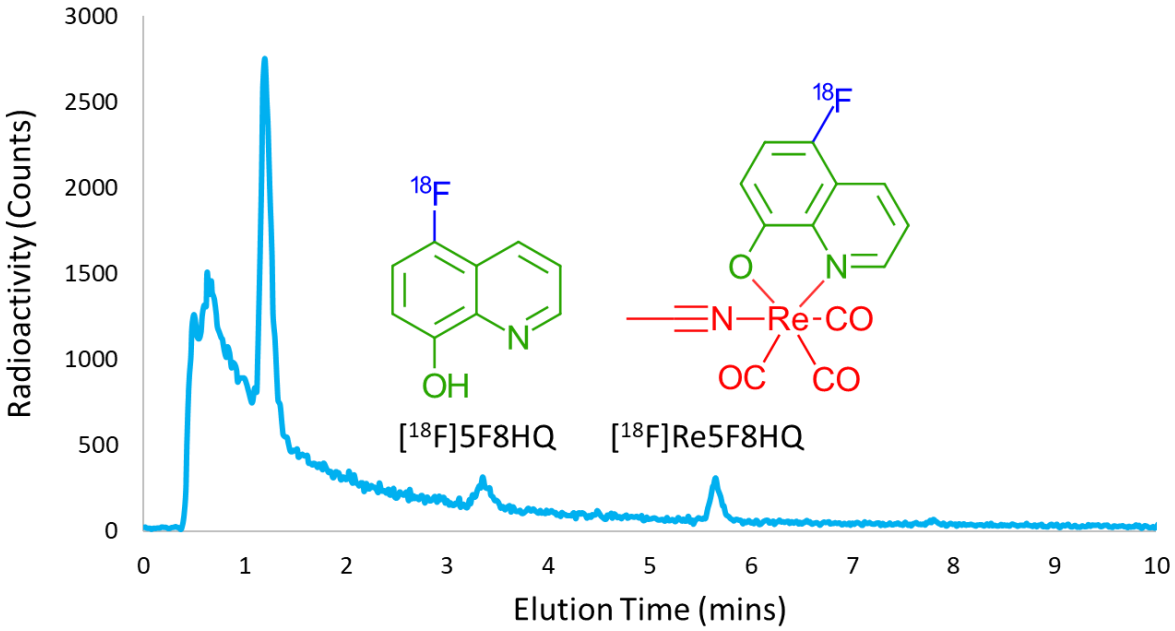

Figure 203. Radiochromatogram obtained for the radiofluorination of 0.08 µmol of **Re5Cl8HQ** precursor in DMSO solution with 29±10 MBq of [^{18}F]fluoride for 47s in *dry* DMSO solvent at 150 °C. These conditions afforded 1% RCY of **[^{18}F]5F8HQ** and 5% **[^{18}F]Re5F8HQ** eluting at 3.4 and 5.7 mins, respectively.

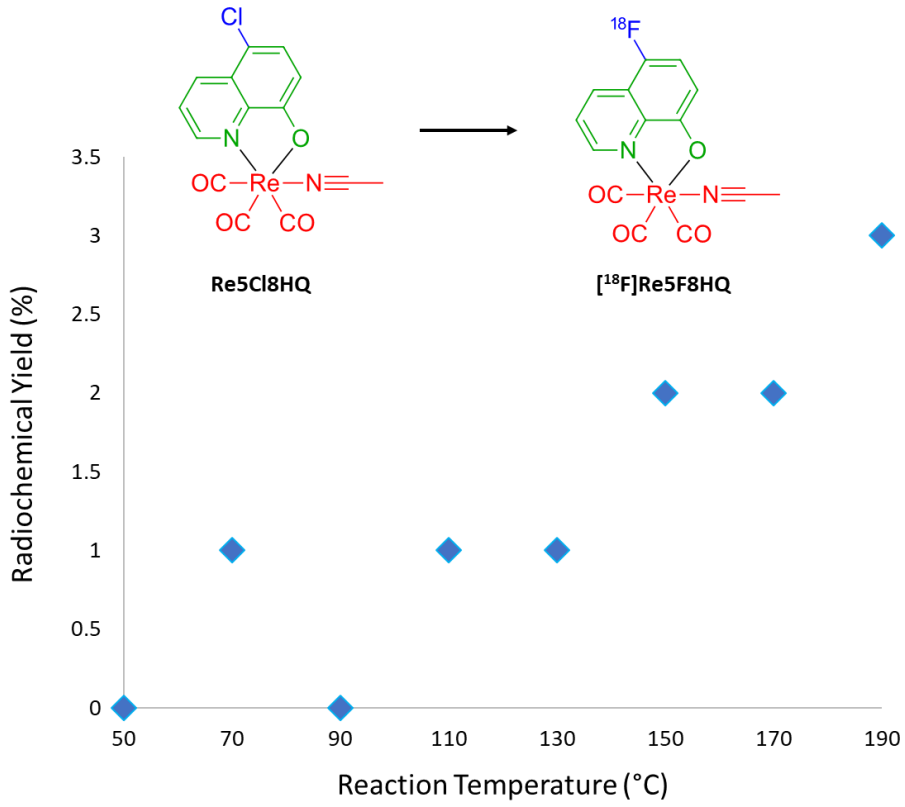

Figure 204. RCY of **[^{18}F]Re5F8HQ** formed from the **Re5Cl8HQ** precursor as a function of reaction temperature under *wet* conditions. Reaction conditions involved 0.08 µmol of precursor, 29±10 MBq of [^{18}F]fluoride and a 47 s reaction time in *wet* DMSO solvent. No **[^{18}F]5F8HQ** was found to form from these reactions.

Owing to the poor RCYs of **[^{18}F]Re5F8HQ** and thus **[^{18}F]5F8HQ** obtained using the **Re5Cl8HQ** precursor, the same experiments were performed using an alternative **Re5NO$_2$8HQ** precursor. Radiofluorinations were hypothesised to afford greater RCYs using this precursor due to the greater electron withdrawing effect of the nitro group, which was also a better leaving group for nucleophilic aromatic substitution for [^{18}F]fluoride. The plot for the RCY of **[^{18}F]Re58HQ** and the dissociated **[^{18}F]5F8HQ** radioproduct per reaction temperature using the standard radiolabelling conditions (0.08 µmol of precursor, 29±10 MBq of radioactivity and 47 s reaction time) is shown in Figure 205. While only 1% RCY of **[^{18}F]Re58HQ** was achieved at 50 and 70 °C, the use of the **Re5NO$_2$8HQ** afforded significantly more of the **[^{18}F]Re5F8HQ** radioproduct than compared with the **Re5Cl8HQ** precursor, with 4% RCY achieved at 130 and 150 °C and as much as 6% RCY achieved at 170 °C. While none of the **[^{18}F]Re58HQ** labelled ligand formed at temperatures equal to and lower than 110 °C, 1% RCY was indeed found to form from 130 to 170 °C and produced as much as 2% RCY at 190 °C. Figure 206 shows an example radiochromatogram obtained at 170 °C which depicts the radiodetection of **[^{18}F]5F8HQ** in 1% RCY at 3.4 mins and **[^{18}F]Re5F8HQ** at 5.7 mins in 6% RCY. Non-azeotropically dried conditions were also trialed, as was consistently tested for the former precursors. Performing the same experiments using the **Re5NO$_2$8HQ** precursor in *wet* DMSO solvent afforded the plot in Figure 207, which shows the RCY of the radioproducts formed as a function of temperature using the standard reaction parameters (0.08 µmol of precursor, 29±10 MBq of radioactivity and 47 s reaction time). Here the RCY of **[^{18}F]Re5F8HQ** increased to 1% at reaction temperatures of 70 and 90 °C, increased to 2% at temperatures of 130 and 150 °C, and finally increased to 3% and 4% RCY at temperatures of 170 and 190 °C, respectively. The **[^{18}F]5F8HQ** radioligand only dissociated in 1% RCY at 190 °C, however. Decreasing the flow rate to 5 µL.min^{-1} at 190 °C resulted in 3% RCY of **[^{18}F]Re5F8HQ** and 2% of **[^{18}F]5F8HQ**. Whereas decreasing the flow rate to 2 µL.min^{-1} at

190 °C produced **[^{18}F]Re5F8HQ** in 4% RCY and **[^{18}F]5F8HQ** in 2% RCY. The final experiment utilising **Re5NO$_2$8HQ** (ten-fold equivalence of 0.80 µmol) under *wet* DMSO conditions applied a flow rate of 4 µL.min^{-1} and afforded **[^{18}F]Re5F8HQ** in 2% RCY and **[^{18}F]5F8HQ** in 1% RCY. Thus, while only comparatively low RCYs no greater than 2% could be attained, the rhenium complexation-dissociation approach was still able to afford the desired **[^{18}F]5F8HQ** radioligand which was unable to be produced using traditional [^{18}F]fluoride substitution techniques.

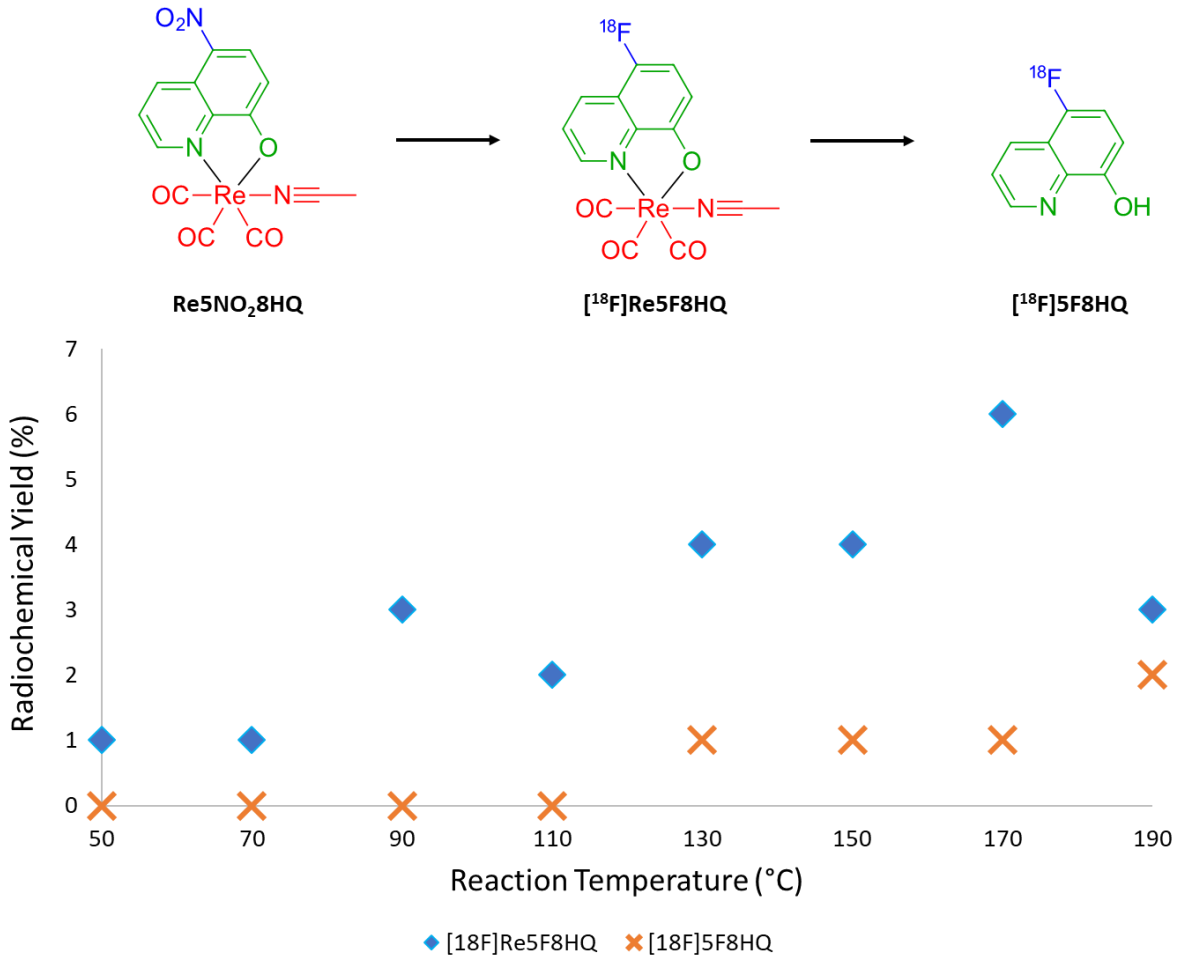

Figure 205. RCY of **[^{18}F]Re5F8HQ** (blue diamonds) and **[^{18}F]5F8HQ** (orange crosses) synthesised from the **Re5NO$_2$8HQ** precursor as a function of reaction temperature while employing the same reaction conditions of 0.08 µmol of the **Re5NO$_2$8HQ** precursor, 29±10 MBq of [^{18}F]fluoride and a 47 s reaction temperature in *dry* DMSO solvent.

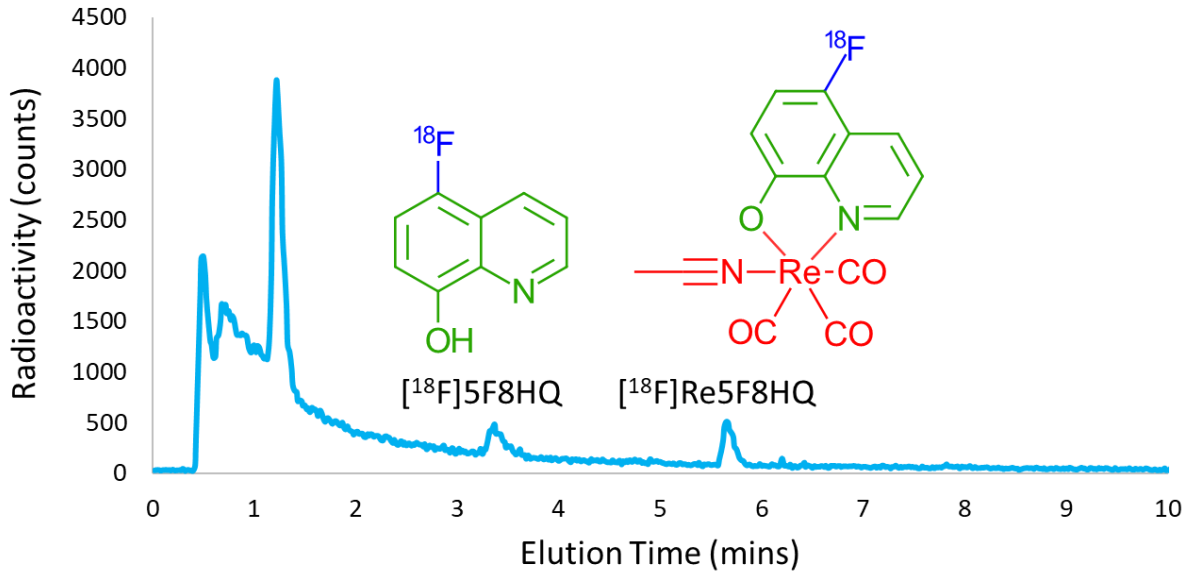

Figure 206. Radiochromatogram obtained for the radiofluorination of 0.08 µmol of **Re5NO$_2$8HQ** precursor in DMSO solution with 29±10 MBq of [^{18}F]fluoride for 47s in *dry* DMSO solvent at 170 °C. These conditions afforded 1% RCY of **[^{18}F]5F8HQ** and 6% **[^{18}F]Re5F8HQ** eluting at 3.4 and 5.7 mins, respectively.

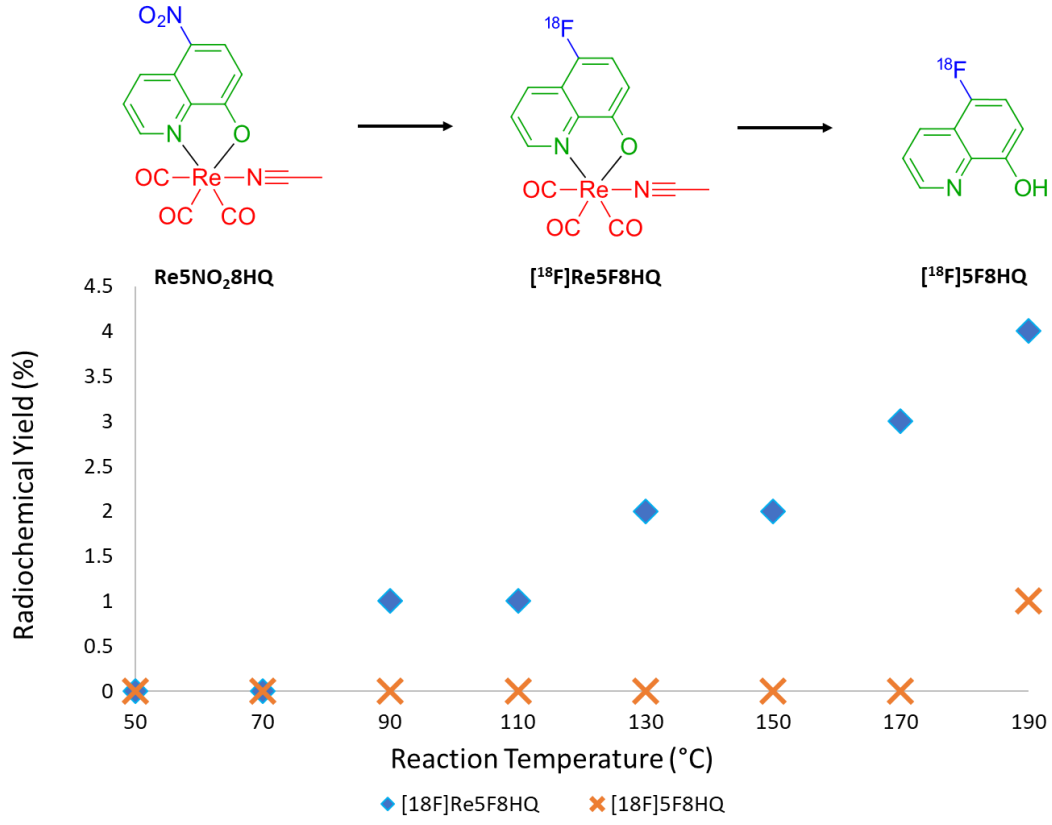

Figure 207. RCY of **[^{18}F]Re5F8HQ** (blue diamonds) and **[^{18}F]5F8HQ** (orange crosses) synthesised from the **Re5NO$_2$8HQ** precursor under *wet* conditions as a function of reaction temperature while employing the same reaction conditions of 0.08 µmol of the **Re5NO$_2$8HQ** precursor, 29±10 MBq of [^{18}F]fluoride and a 47 s reaction temperature in *wet* DMSO solvent.

CHAPTER SIX

RHENIUM-ETHENESULFONYL FLUORIDE CONJUGATION FOR PET-OPTICAL TRACER DEVELOPMENT

6.1 Ethenesulfonyl Fluoride and the Non-Radioactive Synthesis of its Rhenium Complexed Analogue

Ethenesulfonyl Fluoride (ESF) is a small molecule reported as one of the strongest Michael acceptors in the current literature.[105-108] The fluorine-18 analogue of this compound, [^{18}F]ESF, was developed in ANSTO laboratories for use as a prosthetic group for radiolabelling proteins, amino acids and other biomolecules.[109, 110] However, biomolecular conjugations to [^{18}F]ESF demonstrated poor *in vivo* stability overall, leading to its alternative use as a radiofluoride relay agent. Nonetheless, conjugation of [^{18}F]ESF to an amino-phenanthroline rhenium complex was hypothesised to be an alternative useful means of fluorine-18 labelling rhenium complexes for the development of PET-optical tracers. Thus, in order to test such conjugations of the radiolabelled prosthetic groups, non-radioactive standards first needed to be synthesised. Figure 208 shows the synthetic route used to obtain a model rhenium-ESF conjugate used in these experiments. The route first involved the Michael addition of ESF to 5-amino-1,10-phenanthroline (**PhenNH$_2$)** in DMF solution at room temperature, which afforded 5-N-(2-aminoethylsulfonylfluoride)-1,10-phenanthroline (**PhenESF)** in 63% yield. Subsequent complexation of **PhenESF** to bromopentacarbonylrhenium(I) then afforded bromotricarbonyl (5-N-(2-aminoehtylsulfonylfluoride)-1,10-phenanthroline)rhenium(I) (**RePhenESF**) in 79% yield. Similarly, **PhenNH$_2$** was also complexed with bromopentacarbonylrhenium(I) *via* reflux in toluene solution to afford the bromotricarbonyl(5-amino-1,10-phenanthroline)rhenium(I) (**RePhenNH$_2$**) precursor complex in 93% yield.

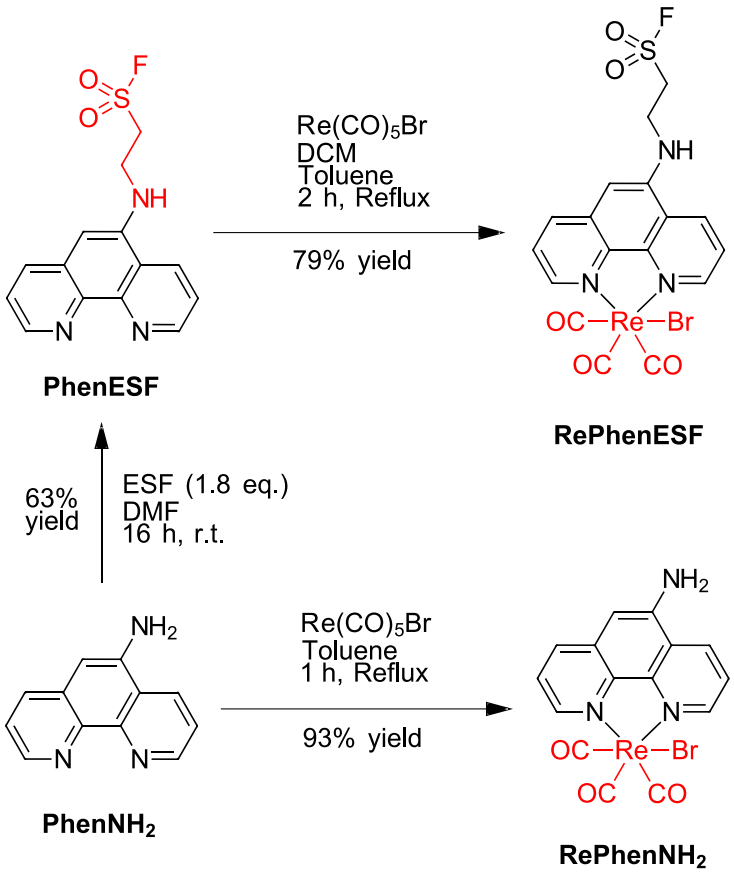

Figure 208. Synthetic route used to synthesise the non-radioactive standards **PhenESF**, *via* Michael-addition between **PhenNH$_2$**, and **RePhenESF** *via* rhenium complexation with **PhenESF**. The **RePhenNH$_2$** precursor was also synthesised *via* rhenium complexation with **PhenNH$_2$**.

6.1.1 Conjugation of ESF to 5-Amino-1,10-Phenanthroline

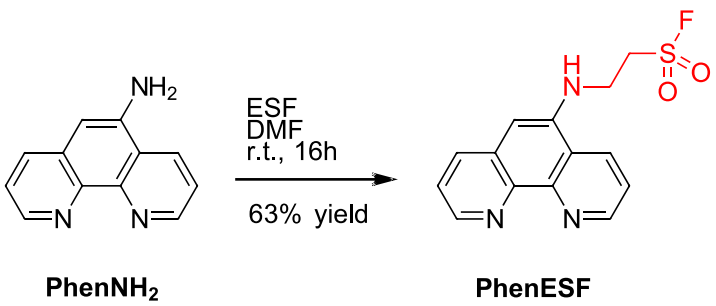

Figure 209. **PhenNH$_2$** was conjugated with ESF in DMF solution to afford **PhenESF** in 63% yield.

Masses of **PhenNH$_2$** (1.000 g, 5.128 mol, 1.0 eq.) and ESF (847.0 mg, 7.7 mol, 1.5 eq.) were dissolved in a volume of DMF (10 mL) and stirred at room temperature (24 h). The resulting orange solution was then poured into a volume of water (300 mL), causing a yellow solid to precipitate. The precipitate was isolated *via* vacuum filtration and washed with water to remove residual DMF. Further purification was achieved by dissolving the crude material in a minimum of DMSO and eluting through a 40 g, C_{18} column using a gradient mobile phase composition of 0.1% TFA in water and acetonitrile (5% to 100% over 8 column volumes). The eluents containing the product were then combined, evaporated down under reduced pressure and dried by lyophilisation to attain a yellow powder (1.125g).

The ^{1}H-NMR spectrum of **RePhenESF** in DMSO-d_6 solvent provided the expected integration for twelve protons, eight of which were relatively downfield shifted corresponding to the protons in the C–H bonds of the phenanthroline ring and the N–H bond of the secondary amine as shown in Figure 210. The retaining four protons existed as two signals arising from overlapping doublets of triplets forming apparent quartets with shared coupling constants of approximately 12 and 6 Hz. The ^{13}C-NMR spectrum in Figure 211 exhibited sixteen carbon-13 resonance signals, twelve pertaining to the carbon nuclei of the phenanthroline ring and the

remaining two resonance signals for the ethyl carbon-13 nuclei forming doublets due to coupling with the fluorine-19 nucleus. The coupling is further evident in the ^{19}F-NMR spectrum of **PhenESF** in Figure 212, whereupon the triplet split resonance signal consisted of a 5.6 Hz coupling constant, closely aligned to that of the apparent quartets in the ^{1}H-NMR spectrum. Elemental analysis further affirmed the purity of the compound with 54.54% carbon, 3.63% hydrogen and 13.64% nitrogen observed against theoretical compositions of 55.07% carbon, 3.96% hydrogen and 13.76% nitrogen.

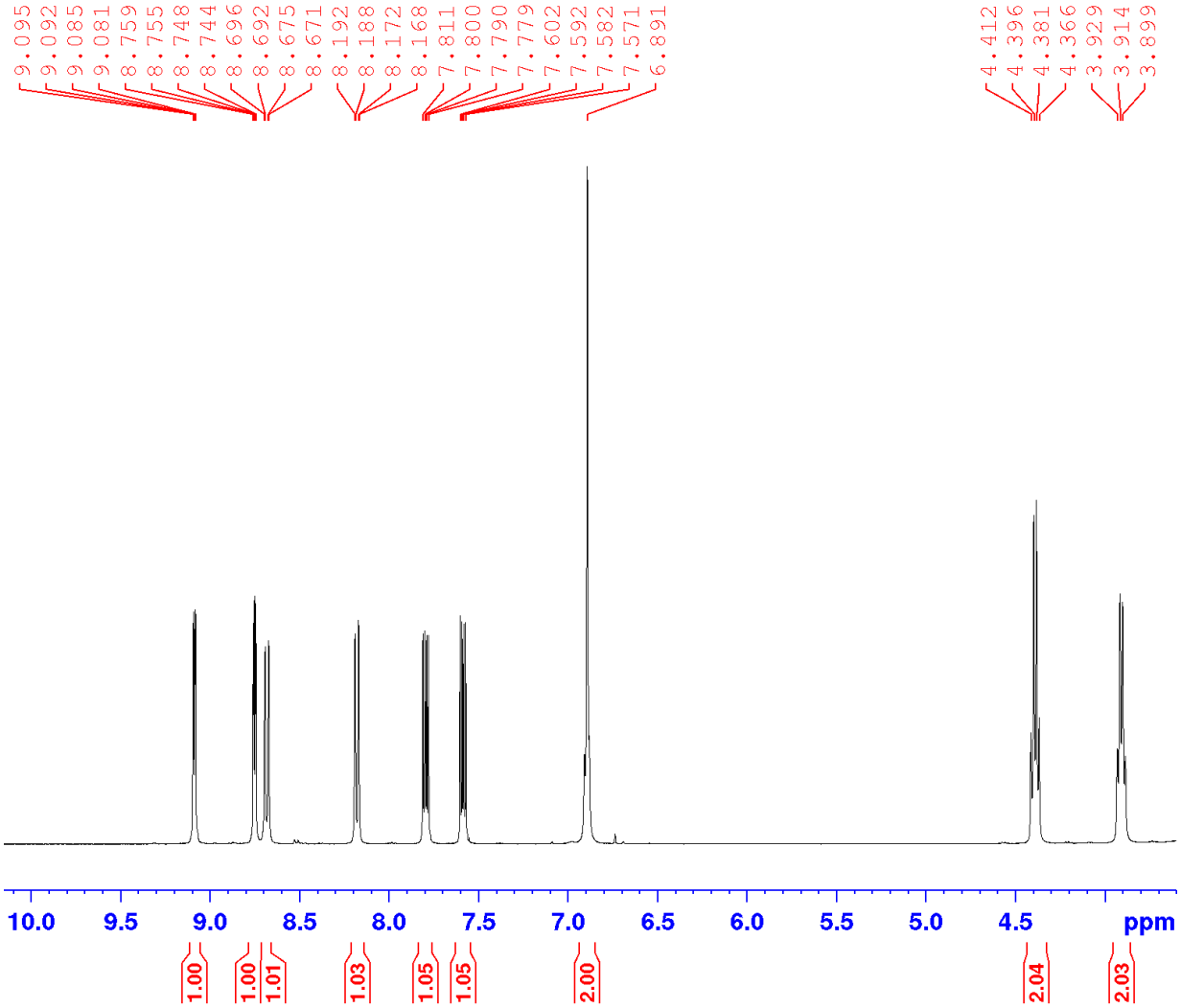

Figure 210. ^{1}H-NMR spectrum of **PhenESF** in DMSO-d_6 showing the expected integration for twelve protons (eight from the phenanthroline ring and amine, four from the ethyl group).

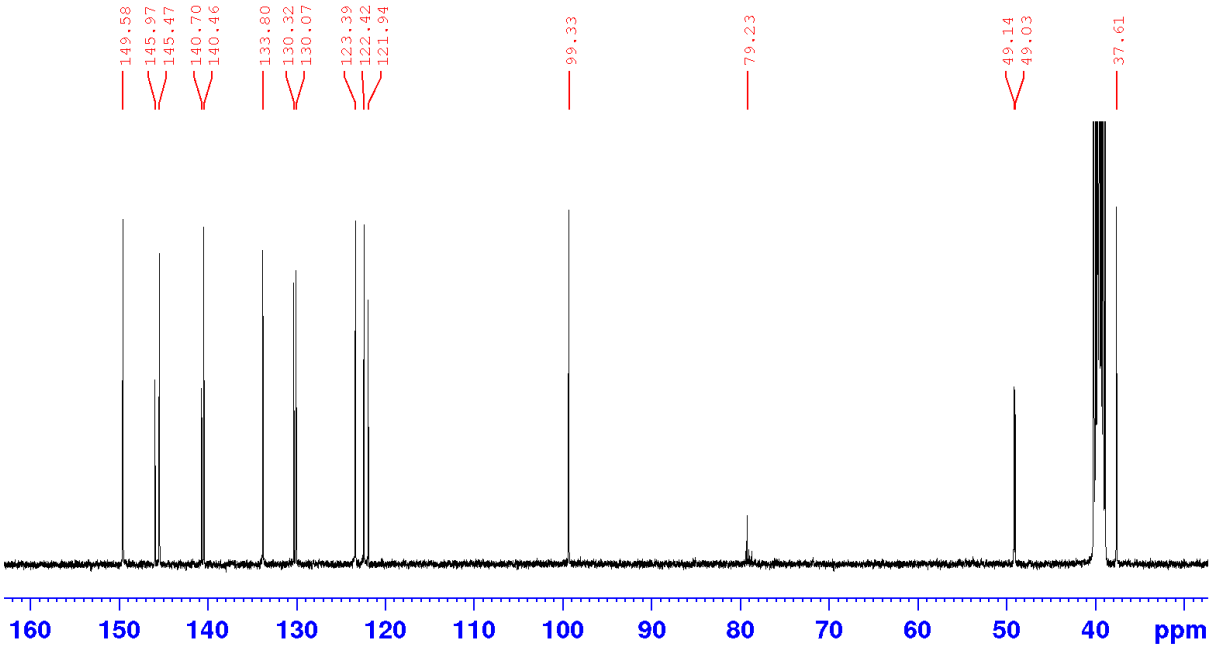

Figure 211. ^{13}C-NMR spectrum of **PhenESF** in DMSO-d_6 showing the expected sixteen carbon-13 signals (twelve from the phenanthroline ring and four from fluorine splitting of the two carbon atoms within the ethylsulfonyl fluoride group).

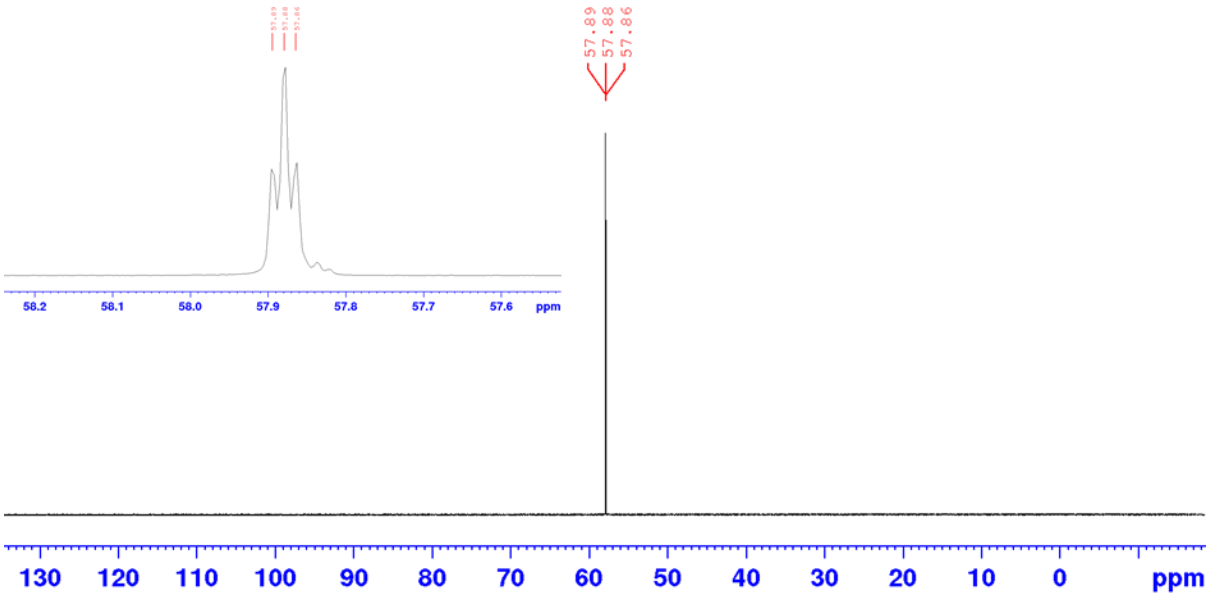

Figure 212. ^{19}F-NMR of **PhenESF** exhibiting the fluorine-19 signal at *approx.* 58 ppm and with a 5.6 Hz coupling constant closely aligned with the coupling constants observed for the ethyl protons in the ^{1}H-NMR spectrum. The expanded spectrum between 57.5-58 ppm, shown in the right-hand corner, clearly demonstrates the coupling of the fluorine-19 nucleus with the hydrogen nuclei.

6.1.2 Rhenium Complexation of the Phenanthroline-ESF Conjugate

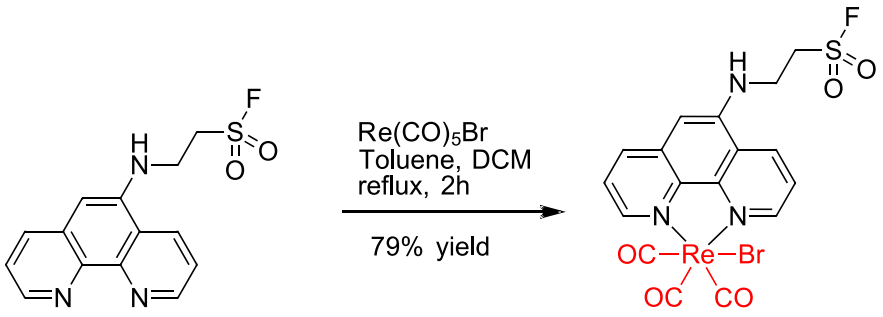

PhenESF **ReESFPhen**

Figure 213. Complexation of **PhenESF** *via* reflux with bromopentacarbonylrhenium(I) to form **RePhenESF** in 79% yield.

A mass of **PhenESF** (65.4 mg, 0.214 mmol, 1.0 eq.) was dissolved in a solution of 50% DCM in toluene (15 mL), to which an additional mass of pentacarbonylrhenium(I) bromide (79.1 mg, 0.195 mmol, 1.1 eq.) was also added. The solution was then stirred and heated at reflux (2h). The solution was left to cool to room temperature and the DCM evaporated, where after the resulting precipitate was filtered *via* vacuum filtration, washed with diethyl ether and dried under vacuum to afford a yellow powder (110.4 mg).

The ^{1}H-NMR spectrum of **RePhenESF**, shown in Figure 214, depicts the same expected integration for twelve protons as was observed in the spectrum of **PhenESF**. However each of the proton resonance signals in the **RePhenESF** spectrum was downfield shifted with respect to **PhenESF**, as shown in Figure 215, due to withdrawal of electron density from the rhenium tricarbonyl center causing the aromatic protons to be more susceptible to the external magnetic field. The ^{13}C-NMR spectrum of **RePhenESF** exhibits three carbon-13 resonance signals at 197.4, 197.3 and 189.5 ppm corresponding to the carbon atoms of the three carbonyl ligands, as shown in Figure 216. An additional sixteen signals are also observed for the fourteen other carbon-13 nuclei due to coupling between the two ethyl carbon nuclei and the fluorine-19

nucleus of the sulfonyl fluoride group. The magnetic resonance signal of this fluorine-19 nucleus is observed in the ^{19}F-NMR spectrum of **RePhenESF** in Figure 217. The FTIR spectrum of the compound exhibits the two distinctive IR absorption bands for excitation of the A'(1) C≡O stretching frequency at 2025 cm^{-1} and the concurrent excitations of the A'(2) & A'' C≡O stretching frequencies at 1919 and 1898 cm^{-1}. The N−H bond stretching frequency of the secondary amine is also observed at 3348 cm^{-1}, as well as weakly absorbing bands for the sp^2 hybridised C−H stretching frequencies at 3050 cm^{-1} and 3005 cm^{-1} in Figure 218. Additionally, the HRMS spectrum of **RePhenESF** depicts the bromine-dissociated $[M\text{-}Br]^+$ ion signal ($ReC_{17}H_{12}N_3O_5SF^+$) with *m/z* 576.00387 against a calculated ratio of *m/z* 576.00337 (Δ 0.86 ppm) for the complex incorporating the ^{187}Re isotope in 62.6% natural abundance, shown in Figure 219. An ion with *m/z* 574.00108 is also observed in this HRMS spectrum, corresponding to the same $[M\text{-}Br]^+$ ion incorporating the ^{185}Re isotope in 37.4% natural abundance. Elemental analysis further verified the purity of the complex as well as the identity of the bromo ancillary ligand, with compositions of 31.61% carbon, 1.85% hydrogen, 6.36% nitrogen, 4.79% sulfur and 12.05% bromine observed against theoretical compositions of 31.15% carbon, 1.85% hydrogen, 6.41% nitrogen, 4.89% sulfur and 12.19% bromine.

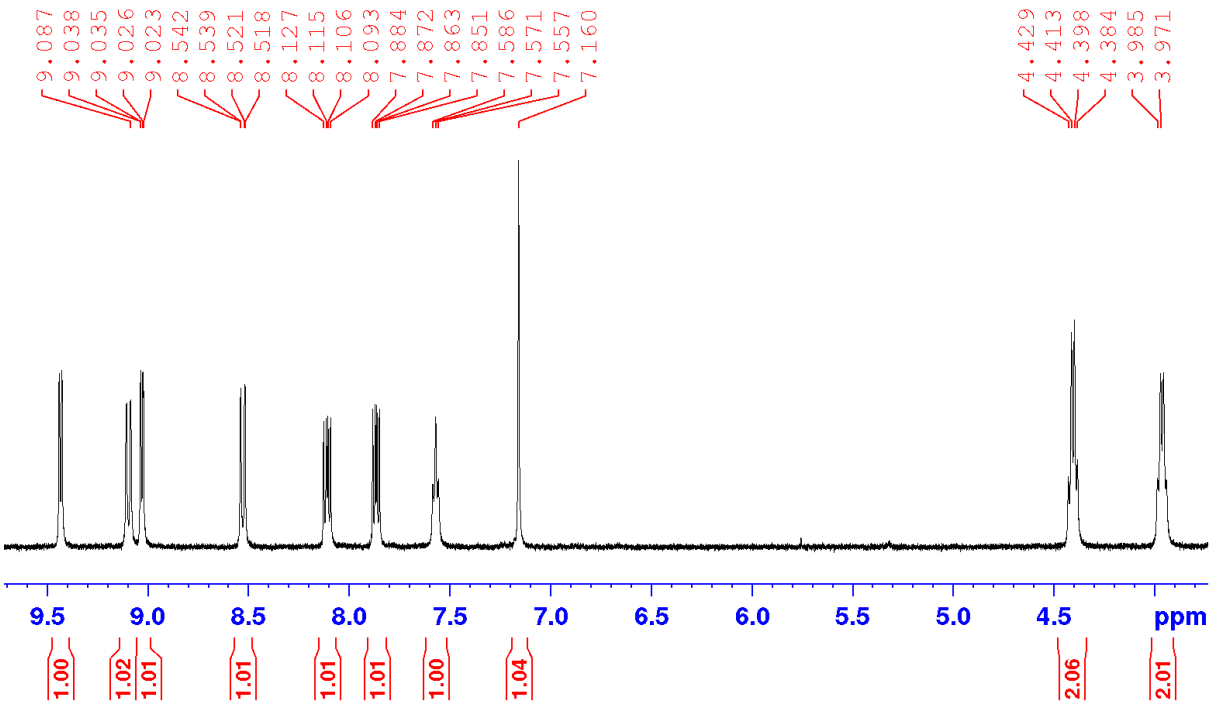

Figure 214. ^{1}H-NMR spectrum of **RePhenESF** in DMSO-d_6 showing the expected integration for twelve protons in the molecule, as well as the expected downfield chemical shifts for the aromatic protons and the relatively upfield chemical shifts of the ethyl group protons.

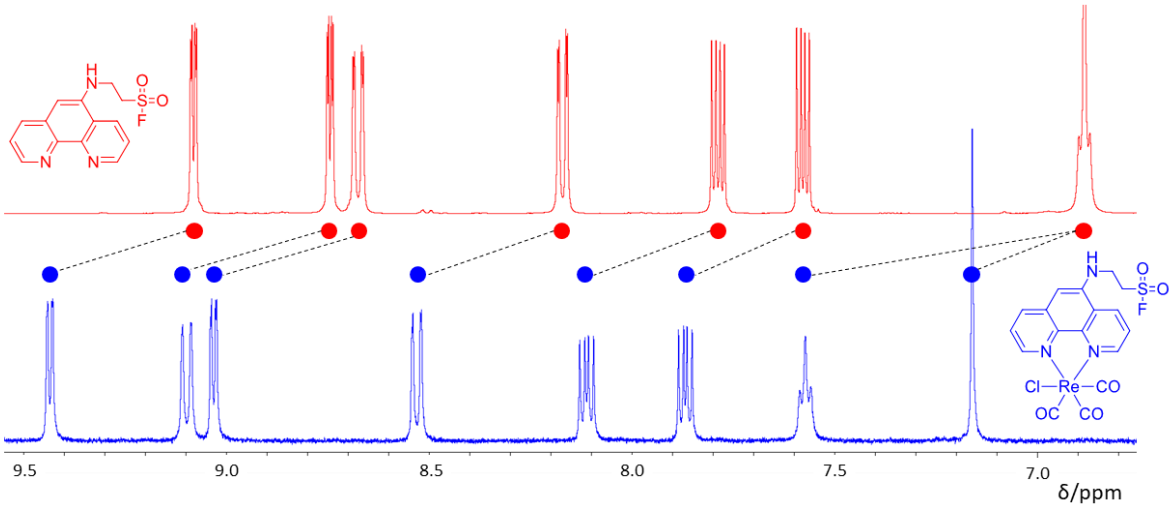

Figure 215. The magnetic resonance signals of the aromatic protons in **RePhenESF** are shifted downfield with respect to the aromatic protons in **PhenESF** in the same DMSO-d_6 solvent due to electron withdrawal of the rhenium tricarbonyl centre.

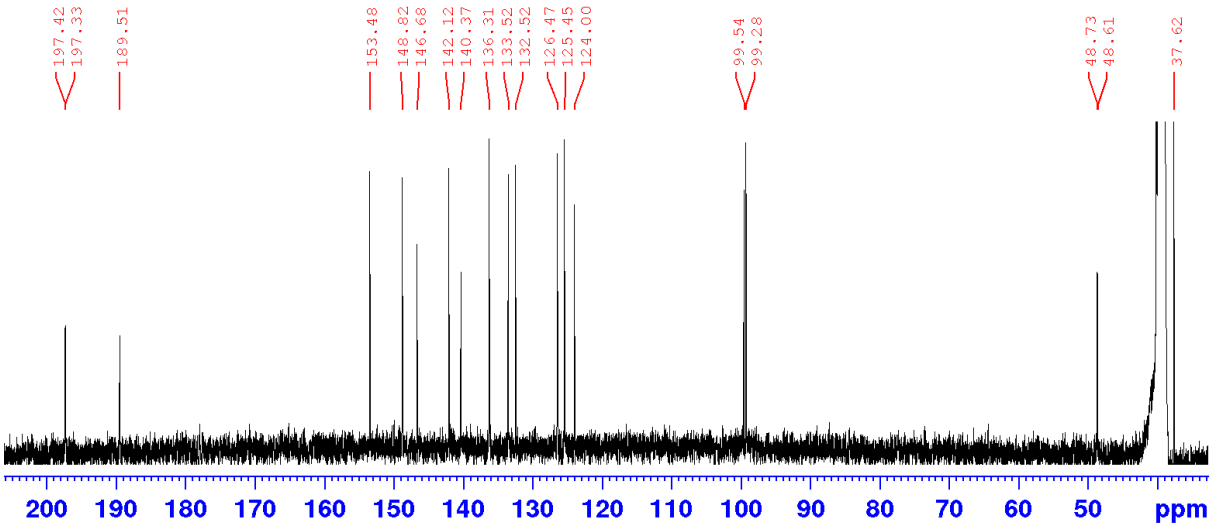

Figure 216. ^{13}C-NMR spectrum of **RePhenESF** in DMSO-d_6 exhibiting nineteen carbon-13 resonance signals, as expected given the perturbation of the carbon-13 nuclei in the three carbonyl ligands at greater than 180 ppm and the splitting of two carbon-13 nuclei in the ethyl group caused by coupling to the fluorine-19 nucleus.

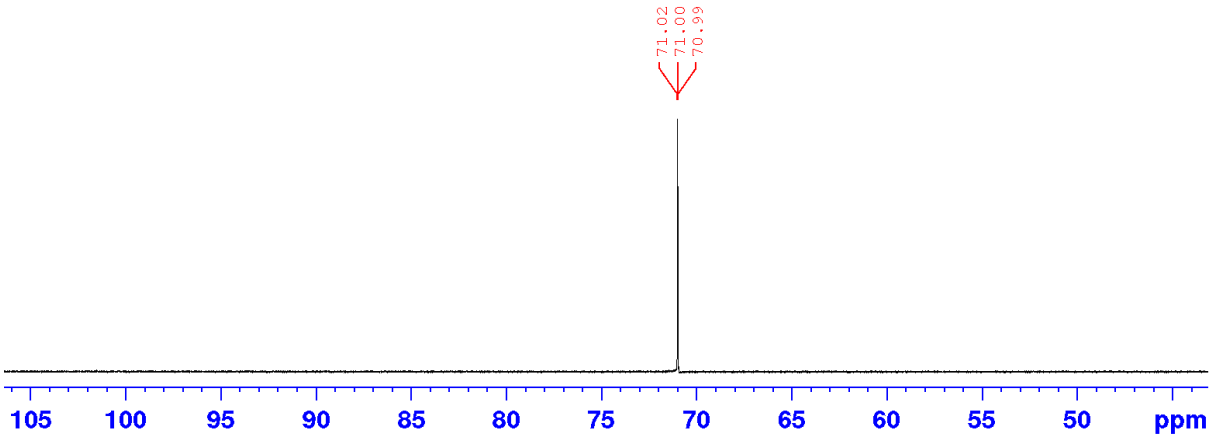

Figure 217. ^{19}F-NMR spectrum of **RePhenESF** in DMSO-d_6 solvent showing the lone magnetic resonance signal of the fluorine-19 nucleus in the molecule at 71 ppm.

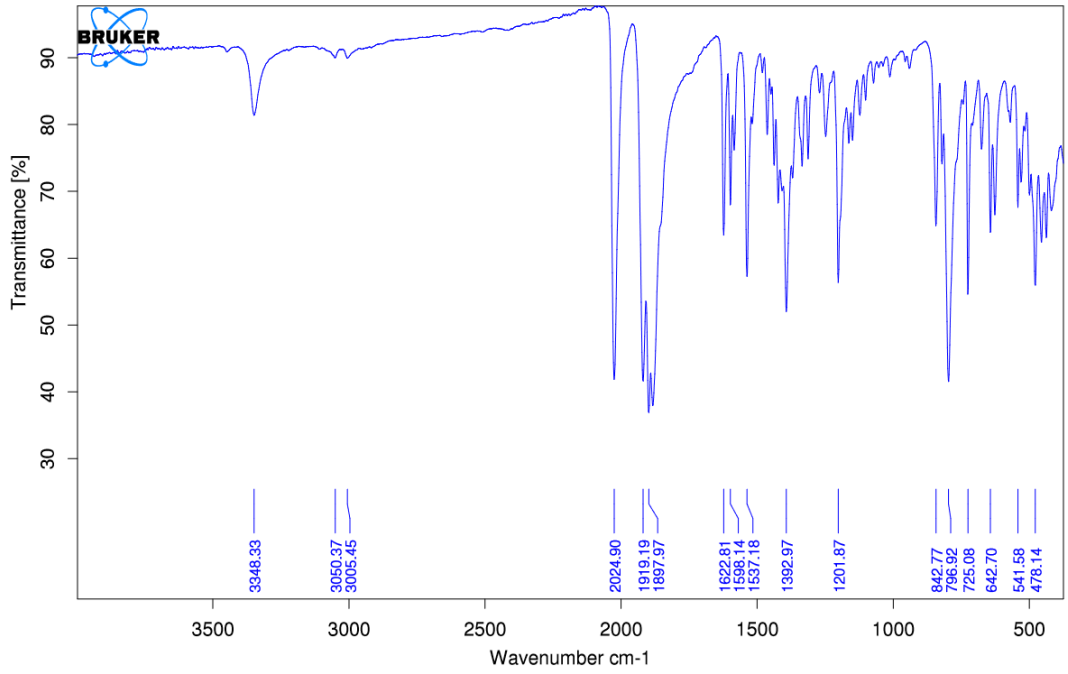

Figure 218. FTIR spectrum of **RePhenESF** exhibiting the two distinctive IR absorption bands for excitation of the A'(1) C≡O stretching frequency at 2025 cm^{-1} and overlapping excitation of the A'(2) & A'' C≡O stretching frequencies at 1919 and 1898 cm^{-1}. Excitations of sp^2 hybridised C−H stretching frequencies are also observed weakly at 3050 and 3005 cm^{-1}, alongside the N−H bond stretching vibration of the secondary amine at 3348 cm^{-1}.

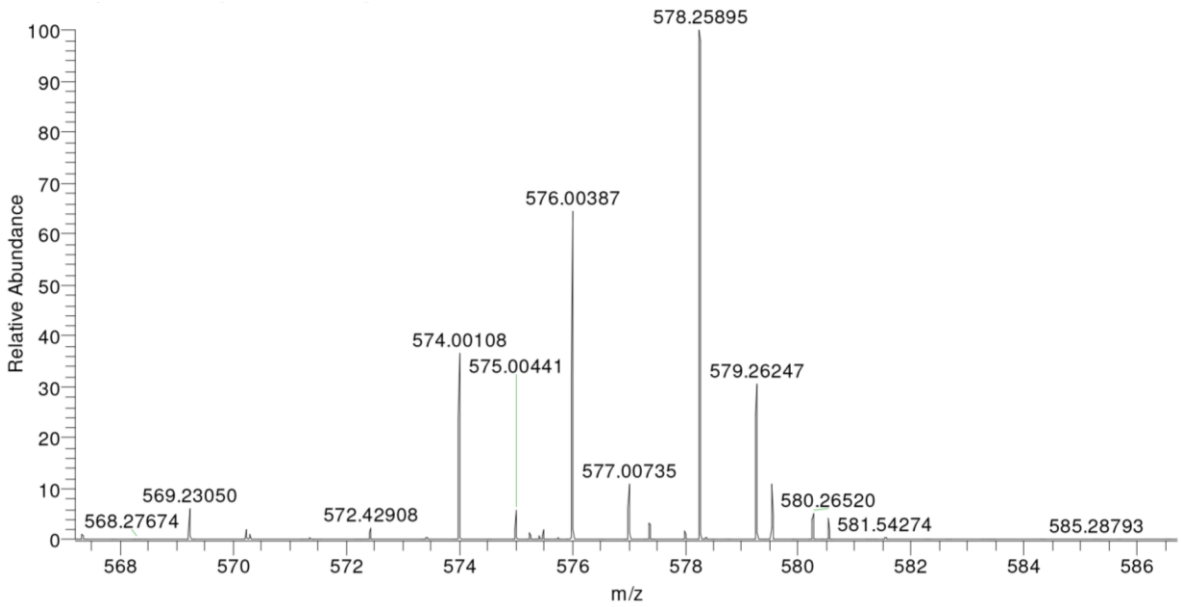

Figure 219. HRMS spectrum of **RePhenESF** depicting the bromine-dissociated $[M\text{-}Br]^+$ ion signal ($ReC_{17}H_{12}N_3O_5SF^+$) observable at *m/z* 576.00387 with a calculated ratio of *m/z* 576.00337 (Δ 0.86 ppm) for the complex incorporating the ^{187}Re isotope in 62.6% natural abundance. An additional signal with *m/z* 574.00108 is also observed for the same ion incorporating the ^{185}Re isotope in 37.4% natural abundance.

6.1.3 Rhenium Complexation of 5-Amino-1,10-Phenanthroline

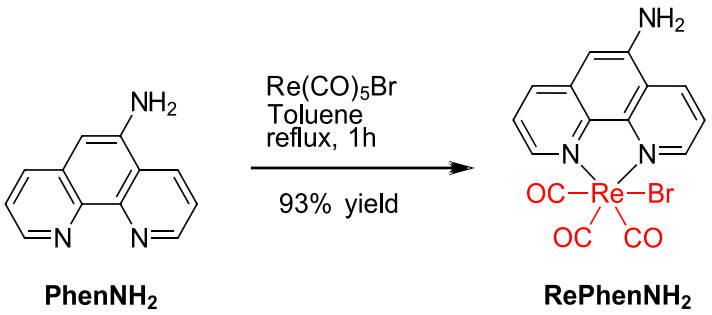

PhenNH$_2$ **RePhenNH$_2$**

Figure 220. Complexation of **PhenNH$_2$** with a source of rhenium to synthesise **RePhenNH$_2$** in 93% yield.

The synthesis of **RePhenNH$_2$** was adapted from a literature method described by Bessette, *et al.*[111]. A mass of 5-amino-1,10-phenanthroline (0.49 g, 2.501 mmol, 1.0 eq.) was dissolved in a volume of toluene (30 mL) and heated to reflux. A mass of bromopentacarbonylrhenium(I) (1.00 g, 2.462 mmol, 1.0 eq.) was then added to the reaction mixture, whereupon the solution turned from yellow to orange in colour. The reaction mixture was left to stir under reflux under a constant supply of nitrogen gas for 1 hour. The solution was then cooled to room temperature and filtered *via* vacuum filtration, whereupon the precipitate was washed with n-hexane and dried to afford an orange powder (1.27 g).

^{1}H-NMR analysis of the compound revealed the expected integration for seven protons in the aromatic region as well as an integration for two protons of a broad resonance signal at 6.90 ppm characteristic of the primary amine functional group, as shown in the spectrum in Figure 221. The 13C-NMR spectrum of **RePhenNH$_2$** shown in Figure 222 exhibited the three carbon-13 resonance signals above 180 ppm as characteristic of the three carbonyl ligands, alongside the expected twelve carbon-13 resonance signals in the aromatic region from the nuclei of the phenanthroline ligand. The FTIR spectrum, shown in Figure 223, depicts the symmetric N−H bond stretching frequency at 3492 cm^{-1} and the asymmetric bond stretching frequency at 3338

cm^{-1}, providing further evidence of the presence of the primary aromatic amine. The spectrum also depicts the characteristic IR excitations of the A'(1) C≡O stretching vibrational mode at 2012 cm^{-1} and overlapping A'(2) & A'' C≡O stretching vibrational modes at 1894 cm^{-1}, respectively, providing further evidence for the existence of the tricarbonyl centre. The HRMS spectrum of **RePhenNH$_2$** also showed a bromine-dissociated $[M\text{-}Br]^+$ ion signal ($ReC_{15}H_9N_3O_3^+$) observable at *m/z* 466.01988 with a calculated ratio of m/z 466.01959 (Δ 0.61 ppm), corresponding to the complex incorporating the ^{187}Re isotope in 62.6% natural abundance, as shown in Figure 224. An additional signal with *m/z* 464.01714 was also observed for the $[M\text{-}Br]^+$ ion corresponding to the incorporation of the ^{185}Re isotope in 37.4% natural abundance. Elemental analysis provided evidence of the bromo ancillary ligand, which was absent in the former analyses, as well as further evidence for the purity of the complex. Compositions of 33.06% carbon, 1.80% hydrogen, 7.64% nitrogen and 14.39% bromine were observed against closely aligned theoretical compositions of 33.04% carbon, 1.66% hydrogen, 7.71% nitrogen and 14.65% bromine.

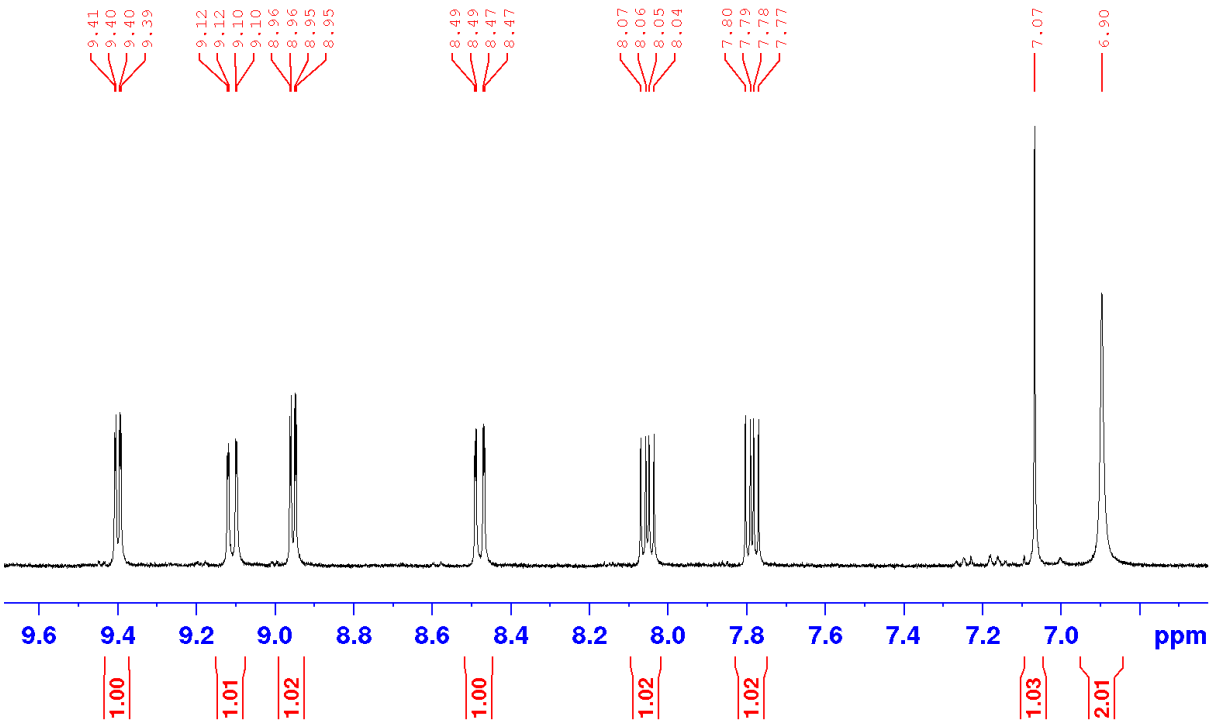

Figure 221. ^{1}H-NMR spectrum of **RePhenNH$_2$** in DMSO-d$_6$ exhibiting integration for the seven C−H aromatic protons and integration of the broad signal at 6.90 ppm for the two protons of the amine functional group.

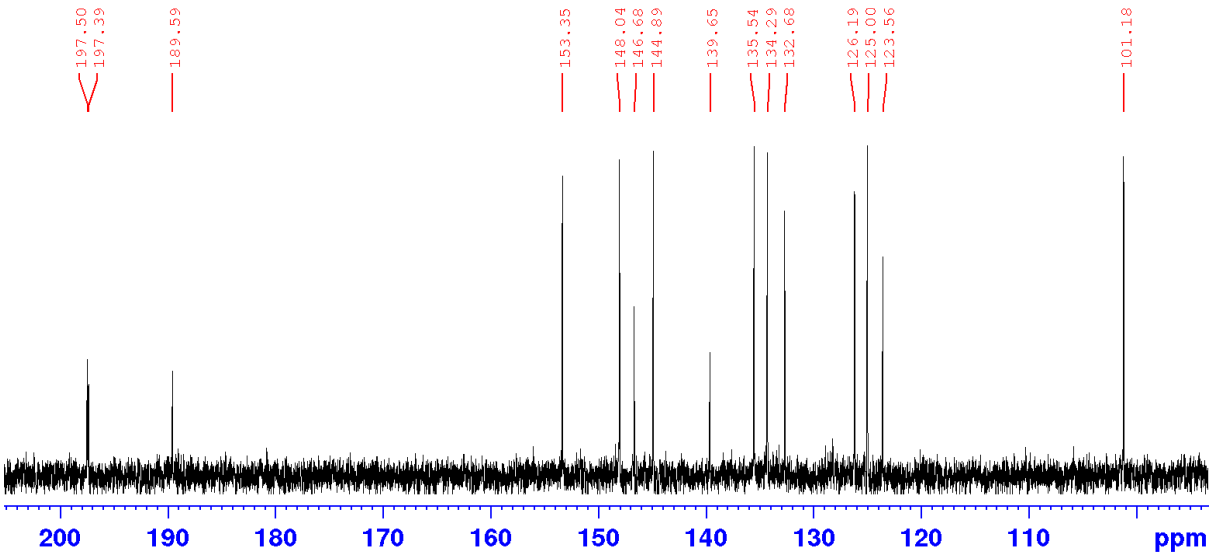

Figure 222. ^{13}C-NMR spectrum of **RePhenNH$_2$** in DMSO-d$_6$ exhibiting the expected fifteen carbon-13 resonance signals, including those for the three carbonyl ligands resonating at greater than 180 ppm.

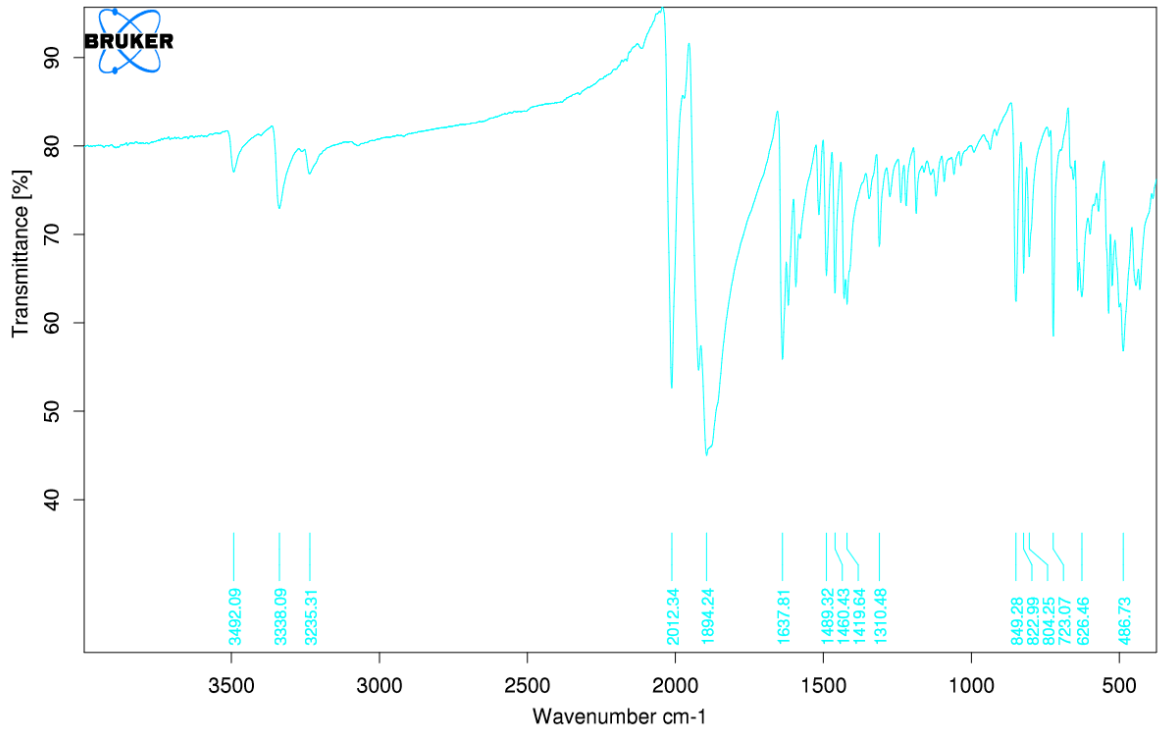

Figure 223. FTIR spectrum of **RePhenNH$_2$** showing the two distinctive IR absorption bands for the A'(1) C≡O stretching vibrational mode at 2012 cm^{-1} and overlapping A'(2) & A'' C≡O stretching vibrational mode at 1894 cm^{-1}. The symmetric and asymmetric N−H bond stretches of the primary amine are also notably excited at 3492 cm^{-1} and 3338 cm^{-1}, respectively.

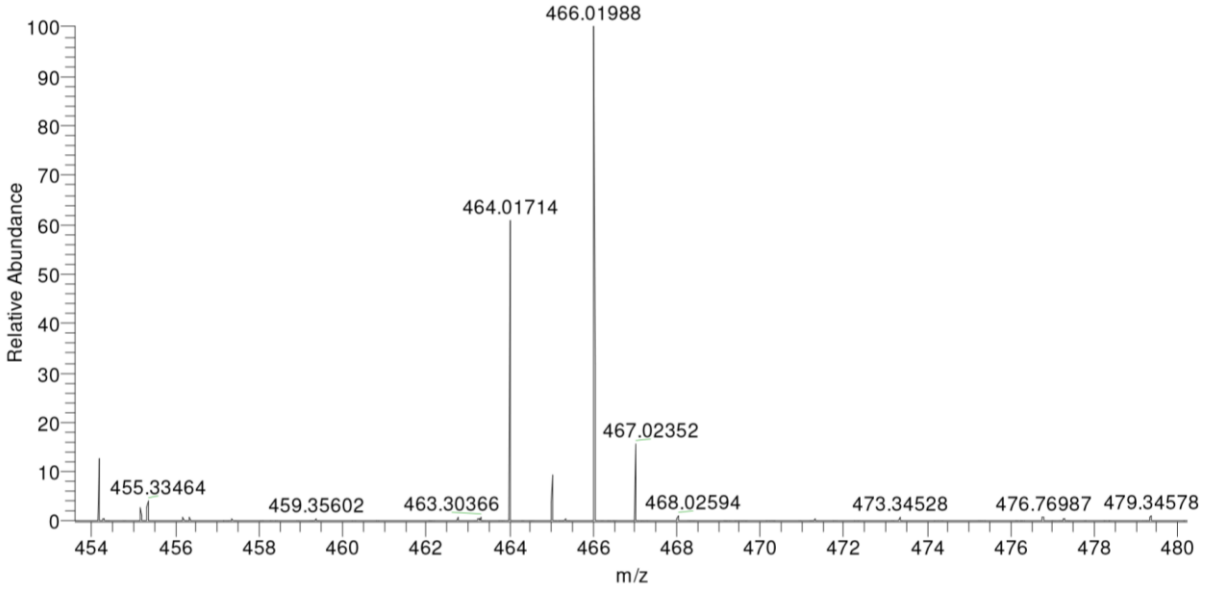

Figure 224. HRMS spectrum of **RePhenNH$_2$** depicting the bromine-dissociated [M-Br]$^+$ ion signal ($ReC_{15}H_9N_3O_3^+$) observable at *m/z* 466.01988 with a calculated ratio of *m/z* 466.01959 (Δ 0.61 ppm) for the complex incorporating the ^{187}Re isotope in 62.6% natural abundance. An additional signal with *m/z* 464.01714 is also observed for the same ion incorporating the ^{185}Re isotope in 37.4% natural abundance.

6.1.4 Characterisation Data for the ESF Conjugates and Rhenium Complexes

5-N-(2-Aminoethylsulfonylfluoride)-1,10-Phenanthroline **(PhenESF)** Orange Solid; MP: 200-205 °C (dec.); 63% yield. ^{1}H NMR (400 MHz, $CDCl_3$, δ/ppm): δ 9.21 (dd, J^d = 4.32, 1.56 Hz, 1H), δ 8.96 (dd, J^d = 4.32, 1.64 Hz, 1H), δ 8.26 (dd, J^d = 8.44, 1.52 Hz, 1H), δ 8.04 (dd, J^d = 8.12, 1.64 Hz, 1 H), δ 7.65 (dd, J^d = 8.40, 4.32 Hz, 1H), δ 7.53 (dd, J^d = 8.08, 4.32 Hz, 1H), δ 7.53 (dd, J^d = 8.08, 4.32 Hz, 1H), δ 6.71 (s, 1H), δ 5.03 (t, J^t = 6.08 Hz, $1H_{\text{-NH-}}$), δ 4.08 (*app.* q, J^q = 12.16, 6.08 Hz, $2H_{\text{-CH2-SO2F}}$), δ 3.89 (td, J^q = 6.16, 4.48 Hz, $2H_{\text{-CH2-}}$). ^{13}C NMR (100 MHz, $CDCl_3$): δ 150.43, δ 147.44, δ 146.91, δ 142.31, δ 138.96, δ 129.59, δ 128.51, δ 123.27. δ 122.58, δ 122.02, δ 101.11, δ 49.66 (J = 15.08 Hz), δ 38.08. ^{19}F NMR (376 MHz, $CDCl_3$): δ 70.67 (t, J^t = 4.63 Hz). FTIR (ATR *corr.* $\tilde{\nu}/cm^{-1}$): 3402 (w, br, N−H *str.*), 2933 (m, sp^2 C−H *str.*), 2872 cm^{-1} (m, sp^3 C−H *str.*), 1596 cm^{-1} (s, sh, *asym.* S=O *str.*), 1384 cm^{-1} (s, sh, *sym.* S=O *str.*), 818 cm^{-1} (m, S-F *str.*). LRMS (ESI^+): *m/z* $[M + H]^+$ *calc.* 306.07; *found* 306.23. HRMS (ESI^+): $[M + H]^+$ *calc.* 306.07070; *found* 306.07093 (Δ 0.74 ppm). UV-Vis (CH_3CN, λ/nm, ε/L.mol^{-1}.cm^{-1}): λ 331 (ε 9099), λ 279 (ε 28578), λ 259 (ε 21861), λ 221 (ε 41646), λ 194 (ε 22289). EA(%): $C_{14}H_{12}O_2N_3SF$ *calc.* C 55.07, N 13.76, H 3.96. *found* C 54.54, N 13.64, H 3.63.

Bromotricarbonyl(5-N-(2-Aminoethylsulfonylfluoride)-1,10-Phenanthroline)rhenium(I) **(RePhenESF)** Yellow solid; MP: 295-301 °C (dec.); 79% yield. ^{1}H NMR (400 MHz, DMSO-d_6): δ 9.28 (d, J^d = 5.04 Hz, 1H), δ 9.10 (d, J^d = 7.88 Hz, 1H), δ 9.03 (dd, J^d = 5.00, 1.12 Hz, 1H), δ 8.53 (dd, J^d = 8.36, 1.12 Hz), δ 8.11 (dd, J^d = 8.82, 5.08 Hz, 1H), δ 7.87 (dd, J^d = 8.36, 5.00 Hz, 1H), δ 7.57 (t, J^t = 5.76 Hz, $1H_{\text{-NH-}}$), δ 7.16 (s, 1H), δ 4.41 (*app.* q, J^q = 11.88 Hz, 5.88 Hz, $2H_{\text{-CH2-SO2F}}$), δ 3.96 (*app.* q, J^q = 11.56, 5.76 Hz, $2H_{\text{-CH2-}}$). ^{13}C NMR (100 MHz, DMSO-d_6): δ 197.42, δ 197.33, δ 189.51, δ 153.48, δ 148.82, δ 146.68, δ 142.12, δ 140.37, δ 136.31,

δ 133.52, δ 132.52, δ 126.47, δ 125.45, δ 124.00, δ 99.41 (d, J^d = 26 Hz), δ 48.67 (d, J^d = 12 Hz), δ 37.62. ^{19}F NMR (376 MHz, DMSO-d_6): δ 70.67 (t, J^t = 4.63 Hz). FTIR(ATR *corr. ṽ/cm^{-1}*): 3347 cm^{-1} (w, sh, N−H *str.*), 3051 cm^{-1} (w, sp^2 C−H *str.*), 3003 cm^{-1} (w, sp^3 C−H *str.*), 2025 cm^{-1} (s, sh, A'(1) C≡O *str.*), 1919 cm^{-1} (s, sh, A'(2) C≡O *str.*), 1898 cm^{-1} (s, sh, A" C≡O *str.*). LRMS (ESI$^+$): *m/z* [M-Br]$^+$ *calc.* 576.00; *found* 576.15. HRMS (ESI$^+$): *m/z* [M-Br]$^+$ *calc.* 576.00337; *found* 576.00387 (Δ 0.86 ppm). UV-Vis (CH_3CN, λ/nm, ε/L.mol^{-1}.cm^{-1}): λ 414 (ε 2517), λ 347 (ε 7341), λ 297 (ε 16255), λ 243 (ε 25956), λ 194 (ε 39590). EA(%): $ReC_{17}H_{12}O_5N_3SFBr$ *calc.* C 31.15, N 6.41, H 1.85, S 4.89, Br 12.19. *found* C 30.61, N 6.36, H 1.85, S 4.91, Br 12.05.

Bromotricarbonyl(5-amino-1,10-phenanthroline)rhenium(I) **(RePhenNH$_2$)** Orange solid; MP: 318-319 °C (dec.); 93% yield. ^{1}H NMR (400 MHz, DMSO-d_6): δ 9.40 (dd, J^d = 5.12, 1.20 Hz, 1H), δ 9.11 (dd, J^d = 8.52, 1.20 Hz, 1H), δ 8.95 (dd, J^d = 5.00, 1.28 Hz, 1H), δ 7.24 (dd, J^d = 8.44, 1.20 Hz, 1H), δ 8.05 (dd, J^d = 8.52, 5.12 Hz, 1H), δ 7.79 (dd, J^d = 8.36, 5.00 Hz, 1H), δ 7.07 (s, 1H), δ 6.90 (s, br, 1H$_{-NH2}$). ^{13}C NMR (100 MHz, DMSO-d_6): δ 197.50, δ 197.39, δ 189.59, δ 153.35, δ 148.04, δ 146.68, δ 144.89, δ 139.65, δ 135.54, δ 134.29, δ 132.68, δ 126.19, δ 125.00, δ 123.56, δ 101.18. FTIR (ATR *corr. ṽ/cm^{-1}*): 3491 cm^{-1} (w, *asym.* N−H *str.*), 3338 cm^{-1} (w, *sym.* N−H *str.*), 3236 cm^{-1} (w, sp^2 C−H *str.*), 2012 cm^{-1} (s, sh, A'(1) C≡O *str.*), 1921 cm^{-1} (s, A'(2) C≡O *str.*), 1894 cm^{-1} (s, A" C≡O *str.*). LRMS (ESI$^+$, cone = 60 V): *m/z* [M - Br]$^+$ calculated: 466.02; found: 466.17; *m/z* [M+H]$^+$ calculated: 545.95 & 547.94, found: 546.05 & 457.05. HRMS (ESI$^+$): *m/z* [M-Br]$^+$ *calc.* 466.01959; *found* 466.01988 (Δ 0.61 ppm). UV-Vis (CH_3CN, λ/nm, ε/L.mol^{-1}.cm^{-1}): λ 416 (ε 2726), λ 348 (ε 10143), λ 296 (ε 24429), λ 244 (ε 36535), λ 194 (ε 58783). EA(%): $ReC_{15}H_9O_3N_3Br$ *calc.* C 33.04, N 7.71, H 1.66, Br 14.65. *found* C 33.06, N 7.64, H 1.80, Br 14.39.

6.2 Radiosynthesis of the [^{18}F]ESF Prosthetic Group

No-carrier added [^{18}F]ESF was first synthesised *via* [^{18}F]fluoride substitution with 2,2,6-trichlorophenylethenesulfonate (TCPE) by the mechanism proposed in Figure 225. The reaction was performed in DMSO using the automated microfluidic set-up assembled as per Figure 226. Here TCPE was supplied through pump 1, whereas the cyclotron eluted and azeotropically distilled [^{18}F]fluoride was supplied through 2. Both solutions were passed through the 15.6 µL microreactor at a flow rate of 20 µL.min^{-1}, whereupon a radioactivity detector monitored the elution of the reaction mixture. The outlet from the microreactor was connected to a closed vial (A) pressurized with nitrogen gas with a flow rate between 0.1 to 0.2 L.min^{-1}.Vial A was heated to 80 °C, resulting in the evaporation of [^{18}F]ESF from the TCPE in DMSO solution. The gaseous effluents were passed through a silica light cartridge which trapped the radioactive impurities and eluted into another vial (B). Pressurisation of vial B from the nitrogen flow resulted in [^{18}F]ESF being trapped on a likewise connected silica Plus SPE cartridge, with a vent attached to alleviate the pressure. An additional radioactivity detector was placed in proximity of the silica plus SPE cartridge to monitor the entrapment of the [^{18}F]ESF radioproduct. The [^{18}F]ESF was then eluted in water for the fluorine-18 radiolabelling of the **PhenNH$_2$** and **RePhenNH$_2$** precursors.

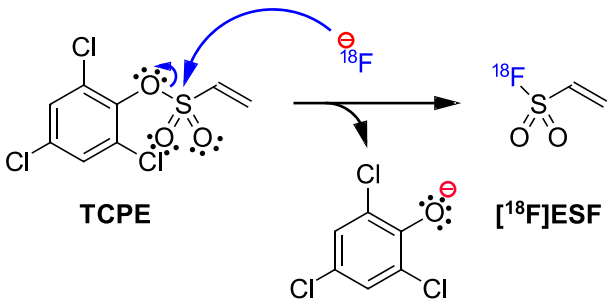

Figure 225. Mechanism for the radiosynthesis of **[^{18}F]ESF** from **TCPE** *via* substitution with complexed [^{18}F]fluoride.

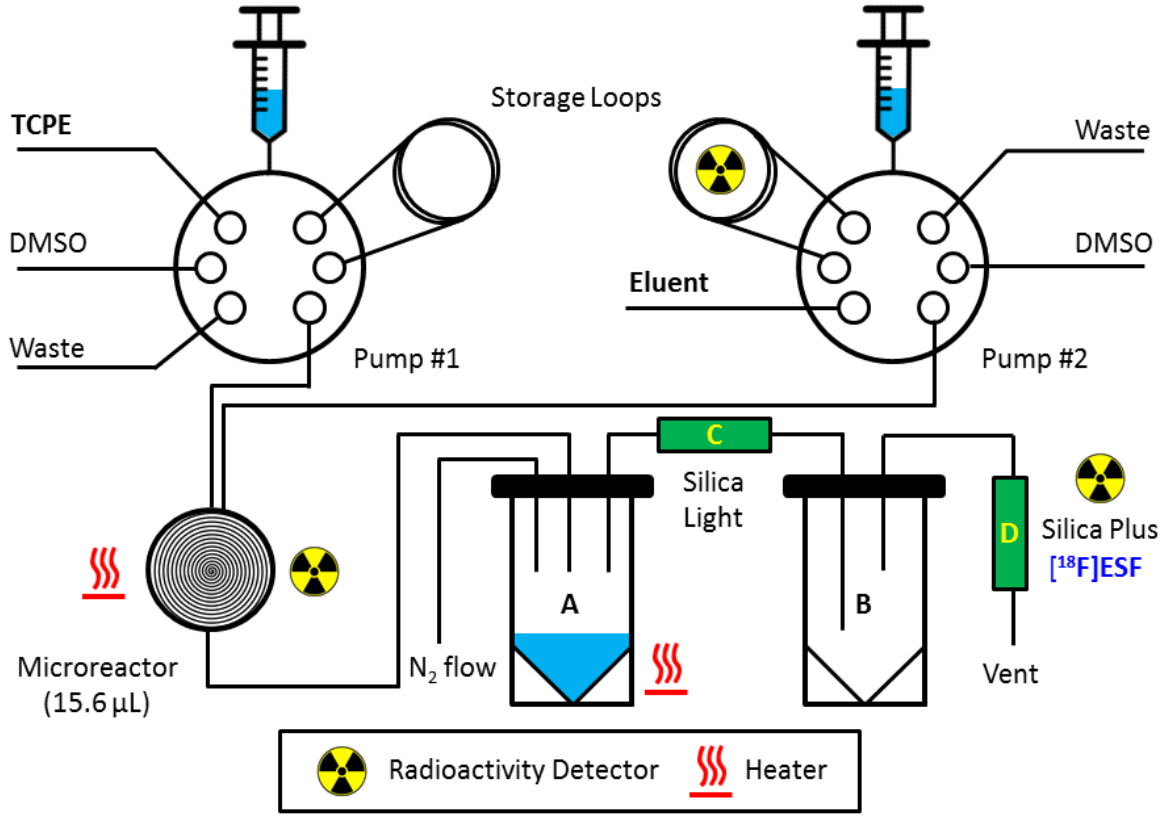

Figure 226. Microfluidic set-up used to produce n.c.a. [^{18}F]ESF. TCPE in DMSO in supplied through pump 1 and azeotropically dried [^{18}F]fluoride (eluent) is supplied through pump 2. Both solutions are passed through a 15.6 µL microreactor whereupon [^{18}F]ESF is formed in solution. The outlet of the microfluidic system was connected to a closed vial (A) heated at 80 °C and pressurized with N_2 gas (0.1 - 0.2 L.min^{-1}). The gaseous effluents from vial A were then directed through a silica light SPE cartridge (C) into a second vial (B). The outlet of vial B was connected to a Silica plus SPE cartridge (D) which trapped the distilled [^{18}F]ESF.

6.2.1 [^{18}F]ESF Conjugation to 5-Amino-1,10-Phenanthroline and its Rhenium Complex

The radiolabelling experiments were performed by mixing 80 µL of 1 mg.mL^{-1} **PhenNH2** and **RePheNH$_2$** solutions in DMSO with 20 µL of 93±19 MBq.mL^{-1} of *no-carrier added* [^{18}F]ESF aqueous solution. The reaction mixture was analysed by radioHPLC, with some reaction RCYs verified by radioTLC analyses, and the radioproduct identity was confirmed *via* retention time comparison with the non-radioactive standards. As shown in Figure 227, for the radiolabelling of the **PhenNH$_2$** ligand with [^{18}F]ESF, the radioproduct eluting at 258 s (4.30 mins) coincides with the UV absorbance peak of the non-radioactive **PhenESF** standard. Curiously, alongside the radiolabelled **[^{18}F]PhenESF** product and unreacted [^{18}F]ESF prosthetic group eluting at 107 s (1.78 mins), degradation of the radiospecies to form [^{18}F]fluoride was observed as well as the elution of an unknown radioactive by-product eluting at 231 s (3.85 mins). One hypothesis for this radioactive by-product may involve η^2 coordination of the ESF allyl functional group to the rhenium centre *via* displacement of the bromo ligand.

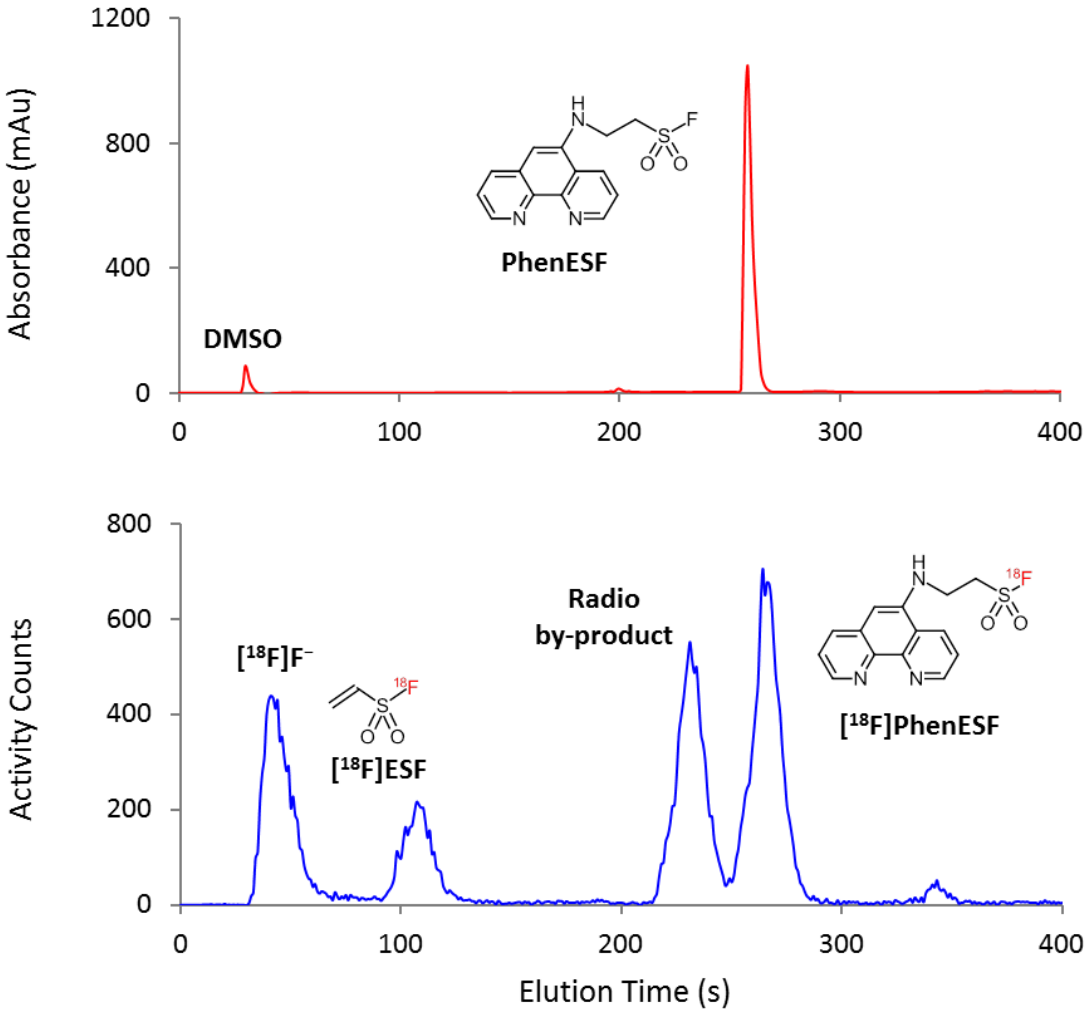

Figure 227. UV absorbance chromatogram providing the 258 s retention time of the non-radioactive **PhenESF** standard (red, top), which aligns with one of the radioproducts in the radiochromatogram (blue, bottom).

An example chromatogram is also shown for the [^{18}F]ESF conjugation of **[^{18}F]RePhenESF** in Figure 228. The consistent degradation to form [^{18}F]fluoride was likewise observed, alongside an unknown radioactive by-product eluting at 210 s (3.50 mins). A minute peak corresponding to the radioproduct can be shown in the zoomed in region at 414 s (6.90 mins), which corresponds to the retention time of the UV absorbance peak for the **RePhenESF** non-radioactive standard in a separate injection.

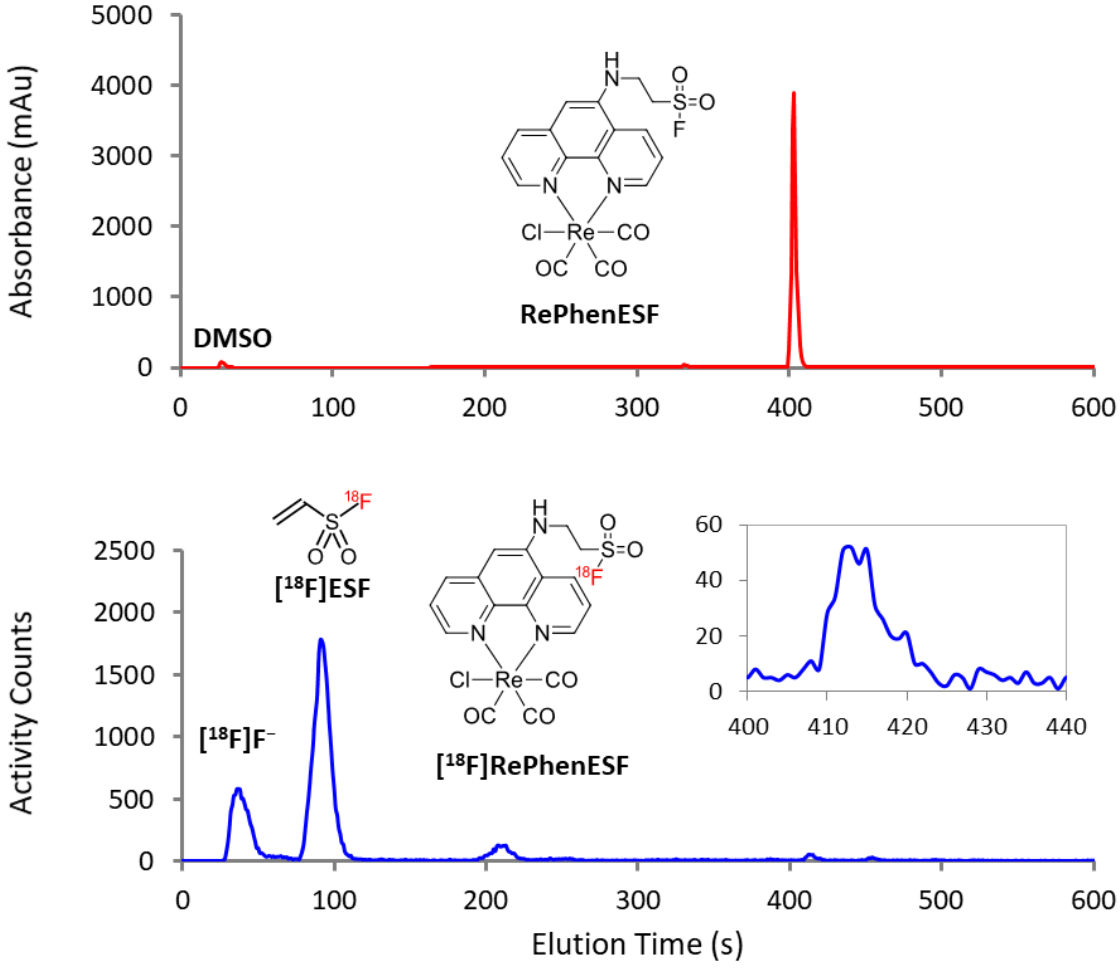

Figure 228. UV absorbance chromatogram providing the 414 s retention time of the non-radioactive **RePhenESF** standard (red, top), which aligns with one of the minor radioproducts in the zoomed in region of the radiochromatogram (blue, bottom).

The non-isolated RCYs for the **[^{18}F]PhenESF** and **[^{18}F]RePhenESF** products provided in Figure 229 for reaction temperatures of 40, 70 and 100 °C. Radiolabelling of the **PhenNH$_2$** precursor ligand increased as a function of reaction temperature; with an RCY of 13% forming at 40°C, 23% RCY forming at 70 °C and 34% RCY forming at 100 °C. The RCYs were also verified by radioTLC with near matching RCYs of 14% and 24% respectively, as shown in Figure 230. Given the volatile nature of [^{18}F]ESF, higher reaction temperatures were not trialled which may afford even greater RCYs under pressurised conditions. The radiolabelling of **PhenNH$_2$** to afford the **[^{18}F]RePhenESF** product was far less efficient, however, with only

1-2% RCY determined by radioHPLC (and 3% RCY determined by radioTLC) irrespective of the reaction temperature. The integration of the radioTLC results are shown for **[^{18}F]PhenESF** at 40 °C and 70 °C in Figure 231 and Figure 232, respectively, and for **[^{18}F]RePhenESF** at 40 °C in Figure 233.

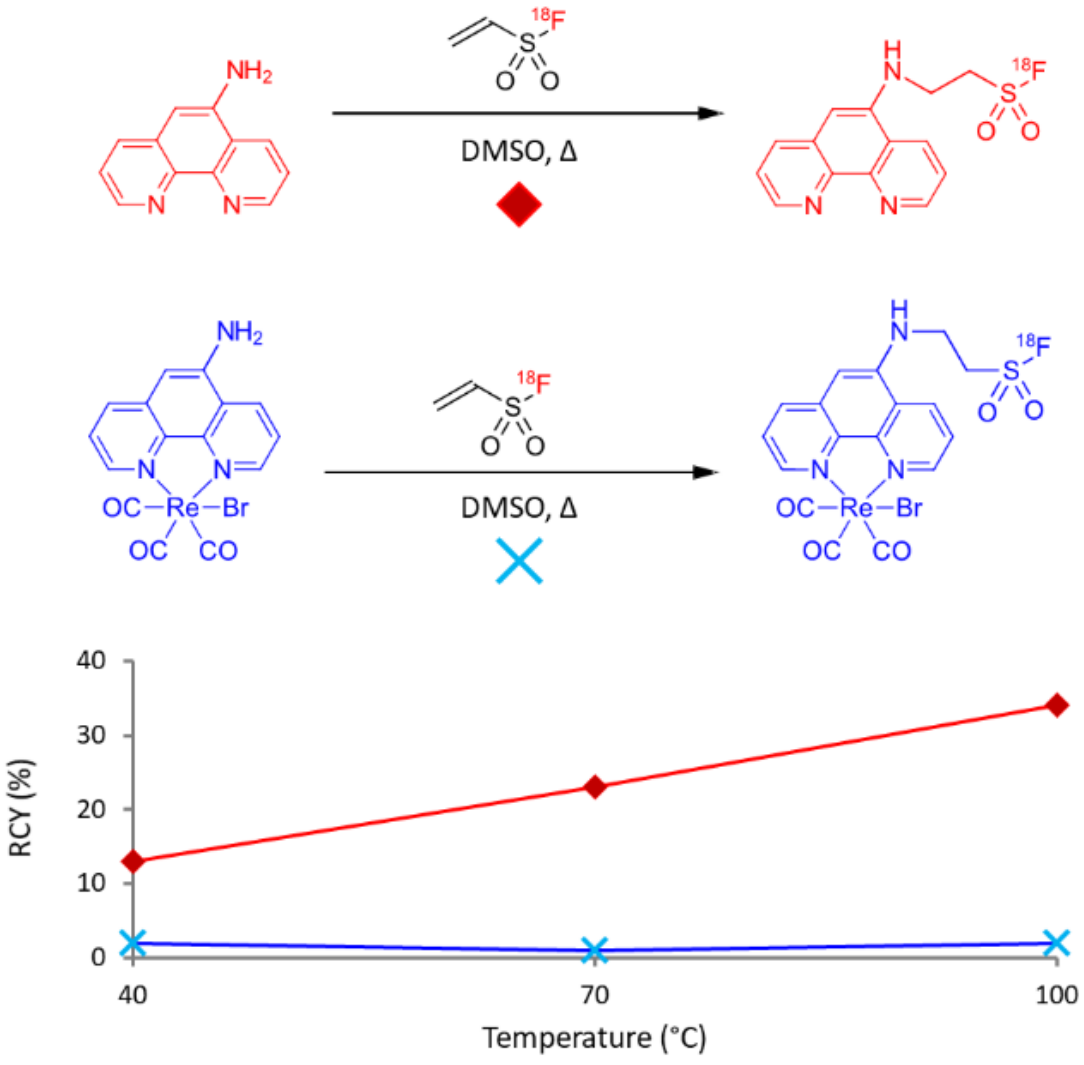

Figure 229. RadioHPLC determined non-isolated RCYs plotted as a function of reaction temperature for the [^{18}F]ESF conjugation reactions to form **[^{18}F]PhenESF** (red, diamonds) and **[^{18}F]RePhenESF** (blue, crosses).

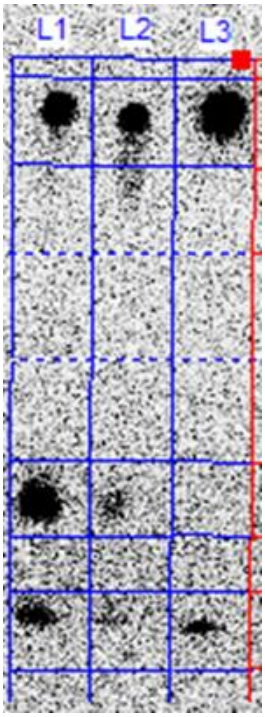

Figure 230. Sampled radioTLC results for the radiosyntheses of **[^{18}F]PhenESF** (70°C L1, 40 °C L2) and **[^{18}F]RePhenESF** (40 °C L3) used to validate RCYs attained by non-isolated radioHPLC peak integrations.

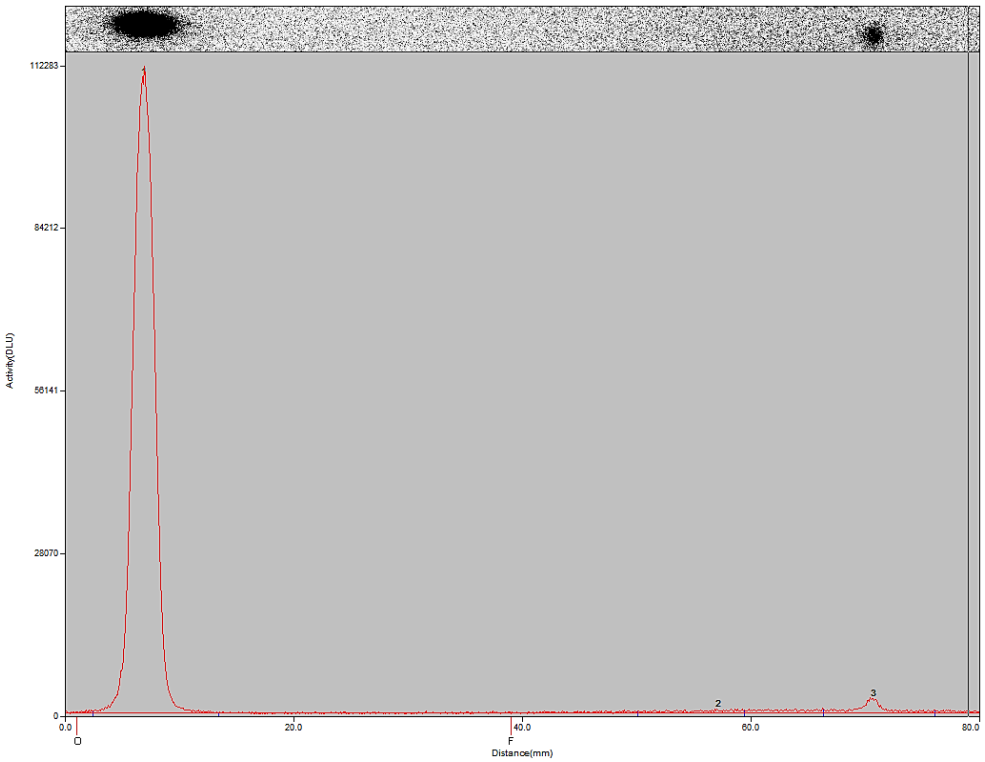

Figure 231. RadioTLC peak integration for reaction forming **[^{18}F]RePhenESF** at 40 °C in 3% RCY (2% by radioHPLC).

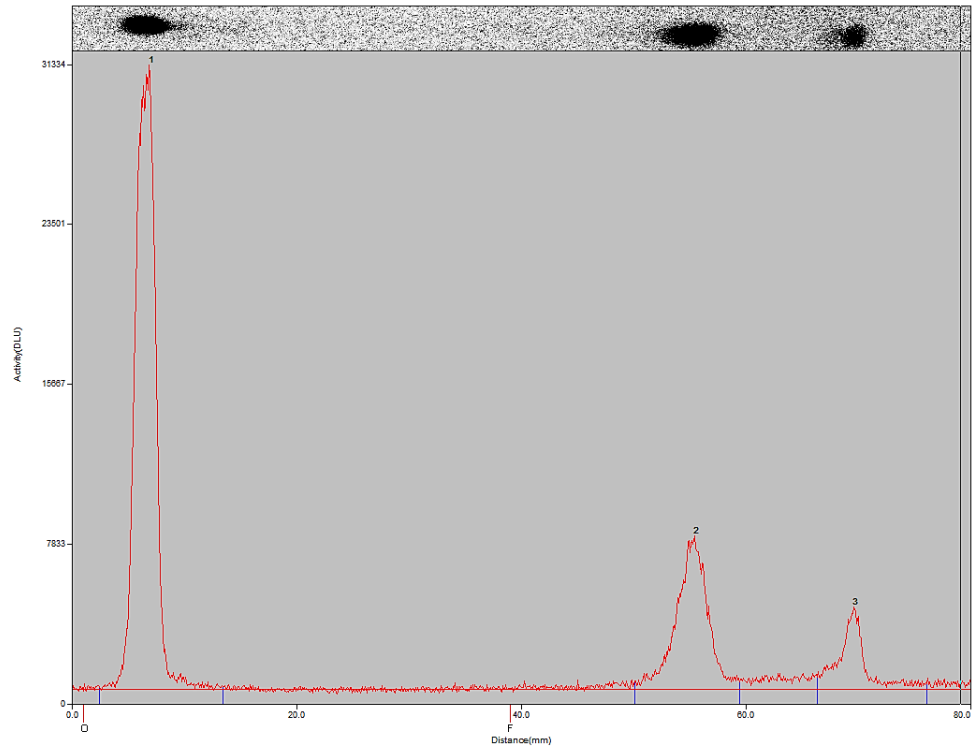

Figure 232. RadioTLC peak integration for reaction forming **[^{18}F]PhenESF** at 70 °C in 24% RCY (23% by radioHPLC), accompanied by an unknown by-product.

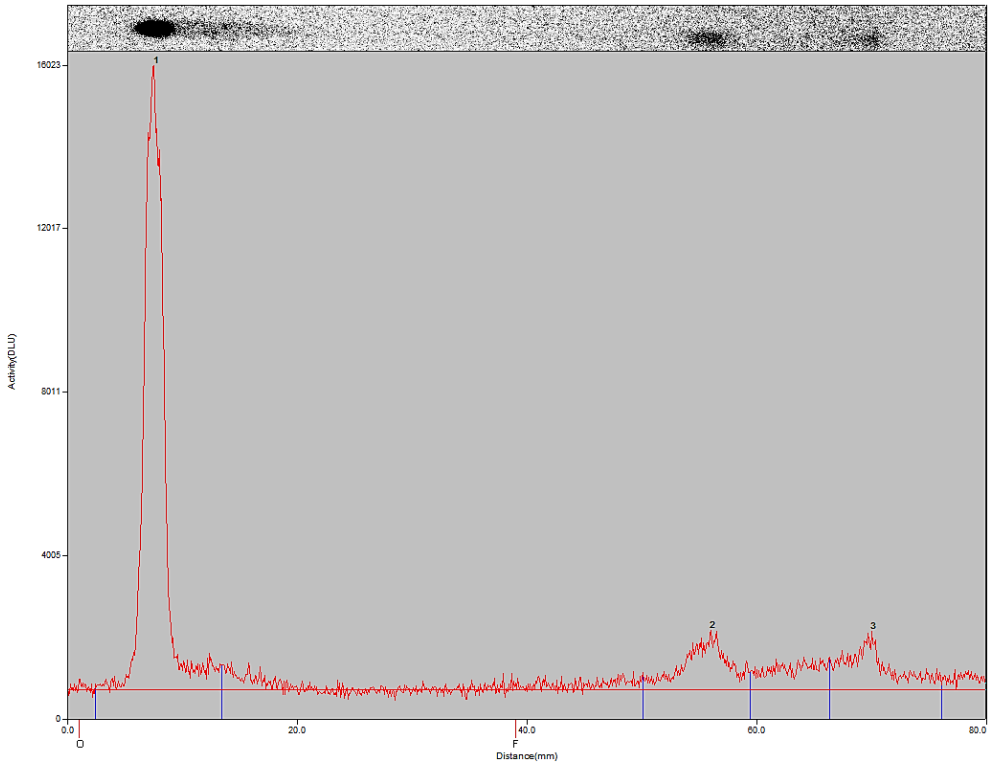

Figure 233. RadioTLC peak integration for reaction forming **[^{18}F]PhenESF** at 40 °C in 14% RCY (13% by radioHPLC), accompanied by an unknown by-product.

6.3 Photophysical Properties of the Rhenium-ESF Conjugate

Towards discerning the value of **[^{18}F]RePhenESF** as a PET-optical agent, photophysical analyses were performed on both the non-radioactive **RePhenNH$_2$** precursor and **RePhenESF** product to comment on their respective optical properties. The UV-Vis spectra for both compounds shown in Figure 234 and Figure 235, exhibit dπ → π* absorption bands to the MLCT excited state at 416 nm (ε 2726 L.mol^{-1}.cm^{-1}) and 414 nm (ε 2517 L.mol^{-1}.cm^{-1}) for **RePhenNH$_2$** and **RePhenESF** respectively. Higher energy π → π* to LC excited states are also notably present at 348, 296, 244 and 194 nm for **RePhenNH$_2$**, and 347, 297, 243 and 194 nm for **RePhenESF** in acetonitrile solution.

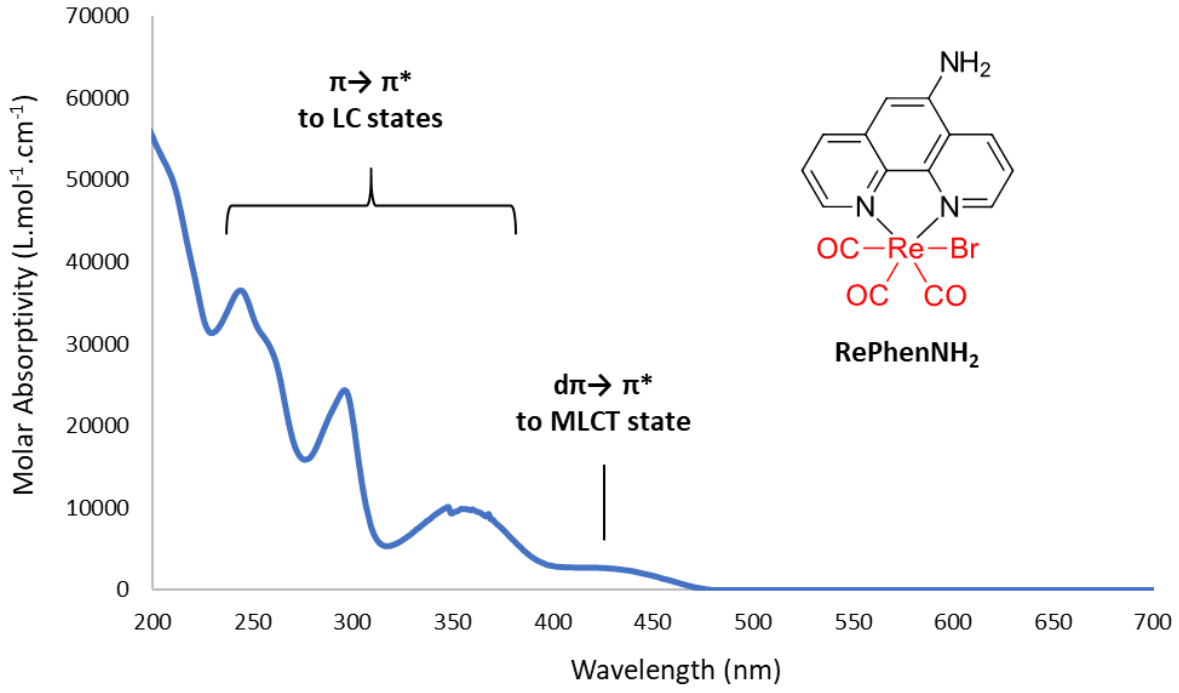

Figure 234. UV-Vis spectrum of **RePhenNH$_2$** (2 mg.mL^{-1}) in acetonitrile solution showing the dπ → π* transition to the MLCT excited state and π → π* transitions to the LC excited state.

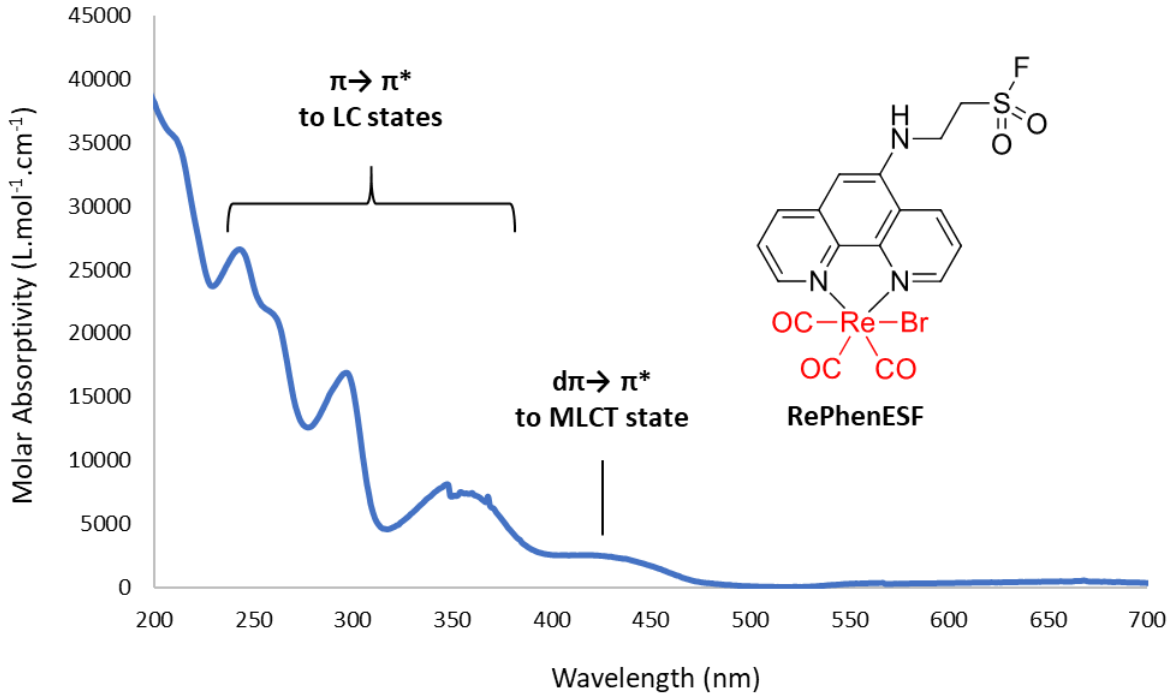

Figure 235. UV-Vis spectrum of **RePhenESF** (5 mg.mL^{-1}) in acetonitrile solution showing the d$\pi \rightarrow \pi^*$ transition to the MLCT excited state and $\pi \rightarrow \pi^*$ transitions to the LC excited state.

Excitation at 410 nm for both compounds in DMSO solution afforded emission maxima of 612 nm for **RePhenNH$_2$** and **RePhenESF** for 621 nm as shown in Figure 236. When measured in aqueous media, containing only 5% v/v DMSO to aid solubility, **RePhenESF** exhibited a solvatochromic shift of the emission maxima to 606 nm. **RePhenNH$_2$** exhibited a relatively short excited state lifetime of less than 10 ns, in agreement with previously obtained photophysical data for the Re−Cl derivative of the compound in DMSO solution.[112] Interestingly, **RePhenESF** instead exhibited a much longer luminescence lifetime of 138 nm with a χ^2 value of 0.995 for the fit of monoexponential decay from the MLCT excited state. Based on a measured absorbance maximum of 0.412 at 410 nm and an integration of 2.75×10^6 counts·nm from the emission spectrum, which were substituted into equation (14) alongside the previously reported variables for [Ru(BiPy)$_3$Cl], the quantum yield of **RePhenESF** in DMSO solution was determined to be 0.4%, as shown in Table 10. The quantum yields of

RePhenESF in 5% v/v DMSO in water solution and **RePhenNH$_2$** in DMSO solution were both determined to be less than 0.1%.

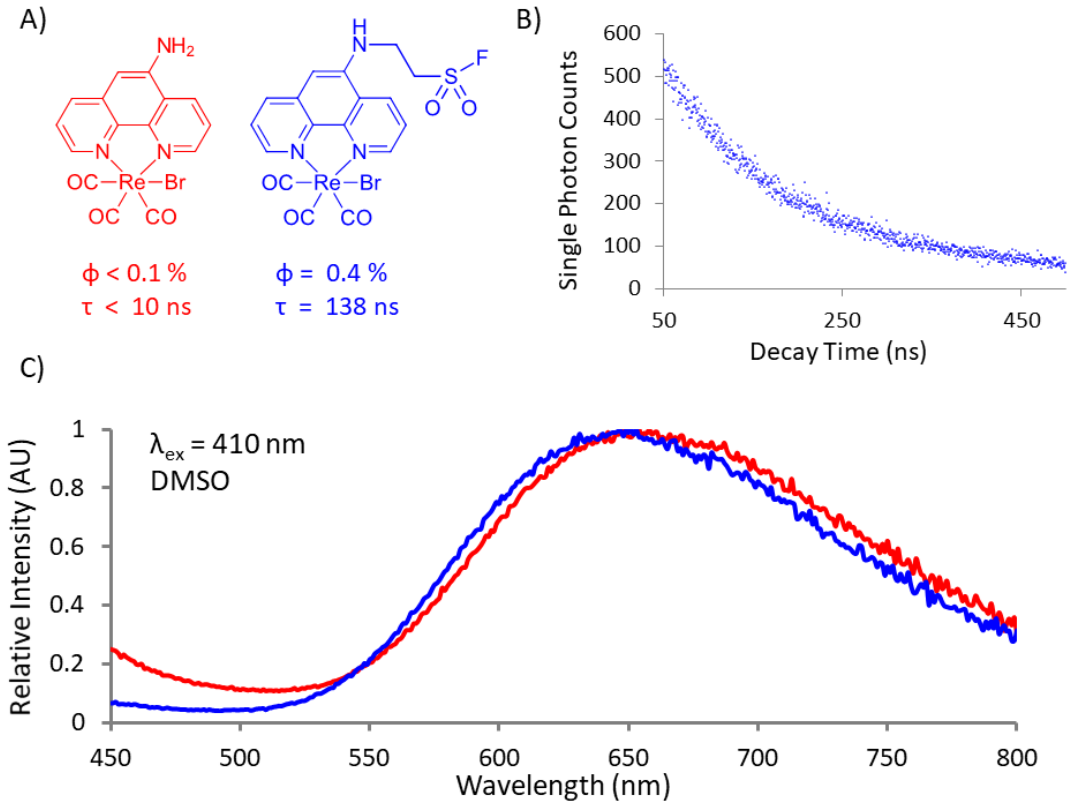

Figure 236. Summary of photophysical properties in DMSO showing A) the quantum yield and lifetime for compounds **RePhenNH$_2$** (red) and **RePhenESF** (blue), B) the monoexponential decay profile for **RePhenESF** and C) the emission spectra of both compounds following excitation at 410 nm wavelength.

Table 10. Quantum yield of **RePhenESF** in DMSO solution as determined by comparison with the [Ru(BiPy)$_3$Cl] reference standard and with correction factors applied for the refractive index of the solvent, absorbance at the 410 nm excitation wavelength and the integration of the emission spectrum, as shown below.

Analyte	Solvent	Refractive Index	Absorbance	Emission Integration (counts·nm)	Quantum Yield (%)
[Ru(BiPy)$_3$]Cl	Water	1.333	0.045	4.71×10^6	2.8%
RePhenESF	DMSO	1.479	0.242	2.75×10^6	0.4%

CHAPTER SEVEN
CONCLUSIONS AND FUTURE WORK

7.1 Conclusions on the Fluorine-18 Labelling of Luminescent Rhenium Complexes

The original intent of this work was to validate the underlying thesis that *a luminescent rhenium complex could be radiolabelled with the fluorine-18 radioisotope and would have desirable properties for use as a PET-optical agent.* Towards verifying this hypothesis, rhenium complexes were synthesised from ligands based on 1,10-phenanthroline and 2,2'-bipyridine *N*-heterocyclic ligands bearing leaving groups for substitution with [^{18}F]fluoride. Radiosynthesis of the 2-[^{18}F]fluoro-1,10-phenanthroline bearing rhenium complex, **[^{18}F]Re2FPhen**, resulted in a reasonable molar activity of 71 MBq.nmol^{-1}. Additionally, the radiolabelled complex was not only found to afford considerable RCY at low temperatures (60 – 80% maximum RCYs formed between 30 to 50 °C) when compared to the radiolabelled ligand, **[^{18}F]2FPhen** (40 – 60% maximum RCYs formed at greater than 170 °C), though was also able to radiofluorinate under non-azeotropically dry reaction conditions. Fluorine-18 radiolabelling reactions which tolerate aqueous conditions are notably rare in the research literature and offer profound benefits for the labelling of drugs or biomolecules which are particularly sensitive to their reaction environments. Such labelling efficiencies were also observed in the rhenium complexed 2,2'-bipyridine systems which afforded RCYs greater than 80% and 60% for the **[^{18}F]Re6FBiPy** and **[^{18}F]Re4FBiPy** complexes, respectively. Given these promising radiofluorination efficiencies it can be claimed that fluorine-18 labelled rhenium complexes certainly have desirable properties for the use in PET tracer development.

The optical properties of the rhenium complexes were also satisfactory, with quantum yields between 0.2% to 1.0% being determined depending on the functionalisation of the ligand and whether it was in DMSO or an aqueous environment. Such quantum yields are within the range of those reported for PET-optical agents based on cyanine dyes with methine chains, such as

the 0.4% quantum yield reported for the fluorine-18 labelled Cy5.5 dye by Priem, *et al.*,[61] though are still notably lower than PET-optical agents based, for instance, BODIPY luminescent structures. Satisfactory luminescent lifetimes between 0.014 μs and 0.138 μs were also measured and represent one of the few examples in literature that reported this crucial parameter for the synthesised PET-optical complexes. Thus, considering these results, it can also be claimed that rhenium complexes also have desirable properties for use in PET-optical tracer development. Further work towards improving the quantum yield of this new class of rhenium(I) based PET-optical agents would be desirable, however, if they are to compete with alternative fluorophores.

7.2 Significance of the Rhenium Mediated Method Discovered to Improve Fluorine-18 Radiotracer Synthesis

Perhaps of greater significance, and certainly serendipitous in its finding, was the discovery that thermal decomplexation of the intended PET-optical rhenium complexes could be used to produce fluorine-18 labelled ligands which could not formerly be synthesised. This was particularly true for the **[^{18}F]6FBiPy** and **[^{18}F]4FBiPy** ligands which were discovered to form in as great as 51% and 27% RCY using the rhenium thermal decomplexation approach and which were unable to be formed from traditional nucleophilic substitution with the ligand precursors using azeotropically dried [^{18}F]fluoride. While this method did not improve upon the radiosynthesis of the [^{18}F]CABS13 Alzheimer's disease imaging agent in preliminary tests, it did enable the radiosynthesis of another alternative fluorine-18 labelled 8-hydroxyquinoline ligand, **[^{18}F]5F8HQ**, which was also unable to be synthesised *via* traditional means. The use of such a method, as summarised in Figure 237, may be a valuable tool towards enabling the radiosynthesis of novel nuclear medicines and presents an exciting academic opportunity to further define the scope of precursors with which it can be applied to.

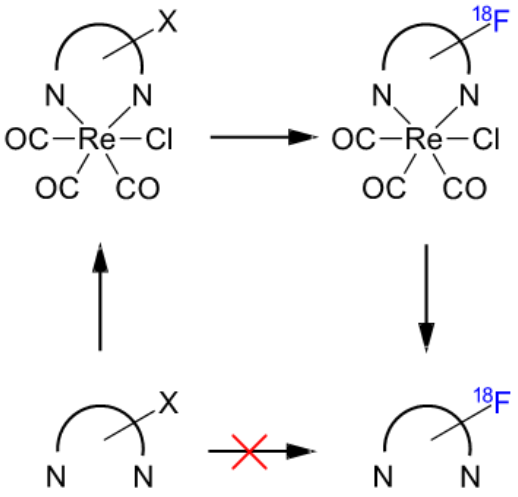

Figure 237. Summary of the rhenium complexation-dissociation approach. A pyridinyl bidentate ligand which would otherwise not substitute for [^{18}F]fluoride can be complexed, radiofluorinated and dissociated to afford the desired radioligand.

7.3 Future Work in Refining the Radiofluorination Method and Rhenium PET-Optical Hybrid Nuclear Medicines

There are certainly many other bidentate ligands which rhenium activation could improve the radiofluorination of and, given sufficient lability of the ligand, could afford the fluorine-18 labelled ligand in greater RCY also. Among these possibilities, testing the radiofluorination of monopyridine ligands could perhaps be of the greatest benefit given the widespread use of fluorine-18 labelled monopyridine systems in the field; such as [^{18}F]MEL050 used in the imaging of melanin in skin cancers, [^{18}F]T807 used to image tau proteins in Alzheimer's disease and [^{18}F]NIDA522131 used for the imaging of acetylcholine receptors, each shown in Figure 238.[113-115] This could be achieved by complexing the monopyridine as an ancillary ligand to the rhenium centre, alongside a bidentate ligand with electron withdrawing groups to aid in the electron withdrawal from the monopyridine π-system, thus improving the nucleophilic aromatic addition of [^{18}F]fluoride. As this would be a monodentate ligand, dissociation could likely be achieved more efficiently and at lower temperatures given its greater lability. This concept could also be applied to the radiofluorination of other such *N*-heterocyclic ligands, such as tetrazoles or triazoles. Alternatively, the addition of such monodentate pyridine ligands with electron withdrawal ligands could also improve radiofluorination on the bidentate ligand, though may be much harder to complex to the rhenium centre. The use of two microreactors in series to control the rates of radiofluorination and decomplexation, as discussed in Chapter Five, could also greatly enhance the RCYs of the fluorine-18 labelled ligands reported herein. Determining the identity of the unidentified by-product that formed from dissociation of the fluorine-18 labelled 2,2'-bipyridine complexes would also greatly help towards designing methods which limit its formation and thus improve the RCY of the desired radioproducts. Towards this aim, loss of the radioproduct following addition of a silicon-based fluoride scavenger could suggest formation of a Re–^{18}F bond.[116]

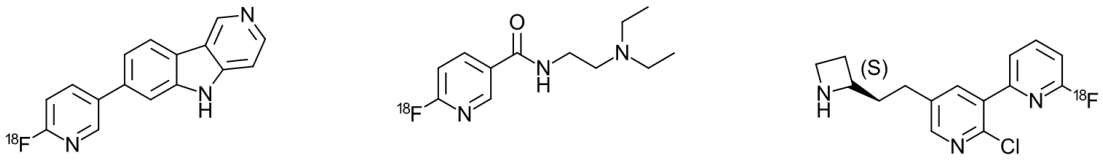

[^{18}F]T807
Imaging of Tau Proteins
(Alzheimer's disease)
14±3 % RCY

[^{18}F]MEL050
Imaging of Melanin
(Skin Cancer)
85% RCY

[^{18}F]NIDA522131
Acetylcholine Receptor
Imaging
4-8% RCY

Figure 238. Examples of fluorine-18 labelled monopyridine radiotracers of varying applications with which the rhenium complexation-dissociation approach could potentially be applied to improve overall RCYs or means of production.

Furthermore, while the thermal dissociation approach proved to be a highly effective strategy for decomplexing the radiolabelled rhenium complexes to achieve the corresponding fluorine-18 labelled ligands, alternative decomplexation strategies are certainly worth investigating. Acid or light induced decomplexation, for instance, may enhance the RCY of the desired fluorine-18 labelled ligand while minimising the formation of the radioactive unidentified by-product. Such alternative approaches may also be useful for dissociating less labile ligands, such as 1,10-phenanthroline, thus expanding the scope of radiotracer product with which this method could be applied to. Verifying the identity of the unknown by-products would furthermore aid in designing improved reaction conditions which circumvent their formation. Also, worth considering is the incorporation of other metal centres. If the activation effect can be explained largely in terms of electron withdrawal from the metal centre, then other metals may perhaps be able to achieve a similar effect with perhaps greater advantages. A manganese tricarbonyl centre, for instance, would certainly be worth investigating given that it is a group VII transition metal akin to rhenium with purportedly lesser complex stability.[117, 118] Thus, decomplexation of such a complex may occur more readily and at lower temperatures to liberate more of the fluorine-18 tracer.

From the perspective of improving the use of these rhenium complexes as PET-optical agents, ancillary ligands bearing conjugated π-systems could significantly improve the quantum yield, as seen in literature examples, compared to other PET-optical agents (for instance of the BODIPY class). The utility of this new class of complexes as PET-optical agents will ultimately rely on their subsequent bioconjugation, the nature of which will depend on the application being explored. In contrast to the Michael-donating strategy used to conjugate the rhenium complex to [^{18}F]ESF in the synthesis of **RePhenESF**, such conjugation strategies could alternatively exploit the electron withdrawing property of the rhenium centre to improve the Michael-acceptor ability of the complex for conjugation to the free amine or thiol groups of lysine or cysteine amino acids. Additionally, these reagents could also find potential utility as SPECT-optical theranostic agents by incorporating the radioactive rhenium-188 radioisotope in the complex centre.[119, 120] Overall there remains a bright future for the use of rhenium in fluorine-18 labelled PET tracers, both for the addition of an optical emission modality and for the improved radiosynthesis of certain ligands, which warrants much greater exploration.

REFERENCES

[1] Moses W.W. Fundamental limits of spatial resolution in PET. *Nucl. Instrum. Methods Phys. Res. A.* **2011**, *648*, 236-240.
[2] Catana C. Principles of simultaneous PET/MR imaging. *Magn. Reson. Imaging Clin. N. Am.* **2017**, *25*, 231-243.
[3] Fernández-Suárez M., Ting A.Y. Fluorescent probes for super-resolution imaging in living cells. *Nat. Rev. Mol. Cell Biol.* **2008**, *9*, 929.
[4] Preshlock S., Tredwell M., Gouverneur V. ^{18}F-Labeling of arenes and heteroarenes for applications in positron emission tomography. *Chem. Rev.* **2016**, *116*, 719-766.
[5] Cole E.L., Stewart M.N., Littich R., Hoareau R., Scott P.J.H. Radiosyntheses using fluorine-18: the art and science of late stage fluorination. *Curr. Top. Med. Chem.* **2014**, *14*, 875-900.
[6] Saha G.B. Basics of PET imaging: physics, chemistry and regulations. *Springer*. **2015**.
[7] Jacobson O., Kiesewetter D.O., Chen X. Fluorine-18 radiochemistry, labeling strategies and synthetic routes. *Bioconjugate Chem.* **2015**, *26*, 1-18.
[8] Gouverneur V., Müller K. Fluorine in pharmaceutical and medicinal chemistry: from biophysical aspects to clinical applications. *Imperial College Press*. **2012**.
[9] Teare H., Robins E.G., Kirjavainen A., Forsback S., Sandford G., Solin O., Luthra S.K., Gouverneur V. Radiosynthesis and evaluation of [^{18}F]Selectfluor bis(triflate). *Angew. Chem. Int. Ed.* **2010**, *122*, 6973-6976.
[10] Teare H., Robins E.G., Årstad E., Luthra S.K., Gouverneur V. Synthesis and reactivity of [^{18}F]-N-fluorobenzenesulfonimide. *Chem. Commun.* **2007**, *23*, 2330-2332.
[11] Kniess T., Laube M., Brust P., Steinbach J. 2-[^{18}F]Fluoroethyl tosylate – a versatile tool for building ^{18}F-based radiotracers for positron emission tomography. *MedChemComm*. **2015**, *6*, 1714-1754.
[12] Vaidyanathan G., Zalutsky M.R. Synthesis of N-succinimidyl 4-[^{18}F]fluorobenzoate, an agent for labeling proteins and peptides with ^{18}F. *Nat. Protoc.* **2006**, *1*, 1655-1661.
[13] Schirrmacher R., Wängler B., Bailey J., Bernard-Gauthier V., Schirrmacher E., Wängler C. Small prosthetic groups in ^{18}F-radiochemistry: useful auxiliaries for the design of ^{18}F-PET tracers. *Semin. Nucl. Med.* **2017**, *47*, 474-492.
[14] Johnström P., Harris N.G., Fryer T.D., Barret O., Clark J.C., Pickard J.D., Davenport A.P. ^{18}F-Endothelin-1, a positron emission tomography (PET) radioligand for the endothelin receptor system: radiosynthesis and *in vivo* imaging using microPET. *Clin. Sci.* **2002**, *48*, 4-8.
[15] Bergmann R., Scheunemann M., Heichert C., Mäding P., Wittrisch H., Kretzschmar M., Rodig H., Tourwé D., Iterbeke K., Chavatte K., Zips D., Reubi J.C., Johannsen B. Biodistribution and catabolism of ^{18}F-labeled neurotensin(8–13) analogs. *Nucl. Med. Biol.* **2002**, *29*, 61-72.
[16] Fredriksson A., Johnström P., Stone-Elander S., Jonasson P., Nygren P-Å., Ekberg K., Johansson B-L., Wahren J. Labeling of human C-peptide by conjugation with N-succinimidyl-4-[^{18}F]fluorobenzoate. *J. Label. Compd. Radiopharm.* **2001**, *44*, 509-519.
[17] Furuya T., Klein J.E., Ritter T. Carbon-fluorine bond formation for the synthesis of aryl fluorides. *Synthesis.* **2010**, *11*, 1804-1821.
[18] Brooks A.F., Topczewski J.J., Ichiishi N., Sanford M.S., Scott P.J.H. Late-stage [^{18}F]fluorination: new solutions to old problems. *Chem. Sci.* **2014**, *5*, 4545-4553.
[19] Palmer A.J., Clark J.C., Goulding R.W. The preparation of fluorine-18 labelled radiopharmaceuticals. *Int. J. Appl. Radiat. Isot.* **1977**, *28*, 53-65.
[20] Jacobson O., Chen X. PET designated flouride-18 production and chemistry. *Curr. Top. Med. Chem.* **2010**, *10*, 1048-1059.

[21] Koren A.O., Chefer S.I., Mukhin A.G., Pavlova O.A., Horti A.G., Vaupel D.B., London E.D., Kimes A.S. 5-IODO-6-[^{18}F]fluoro-3-(2(S)-azetidinylmethoxy)pyridine, a novel pet radioligand for nicotinic acetylcholine receptors: synthesis and initial evaluation. *J. Label. Compd. Radiopharm.* **2001**, *44*, 257-259.

[22] Mühlhausen U., Ermert J., Herth M.M., Coenen H.H. Synthesis, radiofluorination and first evaluation of (±)-[^{18}F]MDL100907 as serotonin 5-HT2A receptor antagonist for PET. *J. label. Compd. Radiopharm.* **2009**, *52*, 6-12.

[23] Bongarzone S., Basagni F., Sementa T., Singh N., Gakpetor C., Faugeras V., Bordoloi J., Gee A.D. Development of [18F]FAMTO: A novel fluorine-18 labelled positron emission tomography (PET) radiotracer for imaging CYP11B1 and CYP11B2 enzymes in adrenal glands. *Nucl. Med. Biol.* **2019**; *68-69*, 14-21.

[24] Dolle F. Fluorine-18 labelled fluoropyridines: advances in radiopharmaceutical design. *Curr. Pharm. Des.* **2005**, *11*, 3221-3235.

[25] Ermert J., Hocke C., Ludwig T., Gail R., Coenen H.H. Comparison of pathways to the versatile synthon of no-carrier-added 1-bromo-4-[^{18}F]fluorobenzene. *J. Label. Compd. Radiopharm.* **2004**, *47*, 429-441.

[26] Kennedy M.D., Jallad K.N., Thompson D.H., Dor B.-A. Optical imaging of metastatic tumors using a folate-targeted fluorescent probe. *J. Biomed. Opt.* **2003**, *8*, 636-641.

[27] Bish S., Wang Y., Tunnell J.W., Zhang X. MEMS scanner based handheld fluorescent hyperspectral imaging system. *Sens. Actuator A Phys.* **2012**, *188*, 450-455.

[28] Zhao Q., Jiang H., Cao Z., Yang L., Mao H., Lipowska M. A handheld fluorescence molecular tomography system for intraoperative optical imaging of tumor margins. *Med. Phys.* **2011**, *38*, 5873-5878.

[29] Cheng S., Cuenca R.M., Liu B., Malik B.H., Jabbour J.M., Maitland K.C., Wright J., Cheng Y-S.L., Jo J.A. Handheld multispectral fluorescence lifetime imaging system for *in vivo* applications. *Biomed. Opt. Express.* **2014**, *5*, 921-931.

[30] Ntziachristos V., Schellenberger E.A., Ripoll J., Yessayan D., Graves E., Bogdanov A., Josephson L., Weissleder R. Visualization of antitumor treatment by means of fluorescence molecular tomography with an annexin V–Cy5.5 conjugate. *Proc. Natl. Acad. Sci.* **2004**, *101*, 12294-12299.

[31] Hong G., Antaris A.L., Dai H. Near-infrared fluorophores for biomedical imaging. *Nat. Biomed. Eng*. **2017**, *1*, 10.

[32] Maestro L.M., Ramirez-Hernandez J.E., Bogdan N., Capobianco J.A., Vetrone F., Solé J.G., Jaque D. Deep tissue bio-imaging using two-photon excited CdTe fluorescent quantum dots working within the biological window. *Nanoscale*. **2012**, *4*, 298-302.

[33] Valeur B., Berberan-Santos M.N. Molecular fluorescence: principles and applications. *Wiley*. 2012.

[34] Raszeja L.J., Siegmund D., Cordes A.L., Güldenhaupt J., Gerwert K., Hahn S., Metzler-Nolte N. Asymmetric rhenium tricarbonyl complexes show superior luminescence properties in live cell imaging. *Chem. Commun*. **2017**, *53*, 905-908.

[35] Gao Q., Zhang W., Song B., Zhang R., Guo W., Yuan J. Development of a novel lysosome-targeted ruthenium(II) complex for phosphorescence/time-gated luminescence assay of biothiols. *Anal. Chem*. **2017**, *89*, 4517-4524.

[36] Zhao Q., Huang C., Li F. Phosphorescent heavy-metal complexes for bioimaging. *Chem. Soc. Rev*. **2011**, *40*, 2508-2524.

[37] Kowalski K., Szczupak Ł., Bernaś T., Czerwieniec R. Luminescent rhenium(I)–chromone bioconjugate: Synthesis, photophysical properties, and confocal luminescence microscopy investigation. *J. Organomet. Chem*. **2015**, *782*, 124-130.

[38] Fernández-Moreira V., Ortego M.L., Williams C.F., Coogan M.P., Villacampa M.D., Gimeno M.C. Bioconjugated rhenium(I) complexes with amino acid derivatives:

synthesis, photophysical properties, and cell imaging studies. *Organometallics*. **2012**, *31*, 5950-5957.

[39] Fernández-Moreira V., Thorp-Greenwood F.L., Coogan M.P. Application of d^6 transition metal complexes in fluorescence cell imaging. *Chem. Commun*. **2010**, *46*, 186-202.

[40] Fernández-Moreira V., Thorp-Greenwood F.L., Amoroso A.J., Cable J., Court J.B., Gray V., Hayes A.J., Jenkins R.L., Kariuki B.M., Lloyd D., Millet C.O., Williams C.F., Coogan M.P. Uptake and localisation of rhenium fac-tricarbonyl polypyridyls in fluorescent cell imaging experiments. *Org. Biomol. Chem.* **2010**, *8*, 3888-3901.

[41] Fernández-Moreira V., Thorp-Greenwood F.L., Amoroso A.J., Cable J., Court J.B., Gray V., Hayes A.J., Jenkins R.L., Kariuki B.M., Lloyd D., Millet C.O., Williams C.F., Coogan M.P. Uptake and localisation of rhenium fac-tricarbonyl polypyridyls in fluorescent cell imaging experiments. *Org. Biomol. Chem.* **2010**, *8*, 3888-3901.

[42] Balasingham R.G., Coogan M.P., Thorp-Greenwood F.L. Complexes in context: attempting to control the cellular uptake and localisation of rhenium fac-tricarbonyl polypyridyl complexes. *Dalton Trans*. **2011**, *40*, 11663-11674.

[43] Gilbert A., Baggott J.E. Essentials of molecular photochemistry. *Wiley*. **1991**.

[44] Szabó Á., Szendi-Szatmári T., Ujlaky-Nagy L., Rádi I., Vereb G., Szöllősi J., Nagy P. The effect of fluorophore conjugation on antibody affinity and the photophysical properties of dyes. *Biophys. J*. **2018**, *114*, 688-700.

[45] McCombs J.R., Owen S.C. Antibody drug conjugates: design and selection of linker, payload and conjugation chemistry. *AAPS. J.* **2015**, *17*, 339-351.

[46] Enciso A.E., Garzoni M., Pavan G.M., Simanek E.E. Influence of linker groups on the solubility of triazine dendrimers. *New J. Chem.* **2015**, *39*, 1247-1252.

[47] French A.N., Wilson S.R., Welch M.J., Katzenellenbogen J.A. A synthesis of 7α-substituted estradiols: synthesis and biological evaluation of a 7α-pentyl-substituted BODIPY fluorescent conjugate and a fluorine-18-labeled 7α-pentylestradiol analog. *Steroids*. **1993**, *58*, 157-169.

[48] Li Z., Lin T.-P., Liu S., Huang C.-W., Hudnall T.W., Gabbaï F.P., Conti P.S. Rapid aqueous [^{18}F]-labeling of a bodipy dye for positron emission tomography/fluorescence dual modality imaging. *Chem. Commun.* **2011**, *47*, 9324-9326.

[49] Liu S., Li D., Shan H., Gabbaï F.P., Li Z., Conti P.S. Evaluation of ^{18}F-labeled BODIPY dye as potential PET agents for myocardial perfusion imaging. *Nucl. Med. Biol*. **2014**, *41*, 120-126.

[50] Chansaenpak K., Wang H., Wang M., Giglio B., Ma X., Yuan H., Hu S., Wu Z., Li Z. Synthesis and evaluation of [^{18}F]-ammonium BODIPY dyes as potential positron emission tomography agents for myocardial perfusion imaging. *Chem. Euro. J*. **2016**, *22*, 12122-12129.

[51] Liu S., Lin T.-P., Li D., Leamer L., Shan H., Li Z., Gabbaï F.P., Conti P.S. Lewis acid-assisted isotopic ^{18}F-^{19}F exchange in BODIPY dyes: facile generation of positron emission tomography/fluorescence dual modality agents for tumor imaging. *Theranostics*. **2013**, *3*,181-189.

[52] Paulus A., Maenen M., Drude N., Nascimento E.B.M., van Marken Lichtenbelt W.D., Mottaghy F.M., Bauwens M. Synthesis, radiosynthesis and in vitro evaluation of ^{18}F-BODIPY-C_{16}/triglyceride as a dual modal imaging agent for brown adipose tissue. *PLOS one*. **2017**, *12*, 1-13.

[53] Ortmeyer C.P., Haufe G., Schwegmann K., Hermann S., Schäfers M., Börgel F., Wünsch B., Wagner S., Hugenberg V. Synthesis and evaluation of a [^{18}F]BODIPY-labeled caspase-inhibitor. *Bioorg. Med. Chem.* **2017**, *25*, 2167-2176.

[54] Kim H., Kim K., Son S-H., Choi J.Y., Lee K-H., Kim B-T., Byun Y., Choe Y.S. ^{18}F-labeled BODIPY dye: a potential prosthetic group for brain hybrid PET/optical imaging agents. *ACS Chem. Neurosci.* **2019**, *10*, 1445-1451.

[55] Ting R., Aguilera T.A., Crisp J.L., Hall D.J., Eckelman W.C., Vera D.R., Tsien R.Y. Fast ^{18}F labeling of a near-infrared fluorophore enables positron emission tomography and optical imaging of sentinel lymph nodes. *Bioconj. Chem.* **2010**, *21*, 1811-1819.

[56] Yamaguchi A., Hanaoka H., Pirmettis I., Uehara T., Tsushima Y., Papadopoulos M., Arano Y. Injection site radioactivity of ^{99m}Tc-labeled mannosylated dextran for sentinel lymph node mapping. *Mol. Pharm.* **2015**, *12*, 514-519.

[57] Sondak V.K., King D.W., Zager J.S., Schneebaum S., Kim J., Leong S.P.L., Faries M.B., Averbook B.J., Martinez S.R., Puleo C.A. Combined analysis of phase III trials evaluating [^{99m}Tc] tilmanocept and vital blue dye for identification of sentinel lymph nodes in clinically node-negative cutaneous melanoma. *Ann. Surg. Oncol*. **2013**, *20*, 680-688.

[58] Rodriguez E.A., Wang Y., Crisp J.L., Vera D.R., Tsien R.Y., Ting R. New dioxaborolane chemistry enables [^{18}F]-positron-emitting, fluorescent [^{18}F]-multimodality biomolecule generation from the solid phase. *Bioconj Chem.* **2016**, *27*, 1390-1399.

[59] Al-Karmi S., Albu S.A., Vito A., Janzen N., Czorny S., Banevicius L., Nanao M., Zubieta J., Capretta A., Valliant J.F. Preparation of an ^{18}F-labeled hydrocyanine dye as a multimodal probe for reactive oxygen species. *Chem. Euro. J.* **2017**, *23*, 254-258.

[60] Wang Y., An F-F., Chan M., Friedman B., Rodriguez E.A., Tsien R.Y., Aras O., Ting R. ^{18}F-positron-emitting/fluorescent labeled erythrocytes allow imaging of internal hemorrhage in a murine intracranial hemorrhage model. *J. Cereb. Blood. Flow. Metab.* **2017**, *37*, 776-786.

[61] Priem T., Bouteiller C., Camporese D., Brune X., Hardouin J., Romieu A., Renard P-Y. A novel sulfonated prosthetic group for [^{18}F]-radiolabelling and imparting water solubility of biomolecules and cyanine fluorophores. *Org. Biomol. Chem.* **2013**, *11*, 469-479.

[62] Heinrich T.K., Gottumukkala V., Snay E., Dunning P., Fahey F.H., Ted Treves S., Packard A.B. Synthesis of fluorine-18 labeled rhodamine B: a potential PET myocardial perfusion imaging agent. Applied Radiation and Isotopes. **2010**, *68*, 96-100.

[63] Damont A., Boisgard R., Dollé F., Hollocou M., Kuhnast B. Avidin/biotin bioinspired platform for dual in vivo ^{18}F-PET/NIRF molecular imaging. *Bioconj. Chem.* **2017**, *28*, 2524-2529.

[64] Ducongé F., Pons T., Pestourie C., Hérin L., Thézé B., Gombert K., Mahler B., Hinnen F., Kühnast B., Dollé F., Dubertret B., Tavitian B. Fluorine-18-labeled phospholipid quantum dot micelles for in vivo multimodal imaging from whole body to cellular scales. *Bioconj. Chem.* **2008**, *19*, 1921-1926.

[65] Coenen H.H., Gee A.D., Adam M., Antoni G., Cutler C.S., Fujibayashi Y., Jeong J.M., Mach R.H., Mindt T.L., Pike V.W., Windhorst A.D. Consensus nomenclature rules for radiopharmaceutical chemistry — setting the record straight. *Nucl. Med. Biol.* **2017**, 55.

[66] Reiss P., Bleuse J., Pron A. Highly luminescent CdSe/ZnSe core/shell nanocrystals of low size dispersion. *Nano Lett.* **2002**, *2*, 781-784.

[67] Hu K., Wang H., Tang G., Huang T., Tang X., Liang X., Yao S., Nie D. In vivo cancer dual-targeting and dual-modality imaging with functionalized quantum dots. *J. Nucl. Med.* **2015**, *56*, 1278-1284.

[68] Liu Q., Sun Y., Li C., Zhou J., Li C., Yang T., Zhang X., Yi T., Wu D., Li F. ^{18}F-labeled magnetic-upconversion nanophosphors via rare-earth cation-assisted ligand assembly. *ACS Nano.* **2011**, *5*, 3146-3157.

[69] Sun Y., Yu M., Liang S., Zhang Y., Li C., Mou T., Yang W., Zhang X., Li B., Huang C., Li F. Fluorine-18 labeled rare-earth nanoparticles for positron emission tomography (PET) imaging of sentinel lymph node. *Biomaterials*. **2011**, *32*, 2999-3007.

[70] Zhou J., Yu M., Sun Y., Zhang X., Zhu X., Wu Z., Wu D., Li F. Fluorine-18 labeled $Gd^{3+}/Yb^{3+}/Er^{3+}$ co-doped $NaYF_4$ nanophosphors for multimodality PET/MR/UCL imaging. *Biomaterials*. **2011**, *32*, 1148-1156.

[71] Lipowska M., Jarkas N., Voll R.J., Nye J.A., Klenc J., Goodman M.M., Taylor A.T. $Re(CO)_3([^{18}F]FEDA)$, a novel ^{18}F PET renal tracer: radiosynthesis and preclinical evaluation. *Nucl. Med. Biol.* **2018**, *58*, 42-50.

[72] Pratt E.C., Shaffer T.M., Grimm J. Nanoparticles and radiotracers: advances toward radionanomedicine. *Wiley Interdiscip. Rev. Nanomed. Nanobiotechnol.* **2016**, *8*, 872-890.

[73] Ory D., Van den Brande J., de Groot T., Serdons K., Bex M., Declercq L., Cleeren F., Ooms M., Van Laere K., Verbruggen A., Bormans G. Retention of $[^{18}F]$fluoride on reversed phase HPLC columns. *J. Pharmaceut. Biomed.* **2015**, *111*, 209-214.

[74] Keng P.Y., van Dam R.M. Digital microfluidics: a new paradigm for radiochemistry. *Mol. Imaging.* **2015**, *14*, 13-14.

[75] Maslan F.D., Stoddard E.A. Acetonitrile–water liquid–vapor equilibrium. *J. Phys. Chem*. **1956**, *60*, 1146-1147.

[76] Horn E., Snow M.R. Coordinated fluoride in rhenium(I) carbonyl complexes. *Aust. J. Chem.* **1984**, *37*, 35-45.

[77] Horn E., Snow M.R. A tetranuclear carbonyl fluoro rhenium(I) cluster, $[Re(CO)_3F]_4.4H_2O$. *Aust. J. Chem.* **1981**, *34*, 737-743.

[78] Corey E.J., Borror A.L., Foglia T. Transformations in the 1,10-Phenanthroline Series. *J. Org. Chem.* **1965**, *30*, 288-290.

[79] Speca A.N., Pytlewski L.L., Karayannis N.M. Transition metal chloride chelates with 1,10-phenanthroline-N-oxide. *Z. Anorg. Allg. Chem.* **1976**, *422*, 182-192.

[80] Weisheng L., Minyu T. Infrared, thermal and fluorescence investigations of 1,10-phenanthroline-N-oxide chelates with lanthanide chlorides. *Thermochimica Acta.* **1991**, *191*, 135-142.

[81] Chassapis C., Pneumatikakis G. Chelates of the rare earth nitrates with 1,10-phenanthroline-N,N′-dioxide. *Inorganica Chimica Acta.* **1978**, *27*, 67-68.

[82] Carmeli M., Rozen S. Synthesis of 1,10-N,N'-phenanthroline dioxides using $HOF{\cdot}CH_3CN$ complex. *J. Org. Chem.* **2005**, *70*, 2131-2134.

[83] Bramley R., Figgis B.N., Nyholm R.S. ^{13}C and ^{17}O NMR spectra of metal carbonyl compounds. *J. Chem. Soc. Faraday Trans.* **1962**, *58*, 1893-1896.

[84] Matesic L., Kallinen A., Wyatt N.A., Pham T.Q., Greguric I., Pascali G. $[^{18}F]$Fluorination optimisation and the fully automated production of $[^{18}F]$MEL050 using a microfluidic system. *Aust. J. Chem*. **2015**, *68*, 69-71.

[85] Klenner M.A., Pascali G., Zhang B., Sia T.R., Spare L.K., Krause-Heuer A.M., Aldrich-Wright J.R., Greguric I., Guastella A.J., Massi M., Fraser B.H. A fluorine-18 radiolabeling method enabled by rhenium(I) complexation circumvents the requirement of anhydrous conditions. *Chem. Euro. J.* **2017**, *23*, 6499-6503.

[86] Ramos L.D., Sampaio R.N., de Assis F.F., de Oliveira K.T., Homem-de-Mello P., Patrocinio A.O.T., Frin K.P.M. Contrasting photophysical properties of rhenium(I) tricarbonyl complexes having carbazole groups attached to the polypyridine ligand. *Dalton Trans.* **2016**, *45*, 11688-11698.

[87] Gonçalves M.R., Frin K.P.M. Synthesis, characterization, photophysical and electrochemical properties of fac-tricarbonyl(4,7-dichloro-1,10-phenanthroline) rhenium(I) complexes. *Polyhedron*. **2015**, *97*, 112-117.
[88] Kirgan R., Simpson M., Moore C., Day J., Bui L., Tanner C., Rillema D.P. Synthesis, characterization, photophysical, and computational studies of rhenium(I) tricarbonyl complexes containing the derivatives of bipyrazine. *Inorg. Chem.* **2007**, *46*, 6464-6472.
[89] Ren W., Li J., Zou D., Wu Y., Wu Y. Palladium-catalyzed Suzuki–Miyaura cross-coupling reaction of potassium 2-pyridyl trifluoroborate with aryl (heteroaryl) halides. *Tetrahedron*. **2012**, *68*, 1351-1358.
[90] Barder T.E., Buchwald S.L. Efficient catalyst for the Suzuki−Miyaura coupling of potassium aryl trifluoroborates with aryl chlorides. *Org. Lett.* **2004**, *6*, 2649-2652.
[91] Sakashita S., Takizawa M., Sugai J., Ito H., Yamamoto Y. Tetrabutylammonium 2-pyridyltriolborate salts for Suzuki–Miyaura cross-coupling reactions with aryl chlorides. *Org. Lett.* **2013**, *15*, 4308-4311.
[92] Molander G.A., Canturk B. Organotrifluoroborates and monocoordinated palladium complexes as catalysts — a perfect combination for Suzuki–Miyaura coupling. *Angew. Chemie. Int. Ed.* **2009**, *48*, 9240-9261.
[93] Matsumura K., Ono M., Kimura H., Ueda M., Nakamoto Y., Togashi K., Okamoto Y., Ihara M., Takahashi R., Saji H. ^{18}F-labeled phenyldiazenyl benzothiazole for in vivo imaging of neurofibrillary tangles in Alzheimer's disease brains. *ACS Med. Chem. Lett.* **2012**, *3*, 58-62.
[94] Walji A.M., Hostetler E.D., Selnick H., Zeng Z., Miller P., Bennacef I., Salinas C., Connolly B., Gantert L., Holahan M., O'Malley S., Purcell M., Riffel K., Li J., Balsells J., Obrien J.A., Melquist S., Soriano A., Zhang X., Ogawa A., Xu S., Joshi E., Della Rocca J., Hess F.J., Schachter J., Hesk D., Schenk D., Struyk A., Babaoglu K., Lohith T.G., Wang Y., Yang K., Fu J., Evelhoch J.L., Coleman P.J. Discovery of 6-(Fluoro-18F)-3-(1H-pyrrolo[2,3-c]pyridin-1-yl)isoquinolin-5-amine ([^{18}F]-MK-6240): a positron emission tomography (PET) imaging agent for quantification of neurofibrillary tangles (NFTs). *J. Med. Chem.* **2016**, *59*, 4778-4789.
[95] Gong B., Cao Z., Zheng P., Vitolo O.V., Liu S., Staniszewski A., Moolman D., Zhang H., Shelanski M., Arancio O. Ubiquitin hydrolase Uch-L1 rescues β-amyloid-induced decreases in synaptic function and contextual memory. *Cell*. **2006**, *126*, 775-788.
[96] Ghavami M., Rezaei M., Ejtehadi R., Lotfi M., Shokrgozar M.A., Abd Emamy B., Raush J., Mahmoudi M. Physiological temperature has a crucial role in amyloid beta in the absence and presence of hydrophobic and hydrophilic nanoparticles. *ACS Chem. Neurosci.* **2013**, *4*, 375-378.
[97] Savelieff M.G., Lee S., Liu Y., Lim M.H. Untangling amyloid-β, tau, and metals in Alzheimer's disease. *ACS Chem. Biol.* **2013**, *8*, 856-865.
[98] Muthuraj B., Layek S., Balaji S.N., Trivedi V., Iyer P.K. Multiple function fluorescein probe performs metal chelation, disaggregation, and modulation of aggregated Aβ and Aβ-Cu complex. *ACS Chem. Neurosci.* **2015**, *6*, 1880-1891.
[99] Mutter S.T., Turner M., Deeth R.J., Platts J.A. Metal binding to amyloid-β1–42: a ligand field molecular dynamics study. *ACS Chem. Neurosci.* **2018**, *9*, 2795-2806.
[100] Liang S.H., Southon A.G., Fraser B.H., Krause-Heuer A.M., Zhang B., Shoup T.M., Lewis R., Volitakis I., Han Y., Greguric I., Bush A.I., Vasdev N. Novel fluorinated 8-hydroxyquinoline based metal ionophores for exploring the metal hypothesis of Alzheimer's disease. *ACS Med. Chem. Lett.* **2015**, *6*, 1025-1029.
[101] Holland J.P., Liang S.H., Rotstein B.H., Collier T.L., Stephenson N.A., Greguric I., Vasdev N. Alternative approaches for PET radiotracer development in Alzheimer's disease: imaging beyond plaque. *J. Labelled. Comp. Radiopharm*. **2014**, *57*, 323-331.

[102] Liang S.H., Collier T.L., Rotstein B.H., Lewis R., Steck M., Vasdev N. Rapid microfluidic flow hydrogenation for reduction or deprotection of ^{18}F-labeled compounds. *Chem. Commun.* **2013**, *49*, 8755-8757.
[103] Vasdev N., Cao P., van Oosten E.M., Wilson A.A., Houle S., Hao G., Sun X., Slavine N., Alhasan M., Antich P.P., Bonte F.J., Kulkarni P. Synthesis and PET imaging studies of [^{18}F]2-fluoroquinolin-8-ol ([^{18}F]CABS13) in transgenic mouse models of Alzheimer's disease. *MedChemComm.* **2012**, *3*, 1228-1230.
[104] Liang S.H., Holland J.P., Stephenson N.A., Kassenbrock A., Rotstein B.H., Daignault C.P., Lewis R., Collier L., Hooker J.M., Vasdev N. PET neuroimaging studies of [^{18}F]CABS13 in a double transgenic mouse model of Alzheimer's disease and nonhuman primates. *ACS Chem. Neurosci.* **2015**, *6*, 535-541.
[105] Chen Q., Mayer P., Mayr H. Ethenesulfonyl fluoride: the most perfect Michael acceptor ever found? *Angew. Chem. Int. Ed.* **2016**, *55*, 12664-12667.
[106] Wang H., Zhou F., Ren G., Zheng Q., Chen H., Gao B., Klivansky L., Liu Y., Wu B., Xu Q., Lu J., Sharpless K.B., Wu P. SuFEx-Based polysulfonate formation from ethenesulfonyl fluoride–amine adducts. *Angew. Chem*. **2017**, *129*, 11355-11360.
[107] Chinthakindi P.K., Arvidsson P.I. Sulfonyl fluorides (SFs): more than click reagents? *Euro. J. Org. Chem.* **2018**, *27-28*, 3648-3666.
[108] Inkster J.A.H., Liu K., Ait-Mohand S., Schaffer P., Guérin B., Ruth T.J., Storr T. Sulfonyl fluoride-based prosthetic compounds as potential ^{18}F labelling agents. *Chem. Euro. J.* **2012**, *18*, 11079-11087.
[109] Zhang B., Pascali G., Wyatt N., Matesic L., Klenner M.A., Sia T.R., Guastella A.J., Massi M., Robinson A.J., Fraser B.H. Synthesis, bioconjugation and stability studies of [^{18}F]ethenesulfonyl fluoride. *J. Labelled Comp. Radiopharm.* **2018**, *61*, 847-856.
[110] Klenner M.A., Pascali G., Zhang B., Ciancaleoni G., Massi M., Fraser B.H. Effect of rhenium(I) complexation on aza-Michael additions to 5-amino-1,10-phenanthroline with [^{18}F]ethenesulfonyl fluoride towards PET optical tracer development. *Aust. J. Chem*. **2018**, *72*, 288-294.
[111] Bessette A., Nag S., Pal A.K., Derossi S., Hanan G.S. Neutral Re(I) complexes for anion sensing. *Supramol. Chem*. **2012**, *24*, 595-603.
[112] Kefalidi C., Koutsouri E., Marchiò L., Zarkadoulas A., Efstathiadou S., Mitsopoulou C.A. Synthesis, characterization and crystal structure of rhenium(I) tricarbonyl diimine complexes coupled with their efficiency in producing hydrogen in a photocatalytic system. *Polyhedron*. **2016**, *110*, 157-164.
[113] Greguric I., Taylor S., Pham T., Wyatt N., Jiang C.D., Bourdier T., Loc'h C., Roselt P., Neels O.C., Katsifis A. Radiosynthesis of a novel PET fluoronicotinamide for melanoma tumour PET imaging; [^{18}F]MEL050. *Aust. J. Chem.* **2011**, *64*, 873-879.
[114] Shoup T.M., Yokell D.L., Rice P.A., Jackson R.N., Livni E., Johnson K.A., Brady T.J., Vasdev N. A concise radiosynthesis of the tau radiopharmaceutical, [^{18}F]T807. *J. Labelled. Comp. Radiopharm.* **2013**, *56*, 736-740.
[115] Zhang Y., Horti A.G. Synthesis of 6-chloro-3-((2-(S)-azetidinyl)methoxy)-5-(2-[^{18}F]fluoropyridin-4-yl)pyridine ([^{18}F]NIDA522131), a novel potential radioligand for studying extrathalamic nicotinic acetylcholine receptors by PET. *J. Labelled. Comp. Radiopharm.* **2004**, *47*, 947-952.
[116] Song Q., Jones R.A. Use of silyl ethers as fluoride scavengers in RNA synthesis. *Tetrahedron Lett.* **1999**, *40*, 4653-4654.
[117] Dai W., Kim S.B., Pike R.D., Cahill C.L., Sweigart D.A. Electrochemical study of manganese and rhenium arene complexes $(C_6R_6)M(CO)_3^+$ (R = Me, Et). *Organometallics*. **2010**, *29*, 5173-5178.

[118] Fang X., Scott B.L., John K.D., Kubas G.J. Synthesis of and small molecule coordination to highly electrophilic cationic manganese(I) and rhenium(I) carbonyl complexes with tied-back phosphites. *Organometallics.* **2000**, *19*, 4141-4149.
[119] Peng C-L., Shih Y-H., Yeh C-H., Tang I.C., Luo T-Y., Shieh M-J. Radioisotope-labeled micelles containing near-infrared dye for dual SPECT and optical imaging. *J. Nucl. Med.* **2012**, *53*, 1683-1683.
[120] Boulay A., Artigau M., Coulais Y., Picard C., Mestre-Voegtlé B., Benoist E. First dinuclear Re/Tc complex as a potential bimodal Optical/SPECT molecular imaging agent. *Dalton. Trans.* **2011**, *40*, 6206-6209.

APPENDICES

A.1 Permissions

Figures 3 and 9 were released into the public domain under the Wikimedia Commons license agreement and the Creative Commons Attribution ShareAlike 3.0 Unported (CC BY-SA 3.0) International Licence.

Figure 7 was reprinted (adapted) with permission from Kennedy M.D., Jallad K.N., Thompson D.H., Dor B.-A. Optical imaging of metastatic tumors using a folate-targeted fluorescent probe. *J. Biomed. Opt.* **2003**, *8*, 636-641. Under the Creative Commons Attribution Non-Commerical 4.0 (CC BY-NC 4.0) International Licence.

Figure 17 was reprinted (adapted) with permission from Li Z., Lin T.-P., Liu S., Huang C.-W., Hudnall T.W., Gabbaï F.P., Conti P.S. Rapid aqueous [^{18}F]-labeling of a bodipy dye for positron emission tomography/fluorescence dual modality imaging. *Chem. Commun.* **2011**, *47*, 9324-9326. Copyright 2019 Royal Society of Chemistry.

Figure 19 was reprinted with permission from Liu S., Lin T.-P., Li D., Leamer L., Shan H., Li Z., Gabbaï F.P., Conti P.S. Lewis acid-assisted isotopic 18F-19F exchange in BODIPY dyes: facile generation of positron emission tomography/fluorescence dual modality agents for tumor imaging. *Theranostics*. **2013**, *3*,181-189. Under the Creative Commons Attribution Non-Commerical 4.0 (CC BY-NC 4.0) International Licence.

Figure 162 was reprinted (adapted) with permission from Liang S.H., Holland J.P., Stephenson N.A., Kassenbrock A., Rotstein B.H., Daignault C.P., Lewis R., Collier L., Hooker J.M., Vasdev N. PET neuroimaging studies of [^{18}F]CABS13 in a double transgenic mouse model of Alzheimer's disease and nonhuman primates. *ACS Chem. Neurosci.* **2015**, *6*, 535-541. Copyright 2019 American Chemical Society.

A.2 Publications

This thesis work was based on the following peer-reviewed publications:

[1] **Klenner M.A**., Pascali G., Zhang B., Sia T.R., Spare L.K., Krause-Heuer A.M., Aldrich-Wright J.R., Greguric I., Guastella A.J., Massi M., Fraser B.H. A fluorine-18 radiolabelling method enabled by rhenium(I) complexation circumvents the requirement of anhydrous conditions. *Chem. Euro. J*. **2017**, *23*, 6499-6503.

[2] **Klenner M.A.**, Pascali G., Zhang B., Ciancaleoni G., Massi M., Fraser B.H. Effect of rhenium(I) complexation on aza-Michael additions to 5-amino-1,10-phenanthroline with [^{18}F]ethenesulfonyl fluoride towards PET optical tracer development. *Aust. J. Chem*. **2018**, *72*, 288-294.

[3] **Klenner, M.A.**, Pascali, G., Ciancaleoni, G., Howard, J. Maynard-Casely, H.E., Clegg, J. Massi, M., Fraser, B.H. Rhenium(I) complexation-dissociation strategy for synthesizing fluorine-18 labelled pyridine bidentate structures. *Under Review.* **2019**.

These articles are attached in the following pages of the appendices with the expressed permission from John Wiley and Sons for article [1] and from the Commonwealth Scientific and Industrial Research Organisation (CSIRO) for article [2].

Contributions were also made to the following articles based on the work described herein:

[4] Zhang, B., Pascali, G., Wyatt, N., Matesic, L., **Klenner, M.A.**, Sia, T.R., Guastella, A.J., Massi, M., Robinson, A.J., Fraser, B.H. Synthesis, bioconjugation and stability studies of [^{18}F]ethenesulfonyl fluoride. *J. Label. Compd. Radiopharm.* **2018**, *61*, 847-856.

[5] Zhang, B., Fraser, B.H., **Klenner, M.A.**, Chen, Z., Liang, S.H., Massi, M., Robinson, A.J., Pascali, G. [^{18}F]Ethenesulfonyl fluoride as a practical radiofluoride relay reagent. *Chem. Euro. J.* **2019**, *Just Accepted*.

This thesis work and contributions therein were also presented to scientific audiences at the following conference proceedings:

[1] **Klenner, M.A.**, Pascali, G., Zhang, B., Sia, T.R., Massi, M., Fraser, B.H. Automated radiosynthesis of PET-optical imaging probes using microfluidics and cyclotron generated [^{18}F]fluoride. *The 50th Symposium of North-Eastern Accelerator Personal (SNEAP) & The 8th Accelerator Technical Forum (ATF).* Sydney, Australia. **2016**.

[2] **Klenner, M.A.**, Pascali, G., Zhang, B., Sia, T.R., Massi, M., Fraser, B.H. Complexation with rhenium(I) allows radiofluorination of a target ligand without the need for preliminary azeotropic distillation. *Innovation in Radiation Applications (IRA)*. Wollongong, Australia. **2017**.

[3] **Klenner, M.A**., Pascali G., Zhang B., Sia T.R., Spare L.K., Krause-Heuer A.M., Aldrich-Wright J.R., Greguric I., Guastella A.J., Massi M., Fraser B.H. Effect of Re(I) complexation in the radiosynthesis of prospective [^{18}F]fluorine labelled PET/optical probes. *The 22nd International Symposium on Radiopharmaceutical Sciences (ISRS).* Dresden, Germany. **2017**.

[4] Zhang, B., Pascali, G., Sia, T.R., **Klenner, M.A.**, Matesic, L., Robinson, A., Guastella, A.J., Fraser, B.H. [^{18}F]Ethenesulfonyl fluoride: a prospective ^{18}F-synthon for the indirect radiolabelling of biological vectors. *The 22nd International Symposium on Radiopharmaceutical Sciences (ISRS)*. Dresden, Germany. **2017**.

[5] **Klenner, M.A.**, Pascali, G., Zhang, B., Sia, T.R., Massi, M., Fraser, B.H. Microfluidic technologies reveal a novel method to expand the accessibility of radiofluorinated nuclear medicines. *The 8th International Nanomedicine Conference.* Sydney, Australia. **2017**.

[6] **Klenner, M.A.**, Pascali, G., Zhang, B., Sia, T.R., Massi, M., Fraser, B.H. The discovery of a new radiofluorination method using rhenium complexes. *The Royal Australian Chemical Institute (RACI) 100th Centenary Conference & The 17th Asian Chemical Congress (ACC).* Melbourne, Australia. **2017**.

[7] Fraser, B.H., Zhang, B., **Klenner, M.A.**, Robinson, A., Pascali, G. New Michael acceptor and rhenium(I) 18F-radiolabelling methods for radiopharmaceutical development. *The Royal Australian Chemical Institute (RACI) 100th Centenary Conference & The 17th Asian Chemical Congress (ACC).* Melbourne, Australia. **2017**.

[8] **Klenner, M.A.**, Pascali, G., Zhang, B., Sia, T.R., Massi, M., Fraser, B.H. New method for improving the radiosynthesis of fluorine-18 labelled nuclear medicines. *The ANSTO Young Researchers Conference (AYRC).* Sydney, Australia. **2017**.

[9] **Klenner, M.A.**, Pascali, G., Zhang, B., Sia, T.R., Massi, M., Fraser, B.H. Expanding the accessibility of [^{18}F]fluoride-labelled pyridinyl-bearing nuclear medicines *via* rhenium activation. *The 3rd Australian Society of Molecular Imaging (ASMI) Scientific Meeting*. Sydney, Australia. **2017**.

[10] Pascali, G., **Klenner, M.A.**, Massi, M., Fraser, B.H. A side route to PET-optical probes: Re(I) complexation enables milder ^{18}F-fluorination conditions. *The 3rd Australian Society of Molecular Imaging (ASMI) Scientific Meeting*. Sydney, Australia. **2017**.

[11] **Klenner, M.A.**, Pascali, G., Zhang, B., Sia, T.R., Massi, M., Fraser, B.H. Applying rhenium coordination towards the improved fluorine-18 radiolabelling of bipyridine nuclear medicines. *The 9th International Symposium on Technetium and Rhenium (ISTR)*. Cronulla, Australia. **2017**.

[12] **Klenner, M.A.**, Pascali, G., Zhang, B., Sia, T.R., Massi, M., Fraser, B.H. Improved synthesis of nuclear medicines *via* rhenium(I) activated radiofluorination. *The 11th Australasian Organometallics Meeting (OZOM)*. Perth, Australia. **2018**.

[13] Fraser, B.H., **Klenner, M.A.**, Pascali, G., Massi, M. Re(I) promoted ^{18}F-fluorinations for the preparation of PET/optical molecular probes. *The 267th American Chemical Society (ACS) National Meeting & Exposition.* New Orleans, USA. **2018**.

[14] **Klenner, M.A.** Creating market application from nuclear medicine research. *Create, Innovate, Translate Conference.* Cronulla, Australia. **2018**.

[15] **Klenner, M.A.**, Fraser, B.H., Massi, M., Pascali, G. Re-mediation for the radiofluorination of pyridine-based structures. *The 22nd International Symposium on Fluorine Chemistry (ISFC).* Oxford, UK. **2018**.

[16] **Klenner, M.A.**, Pascali, G., Massi, M., Ciancaleoni, G., Fraser, B.H. Rhenium enhanced radiopharmaceutical production of fluorine-18 labelled bidentate ligands. *The 10th International Symposium on Technetium and Rhenium (ISTR).* Moscow, Russia. **2018**.

[17] **Klenner, M.A.**, Zhang, B., Pascali, G., Massi, M., Fraser, B.H. Radiofluorinations of pyridine molecular structures assisted by rhenium complexation. *University of Wollongong (UOW)-ANSTO Networking Workshop.* Wollongong, Australia. **2018**.

[18] **Klenner, M.A.**, Zhang, B., Pascali, G., Massi, M., Fraser, B.H. Coupling rhenium with ^{18}F PET chemistry: applications to Alzheimer's disease and prostate cancer imaging. *The 4th Australian Society of Molecular Imaging (ASMI) Scientific Meeting*. Perth, Australia. **2018**.

[19] **Klenner, M.A.**, Pascali, G., Zhang, B. Massi, M., Fraser, B.H. Advances in rhenium coupled ^{18}F PET chemistry: radiofluorinated bidentate ligands. *The 23rd International Symposium of Radiopharmaceutical Sciences (ISRS)*. Beijing, China. **2019**.

[20] Parmar, A., Pascali, G., Hering, A., Rahardjo, G., Arthur, A., Hamze, H., Zahra, D., Zhang, B., Mackay, T.R., Matesic, L., **Klenner, M.A.**, Tran, M., Banati, R., Gregorie, M-C., Muttenthaler, M., Guastella, A.J. Development and characterisation of novel PET tracers for oxytocin receptor imaging. *The World Molecular Imaging Conference (WMIC).* Montreal, Canada. **2019**.

ChemPubSoc Europe

DOI: 10.1002/chem.201700440

CHEMISTRY A European Journal Communication

Radiochemistry

A Fluorine-18 Radiolabeling Method Enabled by Rhenium(I) Complexation Circumvents the Requirement of Anhydrous Conditions

Mitchell A. Klenner,[a, b] Giancarlo Pascali,*[a, c] Bo Zhang,[a, d] Tiffany R. Sia,[a, c] Lawson K. Spare,[e] Anwen M. Krause-Heuer,[a] Janice R. Aldrich-Wright,[e] Ivan Greguric,[a] Adam J. Guastella,[c] Massimiliano Massi,[b] and Benjamin H. Fraser*[a]

Abstract: Azeotropic distillation is typically required to achieve fluorine-18 radiolabeling during the production of positron emission tomography (PET) imaging agents. However, this time-consuming process also limits fluorine-18 incorporation, due to radioactive decay of the isotope and its adsorption to the drying vessel. In addressing these limitations, the fluorine-18 radiolabeling of one model rhenium(I) complex is reported here, which is significantly improved under conditions that do not require azeotropic drying. This work could open a route towards the investigation of a simplified metal-mediated late-stage radiofluorination method, which would expand upon the accessibility of new PET and PET-optical probes.

Positron emission tomography (PET) plays an important clinical role towards unveiling the underlying biochemistry of diseases through the administration of positron (β^+) emitting radiopharmaceuticals. Radiosynthesis of most PET tracers needs to be performed quickly to obtain a large enough dose for a successful PET imaging experiment, owing to the radioactive decay of the β^+ emitting isotope. Therefore, the production of PET radiotracers is performed using automated synthesis modules, and many research groups have worked towards integrating microfluidic technologies to reduce the radiation dose, miniaturize the workspace, and improve production.[1] Fluorine-18 is the most commonly employed PET radioisotope, owing to its 97% β^+ decay profile, ideal 109.7 min half-life, and low 0.64 MeV β^+ energy.[2] However, one drawback is that fluorine-18 is generally produced by the cyclotron-mediated $^{18}O(p,n)^{18}F$ reaction on oxygen-18 enriched water, which affords [^{18}F]fluoride in an aqueous environment, which is typically unreactive towards nucleophilic substitution; nonetheless, the interest in employing this unfavorable aqueous environment has inspired some innovative approaches.[3] Traditionally, to provide an anhydrous environment, the [^{18}F]fluoride in water is trapped on an anion-exchange resin (thus also removing radioactive cationic impurities), eluted with a complexing agent in aqueous/organic solvent mixture, and azeotropically dried in a distillation vial. This azeotropic drying is an inefficient and time-consuming process ($>$15 mins),[4] during which period, radioactivity ($\geq$10%) is lost due to the radioactive decay of the fluorine-18 isotope, as well as non-specific adsorption of [^{18}F]fluoride to the surface of the distillation vial, leading to lower radiochemical yield (RCY) of the PET radiotracer.[3,5]

Having been inspired by recent efforts to couple PET imaging with an optical tracer to complement disease diagnosis,[6] and given our experience in the use of phosphorescent rhenium(I) tricarbonyl diimine systems as optical markers for live cell imaging and diagnosis of pathologies,[7] we sought to investigate the fluorine-18 radiolabeling of this class of rhenium complexes as potential precursors for the future development of PET-optical multimodal markers. Scheme 1 shows the synthetic route used to synthesize the ligand (**3**) and complex (**5**) precursors, as well as the non-radioactive standards **4** and **6**. *N*-Oxidation of 1,10-phenanthroline allowed for selective chlorination in the 2-position by the Vilsmeier reagent to afford **3**. Nucleophilic aromatic substitution with azeotropically dried fluoride, using 18-crown-6 as a phase-transfer catalyst, then afforded the novel 2-fluoro-1,10-phenanthroline ligand (**4**). Ligands **3** and **4** were then chelated to a Re^I metal center to attain complexes **5** and **6**, respectively (see the Supporting Information, sections 1.1–1.5).

The radiosyntheses of [^{18}F]**4** and [^{18}F]**6**, from **3** and **5** precursors, respectively, were automated by means of a flow chemistry set-up adapted from our previous work,[8] as shown in

[a] M. A. Klenner, Dr. G. Pascali, B. Zhang, T. R. Sia, Dr. A. M. Krause-Heuer, Dr. I. Greguric, Dr. B. H. Fraser
Australian Nuclear Science and Technology Organisation (ANSTO)
New Illawarra Rd, Lucas Heights, New South Wales (Australia)
E-mail: Gianp@ansto.gov.au
bfr@ansto.gov.au

[b] M. A. Klenner, Dr. M. Massi
Department of Chemistry, Curtin University
Kent St, Bentley, Western Australia (Australia)

[c] Dr. G. Pascali, T. R. Sia, Prof. A. J. Guastella
Brain and Mind Centre The University of Sydney
Mallett St, Camperdown, New South Wales (Australia)

[d] B. Zhang
Monash University
Wellington Road, Clayton, Victoria (Australia)

[e] L. K. Spare, Prof. J. R. Aldrich-Wright
School of Science and Health, Western Sydney University
Penrith, New South Wales (Australia)

Supporting information and the ORCID identification number(s) for the author(s) of this article can be found under:
http://dx.doi.org/10.1002/chem.201700440.

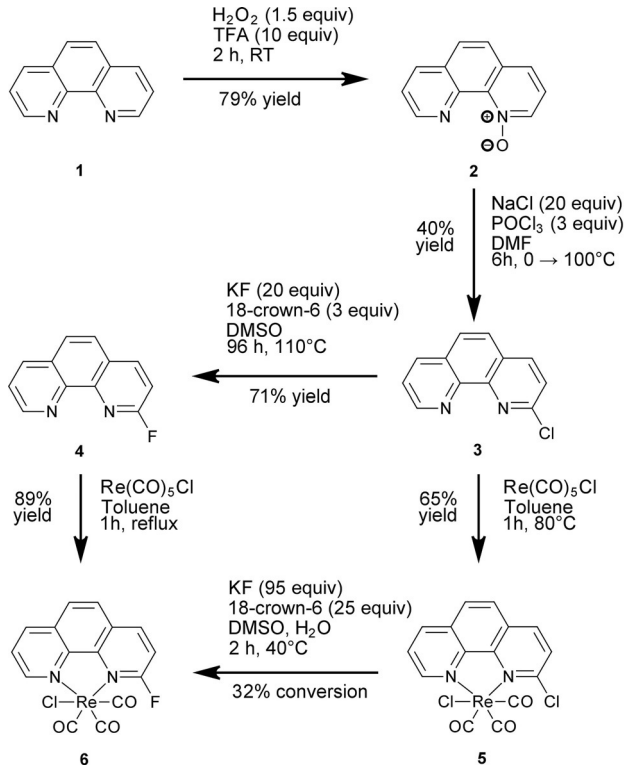

Scheme 1. Synthesis of radiolabeling precursors **3** and **5**, and non-radioactive standards **4** and **6**. Refer to the Supporting Information, sections 1.1–1.5 for detailed procedures.

Figure 1. Within this set-up, aqueous [^{18}F]fluoride was first passed through an MP1 cartridge and eluted with tetraethylammonium bicarbonate ($TEA^+HCO_3^-$) in 90% CH_3CN:H_2O solution. The resulting [^{18}F]TEA^+F^- complex was then either azeotropically dried ("dry" conditions) or not azeotropically dried ("wet" conditions), before being loaded into the microreactor alongside the desired precursor solution (**3** or **5**).

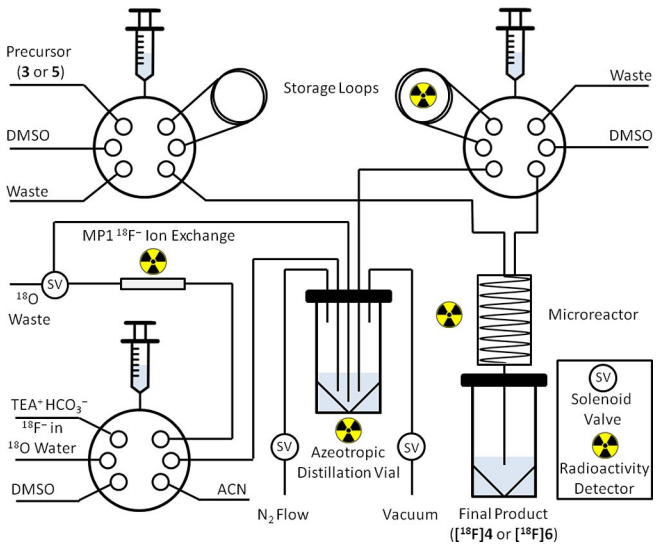

Figure 1. Simplified schematic of the flow chemistry configuration assembled for the automated syntheses of compounds [^{18}F]**4** and [^{18}F]**6**.

The RCYs obtained for the radiosynthesis of [^{18}F]**4** from **3** under varying temperature conditions are illustrated in Figure 2. These conditions employed the same residence times (47 s) and precursor amounts (0.08–0.12 μmol) within the microreactor. Under traditional dry conditions, the RCY of ligand [^{18}F]**4** followed the expected trend, whereupon the yield increases as a function of temperature.[8] In this instance, [^{18}F]**4** only formed at temperatures greater than 130 °C, providing a maximum RCY of 61% at 190 °C. The radiosynthesis of complex [^{18}F]**6** from **5** was then attempted under analogous dry conditions, and the dependence of RCY on temperature is illustrated in Figure 3.

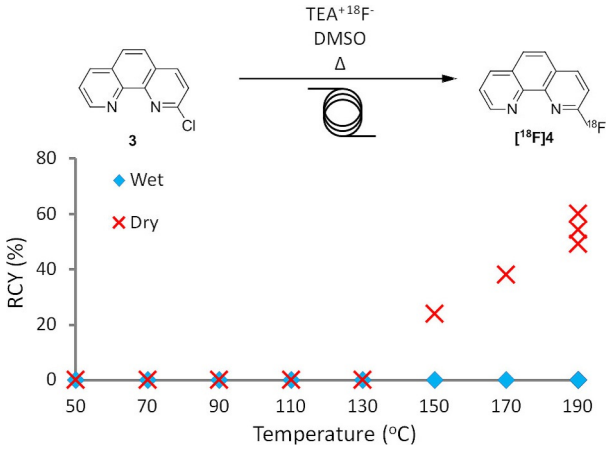

Figure 2. Temperature dependence of nucleophilic aromatic substitution of ligand **3** with [^{18}F]fluoride under azeotropically dried (red crosses) and non-azeotropically dried (blue squares) conditions.

Intriguingly, in this case we observed an opposite trend to the ligand, whereupon the complex [^{18}F]**6** only formed at temperatures below 150 °C (in contrast to the ligand [^{18}F]**4**, which required higher temperatures to afford a radioproduct). The RCYs for the complex [^{18}F]**6** were also noticeably lower than that of the ligand [^{18}F]**4**, with a maximum of 19% RCY obtained

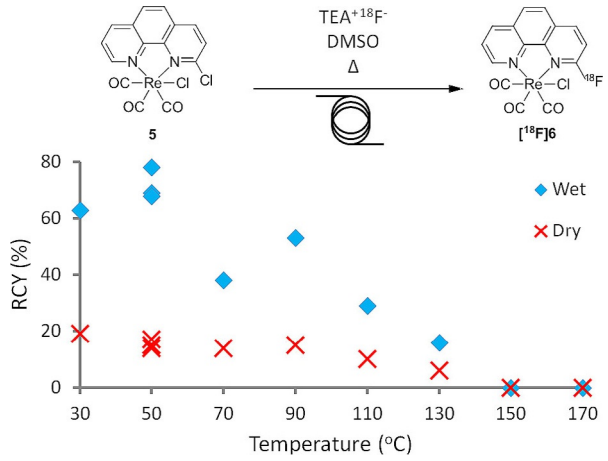

Figure 3. Temperature dependence of nucleophilic aromatic substitution of complex **5** with [^{18}F]fluoride under azeotropically dried (red crosses, "dry") and not azeotropically dried (blue squares, "wet") conditions.

at 30 °C; in addition, there was the clearly noticeable appearance of a UV-absorbing degradation product (Figure 4). We suspected that this byproduct could be due to base-mediated degradation of **5**, and we indeed verified this by analyzing in

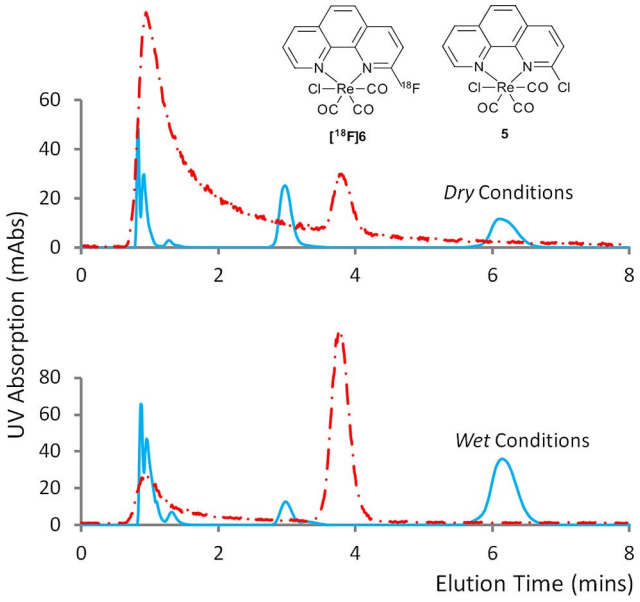

Figure 4. UV absorbance (254 nm, solid blue) and superimposed radioactive (dashed red) profiles, for dry and wet analogous conditions (top and bottom, respectively). UV active degradation byproduct (R_t: 3 min) is reduced under wet conditions. R_t: [^{18}F]F^- (RAD, 1 min), [^{18}F]**6** (RAD, 3.7 min) **5** (UV, 6.2 min).

HPLC a DMSO solution of **5** spiked with 5 μL of 5 N NaOH. Therefore, we sought to suppress this undesired process by modifying the basicity of the reaction media. Thus, the radiosynthesis of [^{18}F]**6** was performed under wet conditions, whereupon azeotropic drying was excluded while preparing the radiofluorinating solution, which realized a 10% v/v content of H_2O. Such wet conditions have been shown previously to be influential in the formation of different reaction products[9] or improved RCYs; to our delight, the radiosynthesis of [^{18}F]**6** under wet conditions was successful and we achieved as large as 78% RCY at a temperature as low as 50 °C. Residence times and precursor amounts were also optimized to maximize the RCY (see the Supporting Information, section 3.1), yielding [^{18}F]**6** in as high as 87% RCY when using 0.38 μmol of precursor within a residence time of 47 s. Significantly less of the degradation product from **5** was observed under these wet and low temperature conditions, confirming the desired switch from degradation to improved nucleophilic displacement by [^{18}F]fluoride in these aqueous conditions. To verify that the Re^{I} center was influential in facilitating nucleophilic substitution in the 2-position in such extremely mild conditions, we also performed the radiosynthesis of the ligand [^{18}F]**4** under identical wet conditions, which, as expected, afforded no radioproduct at all, as shown in Figure 2. It is suspected that the electron-withdrawing nature of the Re^{I} metal center, due to the π-acceptance of the CO ligands, may activate the 2-position of phenanthroline for improved nucleophilic substitution at low temperatures. Mechanistic studies are currently underway in our labs to explain why the presence of water favors the radiofluorination reaction so greatly.

The direct radiolabeling of the Re^{I} tricarbonyl diimine complex was also compared to a two-step automated radiosynthetic process.[10] Using microfluidic technology, we assembled a second microreactor in series, alongside a fourth pump to supply the $Re(CO)_5Cl$ precursor, as shown in Figure 5. RCYs as great as 35% were able to be achieved using ≥5× stoichiometric equivalents of $Re(CO)_5Cl$ compared to **3**, as shown in Figure 6, despite the residual basic conditions from the reaction in the first microreactor. Therefore, this unprecedented two-step microfluidic approach indeed led to the desired final

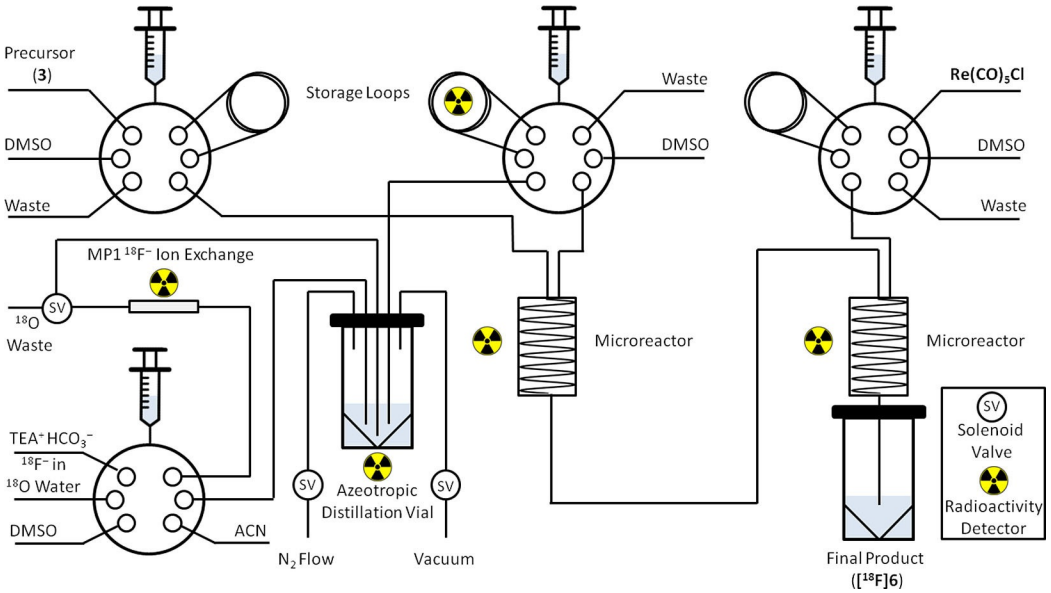

Figure 5. Simplified schematic of the flow chemistry configuration assembled for the automated two-step radiosynthesis of [^{18}F]**6**.

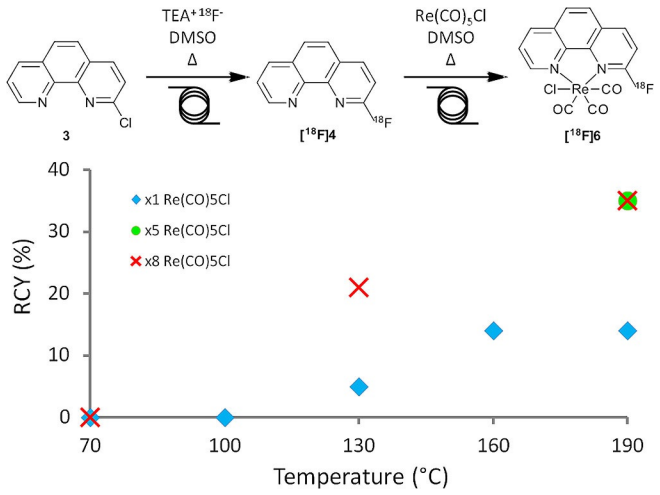

Figure 6. Temperature dependence (2nd step) of the two-step radiofluorination to form complex [^{18}F]**6** under azeotropically dried conditions using one (blue squares), five (green circle), and eight (red crosses) stoichiometric equivalents of the $Re(CO)_5Cl$ precursor.

product by marginally increasing total process time (4 vs. 10 min), but provided a reduced RCY compared to the direct milder radiofluorination of **5**. A process involving the purification of [^{18}F]**4** and performance of a separate 2nd step reaction was not attempted, as it would have involved a much longer and more complex system resulting in further radioactive decay.

Before performing the radiolabeling using microfluidic systems, we were unable to synthesize **6** from **5** using the usual heated and anhydrous conditions that afforded **4** from **3**. Given the resulting formation of [^{18}F]**6** from **5** under wet, low temperature conditions, we revisited the bulk non-radioactive synthesis and attempted the reaction of **5** to **6** under analogous conditions. UV reaction monitoring revealed that complex **6** did indeed form under these wet and low temperature conditions (32% HPLC conversion), thus demonstrating how fast and efficient microfluidic optimization can be also used to identify the best reaction conditions for bulk syntheses.

Photophysical properties of **6** were also assessed, to investigate the effect of replacing a chloro for a fluoro substituent in the 2-position of phenanthroline, given our initial research incentives to develop PET-optical probes. We therefore verified that these Re^{I} complexes afforded similar quantum yields ($\Phi =$ 0.3%), lifetimes ($\tau = 27$–41 ns), emission maxima ($\lambda_{ex} = 410$ nm, $\lambda_{em} = 653$–654 nm) and monoexponential decay profiles in DMSO (see the Supporting Information, sections 4.1–4.3).

In summary, the fluorine-18 radiolabeling of a ligand complexed to Re^{I} was found to afford optimal RCYs under remarkably mild conditions, without the need for azeotropic distillation and with a reduction of $>100\,^{\circ}C$ for the optimal temperature. Further investigations will clarify the involvement of the Re^{I} center in the radiofluorination mechanism, and will seek to apply this radiolabeling strategy toward improving the RCY of existing PET tracers, as well as toward accessing new PET and PET-optical probes.

Experimental Section

Aqueous [^{18}F]fluoride was produced on an IBA Cyclone 18 Twin cyclotron (ANSTO, Camperdown, Australia) using the $^{18}O(p,n)^{18}F$ nuclear reaction. Microfluidic radiosyntheses were performed in Discovery Mode using a NanoTek LF Microfluidic Synthesis System (Advion, Ithaca, NY) connected to a standard laptop using the NanoTek software, V1.4.0 GMP Lite. Microreactors were made of fused silica tubing (100 μm × 2 m), coiled tightly into a brass ring containing a thermoresistent polymer to hold the tubing in place. RadioHPLC analyses were carried out using a Shimadzu system comprised of a CBM-20 controller, LC-20AD pump, SIL-20AHT autoinjector, SPD-M20A PDA detector (for UV analyses) and a Lablogic Posi-RAM gamma detector. Analyses were performed using isocratic conditions consisting of CH_3CN/H_2O/TFA mobile phases (7.95:91.95:0.10% v/v for [^{18}F]**4** and 64.95:34.95:0.10% v/v for [^{18}F]**6**), on a Chromolith RP column (monolith system, Merck, 50 × 4.6 mm). RCYs were calculated using the radio-HPLC profiles, integrating the radioproduct peak against all the other radioactive peaks (inclusive of the unreacted [^{18}F]fluoride), using Laura V4.1.70 SP2 HPLC data analysis software.

The microfluidic experiments were carried out on the scale of 29 ± 10 MBq, and afforded [^{18}F]**6** with a molar activity of 71 ± 12 MBq nmol^{-1}.

Experimental details concerning the general syntheses, structure elucidation, radiochemistry, and photophysical characterizations of the reported compounds can be found in the Supporting Information, sections 5.1–5.3.

Acknowledgements

This work has been partially funded by the Australian Institute for Nuclear Science and Engineering (AINSE) through the provision of a Postgraduate Research Award (PGRA), and the Australian Research Council (ARC): Linkage grant LP1590101307. We also acknowledge Nikolas Paneras for the cyclotron production, as well as Dr. Lidia Matesic and Iveta Kurlapski for laboratory support.

Conflict of interest

The authors declare no conflict of interest.

Keywords: fluorine-18 radiolabeling · late-stage fluorination · microfluidics · pet chemistry · rhenium complexes

[1] Representative examples: a) G. Pascali, P. Watts, P. A. Salvadori, *Nucl. Med. Biol.* **2013**, *40*, 776–787; b) A. Lebedev, R. Miraghaie, K. Kotta, C. E. Ball, J. Zhang, M. S. Buchsbaum, H. C. Kolb, A. Elizarov, *Lab Chip* **2013**, *13*, 136–145; c) C.-C. Lee, G. Sui, A. Elizarov, C. J. Shu, Y.-S. Shin, A. N. Dooley, J. Huang, A. Daridon, P. Wyatt, D. Stout, H. C. Kolb, O. N. Witte, N. Satyamurthy, J. R. Heath, M. E. Phelps, S. R. Quake, H.-R. Tseng, *Science* **2005**, *310*, 1793–1796; d) C. J. Steel, A. T. O'Brien, S. K. Luthra, F. Brady, *J. Labelled Compd. Radiopharm.* **2007**, *50*, 308–311; e) P. W. Miller, H. Audrain, D. Bender, A. J. deMello, A. D. Gee, N. J. Long, R. Vilar, *Chem. Eur. J.* **2011**, *17*, 460–463.

[2] S. M. Ametamey, M. Honer, P. A. Schubiger, *Chem. Rev.* **2008**, *108*, 1501–1516.

[3] Representative examples: a) C. F. Lemaire, J. J. Aerts, S. Voccia, L. C. Libert, F. Mercier, D. Goblet, A. R. Plenevaux, A. J. Luxen, *Angew. Chem. Int. Ed.* **2010**, *49*, 3161–3164; *Angew. Chem.* **2010**, *122*, 3229–3232;

b) R. Richarz, P. Krapf, F. Zarrad, E. A. Urusova, B. Neumaier, B. D. Zlatopolskiy, *Org. Biomol. Chem.* **2014**, *12*, 8094 – 8099; c) J. Aerts, S. Voccia, C. Lemaire, F. Giacomelli, D. Goblet, D. Thonon, A. Plenevaux, G. Warnock, A. Luxen, *Tetrahedron Lett.* **2010**, *51*, 64 – 66; d) S. H. Wessmann, G. Henriksen, H. J. Wester, *Nuklearmedizin* **2012**, *51*, 1 – 8; e) F. Basuli, X. Zhang, E. M. Jagoda, P. L. Choyke, R. E. Swenson, *Nucl. Med. Biol.* **2016**, *43*, 770 – 772; f) J.-H. Chun, S. Telu, S. Lu, V. W. Pike, *Org. Biomol. Chem.* **2013**, *11*, 5094 – 5099.

[4] L. Matesic, A. Kallinen, N. Wyatt, T. Q. Pham, I. Greguric, G. Pascali, *Aust. J. Chem.* **2015**, *68*, 69 – 71.

[5] S. Lindner, C. Rensch, S. Neubaur, M. Neumeier, R. Salvamoser, V. Samper, P. Bartenstein, *Chem. Commun.* **2016**, *52*, 729 – 732.

[6] Representative examples: a) Z. Li, T. P. Lin, S. Liu, C. W. Huang, T. W. Hudnall, F. P. Gabbai, P. S. Conti, *Chem. Commun.* **2011**, *47*, 9324 – 9326; b) S. Liu, D. Li, Z. Zhang, S. G. K. Prakash, P. S. Conti, Z. Li, *Chem. Commun.* **2014**, *50*, 7371 – 7373; c) T. Temma, N. Kondo, M. Ono, H. Saji, *J. Nucl. Med.* **2015**, *56 (S3)*, 1127; d) J. A. Hendricks, E. J. Keliher, D. Wan, S. A. Hilderbrand, R. Weissleder, R. Mazitschek, *Angew. Chem. Int. Ed.* **2012**, *51*, 4603 – 4606; *Angew. Chem.* **2012**, *124*, 4681 – 4684; e) K. Chen, Z.-B. Li, H. Wang, W. Cai, X. Chen, *Eur. J. Nucl. Med. Mol. Imaging* **2008**, *35*, 2235 – 2244; f) F. Ducongé, T. Pons, C. Pestourie, L. Hérin, B. Thézé, K. Gombert, B. Mahler, F. Hinnen, B. Kühnast, F. Dollé, B. Dubertret, B. Tavitian, *Bioconjugate Chem.* **2008**, *19*, 1921 – 1926; g) W. Guo, X. Sun, O. Jacobson, X. Yan, K. Min, A. Srivatsan, G. Niu, D. O. Kiesewetter, J. Chang, X. Chen, *ACS Nano* **2015**, *9*, 488 – 495.

[7] Representative examples: a) M. V. Werrett, P. J. Wright, P. V. Simpson, P. Raiteri, B. W. Skelton, S. Stagni, A. G. Buckley, P. J. Rigby, M. Massi, *Dalton Trans.* **2015**, *44*, 20636 – 20647; b) C. A. Bader, R. D. Brooks, Y. S. Ng, A. Sorvina, M. V. Werrett, P. J. Wright, A. G. Anwer, D. A. Brooks, S. Stagni, S. Muzzioli, M. Silberstein, B. W. Skelton, E. M. Goldys, S. E. Plush, T. Shandala, M. Massi, *RSC Adv.* **2014**, *4*, 16345 – 16351.

[8] G. Pascali, L. Matesic, T. L. Collier, N. Wyatt, B. H. Fraser, T. Q. Pham, P. A. Salvadori, I. Greguric, *Nat. Protoc.* **2014**, *9*, 2017 – 2029.

[9] Representative examples: a) G. Pascali, M. De Simone, L. Matesic, I. Greguric, P. A. Salvadori, *J. Flow Chem.* **2014**, *4*, 86 – 91; b) T. R. Neal, S. Apana, M. S. Berridge, *J. Labelled Compd. Radiopharm.* **2005**, *48*, 557 – 568.

[10] G. Pascali, G. Nannavecchia, S. Pitzianti, P. A. Salvadori, *Nucl. Med. Biol.* **2011**, *38*, 637 – 644.

Manuscript received: January 29, 2017
Accepted Article published: March 22, 2017
Final Article published: April 11, 2017

CSIRO PUBLISHING

Aust. J. Chem. **2019**, *72*, 288–294
https://doi.org/10.1071/CH18512

Full Paper

Effect of Rhenium(I) Complexation on Aza-Michael Additions to 5-Amino-1,10-Phenanthroline with [^{18}F] Ethenesulfonyl Fluoride towards PET Optical Tracer Development

Mitchell A. Klenner,[A,B,F] *Giancarlo Pascali,*[A,C,F] *Bo Zhang,*[A,D] *Gianluca Ciancaleoni,*[E] *Massimiliano Massi,*[B] *and Benjamin H. Fraser*[A]

[A]Human Health, Australian Nuclear Science and Technology Organisation (ANSTO), Lucas Heights, NSW 2229, Australia.
[B]Department of Chemistry, Curtin University, Bentley, WA 6102, Australia.
[C]Brain and Mind Centre, University of Sydney, Sydney, NSW 2050, Australia.
[D]School of Chemistry, Monash University, Melbourne, Vic. 3800, Australia.
[E]Dipartimento di Chimica e Chimica Industriale Università di Pisa, Pisa 56127, Italy.
[F]Corresponding authors. Email: mitchk@ansto.gov.au; gianp@ansto.gov.au

Conjugations with the recently developed [^{18}F]ethenesulfonyl fluoride ([^{18}F]ESF) were performed on 5-amino-1,10-phenanthroline, in its free form and coordinated to a rhenium(I) tricarbonyl complex, as a means of radiosynthesizing dual-modal optical and positron emission tomography (PET) tracers. The Michael-donating ability of the aromatic amine was noticeably perturbed on coordination with the rhenium(I) centre, resulting in decreased radiochemical yields from 34 %, in the case of the free ligand, to 1 %. We attribute the decreased nucleophilicity of the amine to metal deactivation from the electron-withdrawing feature of the rhenium(I) tricarbonyl centre, based on spectroscopic and computational evidence, thus highlighting this effect as a crucial parameter in designing late-stage metal coordination methods employing related aza-Michael additions. Photophysical analyses were also performed on the ESF-conjugated rhenium(I) complex, exhibiting a longer decay lifetime from the triplet metal-to-ligand charge transfer excited state when compared with the non-conjugated analogue.

Manuscript received: 17 October 2018.
Manuscript accepted: 10 December 2018.
Published online: 14 January 2019.

Introduction

Aza-Michael additions are an invaluable tool for forming molecular linkages as well as bioconjugating peptides and proteins, typically through the free ε-amino groups of lysine units or alternative N-terminals of end-chain amino acids.[1–3] The reaction mechanism involves the bonding of free amine Michael donors to α,β-unsaturated olefin Michael acceptors, and generally progresses relatively fast compared with other enolate or thia-Michael additions.[4] Furthermore, aza-Michael additions can function under physiological temperatures and do not require deprotonation of the donating group by an external base,[5,6] thus suppressing the likelihood of denaturing any biomolecular target. However, limited applicability of aza-Michael additions has been noted in the conjugation of organometallic complexes bearing a Michael-donating moiety. As the presence of a metal centre can reduce the nucleophilicity of the donating group, synthetic routes tend to synthesize conjugated ligands before late-stage metal complexation.[6–8] Despite this hindrance, towards our development of positron emission tomography (PET) optical tracers coupling the fluorine-18 radioisotope (109.7 min half-life) with luminescent rhenium complexes,[9] it was hypothesized that any loss of radiochemical yield (RCY) due to metal deactivation effects may in fact be less detrimental than the loss of RCY due to radioactive decay during the metal complexation phase. We compared Michael addition reactions on 5-amino-1,10-phenanthroline ($PhenNH_2$) as a stand-alone substrate or coordinated to a rhenium(I) tricarbonyl centre with our recently developed peptide-labelling prosthetic group, [^{18}F]ethenesulfonyl fluoride ([^{18}F]ESF).[10] In addition, we modelled the reaction pathway via density functional theory (DFT) techniques to gain an improved mechanistic insight on the influence of rhenium deactivation, and characterized the photophysical properties of the rhenium complexes for use as optical probes.

Results and Discussion

Non-Radioactive Syntheses

The synthetic route used to obtain **PhenESF**, **RePhenNH$_2$**, and **RePhenESF** is shown in Fig. 1 (rt, room temperature). To bioconjugate the probe for use as a PET optical imaging agent, the bromo-ancillary ligand of the **RePhenESF** complex is envisioned to be easily substituted for a suitable ancillary monodenate ligand, either bearing or modified with a

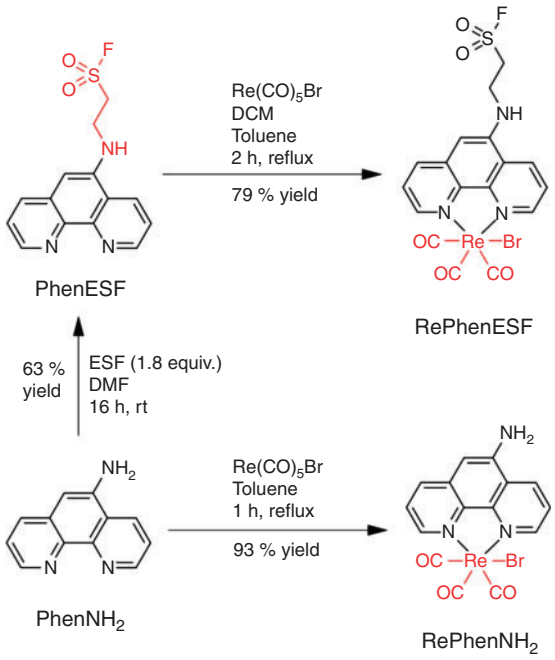

Fig. 1. Conditions used to synthesize the novel compounds **PhenESF** via Michael addition between **PhenNH$_2$** and ESF, and **RePhenESF** via rhenium complexation with **PhenESF**.

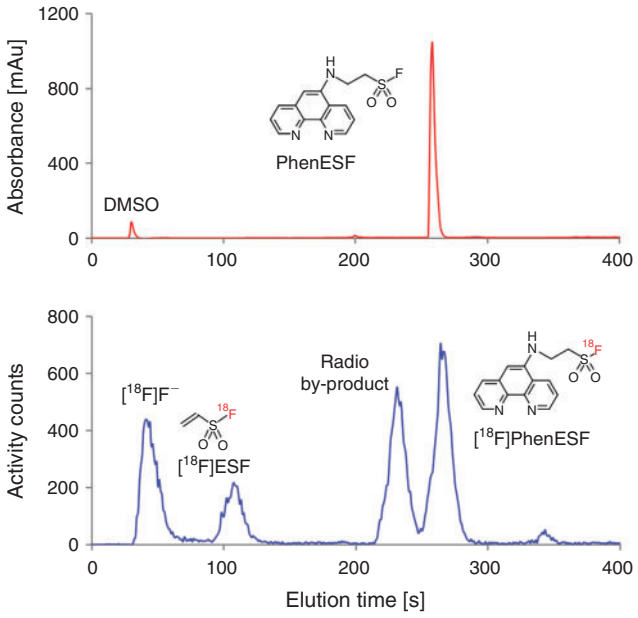

Fig. 2. UV-absorbance chromatogram for the non-radioactive **PhenESF** standard (red, top), the peak of which aligns with the 258 s retention time of the product depicted in the radiochromatogram for the reaction forming **[^{18}F]PhenESF** (bottom, blue). An unknown product (231 s) is also observed, alongside unreacted [^{18}F]ESF and degraded [^{18}F]fluoride.

pyridine,[11–13] tetrazole[14] or similar N-heterocyclic functional group,[15] for conjugation to a biological vector. The synthesis of the non-radioactive **RePhenESF** standard was performed by Michael addition of ESF to **PhenNH$_2$**, which afforded a reaction yield of 63 % in DMF at room temperature. Subsequent complexation of **PhenESF** to bromopentacarbonylrhenium(I) afforded the desired product in 79 % yield when refluxed in a 1 : 1 DCM/toluene mixture, from which the targeted complex could be separated with high purity by simple filtration. Similarly, **PhenNH$_2$** was complexed with bromopentacarbonylrhenium(I) in toluene solution, in accordance with the previously reported synthesis of **RePhenNH$_2$**,[16] affording the complex in 93 % yield. NMR and IR spectra can be viewed in Figs S1–S11 and Figs S1, S2 of the Supplementary Material respectively.

*Direct ^{18}F/^{19}F Exchange of **PhenESF** and **RePhenESF***

In a preliminary attempt towards the radiosynthesis of **[^{18}F]PhenESF** and **[^{18}F]RePhenESF**, we tested the ^{19}F/^{18}F direct exchange of the non-radioactive analogues using cyclotron-produced [^{18}F]fluoride. The [^{18}F]fluoride was eluted off a QMA cartridge using tetraethylammonium (TEA) hydrogen carbonate, azeotropically dried with anhydrous acetonitrile, and reconstituted in anhydrous DMSO. The resulting solution afforded 32 ± 7 MBq mL^{-1} of activity. The [^{18}F]fluoride solution (20 µL) was then added to a volume of **PhenESF** (80 µL, 2.5 mg mL^{-1}), which afforded a 2 % RCY for **[^{18}F]PhenESF** and 3 % RCY for an unknown product. The ^{19}F/^{18}F direct exchange on **RePhenESF** (5 mg mL^{-1}), however, did not afford any radioproduct. The direct exchange on **RePhenESF** was also attempted in a solution of ethanol under analogous conditions using 107 ± 22 MBq mL^{-1} of radioactivity, though still exhibited no yield. Thus, [^{18}F]ESF was instead used to produce the radiotracers via aza-Michael addition.

*Radiolabelling of **PhenNH$_2$** and **RePhenNH$_2$** with [^{18}F]ESF*

The aza-Michael additions were performed by mixing 80 µL of 1 mg mL^{-1} **PhenNH$_2$** and **RePhenNH$_2$** solutions in DMSO with 20 µL of 93 ± 19 MBq mL^{-1} no-carrier added [^{18}F]ESF aqueous solution. The reaction mixture was analysed by radio-HPLC, and the radioproduct identity was confirmed via retention time comparison against the UV absorbance peak of the non-radioactive standard. As can be seen in Fig. 2, related to the conjugation of **PhenNH$_2$**, the radioproduct eluting at 258 s coincides with the UV absorbing peak of the separately injected **PhenESF** non-radioactive standard. Curiously, alongside the radiolabelled **[^{18}F]PhenESF** product and unreacted [^{18}F]ESF (107 s elution), we observed not only degradation to form [^{18}F]fluoride but also an unknown radio by-product eluting at 231 s. In Fig. 3, example chromatograms are also shown for the UV absorbance of the non-radioactive standard **RePhenESF** and the elution profile for the radiosynthesis of **[^{18}F]RePhenESF** from **RePhenNH$_2$**. Here, we observed also the consistent degradation of unreacted [^{18}F]ESF to form [^{18}F]fluoride, accompanied by an unknown by-product eluting at 210 s. One hypothesis for the identity of this unknown by-product could involve the direct interaction of the allyl functional group with the rhenium(I) centre by displacement of the bromo ligand, for instance through η^2 coordination. At 414 s, we observe a minute peak for a radioproduct, shown in the zoomed-in region of Fig. 3, which corresponds with the UV absorbance peak for **[^{18}F]RePhenESF**. The non-isolated RCYs for these radioproducts were then determined by calculating the ratio of the integrated peak area for the radioproduct against the integrated area of the entire radiochromatogram. The determined RCYs for these radiolabelled products are shown in Fig. 4 for each of the three tested temperature conditions. Radiolabelling of the ligand resulting in **[^{18}F]PhenESF** improved as a function of higher temperature, with an RCY of 13 % forming at 40°C, 23 % RCY forming at 70°C, and an improved RCY of 34 % forming at 100°C. The

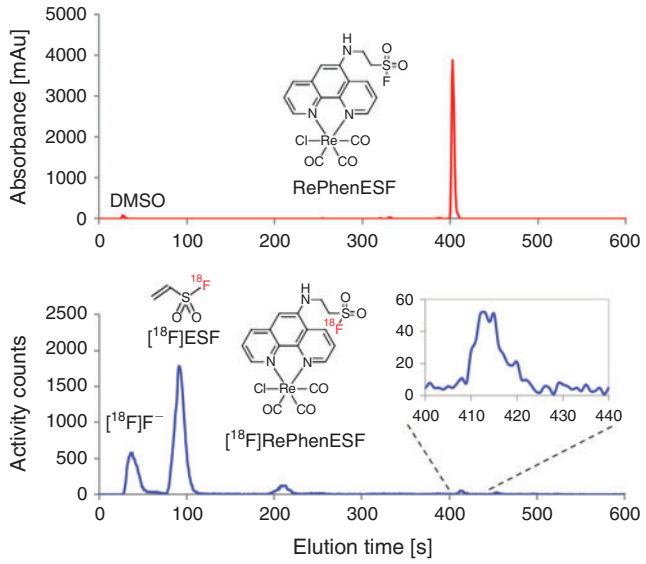

Fig. 3. UV-absorbance chromatogram for the non-radioactive **RePhenESF** standard (red, top), the peak of which aligns with the 414 s retention time of the zoomed-in peak depicted in the radiochromatogram for the reaction forming **[^{18}F]RePhenESF** (bottom, blue). An unknown product (210 s) is also observed, alongside unreacted [^{18}F]ESF and degraded [^{18}F] fluoride.

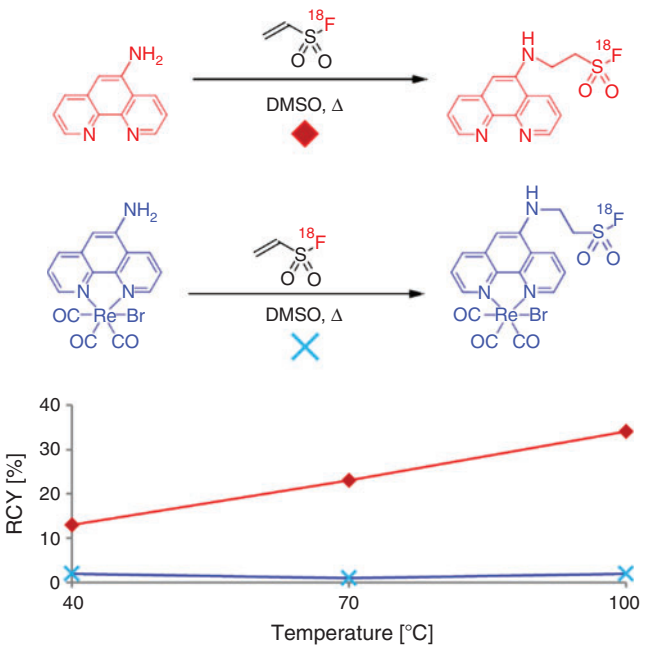

Fig. 4. Non-isolated RCYs plotted as a function of temperature for the aza-Michael addition reactions with [^{18}F]ESF to form **[^{18}F]RePhenESF** (red, diamonds) and **[^{18}F]RePhenESF** (blue, crosses).

RCYs at 40°C and 70°C were also further verified by radio-TLC with closely matching yields of 14 and 24 % respectively, as shown in Fig. S3.1–S3.4 of the Supplementary Material. Higher temperature conditions were not trialled given the volatile nature of ESF within our experimental set-up. The radiolabelling of **RePhenNH$_2$** to afford **[^{18}F]RePhenESF** was not as efficient, however, forming only 1–2 % RCY by radio-HPLC (3 % by radio-TLC) irrespective of the reaction temperature (Fig. 4).

*Mechanism of ESF aza-Michael Additions with **PhenNH$_2$** and **RePhenNH$_2$** by DFT Analyses*

To investigate the difference in these radiolabelling efficiencies, we studied the mechanisms of the two reactions by DFT, using crystal structures previously obtained by Świtlicka-Olszewska et al.[17] In both cases, the first molecular event occurs via nucleophilic addition ('attack') by the lone electron pair of the amino group at the β-carbon of ESF, thus forming the first transition state (TS_{attack}). The attack is directed by a hydrogen bond existing between the amino group and the oxygen atom of ESF and leads to an intermediate species (Int) with charge separation. The negative charge is present on the α-carbon and the positive charge is present on either the nitrogen (uncoordinated phenanthroline) or shared between the sulfur and the oxygen atoms (coordinated phenanthroline). Successively, one proton shifts from the nitrogen to the α-carbon, affording the final product (Fig. 5). In agreement with experimental results, the activation free energy of all the steps is higher in the presence of the metal centre (40.8 instead of 36.8 kcal mol^{-1} (1 kcal mol^{-1} = 4.186 kJ mol^{-1}) for the rate-determining step), indicating that the amine group on the phenanthroline is less reactive when coordinated to the rhenium. When also comparing the electronic and geometrical properties of **PhenNH$_2$** and **RePhenNH$_2$**, the C–NH$_2$ bond is noticeably longer for the complexed ligand than in the free ligand (1.394 and 1.389 Å respectively), and the lone pair of the nitrogen atom is also more occupied in the uncoordinated ligand than in the coordinated analogue (natural orbital occupancy of 1.79 and 1.75 e respectively), in accordance with the natural bond order (NBO) analysis (refer to Fig. S4 of the Supplementary Material for more detail). This information suggests that greater electron density resides in the C=N π-bond when coordinated to rhenium(I) and therefore is less available for nucleophilic attack by the amine, in agreement with the experimental data. The natural orbital for chemical valance–charge displacement (NOCV-CD) analysis of **RePhenNH$_2$** reveals that the rhenium–**PhenNH$_2$** bond can be decomposed into four main contributions, two of which are related to **PhenESF** → Re σ-donation and the other two describe the Re → **PhenESF** π-backbonding donation. In all of these contributions, the ligand is polarized, with a depauperation of the ligand electronic density (depicted in Fig. S4.1–S4.2 in the Supplementary Material). This hypothesis is further backed by the downfield shift in proton signals displayed in the comparative NMR spectra between **PhenESF** and **RePhenESF**, shown in Fig. 6, which is consistent with a loss of electron density evident from the diminished effect of magnetic shielding. Also in this case, the NOCV-CD analysis on **RePhenESF** denotes a depauperation of the ligand electronic density qualitatively similar to that for **RePhenNH$_2$** in agreement with the NMR data.

*Photophysical Characterization Following Michael Addition of **PhenNH$_2$** with ESF*

In accordance with our intentions to further develop the probe for PET optical imaging, we assessed the photophysical properties of **RePhenNH$_2$** in comparison with its Michael addition product **RePhenESF**. The UV-vis spectra for both compounds, shown in Fig. S6.1–S6.2 of the Supplementary Material, exhibit d$\pi \rightarrow \pi^*$ absorption bands to the metal-to-ligand charge transfer (MLCT) excited state at 416 nm (extinction coefficient ε 2726 L mol^{-1} cm^{-1}) and 414 nm (ε 1835 L mol^{-1} cm^{-1}) for **RePhenNH$_2$** and **RePhenESF** respectively. Higher-energy $\pi \rightarrow \pi^*$ bands are also present at shorter wavelengths, 348, 296,

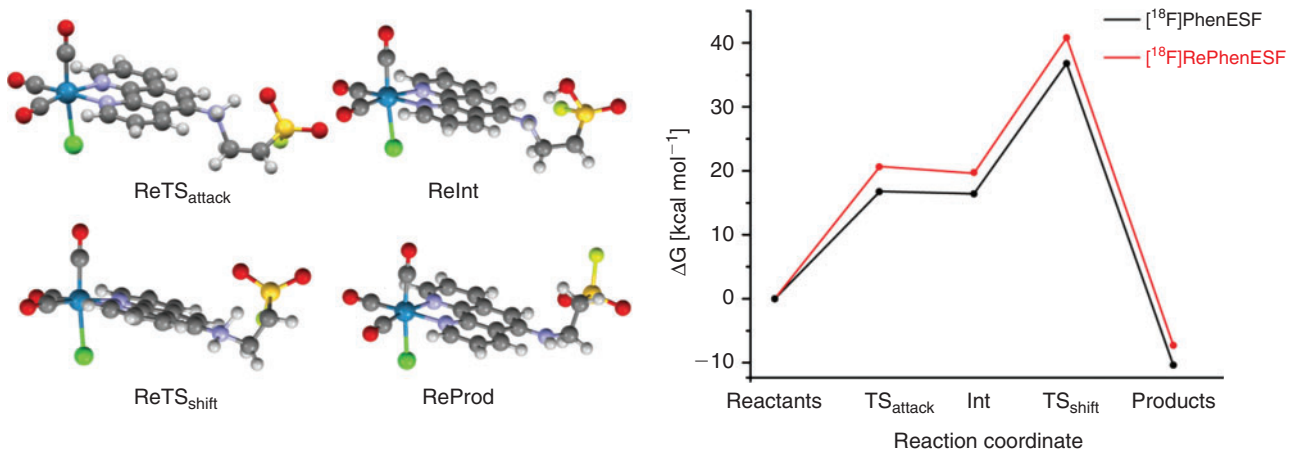

Fig. 5. Reaction pathway depicting the attack transition state (TS_{attack}), intermediate (Int), shift transition state (TS_{shift}), and final product (left for the rhenium complex). The Gibbs free energy is calculated along the reaction coordinate (shown right). The Gibbs free energy of each step in the reaction coordinate is higher for the formation of **[^{18}F]PhenESF** (black) than for **[^{18}F]RePhenESF** (red).

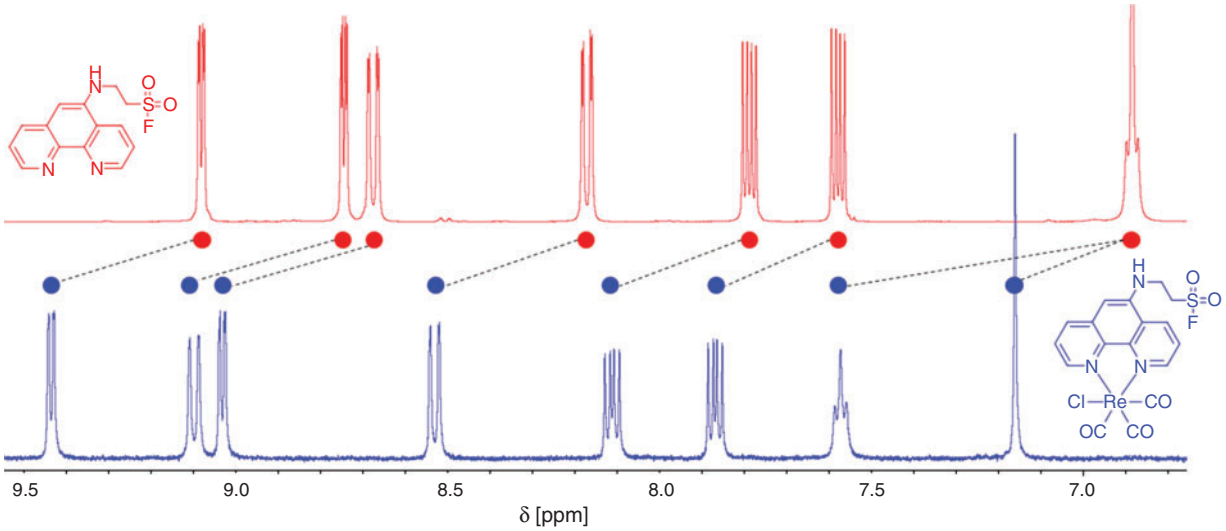

Fig. 6. Aromatic ^{1}H NMR signals of **PhenESF** (top, red) are seen to undergo downfield shifts when complexed to form **RePhenESF** (bottom, blue). These downfield shifts suggest an electron-withdrawal effect from the rhenium.

244, and 194 nm for **RePhenNH$_2$**, and 347, 297, 243, and 194 nm for **RePhenESF**. Following excitation at 410 nm for both compounds in DMSO solution, emission maxima of 612 nm for **RePhenNH$_2$** and 621 nm for **RePhenESF** were obtained, as shown in Fig. S7.2 of the Supplementary Material. Whereas **RePhenNH$_2$** exhibited a relatively short excited state decay lifetime of less than 10 ns, in agreement with previously obtained photophysical data for the Re–Cl derivative in DMSO,[18] **RePhenESF** instead exhibited a longer luminescent lifetime of 138 ns with a χ^2 value of 0.995 for the fit of mono-exponential decay from the MLCT excited state. The photophysical properties of **RePhenESF** were also assessed in aqueous media, containing 5 % DMSO to aid solubility, which resulted in a solvatochromic shift of the emission maxima to 606 nm.

Conclusion

Rhenium(I) deactivation was evident in both the obtained NMR spectra and difference in Gibbs free energy calculated along the reaction coordinate of our mechanistic studies by DFT analysis. Despite our underlying hypothesis that a loss of RCY could be minimized by circumventing multistep radiosynthesis via aza-Michael addition of [^{18}F]ESF to an already rhenium(I) deactivated complex, the RCYs attained for this radiolabelled complex were negligible compared with the ligand under all temperature conditions. Photophysical studies of the conjugated complex affirm the typical longer decay lifetime from the MLCT excited state exhibited by rhenium(I) tracers and mark potential for development of the compound as an optical probe coupled with PET imaging modality.

Experimental and Computational Methods

Chemical Reagents

All chemical reagents, including the 5-amino-1,10-phenanthroline, bromopentacarbonylrhenium(I), and ESF reactants, were purchased from Sigma–Aldrich. All solvents were purchased from Merck. Water was purified using a Merck Millipore Milli-Q integral water purification system.

Instruments Used in Non-Radioactive Characterization

Quality control HPLC analyses were performed on a Waters HPLC system equipped with a Waters 626 pump, inline degasser AF unit, 717-plus autosampler, 2996 photodiode array (PDA) detector, 2424 evaporative light scattering (ELS) detector, and 600S controller. A Waters Bridge Columns XBridge (C_{18}, 3.5 µm pore size, 4.6 mm internal diameter (ID), 50 mm length) column was employed. An isocratic method was applied using 10 % acetonitrile in water containing 0.1 % TFA modifier with a 1.5 mL min^{-1} flow rate. Low resolution mass spectrometry (LRMS) was performed using a Waters micromass ZQ, equipped with an electrospray ionization (ESI (+)) source with the following conditions: voltages: 3 kV capillary voltage, 25 V cone voltage for **PhenESF** and 70 V cone voltage for **RePhenNH$_2$** and **RePhenESF** (higher cone voltage was required to dissociate Re–Br bonds), 5 V extractor voltage, 0.2 V radiofrequency (RF) lens voltage; temperatures: 45°C source temperature, 300°C desolvation temperature; gas flows: 350 L h^{-1} desolvation N_2 gas flow, 90 L h^{-1} cone N_2 gas flow. Samples for high-resolution mass spectrometry (HRMS) analyses were sent to the Mass Spectrometry User Resource and Research Facility (MSURRF) at the University of Wollongong. Melting point analyses were performed using a Stanford Research Systems Optimelt automated melting point system with digital imaging processing technology. IR analyses were performed using a Brucker ALPHA-p IR spectrometer. UV-vis analyses were performed using an Agilent technologies Cary 100 UV-vis spectrometer. NMR analyses were performed using a Bruker Spectrospin 400 MHz UltraShield NMR spectrometer. TMS was used as the internal standard for ^{1}H and ^{13}C measurements, and *para*-difluorobenzene (*p*-DFB) as the internal standard for ^{19}F measurements. Samples for elemental analyses were sent to the Campbell Microanalytical Laboratory at the University of Otago in New Zealand for C, H, N, and Br analyses.

Equipment Used for Radiosynthesis

Aqueous [^{18}F]fluoride was produced on an IBA Cyclone 18 Twin cyclotron (ANSTO, Sydney, NSW, Australia) using the $^{18}O(p,n)^{18}F$ nuclear reaction. Analyses were performed using gradient conditions consisting of 0.1 % v/v TFA in both acetonitrile (A) and water (B) mobile phases on a Chromolith column (Merck, 50 × 4.6 mm). The method duration was 12 min with 5 % A held for 1 min, %A increased to 95 % over 7 min, %A held at 95 % for 2 min, %A reduced to 5 % over 30 s, and then held at 5 % for the remaining 1 min 30 s for equilibration. RCYs were calculated using the radio-HPLC profiles, integrating the radioproduct peak against all the other radioactive peaks (including the unreacted [^{18}F] fluoride), using *Laura V4.1.70 SP2* HPLC data analysis software.

Radiochemical Production of [^{18}F]ESF

No-carrier added [^{18}F]ESF was formed from a 2,4,6-trichlorophenylethenesulfonate (TCPE) precursor in DMSO solvent under microfluidic conditions.[10] The TCPE in DMSO solution was radiofluorinated from non-azeotropically dried TEA [^{18}F]fluoride complex in acetonitrile, both of which were pumped from storage loops into a fused silica microreactor (2 m × 100 µm, 15.6 µL) heated to 100°C, at an overall flow rate of 40 µL min^{-1} (24 s residence time). The reaction mixture underwent distillation, following conditions reported in the literature,[10] and the pure product was trapped in a Silica Plus cartridge and eluted with purified water. Such conditions provided an optimal non-isolated 86 ± 10 % RCY solution of [^{18}F]ESF with 31.8 ± 6.4 MBq mL^{-1} of activity. Refer to Fig. S5.1 and S5.2 of the Supplementary Material for schematics of the microfluidic set-up.

Equipment Used for Photophysical Characterization

Photophysical measurements were performed using an Edinburgh FLS980 spectrometer. Light from a 450 W xenon arc lamp source was passed through excitation and emission monochromators to acquire the corresponding spectra. Emission lifetimes were determined using the time correlated single-photon counting (TCSPC) technique with a pulsed picosecond light-emitting diode (LED, 377 nm).[19,20] The goodness-of-fit was assessed by minimizing the reduced χ^2 function and by visual inspection of the weighted residuals.

Computational Details and Methods

The geometry optimizations and bond analyses were computed using *ORCA* software[21] at the DFT level using def2-TZVP basis sets, B97 functional[22] corrected using the Grimme D3 correction with Becke–Johnson damping to the DFT energy.[23] The resolution of identity (RI) approximation[24] and the Effective Core potential LANL2DZ were also applied.[25–27] All of the structures were confirmed to be local energy minima (no imaginary frequencies) except the transition states (one imaginary frequency). Thermodynamic properties were computed at the def2-TZVP/B97-D3 level of theory and calculated at 298 K. Zero-point energy corrections are included. NBO analyses were performed using the *NBO6* suite of programs.[28] Charge displacement function analysis is based on Eqn 1[29,30] wherein $\Delta\rho(x, y, z)$ is the difference between the electron density of a complex and that of its non-interacting fragments placed in the same position as they occupy in the complex. These fragments are [PhenNHR] (R = H or $CH_2CH_2SO_2F$) and [Re(CO)$_3$Cl]. The function $\Delta q(z)$ defines, at each point z along a chosen axis, the amount of electronic charge that, on formation of the bond between the fragments, moves across a plane perpendicular to the axis through the point z. A negative value corresponds to electron density flowing in the direction of increasing z. Charge accumulates where the slope of Δq is positive and decreases where it is negative.

$$\Delta q(z') = \int_{-\infty}^{+\infty} dx \int_{-\infty}^{+\infty} dy \int_{-\infty}^{z'} dz \Delta\rho(x, y, z) \qquad (1)$$

In the natural orbital for chemical valence theory (NOCV),[31] $\Delta\rho$ is built from the occupied orbitals of A and B, suitably orthogonalized to each other and renormalized (*promolecule*), using the valence operator in Eqn 2.[32–34]

$$\hat{V} = \sum_i \left(\left|\psi_i^{(AB)}\right\rangle \left\langle\psi_i^{(AB)}\right| - \left|\psi_i^0\right\rangle \left\langle\psi_i^0\right| \right) \qquad (2)$$

Here, ψ_i^0 is the set of the occupied Kohn–Sham orbitals of fragments A and B, mutually orthonormalized, and $\psi_i^{(AB)}$ is the set of occupied orbitals of the adduct. The NOCVs can be grouped in pairs of complementary orbitals (φ_k, φ_{-k}) corresponding to eigenvalues with same absolute value but opposite

sign (Eqn 3). Herein the term v_k represents the fraction of electrons transferred from the φ_{-k} to the φ_k orbital.

$$\hat{V}\varphi_{\pm k} = \pm v_k \varphi_{\pm k} (v_k > 0) \quad (3)$$

whereby k numbers the NOCV pairs ($k = 0$ for the largest value of $|v_k|$). In this framework, $\Delta\rho'$ can be defined as per Eqn 4.

$$\Delta\rho' = \sum_k v_k \left(|\varphi_k|^2 - |\varphi_{-k}|^2 \right) = \sum_k \Delta\rho'_k \quad (4)$$

The different $\Delta\rho'_k$ can then be separately integrated using Eqn 1.[35,36] The boundary between the two fragments was defined as the point on the z axis at which equal-valued isodensity surfaces of the isolated fragments are tangential. The NOCV orbital cubes were manipulated through the software *Gabedit*,[37] whereas the electronic density matrices were manipulated through the suite of tools *Cubes*.[38] NBO analysis was performed using the *NBO6* suite of software.[39]

*Synthesis of Bromotricarbonyl(5-amino-1,10-phenanthroline) Rhenium(I) (**RePhenNH$_2$**)*

The synthesis of **RePhenNH$_2$** was adapted from a literature method described by Bessette et al.[16] 5-Amino-1,10-phenanthroline (0.49 g, 2.501 mmol, 1.0 equiv.) was dissolved in toluene (30 mL) and heated to reflux. Bromopentacarbonylrhenium(I) (1.00 g, 2.462 mmol, 1.0 equiv.) was then added to the reaction mixture, whereupon the solution turned from yellow to orange. The reaction mixture was stirred under reflux under a constant supply of nitrogen gas for 1 h. The solution was then cooled to room temperature and filtered via vacuum filtration, whereafter the precipitate was washed with *n*-hexane and dried to afford an orange powder (1.27 g, 93 %); mp 318–319°C (dec.). δ_H (400 MHz, [D6]DMSO) 9.40 (dd, J^d 5.12, 1.20, $1H_{Ar}$), 9.11 (dd, J^d 8.52, 1.20, $1H_{Ar}$), 8.95 (dd, J^d 5.00, 1.28, $1H_{Ar}$), 7.24 (dd, J^d 8.44, 1.20, $1H_{Ar}$), 8.05 (dd, J^d 8.52, 5.12, $1H_{Ar}$), 7.79 (dd, J^d 8.36, 5.0, $1H_{Ar}$), 7.07 (s, $1H_{Ar}$), 6.90 (s, br, $1H_{NH2}$). δ_C (100 MHz, [D6]DMSO) 197.50, 197.39, 189.59, 153.35, 148.04, 146.68, 144.89, 139.65, 135.54, 134.29, 132.68, 126.19, 125.00, 123.56, 101.18. ν_{max}/cm^{-1} (attenuated total reflectance (ATR) corrected) 3491.45 (w, asym N–H str), 338.00 (w, sym N–H str), 3235.51 (w, sp^2 C–H str), 2012.36 (s, sh, A′(1) C≡O str), 1921.25 (s, A′(2) C≡O str), 1894.37 (s, A″ C≡O str). *m/z* (LRMS ESI$^+$, cone 60 V) 466.17 $[M - Br]^+$; calc. 466.02; 546.05 and 457.05 $[M + H]^+$; calc. 545.95 and 547.94. *m/z* (HRMS ESI$^+$) 466.01988 $[M–Br]^+$; calc. 466.01959 (Δ 0.61 ppm). λ_{max}/nm ($\varepsilon/M^{-1}\,cm^{-1}$) ($CH_3CN$) 416 (2726), 348 (10142), 296 (24429), 244 (36534), 194 (58783). Anal. Calc. for $ReC_{15}H_9O_3N_3Br$: C 33.04, N 7.71, H 1.66, Br 14.65; found C 33.06, N 7.64, H 1.80, Br 14.39 %.

*Synthesis of 5-N-(2-Aminoethylsulfonylfluoride)-1,10-phenanthroline (**PhenESF**)*

5-Amino-1,10-phenanthroline (1.000 g, 5.128 mol, 1.0 equiv.) and ESF (847.0 mg, 7.7 mol, 1.5 equiv.) were dissolved in DMF (10 mL) and stirred at room temperature (24 h). The resulting orange solution was then poured into water (300 mL), causing a yellow solid to precipitate. The precipitate was isolated via vacuum filtration and washed with water to remove residual DMF. Further purification was achieved by dissolving the crude material in a minimum of DMSO and eluting through a 40-g C_{18} column using a gradient mobile phase of 0.1 % TFA in water and acetonitrile (5 to 100 % over 8 column volumes). The eluents containing the product were then combined, evaporated under reduced pressure, and dried by lyophilization to obtain a yellow powder (1.125 g, 63 %); mp 200–205°C (dec.). δ_H (400 MHz, $CDCl_3$) 9.21 (dd, J^d 4.32, 1.56, $1H_{Ar}$), 8.96 (dd, J^d 4.32, 1.64, $1H_{Ar}$), 8.26 (dd, J^d 8.44, 1.52, $1H_{Ar}$), 8.04 (dd, J^d 8.12, 1.64, 1 H_{Ar}), 7.65 (dd, J^d 8.40, 4.32, $1H_{Ar}$), 7.53 (dd, J^d 8.08, 4.32, $1H_{Ar}$), 7.53 (dd, J^d 8.08, 4.32, $1H_{Ar}$), 6.71 (s, $1H_{Ar}$), 5.03 (t, J^t 6.08, $1H_{NH}$), 4.08 (app. q, J^q 12.16, 6.08, $2H_{CH2–SO2F}$), 3.89 (td, J^q 6.16, 4.48, $2H_{CH2}$). δ_C (100 MHz, $CDCl_3$) 150.43, 147.44, 146.91, 142.31, 138.96, 129.59, 128.51, 123.27. 122.58, 122.02, 101.11, 49.66 (*J* 15.08 Hz), 38.08. δ_F (376 MHz, $CDCl_3$) 70.67 (t, J^t 4.63). ν_{max}/cm^{-1} 3402.28 (w, br, N–H str), 2933.34 (m, sp^2 C–H str), 2872.24 (m, sp^3 C–H str), 1595.69 (s, sh, asym S=O str), 1384.34 (s, sh, sym S=O str), 818.10 (m, S–F str). *m/z* (LRMS ESI$^+$) 306.23 $[M + H]^+$; calc. 306.07. *m/z* (HRMS ESI$^+$) 306.07093 $[M + H]^+$; calc. 306.07070 (Δ 0.74 ppm). λ_{max}/nm ($\varepsilon/M^{-1}\,cm^{-1}$) ($CH_3CN$) 331 (9098.68), 279 (28578.41), 259 (21861.26), 221 (41646.31), 194 (22288.72). Anal. Calc. for $C_{14}H_{12}O_2N_3SF$: C 55.07, N 13.76, H 3.96; found C 54.54, N 13.64, H 3.63 %.

*Synthesis of Bromotricarbonyl(5-N-(2-Aminoethylsulfonylfluoride)-1,10-phenanthroline) Rhenium(I) (**RePhenESF**)*

5-*N*-(Aminoethylsulfonylfluoride)-1,10-phenanthroline (65.4 mg, 0.214 mmol, 1.0 equiv.) was dissolved in a solution of 50 % DCM in toluene (15 mL), to which pentacarbonylrhenium (I) bromide (79.1 mg, 0.195 mmol, 1.1 equiv.) was added. The solution was then stirred and heated at reflux (2 h). The solution was left to cool to room temperature and the DCM evaporated, after which the resulting precipitate was filtered via vacuum filtration, washed with diethyl ether, and dried under vacuum to afford a yellow powder (110.4 mg, 79 %); mp 295–301°C (dec.). δ_H (400 MHz, [D6]DMSO) 9.28 (d, J^d 5.04, $1H_{Ar}$), 9.10 (d, J^d 7.88, $1H_{Ar}$), 9.03 (dd, J^d 5.00, 1.12, $1H_{Ar}$), 8.53 (dd, J^d 8.36, 1.12 Hz), 8.11 (dd, J^d 8.82, 5.08, $1H_{Ar}$), 7.87 (dd, J^d 8.36, 5.00, $1H_{Ar}$), 7.57 (t, J^t 5.76, $1H_{NH}$), 7.16 (s, $1H_{Ar}$), 4.41 (app. q, J^q 11.88, 5.88, $2H_{CH2–SO2F}$), 3.96 (app. q, J^q 11.56, 5.76, $2H_{CH2}$). δ_C (100 MHz, [D6]DMSO) 197.42, 197.33, 189.51, 153.48, 148.82, 146.68, 142.12, 140.37, 136.31, 133.52, 132.52, 126.47, 125.45, 124.00, 99.41 (d, J^d 26), 48.67 (d, J^d 12), 37.62. δ_F (376 MHz, [D6]DMSO) 70.67 (t, J^t 4.63). ν_{max}/cm^{-1} 3347.38 (w, sh, N–H str), 3051.21 (w, sp^2 C–H str), 3003.10 (w, sp^3 C–H str), 2025.18 (s, sh, A′(1) C≡O str), 1919.09 (s, sh, A′(2) C≡O str), 1898.11 (s, sh, A″ C≡O str). *m/z* (LRMS ESI$^+$) 576.15 $[M–Br]^+$; calc. 576.00. *m/z* (HRMS ESI$^+$) 576.00387 $[M–Br]^+$; calc. 576.00337 (Δ 0.86 ppm). λ_{max}/nm ($\varepsilon/M^{-1}\,cm^{-1}$) ($CH_3CN$) 414 (1835.32), 347 (7341.28), 297 (16255.69), 243 (25956.66), 194 (39590.46). Anal. Calc. for $ReC_{17}H_{12}O_5N_3SFBr$: C 31.15, N 6.41, H 1.85, S 4.89, Br 12.19; found C 30.61, N 6.36, H 1.85, S 4.91, Br 12.05 %.

Supplementary Material

The NMR and FTIR spectra for each of the compounds synthesized, the radioTLC results used for RCY verification, a more detailed analysis of the DFT computed mechanism, details for the microfluidic set-up used in the production of [^{18}F]ESF, as well as the UV-Vis spectra and photophysical characterization data for the synthesized rhenium complexes are available on the Journal's website.

Conflicts of Interest

The authors declare no conflicts of interest.

Acknowledgements

This work was generously funded by the Australian Institute for Nuclear Science and Engineering (AINSE) through the provision of a Postgraduate Research Award (PGRA), and the Australian Research Council (ARC) Linkage Grant LP1590101307. The authors also acknowledge the kind efforts of Amanda McDonald and Cathy Jiang in their laboratory support at ANSTO, as well as Gary Perkins and Nikolas Paneras for cyclotron production.

References

[1] H. Chen, R. Hong, Z. Li, W. Zhu, J. Chen, Y. Zhang, B. Jiang, *Org. Biomol. Chem.* **2017**, *15*, 7339. doi:10.1039/C7OB01866E

[2] A. M. Freedy, M. J. Matos, O. Boutureira, F. Corzana, A. Guerreiro, P. Akkapeddi, V. J. Somovilla, K. Nicholls, B. Xie, G. Jimenez-Oses, K. M. Brindle, A. A. Neves, G. J. L. Bernardes, *J. Am. Chem. Soc.* **2017**, *139*, 18365. doi:10.1021/JACS.7B10702

[3] J. L. Furman, M. Kang, S. Choi, Y. Cao, E. D. Wold, S. B. Sun, V. V. Smider, P. G. Schiltz, C. H. Kim, *J. Am. Chem. Soc.* **2014**, *136*, 8411. doi:10.1021/JA502851H

[4] A. Narayanan, B. Maiti, P. De, *React. Funct. Polym.* **2015**, *91–92*, 35. doi:10.1016/J.REACTFUNCTPOLYM.2015.04.001

[5] B. C. Ranu, S. Banerjee, *Tetrahedron Lett.* **2007**, *48*, 141. doi:10.1016/J.TETLET.2006.10.142

[6] H. D. Batey, A. C. Whitwood, A.-K. Duhme-Klair, *Inorg. Chem.* **2007**, *46*, 6516. doi:10.1021/IC700554N

[7] C.-O. Ng, S.-W. Lai, H. Feng, S.-M. Yiu, C.-C. Ko, *Dalton Trans.* **2011**, 10020. doi:10.1039/C1DT10831J

[8] A. M. Fracaroli, K. Tashiro, O. M. Yaghi, *Inorg. Chem.* **2012**, *51*, 6437. doi:10.1021/IC300744X

[9] M. A. Klenner, G. Pascali, B. Zhang, T. R. Sia, L. K. Spare, A. M. Krause-Heuer, J. R. Aldrich-Wright, I. Greguric, A. J. Guastella, M. Massi, B. H. Fraser, *Chem. – Eur. J.* **2017**, *23*, 6499. doi:10.1002/CHEM.201700440

[10] B. Zhang, G. Pascali, N. Wyatt, L. Matesic, M. A. Klenner, T. R. Sia, A. J. Guastella, M. Massi, A. J. Robinson, B. H. Fraser, *J. Labelled Comp. Radiopharm.* **2018**, *61*, 847. doi:10.1002/JLCR.3667

[11] K. Y. Zhang, K. K.-S. Tso, M.-W. Louie, H.-W. Liu, K. K.-W. Lo, *Organometallics* **2013**, *32*, 5098. doi:10.1021/OM400612F

[12] V. Fernandez-Moreira, M. L. Ortego, C. F. Williams, M. P. Coogan, M. D. Villacampa, M. C. Gimeno, *Organometallics* **2012**, *31*, 5950. doi:10.1021/OM300610J

[13] K. K.-W. Lo, W.-K. Hui, D. C.-M. Ng, *J. Am. Chem. Soc.* **2002**, *124*, 9344. doi:10.1021/JA026598N

[14] C. A. Bader, R. D. Brooks, Y. S. Ng, A. Sorvina, M. V. Werrett, P. J. Wright, A. G. Anwer, D. A. Brooks, S. Stagni, S. Muzzioli, M. Silberstein, B. W. Skelton, E. M. Goldys, S. E. Plush, T. Shandala, M. Massi, *RSC Adv.* **2014**, *4*, 16345. doi:10.1039/C4RA00050A

[15] S. Ranjan, S.-Y. Lin, K.-C. Hwang, Y. Chi, W.-L. Ching, C.-S. Liu, *Inorg. Chem.* **2003**, *42*, 1248. doi:10.1021/IC0259181

[16] A. Bessette, S. Nag, A. K. Pal, S. Derossi, G. S. Hanan, *Supramol. Chem.* **2012**, *24*, 595. doi:10.1080/10610278.2012.691500

[17] A. Świtlicka-Olszewska, T. Klemens, I. Nawrot, B. Muchura, R. Kruszynski, *J. Lumin.* **2016**, *171*, 166.

[18] C. Kefalidi, E. Koutsouri, L. Marchio, A. Zarkadoulas, S. Efstathiadou, C. A. Mitsopoulou, *Polyhedron* **2016**, *110*, 157. doi:10.1016/J.POLY.2016.02.043

[19] P. J. Wright, S. Muzzioli, M. V. Werrett, P. Raiteri, B. W. Skelton, D. S. Silvester, S. Stagni, M. Massi, *Organometallics* **2012**, *31*, 7566. doi:10.1021/OM300870A

[20] R. G. LeBel, D. A. I. Goring, *J. Chem. Eng. Data* **1962**, *7*, 100. doi:10.1021/JE60012A032

[21] F. Neese, *WIREs Comput. Mol. Sci.* **2012**, *2*, 73. doi:10.1002/WCMS.81

[22] A. D. Becke, *J. Chem. Phys.* **1997**, *107*, 8554. doi:10.1063/1.475007

[23] S. Grimme, J. Antony, S. Ehrlich, H. Krieg, *J. Chem. Phys.* **2010**, *132*, 154104doi:10.1063/1.3382344

[24] R. A. Kendall, H. A. Früchtl, *Theor. Chem. Acc.* **1997**, *97*, 158. doi:10.1007/S002140050249

[25] P. J. Hay, W. R. Wadt, *J. Chem. Phys.* **1985**, *82*, 270. doi:10.1063/1.448799

[26] W. R. Wadt, P. J. Hay, *J. Chem. Phys.* **1985**, *82*, 284. doi:10.1063/1.448800

[27] P. J. Hay, W. R. Wadt, *J. Chem. Phys.* **1985**, *82*, 299. doi:10.1063/1.448975

[28] E. D. Glendening, C. R. Landis, F. Weinhold, *J. Comput. Chem.* **2013**, *34*, 1429. doi:10.1002/JCC.23266

[29] N. Salvi, L. Belpassi, F. Tarantelli, *Chem. – Eur. J.* **2010**, *16*, 7231. doi:10.1002/CHEM.201000608

[30] G. Ciancaleoni, L. Belpassi, F. Marchetti, *Inorg. Chem.* **2017**, *56*, 11266. doi:10.1021/ACS.INORGCHEM.7B01635

[31] M. Mitoraj, A. Michalak, *J. Mol. Model.* **2007**, *13*, 347. doi:10.1007/S00894-006-0149-4

[32] R. F. Nalewajski, A. M. Koster, K. Jug, *Theor. Chim. Acta* **1993**, *85*, 463. doi:10.1007/BF01112985

[33] R. F. Nalewajski, J. Mrozek, *Int. J. Quantum Chem.* **1994**, *51*, 187. doi:10.1002/QUA.560510403

[34] R. F. Nalewajski, J. Mrozek, A. Michalak, *Int. J. Quantum Chem.* **1997**, *61*, 589. doi:10.1002/(SICI)1097-461X(1997)61:3<589::AID-QUA28>3.0.CO;2-2

[35] G. Bistoni, S. Rampino, F. Tarantelli, L. Belpassi, *J. Chem. Phys.* **2015**, *142*, 084112doi:10.1063/1.4908537

[36] M. De Santis, S. Rampino, H. M. Quiney, L. Belpassi, L. Storchi, *J. Chem. Theory Comput.* **2018**, *14*, 1286. doi:10.1021/ACS.JCTC.7B01077

[37] A.-R. Allouche, *J. Comput. Chem.* **2011**, *32*, 174. doi:10.1002/JCC.21600

[38] S. Rampino, *VIRT&L-COMM* **2015**, *7*, 6.

[39] E. D. Glendening, J. K. Badenhoop, A. E. Reed, J. E. Carpenter, J. A. Bohmann, C. M. Morales, C. R. Landis, F. Weinhold, *NBO 6.0* **2013** (Theoretical Chemistry Institute, University of Wisconsin: Madison, WI).

Rhenium Complexation-Dissociation Strategy for Synthesizing Fluorine-18 Labeled Pyridine Bidentate Radiotracers

Mitchell A. Klenner,[a,b] Giancarlo Pascali,*[a,c] Bo Zhang,[a,d] Gianluca Ciancaleoni,[e] James Howard,[a] Helen E. Maynard-Casely,[a] Jack Clegg,[f] Massimiliano Massi,[b] Benjamin H. Fraser.*[a]

Abstract: A novel fluorine-18 labelling method referred to as pyridine fluorination activated by rhenium (PYFLARE) is described herein. The PYFLARE method was found to afford high to moderate radiochemical yields of labelled rhenium complexes. More significantly, by exploiting thermal dissociation, the PYFLARE method enabled the radiosynthesis of fluorine-18 labelled bipyridine structures which could not be radiofluorinated by traditional means. The PYFLARE method was further applied to the radiosynthesis of [^{18}F]CABS13, an Alzheimer's disease imaging agent, alongside other phenanthroline and 8-hydroxyquinoline radiotracers. Computational modelling was also performed to elucidate the reaction mechanism. This data suggests that the efficiency of the PYFLARE method may be attributed to both an electron withdrawal effect by the rhenium and the formation of an acylfluoride intermediate which may 'anchor' the fluoride subsequent to nucleophilic addition.

Radiotracers are commonly used to investigate biochemical systems in living organisms and are routinely employed as nuclear medicines to diagnose cancers and other disease pathologies.[1] The discovery of new radiolabeling methods is critical to the improved synthesis of new radiotracers needed to diagnose currently untreated disease states. Positron emission tomography (PET) is the most sensitive of all nuclear imaging techniques and fluorine-18 is the most widely utilized radioisotope in existing PET medicines.[2,3] Given the difficulties associated with fluorine-18 labeling pyridine-containing bidentate structures, it was hypothesized that a rhenium activation approach could be a powerful tool towards expanding the scope of such radiotracers.[4] To test this hypothesis, we selected three common bidentate structures throughout our investigation; 1,10-phenanthroline, 2,2'-bipyridine and 8-hydroxyquinoline. In each of these studies we systematically tested the nucleophilic substitution of chloro, bromo and/or nitro leaving groups for [^{18}F]fluoride on different positions of the molecule to establish the advantages and limitations of a thermally mediated rhenium complexation-dissociation strategy, following a method herein referred to as pyridine fluorination activated by rhenium (PYFLARE). Additionally, the PYFLARE method fits within a limited scope of fluorine-18 labelling methods which can substitute under aqueous conditions, inclusive of AlF,[4-7] boron-dipyrromethene (BODIPY)[8-10] and ethenesulfonyl fluoride (ESF) agents.[11,12] This discovery lead us to compare reaction conditions employing azeotropically distilled ('*dry*') and non-distilled ('*wet*') fluorine-18 sources, the latter of which typically suppresses radiochemical yield (RCY) due to the decreased nucleophilicity of the [^{18}F]fluoride in aqueous media.[3]

Each precursor was reacted under microfluidic conditions using an automated synthesis module assembled as per the schematic in Figure 1. Herein cyclotron generated [^{18}F]fluoride was trapped on an ion-exchange cartridge and eluted to an azeotropic distillation vial using a solution of tetraethylammonium (TEA) bicarbonate in 9:1 acetonitrile: water solution. *Dry* reaction conditions were then achieved by azeotropically drying the [^{18}F]fluoride complex *via* the heated dropwise addition of acetonitrile followed by reconstitution in anhydrous DMSO to enhance the nucleophilicity of the fluoride. Whereas *wet* reaction conditions omitted this distillation step and thus consisted of a 5%

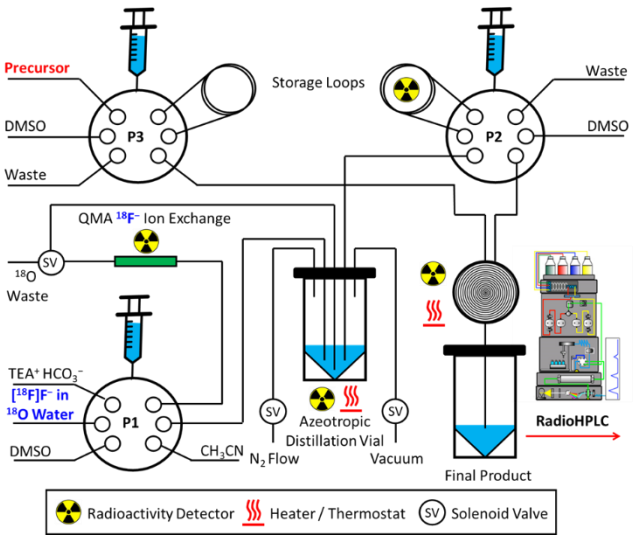

Figure 1. Automated synthesis module assembled from microfluidic components for the azeotropic drying of cyclotron generated [^{18}F]fluoride and subsequent PYFLARE radiolabeling reactions with a precursor molecule in a microreactor of varying temperature.

[a] Mr. M. A. Klenner, Dr. G. Pascali, Mr. B. Zhang, Dr. J. Howard, Dr. H. Maynard-Casely, Dr. B. H. Fraser.
Human Health
ANSTO
Lucas Heights, NSW, Australia. 2234.
E-mail: gianp@ansto.gov.au, bfr@ansto.gov.au
[b] Mr. M. A. Klenner, Dr. M. Massi.
School of Molecular and Life Sciences
Curtin University
Bentley, WA, Australia. 6102.
[c] Dr. G. Pascali.
Brain and Mind Centre
University of Sydney
Camperdown, NSW, Australia. 2050.
[d] Mr. B. Zhang.
School of Chemistry
Monash University
Melbourne, VIC, Australia. 3800.
[e] Dr. G. Ciancaleoni.
Dipartmento di Chimica e Chimica Industriale
Università di Pisa
Pisa, Italy. 56127.
[f] Assoc. Prof. J. Clegg
Department of Chemistry
University of Queensland
St. Lucia, QLD, Australia. 4072.

Supporting information (SI) for this article is given via a link at the end of the document.

	1			2		3
Compound	Structure	Re Complex	R_1	R_2	R_3	
Phen	1	Ligand	H	H	-	
2ClPhen	1	Ligand	Cl	H	-	
5ClPhen	1	Ligand	H	Cl	-	
2BrPhen	1	Ligand	Br	H	-	
5NO_2Phen	1	Ligand	H	NO2	-	
2FPhen	1	Ligand	F	H	-	
5FPhen	1	Ligand	H	F	-	
RePhen	1	Complex	H	H	-	
Re2ClPhen	1	Complex	Cl	H	-	
Re5ClPhen	1	Complex	H	Cl	-	
Re2BrPhen	1	Complex	Br	H	-	
Re5NO_2Phen	1	Complex	H	NO2	-	
Re2FPhen	1	Complex	F	H	-	
Re5FPhen	1	Complex	H	F	-	
BiPy	2	Ligand	H	H	H	
6ClBiPy	2	Ligand	Cl	H	H	
5ClBiPy	2	Ligand	H	Cl	H	
4ClBiPy	2	Ligand	H	H	Cl	
6BrBiPy	2	Ligand	Br	H	H	
6FBiPy	2	Ligand	F	H	H	
5FBiPy	2	Ligand	H	F	H	
4FBiPy	2	Ligand	H	H	F	
ReBiPy	2	Complex	H	H	H	
Re6ClBiPy	2	Complex	Cl	H	H	
Re5ClBiPy	2	Complex	H	Cl	H	
Re4ClBiPy	2	Complex	H	H	Cl	
Re6BrBiPy	2	Complex	Br	H	H	
Re6FBiPy	2	Complex	F	H	H	
Re5FBiPy	2	Complex	H	F	H	
Re4FBiPy	2	Complex	H	H	F	
2Cl8HQ	3	Ligand	Cl	H	-	
5Cl8HQ	3	Ligand	H	Cl	-	
2F8HQ*	3	Ligand	F	H	-	
5F8HQ	3	Ligand	H	F	-	
Re2Cl8HQ	3	Complex	Cl	H	-	
Re5Cl8HQ	3	Complex	H	Cl	-	
Re2F8HQ	3	Complex	F	H	-	
Re5F8HQ	3	Complex	H	F	-	

Figure 2. List of rhenium complex and ligand structures based on 1,10-phenanthroline (**1**), 2,2'-bipyridine (**2**) and 8-hydroxyquinoline (**3**) N-heterocycles used as precursors or standards in this study. *Note that [^{18}F]2F8HQ is also known as the [^{18}F]CABS13 Alzheimer's disease PET diagnostic radiotracer.

v/v content of water and acetonitrile. Both the [^{18}F]fluoride (29±10 MBq) and precursor solution (0.08 μmol) in DMSO were then dispensed concurrently from pumps 2 and 3 (P2, P3) respectively through a heated microreactor at a rate of 20 μL.min^{-1} (47 s reaction time). Reaction temperatures between 50 and 190 °C were trialed for each experiment in 20 °C increments. The solution was then dispensed into a final product vial where the solution was subsequently analysed by radioHPLC and/or radioTLC to determine the non-isolated RCYs of the radioproducts.

A list of each of the tested precursors and fluorinated standards are provided in figure 2. Initial PYFLARE reactions employing the **Re2ClPhen** precursor provided the fluorine-18 labelled **[^{18}F]Re2FPhen** in a considerable 90% RCY at 90 °C under *dry* conditions and exhibited some minor thermal dissociation to form the **[^{18}F]2FPhen** ligand in 13% RCY at 170 °C. Curiously, the same reaction under *wet* conditions afforded **[^{18}F]Re2FPhen** in 59% RCY at a much lower temperature of 50 °C though exhibited no dissociation to form **[^{18}F]2FPhen** at all. Radiofluorination of **Re2BrPhen** under *dry* conditions *via* PYFLARE demonstrated a similar trend whereupon **[^{18}F]Re2FPhen** formed in a maximum 73% RCY at 70 °C and afforded a small 8% RCY of **[^{18}F]2FPhen** *via* thermal dissociation at 170 °C. To widen the scope of available fluorine-18 labelled rhenium complexes we then trialed radiolabeling reactions in the 5-position using PYFLARE. Fluorine-18 labeling of **Re5ClPhen** afforded **[^{18}F]Re2FPhen** in 33% RCY under *dry* conditions, though only 2% of **[^{18}F]Re2FPhen** under *wet* conditions, with neither reaction thermally decomplexing to form the **[^{18}F]5FPhen** ligand. Thus, PYFLARE reactions were attempted with **Re5NO$_2$Phen** bearing the more electron withdrawing nitro group which we hypothesized would improve nucleophilic substitution for [^{18}F]fluoride. Indeed under *dry* conditions using **Re5NO$_2$Phen** we not only observed **[^{18}F]Re2FPhen** radiolabeling in 39% RCY at 110 °C though also observed some very minor ligand dissociation forming **[^{18}F]5FPhen** in 2% RCY. Worth mentioning is that each of these reactions appeared to also form another unknown ('mystery') radio by-product for which we did not have a non-radioactive standard to confirm the identity of. Plots illustrating the RCY of the fluorine-18 labelled complex, ligand and mystery compounds as a function of increasing reaction temperature can be found in S.3 of the SI.

Based on these results we opted to trial a dissociation strategy using similarly complexed 2,2'-byridine ligands. Intriguingly, **Re2ClBiPy** did not only radiolabel to form **[^{18}F]Re2FBiPy** in 82% RCY at 130°C under *dry* conditions, though also readily dissociated with increasing temperature to form the desired **[^{18}F]2FBiPy** ligand in 64% RCY at 190°C. To our surprise the **[^{18}F]2FBiPy** radioproduct would not form from the **2ClBiPy** precursor under analogous conditions and hence could only be synthesised using the PYFLARE method. Radiolabeling reactions using the **Re2BrBiPy** precursor similarly formed **[^{18}F]Re2FBiPy** in a maximum of 72% RCY at 110°C under *dry* conditions and dissociated to form **[^{18}F]2FBiPy** in 51% at 190°C. Substituting for [^{18}F]fluoride in the *para* instead of *ortho* position using the **Re4ClBiPy** precursor provided **[^{18}F]Re4FBiPy** in 68% RCY and dissociated to form **[^{18}F]4FBiPy** in 31% RCY at 190°C, which likewise could not be synthesized from the **4ClBiPy** ligand precursor under analogous conditions. Using PYFLARE to synthesize **[^{18}F]Re5FBiPy** from **Re5ClBiPy** afforded less than 1% RCY of the radiolabeled complex, however, which proved too little of an amount to dissociate any of the **[^{18}F]5FBiPy** ligand. A summary of the RCYs formed per temperature for each of the bipyridines successfully radiolabeled under *dry* conditions using PYFLARE is shown in figure 3. Example chromatograms in this figure also show the dissociation of the complex to form the

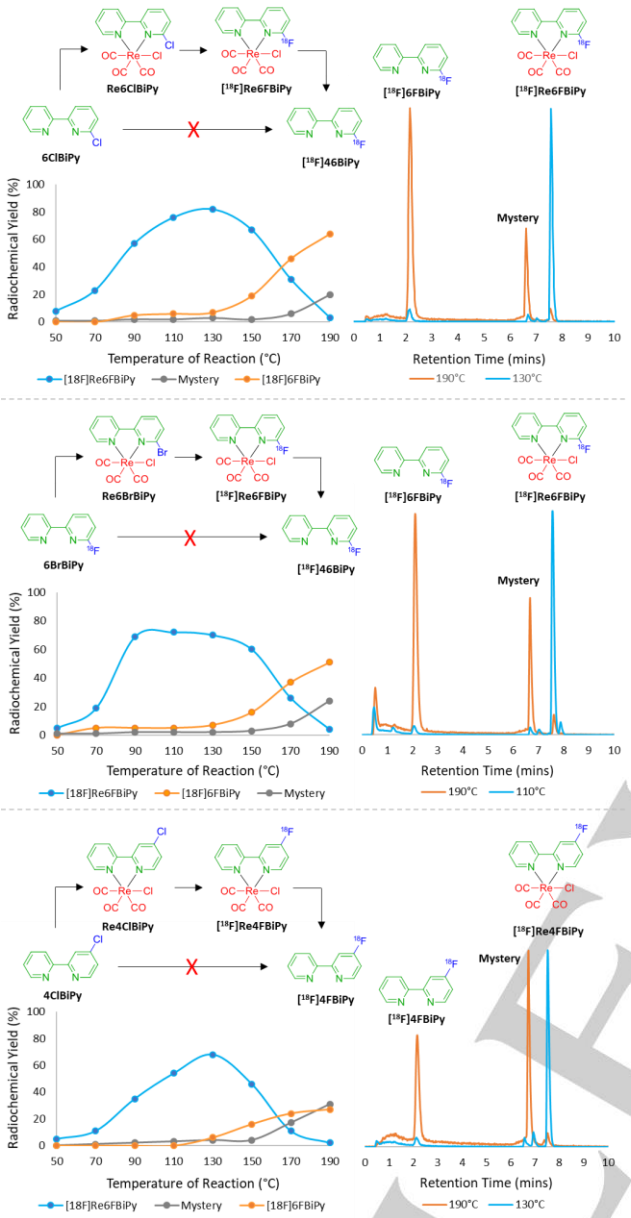

Figure 3. RCY plotted as a function of reaction temperature alongside radiochromatograms for **Re6ClBiPy** (top), **Re6BrBiPy** (middle) and **Re4ClBiPy** (bottom) precursors. These trends show the formation of a fluorine-18 labelled complex and subsequent dissociation of the formerly unobtainable fluorine-18 labelled ligand at higher temperatures.

radiolabeled ligand at two differing temperatures, alongside the appearance of the mystery by-product. Reactions under *wet* conditions also demonstrated lower yielding yet similar trends with **[^{18}F]Re6FBiPy** forming from **Re6ClBiPy** and **Re6BrBiPy** in 29% RCY at 130 °C and 9% RCY at 150 °C respectively, and dissociating to form **[^{18}F]6FBiPy** in 24% RCY at 190 °C and 10% RCY at 190 °C respectively. RCY *vs.* temperature plots for these *wet* reactions can be found in S.3 of the SI. One hypothesis as to why the 2,2'-bipyridine complexes thermally dissociate with greater efficiency than the 1,10-phenanthroline rhenium complexes, and thus form their respective fluorine-18 labeled ligands in greater RCY, may be due to the lesser rigidity exhibited by bipyridine molecules in comparison to phenanthroline ring systems. [13]

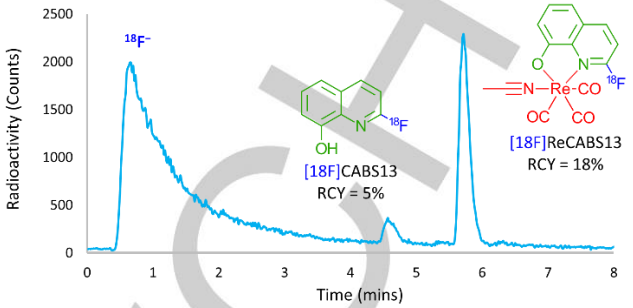

Figure 4. Radiochromatogram obtained for the **[^{18}F]ReCABS13** tracer (5.7 min) forming in 18% RCY and thermally dissociating to form the **[^{18}F]CABS13** Alzheimer's PET radiotracer (4.6 min) in 5% RCY.

After establishing the efficiency of the PYFLARE method, and its subsequent thermal dissociation of fluorine-18 labelled 2,2'-bipyrine ligands, we were interested in translating the method to 8-hydroxyquinoline structures. Notably because of the documented use of these structures as markers of amyloid-β (Aβ) plaques characterized by Alzheimer's disease.[14-18] Though also because complexation of the hydroxyl group to rhenium was hypothesized to circumvent multiple step radiosynthesis, which is usually required to protect the alcohol, during which time radioactivity is lost due to decay. The first of these precursor structures to be radiolabeled was **Re2Cl8HQ** in the hopes of radiosynthesising **[^{18}F]CABS13** (*i.e.* **[^{18}F]2F8HQ**), a radiotracer which provided efficient PET imaging of Aβ plaques in transgenic mouse models of Alzheimer's disease,[19] though which failed when translating to a non-human primate due to low brain uptake and rapid metabolism.[20] Radiolabeling of **Re2Cl8HQ** afforded only 2% RCY of both **[^{18}F]ReCABS13** (*i.e.* **[^{18}F]Re2F8HQ**) and **[^{18}F]CABS13** at 190°C under *dry* conditions, thus prompting us to increase the molar amount of precursor used. Using ten-fold the mass of **Re2Cl8HQ** (0.8 μmol) resulted in a remarkable increase to 18% RCY of **[^{18}F]ReCABS13** and 5% RCY of the dissociated **[^{18}F]CABS13** PET radiotracer at 190°C. This RCY of **[^{18}F]CABS13** obtained using PYFLARE is still below the 19±5% RCY achieved by Liang and coworkers using multi-step radiosynthesis,[20] however these results suggest that further optimizations could be made for all analyses by increasing the molar amount of the precursor. More interestingly, the **[^{18}F]5F8HQ** radiotracer which was hypothesized to be more efficient at disaggregating Aβ plaques,[21] though which was unable to be synthesized by traditional means, was able to be formed from both **Re5Cl8HQ** and **Re5NO$_2$8HQ** precursors in 1% and 2% RCY respectively, with the radiolabeled complex **[^{18}F]Re5F8HQ** also forming in 3% and 6% RCY respectively, under *dry* conditions. Under *wet* conditions **[^{18}F]ReCABS13** and **[^{18}F]Re5F8HQ** could both be formed from their respective precursors, albeit in lower RCY. Only **Re5NO$_2$8HQ** was able to undergo ligand dissociation to afford **[^{18}F]5F8HQ** under such *wet* conditions, however. RCY plots for the rhenium complexed and dissociated 8-hydroxyquilone tracers as a function of reaction temperature can be viewed in S.3 of the SI. A list of the RCYs obtained for each of the fluorine-18 labelled rhenium complexes

and dissociated ligands under comparable conditions is provided in Table 1.

Table 1. Optimum RCYs obtained for varying temperatures when reacting TEA [^{18}F]fluoride with each of the rhenium precursors under the same *dry* experimental conditions (solvent: DMSO, reaction time: 47 s, precursor amount: 0.08 μmol, radioactivity: 29 ± 10 MBq). Save for these exceptions: *Reaction time of 188 s used. **Ten-fold mass (0.8 μmol) of precursor used.

Radiotracer	Precursor	Temperature (°C)	RCY (%)
[^{18}F]Re2FPhen	Re2ClPhen	90	91
	Re2BrPhen	110	69
[^{18}F]Re5FPhen	Re5ClPhen	170	33
	Re5NO_2Phen	110	39
[^{18}F]Re6FBiPy	Re6ClBiPy	130	82
	Re6BrBiPy	110	72
[^{18}F]Re4FBiPy	Re4ClBiPy	130	68
[^{18}F]Re2F8HQ**	Re2Cl8HQ	190	18
[^{18}F]Re5F8HQ	Re5Cl8HQ	130	3
	Re5$NO_2$8HQ	170	6
[^{18}F]2FPhen	Re2ClPhen	170	13
	Re2BrPhen	170	8
[^{18}F]5FPhen	Re5ClPhen	-	0
	Re5NO_2Phen	130	2
[^{18}F]6FBiPy	Re6ClBiPy	190	64
	Re6BrBiPy	190	51
[^{18}F]4FBiPy*	Re4ClBiPy	190	37
[^{18}F]2F8HQ**	Re2Cl8HQ	190	5
[^{18}F]5F8HQ	Re5Cl8HQ	190	1
	Re5$NO_2$8HQ	190	2

Towards understanding the mechanism by which PYFLARE improves fluorination of a pyridine bidentate structure, we opted to model the reaction *via* DFT calculations at the B97-D3/def2-TZVP level of theory. The input coordinates were acquired from the XRD data of crystals of the rhenium complexes grown from slow evaporation in DMSO solution. First, the coordination on the rhenium center leads to a depletion of electron density on the ligand, a phenomenon also realised by the downfield chemical shifts observed in NMR spectra of the rhenium complexes. This depletion can be quantified by the Natural Orbitals for Chemical Valence-Charge Displacement (NOCV-CD),[22] according to which the L → M σ-donation is 0.266 e and the L ← M π back-donation is 0.116 e in the case of **Re6FBiPy**. Such electronic depletion favours nucleophilic addition of the fluoride on the carbon bound to the chlorine atom. The DFT-computed activation

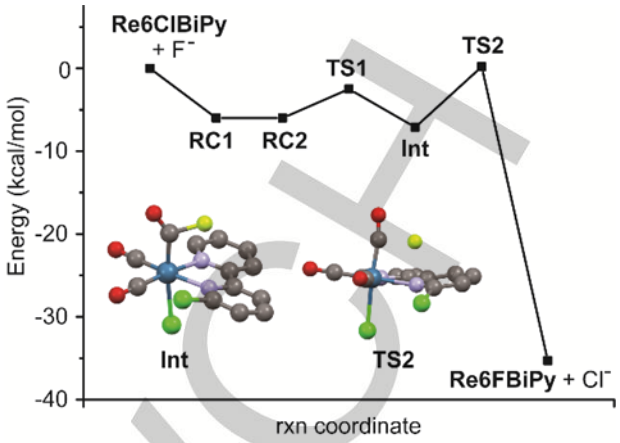

Figure 5. DFT modelling of the reaction mechanism forming **Re6FBiPy** from **Re6ClBiPy**. The optimized geometries of the intermediate species (**Int**) and the rate-determining transition state (**TS**) are shown.

energies are 6.3 and 34 kcal.mol^{-1} in the presence and absence of the metal fragment, respectively. Notably the fluoride primarily bonds to the carbonyl in the *cis* position relative to the diimine ligand, forming an acylfluoride intermediate as shown in figure 5. This intermediate is unstable, however, and quickly detaches from the carbonyl anchor to undergo nucleophilic aromatic substitution for the chlorine atom. From the experimental data is was observed that **Re6FBiPy** formed in a greater fluorination yield than **Re4FBiPy**, whereas the **Re5FBiPy** complex formed in almost no appreciable yield at all. This trend can be explained by calculating the atomic charges by Natural Population Analysis, whereupon it was shown that the carbon atoms bound to the chlorine consisted of partial charges equal to 0.29, -0.01 and 0.04 e for the **Re6ClBiPy**, **Re5ClBiPy** and **Re4ClBiPy** precursors respectively. Clearly a positive partial charge facilitates fluorination and a negative partial charge inhibits nucleophilic addition of the fluoride.

In a former study we also verified the photophysical properties of the **Re2ClPhen** and **Re2FPhen** complexes for potential use of the latter as a PET-optical multimodal imaging agent.[4] Given the reasonable RCYs which were likewise obtained for the rhenium bipyridine complexes in this study, we further determined quantum yields of 5.8 ×10^{-3}, 1.1×10^{-2}, 4.7×10^{-3} and 6.1×10^{-3} for **Re4ClBiPy**, **Re5ClBiPy**, **Re6ClBiPy** and **Re6FBiPy** complexes in DMSO solution respectively.

In conclusion, we report the novel PYFLARE method for radiolabeling rhenium tricarbonyl complexes with the fluorine-18 radioisotope. The rhenium center improves radiofluorination *via* an electron withdrawal effect and, in accordance with our computational models, may facilitate radiofluorination reactions *via* formation of an acylfluoride intermediate with a carbonyl ligand. Through a series of radiosyntheses under microfluidic conditions we verified that high to moderate RCYs could be obtained by substituting [^{18}F]fluoride in the rhenium-activated *ortho* and *para* positions of bidentate pyridine ligands, as well as in the 5-position of a phenanthroline ligand. Radiolabeling in the *meta* position, however, proved challenging and lies outside the scope of the PYFLARE method. In addition to providing reasonable RCYs of

many radiolabeled complexes, which may find applications in the development of PET-optical multimodal tracers, a thermal decomplexation approach has also been shown to dissociate more labile bidentate ligands. This rhenium complexation-dissociation approach was particularly useful for synthesizing fluorine-18 labelled bipyridine compounds in considerable RCYs, which were unable to be synthesised under analogous conditions without using PYFLARE. Such a method may thus expand the scope of new PET radiotracers which can be developed. Furthermore, the PYFLARE method also joins the limited suite of radiofluorinating methods which can afford radiotracers under aqueous conditions. This discovery may expand the scope for PYFLARE to be used at low temperatures following subsequent bioconjugation for further PET-optical development. Future work towards alternative decomplexation methods (*e.g.* photodissociation or acid dissociation), as well as attempts to fluorine-18 label monodentate pyridine ligands complexed to the rhenium center, may further expand the scope of radiotracer syntheses which PYFLARE could be applied to.

Experimental Section

Synthesis of rhenium complexes

Complex diveratives of **ReXPhen** and **ReXBiPy** were prepared by refluxing rhenium(I) pentacarbonyl chloride (300 mg, 830 µmol, 1.0 eq.) and the appropriately substituted chloro, bromo or nitro 2,2-bipyridine or 1,10-phenanthroline (1.1 eq.) in a solution of anhydrous toluene (10 mL) for 4 hours in an inert nitrogen environment, resulting in a colour change from blue or colourless to yellow or orange. The solid precipitate was isolated by vacuum filtration and washed with diethyl ether. The crude material was then dissolved in a minimum of DCM and eluted over neutral alumina Brockmann grade II using a DCM/MeOH gradient mobile phase. The eluents containing the product were subsequently combined and evaporated down under reduced pressure to afford the yellow or orange powder.

Complex derivatives of **ReX8HQ** were prepared by first refluxing rhenium(I) pentacarbonyl chloride (100 mg, 275 µmol, 1.0 eq.) in anhydrous acetonitrile (10 mL) for 4 hours in an inert nitrogen environment (purged by vacuum for 3 cycles) in order to make the rhenium(I) diacetonitrilo tricarbonyl chloride intermediate, which can be monitored by HPLC or IR spectroscopy. Simultaneously, the appropriate chloro or nitro substituted 8-hydroxyquinoline (1.0 eq.) was deprotonated with sodium hydride (60% wt/wt in mineral oil washed with hexanes) in anhydrous acetonitrile (2 mL) at room temperature under an inert nitrogen environment, resulting in a vibrant green solution. The green solution was then filtered (0.2 µm PTFE) and added drop wise to the solution containing rhenium. This solution was then left to stir for 12 hours at room temperature eventually forming an orange solution. The orange solution was then added to a volume of aqueous triflic acid (0.1 M, 10 mL) and evaporated under reduced pressure to remove the acetonitrile, thus precipitating out a a yellow or orange solid in aqueous suspension. The crude material was then isolated by vacuum filtration, dissolved in acetonitrile and eluted over neutral alumina Brockmann grade II using an isocratic acetonitrile mobile phase. The eluents containing the product were subsequently combined and evaporated down under reduced pressure to afford the yellow or orange powder.

Radiolabeling protocol

Aqueous [^{18}F]fluoride was produced on an IBA Cyclone 18 Twin cyclotron *via* the ^{18}O(p,n)^{18}F nuclear reaction. The [^{18}F]fluoride was trapped by a QMA catridge and eluted off with tetraethylammonium bicarbonate in 10% v/v water/acetonitrile for *wet* conditions, and azeotropically dried using anhydrous DMSO for *dry* conditions. Microfluidic radiosyntheses were performed in in Doscovery Mode using a NanoTek LF Microfluidic Synthesis System (Advion) connected to a standard laptop using NanoTek software v1.4.0 GMP Lite. Microreactors were made of fused silica tubing (100 µm × 2 m, 15.6 µL) coiled tightly into a brass ring and held by a thermoresistent polymer. RadioHPLC analyses were carried out using a Shimadzu system comprised of a CBM-20 controller, LC-20AD pump, SIL-20AHT autoinjector, SPD-M20A PDA detector and a Lablogic Posi-RAM gamma detector. Analyses were performed using gradient conditions over 15 minutes, consisting of 95:5 water: acetonitrile for the first 3 minutes followed by a a linear transposition to 5:95 water:acetonitrile over the remaining 12 minutes using a 2 mL.min^{-1} flow rate. A Chromolith RP column (monolith system, Merck 50 × 4.6 mm), demonstrated to have >92% [^{18}F]fluoride retention in low pH ranges,[23] was employed as the stationary phase. RadioHPLC derived non-isolated RCYs were calculated *via* the integrated peak area ratio between the radioproduct and other radioactive species present, inclusive of any unreacted [^{18}F]fluoride, using Laura V4.1.70 SP2 HPLC data analysis software.

Computational, photophysical and characterisation data

Further information on the characterisation data, computational details and photophysical experiments can be found in sections S.1-S.2, S.4 and S.5 of the SI respectively.

Acknowledgements

The authors kindly acknowldege the Australian Institute for Nuclear Science and Engineering (AINSE) for the provision of a Postgraduate Research Award (PGRA). The Australian Research Council (ARC) is also kindly acknowledged for the provision of a Linkage Grant (LP1590101307). Crystal structure data for this contribution was collected on the MX beamline, Australian Synchrotron as part of CAP11195. Finally, the authors also ackowledge the efforts of Michael Tran and Gary Perkins for cyclotron production at ANSTO.

Keywords: fluorine-18 • rhenium • pyridine • PET • Alzheimer's

[1] S. M. Ametamey, M. Honer, P. A. Schubiger. *Chem. Rev.* **2008**, *108*, 1501-1516.

[2] D. van der Born, A. Pees, A. J. Poot, R. V. A. Orru, A. D. Windhorst, D. J. Vugts. *Chem. Soc. Rev.* **2017**, *46*, 4709-4773.

[3] O. Jacobson, D. O. Kiesewetter, X. Chen. *Bioconjugate Chem.* **2015**, *26*, 1-18.

[4] M. A. Klenner, G. Pascali, B. Zhang, T. R. Sia, L. K. Spare, A. M. Krause-Heuer, J. R. Aldrich-Wright, I. Greguric, A. J. Guastella, M. Massi, B. H. Fraser. *Chem. Euro. J.* **2017**, *23*, 6499-6503.

[4] F. Cleeran, J. Lecina, J. Bridoux, N. Devoogdt, T. Tshibangu, C. Xavier, G. Bormans. *Nat. Protoc.* **2018**, *13*, 2330-2347.

[5] P. Laverman, W. J. McBride, R. M. Sharkey, D. M. Goldenberg, O. C. Boerman. *J. Label. Comp. Radiopharm.* **2014**, *57*, 219-223.

[6] S. H. Hausner, B. Bauer, J. L. Sutcliffe. *Nucl. Med. Biol.* **2014**, *41*, 43-50.

[7] N. Malik, B. Baur, G. Winter, S. N. Reske, A. J. Beer, C. Solbach. *Mol. Imaging. Biol.* **2015**, *17*, 777-785.

[8] Z. Li, T-P. Lin, S. Liu, C-W. Huang, T. W. Hudnall, F. P. Gabbi, P. S. Conti. *Chem. Commun.* **2011**, *47*, 9324-9326.

[9] S. Liu, D. Li, Z. Zhang, G. K. Surya-Praskash, P. S. Conti, Z. Li. *Chem. Commun.* **2014**, *50,* 7371-7373.

[10] H. Kim, K. Kim, S-H. Son, J. Y. Choi, K-H. Lee, B-T. Kim, Y. Byun, Y. S. Choe. *ACS Chem. Neurosci.* DOI: 10.1021/acschemneuro.8b00480 just accepted.

[11] B. Zhang, G. Pascali, N. Wyatt, L. Matesic, M. A. Klenner, T. R. Sia, A. J. Guastella, M. Massi, A. J. Robinson, B. H. Fraser. *J. Label. Comp. Radiopharm.* **2018**, *61*, 847-856.

[12] M. A. Klenner, G. Pascali, B. Zhang, G. Ciancaleoni, M. Massi, B. H. Fraser. *Aust. J. Chem.* **2019**, *72*, 288-294.

[13] M. Zhang, P. Lu, Y. Ma, J. Shen. *J. Phys. Chem. B* **2003**, *107*, 6535-6538.

[14] M. I. Fernandez-Bachiller, C. Perez, G. C. Gonzalez-Munoz, S. Conde, M. G. Lopez, M. Villarroya, A. G. Garcia, M. I. Rodriguez-Franco. *J. Med. Chem.* **2010**, *53*, 4927-4937.

[15] C. Deraeve, M. Pitie, H. Mazarguil, B. Meuiner. *New J. Chem.* **2007**, *31*, 193-195.

[16] C. Deraeve, C. Boldron, A. Maraval, H. Mazarguil, H. Gornitzka, L. Vendier, M. Pitie, B. Meuiner. *Chem. Euro. J.* **2008**, *14*, 682-696.

[17] F. Prati, C. Bergamini, R. Fato, O. Soukup, J. Korbecny, V. Andrisano, M. Bartolini, M. L. Bolognesi. *ChemMedChem* **2016**, *11*, 1284-1295.

[18] D. Antequera, M. Bolos, C. Spuch, C. Pascual, I. Ferrer, M. I. Fernandez-Bachiller, M. I. Rodriguez-Franco, E. Carro. *Neurobiol. Dis.* **2012**, *46*, 682-691.

[19] N. Vasdev, P. Cao, E. M. van Oosten, A. A. Wilson, S. Houle, G. Hao, X. Sun, N. Slavine, M. Alhasan, P. P. Antich, F. J. Bonte, P. Kulkarni. *MedChemComm.* **2012**, *3*, 1228-1230.

[20] S. H. Liang, J. P. Holland, N. A. Stephenson, A. Kassenbrock, B. H. Rotstein, C. P. Diagnault, R. Lewis, L. Collier, J. M. Hooker, N. Vasdev. *ACS Chem. Neurosci.* **2015**, *6*, 535-541.

[21] S. H. Liang, A. G. Southon, B. H. Fraser, A. M. Krause-Heuer, B. Zhang, T. M. Shoup, R. Lewis, I. Volitakis, Y. Han, I. Greguric, A. I. Bush, N. Vasdev. *ACS Med. Chem. Lett.* **2015**, *6*, 1025-1029.

[22] G. Bistoni, S. Rampino, F. Tarantelli, L. Belpassi, *J. Chem. Phys.* **2015**, *142*, 084112.

[23] D. Ory, J. Van den Brande, T. de Groot, K. Serdons, M. Bex., L. Declercq, F. Cleeren, M. Ooms, K. Van Laere, A. Verbruggen, G. Bormans. *J. Pharm. Biomed. Anal.* **2015**, *111*, 209-

A.3 Attribution Statement

I, Mitchell Klenner, contributed the synthesis of the investigated molecules, their subsequent radiolabelling with fluorine-18 and the analysis of their photophysical properties; alongside project conceptualisation, data curation, interpretation of the results, funding acquisition and the writing & editing of the publications entitled "*A Fluorine-18 Radiolabelling Method Enabled by Rhenium(I) Complexation Circumvents the Requirement of Anhydrous Conditions"*, "*Effect of Rhenium(I) Complexation on Aza-Michael Additions to 5-Amino-1,10-Phenanthroline with [^{18}F]Ethenesulfonyl Fluoride towards PET Optical Tracer Development"* and *"Rhenium(I) Complexation-Dissociation Strategy for Synthesising Fluorine-18 Labelled Pyridine Bidentate Radiotracers"*.

All co-authors on the each of the above listed publications have endorsed that this level of contribution is appropriate.